

An Experimental and Theoretical Investigation of Novel Aircraft  
Drag Reduction

John Kester Onyebuchi Momoh

A thesis submitted in partial fulfilment of the requirement of the University of  
Hertfordshire for the degree of Doctor of Philosophy

The programme of research was carried out in the School of Engineering and  
Technology, University of Hertfordshire

August 2018

## Abstract

Air transportation is an important part of the world's economic and indispensable transportation system. The major institutions in the world and the aviation authorities are well aware of the demanding expectations of the public for cheaper transportation cost and at the same time the need to reduce the negative impact of aircraft or air-transportation system on the atmosphere which include noise around airports and global warming to attain sustainability, reduction in the emission of green-house gases such Nitrogen oxides (x) and Carbon di-oxide.

In order to achieve such a balance in the future, a strategy is required to match competitive excellence dedicated to meeting the demands of society while at the same time being cost effective for the airline companies and operating aviation authorities. Such a vision or concept cannot be realised without making further technological breakthroughs in engineering fields such as Aerodynamics and other discipline including materials and structures. Improving aircraft aerodynamic performance will have a direct impact on helping to implement these goals. Improving aircraft drag capabilities remains one of the big challenges faced by manufacturers of transport aircraft. It is known that for a typical transport aircraft drag, the induced drag amounts to about 40% of the total drag at cruise flight conditions and about 80 –90 percent of the total drag during aircraft take off. The skin friction drag constitute approximately one half of the total Aircraft drag at cruise flight configuration making up most of the remaining percentage of drag at cruise condition.

The use of winglets or other wing-tip devices as a drag reduction device play a significant role in improving aircraft performance by acting as passive devices to reduce drag and enhance aircraft performance. In this thesis, four novel spiroid drag reduction devices are presented which were designed and optimised using STAR-CCM+ Optimate + which uses the SHERPA search algorithm as its optimisation tool. The objective of the optimisation process was set to maximise the lift-to-drag ratio. A low fidelity mesh model was used during the optimisation and the results were verified by using high-fidelity physics and mesh model. The developed devices showed an improve  $C_L/C_D$  ratio of up to 11 percent and improved  $C_L$  by up to 7 percent while reducing  $C_D$  by up to 4 percent with an 18 - 24 percent reduction in induced drag observed as well. The devices showed consistency in performance at several Mach numbers and angles of attacks. Thus, suggesting that such devices could be used over a wide range of flight regimes on aircraft or UAVs. The study also successfully demonstrated the capability to using this optimisation process in the design and development of such devices.

Furthermore, a numerical investigation and wind tunnel verification study was performed on a wing tip turbine to ascertain the aerodynamic performance modification of using such a device at several Mach numbers, angles of attack, propeller rpms and sensitivity of propeller nacelle positions at the wing tip. The obtained results revealed a trend on the nacelle position to achieve the most improved aerodynamic performance. A  $C_L/C_D$  ratio improvement of up to 7 percent,  $C_L$  modification of approximate 4 percent and  $C_D$  reduction of up to 4 percent were achieved.

In addition to demonstrate an appreciation of some of the wider implication of installing wing tip devices, a flutter analysis on a rectangular clean wing with added variable mass at the wing tip was performed. The result showed that the added masses had no significant implication on the flutter characteristics of the wing.

## **Acknowledgement**

Firstly, I would like to express my sincere gratitude to my principal supervisor Dr. Andrew Lewis for the continuous support of my Ph.D. study, for his patience, motivation, and knowledge. His guidance helped me in all the time of research and writing of this thesis. I could not have imagined having a better supervisor and mentor for my Ph.D. study.

Besides my advisor, I would like to thank both of my second supervisors Dr. Mohammed Reza Herfatmanesh and Dr. Jason Knight for their continuous support during my Ph.D. study.

Last but not the least, I would like to thank my family: my parents and to my brothers and sister for supporting me throughout writing this thesis and my life in general.

## Table of Contents

Abstract.....	2
Acknowledgement.....	4
Table of tables .....	8
Table of figures.....	9
Chapter 1: Introduction.....	13
1.1. Motivation for research.....	13
1.2. Contributions to knowledge.....	14
1.2.1. Aims and objectives .....	15
1.2.2. Layout of the thesis .....	15
Chapter 2: Literature review .....	18
2.1. Introduction.....	18
2.2. Basic Lift concept.....	18
2.3. Basic Drag Concept .....	20
2.4. Novel Induced Drag Reduction Technologies .....	22
2.4.1. Induced drag reduction - Wing-tip devices and winglets.....	22
2.4.1.1. Vortex Diffuser .....	28
2.4.1.2. Wing tip sails and Grid .....	29
2.4.1.3. Tip Fence.....	33
2.4.1.4. Blended wingtip device.....	34
2.4.1.5. Tip Turbine .....	36
2.4.1.6. Spiroid winglet.....	38
2.4.2. Non-planar wing concepts.....	41
2.4.3. C-Wing concept .....	42
2.4.4. Box Wing.....	43
2.5. Skin Friction Drag Reduction.....	45
2.5.1. Extended Laminar Flow for drag reduction .....	45
2.5.2. Natural Laminar Flow (NLF).....	49
2.5.3. Hybrid Laminar Flow (HLF).....	52
2.5.4. Alternative Laminar Flow Control Technologies.....	59
2.5.5. Micro Sized Roughness.....	60
2.5.6. Localized heating .....	64
2.5.7. Plasma Actuation .....	64
2.5.8. Polishing of Surface .....	67
2.5.9. Wave Cancellation .....	67
2.6. Turbulent Skin Friction Reduction .....	72
2.6.1. Riblets .....	72
2.6.2. Dimples .....	73
2.7. New Technologies for Turbulent skin friction drag reduction.....	74
2.8. Separation control technologies .....	78
2.9. Conclusion.....	82
Chapter 3: Computational Fluid Dynamics .....	85
3.1. Introduction.....	85
3.1.1. Brief History .....	86
3.2. Application of Computational Fluid Dynamics as a Drag Prediction Tool .....	88
3.2. Theory.....	90
3.2.1. Governing Equations.....	91
3.2.2. Turbulence .....	93
3.2.3. Reynolds Average Navier Stokes Equations.....	96

3.2.4. Turbulence Closure .....	98
3.2.5. One Equation Model (Spalart-Allmaras Turbulence Model) .....	100
3.2.6. Two Equation model .....	100
3.2.7. Near Wall Treatment .....	108
3.2.8. Discretisation .....	113
3.2.9. Finite Volume Method .....	114
3.2.10. Grid or Mesh Generation.....	114
Chapter 4: Initial CFD results.....	117
4.1. CFD Test cases to validate numerical method .....	117
4.1.1. Geometry.....	118
4.1.2. Mesh and Computational Domain.....	119
4.1.3. Computational Approach and Turbulence modelling .....	123
4.1.4. Force coefficients ( $C_L$ and $C_D$ ) – Spiroid winglet.....	124
4.1.5. Force Coefficients ( $C_L$ and $C_D$ ) – Blended winglet .....	125
4.1.6. Force coefficients ( $C_L$ and $C_D$ ) – Lift Prediction Workshop 1.....	127
4.2. Initial CFD results and proposed designs.....	128
4.2.1. Geometry (Initial CFD results) .....	128
4.2.2. Mesh and Computational Domain.....	131
4.2.3. Computational approach .....	134
4.2.4. Force Coefficients .....	134
4.3. Proposed designs for optimisation study.....	144
4.4. Effect of fuselage on wing aerodynamic forces .....	150
4.5. Conclusion .....	155
Chapter 5: Aerodynamic optimisation of spiroid wing tip devices.....	156
5.1. Introduction.....	156
5.2. Aerodynamic shape optimisation.....	157
5.2.1. Gradient based methods .....	157
5.2.2. Non-gradient based methods (derivative-free methods) .....	158
5.2.3. Surrogate based methods.....	158
5.2.4. SHERPA - Simultaneous Hybrid Exploration that is Robust, Progressive and Adaptive.....	159
5.3. Design Evaluation.....	161
5.3.1. Optimisation Post-processing.....	165
5.3.5. Lift per unit span.....	194
5.3.6. Flow visualisation .....	195
5.4. Sensitivity of design variables on aerodynamic forces .....	208
5.5. Conclusions.....	218
Chapter 6: Investigation on the use of wing tip turbine as a wing aerodynamic improvement device .....	221
6.1. Introduction .....	221
6.2 Validation of CFD modelling approach with SVA Potsdam experimental data of a controllable pitch propeller.....	221
6.2.1. Geometry, mesh, physics models.....	222
6.2.2. Comparison of CFD and experimental propeller performance data.....	224
6.3. Wind tunnel experiment at UH and CFD validation model.....	224
6.3.1. Test description and CFD modelling approach.....	228
6.3.2. Force coefficients.....	229
6.4. Investigated design configuration .....	231
6.4.1. Mesh and computational approach.....	234
6.4.2. Results for the effect of propeller nacelle position on wing aerodynamic performance .....	236
6.4.3. The effect of the direction of propeller rotation on wing aerodynamic characteristics .....	238

6.4.4. The effect of the Mach number on the wing propeller nacelle performance .....	242
6.4.5. Effect of angle of attack on propeller wing aerodynamic performance – take-off condition .....	264
6.4.6. Propeller RPM effect on wing performance.....	265
6.5. Conclusion .....	266
Chapter 7: Discussion and error analysis of results .....	268
7.1. Re-introducing the wing-tip devices .....	268
7.2. Error analysis and applied correction factors .....	270
7.3. Potential application of the technologies .....	275
Chapter 8: Conclusion .....	277
Chapter 9: Recommendations.....	282
References .....	283
Appendices .....	291
Appendix A: Flutter analysis of wing with winglet.....	291
A-I: Wing Structural Model, Aerodynamic modelling and solving the flutter equation.....	291
A-II: Initial test case to validate Flutter Model .....	293
A-III: Investigated wing model with concentrated mass (winglet) at wing tip .....	295
A-IV: Location of centre of mass, Elastic axis location, concentrated mass with results and conclusion .....	296
Appendix B: Kriging response surfaces .....	299
B-I: Kriging response surface for initial design phase of Design-2 .....	299
B-II: Kriging response surface for the second phase of the optimisation process of Design-2.....	306
B-III: Kriging response surfaces produced for Design-1 .....	313
B-IV: Kriging response surfaces for Design-3.....	324

## Table of tables

Table 1: Design parameters for clean wing and spiroid winglet.....	119
Table 2: Design parameters clean wing and blended winglet.....	119
Table 3: Lift Prediction Workshop 1 wing design specification.....	119
Table 4: Mesh specifications .....	120
Table 5: Summarized boundary conditions .....	122
Table 6: Numerical data and data from literature (Rumsey et al., 2011b).....	128
Table 7: Design specification .....	129
Table 8: Mesh specification.....	131
Table 9: Physics set-up .....	134
Table 10: Lift coefficient .....	135
Table 11: Range of different wing tip devices at cruise at constant altitude .....	143
Table 12: Performance of the full-scale trapezium spiroid winglet against a clean wing.....	146
Table 13: Design specification wing with and without winglets .....	146
Table 14: Performance of the devices against the clean wing pre-optimisation at 4 degrees angle of attack and Mach 0.74 .....	150
Table 15: Aerodynamic coefficients wing only and wing plus fuselage .....	151
Table 16: Design 1 design variables with upper and lower limits .....	163
Table 17: Design 2 design variables with upper and lower limits .....	164
Table 18: Design 3 design variables with upper and lower limits .....	164
Table 19: Spiroid trapezium design variables with lower and upper limits .....	165
Table 20: Coefficient of lift and drag mesh dependency study .....	185
Table 21: Aerodynamic coefficients for Designs 1 - 3 .....	186
Table 22: Aerodynamic coefficients Spiroid trapezium .....	186
Table 23 : Test conditions (Re, Mach No, air speed) .....	190
Table 24: Simulation initial conditions.....	223
Table 25: Wing and propeller specification.....	228
Table 26: Propeller design specification and test initial conditions.....	234
Table 27: Coefficient of lift and drag mesh dependency study .....	235
Table 28: Mesh settings .....	235
Table 29 (a): Propeller nacelle sensitivity to aerodynamic force coefficients and $C_L/C_D$ ratio, the results for steady state simulation .....	237
Table 30: Propeller nacelle sensitivity aerodynamic force coefficients and $C_L/C_D$ ratio, the results for the unsteady state simulation .....	237
Table 31: Results clockwise and anti-clockwise rotation .....	238
Table 32: RPM effect on wing performance.....	266
Table 33: Numerical data and data from literature (Rumsey et al., 2011b).....	271
Table 34: Aerodynamic coefficients for Designs 1 – 3, before correction was applied .....	271
Table 35: Aerodynamic coefficients for Designs 1 – 3 corrected data .....	272
Table 36: Aerodynamic coefficients Spiroid trapezium, before correction was applied .....	272
Table 37: Aerodynamic coefficients Spiroid trapezium corrected data .....	272
Table 38: UH wind tunnel experimental data and CFD results for the clean wing before correction .....	273
Table 39: UH wind tunnel experimental data and CFD results for the wing with propeller before correction ..	273
Table 40: UH wind tunnel experimental data and CFD clean wing corrected data .....	273
Table 41: UH wind tunnel experimental data and CFD wing with propeller corrected data .....	274
Table 42 : Propeller nacelle sensitivity to aerodynamic force coefficients and $C_L/C_D$ ratio, the results for steady state simulation at 4 degrees AOA and Mach 0.64 data before corrections applied .....	274
Table 43 : Propeller nacelle sensitivity to aerodynamic force coefficients and $C_L/C_D$ ratio, the results for steady state simulation at 4 degrees AOA and Mach 0.64 corrected data .....	274
Table 44: Propeller nacelle sensitivity to aerodynamic force coefficients and $C_L/C_D$ ratio, the results for steady state simulation showing percentage improvements at 4 degrees AOA and Mach 0.64, before corrections applied.....	275
Table 45: Propeller nacelle sensitivity to aerodynamic force coefficients and $C_L/C_D$ ratio, the results for steady state simulation showing percentage improvements at 4 degrees AOA and Mach 0.64, after corrections applied.....	275

## Table of figures

Fig. 1: Aerodynamic forces acting on an aircraft in level flight condition .....	18
Fig. 2: Wing lift curve (Raymer, 1992) .....	19
Fig. 3: Showing aircraft trailing vortices at take-off (Image courtesy of Asim Ghatak) .....	22
Fig. 4 Winglet on an Airbus A350 (Picture © Airbus S.A.S./computer rendering by Fixion) .....	23
Fig. 5: Wing-tip looking devices on Birds (Al-Atabi, 2006) .....	23
Fig. 6: Side view of some winglets (Filippone, 2012) .....	24
Fig. 7: Shows various wing-tip devices (Guerrero et al., 2012a).....	25
Fig. 8: Hoerner wing-tip design on a glider plane (Falcao da Luz, 2013) .....	26
Fig. 9: Learjet Business jet with winglet (Falcao da Luz, 2013) .....	28
Fig. 10: Vortex diffuser by (Hackett, 1980) .....	29
Fig. 11: Configurations considered better, A is the leading winglet, B is the central and C is the trailing one by (Cerón-Muñoz and Catalano, 2006).....	30
Fig. 12: (a) The wing balance with the base wing and the Clark Y tip attached. The vertical structure is the streamlined shroud that covers the force transducer. The tip shaft can be seen between the base wing and the tip. It extends through the base wing and supports the tip. The shroud is 152mm high (Tucker, 1993)	31
Fig. 13: (a) Wing tunnel configuration ; (b) Sample Euler Grid for the Baseline (Smith et al., 2001).....	32
Fig. 14: wingtip fence (Whomsley, 2018) .....	34
Fig. 15: Boeing MAX 737 Winglet (Boeing, 2015) .....	35
Fig. 16: Spiroid loop (left) and downward pointing (right) wing tip devices (Hantrais-Gervois et al., 2009).....	36
Fig. 17: Comparison of CFD-Based drag prediction and flight test for API blended winglets on 737NG (McLean, 2005).....	38
Fig. 18: (a) Span efficiency for various optimally loaded non-planar systems (b) Induced drag variation with allowable height for non-planar systems (Kroo, 2005) .....	42
Fig. 19: Conceptual design for a large aircraft with span constraints (McMasters and Kroo, 1998).....	43
Fig. 20: Example of non-planar wing configuration, Lockheed box-wing (Frediani et al., 2003) .....	44
Fig. 21: showing stationary CF- Waves on a wing (Warsop, 2003).....	46
Fig. 22: F-16XL Ship B2 SLFC-in flight configured with SLFC glove (Bushnell, 2003) .....	48
Fig. 23: (a) TELFONA PATHFINDER Model in ETW wind tunnel test section (b) Position of TSP patches and pressure tap sections (Streit et al., 2011).....	51
Fig. 24: Hybrid Laminar Flow concept (Reneaux, 2004) .....	53
Fig. 25: Leading edge (upper half) with a positive bracelet. Grid for RANS computations (Arnal and Archambaud, 2008).....	54
Fig. 26: Classical suction system and simplified suction system (Reneaux, 2004) .....	57
Fig. 27: Suction test definition in SUPERTRAC (Hein et al., 2010).....	58
Fig. 28: Stream-wise transition as a function of the suction velocity for different test cases from SUPERTRAC project (Hein et al., 2010) .....	58
Fig. 29: Applications of NLF & HLFC concept on a supersonic test (Abbas et al., 2012). .....	59
Fig. 30: Swept wing in flight tests (SWIFT) (Saric et al., 2011) .....	62
Fig. 31: Flight measurements carried by W. Saric (2011) with painted LE et DRE concept .....	62
Fig. 32: Visualization of Boundary Layer transition for the NLF (2) -0415 Aerofoil are $Re=2.2$ Million. (a) uncontrolled and (b) controlled (Sui-Han et al., 2010) .....	63
Fig. 33: Two-dimensional model of the Onera-D aerofoil mounted inside the wind tunnel (Kurz et al., 2013) ..	66
Fig. 34: Cross-sectional view of the Onera-D wing model equipped with one DBD actuator ((Kurz et al., 2013) .....	67
Fig. 35: Active control principle (Arnal and Archambaud, 2008).....	68
Fig. 36: Principle of an active wave control system (TU Berlin) (Engert and Nitsche, 2008) .....	68
Fig. 37: Generic wing model with a) control - and b) reference insert (Engert and Nitsche, 2008).....	70
Fig. 38: Principle of a (a) surface hot wire and (b) membrane actuator (Engert and Nitsche, 2008) .....	70
Fig. 39: Grob G103 with glove and sensor actuator arrangement (Erdmann et al., 2011).....	71
Fig. 40: Typical Riblets geometry (García-Mayoral and Jiménez, 2011).....	73
Fig. 41: Structure of “smart surface”, (a) the components (b) Before compressed, (c) After Compressed (Zheng and Yan, 2010).....	75
Fig. 42: Compressions under different flow regimes (Zheng and Yan, 2010).....	75
Fig. 43: Schematic of the SINHA Flexible composite surface (FCSD) (Sinha and Ravande, 2006) .....	76
Fig. 44: (a) Sinha tech slow speed wind tunnel and (b) close up of tunnel section showing the NFL-0414F aerofoil (Sinha and Ravande, 2006).....	77
Fig. 45: Schematic view of the proposed flow separation control actuation concept – AEROMEMS II project (Warsop et al., 2007).....	80

Fig. 46 : SBVG on flap in the AWIATOR Project (Bohannon, 2006) .....	82
Fig. 47: Illustrates the sub-divisions of the Near-Wall region (CD-ADAPCO, STAR-CCM+, 2015).....	110
Fig. 48: Wing with spiroid winglet.....	118
Fig. 49: Wing with blended winglet .....	118
Fig. 50: Wing and fuselage configuration Lift Prediction Workshop 1 (Rumsey et al., 2011b).....	118
Fig. 51: Volumetric mesh representation (a.) clean wing and (b.) spiroid winglet.....	120
Fig. 52: Volumetric mesh representation (a.) clean wing and (b.) blended winglet .....	121
Fig. 53: Volumetric mesh representation - Lift Prediction Workshop 1 (Rumsey et al., 2011b) .....	121
Fig. 54: Domain and boundary conditions.....	122
Fig. 55: Domain and boundary conditions.....	123
Fig. 56: Domain and boundary conditions (Lift Prediction Workshop 1) .....	123
Fig. 57: $C_L$ vs Alpha – numerical data and data from literature (Guerrero et al., 2012b).....	125
Fig. 58: $C_D$ VS Alpha - numerical data and data from literature (Guerrero et al., 2012b).....	125
Fig. 59: $C_L$ vs Alpha - numerical data and data from literature (Beechook and Wang, 2013).....	126
Fig. 60: $C_D$ VS Alpha - numerical data and data from literature (Beechook and Wang, 2013).....	126
Fig. 61: $C_L$ vs Alpha - numerical data and data from literature (Rumsey et al., 2011b).....	127
Fig. 62: $C_D$ VS Alpha - numerical data and data from literature (Rumsey et al., 2011b) .....	127
Fig. 63: Clean wing configuration .....	129
Fig. 64: Spiroid Trapezium configuration .....	130
Fig. 65: Spiroid Loop configuration .....	130
Fig. 66: Blended winglet configuration .....	130
Fig. 67: Mesh on Wing and spiroid trapezium model .....	132
Fig. 68: Spiroid loop and Blended winglet model .....	132
Fig. 69: Cross-section of wing showing prism layers (a.) Whole aerofoil, (b.) zoomed leading edge view.....	132
Fig. 70: Graph showing $C_L$ vs Number of nodes .....	133
Fig. 71: Graph showing $C_D$ vs Number of nodes.....	133
Fig. 72: $C_L$ vs Angle of attack.....	135
Fig. 73: $C_D$ vs Angle of attack .....	137
Fig. 74: Induced drag reduction.....	138
Fig. 75: lift-to-drag ratio.....	139
Fig. 76: Vorticity plot - Clean wing.....	140
Fig. 77: Vorticity scalar - Blended winglet.....	140
Fig. 78: Vorticity scalar - Spiroid trapezium .....	141
Fig. 79: Vorticity scalar - Spiroid Loop.....	141
Fig. 80: Q-Criterion 3D volume rendering - Clean wing (Left normal view and Right transparent view).....	142
Fig. 81: Q-Criterion 3D volume rendering – Blended winglet (Left normal view and Right transparent view) .....	142
Fig. 82: Q-Criterion 3D volume rendering – Spiroid trapezium (Left normal view and Right transparent view) .....	142
Fig. 83: Q-Criterion 3D volume rendering – Spiroid Loop (Left normal view and Right transparent view) .....	142
Fig. 84: Clean wing range % improvement vs Wing-tip device.....	144
Fig. 85: (a) scaled spiroid trapezium winglet model in section 3.4.1. (b) Full scale model on a wing model resembling a Boeing 737 wing (c) Clean wing model for comparison .....	145
Fig. 86: (a) clean wing (b) Design-1 (c) Design-2 (d) Design-3 .....	149
Fig. 87: Fuselage plus wing and mesh.....	150
Fig. 88: Lift per unit span .....	151
Fig. 89: Drag per unit span .....	152
Fig. 90: Pressure contour (i,ii,iii,iv).....	153
Fig. 91: Skin friction coefficient (i,ii,iii,iv) .....	154
Fig. 92: Traditional and SHERPA optimisation approach (CD-ADAPCO, STAR-CCM+, 2015) .....	161
Fig. 93: Lift-to-drag ratio as a function of the design number – Design-1 .....	166
Fig. 94: Designs performance plot – Design-1 .....	167
Fig. 95: Lift-to-drag ratio as a function of the design number – Design-2, Mid-point optimisation .....	167
Fig. 96: Designs performance plot – Design-2, Mid-point optimisation .....	168
Fig. 97: Lift-to-drag ratio as a function of the design number – Design-2 .....	168
Fig. 98: Designs performance plot – Design-2 .....	169
Fig. 99: Lift-to-drag ratio as a function of the design number – Design-3, Mid-point optimisation .....	169
Fig. 100: Designs performance plot – Design-3, Mid-point optimisation .....	170
Fig. 101: Lift-to-drag ratio as a function of the design number – Design-3 .....	170
Fig. 102: Designs performance plot – Design-3 .....	171
Fig. 103: Lift-to-drag ratio as a function of the design number – Spiroid trapezium .....	171

Fig. 104: Designs performance plot – Spiroid trapezium .....	172
Fig. 105: (a.) Clean wing, (b.) Design-1, (c.) Design-2, (d.) Design-3, (e.) Spiroid trapezium .....	173
Fig. 106: Design-1 before and after optimisation as well as the design dimensions and control points .....	176
Fig. 107: Design-2 before and after optimisation as well as the design dimensions and control points .....	178
Fig. 108: Design-3 before and after optimisation as well as the design dimensions and control points .....	180
Fig. 109: Spiroid trapezium before and after optimisation as well as the design dimensions and control points .....	183
Fig. 110: Mesh dependency study showing convergence - (a.) coefficient of lift and mesh count (b.) drag coefficient .....	184
Fig. 111: $C_L/C_D$ ratio – take-off condition .....	187
Fig. 112: Lift coefficient – take-off condition .....	187
Fig. 113: Drag coefficient – take-off condition .....	188
Fig. 114: $C_{D_{induced}}$ vs angle of attack – take-off condition .....	189
Fig. 115: Coefficient of pitching moment ( $C_M$ ) vs angle of attack (AOA) .....	189
Fig. 116: Lift coefficient as a function of Mach number .....	191
Fig. 117: Drag coefficient as a function of Mach number .....	192
Fig. 118: $C_L/C_D$ ratio as a function of Mach number .....	192
Fig. 119: $C_{D_{induced}}$ as a function of Mach number .....	193
Fig. 120: $C_M$ as a function of Mach number .....	193
Fig. 121: Lift per unit span - (Mach 0.74) .....	194
Fig. 122: lift per unit span - clean wing and spiroid trapezium (Mach 0.24) .....	195
Fig. 123 – Clean wing vorticity scalar contour .....	196
Fig. 124 – Design – 1 vorticity scalar contour .....	196
Fig. 125 – Design – 2 vorticity scalar contour .....	197
Fig. 126 – Design – 3 vorticity scalar contour .....	197
Fig. 127: Clean wing vorticity volume rendering .....	198
Fig. 128: Design – 1 vorticity volume rendering .....	198
Fig. 129: Design – 2 vorticity volume rendering .....	199
Fig. 130: Design – 3 vorticity volume rendering .....	199
Fig. 131: Clean wing – vorticity scalar contour – Mach 0.24 .....	200
Fig. 132: Spiroid trapezium – vorticity scalar contour – Mach 0.24 .....	200
Fig. 133: Clean wing – vorticity volume rendering – Mach 0.24 .....	201
Fig. 134: Spiroid trapezium – vorticity volume rendering – Mach 0.24 .....	201
Fig. 135: Clean wing (a.) top, (b.) bottom – pressure contour – Mach 0.74 .....	202
Fig. 136: Design – 1 (a.) top, (b.) bottom – pressure contour – Mach 0.74 .....	203
Fig. 137: Design – 2 (a.) top, bottom (b.) right – pressure contour – Mach 0.74 .....	204
Fig. 138: Design – 3 (a.) top, (b.) bottom – pressure contour – Mach 0.74 .....	205
Fig. 139: Clean wing (a.) top left, (b.) bottom – pressure contour – Mach 0.24 .....	206
Fig. 140: Spiroid trapezium (a.) top, (b.) bottom – pressure contour – Mach 0.24 .....	207
Fig. 141: The influence of the factors (variables) on lift-to-drag ratio, lift (N) and drag forces (N) .....	210
Fig. 142: Chord 4 length (m), Chord 2 length (m) .....	211
Fig. 143: Chord 5 sweep, Chord 4 twist .....	211
Fig. 144: Chord 1 size (m), Chord 5 length (m) .....	212
Fig. 145: Chord 2 size, Chord 1 twist .....	212
Fig. 146: Chord 3 size, Chord 2 twist .....	213
Fig. 147: Chord 4 size, Chord 3 twist .....	213
Fig. 148: Chord 5 size, Chord 5 size .....	214
Fig. 149: Chord 4 length (m), Chord 2 length (m) .....	214
Fig. 150: Chord 5 sweep, Chord 4 twist .....	215
Fig. 151: Chord 1 size, Chord 5 length (m) .....	215
Fig. 152: Chord 2 size, Chord 1 twist .....	216
Fig. 153: Chord 3 size, Chord 2 twist .....	216
Fig. 154: Chord 4 size, Chord 3 twist .....	217
Fig. 155: Chord 5 size .....	217
Fig. 156: The influence of the factors (variables) on lift-to-drag ratio, lift (N) and drag forces (N) .....	218
Fig. 157: (a.) Geometry (b.) boundary conditions .....	222
Fig. 158: Graph plot - Exp. (Barkmann, 2011b) and CFD propeller performance data .....	224
Fig. 159: (a.) wind tunnel set-up (b.) wind tunnel configuration showing the two strut and the incidence .....	226
Fig. 160: CFD models (a.) simulation domain, (b.) clean wing (c.) wing plus propeller .....	227

Fig. 161: Force coefficients (a.) Wing $C_L$ from experiment and CFD (b.) Wing $C_D$ from experimental and CFD (c.) Wing plus turbine $C_L$ from experimental and CFD (steady and unsteady) (d.) Wing plus turbine $C_D$ from experimental and CFD (steady and unsteady), .....	231
Fig. 162: Top view – the main difference in these is the distance that the propeller is aft the wing trailing edge (a.) propeller nacelle position 1 (b.) propeller nacelle position 2, (c.) propeller nacelle position 3, (d.) propeller nacelle position 4, (e.) propeller nacelle tractor position, (f) far view of configuration- propeller on wing tip .....	233
Fig. 163: Coefficient of lift mesh dependency study .....	234
Fig. 164: Coefficient of drag mesh dependency study.....	235
Fig. 165: Simulation domain with boundary conditions.....	236
Fig. 166: Wing and propeller geometry with rotation directions.....	239
Fig. 167: Velocity component of the rotating region – showing direction of blade rotation .....	240
Fig. 168: Direction of rotation – Vorticity.....	242
Fig. 169: Lift per unit span .....	242
Fig. 170: Coefficient of lift as a function of Mach number .....	244
Fig. 171: (a.) Coefficient of drag as a function of Mach number for all studied cases (b.) Coefficient of drag as a function of Mach numbers < 0.65.....	245
Fig. 172: $C_L/C_D$ ratio vs Mach number .....	245
Fig. 173: Velocity experienced by the propellers .....	249
Fig. 174: Pressure distribution of wing lifting surface.....	256
Fig. 175: Skin friction coefficient.....	263
Fig. 176: $C_L$ vs AOA .....	264
Fig. 177: $C_D$ vs AOA .....	265
Fig. 178: $C_L/C_D$ vs AOA.....	265
Fig. 179: Design-1 .....	268
Fig. 180: Design-2 .....	268
Fig. 181: Design-3 .....	269
Fig. 182: Spiroid trapezium .....	269
Fig. 183: Wing tip turbine .....	270

## Chapter 1: Introduction

### 1.1. Motivation for research

The high prices of aviation fuel and the environmental issues the world is currently facing, for instance global warming, have forced aircraft manufacturers and airline companies to explore ways to reduce the negative environmental effect of aviation on the world's atmosphere with the aim to improve aircraft fuel efficiency during flight while at the same time meeting the demand of society for cheaper flight fares. Aircraft configurations yielding a more economical and eco-friendly transportation system are highly desired by aircraft manufacturers and air-line companies due to the fact that such configurations would play a key role in improving the standards of current aircraft and proving a means to achieving these goals. This has significantly affected the way the aeronautical community foresees aircraft development in the future. To this effect, a Group of leading authorities in the aerospace community formulated a clear set of requirements for civil transport aircrafts under the programme ACARE Vision for 2020. The following goals were set out to be achieved based on these requirements:

Quality and affordability of aircraft.

- Quality in the sense that cheaper and competitive fares be made available to air-line flyers
- increased options for passengers' transportation freight operation and,
- reduced 50% marketing time for newly manufactured aircraft

in the environment

- By effectively reducing the emissions of CO<sub>2</sub> by 50% where possible;
- 50% reduction of Nitrogen oxide, and emissions,
- reduction in perceived external noise by 50% and,
- To show progress towards Green multi-material design (MMD).

Safety improvement propositions were also made which include:

- Accident rate reduction by 80%,
- Heavy reduction in human error and associated consequences.

The efficiency of the air transport system

- To achieve three times capacity increase,

- 99% of flights to be within 15 minutes of schedule time,
- Less than 15 minutes of waiting time in airport before short flights take off.

Measures to tighten the security on aircrafts were proposed as well; most of these goals can only be achieved by collective effort and innovative ideals of expertise from multi-disciplinary engineering fields.

These goals have a direct impact on the aerodynamic performance of an aircraft and thus improved performance is required. They also have an impact on the decisions to be made based on the type of technologies which can be used to help bring about a more eco-friendly, effective transportation system.

Aircraft drag reduction plays a key role in achieving some of the set-out goals; the drag reduction of a civil aircraft directly impacts on the performance of an aircraft, but also it affects the operating cost of aircraft and has an indirect positive impact on the environment. Aircraft fuel consumption represents an estimate 22% of the Direct Operating Cost (Reneaux, 2004) which is very important to airline companies as any fuel reduction will be beneficial. For a standard long-range civil transport aircraft, drag reduction has a direct impact on the Direct Operating Cost; a drag reduction of 1% can lead to a Direct Operating Cost decrease of about 0.2% for a large transport aircraft (Reneaux, 2004). Other trade-offs corresponding to a 1% drag reduction are 1.6 tons on the Operating empty weight or approximately 10 passengers. Drag reduction would in-directly contribute to dealing with issues of Carbon dioxide and Nitrogen oxide reduction by 50% and aircraft noise reduction by 50% thereby creating a more sustainable and eco-friendly transportation system.

## **1.2. Contributions to knowledge**

This project contributes to knowledge in the field of aerodynamics and aircraft performance. The contribution in aerodynamics is based on the design and understanding of the performance characteristics of a set of new spiroid or circular lift induced drag reduction devices. The device has been optimised and demonstrates the capability of using CFD coupled with optimisation algorithms for the design and development of wing-tip devices. Four novel wing tip devices have been presented with a drag reduction of up to 4 percent achieved by retrofitting and using the devices on a clean wing as well as  $C_L$  improvement of about 7 percent and lift-to-drag ratio increase by 11 percent.

A wing-tip turbine has also been extensively investigated by CFD methods to enhance the knowledge on the performance characteristics of using such a device on aircraft wing as a lift-to-drag ratio or simply as a lift induced drag reduction mechanism which could potentially be used to generate power for systems.

The introduction of wing tip devices has other implications on aircraft design. For example, aeroelasticity. In recognition of this, an investigation of the flutter characteristics of using wing-tip devices on aircraft wing was undertaken, providing evidence that by using such devices, the flutter characteristics of the wing changes little.

### **1.2.1. Aims and objectives**

The aim of this research programme is to investigate several of these novel drag reduction techniques and in particular the spiroid winglet and wing tip turbines, to gain a greater understanding of the technologies in terms of the amount of drag reduction achievable and design optimisation. Furthermore, it will improve understanding of the capabilities of CFD to analyse new drag reduction methodologies.

#### **Aim of the project**

- To investigate aircraft drag reduction methodologies

#### **Objectives of the Project**

- To reduce aircraft drag by using novel drag technologies with particular interest in spiroid wing tip device and wing tip turbine.
- To reduce aircraft drag by up to 4% by using an optimised spiroid winglet device and wing tip turbine.

#### **Some of the issues that need to be addressed are;**

For spiroid winglets:

- To identify what may constitute an optimal design for a spiroid winglet.
- The optimisation of such design with possible surrogate modelling (SHERPA search algorithm.) to achieve its optimal aerodynamic performance capabilities.

These afore mentioned points are to be addressed by numerical means (computational fluid dynamics) and by experimental verification of numerical approach.

- The drag reduction potential of wing tip turbines

Broader implications for aircraft design e.g. aeroelasticity.

### **1.2.2. Layout of the thesis**

The work that is presented in this report is set out in eight chapters.

- Chapter 1
  - Research motivation together with research contribution and research aims and objectives.
- Chapter 2
  - Background knowledge and comprehensive literature review on the aerodynamic lift and drag forces acting on an aircraft. A detailed literature review on various aircraft drag reduction and performance improvement technologies.
- Chapter 3
  - Background on the principles of CFD.
  - Literature review on the use of CFD as an aerodynamic performance prediction tool.
- Chapter 4
  - CFD test cases to validate numerical method adopted all through the research.
  - Initial CFD results and proposed designs.
  - Proposed design for optimisation study
  - Effect of fuselage on wing aerodynamic forces
- Chapter 5
  - General overview on optimisation algorithms
  - Detailed description of the optimisation method and algorithm adopted for this research
  - Optimisation of the proposed designs
  - Further CFD simulations to validate the designs
  - Results and analysis
  - Sensitivity study of the optimised designs
- Chapter 6
  - Investigation on the use of a wing tip turbine as a performance enhancement device
  - Test cases to validate the numerical method adopted for the steady and unsteady CFD simulation of the wing tip turbine
  - Proposed turbine configurations
  - Results and analysis of the proposed turbine configurations
- Chapter 7
  - Discussion and error analysis of results
- Chapter 8

- Research conclusions
- Chapter 9
  - Recommendation for future work

## Chapter 2: Literature review

### 2.1. Introduction

There are four main forces acting on aircraft in a level flight condition. These forces are the lift force, the drag force, thrust and the weight of the aircraft. Fig. 1 gives a virtual illustration of the direction in which these forces act during flight. The thrust force acts as the force required to overcome the drag and in the level cruise flight condition  $\text{Thrust} = \text{Drag}$  and the  $\text{Lift} = \text{Aircraft Weight}$ . Further detailed analysis on the concept of lift and drag together with drag reduction technologies are discussed in this chapter.

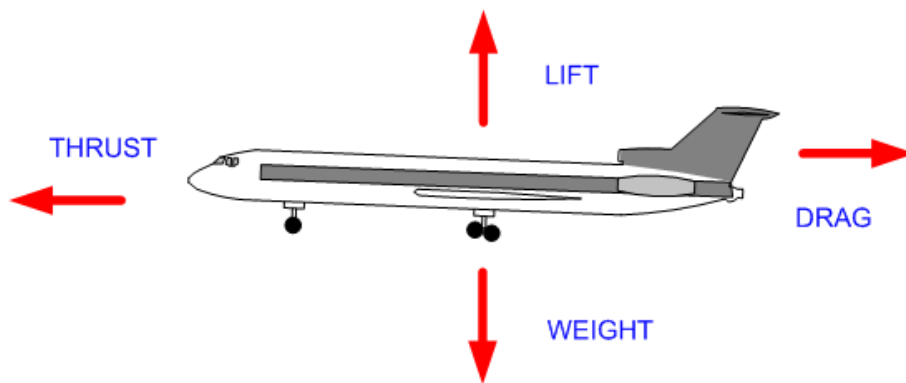


**Fig. 1: Aerodynamic forces acting on an aircraft in level flight condition**

### 2.2. Basic Lift concept

The lift force is the force acting perpendicular to the flight direction. Lift is typically characterised by a non-dimensional coefficient which is defined through (Raymer, 1992):

$$L = \frac{1}{2} \rho v^2 S C_L \quad (1)$$

Where  $\rho$  is the density of air,  $v$  is the free stream velocity of air,  $S$  is the reference area of the wing; which is the full rectangular or trapezoidal area which extends towards the centre axis of the aircraft.  $C_L$  is the non-dimensional lift coefficient. The lift coefficient is used to model the dependencies of object shape, inclination angle, viscosity and compressibility effect on the lift force generated by a wing.

The lift is generated due to the difference in pressure between the lower and upper surfaces of the wing aerofoils. Air travels faster on the top surface of the wing resulting in a lower pressure region and slower at the bottom

surface of the wing leading to a higher-pressure region. This creates a net pressure force acting upwards on the aerodynamic surface.

A typical plot of the coefficient of lift vs the angle of attack is illustrated in Fig. 2. The slope of the lift curve is linear below the stall angle of attack. At stall the wing experiences flow separation nearer the upper leading-edge section of the wing. The stall angle corresponds to maximum coefficient of lift ( $C_{Lmax}$ ). The stall characteristics of the wing are not only dependent on the angle of attack but also on the wing camber, maximum thickness and the wing nose radius (Taylor, 1976). Reynolds number also plays an important role in determining the  $C_{Lmax}$  as higher Reynolds number tends to create an energised boundary layer which stays attached resulting in higher  $C_{Lmax}$  at higher angles of attack. Fig. 2 also shows the typical effect of camber and aspect ratio on lift. A cambered aerofoil has positive lift at a zero angle of attack. To produce zero lift for a cambered aerofoil a negative angle of attack is needed. An un-cambered aerofoil has zero lift at zero degrees angle of attack.

Higher wing aspect ratios corresponds to higher lift produced by the aerofoil at lower angles of attack, as the aspect ratio reduces the lift slope is decreased. The ability of the flowing air to escape from the wing tip at lower aspect ratios tends to promote late stall characteristics of the wing at the expense of lower lift values, as shown in Fig. 2.

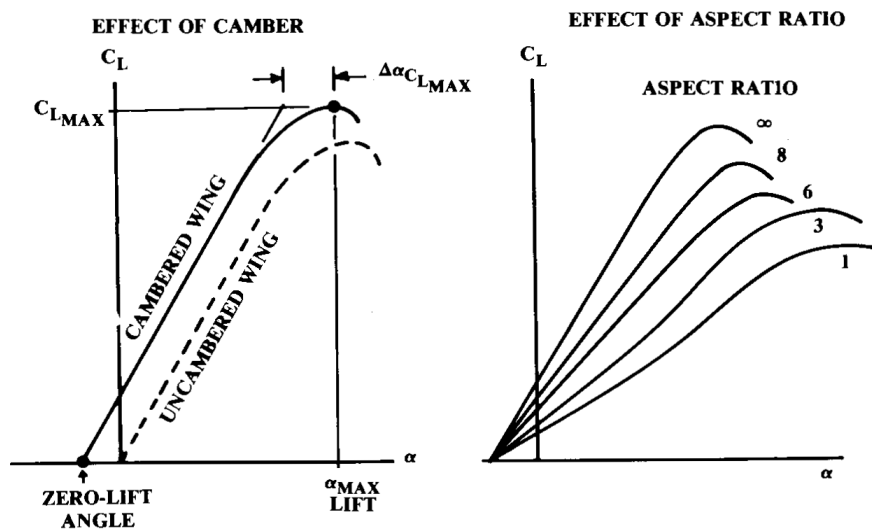


Fig. 2: Wing lift curve (Raymer, 1992)

Lift generated by a 3-dimensional wing produces an undesirable by-product due to down wash created by the flow circulation around the wing tip called the induced drag. The concept and method for reducing this drag is discussed further in sections 2.3 – 2.5.

### 2.3. Basic Drag Concept

Drag is the rearward aerodynamic force acting on a moving object. The precise definition of drag and the contribution of its components are essential for the prediction of drag and also for the appreciation of drag reduction technology (Torenbeek, 2013). The drag of an aircraft depends on the aircraft's aerodynamic shape and speed, which are design dependent parameters, as well as on the properties of the air (Kundu, 2010). Drag is a complex occurrence caused by several sources which includes viscous effects that result in skin friction, pressure differences as well as the induced flow field of the lifting surfaces and the effect of compressibility on the aerodynamic surface (Kundu, 2010). According to Torenbeek, (2013) drag can be broken down for simplicity in one of the following ways:

- An aerodynamic surface that is exposed to a fluid flow field can be sub-divided into several parts and the forces on each part can be broken down into the normal pressure component and friction component tangential to it. All components in the direction of the air flow are added to give the total drag experienced by the aerodynamic surface.
- Drag can be broken down according to the mechanisms that are contributing to the drag. i.e. the viscous properties of the fluid, pressure acting perpendicular to the lifting surface and the shockwaves.
- The drag can be sub-classified into parasite drag and the lift induced drag.

Typically, the process of estimating an aircraft drag begins by taking into consideration the individual components of the aircraft. The drag generated by each component is heavily dependent on its shape, size and surface contact with the fluid. The total drag is then obtained by summing the drag produced by the individual components plus the interference effects when the components are combined. The total drag produced by adding two or more aircraft components with their interference effects is higher than that obtained without interference effect due to the extra disturbance created in the flow fields.

In this research, the drag is classified into parasite and induced drag. The parasite drag encompasses the resistance to the movement of the flowing fluid (air) of all the aircraft components. i.e. aircraft wing, fuselage, tail surfaces, nacelles and undercarriage. The parasite drag can be sub-divided into:

- Profile drag (boundary layer drag)
  - Pressure drag (drag due to pressure force in the boundary layer of the aircraft component).
  - Skin friction drag (drag caused as a result of skin friction effect on the aircraft component). The Reynolds number plays a critical role in determining the associated skin friction drag over an

affected aerodynamic surface. It determines to what extent it affects the surface and also it determines the steadiness of the boundary layer on the surface which affects the parasite drag experienced.

- Interference drag: Drag due to the proximity of two aircraft components i.e. wing-fuselage, wing-engine junction.
- Wave drag (drag due to shock waves in transonic and supersonic flight conditions): As an aircraft speed approaches the speed of sound, shock waves are generated along the surface which result in an additional drag component (NASA, 2015). The pressure drag increases dramatically in the region as the aircraft approaches supersonic speeds, this is because of the shock waves which are generated by the aircraft structures in contact with air and other aircraft systems. i.e. engines.
- Excrescence drag: This drag can be identified as being associated with small items attached to aircraft surfaces. i.e. instruments (pitot tubes), ducts (cooling), blisters and some necessary gaps required to accommodate moving aircraft surfaces. In addition, the excrescence drag can be attributed to discrete surface roughness as a result of mismatching for example at assembly joints and from imperfections which are seen as defects caused by limitations in the manufacturing process. To this effect, the excrescence drag is classified by (Kundu, 2010) into:
  - Excrescence drag due to manufacturing origin, this includes aerodynamic mismatch such as roughness due to tolerance allocation.
  - Excrescence drag due to non-manufacturing origins, which includes flap tracks and gaps, bumps, blisters and protrusions.

Much research on excrescence drag has been conducted and some of the work carried out have been documented in Young and Paterson, (1981) and by Haines, (1968).

The induced drag: This is drag directly associated with the generation of lift and lifting mechanisms which at subsonic speeds is primarily generated by the trailing vortices such as the wing-tip vortices which are caused because of the fluid flow field passing from the bottom of the wing to the top. The drag reduction and aircraft performance improvement devices that are considered in this project are based on reducing the effect of this drag.

## 2.4. Novel Induced Drag Reduction Technologies

### 2.4.1. Induced drag reduction - Wing-tip devices and winglets

A typical break-down of a transport aircraft shows that the lift induced drag can be accounted for as much as 40% to 43% (Abbas et al., 2013) of the total drag of an aircraft at cruise conditions and around 80% - 90% of the total drag during take-off conditions (Guerrero et al., 2012a). The induced drag which is the second largest source of drag on a commercial airliner depends on the wing span and the lift distribution along the wing span (Abbas et al., 2013). This drag is directly associated with the generation of lift and lifting mechanisms which at subsonic speed is generated by trailing vortices such as the wing tip vortices. The wing-tip of an aircraft is a crucial area of the wing since this is the region where the higher pressure of air flowing from the bottom of the wing can flow around the wing to the top of the wing which has a lower pressure. This vortex flowing from beneath the wing to the top of the wing reduces the efficiency of the wing and poses a hazard to other aircraft in the area (vicinity) as shown Fig. 3.



**Fig. 3: Showing aircraft trailing vortices at take-off (Image courtesy of Asim Ghatak)**

In a large commercial aircraft, the lift distribution is well optimised and as a result, there is little margin to reduce the lift induced drag by wing span extension with current aircraft designs. The typical way to decrease the lift induced drag is to increase the aspect ratio of the wing. This was done with the A340 wing, which is reported to have an aspect ratio that reaches 9 (Reneaux, 2004). However, wing aspect ratio is a compromise between aerodynamic and structural characteristics, and it is clear that with the current technology there is not a great possibility to increase aspect ratios. An alternative approach to deal with this issue is by placing a physical barrier to the flow of air moving from the bottom of the wing to the top of the wing (Abbas et al., 2013). Several designs

of such barriers have been investigated and are generally known as winglets which acts on the tip vortex which is at the origin of lift induced drag. Fig. 4 shows a wing-tip device on an Airbus aircraft.



**Fig. 4 Winglet on an Airbus A350 (Picture © Airbus S.A.S./computer rendering by Fixion)**

The idea of fitting winglets on a wing is not a new concept and is actually not only exclusive to applications in aviation. Fig. 5 shows the existence of such mechanisms in birds and other flying animals; also, similar mechanisms have been applied to hydrodynamic structures and a variety of aerodynamic machines. An example is the winglet found on the tip-blade of an Osprey.

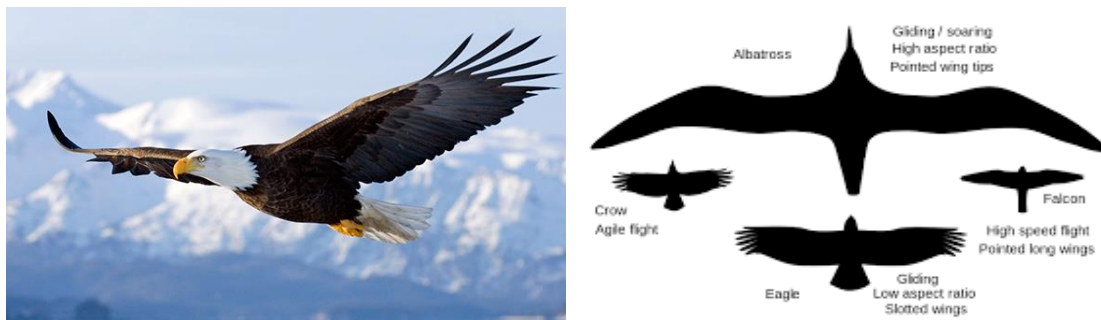


**Fig. 5: Wing-tip looking devices on Birds (Al-Atabi, 2006)**

Over the last few decades, various types of winglets have been studied, currently researched or are already incorporated into existing aircraft.

The use of winglets on aircraft is one of the most noticeable fuel economic technologies on aircraft. It improves aircraft efficiency by diffusing strong vortices produced at the tip of the wing and thereby changing the lift distribution in the span-wise direction, while maintaining the additional moments of the wing within a desired limit. This reduces the induced drag created by the wing tip vortices on the aircraft thereby improving the lift-to-

drag ratio of the aircraft. To this effect, researchers have been investigating numerous technologies to produce favourable effects on the flow field around an aircraft wing tip by using wing tip devices to reduce the strength of the trailing vortices sheets in this region. Winglets with several platforms, for example, wing sails, wing diffusers, wing tip grid, several modifications of a wing tip side edge and adapting various non-planar configurations such as the box-wing and C-planar wing-tip device have all been studied by McMasters and Kroo, (1998). Winglets are usually cambered to reduce the effective surface area thereby having a significant effect reducing the profile drag while reducing the induced drag and are twisted to enable the rotation flow at the tip of the wing to create a lift force on the winglet and to improve the stall characteristics of the wing.

From an aeronautical point of view, the main reason behind the research work and new developments of all wing tips devices is to reduce the induced drag of an aircraft. The essential parameters of a winglet are the height measured from the base of the winglet, the tip chord, the base chord of the winglet and the cant angles of the winglet (Filippone, 2012). The aircraft wing span is increased by the cant angle (Filippone, 2012). Fig. 6 shows the side view of winglets on Airbus and Boeing aircraft. The graph shows the control points used for constructing and re-constructing the geometry of the winglets.

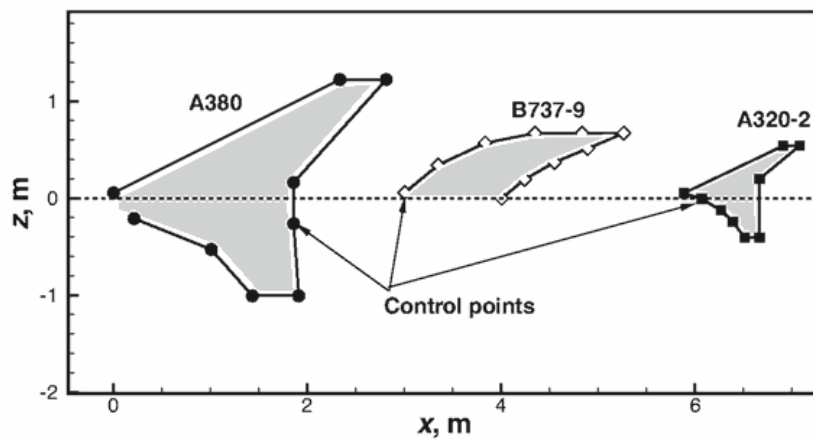


**Fig. 6: Side view of some winglets (Filippone, 2012)**

The principle of the winglet is based on the bio-mimicry of birds (such as the Albatross) which have been studied over the years. Several wing tip devices have been used and/or are been tested by various companies all with the objective of achieving aircraft induced drag reduction directly and in-directly creating an eco-friendlier transport system at the same-time satisfying the needs of society for cheaper fares and safety. Fig. 7 gives a schematic view on some wing-tip devices.

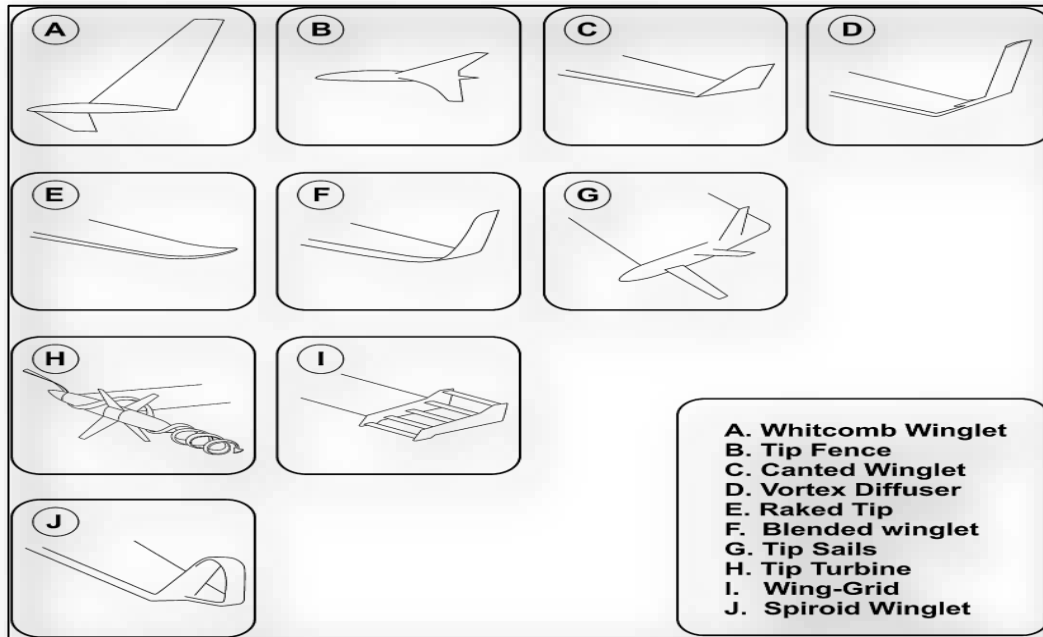


**Fig. 7: Shows various wing-tip devices (Guerrero et al., 2012a)**

The importance of using wing tip devices as a means of improving aircraft aerodynamic efficiency is the fact that these devices could be retrofitted on an already existing aircraft without having to change the entire design and or configuration of the aircraft to accommodate the device. They can also be considered as an alternative method to wing extensions which can enhance the lift-drag ratio of aircraft thereby improving the aircraft performance (Kravchenko, 1996). However, the effectiveness of wings with various wing-tip devices is substantially dependent on the flight regime parameters i.e. flight Mach number, flight Reynolds number and angle of attack (Wan and Lien, 2009).

The concept of winglets was originally developed in the 1890s by Frederick W Lanchester who patented the concept of placing a vertical surface at the wing tip to reduce the induced drag. Frederick W Lanchester's patent was in an end-plate, this concept was based on the ideal that the end-plate will reduce the lift induced drag by controlling the wing-tip vortices (Jupp, 2001). Unfortunately, the concept was not very effective at cruise conditions as the end-plate created large separations which in turn resulted in an increase in the profile drag; therefore, the skin friction drag and flow separation out-weighed any benefits obtained from reducing the lift induced drag.

In a later patent, Lanchester presented a wing-tip set up which has the outer portions of the wings sloped in an upwards direction to approximately 30 degrees resulting in a wing design which looked very like today's raked wing-tip devices. Although his original idea was to increase the directional stability of the aircraft rather than improve the aerodynamic characteristics of the wing (Falcao da Luz, 2013). Research on wing-tip devices continued, Langley Research Centre was the site of much important research work on wingtip devices both theoretically and experimentally (Reid, 1925), (Hemke, 1928). Hoerner, (1952) did some investigation on wingtip devices at the Wright Patterson Air Force base in the U.S.A. During his research work, he created a design known as the Hoerner tip and his design was the first wing-tip design to achieve some success. Fig. 8 shows a Hoerner wing tip device on a glider plane. This configuration of wing-tip device was mostly adopted for glider planes.



**Fig. 8: Hoerner wing-tip design on a glider plane (Falcao da Luz, 2013)**

Hoerner's conclusion was that such a design can be achieved with an additional cost during manufacturing but he also claimed that his wing-tip device did not provide much benefits or performance improvements (Hoerner, 1952). In summary, earlier work on wing tip devices suffered from either of two problems:

- Increased profile drag which outweighed a drag reduction benefit of the winglets due to induced drag reduction.
- Increase in the wing's root bending moment which would require a much stronger structure with the consequence of added production and manufacturing cost and more weight.

Reid, (1925), carried out an experiment bearing in mind the afore mentioned barriers in an attempt to reduce the added parasite drag created by using wing-tip devices. A trapezoidal shape wing-tip device was used during his investigation. It was concluded that the practicality of applying such devices to aircraft remained in doubt until more was learnt about the load impact of using such a configuration on the wing span (Reid, 1925).

A more recent breakthrough for wing tip designs came in the 1970s with Richard T Whitcomb's comprehensive studies. Due to the oil price increases in the 1973, airline companies together with aircraft manufacturers exploited several ways to reduce their aircraft fuel consumptions by improving the operating efficiency of their aircrafts (Guerrero et al., 2012a). In an attempt to find ways to reduce cruise drag and improve aircraft performance, Richard T Whitcomb patented a wing-tip design concept. Whitcomb (1976) designed the winglet using advanced aerofoil concepts integrated into a swept, tapered platform that would be able to interact with the wing-tip air-flow to reduce aircraft drag. The research was conducted in the Langley 8 foot transonic pressure wind tunnel at high subsonic speeds with the winglets mounted on the tip of a first generation, narrow body jet transport wing, and after numerous experimentations, a small and nearly vertical winglet was installed on a KC-135A and flights were tested in 1979 and 1980 (Hossain et al., 2008), (Whitcomb, 1976), (Whitcomb, 1981). Whitcomb's research showed that winglets could improve an aircraft range by as much as 7%, and also improved the lift to drag ratio by 9% with an induced drag reduction of approximately 20% which was twice the magnitude capabilities by compared with a wing tip extension. Whitcomb's analysis of the air flow around the wing tip of a typical transport aircraft showed the air flow in this region of the wing was characterised by a flow that is directed inwards above the wing tip and a flow which is directed out-ward below the wing tip. Whitcomb's winglet concept attracted further research on winglets for aircraft.

Heyson et al., (1977) carried out an investigation of numerous winglets by comparing their characteristics with wing extension devices. From his investigation, he reported that in an identical level of root bending moment, a winglet provided better induced drag reduction capabilities than those of a wing tip extension. This agreed with Whitcomb's research in NASA TND -8260 (Whitcomb et al., 1976). The first aircraft to use the concept of a winglet was Burt Rutan's light home-built Vari-eze, Fig. 9 Shows the design. In 1974, a Learjet 28 was the first jet to incorporate the concept of winglets on a jet aircraft. Their success has led to extensive usage of winglets on aircraft.



**Fig. 9: Learjet Business jet with winglet (Falcao da Luz, 2013)**

A NASA contract Yates and Donald, (1986) assessed winglets and other drag reduction devices in the 1980s. They found wing tip devices such as winglets, sails, feathers etc. could improve the induced drag efficiency by 10% to 15% if they are designed as an integral part of the wing.

The first industrial application of the winglet concept was in the sail plane. The Pennsylvania State University (PSU) 94-097 aerofoil was designed for use on winglets of high performance sail planes (Maughmer et al., 2002). To validate the design tools as well as the design itself, the aerofoil was tested in the Pennsylvania State University low speed low turbulence wind tunnel at Reynolds numbers of  $2.4 \times 10^5$  to  $1.0 \times 10^6$ , and the results obtained were compared with results from two source panel codes PROFILE and XFOIL. They were found to produce results which were in good agreement with the experimental data. Kuhlman and Liaw, (1988) from their investigation on winglets predicted a reduction in the total drag for low aspect ratio wings by up to 12%.

#### **2.4.1.1. Vortex Diffuser**

Hackett, (1980) proposed the vortex diffuser, a device which uses a mechanism to intercept the wing tip vortex just at the back of the wing trailing edge thus diffusing the trailing vortices and thereby reducing the lift induced drag of the wing, (see Fig. 10). Hackett's results showed that the aft mounting features of the vortex diffuser wing tip device allow for the greater reduction of the drag at transonic Mach numbers and the inboard cant eases the stress on the structures. The design was claimed to be capable of being retro-fitted into existing aircraft wings without major re-constructions needed which seem very possible.

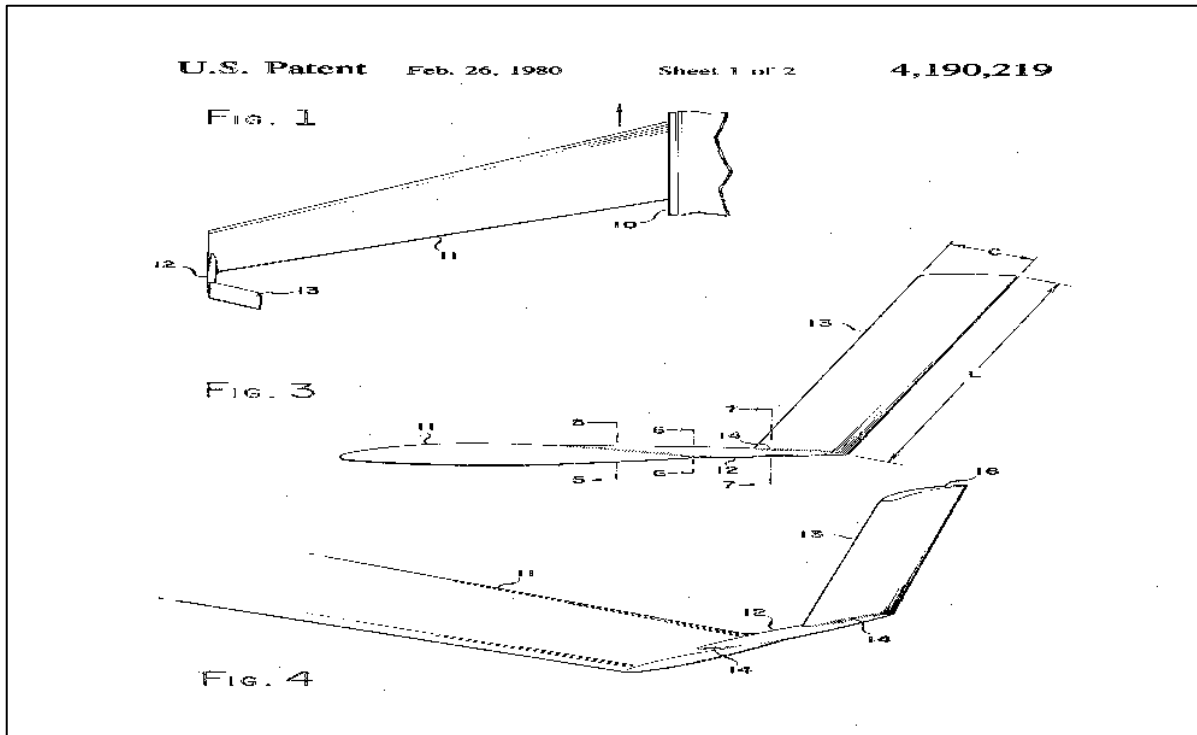


**Fig. 10: Vortex diffuser by (Hackett, 1980)**

#### 2.4.1.2. Wing tip sails and Grid

Spillman, (1978) patented wing-tip sails. This wing tip device concept is characterised by multiple high aspect ratio lifting elements at several dihedral angles. The device was designed to diffuse the wing tip vortex. Flight and wind tunnel experiments confirmed that the design reduced the fuel consumption and reduced the take-off roll of a Paris MS 760 Trainer Aircraft. A further study on the design was performed by Cerón-Muñoz and Catalano, (2006) in which the investigation was performed using a NACA 65<sub>3</sub>-018 profile with three winglets (tip sails) as shown in Fig. 11. The three winglets were added to three cylindrical modules at the tip tank with varying angles and configuration and was tested in a wind tunnel at Reynolds number 350 000. Wind tunnel experiments showed that by using a combined three winglet configuration some potential benefits can be achieved and they proposed an optimisation of the concept which would be capable of improving the whole flight envelope from climb to maximum range.

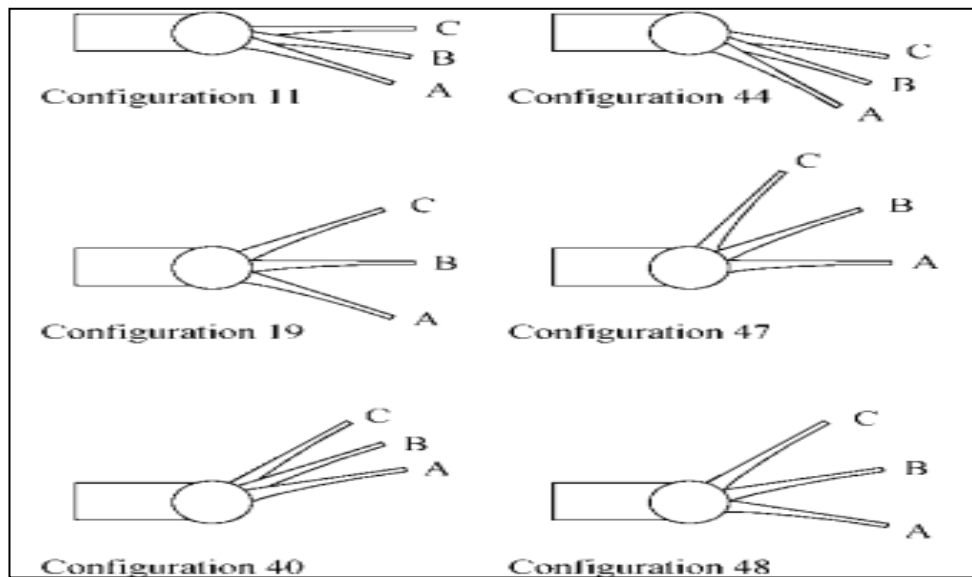
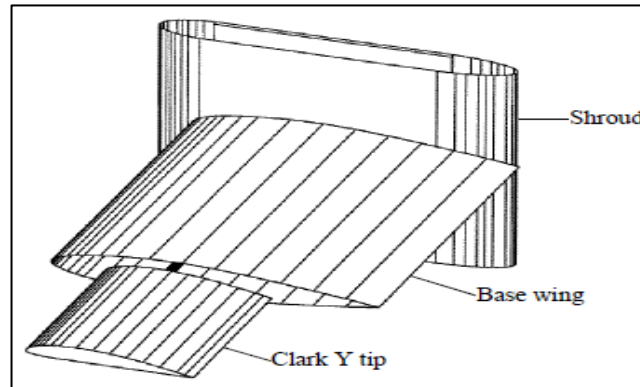


**Fig. 11: Configurations considered better, A is the leading winglet, B is the central and C is the trailing one by (Cerón-Muñoz and Catalano, 2006)**

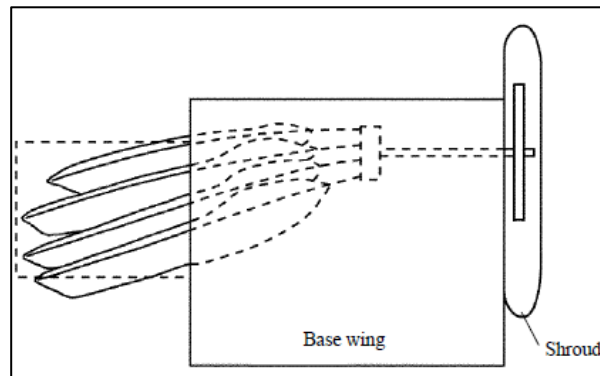
Klug, (1988) patented a wing-tip design known as the wing grid. The wing grid device consists of a set of multiple wing extensions added to the wing at various angles in a way that their vortices do not interact to form a stronger vortex. The smaller vortex distorts the energy so that the lift distribution on the wing is increased and lift induced drag reduced. The design is known to have flaws since it is unable to change its configuration in flight to optimise drag reduction and also the closed lattice work that is used at the end of the wing or at the wing tip does not allow the freedom to control the individual winglets for optimum configuration and performance.

Tucker, (1993) to further the knowledge on the wing grid, performed an extensive study on the split tip of soaring birds to demonstrate the potential of using such a configuration to improve wing performance. An experiment was performed in a closed wind tunnel at an air speed of 12.6 m/s by using a baseline wing which was fitted with slotted wing-tips and another baseline wing fitted with an extension of the Clark Y tip see (Fig. 12 a). The results obtained from this study demonstrated that with the same number of increases in the angle of attack, the Clark Y tip increased the baseline wing drag by 25%, whereas, the feathered tip reduced the drag by up to 6%. The feathered wing tip maintained a high span factor under increasing angle of attack. Flow visualisation was achieved by using helium filled bubbles to show that by attaching two winglets to the tip of a wing model, vortices sheets are spread horizontally and vertically in the wake of the tip. The investigation provided evidence that the tips of slotted wing-tip-like feathers on soaring birds reduced the lift induced drag which in reality is achieved by

separated tip feathers of birds which acted as winglets and increased the span factors (efficiency factor) of the wing.



(a)

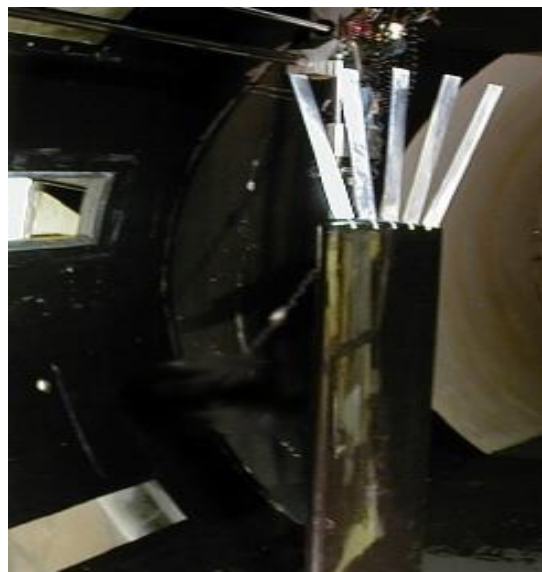


(b)

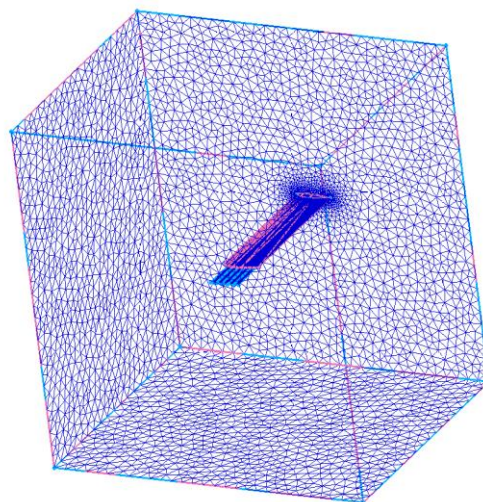
**Fig. 12: (a) The wing balance with the base wing and the Clark Y tip attached. The vertical structure is the streamlined shroud that covers the force transducer. The tip shaft can be seen between the base wing and the tip. It extends through the base wing and supports the tip. The shroud is 152mm high (Tucker, 1993)**  
**(b) A top view of the wing balance with the base wing and the feathered tip mounted on it. Dashed lines show the tip shaft, the feather clamp and the parts of the tip feathers that are inside the base wing. Dashed lines also show the outline of the Clark Y tip (Tucker, 1993)**

Smith et al., (2001) demonstrated the advanced performance potential of the multi winglet design over a baseline wing and equivalent single winglets. Their purpose was to investigate the potential of multi-winglets for the reduction of induced drag without increasing the span of aircraft wings. A wind tunnel model of the winglets was constructed using a NACA 0012 aerofoil section, see Fig. 13 (a). A wing measuring 1.219 m span and 0.3 m chord length was used. Five separate winglets were tested with a mechanism placed in the wing tip to allow for the independent adjustment of the rotation and angle of attack about the wing tip. A CFD code Cobalt was used for

the optimisation of the winglet configurations. Wing configurations which included the baseline wing (no winglet), baseline winglet and wing with 5 winglets located at the wing tip with no dihedral angle, (Fig. 13b) and finally the optimised winglet and wing with 5 winglets located at  $20^\circ$ ,  $10^\circ$ ,  $0^\circ$ ,  $-10^\circ$ ,  $-20^\circ$  dihedral angle measured from the leading edge to the trailing edge were studied. Wind tunnel and Numerical testing indicated that certain multi-winglet configurations reduced the wing induced drag and improved the lift to drag ratio by 15-30% compared with the baseline wing. A substantial increase in lift curve slope occurs with dihedral spread of winglets set at zero incidences relative to the wing. Dihedral spread also distributes the tip vortex. However, the wing grid may also have limitation due to aero-elastic effects in the compressible flight regime that have not yet been evaluated on the optimal configuration.



(a)



(b)

**Fig. 13: (a) Wing tunnel configuration ; (b) Sample Euler Grid for the Baseline (Smith et al., 2001)**

### 2.4.1.3. Tip Fence

Wolfgang Liebe patented a wing tip fence (see Fig. 14) concept in 1938 at the time of his work on the Messerschmitt Bf 109B. The design is a flat plate attached perpendicularly to the wing and in line with the air flow. He discovered that the Bf 109B had a peculiar stall which was initiated at the wing root and cross span flow near the wing leading edge which then travelled outward towards the wing tip at high speed. The aerodynamic result of such characteristics was that the entire wing stalled at the same time, but the installation of a wing tip fence prevented the cross flow thereby removing the stall issue. This type of wing tip device has been used on aircraft with swept wings for over 50 years. The MiG-15 and the F-86 were some of the earliest aircraft which used such configuration for drag reduction. More recent usage has been on aircraft such as the Fiat G91, BAE Hawk and Harrier and on some Boeing series aircraft i.e. Boeing 737-800. Low speed wind tunnel and flight tests were conducted by Williams, (2009) to check the effect of a wing fence on a T-38A. The wind tunnel results were based on force and moment data which were collected with a six-component balance and flow visualisation. The experiment was conducted at Reynolds number  $0.3 \times 10^6$  and wind tunnel results showed an increase in lift coefficient by up to 0.6% and reduced span-wise flow and separated flow outboard towards the wing fence. Flight test also confirmed the results.

Most recent work on the tip fence is presented in Gavrilović et al., (2015). Here several numerical investigations using different types of winglets which included wing-tip fence, winglet MAX (a blended winglet with split tip), blended winglet, and two spiroid winglets modelled using a NACA0012 aerofoil was undertaken. The CFD code FLUENT was used as the Reynolds Average Navier Stokes' solver in compressible turbulent flow conditions and the Realisable  $k - \epsilon$  model as the turbulence closure model with 8 million cells to obtain the solution. Although there appears to be no way to replicate their work as no exact design parameters or domain parameters were provided, they claimed a considerable amount of benefit was obtained by using all winglets with the tip fence offering the most benefits in terms of most improved lift to drag ratio for short range flights.



**Fig. 14: wingtip fence (Whomsley, 2018)**

#### **2.4.1.4. Blended wingtip device**

A new and well renowned wingtip device is the blended winglet concept consisting of a winglet extending smoothly from the wing to eliminate interference drag found in most conventional winglets. It is reported that the blended winglet reduces drag by eliminating the discontinuity between the wing tip and the winglet (French, 1978). A smoothed version is attached to the Boeing 737-400 and Boeing 7xx series jetliners. Flight tests of Blended Winglets on the Boeing Business Jet 737-400 have indicated significant overall aerodynamic improvement and resulted in a 7% drag reduction. Theoretical predictions had indicated that the configuration would have only a 1-2% improvements in drag reduction, and wind tunnel tests had shown only 2% drag reduction (Clark, 1999). In a publication by Airbus in 2012, Airbus attributes the reduction of fuel burn by 15% to using blended winglets mounted on the A320neo family which was eventually fitted to the A320 and 50% of all A320 type aircrafts that have been delivered since 2013 and to all that were delivered from 2014. A newer version of the blended winglet has been developed by Boeing called the MAX737 winglet, the winglet began in operation in 2017 (See Fig. 15).



**Fig. 15: Boeing MAX 737 Winglet (Boeing, 2015)**

The Boeing MAX 737 winglet configuration is reported by Boeing to deliver 8% lower operating costs than its main competitors, increasing fuel efficiency by 1.8% and having reliability with excellent passenger experience (reduced noise) and better environmental performance. “The superior fuel efficiency of the 737 MAX reduces carbon emissions” (Boeing, 2015) with a 40% smaller noise footprint than today’s single-aisle airplanes is claimed (Boeing, 2015).

Airbus, Onera and the University of Braunschweig performed an investigation within the M-DAW project (Modelling and Design of Advanced Wing Tip Devices) which can be found in Mann, (2006), Buscher et al, (2006). Two wing tip devices were investigated and optimised (see Fig. 16), namely the spiroid loop and the downward pointing winglet design. A typical long-range aircraft wing was used as the baseline reference wing before comparing the results obtained from their investigation with the performance data of a blended winglet. The new design configurations were assessed using CFD methods which were then validated using cryogenic European transonic wind tunnel testing. The downward pointing winglet was designed for retro-fitting with wing modification up to 4% allowed; this was done to keep the max wing root bending moment the same so as not to require further modifications to the wing. As a result, any gains obtained were solely based on the aerodynamic performance of the devices. The winglets were designed for cruise Mach number of 0.85. A previous study Grenon and Bourdin, (2002) carried out on the spiroid loop design reported some drag gain for slightly lower rooting bending moment when compared with other similar wing tip devices. Also it was reported that the configuration suffered from the formation of shock waves in spiroid loops (Abbas et al., 2013). To tackle this problem, optimisation was performed on the designs. The winglet optimisation was based on 45 design parameters of which the most important parameters are; maximum thickness of winglet, winglet twist, sweep angle and

winglet camber. Other parameters considered included, but, were not limited to, spiroid loop size, minimum chord length, minimum aerofoil relative thickness set at (5%), and identical wetted area with the equivalent blended winglet. Their reported result showed that the spiroid loop had a better efficiency at high coefficient of lift values in keeping the root bending moment the same, but an under performance in terms of drag reduction estimated at 86% of the drag reduction of the identical blended winglet. The investigation of the downward pointing winglet which was based on high and low speed conditions, showed some benefits estimated as 1 – 3% in range improvement over the long range flight setting and improvement of 4 – 6% lift to drag ratio at low speed conditions (Hantrais-Gervois et al., 2009), (Abbas et al., 2013).

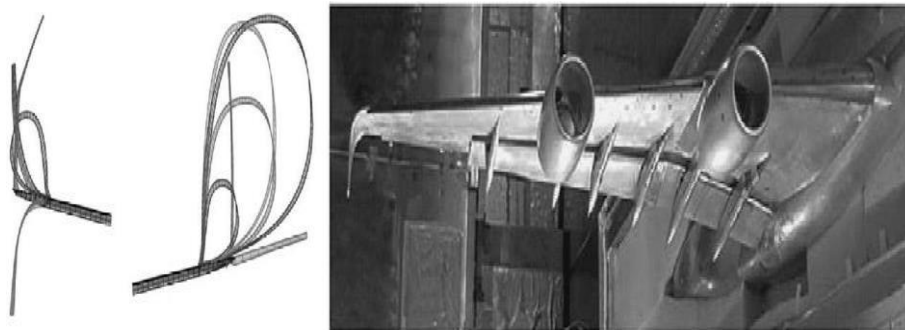


**Fig. 16: Spiroid loop (left) and downward pointing (right) wing tip devices (Hantrais-Gervois et al., 2009)**

While acknowledging these positive accomplishments made by the aviation industry in reducing induced drag by using winglets, it should not be forgotten that winglets still carry some weight penalties in terms of the structural improvements required to support the additional weight and increase in the wing root bending moments. Buscher et al. (2006) stated that the extra weight penalty associated with incorporating a wingtip device on a wing must be considered when designing a winglet for application on an aircraft. This is essential since a winglet which has been designed solely to improve the aerodynamic performance of an aircraft such as to reduce the induced drag may not be the optimum design if the added weight penalty is taking into consideration (Falcao da Luz, 2013). To this effect much research work has been focused on optimising winglets so that the cost benefit balance can be improved (Jansen et al., 2010), (Ning and Kroo, 2010), (Ning and Kroo, 2008), (Ursache et al., 2007), (Khosravi and Zingg, 2014) (Wakayama, 2000), (Elham and van Tooren, 2014a).

#### **2.4.1.5. Tip Turbine**

Established by James Patterson in 1985, the tip turbine reduces the strength of the vortices and recovers energy required to overcome drag. The concept is to have a turbine mounted at the tip of the wing which rotates or is driven solely by the wing tip vortex cross-flow that is created by the lifting wing during flight. If the wing is not

producing lift and consequently there will be no vortex as in the case of a wing having a symmetrical aerofoil section set to zero angle of attack in the wing tunnel, the wing tip vortex will not rotate.

In August 1987, James c. Patterson, Jr., and Glynn R. Bartlett conducted a preliminary investigation at the NASA Langley Research Centre to determine the installed performance of a wing tip-mounted pusher turboprop. Tests were conducted in the Langley 7- by 10-Foot High-Speed Tunnel using a semi-span model having an un-swept, un-tapered wing with an air-driven turbine motor located on the tip of the wing, with an SR-2 design high speed propeller installed on the rear shaft of the motor. All tests were conducted at;

- a Mach number of 0.70,
- at angles of attack of approximately  $-2^{\circ}$  to  $+4^{\circ}$ , and
- at a Reynolds number of 3.82 million based on the wing chord of 13 inches.

The data reported indicated that, due to locating the propeller behind the wing trailing edge, at the wingtip, in the cross flow of the tip vortex, it was possible to recover part of the vortex energy as an increase in propeller thrust and, therefore, a reduction in the lift-induced drag as well. Also, the propeller performance enhancement and the reduction in drag due to lift associated with the wing tip pusher turboprop is forfeited when the turboprop is located inboard of the wing tip (wing tip extended) and a  $-3^{\circ}$  turboprop nacelle incidence resulted in an additional drag reduction of approximately  $10^0$  at a lift coefficient of 0.3 (Patterson Jr and Bartlett, 1987). This investigation did provide details on issues such as sensitivity to nacelle positions, rpm effect on wing, tractor propeller configuration, Mach number and Reynolds thereby not giving a broader scope on the application of such configuration. Other research work on the use of propellers for induced drag or overall drag reduction have focused on optimising the engine's nacelle position in board of wing with CFD as shown in Veldhuis, (2004), Alba et al., (2018), application of the propeller in board wing to improve the wing performance by using experimental and or CFD see Williams and Cho, (1990), Stone, (2008), Selig, (2010), Rakshith et al., (2009), Moens and Gardarein, (2001), Samant et al., (1987), Traub, (2016) with the reported findings showing substantial improvement in lift-to-drag ratio, lift improvement and drag reduction. Irrespective of this, the afore mentioned issues still need to be addressed as it can be assumed that wing tip mounted propeller configuration carries a better benefit potential than an in board mounted configuration.

### 2.4.1.6. Spiroid winglet

The first spiroid winglet concept was developed by Aviation Partner Incorporation. Wind tunnel and CFD analysis from Aviation Partner Incorporation indicated that spiroid wingtip device could be 40% to 50% more efficient than the conventional dihedral blended winglet. According to Aviationpartners, (2013) it is claimed that whereas the blended winglet reduces cruise drag by estimated 7% the spiroid winglet has the potential to reduce the drag by an estimated 10%. The spiroid design is a hybrid configuration of Whitcomb’s single configuration winglet and the multiple slit feathers of most birds; the spiroid winglet is a split-wing loop extending from the tip of the wing and aims to combine the optimal vorticity distribution of multiple winglets with simplicity and absence of interference of single winglets (Guerrero et al., 2012a). It has been proposed by several researchers that problems encountered by most winglets which include increased interference drag and larger skin friction drag can be resolved by using spiroid winglet (Bannasch, 2001) , (Gratzer, 1992), (Guerrero et al., 2012a). A research paper by McLean, (2005) of Boeing results showed flight test and Computational Fluid Dynamics based drag prediction for several winglets (including spiroid winglets). From the data presented in his work, the spiroid winglet gave a better cruise drag reduction percentage at constant lift coefficient with a slight increase in the cruise gross weight increase percentage (See Fig. 17).

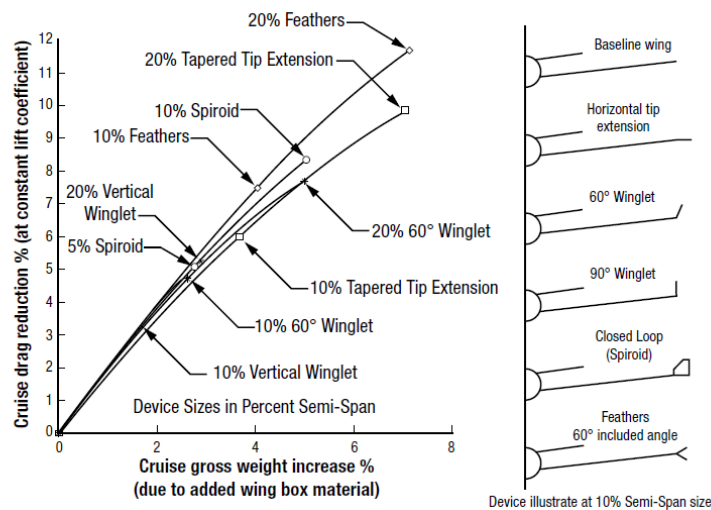


**Fig. 17: Comparison of CFD-Based drag prediction and flight test for API blended winglets on 737NG (McLean, 2005)**

Guerrero et al., (2012a) proposed a spiroid concept by joining the tip of a vertical winglet which was an extended half of the tip chord of the wing with a horizontal extension from the vertical winglet extending from the other

half of the wing and tip chord. Preliminary numerical simulation using a rectangular clean wing and wing with spiroid winglet configurations showed the design can improve the coefficient of lift values by 9%, drag reduction at higher angles of attack of over 8 degrees plus, improved stall characteristics of the wing and considerable induced drag reduction. Shortcomings of the design were due to increased parasite drag from interference edges, increased wetted surface area and increased weight.

Tucker, (1995) for the first time demonstrated that the presence or absence of tip slots has a significant impact on the drag force experienced by living and flying birds. The drag force experienced by a Harris' Hawk in a gliding set up at level flight was measured in a wind tunnel. It was observed that the drag force increased significantly when the tip slots which were the primary feathers, were removed. The unclipped hawk had 70–90 % of the drag of the clipped hawk (removed primary feathers) at speeds between 7.3m/s and 15.0m/s. The unclipped hawk had a mean induced drag factor of 0.56, compared with the value of 1.10 for the clipped hawk. The slots appeared to reduce the drag by spreading the wing tip vortex vertically, this is because the larger wing span and the other differences that were observed with the bird that had its tip slot did not completely account for its lesser drag.

The research paper Nazarinia et al., (2006) presented a wind tunnel test carried out on the spiroid wing-tip configuration. The investigation was performed experimentally on different winglet shapes and orientations, using static surface pressure measures over the wing's wake at various angles of attack. Four types of winglets, spiroid (forward and aft), blended, and wing grid were used in this investigation. Wing static surface pressure measurements were obtained both chord wise and span wise as well as the wake profiles at various angles of attack using the afore mentioned winglets. The data were compared with a bare wing. The experiment was conducted using a low speed wind tunnel at Reynolds number  $0.2 \times 10^6$ . The results show that integration of winglets changes the flow field over and around the wing significantly. Further, it was found that certain winglet configurations improve both the wake and the wing pressure distribution. The total pressure in the wake of the model varied drastically when the wing is equipped with winglets. It was also reported that a Forward Spiroid winglet seems to be more suitable for the cruise flight phase as the angle of attack is low, whereas the Aft Spiroid winglet is more suitable for the climb phase where the angle of attack is higher than that of the cruise, however, no quantitative results on lift and drag coefficients are provided, which makes it difficult to replicate their work.

Maksoud and Seetloo, (2014) presented investigations on several wing-tips devices which include the blended winglet, wing tip fence, wing tip rake, spiroid winglet and a new design concept triple blended winglet. The investigation was performed by using the CFD code Phoenix solving RANS equations at a velocity of 80m/s, and Reynolds number  $6.712 \times 10^7$ . The research findings showed each wing-tip configuration worked differently

and were most effective at different flight phases. At cruise the raked winglet offered the highest lift to drag ratio 8.24 percentage, at take-off the triple blended winglet was reported to be the most effective having a lift to drag ratio of 8.89 percentage. Their results also showed that the spiroid winglet was more effective than the Blended winglet in both cruise and climb flight phases.

Mostafa et al., (2014) proposed several spiroid winglet configurations on a Falcon 50 aircraft. 14 spiroid configurations were studied by using 30 percentage of the baseline wing span to design the spiroids, NACA2412 and NACA0012 aerofoil sections. CFD was used for their investigations with results compared with the data for a simple wing and blended winglet configuration. The results for their investigation showed a superior induced drag reduction capability of a certain spiroid winglet configuration by up to 50% compared with the simple wing and blended winglets which were much lower. They also reported some improvement in range and endurance of the Falcon aircraft. In this regard, further research work could be carried out by using such configurations on a more realistic approach in terms of the percentage of wing that is used for the winglet design; thus, using 25% or less of the baseline wing as the winglet size. This would have a less negative impact on the structural loading and bending moment on the wing as opposed to using 30% of the wing which might require a new structural study on the wing.

Wan and Lien, (2009) presented work on validating the flight test that was performed on the spiroid winglet in 1993 by Aviation partners Inc. by using a spiroid wing-tip design of 5% of vertical height with an added blowing device to reduce the total drag and reduce the trailing vortex strength which was mounted on a Gulfstream IV. The spiroid was designed using a NACA64206 aerofoil section, at Mach 0.8. The investigation used the computational fluid dynamics Reynolds Averaged Navier Stokes solver and turbulence closure modelled used the Spalart-Allmaras turbulence model. The results obtained showed the forward spiroid winglet had a better performance at low angles of attack than the aft spiroid winglet configuration which was confirmed by the work of Nazarinia et al., (2006). The results of their investigation also showed some fuel consumption reduction and up 5% drag reduction.

In addition to the different spiroid wing tip concepts proposed or investigated by the afore mentioned researchers, the MAX 737 winglet that was discussed in section 2.4.1.4 can possibly be modified by adding an arc to the tips of the device to form a close loop which could potentially reduce the wing tip vortices and possibly decrease the induced drag. Other configurations could be the use of hollowed circular cylindrical closed loop wing tip device which could potentially diffuse any strong wing tip vortices concentrations.

### 2.4.2. Non-planar wing concepts

The concept of a non-planar wing goes beyond wing tip devices and opens the possibility of using a range of complex designs to reduce aircraft induced drag with higher efficiency compared to planar wings of the same wing span and lift force.

Studies by Kroo, (2005) of Stanford University, U.S.A on a non-planar wing showed numerical comparisons, using optimising vortex lattice code, between the efficiency of different non planar configurations (see Fig. 18) for several non-planar wing concepts for which the geometry was allowed a vertical extension of up to 20% of the initial wing span. These types of designs can be of interest to engineers due to the potential for reducing the lift induced drag of aircrafts at fixed wing span which is a key constraint as structural and other considerations limit wing span. These unconventional wing concepts provide the technological advancement to achieve such goals. Among the studied designs, the joined (box plane) wing concept probably presents the best solution (Kroo, 2005).

Fig. 18 shows the minimum vortex drag achievable by the studied design concepts having the same span and carrying the same lift with variations in the ratios of height to span. The design concepts shown are biplanes, box planes, winglets and ring wing concepts. Kroo, (2005) claimed that a ring wing had 50% the vortex drag of a monoplane having the same lift and span. From observing the plot in Fig. 18, it is observed that a box plane achieves the least possible vortex drag for a specified span and height, winglets follow closely and the bi plane achieves the same amount of vortex drag savings in the limit of very large vertical gap. Kroo, (2005) suggests that a good number of savings in vortex drag are possible for a specified wing with fixed wing span, if large vertical extensions are permitted with a suggested 30% vortex drag reduction possible with a height to span ratio of 0.2. In short, the investigation showed the potential of using a closed system wing or devices to effectively reduce the induced drag and showing improved span efficiency. A more detailed literature review on c-wing and box plane concepts is presented in the following sections.

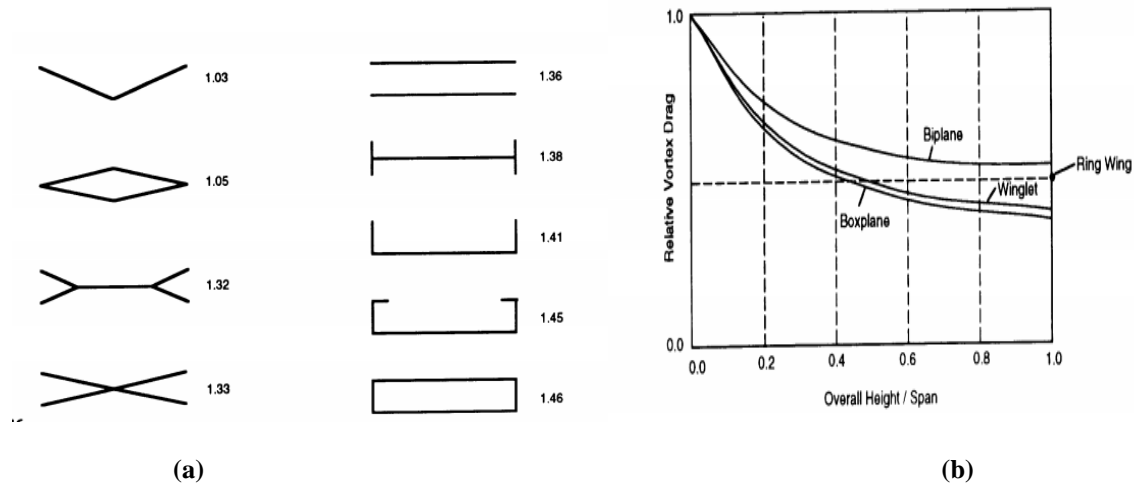


**Fig. 18: (a) Span efficiency for various optimally loaded non-planar systems (b) Induced drag variation with allowable height for non-planar systems (Kroo, 2005)**

### 2.4.3. C-Wing concept

This system uses a winglet and then adds a horizontal extension of the winglet inwards to form a C like shape. The horizontal pointing winglet at each tip acts as a horizontal stabilizer and pitch controlling device (Torenbeek, 2013). The optimum lift distribution of the C wing shows all upward lift is been generated by the main wing, the vertical fins carry a certain amount of inward air while the horizontal winglets pointing inwards carry a small download. It is suggested that since the C wing concepts have already been investigated primarily for large transport aircraft it might be worthwhile investigating the concept on other types of aircraft. The advantage of using the C wing is based on improving the performance and flight characteristics of large aircrafts with a highly constrained span; this benefit could also be observed in smaller aircraft but has yet to be investigated. The concept achieves close to the induced drag reduction that is associated with the box plane as shown in Fig. 18 (b) but eliminates the added area needed to complete the box plane design. Studies showed that the optimal loading on the horizontal winglet acting inwards is directed downwards, reducing the root bending moment and providing a positive pitching moment when mounted on an aft swept wing. This potential lead to some interesting studies by Boeing on the application of the C wing concept on a large commercial aircraft see Fig. 19 (McMasters and Kroo, 1998). The investigation was carried out based on the strict span constraints associated with the airport for large aircraft. The ideal concept was to use thick aerofoils on the wing to accommodate some payload which would be mounted on the inner wing section. This concept was not further investigated due to the level of complexity that is associated with such a design, but it does suggest some interesting variants.

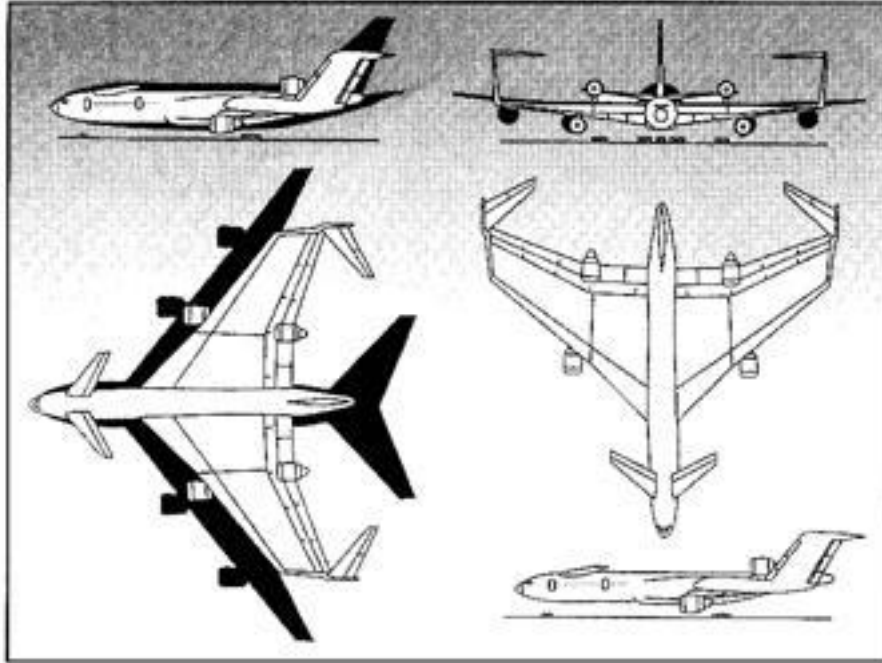


**Fig. 19: Conceptual design for a large aircraft with span constraints (McMasters and Kroo, 1998)**

#### **2.4.4. Box Wing**

From the results of Fig. 18, the box plane concept achieves the minimum possible induced drag (due to the almost closed wing tip section) for a given lift, span and vertical extent of all the concepts considered. The optimal lift distribution of the box plane concept is generally shown to arise from two horizontal wings that carry the same lift which are connected by vertical wings whose air circulation goes to zero at their centre (von KÁRMÁN and Burgers, 1935). However, a fixed circulation can be added to the concept so that the lower wing carries all the lift and the upper wing section carries no lift; this was noticed not to affect the lift and vortex drag which remained unchanged as observed by Kroo, (2005). This is the reason why the c-wing concept shown in Fig. 18 (a) has an induced drag reduction factor that is close to that of the box plane concept.

A practical application of the box wing concept can be seen in the joint wing design Fig. 20. This concept was first introduced by Wolkovitch, (1986). The joined wing model is proposed to be able to increase aspect ratio significantly with a suggested theoretical induced drag reduction of estimate 40% (Sivaji, 2004), (Frediani et al., 2003). However, some issues related to this concept needs to be investigated before the concept can be used in practice. These includes the effect of the design stability and control, structural issues which may arise from using such a design concept and detailed investigations on the behaviour and pattern of the wake vortices. Frediani et al., (2003) applied this concept on a modified Airbus A380 aircraft, with the project aimed at the stability and

structural effect of using such a configuration on an established aircraft model. Optimisation of the model was carried out during which process they found it impossible to connect the rear wing to the fuselage and thus the solution was to position the wing over the fuselage and connect the wings using fins as shown in Fig. 20



**Fig. 20: Example of non-planar wing configuration, Lockheed box-wing (Frediani et al., 2003)**

This new concept proved to be stable in cruise flight conditions and the maximum lift to drag ratio was greatly improved due to an even distribution of lift across the entire wing platform. From analysing the design concept based on its structural characteristics, the bending stresses on the fuselage were noted to be close to zero in the roots of the front and rear wing. The observed vibration modes for the aircraft were completely different from these of a conventional aircraft. This was particularly observed for the fuselage lateral bending modes which were completely absent. Also, the moment of inertia and damping moment along the pitch axis was observed to be greater than that observed for conventional aircraft. Because of these qualities, the flight characteristics of the concept were considered to be satisfactory but then again there is the issue on how to properly design the pitch control system for the concept (Torenbeek, 2005).

“Munk’s stagger theorem, which implies that sweeping a wing does not affect the vortex drag based on the assumption that the lift distribution remains constant when staggering the lifting surfaces, was applied to a transonic box plane. The transonic box plane concept consisted of a forward mounted swept back lower wing and a rear forward swept upper wing which is interconnected by a swept vertical plane at the tips” (Torenbeek, 2013). The transonic box plane concept was invented by L. Miranda of the Lockheed company, who named it the transonic biplane. The transonic biplane concept is said to have less vortex drag than a monoplane with the same wing span set-up and also it allows for a constant given section of the fuselage shape at the same time trying to

maintain the lift magnitude and distribution required to cruise at transonic Mach numbers. Some advantages associated with this design concept includes using aerofoils which have different camber from those used in monoplanes to avoid unnecessary premature flow separations, high profile drag and low lift (Addoms and Spaid, 1975). A feasibility study by Lockheed Lange et al., (1974) on the transonic bi-plane design for an operating Mach number of 0.95 using wind tunnel testing verified the estimated reduction in vortex drag at high speed. The investigation revealed some disadvantages in using the design as the flutter analysis revealed both symmetric and anti-symmetric instabilities occurring below the desired flutter speed which could not be properly controlled. Also, they claimed no significant weight reduction was observed for the wing and tail of the box plane when compared to a monoplane having the same capabilities. This led to the project been abandoned with recommendations on applying a similar concept to low speed aircrafts, which might not be as susceptible to these draw backs.

## **2.5. Skin Friction Drag Reduction**

Skin friction drag accounts for about 50% of the total drag at cruise (Houghton and Carpenter, 2003), (Cortelezzi et al., 1998),(Viswanath, 2002), (Hough, 1980). This area shows a promising area for aircraft drag reduction in coming years. Two main approaches have been researched by various countries under projects such as Supertrac, Telfona, Hlyt projects etc (Chernyshev et al., 2009), (Abbas et al., 2013). These are laminar flow and turbulent flow drag reduction methodologies.

### **2.5.1. Extended Laminar Flow for drag reduction**

Although this research focuses on the use of wing tip devices to reduce induced drag, other forms of drag reduction technologies are also reviewed to give a wider picture. There are basically two different instability mechanisms which may produce turbulent transition in a boundary layer of an aircraft at subsonic and transonic Mach numbers, these are TS-waves and Cross-flow waves (CF). Other instabilities exist such as the Mack mode instabilities, Gortler instabilities and attachment-line instabilities (Yu and Yuan, 2016). These are predominately responsible for early laminar turbulent transition in concave bodies at hypersonic flows (Whang and Zhong, 1999), (Whang and Zhong, 2000) but are not discussed in this thesis.

- Tollmein Schlicting (TS) waves are driven by viscous effect on the surface, they occur in a 2-D flow and in the mid chord region of a swept wing. The wave vectors of TS-waves are approximately oriented parallel to the flow direction.

- Cross flow (CF): These instabilities occur in the regions of positive gradients on swept wings. The imbalance between the pressure gradient and the stream wise velocity inside and outside the boundary layer provokes a secondary boundary layer flow called cross flow which presents a typical inflection point instability (A. Abbas, 2012).

These two types of disturbance grow under different conditions. TS-waves grow faster in a flow with positive pressure gradient as on the back of the wing. TS are free of stream sound and 2D roughness and the CF-waves grow stronger in flows with a negative pressure gradient that is in accelerated flows for example close to the leading edge.

See Fig. 21 for an experiment at ONERA showing stationary CF-waves on a wing.



**Fig. 21: showing stationary CF- Waves on a wing (Warsop, 2003)**

The transition from laminar to turbulent flow is always initiated by a receptivity process in which a disturbance entrains the laminar boundary layer. The unstable disturbance grows until it reaches a critical amplitude and breaks down to turbulence.

Receptivity is the process by which disturbances in the free stream such as sound or vorticity enters the boundary layer as steady and or unsteady fluctuations of the basic state. It provides the vital initial conditions of amplitude, frequency and phase for the break-down of laminar flow (Morkovin, 1969).

The goal of Receptivity theory is to estimate the receptivity coefficient, i.e. the relationship between the disturbance environment and the initial disturbance that is triggered in the boundary layer. Transition can be caused by a range of disturbances; the character of the transition process is decided by which type of disturbance the boundary layer is subjected to:

- Acoustic disturbances in a 2-D boundary layer trigger exponentially growing TS-waves. The long wavelength of the acoustic disturbance must be reduced to the short wavelength of the TS-waves, this can happen at the leading edge or at surface roughness where the flow experience a sharp gradient in the stream wise direction
- Free-stream turbulence or roughness in a 2-D boundary layer gives rise to stream wise streaks of alternating low and high velocity. Due to the sharp wall-normal gradient of the boundary layer, a small disturbance in the wall-normal velocity can cause a large disturbance in the stream wise velocity; this is known as the lift-up effect.

Free-stream turbulence or roughness in a 3D boundary layer triggers cross-flow waves.

CF is very sensitive to free stream and 3D roughness whilst TS are sensitive to free of stream sound and 2D roughness. A negative pressure gradient is favoured in damping the TS while that could be destabilise CF. In the case of a real wing the transition is triggered by a combination of all these effects.

Other instabilities which may produce turbulent transition in a boundary layer are:

- Attachment line contamination which is provoked by the boundary layer of the fuselage which propagates from the wing fuselage junction along the attachment line and contaminates the boundary layer of the leading edge.
- Curvature induced instability appears on shear layers over concave surfaces.

Different concepts for Laminar Flow Technologies include:

Natural laminar flow: This is the easiest method to apply to an aircraft. This involves tailoring the aerofoil shape to inhibit disturbances. This, for example, could include a very short pressure recovery zone on the back of the aerofoil to prevent growth of TS-waves.

Laminar Flow Control (LFC): The idea is to prevent the boundary layer from developing and thereby also preventing disturbances from growing. This is accomplished by using a perforated surface with a suction system around the wing's leading edge in front of the front spar, this could also only be applied to the upper wing since the wing upper surface has the highest boundary layer edge velocity thus very high skin friction drag associated to this region (Bushnell, 2003). Fig. 22 shows a NASA flight test with a suction wing.

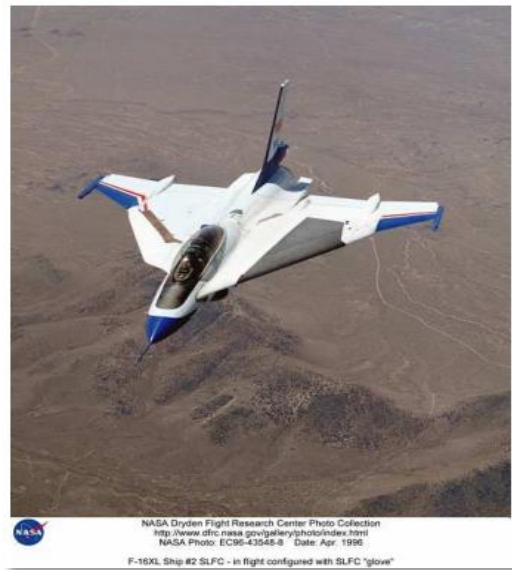


**Fig. 22: F-16XL Ship B2 SLFC-in flight configured with SLFC glove (Bushnell, 2003)**

**Hybrid Laminar Flow Control:** This is a combination of NLF (see section 2.5.2.) and LFC. This method involves using a suction device at the leading edge of the wing and wing optimisation performed down-stream towards the wing trailing edge. A practical application is to use suction close to the leading edge to inhibit the CF – waves while modifying the trailing edge of the wing to control TS-waves.

**Micro Sized Roughness:** This is the arrangement of small bumps at the leading edge. Small bumps create chosen disturbance to take out unwanted disturbances. Transition is caused by growth and break down of disturbances. Disturbances with different wave numbers grow at different rates. The concept is to generate disturbances with a wave length called the killer which will modify the boundary layer in order to damp the most dangerous disturbances called the target. The killer disturbance is generated by micron sized roughness elements close to the leading edge.

**Gaster bump:** These are big bumps on the leading edge of a wing. It prevents the turbulent boundary layer on the aircraft fuselage contaminating the boundary layer on the wing. As the boundary layer develops along the fuselage it becomes turbulent. The turbulent boundary layer spreads from the fuselage down along the leading edge of the wing and contaminates the boundary layer of the wing. A Gaster bump is a bracelet or a bump that is put on the leading edge of the wing close to the fuselage. If they are designed well, they will be able to stop the turbulent boundary layer from the fuselage to develop on the wing surface (Martin Bystrom, 2006).

The ideal of delaying boundary layer transition is a well-known concept of reducing drag. Some prototypes have already been developed to this effect of which include;

- Advanced Technologies Testing Aircraft System designed by German Aerospace Centre DLR.
- The Fokker F100
- The Piaggio P180 aircraft or the 757 HLHC Flight Program
- Falcon 50 and 900.

### **2.5.2. Natural Laminar Flow (NLF)**

This is essentially the development of a wing design which allows the provision of a natural laminar flow on a large section of the wing chord. It is known that the NLF concept cannot be adopted for high Reynolds number (Sawyers, 2006) . Some of the most recent developments in NLF technologies for transonic and subsonic flow problems are illustrated by the emergence of projects such as TELFONA (Testing for Laminar Flow on New Aircraft) and NACRE (New Aircraft Concept Research) projects while supersonic flow problems are considered within SUPERTRAC (Supersonic Transition Control) and HISAC (environmentally friendly High-Speed Aircraft) projects.

The European FP6 project adopted the concept of HARLS (High Aspect Ratio Low Sweep) wing concept. This is a wing concept optimised for the purpose of fuel burn rather than for the operating cost of the aircraft. The idea behind this concept was the suggestions that using a wing that was slightly swept would potentially unlock the concept of laminar flow i.e. laminar flow that is more controllable (Meheut et al., 2009).

The New Aircraft Concept Research (NACRE) was one project that used the HARLS concept (Godard and Stanislas, 2006b), (Frota, 2010). In the project, a multi-disciplinary investigation of a turbulent HARLS setup was carried out and also the practical application of using NLF on forward swept wing designs were studied. The aircraft model used for the investigation was a civil aircraft which had a passenger payload of 180, cruise Mach number of 0.76 at cruising altitude of 35,000 feet and Reynolds number of  $23.7 \times 10^6$ . The wing had an aspect ratio of 9.5 and a leading-edge sweep of 17.8 degrees. The project also focused on the optimisation of the laminar flow region by optimising the pressure distribution on the wing. The method adopted for this process was based on using a code to solve the Navier stokes equations on the starting design and taking the observed differences between the pressure distributions of the desired and obtained pressure. The final design obtained for the project yielded a wing design which had inboard transition characteristics moving in the down-stream regions of the wing

(upper and lower sides) with the lower side of the wing being dominated by CF and the upper side by TS and an estimated drag reduction of 14% of the aircraft total drag.

The TELFONA project in Streit et al., (2011), Perraud et al., (2010), Wild, (2013) also used the HARLS wing concept for its investigations based on developing the tools that could be used to design and test a wing model and also a tool which is capable of predicting the in-flight performance standard of an NLF aircraft. The different activities performed in the TELFONA project included the calibration of the European Transonic wing tunnel, the investigation of the impact of the effect of noise and free stream turbulence on transition location in a 2-D flow in the TsAGi wind tunnel, A receptivity study on the vortices of traveling cross flows to free stream turbulence and also that of cross flows vortices to the surface roughness. The testing of the performance of an NLF wing in the European Transonic Wind tunnel was also carried out.

The project work was structured based on the design, manufacturing, testing and the analysis of two wing concepts. These were:

- The concept of the pathfinder wing model which was used to calibrate the transition methods for the European Transonic Wind tunnel see Fig. 23 (a),
- The performance of the wing which had to demonstrate the capabilities of the HARL and NLF configurations for various Reynolds numbers.

The test performed on the pathfinder wing were performed based on the following flight conditions:

- Mach number of  $0.78 \pm 0.02$
- The Reynolds number given as  $15 \times 10^6 - 23 \times 10^6$
- The specified ambient temperature as 117 K
- $C_L$  is given as 0.1 to 0.5
- Side slip  $\beta = 0$  and  $-4$  degrees.
- Wing pressure taps which were located on the diagonal sections which are located at normalised span positions  $\eta = 0.33, 0.067$  see Fig. 23 (b).

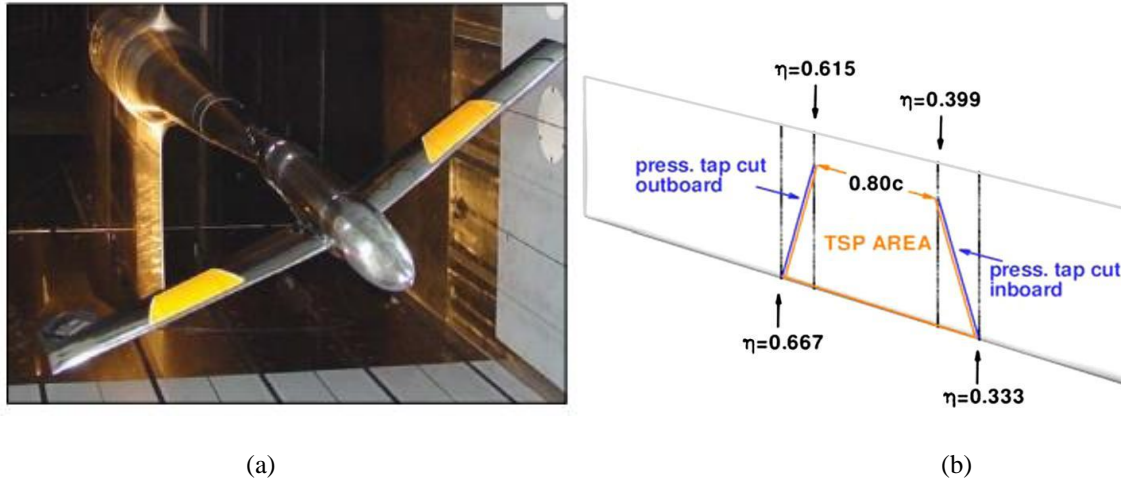


**Fig. 23: (a) TELFONA PATHFINDER Model in ETW wind tunnel test section (b) Position of TSP patches and pressure tap sections (Streit et al., 2011)**

The results obtained from the investigation proved the capability of using the ETW wind tunnel for NLF design testing also it shows the successful application of the NLF concept on a swept wing. More details regarding the investigation can be found in Streit et al., (2011).

SUPERTRAC, CIRA (Centro Italiano Ricerca Aeronautica) in Arnal et al., (2006a), Iuliano et al., (2009), Arnal and Archambaud, (2008) proved the feasibility of a numerical optimisation process in the design of a laminar supersonic wing. The optimisation was performed with an evolutionary optimisation library, which used a 3-D Euler solver coupled with a full 3-D boundary layer model, and a boundary layer stability tool which made use of the ONERA-CIRA database stability computations. 25 twist control sections plus 68 shapes were defined as design variable functions for each section giving a total of 1700 variables. The following design points were considered in the computations:

- Mach = 1.6
- Reynolds Number =  $51.8 \times 10^6$
- Length = 6.27 m
- Wing Area  $50.0 \text{ m}^2$
- CL = 0.182
- CM = 0.05

Maximum trailing edge angle = 6 degree and minimum leading-edge radius 0.15 mm.

The optimisation process returns a damping of the pressure peaks and mid-chord shocks and an important enhancement of laminar flow, from 2% to about 10–12% of wing surface. They proved the feasibility of using optimisation tools in the design of laminar wings.

A major challenge in the use of LFC is not whether the technology can be achieved but if it can be maintained in a reliable way and in an economically reduced fashion. Economics is at the heart of the decision on whether or not to employ LFC in aircraft; the economics involved in maintenance and also the economics of the initial capital cost of the technology plays a big part in the decision making since for new aircraft over half of the direct operating costs is debt service. The LFC concept is not a retrofittable technology so the wing would have to undergo major changes or complete modification or development.

### **2.5.3. Hybrid Laminar Flow (HLF)**

Hybrid Laminar Flow is basically a combination of the natural laminar flow technique and the laminar flow control technique. It combines the benefits of using both techniques which could include but not be limited to using suction at the leading edge of the wing to inhibit cross flows (CF flows) and modifying the trailing edge region of the wing to control Tollmien Schlichting waves (TS-waves).

The Hybrid Laminar flow technique can be adopted to obtain a substantial level of reduction in fuel consumption and in carbon dioxide emissions into the atmosphere by aircraft. This could be achieved by reducing the skin friction drag associated with the aircraft wing. Natural laminar flow can be adopted for small aircraft with low swept wings, at Reynolds number less than  $20 \times 10^6$  and leading edge angles of no more than 20 degrees by shaping the aerofoil section (Jahanmiri, 2011) as discussed in section 2.2.1.1. However, for aircraft wings operating at high Reynolds number regimes and high sweep angles, suction has to be applied (Reneaux, 2004), for example, on large transport aircraft. The use of suction to remove the boundary layer is a way of maintaining extensive regions of laminar flow on the aircraft wing and has been studied widely both experimentally and theoretically since the 1940s and 1950s. Some of the earliest work based on this concept can be found in Loftin Jr and Horton, (1952), Braslow et al., (1948).

One fundamental issue that arises from using laminar flow control is based on identification of the mechanisms that are responsible for the transition that occur in a particular problem. This is especially related to understanding whether the linear (basic) instability mechanisms dominate the process or whether it is dominated by the non-linear or so called “bypass mechanisms”. Bypass as a term is used to describe any flow transition which is not

dominated by a single instability (Morkovin, 1985), and (Bushnell, 2003). Examples of these could include early flow transition caused by span wise contamination on the swept wing leading edge, sound, insects, surface roughness and the interaction of a limited amplitude mode. A successful application of laminar flow control techniques would require that factors which causes bypass transition be identified and controlled completely. An example on how to approach and tackle this problem on a wing's leading edge could be to bleed off factors causing transition (contamination) from this region of the wing and re-establish a laminar attachment line flow. It has been noted by Bushnell, (2003) that such a method might not be possible for a large leading edge of a 600-800 capacity passenger large transport aircraft and therefore, some form of active transition control measure may be required in the region of the attachment line. To use HLFC, it is necessary to first ensure that the attachment line remain in the laminar flow region to prevent contamination from occurring which could annihilate any effort in laminarisation of a swept wing. To this effect, anti-contamination devices needs to be employed to avoid the contamination of the attachment line by turbulent structures coming from the fuselage. See Fig. 24 for an applied concept of the HFL also showing anti-contamination devices.

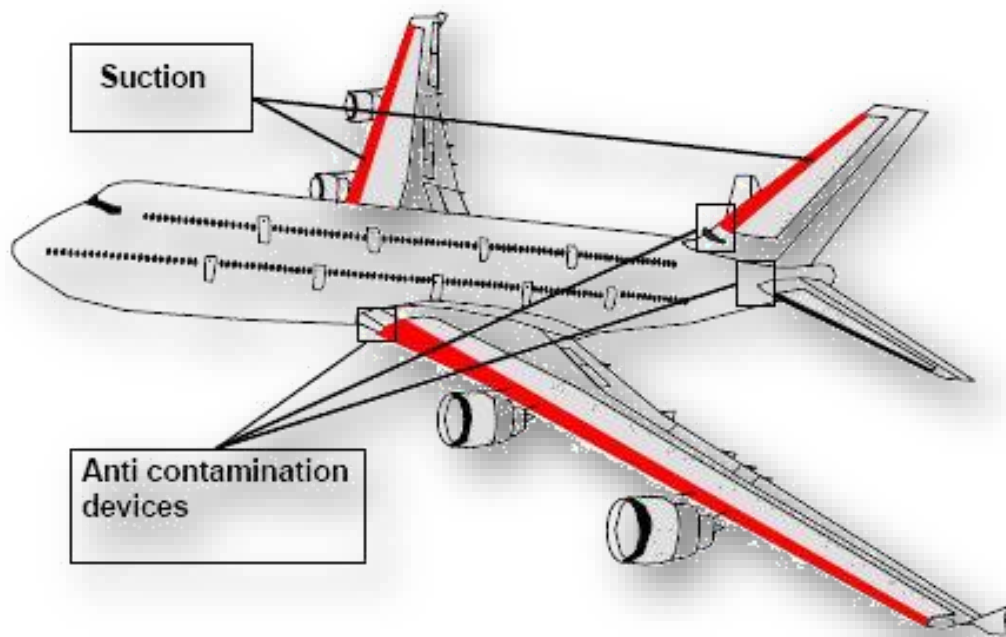


**Fig. 24: Hybrid Laminar Flow concept (Reneaux, 2004)**

For low speed flight regime, the important parameter is the leading-edge Reynolds number  $\bar{R}$ . For a given cylinder with the radius  $R$ ,  $\bar{R}$  is given as (Arnal et al., 2006b):

$$\bar{R} = \left[ \frac{V_0 R \sin \phi t g \phi}{\nu} \right]^{1/2}$$

$\nu$  is given as the kinematic viscosity,  $V_o$  is the free stream velocity of the fluid,  $\varphi$  is the wing sweep angle. Results obtained by experimental means have shown that the wing's leading edge contamination occurs when  $\bar{R}$  exceeds a value of 250 (Arnal et al., 2006b), (Pfenninger, 1965), (Poll, 1978). For high speed flows, this criterion can be used by adopting a modified Reynolds number  $\bar{R}^o$  which is derived from  $\bar{R}$  by using an “ empirical compressibility function”(Arnal et al., 2006b), (Poll, 1985). In most flight conditions, it is probable that the critical value of  $\bar{R}^o$  would be surpassed, so wing leading edge contamination will most likely occur. To delay the onset of contamination or onset of the attachment line, several tools have been developed and adopted. One such tools is the Gaster bump device and localised suction technique, which have been successfully adopted and proven efficient for subsonic and transonic flows. The Gaster bump is a bracelet or simply a bump that is placed on the leading edge of an aircraft wings close to the fuselage. The Gaster bump acts by creating a stagnation point on the wing thereby allowing a new laminar flow boundary layer to be created in the region aft the device. This concept of using anti-contamination devices was employed in the Supertrac project. In the Supertrac project (Arnal et al., 2006b) they made use of a simple geometry which consisted of a half cylinder with radius 10 mm which was followed by a flat plate see Fig. 25.

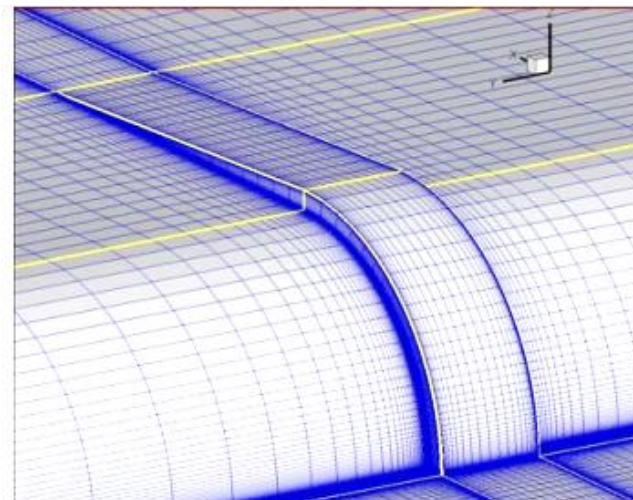


**Fig. 25: Leading edge (upper half) with a positive bracelet. Grid for RANS computations (Arnal and Archambaud, 2008)**

The Bump was fixed on a wing at a swept angle of 65 degrees to a solid wall within a CFD domain which represented the wall in the wind tunnel. Their goal was not to predict the transition but to model the mechanisms by which turbulence coming from the wall could be damped by using the right device which could be mounted on the wing leading edge or by changing the Reynolds number. To this end, a Reynolds Average Navier Stokes computation were performed in a CFD simulation setup consisting of a simple model and the lateral wall. The

first CFD simulations was carried out on a clean leading edge. i.e. a model without the anti-contamination devices. The incompressible shape factor  $Hi$  was selected as the parameter to determine the nature of the boundary layer. This parameter is used to show the correlation between the  $\bar{R}^o$  parameter and the nature of the boundary layer. From the results they found that RANS computations provided the right trends but were unable to mimic the complex physics of leading-edge contamination. This was also observed by ONERA, CIRA and IBK.

Another numerical experiment using CFD RANS solvers considers an anti-contamination device which was mounted on the leading edge of the wing. The anti-contamination device was in the shape of a bracelet. The bracelet is defined as a device of rectangular cross section (upper half of the leading-edge region). As stated by Creel, (1991) such a device could be efficiently used to relaminarise the attachment line flow at Mach number at supersonic Mach numbers. A triangular shaped bracelet was also investigated. They performed a parametric study by varying the height of the bracelets by keeping  $\bar{R}^o$  constant and equal to 440. The results obtained in the investigation were, for small values of the bracelet's height that, the turbulence coming from the wall jumps over the bracelets without any significant modification and also for larger values of height of the bracelets ( $h$ ), a stagnation point is created on the windward face of the device. The streamlines observed showed the existence of vortices in the flow roughly aligned in the chordwise direction. It was also observed that the new boundary layer that was generated at the stagnation point becomes turbulent very quickly aft the stagnation point in the span-wise direction. Concise re-laminarisation was never observed. The inference from these findings, shows that leading edge contamination is impossible to contain using this device. But then again, CFD RANS models used had shown their inability to appropriately capture the complex flow phenomenon of leading-edge contamination as demonstrated in the clean leading edge CFD investigation performed. Due to this, one could argue that the turbulence generated aft of the stagnation point of the large devices is not realistic. As a result, the criterion for an efficient anti-contamination device was based on the appearance of a stagnation point. On the contrary to what was observed in the supertrac project for supersonic flow conditions, the successful use of a gaster bump device as an anti-contamination mechanism was investigated in the ONERA F2 wind tunnel (Reneaux et al., 1996). The results showed the gaster bump delayed the contamination on the wing up to  $\bar{R} = 400$  when compared to the critical Reynolds number  $\bar{R} = 250$  observed for the clean wing leading edge. Also, higher attachment line Reynolds numbers such as those observed for large transport aircraft were observed by Arnal et al., (1997). The investigation was based on an experimental study of the leading-edge contamination of a swept wing by turbulence coming from the wing wall junction with the aim to delay the contamination onset by applying suction along the attachment line. The results of their investigation showed that suction could be used successfully to re-laminarise

the attachment line with transition delayed. The results of their investigation proved that attachment line contamination can be contained, and attachment line transition can be avoided in flight conditions.

Turning now to suction systems, these are designed in accordance with a number of aerodynamic and structural requirements of which the main features include laser drilled titanium panels, suction chambers which are controlled by independent ducts. The characteristics of the geometry of the perforated panel such as the hole diameter, porosity of the panels, also the chamber size is determined by taking into consideration the suction velocity range to be used. These are computed by using the stability method as well as the pressure distribution that is applicable for various aerodynamic conditions (Reneaux, 2004). Also, it is worth noting that by using suction systems, in some cases, premature transition can occur due to outflow, and also as a result of roughness effects resulting from high velocities in the suction holes. To prevent this phenomenon, pressure drop methods and suction criteria must be adopted.

The first practical application of HLFC for in flight demonstration on a jet transport aircraft was performed on a modified version of a Boeing 757 in 1990 (Collier Jr, 1993). Since then, the use of the HLFC concept has been successfully demonstrated by Dassault Aviation on the wing of a Falcon 900 business jet aircraft (Young et al., 2001). In addition, two separate HLFC engine nacelle flight test campaigns (on a GEAE nacelle installed on an A300 test bed and on the Rolls-Royce/DLR nacelle on a VFW 614 test aircraft) have taken place (Joslin, 1998) and (Mullender and Riedel, 1996). Supersonic demonstration of HLFC was accomplished on a modified F-16XL aircraft in 1996 (Joslin, 1998).

An interesting concept for a suction system has been designed by Airbus based in Germany and DLR (Schrauf and Horstmann, 2004) in the ALTTA European programme (see Fig. 26). The concept allows for a very efficient structure with stringers aligned in the span-wise direction. The local disturbances created by wing structures are removed. The whole wing leading edge box is adopted as a single suction unit (duct). The suction system is also self-adaptive, therefore, it works without controlling the internal flow with the help of flow meters and valves (Reneaux, 2004).

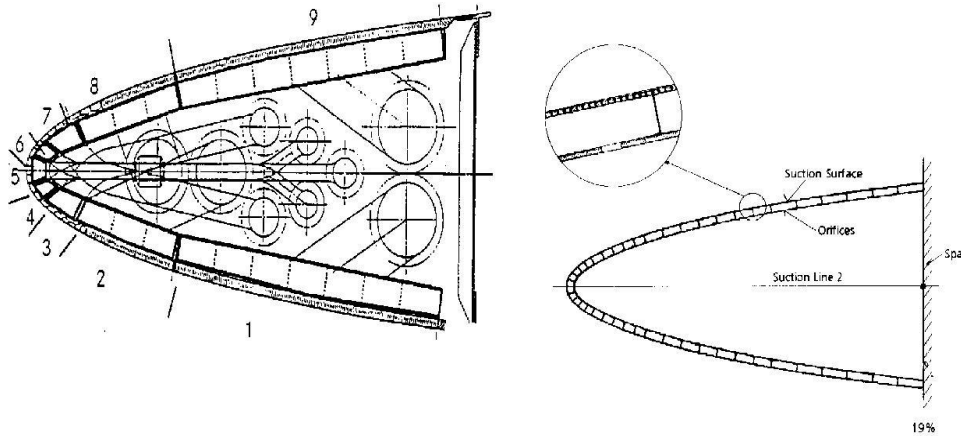


**Fig. 26: Classical suction system and simplified suction system (Reneaux, 2004)**

A high Reynold's number application of the HLFC concept for supersonic aircraft wings was investigated in the SUPERTRAC and HISAC European projects (Hein et al., 2010). Before this experiment no previous work had been done for HLFC on supersonic aircraft wings. In SUPERTRAC (Hein et al., 2010), the laminar flow control on a wing by using suction of cross flow dominated laminar to turbulent transition was studied at Mach 0.2. After initial numerical analysis, a wind tunnel model was built using a symmetrical shaped aerofoil which had a thickness of 13%, a chord length of 300mm and designed with a shaped leading edge. The wing model was tested at sweep angle configurations of 20 degrees and 30 degrees. Suction was applied between the 5% and 20% chord position through a single suction chamber covered by porous sinter material. The diameter of the suction hole used was 17  $\mu\text{m}$ . The designed model was set up in a wind tunnel and tested at 0-degree angle of attack (see Fig. 27). The experiment was conducted in the Ludwig Tube Facility (RWG) at DLR. The suction pressure used ranged from 1.2 bar to 4.8 bars with corresponding Reynolds number of  $6 \times 10^6$  and  $24 \times 10^6$ . The result showed a significant delay in laminar to turbulent transition can be obtained (within 20% to 60% of the chord). It was also observed that beyond a certain level of suction velocity, no further improvement was achieved.

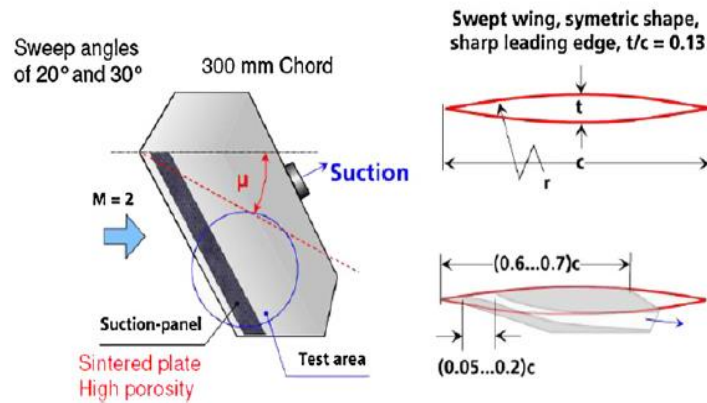


Fig. 27: Suction test definition in SUPERTRAC (Hein et al., 2010)

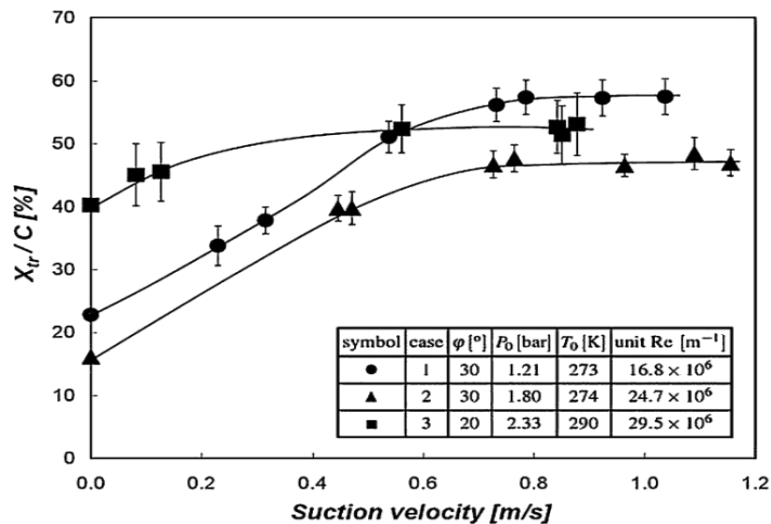
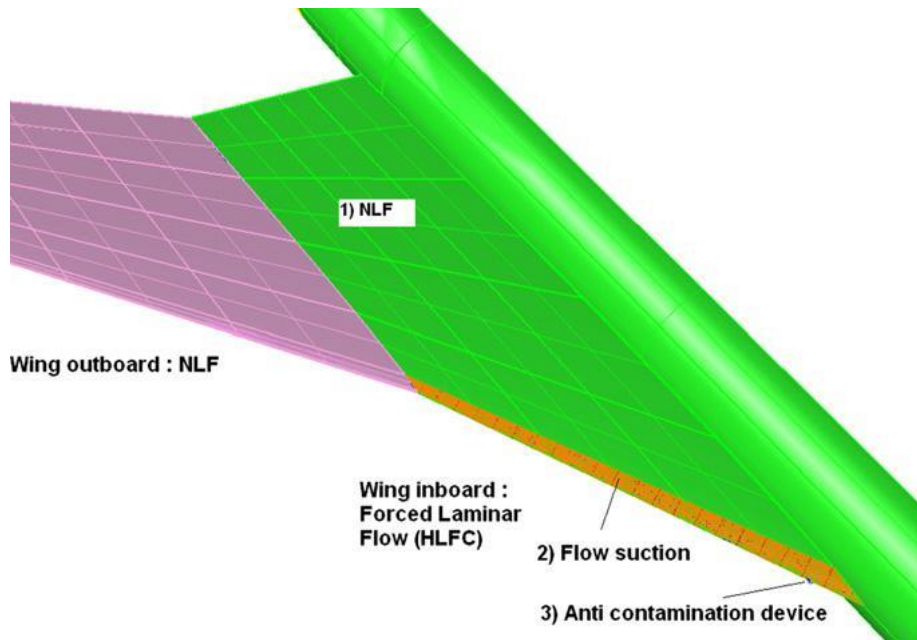


Fig. 28: Stream-wise transition as a function of the suction velocity for different test cases from SUPERTRAC project (Hein et al., 2010)

The HISAC project (Abbas et al., 2012) investigated the application of laminar flow technology to a supersonic small size aircraft with swept wing. The wing and the horizontal tail wing were designed to keep the flow over a large part of the wing and tail area laminar. The wings designed were tested in the ONERA-S2MA wind tunnel at Mach 1.6, Reynolds number of  $7 \times 10^6$ . The investigation used suction, cooling and anti-contamination devices on the swept wings. The results of the study showed the NFL can be achieved on the outboard wing which could be enhanced by using laminar flow cooling, whilst suction and the use of anti-contamination devices were needed in order to sustain the laminar flow on the inboard wing (see Fig. 29). The suction rates used for the study proved to increase the upper wing surface transition location by up to 50% of the chord length and reduced the viscous drag by an estimated 28.5%. A major challenge encountered to further develop the concept was in the

development of the high lift devices and the development of the de-icing system which are compatible with the LF concept.



**Fig. 29: Applications of NLF & HLFC concept on a supersonic test (Abbas et al., 2012).**

In general, the development of HLFC for high subsonic transport aircraft has made significant progress over the last 20 years. One issue that has been a common problem is the design and manufacture of the porous or perforated skin surface (through which the air is sucked) and the supporting substructures. Recent studies have shown that modern manufacturing methods can produce smooth surfaces which are compatible with laminar flow conditions; this could also combat the issues with surface imperfections i.e. isolated roughness, gaps which could cause premature transition. It is also important to study and understand the effects on transition posed by waviness, surface imperfection and other premature transition contributors, to develop methods and prediction criterias which will enable engineers to estimate their effect.

#### **2.5.4. Alternative Laminar Flow Control Technologies**

Besides the classical laminar flow control technologies already discussed earlier other approaches are being investigated. Advances in micro, nano-machining and electromechanical fabrication have facilitated the development of these alternate methods for laminar flow control of which the research areas include;

- Micro sized roughness concept
- Polishing of surface

- Wave cancellation
- Localized heating to control laminar flow

Micron size roughness concepts and stream wise streaks can be considered as passive techniques in the sense that they do not require any energy supply to implement them while the remainder can be classified as active.

These technologies may offer a lighter weight solution than the conventional hybrid laminar flow system. However, more research is required to understand the viability of such approaches both in terms of the fundamental flow physics of how the transition can be delayed and the resultant control system requirements.

### **2.5.5. Micro Sized Roughness**

The micron sized roughness concept or periodic discrete roughness elements can control stationary cross flow vortices. The idea is to create an artificial surface roughness which introduces a wave with a weakly growing wavelength, which generates a modified mean flow which is stable for all wavelengths greater than the weakly growing wavelength. Transition is caused by the growth and break down of disturbances. Disturbances with different wave numbers grow at different rates. The idea is to generate disturbances with a certain wavelength (killer) to modify the boundary layer to damp the most dangerous disturbances (target) (Saric and Reed, 2002). The killer wavelength distance is generated by micron sized roughness elements close to and parallel to the leading edge at a chord wise position corresponding to the critical point that is close to the attachment line (Arnal and Archambaud, 2008).

For particular values of the killer wavelength and for particular pressure gradients (which should be optimised), the artificial vortices interact non-linearly (randomly) with the natural vortices and with the mean flow field in such a way that the amplitude of the natural vortices is strongly reduced through the distortion of the mean flow field. If at the same time the amplitude of the artificial vortices remains below some critical threshold transition is delayed (Arnal and Archambaud, 2008).

One of the difficulties with this concept is to find a killer wave that only reduces the target. The killer wave affects different wavelengths and there is a risk that the energy is put into another mode that causes early transition. It is important to choose a killer wave that grows rapidly in the beginning and decays further back on the wing. Otherwise it could cause transition on its own (Martin Bystrom, 2006).

This concept was developed by W.S Saric and his team at Arizona State University (A.S.U) and validated by experiments carried out on a swept wing in a subsonic wind tunnel can be found in William and Ruben Jr, (1998), Arnal and Archambaud, (2008).

The efficiency of this passive control system was first demonstrated in subsonic wind tunnels at A.S.U (William and Ruben Jr, 1998). More recent investigations extended this work to supersonic conditions (Saric and Reed, 2003), (Saric and Reed, 2002) and (Saric et al., 2008).

it is possible to determine the optimum value of the killer wave from nonlinear Parabolised Stability Equation (PSE) computations. It has been demonstrated that two conditions need to be fulfilled for a successful application of this control system (Arnal and Archambaud, 2008):

- The uncontrolled transition of the total growth rate of the most unstable disturbances ( $N$  factor) for stationary vortices must be large enough (around 10) to be sure that these vortices dominate the transition process.
- The total growth rate of the most unstable disturbances ( $N$  factor) curves for the killer mode must exhibit a maximum upstream of the natural transition location, with a value around 6.

When these conditions are fulfilled, nonlinear Parabolised Stability Equation (PSE) computations show that increasing the initial amplitude of the killer mode can delay the appearance of the numerical transition. Basically, the beginning of the nonlinear saturation and the point where the computation breaks down move downstream. Another important result is that there are no good and bad pressure gradients which means a given pressure gradient can be convenient or not, depending on the Reynolds number.

The determination of the roughness height remains a key issue, Piot et al., (2007), using direct numerical simulation of the flow around a swept cylinder using micro-roughness arrays, showed that a roughness element of height which is equal to  $1/10^{\text{th}}$  of the boundary layer thickness generates vortices with an initial amplitude around  $10^{-3} U_e$ . This is the order of magnitude of the most appropriate values of the killer initial amplitude determined from the non-linear analyses (Arnal and Archambaud, 2008).

Saric et al., (2011) showed that the Micro sized roughness could increase the laminar region from 30% to 60% of the chord at a Reynolds number  $8.1 \times 10^6$  sweep angle of 30 degrees and velocity of 92 m/s which corresponds to Mach 0.28. The experiment was performed on the Swept Wing in Flight Tests (SWIFT), mounted on a Cessna O-2A Sky master at the Texas A&M Flight Research Laboratory (see Fig. 30).



**Fig. 30: Swept wing in flight tests (SWIFT) (Saric et al., 2011)**

The design resulted in a pressure minimum between 0.7 to 0.8 chord position, making the boundary layer subcritical to TS instability whilst disrupting the cross-flow waves. The nose radius region of the wing was restricted to an attachment-line Reynolds number less than 100, making an attachment-line subcritical to instabilities and contamination. Finally, the coefficient of pressure distribution was optimized by cross flow control. The computation was performed using the Navier–Stokes equations solver for the calculations of the coefficient of pressure and boundary layer, Orr–Sommerfeld was used for stability analysis and Parabolised Navier–Stokes equations for the final assessment (Haynes and Reed, 2000). The stability calculations performed verified that a 4.5 mm wavelength was very unstable and that using a killer value of 2.25 mm was the candidate to control cross flow. Two layers of Micro sized roughness were placed at 1% of the chord on the inboard pressure row (tapping), and 1.3% of the chord on the outboard pressure row (tapping). The Micro sized roughness had 2.25 mm spacing, 1 mm of diameter was 30 microns high. For this configuration, the transition of the chord moves from 30% to 60% (Fig. 31).

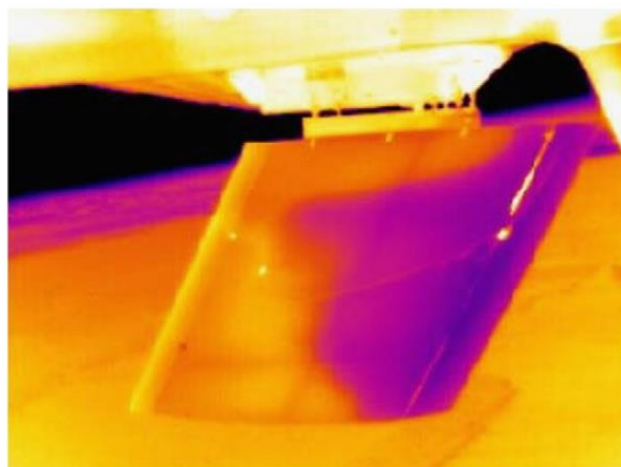


**Fig. 31: Flight measurements carried by W. Saric (2011) with painted LE et DRE concept**

Sui-Han et al., (2010) carried out experiments by using two different wind tunnels (A low turbulence wind tunnel and a NF-3 Wind tunnel) at the North-western Polytechnic University (NPU), the purpose was to investigate cross flow instability and the transition control technique on swept wings. The low turbulence wind tunnel was used to provide an ideal situation to investigate the stationary cross flow instabilities while the NF-3 wind tunnel was used as it offers a higher Reynolds number for the experiment to study the transition control technique. Both wind tunnels were open circuit wind tunnels. In order to provide an isolated situation for the cross-flow instability investigation, the NLF (2)-0145 aerofoil with a 45 degrees sweep was selected for the experiment. They used two models for the experiment, one which had two rows of pressure taps and the other had a high polish mode. The 3-D artificial roughness in the experiment was applied for the introduction of cross-flow disturbance; a sublimation technique was used for flow visualisation, and for this experiment Naphthalene acetone spray was used.

The experiments were conducted at an angle of attack of - 4 degrees, Reynolds number  $1.65 \times 10^6$ ,  $1.10 \times 10^6$  and  $1.38 \times 10^6$  for the low turbulence wind tunnel, with Reynolds number  $1.38 \times 10^6$  and  $2.20 \times 10^6$  for the NF-3 Wind tunnel experiment (see Fig. 32). For the experimental investigation in the low turbulence wind tunnel, straight transition lines behind the minimum pressure point which are dominated by TS instabilities appeared on the model without artificial roughness in the Reynolds number range of  $5.50 \times 10^5 - 1.65 \times 10^6$ . It was discovered that when the Reynolds number exceeded  $1.38 \times 10^6$  the traces of the most amplified stationary cross-flow waves were detected. For the experiment conducted in the NF-3 wind tunnel, the favourable pressure gradient was stronger at the same angle of attack as the low turbulence wind tunnel.

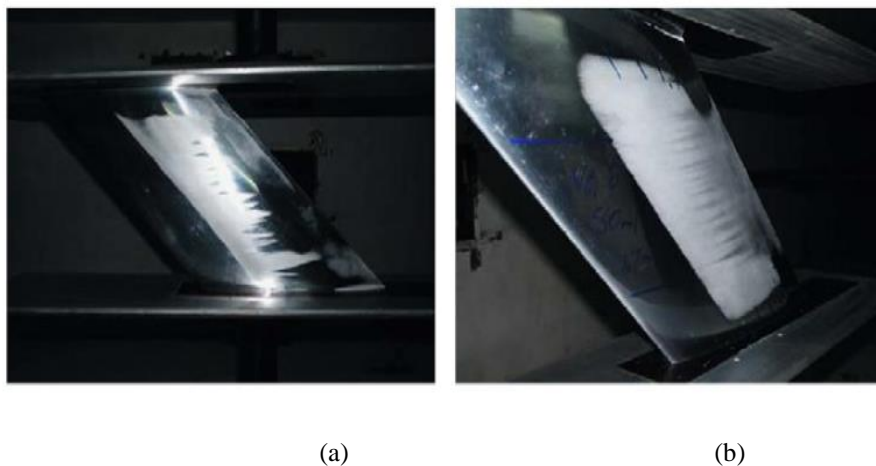


**Fig. 32: Visualization of Boundary Layer transition for the NLF (2) -0415 Aerofoil at  $Re=2.2$  Million. (a) uncontrolled and (b) controlled (Sui-Han et al., 2010)**

From the Fig. 32 it can be observed that in the region downstream of the roughness on the wing, the transition was suppressed effectively until the trailing edge region. More details on the experiment can be found in (Sui-Han et al., 2010).

### **2.5.6. Localized heating**

Transition control on a wing is possible by adopting a localized surface heating technique (in air). The principle is for the wall to be heated over a short distance in the chord-wise direction (stream-wise), and a relaxation region develops downstream of the heating strip. In the relaxation region, the boundary layer temperature close to the wall is larger than the wall temperature, so that the boundary layer sees or meets a cold wall. Based on the linear stability theory, this leads to a decrease in the unstable disturbance growth rates.

Laminar flow control can also be achieved by heat transfer and plasma actuation. In the past, controlling the temperature of the wing skin was found to be relatively inefficient. However, with the use of micro fabricated films and sensors, it may be possible to control the heat transfer using relatively small amounts of energy which could make this method more interesting. The HISAC project considered this new approach and showed that such a concept could be applied to nacelles in the future (A. Abbas, 2012).

### **2.5.7. Plasma Actuation**

Plasma actuation is a method of introducing perturbations for low speed flow control. Kurz et al., (2013) classified these actuators into two groups, depending on the kind of plasma that is generated:

- Non-thermal plasma
- Thermal plasma

Thermal plasma actuators are based on the generation of an equilibrium discharge, in order to locally increase the pressure and the temperature of the surrounding gas, for example, plasma synthetic jet actuators which generate a spark discharge inside a small cavity having a pin hole exit at the wall. The pressure increase inside this cavity induces a wall normal jet which acts on the boundary layer as a vortex generator. These actuators have shown promising results in controlling several academic aerodynamic configurations, such as compressible jets or incompressible separated boundary layers (Caruana et al., 2009), (Hardy et al., 2010).

Non-thermal plasma actuators such as Dielectric Barrier Discharge (DBD) are based on the generation of a non-equilibrium surface discharge, which induces a body force parallel to the wall called ionic wind inside the boundary layer. This kind of actuator has been investigated and has shown an ability to control airflows around different kinds of bodies such as aerofoils.

Kurz et al., (2013) carried out experimental and numerical investigations dealing with 2D boundary layer transition control on an Onera-D aerofoil using Dielectric Barrier Discharge actuators. The aim of the study was to show the ability of a DBD plasma actuator to delay transition on an aerofoil by means of either steady or unsteady actuation. This is because the actuator is able to induce either continuous or unsteady momentum adding to the boundary layer depending on the electrical parameters of the high voltage signal. These actuators generate a non-thermal surface discharge, which induces a momentum which is added tangentially and close to the wall. In this case, the ability of this kind of plasma actuator to delay transition has been assessed using both steady and unsteady modes of actuation. Wind tunnel investigations are conducted, as well as linear stability analyses to study the effect of a steady operated DBD actuator on boundary-layer stabilisation. A two-dimensional model based on an Onera D symmetric profile, having a chord length of 0.35m, is mounted horizontally in the test section of the wind tunnel. The angle of attack can be adjusted between  $-8^{\circ}$  to  $+3^{\circ}$ , to permit the modification of the pressure gradient and thus the natural transition location. The model was equipped with 15 pressure taps on the upper side. The DBD plasma actuator adopted for the experiment is made up of a 5mm thick dielectric layer as shown in Fig. 33 and Fig. 34, made of Lab850 material, placed at the leading-edge region and placed to match the shape of model. The model is mounted to allow it to be outfitted with the desired number of DBD actuators, adhering electrodes asymmetrically on both sides of the dielectric material. e.g. Fig. 34 shows the one single DBD actuator located at 10 % chord, downstream edge of the air exposed electrodes. The electrodes are 30 cm-long in the span-wise direction and made of copper tape. The air-exposed electrodes are connected to a TREK power amplifier (model 30/20,  $\pm 30$  kV, 20 mA peak) and supplied with high AC voltage, while other electrodes are grounded. Moreover, these air-exposed electrodes were polished, in order to reduce their thickness down to 0.05 mm to prevent them from promoting transition. This value is one order of magnitude lower than the displacement thickness of the boundary layer measured at the 10 % chord in the two following experiments. Hot wire anemometry (Dantec Streamline, 90C10 CTA modules, 55P15 probes) has been employed for boundary-layer explorations. The boundary layer transition delay was investigated experimentally using one single DBD actuator located at the 10% chord and operated continuously. The angle of attack of the model was set to 2.5 degrees and the experiment was performed for two different free stream velocities of 7 m/s and 12 m/s. The plasma actuator

was supplied with an high AC voltage having three different amplitudes 8.5, 12 and 17kV and an operating frequency set to 2kHz. The maximum velocity of the ionic wind induced by the actuator in quiescent air was about 4.5 m/s at the highest voltage amplitude. Velocity fluctuations are computed from boundary-layer explorations along the chord, moving the hot-wire probe at a constant distance from the wall, with and without control. The location of the transition is deduced from the fluctuation increase. The natural transition is located at the 40 % chord for air velocity 7 m/s and at the 26 % chord for air velocity of 12 m/s. In all cases, the ignition of the plasma actuator was repeated to lead to a transition delay. The transition was shifted progressively downstream when the amplitude of the voltage is increased, since the mechanical effect of the actuator (ionic wind) increases.

The results show a maximum transition delay of about 66% of the chord for studied air velocities. On the other hand, an experiment has been performed using the unsteady force produced by the DBD actuator, to achieve Active Wave Cancellation in a direct frequency mode. With the help of a closed loop control system, a significant transition delay has been achieved by damping artificially introduced TS waves for air velocities up to 20 m/s.

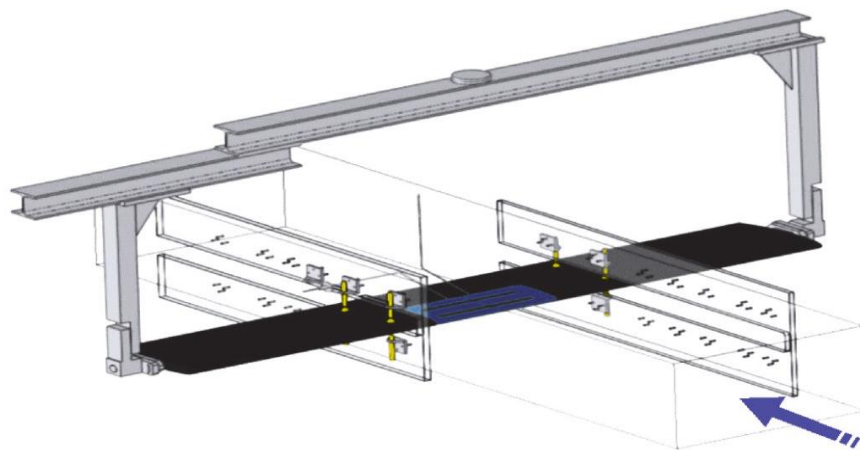


**Fig. 33: Two-dimensional model of the Onera-D aerofoil mounted inside the wind tunnel (Kurz et al., 2013)**

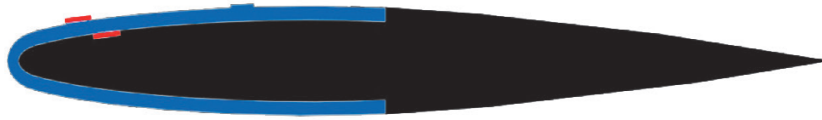


**Fig. 34: Cross-sectional view of the Onera-D wing model equipped with one DBD actuator ((Kurz et al., 2013)**

The maximum transition delays recorded during this experiment were 35 % of the chord for air velocity 7 m/s and 20 % of the chord for  $U$  a freestream speed of 12 m/s.

### **2.5.8. Polishing of Surface**

Polishing the leading edge is another way to extend the laminar flow region on an aircraft wing. Test flights conducted by the Texas A & M Flight research laboratory on a Cessna O-2A Sky master showed 80% laminar flow at Reynolds Number of  $8 \times 10^6$ , wing sweep angle of 30 degrees, obtaining the total growth rate of the most unstable disturbances (N factor)  $> 16$ . The advantage was that it was necessary to polish only 10% of the chord to be efficient. However, typical of flight conditions, adequate evaluation requires very low free-stream turbulence, which makes it impossible to calibrate in wind tunnel testing. Other disadvantages are associated with the manufacturing process such as the necessity to use harder surfaces to reduce roughness or the use of leading edge Krueger flaps to protect during landing and take-off (Abbas et al., 2013).

### **2.5.9. Wave Cancellation**

Active control of TS waves could allow the laminar flow to extend in difficult conditions (adverse pressure gradient, at high Reynolds numbers) to achieve aircraft drag reduction (see Fig. 35). Active control can be used to cancel growing linear fluctuations based on the wave superposition principle. This requires;

- The detection of the frequencies, orientations and phase angles of the dominant waves (Natural waves) with a reference sensor.

- Introduction of out-of-phase (artificial) disturbances that cancel the initial waves by simple linear superposition. It involves the monitoring of results with an error sensor which allows the control to be adapted.

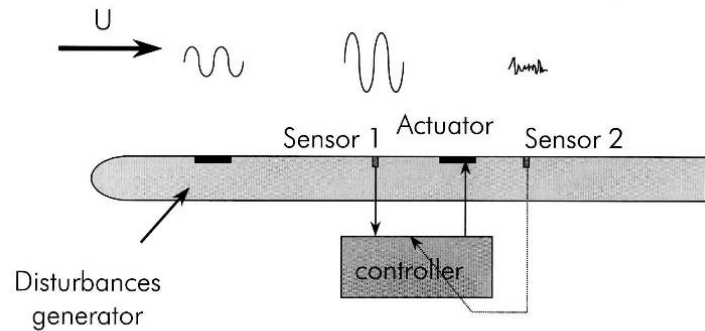


**Fig. 35: Active control principle (Arnal and Archambaud, 2008)**

Experiments on transition active control have been performed on 2D bodies at low speed with transition dominated by TS waves. Two TS waves generators are often used; the first one creates disturbances playing the role of “natural” TS waves; the second one (actuator) is placed some distance downstream and creates “artificial” waves. The frequency, the amplitude and the phase of the latter waves are optimised through an open or closed loop system in order to obtain the best cancelling effect as shown in Fig. 35.

Engert and Nitsche, (2008) conducted an experiment on Active wave cancellation in the TU Berlin transonic wind tunnel using a modified un-swept NACA 0004 wing section at Mach numbers ranging from 0.2 to 0.4. The principle approach for active wave cancellation that has been adapted in TU Berlin is shown in Fig. 36.

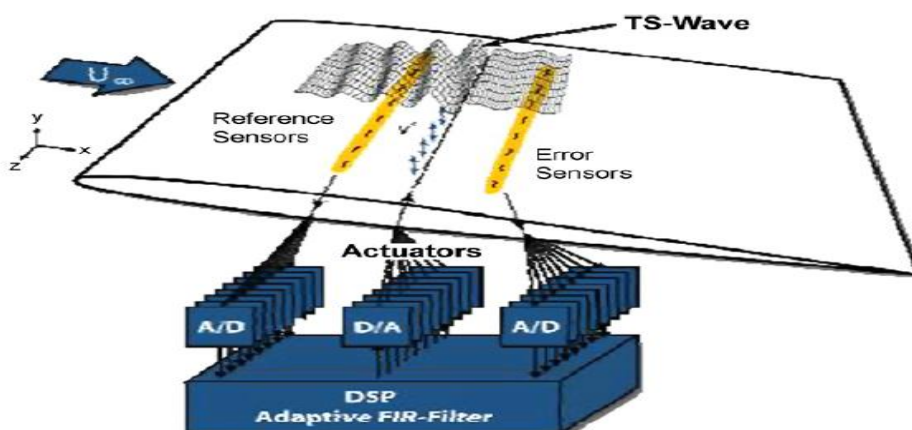


**Fig. 36: Principle of an active wave control system (TU Berlin) (Engert and Nitsche, 2008)**

The convective TS wave is detected by a reference sensor upstream of the actuator. The actuator signal to excite the cancelling wave is generated by applying an adaptive transfer function (adaptive digital filter) to the disturbance signal of the reference sensor. The filter is adapted to minimize the signal power of the error sensor located downstream. It is well known that a complete cancellation of TS instabilities is impossible but reducing the impact it has on the flow is possible. This is because of technical limits due to the signal to noise ratio of the sensors, non-linear characteristics of the actuator or weak non linearities of the TS waves between the reference and error sensor (Engert and Nitsche, 2008). Therefore, a multiple channel system in the span wise and the flow direction should be implemented (Engert and Nitsche, 2008). The experiment was conducted in a low turbulence wind tunnel. Adjustable top and bottom fibre-glass walls of the test section can be individually deflected by 13 computer-controlled servo-motors. This allows artificial/controlled pressure gradients along the wing profile to be introduced in order stabilise or destabilise the natural transition process. The un-swept test wing has a modified NACA 0004 profile at the leading edge. At the maximum thickness of 30mm the NACA nose is tangentially extended with a flat plate and ends with a flap at the trailing edge (chord 750mm) as shown in . The highly polished aluminium profile is equipped with a rectangular opening located between the 0.1% to 0.6% chord from the model's leading edge for the installation of different sensor-actuator arrangements depending on the experimental configuration. The pressure distribution is instantaneously measured by 18 equidistantly arranged pressure orifices in the flow direction. The model was horizontally fixed 5mm below the centre of the two-dimensional adaptive test section to reduce blockage effects on the model's sensor side at higher Mach numbers. One plate inserts (Fig. 38 b) consists of an array of surface hot wires (SHW) which are symmetrically aligned to the centre line span-wise (three rows,  $Dz = 15\text{mm}$  spacing) and stream-wise ( $0.12-x/c- 0.57$ ,  $Dx = 10\text{mm}$  spacing) directions. By means of this 'baseline configuration, the general development of TS waves up to Mach 0.4 was investigated.

The sensors used were surface hot-wire, the actuator was a voice-coil driven membrane actuator Fig. 38. Finally, an FxLMS closed-loop control model (Filtered-x least mean square) which is a real-time filter model, based on the least mean square (LMS) algorithm autonomously adapted a transfer function for the adaptive path between the reference sensor and the actuator in real time. The adaptive controller achieves a powerful cancellation of naturally occurring 2-D TS instabilities on an un-swept wing. It enables a local TS amplitude reduction of about 90% on the error-sensor (Engert and Nitsche, 2008).

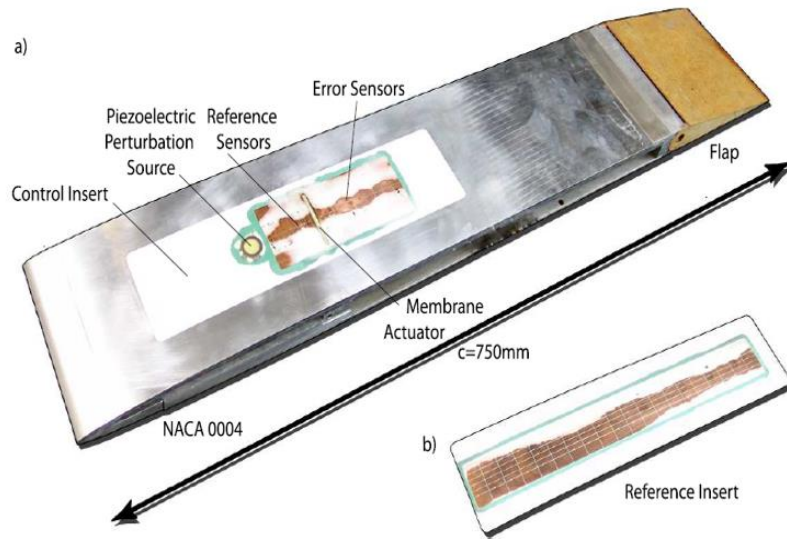


**Fig. 37: Generic wing model with a) control - and b) reference insert (Engert and Nitsche, 2008)**

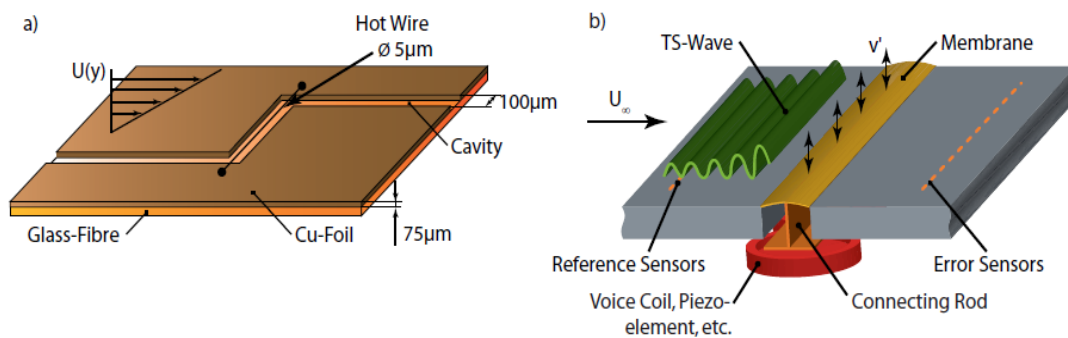


**Fig. 38: Principle of a) surface hot wire and b) membrane actuator (Engert and Nitsche, 2008)**

Erdmann et al., (2011) compiled a report on the work they have done on drag reduction on aerofoils by means of active control of Tollmien–Schlichting (TS) waves. Wind-tunnel experiments at Mach numbers of up to  $M = 0.42$  and model Reynolds numbers of up to  $Re = 2 \times 10^6$ , as well as in-flight experiments on a wing glove (see Fig. 39) at a Reynolds number of  $Re = 2.4 \times 10^6$ , flight velocities ranging from 20 to 27  $m/s$  were presented in the report. Surface hot wires were used to detect the linearly growing TS waves in the transitional boundary layer. Different types of voice-coil and piezo-driven membrane actuators, as well as active-wall actuators, located between the reference and error sensors, were demonstrated to be effective in introducing counter waves into the boundary layer to cancel the travelling TS waves. A control algorithm based on the filtered-x least mean square (FxLMS) approach was employed for inflight and high-speed wind-tunnel experiments. A model-predictive control algorithm was tested in low-speed experiments on an active-wall actuator system. For the in-flight experiments, a reduction of up to 12 dB (75% TS amplitude) was accomplished in the TS frequency range between 200 and

600 Hz. A significant reduction of up to 20 dB (90% TS amplitude) in the flow disturbance amplitude was achieved in high-speed wind-tunnel experiments in the fundamental TS frequency range between 3 and 8 kHz. A downstream shift of the laminar–turbulent transition of up to seven TS wavelengths was presented. The cascaded sensor–actuator arrangement given by Sturzebecher and Nitsche., (2003) for low speed wind-tunnel experiments was able to shift the transition 18% chord downstream by a TS amplitude reduction of 96 per cent (30 dB). By using an active-wall actuator, which is much shorter than the cascaded system, a transition delay of seven TS wavelengths (16 dB TS amplitude reduction) was reached. More detailed results can be found in Erdmann et al., (2011).



**Fig. 39: Grob G103 with glove and sensor actuator arrangement (Erdmann et al., 2011)**

In 2D flows, the wave cancellation concept can also be used by exploiting the results of receptivity theories. Let us consider a flat plate with a blunt leading edge, placed in a subsonic wind tunnel. A thin 2D roughness element is attached to the surface some distance downstream of the junction between the leading edge and the flat plate. According to the results of the receptivity theories, this set-up generates two series of TS waves, one in the leading-edge region (leading edge receptivity) and the other around the roughness element (localised receptivity). A coupling of the different waves initiated by these mechanisms takes place around the roughness. If the disturbance amplitudes are small, the coupling is in the form of linear superposition which gives rise to destructive or constructive interference. This concept of wave cancellation was tested successfully by Kosorygin et al., (1995). A destructive interference was observed for a proper choice of roughness height and position. It is clear that this passive control technique is far from suitable for practical applications. However, such experiments are of great interest to validate receptivity theories.

## 2.6. Turbulent Skin Friction Reduction

The skin friction drag due to turbulence remains, even after the successful application of Laminar flow control. Skin friction drag due to turbulence can be reduced with the use of passive boundary layer manipulators. Among the various devices, V-groove Riblets have demonstrated substantial reductions of up to 8% of the local skin friction (Coustols and Schmitt, 1990). Work done on some of these devices such as Riblets, dimples or surface actuation that aims to reduce the drag caused by turbulent effects and other new concepts will now be discussed.

### 2.6.1. Riblets

Riblets are small surface protrusions, aligned with the direction of flow, which offer an anisotropic roughness to a surface. They are part of the few techniques that have been successfully applied both in laboratories and on full aerodynamics configurations to reduce turbulent skin friction drag. They could be classified as a mature technology which can reduce skin friction drag caused by turbulence.

An experimental verification in a large T2- transonic cryogenic wind tunnel at ONERA was conducted in 1988. Coustols and Schmitt, (1990) conducted test on a 1/11<sup>th</sup> scale model of an Airbus A320. For the test, 2/3 of the wetted model surface was covered with the Riblets for which a V-grooved cross-section was selected. Viscous flow computations on the wing and on the fuselage showed that Riblets depth of 0.023mm can allow an average value of  $h^+ = 8$  to be obtained, this data was used based on the generated data obtained from 3-M riblets which showed optimum drag reduction occurs when  $h^+ = hu^+/\nu$  is in the range of 8 -15 (Walsh, 1990). The Wind tunnel test was successful and total drag reductions up to 1.6% have been demonstrated at corresponding cruise Mach number conditions. The Flight test was prepared with the Airbus A320 No 1. 600 m<sup>2</sup> Riblets film covering 75% of the wetted surface installed on the aircraft and the test was carried out in 1989. Overall performance and local data were measured with and without the Riblets and drag reduction predictions based on the wind tunnel tests were confirmed. Earlier work on Riblets (Bruse et al., 1993), (Walsh and Lindemann, 1984) at low speed which focused on Riblets geometry optimisation reported a drag reduction up to 10%.

Operational aspects and maintenance problems (Robert, 1992) have then been investigated and in-service applications have been decided upon by Cathay Pacific Airways on an A340. Significant reduction in fuel consumption has been reported. However, this in-service application showed that the Riblets film has to be replaced after 2-3 years. The applications of this technology depend now on the quality improvement of the Riblets

film. The characteristics of the film should be maintained for at least for 5 years to obtain benefits. The current development of Riblets is in line with a better understanding of the physics and the application of surface technologies such as the aerodynamic evaluation of Riblets material for turbulent skin friction drag reduction.

Recent analyses of the status of these devices can be found in Bushnell, (2003) and Choi, (2000). The physical mechanism of the Riblets drag reduction effect is caused by a protrusion height between the virtual origin seen by the stream-wise shear flow and some mean surface location. This offset would result in a greater separation between the wall and the turbulent stream-wise vortices, hereby reducing the exchange of momentum at the wall (Jiménez, 1994), (Bechert and Bartenwerfer, 1989). The correct explanation for the underlying physics is still yet to be fully understood and remains a topic of debate and discussion.

García-Mayoral and Jiménez, (2011) found that the groove cross section  $A_g^+$ , expressed in wall units, was a better characterization of this breakdown than the Riblets spacing, with an optimum  $(A_g^+)^{1/2} = 11$  (see Fig. 40). However, the drag reduction was affected greatly by the Riblets spacing and size or orientation which, in some cases, could produce a drag increase. Other non-aerodynamic issues were maintenance of Riblets shape and adhesive over operational life (hydraulic fluid, dirt, deformation by hail and maintenance), visual appearance, and time required to install, remove and re-apply Riblets.

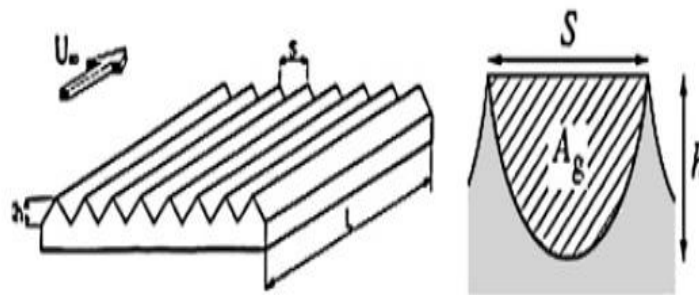


**Fig. 40: Typical Riblets geometry (García-Mayoral and Jiménez, 2011)**

### 2.6.2. Dimples

Dimples are regular arrangement of surface depressions distributed along the wall. Dimples are a well known measure to increase the heat transfer from a wall (Case et al., 2011).

Russian scientists Alekseev et al., (1998) discovered that apart from heat-transfer enhancement, dimples might be useful for drag reduction. This finding is based on experimental measurements of turbulent flows over surfaces with a regular arrangement of shallow dimples leading to a decrease of the skin-friction drag of a turbulent flow up to 20%. (Note that this is not the “golf ball” effect!) (Lienhart et al., 2008).

Dimples can be used for drag reduction, when compared to Riblets they have advantages since they are composed of microscopic structures which are less sensitive to dirt and mechanical degradation. Furthermore, their effectiveness should not depend on the flow direction. Since, the drag reduction promised by the use of dimples would have a tremendous economic influence. Lienhart et al., (2010), conducted an experimental investigation as well as direct numerical simulations of the turbulent flow inside a channel with dimpled walls in order to investigate the physical mechanism. Based on what was reported from the experiment, success was not achieved as no significant difference was observed between the configurations with dimples and without dimples.

## **2.7. New Technologies for Turbulent skin friction drag reduction**

### **2.7.1. Smart Surfaces**

This is a new concept which was proposed by Zheng and Yan, (2010). It consists of using a composite surface that combines riblets with an elastic coating which acts as the base and the elastic layer respectively. This concept was Inspired by the self-adjustable skin of marine animals such as sharks and dolphins. it is designed to modify the traditional Riblets technique and enable it to sense and interact with the flow by adjusting the wall structure accordingly to the fluid flow condition.

A trapezoidal Riblets surface is used as the base of the smart surface configuration as it shows good durability and easy manufacturing implementation. It also allows crack inspections through the flat valley when the elastic coating is transparent (Zheng and Yan, 2010) (see Fig. 41 and Fig. 42) for configuration.

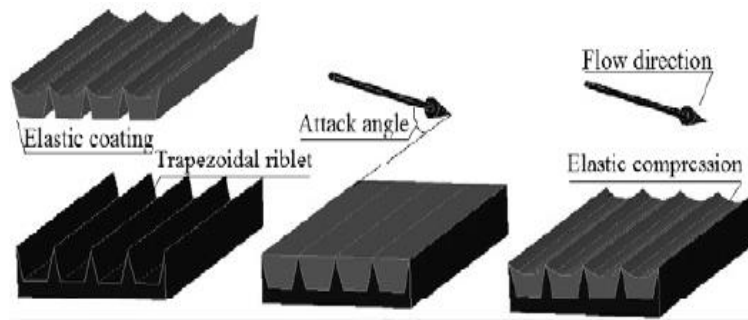


**Fig. 41: Structure of “smart surface”, (a) the components (b) Before compressed, (c) After Compressed (Zheng and Yan, 2010)**

Before compression of the surface takes place, the surface keeps the smooth contour which is beneficial for maintaining laminar flow drag at a low level. When the flow becomes turbulent, the drag on the smooth surface will be increased to a higher level compared to laminar flow. In this case, the “smart surface” adjusts its surface according to the flow velocity to keep itself in a condition which enables a more effective drag reduction in a wider flow range. The self-adjusting is not an abrupt event but a gradual change. The key issue is to make sure the extent of self-adjustment meets the requirement of effective drag reduction. Either premature or overdue adjustment would increase the flow drag oppositely if it is not designed appropriately.

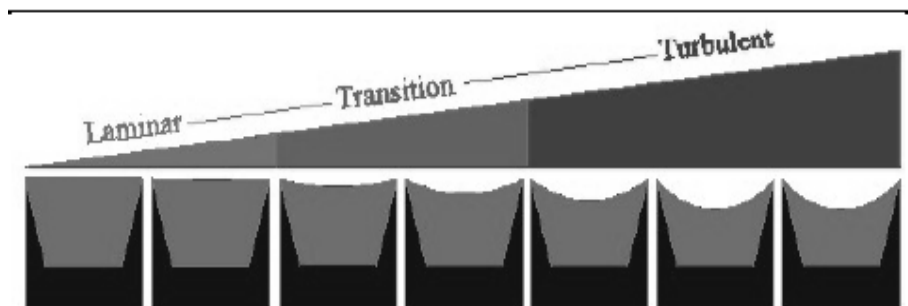


**Fig. 42: Compressions under different flow regimes (Zheng and Yan, 2010)**

The attack angle of flow and the material of the elastic layer determine the sensibility of smart surface. The way these interact needs to be understood. Further experimental and numerical research work is required to verify the validity of the smart surface approach. The concept was tested on a test shuttle in a water channel by Zheng and Yan, (2010) taking into consideration for the investigation the spacing and height of the trapezoidal Riblets which were coated with a smart surface, drag reduction and characteristics of the shear stress were reported. More studies into the compression mechanisms of elastic coating, other flow separation and self-adjustable design could be carried out.

## 2.7.2. Flexible Composite Surface Deturbulator

Inspired by the electrically powered Active Flexible Wall Transducer from Sinha, (1999). Sinha and Ravande, (2006) patented the concept of the flexible composite deturbulator (see Fig. 43).

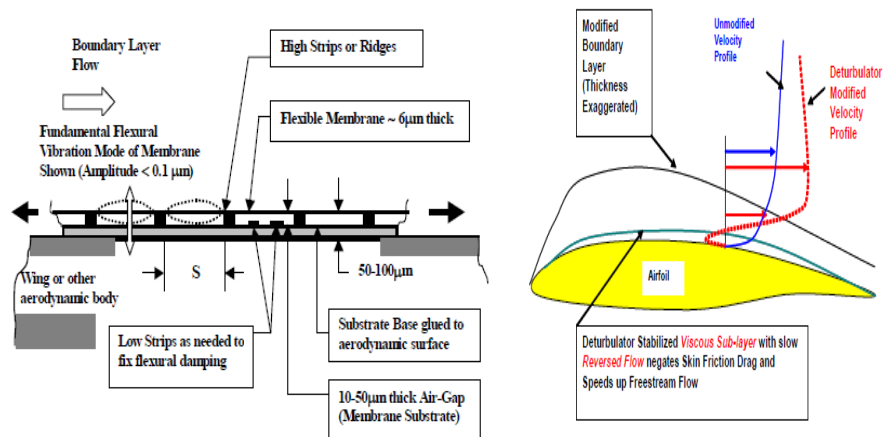


**Fig. 43: Schematic of the SINHA Flexible composite surface (FCSD) (Sinha and Ravande, 2006)**

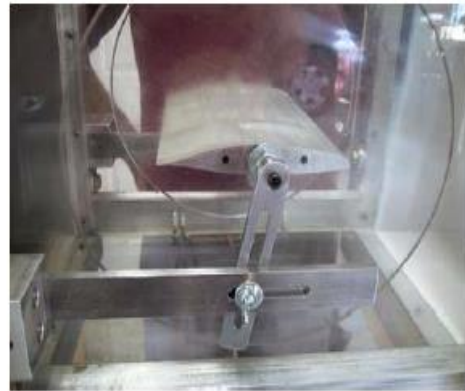
The FCSD is a micro structured compliant wall and the interaction of compliant walls (Sinha, 2008) with zero pressure gradient laminar, transitional and turbulent boundary layers is well documented in Bushnell et al., (1977) and Carpenter et al., (2001). The stand out characteristics of the FCSD approach is that it relies on reducing the overall aerodynamic drag by helping maintain a thin layer of separated flow near the surface by attenuating turbulent mixing in the shear layers (Sinha and Ravande, 2006), (see Fig. 43) for schematics of the concept. The presence of a changing pressure gradient in the chord wise direction which notably occurs in aerofoils and streamlined aerodynamics objects, was reported to be essential for this phenomenon. In this concept, the FCSD helps maintain a laminar separation bubble-like flow structure, except that it is stretched over a larger extent of the chord (Sinha and Ravande, 2006). In this way, the bubble behaves like a slip-layer to the external flow and can eliminate skin-friction drag. In practice, FCSD modification of boundary layer flows significantly lowers the skin friction coefficient as evidenced by a speed up of the external inviscid flow (Sinha and Ravande, 2006). This can help increase circulation and lift generation similar to Liebeck High-lift aerofoils (Liebeck, 1973). However, such aerofoils require close control of transition. The FCSD makes transition control less critical, thereby extending the low drag conditions in larger ranges of flight conditions.

Sinha and Ravande, (2006) conducted an investigation on flow modifications resulting from integrating the FCSD with existing low-drag aerofoils which rely on maintaining laminar flow over an extended region of the chord. The NLF-0414F aerofoil which was developed by NASA was selected for the test since an all composite single engine trainer, the Global GT-311, was available for testing which incorporated this aerofoil. However, at low Reynolds numbers which can be associated with long-endurance UAVs, the ability to improve lift to drag ratios for this aerofoil was also important. Hence, a low speed wind-tunnel was used for the low Reynolds number tests with flight tests on the GT-3 for the investigation on higher Reynolds numbers.

A 0.127m chord electro-discharge wire cut from aluminium to form aerofoil was customarily made as shown in Fig. 44 (b). All wind tunnel investigations were carried out in a low speed tunnel (see Fig. 44 (b)). The surface of the wing model was polished with 1000 grit emory paper. The wing model had a span of 0.197m and was supported in the wind tunnel between two Plexiglas end plates to restrict the corner vortices. The flow in the middle 0.100m span of the wing model was used for tests with measurements being conducted in the central vertical plane. A 5  $\mu\text{m}$  diameter hot wire probe incorporated with a 1 channel min CTA constant temperature anemometer was adopted to measure boundary layer velocities and turbulence levels. The tests were run at the maximum speed setting of the wind tunnel at Reynolds number  $0.3 \times 10^6$  and Mach 0.09 with the aerofoil set at angle of attack -1 degree.



(a)



(b)

**Fig. 44: (a) Sinha tech slow speed wind tunnel and (b) close up of tunnel section showing the NFL-0414F aerofoil (Sinha and Ravande, 2006).**

From the wind tunnel experiment, it was reported that the  $C_L$  value increased by 12% and the pressure drag coefficient decreased by about 45%, which surely proves that this technique is credible. A flight test was also conducted to verify the results obtained from the wind tunnel testing. The optimized FCSD has the potential of

reducing overall fuel consumption of large transport aircraft by at least 10% through retrofitting, resulting in similar reductions in fossil fuel usage and emissions of NO<sub>x</sub> and greenhouse gases. The enhancement of lift measurements obtained could make the complicated flap structure on a commercial aircraft simpler, thereby reducing the weight and drag of the aircraft. This along with reducing the profile drag and induced drag using the FCSD tape could make the existing aircraft highly fuel efficient (Sinha and Ravande, 2006). The FCSD concept was also adopted in Sinha, (2007) on the flight test of a Standard Circus sailplane which demonstrated an 18% improvement on the lift to drag ratio by treating 8% the upper surface of the wing aerodynamic chord with passive FCSD.

## **2.8. Separation control technologies**

Separated flows can appear in two different conditions. These are;

- The progressive boundary layer separation; e.g. The trailing edge separation which displaces progressively upstream when the angle of attack is increased
- The Localized boundary layer separation; e.g. Those generated by geometrical discontinuities.

### **2.8.1. MEMS**

Developments in advanced manufacturing technology have made possible the fabrication of Micro-Fabricated-Electro-Mechanical-Systems (MEMS) which has enabled sensors and actuators, having dimensions of a few hundreds of microns, to be integrated with controlling electronics. The reduction of boundary layer separation regions can be obtained by an active system (device) avoiding the drawbacks of conventional flow separation control technologies, which increase the coefficient of drag at low lift coefficient. The recent development of MEMS technologies can be used to control the flow through active manipulation of the coherent structures that are developed in the near wall region of the thin boundary layer that exist on the aerodynamic surfaces of aircraft and their propulsion systems (Reneaux, 2004), (Warsop et al., 2007).

MEMS is a new technology that has developed rapidly over the last decade. Its application to commercial products is only now becoming widespread with the advent of products such as ink-jet printer heads, and accelerometers and gyroscopes for automotive and aerospace applications. The application of MEMS for industrial boundary layer flow control is extremely novel. No other attempts to move this technology application to the proposed levels of industrial development at either a national or European level are known. The development of these

boundary layer flows around aerodynamic surfaces of aircraft and their propulsion systems directly affects the performance of the aircraft since these boundary layers give rise to the skin friction drag and flow separation, which leads to buffet and limits maximum achievable lift. MEMS technology offers, in the medium to long term, a means whereby these boundary layers can be actively controlled during certain phases of flight to achieve a performance benefit whilst not incurring penalties at other stages as is the case with more conventional passive flow control systems.

Application of MEMS technology have been investigated under the EU 4<sup>th</sup> frame work project AEROMEMS 1 & AEROMEMS 2. In AEROMEMS 1, (Warsop, 1999) a “basic research” study to assess the viability of applying MEMS for boundary layer control on aircraft was conducted. The project demonstrated that;

- MEMS can be used to delay boundary layer separation,
- MEMS actuators and sensors could meet the necessary full-scale requirement.
- Medium term applications are aircraft high lift systems, intakes and engine components.

As a result of these findings, the AEROMEMS 2 (Warsop, 2006) investigation was carried out to further develop the MEMS flow separation control technologies that were identified under the AEROMEMS project to the level of demonstrating the concepts in large, industrial-scale wind-tunnel experiments and undertaking complete industrial cost/benefit assessments and engineering integration studies. A further goal was the development and validation of the theoretical tools needed to treat flows with active MEMS-based control and to extrapolate the results obtained from large-scale wind tunnel tests to full-scale flight. Finally, it was proposed to further develop the current prototype MEMS flow sensor and actuator hardware towards the realisation of flight-worthy status. It was also proposed to improve the efficiency of the devices and to resolve issues concerning the packaging and interconnection of the devices with each other and with aircraft systems. The proposed concept comprised arrays of a sub-boundary layer device of pulsed air jet, micro jet nozzles which act as a vortex generator and is placed up stream of the expected region of flow separation. In operation the vortex generator produces vortices in the stream-wise direction in the middle region of the boundary layer. Using this approach has demonstrated some improvement in the shape factor as result leading to reduced flow separation capabilities (Warsop et al., 2007), (Stanislas and Godard, 2005). The configuration of the actuation concept used is shown in Fig. 45, and comprises an orifice that is placed at 45 degrees to the surface and skewed at 90 degrees to the local flow. The diameter of the of the micro jet nozzles (orifice) is between 5 – 15 % of the boundary layer thickness. Pressurised air is supplied to each orifice and its controlled by a valve that is mounted below each orifice making it independently controlled and been able to produce injected air based on the response from a command signal. Each of the

actuators is capable of exiting flow which is of the same order as the local free stream velocity. As suggested by Warsop et al., (2007) for the application of this concept to the trailing edge slat or leading edge of moderately large aircraft the required orifice should have a diameter of the order of  $200 - 400 \mu\text{m}$  with the upper values of the jet velocity of the order of  $200 - 300 \text{ m/s}$ . The actuation mechanism was optimised and details can be found in Godard and Stanislas, (2006b) with the optimised configuration obtained compared with performance data for an optimised passive vortex generator (Godard and Stanislas, 2006a) and an optimised slotted jet vortex generator (Godard et al., 2006). The results reported showed comparable performance in terms of the skin friction.

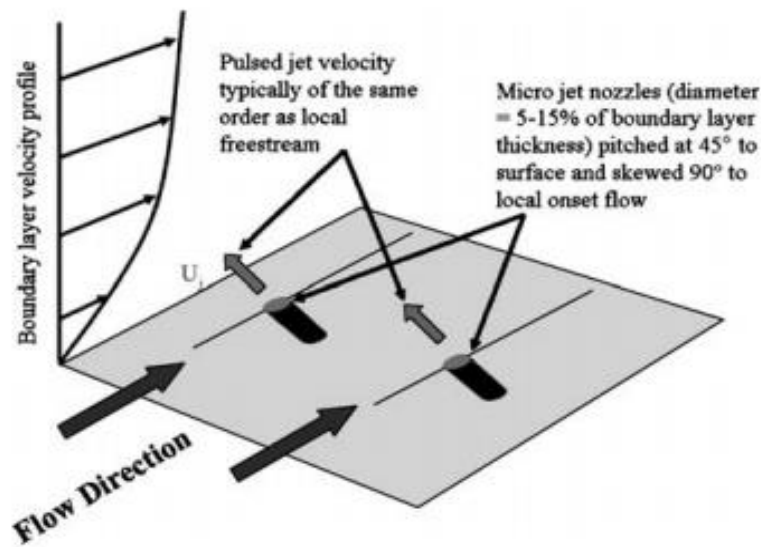


**Fig. 45: Schematic view of the proposed flow separation control actuation concept – AEROMEMS II project (Warsop et al., 2007)**

Warsop et al., (2007) described the design and validation of a micro-fabricated pulsed air-jet actuator for practical application to flow-separation control at full-scale operating conditions on a medium to large air vehicle. This was a high-authority, piezo-electrically driven MEMS micro-valve-operated pulse-jet actuator suitable for application to flow-separation control. Steady and unsteady CFD simulations using Fluent CFX coupled with analytical and finite-element structural modelling of the electromechanical behaviour of the device was used to validate the internal flow in the device. The design was reported to be capable of generating peak velocities up to  $300 \text{ m/s}$  and at frequencies up to  $500 \text{ Hz}$ , through an orifice with diameter  $200 \mu\text{m}$  which uses a voltage of  $90 \text{ V}$  at  $50 \text{ mW}$  power consumption level. Reported CFD results also showed that using such a configuration is dependent on the state of the internal flow within the micro-valves and the shaping of the flow entering the valve orifice, with a

suggested best configuration being a jet orifice normal to the aerodynamic surface as opposed to 45 degrees pitched nozzle which was used in the AEROMEMS II project. A planar MEMS-fabrication route for the device that enables the incorporation of high activity bulk piezoelectric materials with low-temperature (sub 200°C) processing techniques was developed and successfully demonstrated with the intension to patent. More details regarding the project can be found in Warsop et al., (2007).

More recently, Joseph et al., (2013) with the intension to extend this application of MEMS to the automotive industry performed a wind tunnel experiment using a bluff body equipped with micro jets made of full silicon electrostatic micro sized actuators. A drag reduction of 10% was reported with considerable modification to the wake vortices of the bluff body. Ho et al., (2003) extends the application of MEMS to Micro Air Vehicles (MAVs) as an active flow control, flow separation mechanism.

### **2.8.2. Vortex Generators**

Passive vortex generators are small aspect ratio aerofoils which are mounted normally to the lifting surfaces ahead of the flow separation point in the boundary layer in order to energise the boundary layer and to prevent flow separation at the lifting surfaces. Vortex generators and sub boundary-layer Vortex generators can be classified as Progressive boundary layer separation flow control actuators. A classical application of these devices is the control of low speed separated flows in adverse pressure gradients and supersonic shock-induced separation.

The most recent application of the sub boundary layer vortex generator is in the AWIATOR project (Bohannon, 2006), where the SBVGs were mounted on a flap upper surface so that they delay flap boundary layer separation only when the flap was deployed. When the flap is stowed, the SBVGs are contained in the cove region, under the shroud see Fig. 46. These SBVGs control the flap boundary layer by adding momentum to the boundary layer at the flap surface, by doing so SBVGs control the boundary layer separation.

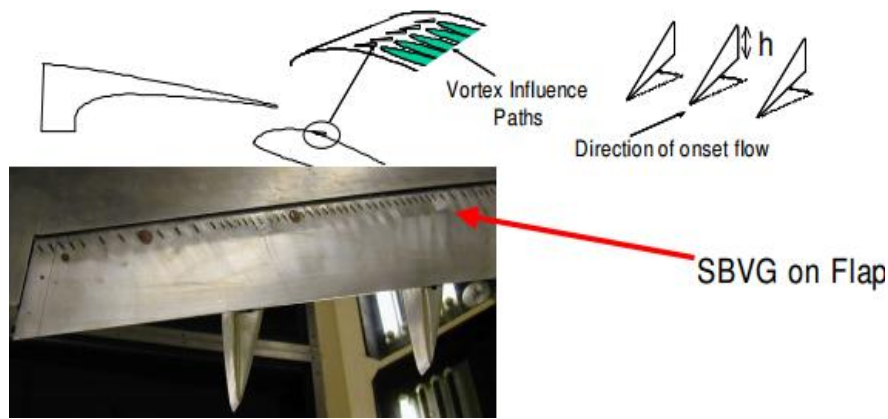


**Fig. 46 : SBVG on flap in the AWIATOR Project (Bohannon, 2006)**

The design was tested on an A340. Computational fluid dynamics analysis, wind tunnel testing and flight test validation were carried out to optimise the design. The optimised SBVG array significantly reduced the extent of boundary layer separation of the flap at an increased flap deflection of 35 degrees. The addition of the SBVGs to the flap at flap deflection angle of 35 degree increased the lift coefficient by up to 2.2% over a wide range of incidence angle when compared to the baseline configuration of flap deflection angle of 32 degrees without SBVGs. The effect of the SBVGs at a fixed deflection increased the lift coefficient  $C_L$  by 0.01 to 0.04 over part of the incidence range indicating as expected, that the vast majority of the lift increase is due to increase in flap angle. A trend of a small increase in drag of 4 counts ( $C_d = 0.0004$ ) in the take-off configuration is within the repeatability of the wind tunnel balance and therefore deemed not significant. Although stall occurred 0.3 degree early, the flight test confirmed the improvement in the behaviour of the flap at 35 degrees with an increment of  $C_L$  of approximately 2.5% at reference angle of attack.

## 2.9. Conclusion

This chapter focused on the literature review on drag reduction technologies and techniques. The purpose of this chapter was to give a comprehensive oversight on several induced drag reduction technologies with an extension and broader look on other aspect of drag reduction which included skin friction drag and flow separation, with the aim to identify areas for potential drag reduction.

Planar and non-planar wing configurations and devices have been discussed, as well as flow control technologies for the purpose of aerodynamic performance improvement. The potential benefits which these concepts offer have also been discussed by accessing performance merit criteria such as improvement in lift to drag ratio, drag reduction (skin friction and induced drag), laminar flow control and the mitigation of flow separation. The following areas shows potential areas for improvement.

The sail tips developed by J.J Spillman could be further investigated in terms of trying out different surfaces which could be investigated to find the optimum value for this configuration.

Further work is possible on the optimisation of shape of novel spiroid winglets, as this configuration shows more promise in drag reduction when compared to other wing tip devices which have already been tested or are currently in use. Optimisation could be achieved by using optimisation criteria to obtain various benefits such as increased operating range, improved take-off performance, higher operating altitudes, improved aircraft roll rates, less take off noise, shorter climb rates, increased cruise speed and reduced engine emissions. Also, it could meet gate clearance with minimal span and height as well as reduced separation distances and improved safety in take-off and landing operations due to weak vortex turbulence reduction. Drag reduction may be possibly up to 4% and includes possible drag reduction at take-off.

The C-Wing is another configuration that looks interesting as it remains a fascinating design concept although the design may possibly be found to be penalised by a significant parasite drag increment and considerable structural and aero-elastic complications. It also has many beneficial characteristics when applied to large aircraft or tailless design and the possibility of using such a configuration for a smaller aircraft is worth investigating to fully exploit its benefits.

The box-plane is aerodynamically and structurally complex and possibly expensive to develop into a fully efficient lifting system with some aero-elastic challenges. The low induced drag for a given wing span will have to be paid for by increased parasite drag and reduced maximum lift due to low chord Reynolds numbers and the presence of non- lifting vertical tip planes. Due to this reasons, (Torenbeek, 2013) suggested that due to the integrated character, the application of these types of aircraft concept might be impossible as it will require a major re-design of all the major components of the Aircraft.

Another area that might be worth investigating is the possibility of reducing excrescence drag but in order to do this, the appropriate technologies to accurately predict the magnitude of this type of drag will have to be enhanced.

Natural laminar flow control offers a considerable amount of skin friction drag reduction. Further work is required in to develop new wing concepts, which supports natural laminar flow control and to fully understand the underlying fundamental flow physics for this concept.

Hybrid Laminar Flow Control offers up to 15% of total aircraft drag reduction which is a very good amount when compared to other drag reduction techniques. The design of the suction surface and the chambers underneath the perforated skin represents one of the most significant engineering challenges concerning the implementation of Hybrid Laminar Flow Control and the current technique used has a weight penalty, cost and energy expenditure which often exceeds the benefits of using it. However, the application of MEMS technology and distributed roughness could yield greater benefits and are much lighter in weight and so, it might be worth investigating.

Flow separation control offers a means of reducing aircraft weight for the same level of performance. It has the potential in terms of improving the lift and control device effectiveness. Sub Boundary Layer Vortex Generators are already well known; however, the use of mass-less-jets may enable a more effective method of flow separation control.

The use of wing tip turbines as aircraft performance devices also provides an interesting concept which could be further investigated in terms of sensitivity studies on the effect of the nacelle and propeller position for aircraft drag and lift to drag ratio improvement. This concept could also be investigated on its practicality on aerodynamic performance improvement for UAVs and general commercial aircraft. Also, an extra source of power for systems.

After carefully reviewing the performance and practical application of the aircraft performance devices discussed so far, the wing tip turbine and novel spiroid wing tip concepts were selected to be further investigated in this project based on their performance in terms of reduction in the coefficient of drag, improvement in the coefficient of lift and improvement in lift-to-drag ratio. This has a direct impact on the range of an aircraft and on the general aerodynamic performance.

## Chapter 3: Computational Fluid Dynamics

In this chapter, the underlying principles and the CFD modelling approach employed throughout this study for the design and investigation of the proposed set of wing tip devices is discussed. Section 3.1 introduces CFD, Section 3.1.1 gives a brief history on CFD, Section 3.1.2 presents the application of Computational Fluid Dynamics as a drag prediction tool, Section 3.2.1. presents the governing equations, Section 3.2.2 reviews turbulence models, Section 3.2.3 depicts the Reynolds Average Navier Stokes Equations, Section 3.2.4 presents turbulence closure, Section 3.2.5. describes one equation turbulence models, Section 3.2.6 describes the two equation turbulence models in which Section 3.2.6.1 gives an overview of the standard  $k-\epsilon$  model, Section 3.2.6.2 gives an overview of the renormalization  $k-\epsilon$  model, Section 3.2.6.3 presents the realisable model, Section 3.2.6.4 gives an overview of the standard  $k-\omega$  model, Section 3.2.6.5 describes the shear stress transport model, Section 3.2.7 discusses near wall treatment, Section 3.2.7.1 discusses boundary the layer velocity profile, Section 3.2.8 describes mesh discretisation, Section 3.2.9 describes the finite volume method and Section 3.2.10 discusses mesh generation techniques.

### 3.1. Introduction

Computational Fluid Dynamics (CFD) is the solution of a system of partial differential equations (PDEs) in order to determine the numerical solution of a fluid flow problem (McGuffie, Porte, & Hirst, 2013). Computational Fluid Dynamics can also be defined as the *prediction of the behaviour of fluids and of the effects of the fluid motion past objects by numerical methods rather than model experiment*. Generally, the solution of partial differential equations of fluid flow are very difficult to obtain, impossible and cannot be solved analytically except for some special cases (Joel and Peric, 1999). Being able to obtain numerical solutions means fewer experiments are required. Several of mathematical formulations are used to numerically solve a system of partial differential equations. These include:

- Finite Volume Method
- Finite Difference Method
- Finite Element Method

Recently most Commercial Computational Fluid Dynamics Packages makes use of the Finite Volume Method as the approach to solve a system of partial differential equations. However, it should be noted that other methods have been proven to produce accurate results. Finite Volume methods are also used to create approximations using discretisation of the fluid flow problem (Ferziger and Peric, 2012).

Computational Fluid Dynamics has become more popular due to some of the following reasons: Computational fluid dynamics allows the observations of a fluid flow property without disturbing the flow. It also allows the numerical solutions to be solved and made available for much subsequent analysis as even desired after the computation (Blazek, 2015). Computational fluid dynamics allows for the observation of a flow property at a location within the flow which may not be accessible experimentally or through flight testing. Computational fluid dynamics can be used a qualitative tool to define design variables for design optimisation enabling a rapid turnaround time compared to experiment methods.

### **3.1.1. Brief History**

The end of the cold war in the 1990s with defence budgets being cut gave rise to a new paradigm: “design –to-cost which meant better, faster and cheaper ways of develop designs and numerically solving fluid physics problems. As a result, both military and civil aircraft markets now demand technological products to fulfil the mission with low cost to design and manufacture and an integral part of fulfilling this demand is computational Fluid Dynamics. Over the last 50 years, the use of CFD has advanced to the point that currently CFD codes solving Navier-Stokes equations are now used as an integral part of the aircraft design process as well as in other fields for other purposes such as Biomedical science, chemical and mineral processing, civil and environmental engineering, sports, power generation etc.

The earliest use of computational fluid dynamics for aerospace application was in the 1960s; it was mainly used as an aircraft design tool. Over the years, the uses of computational fluid dynamics have seen much progress mainly due to three factors:

- Increase in computing resources
- Development of efficient numerical methods for simulating physics problems
- The progress made in Physics modelling

In the earlier years of the use of computational fluid dynamics (late 1960s), its application was based on aircraft design. The application consisted of using linear models such as the Laplace or Prandtl-Glauert equations (Potential flow equations). At first, lifting surface theories and the lifting line theories underpinned these numerical methods. Afterwards the vortex-Lattice procedure and developed these methods were used to represent the mean surface and made use of vortex filaments singularities. In this period, methods such as the panel methods were developed. These methods discretized the actual surface of the created geometry (Vos et al., 2002). In the early 1970s boundary layer methods, which can be used to study the viscous effects in the fluid flow became

relatively well developed and were applied in design. In the last two decades, much research was performed on integrating the boundary layer method with the panel method and on developing non-linear compressible potential formulations which were then used to simulate transonic fluid flows with shock waves. The non-linear inviscid method was later integrated with the boundary layer method for computations. An example of this class is the TRANAIR code (Jou et al., 1995), (Samant et al., 1987) and Navier aircraft solvers which after several years of modification now includes multi-point design optimisation. The development of super-computers i.e. (Cyber 205) in the late 1970s made it possible to apply nonlinear methods for more complicated flows other than for irrotational flows and isentropic flows. The development of the first Euler codes that were ever used in aircraft design were developed in the late 1980s and introduced followed by further advances in the Euler methods coupled with boundary layer codes (Vos et al., 2002). At first these codes and methods were only applied on steady aerodynamics flows while the panel methods were improved to be able to treat unsteady fluid flow problems. The advancement of computer capacity to be able to compute in parallel has provided a means to solving more realistic type of fluid flow physics problems within reasonable turn a-round time to obtain results to be used in industrial design. Parallel simulation capabilities of computers enabled the simulation methods to move from Euler into solving Navier Stokes equations for steady fluid flow problems and the study of transient fluid flows by using Euler formulations. At the same time, there began the increasing need to couple Computational Fluid Dynamic codes into the aircraft engineering design set-up in order to be able to tackle some of the new challenges caused by the economic market for aircraft (Vos et al., 2002). To this effect efforts have been focused since the early 1990s to integrate known knowledge of computational fluid dynamics methods and codes into methods and tools used for aerodynamics design analysis in terms of performance.

CFD is regarded as a relatively mature tool complimentary to flight test and wind tunnel testing. As a result of the rapid increase in the reliability of CFD due to the advancement in the computing power of computers and computing capabilities, it has found its way into engineering companies. At the same time numerical methods still need to be improved to meet the requirements with respect to the efficiency (computing time/ simulation time) mostly on the turnaround time for meshing which may consume a huge amount of time when high quality (fine mesh quality) is required, improved turbulence and transition modelling, improved numerical schemes and also improvement needs to be made to increase the accuracy and the time for simulating complex physics problems even if the physics problems and the simulated geometry becomes more complex (Vos et al., 2002), (Schwamborn et al., 2006).

The major challenge is to produce advanced CFD codes which can deliver high levels of accuracy in aircraft performance analysis and design for new configurations and test cases in order for it to become an ever more reliable tool which can be incorporated properly as a design and aircraft performance analysis tool in the process chain in the aerospace industry in order to be fully accepted (Schwamborn et al., 2006). The level of accuracy in computational fluid dynamics should enable the prediction of drag within acceptable error margins. As a result of this, it is important to assess the capabilities of the state-of-the-art numerical methods as tools for predicting aerodynamic coefficients.

### **3.2. Application of Computational Fluid Dynamics as a Drag Prediction Tool**

The use of computational fluid dynamics as a drag prediction tool has seen much progress over the last decades since the introduction of super-computers (cluster computing). This is because such computers allow for more realistic type of physics problem conditions to be solved and analysed in a robust way. i.e. the numerical simulation of full body aircraft for performance analyses, not just for research, but at an industry level. There is an increasing confidence and reliance of CFD tools for design tool and design performance analysis in the Aerospace industry to determine aircraft performance parameters, although testing remains critical.

Many papers have been published on the research and application of CFD methods using CFD to solve industry type problems to determine lift, drag and moments either to replicate a wind-tunnel set-up and or a real-life condition (atmosphere simulation). Some of the Computational methods and findings from a few selected papers are discussed in the following paragraphs as evidence of the advancement in CFD for industrial type physics problems.

In an article by Eliasson, (2007) a numerical investigation on the flow around a half model of civil aircraft was described. The numerical calculations were performed using an unstructured prismatic grid line-up in order to resolve the boundary layer. The algorithms used for the grid configuration inside the boundary layer and the algorithm used for the main inviscid flow stream were different away from the body. TRITET grid generators were used and the numerically calculated results and experimental data that were obtained with and without applied wall's interference were compared (Van Leer, 1979). The results from the comparison showed that the numerical calculations provided a reasonable description of the flow fluid. Melber-Wilkending et al., (2006) present investigations conducted to replicate the experimental data obtained from two wind tunnels. The numerical simulations were performed using the TAU Code (Melber-Wilkending et al., 2006) which featured an unstructured grid. The calculations were performed using an implicit numerical scheme using the

*SST turbulence model* of the Reynolds Averaged Navier Stokes equation system and results showed good correlation with the wind tunnel results, although the purpose of their investigation was to propose a new wind tunnel CFD supported testing system. Due to the importance of aerodynamic performance of aircraft during the design phase of aircraft development, it is important to be able to accurately model these conditions particularly in a manner which is suited for industrial application and not just for research purposes. To this aspect, the High Lift Prediction workshops were organised to check the capabilities of current computational fluid dynamic packages in terms of meshing, numerical algorithms, turbulence modelling and high-performance computing.

In an article written by Shankara and Snyder, (2012) to satisfy the requirements for the AIAA Applied Aerodynamics Conference for the drag prediction work-shop, numerical simulations on a high lift trap wing were performed using commercial simulation package STAR-CCM+. This was a benchmark case used in the conference. An Un-structured mesh was used to reduce the number of nodes required to obtain a reasonably accurate solution also as a point-to-point conformal meshing could be difficult for such a complex geometry. A density based discretization approach was employed with “second order upwind partial discretisation for the convective flux term” (Shankara and Snyder, 2012). A Pseudo-time marching scheme were used, pre-conditioning of the coupled approach was used to make this approach suitable for low Mach numbers as the simulation was run at a Mach number of 0.2; isothermal- conditions assumed, Gauss-Seidel linear system solver was used with algebraic multi-grid (AMG) acceleration to solve the resulting discrete linear system at each iteration. To model turbulence, the *SST  $k - \omega$  model* Menter, (1994), Durbin, (1996) was used with the *correlation – based  $\gamma - Re - \theta$  transition model* to model transition. Near wall thickness  $y +$  values of 0.1 to 1.0 were used to accurately capture the flow in the boundary layer next to the wall. The results presented showed very good correlation with the wind-tunnel test previously carried out by NASA for the 1<sup>st</sup> AIAA conference. It was observed that the use of the predictive transition model (*Gamma  $\gamma$  theta model*) improved the accuracy considerably also and a very refined mesh were required to properly capture the flow characteristics around the wing model. A similar approach has been adopted in simulation validation work by CD-ADAPCO to validate the use of STAR-CCM+ as a drag prediction code by comparing numerical data with well know data for a 2-D NACA 0012 aerofoil profile. Numerical data obtained correlated within acceptable margins with the experimental data recorded for the NACA 0012 (Rumsey, 2015).

Other Authors adopted a different approach known as the far-field drag prediction and decomposition method. Such methods were adapted by Gariépy et al., (2013) to presents numerical data for the AIAA drag prediction workshop 5. The far-field method is a technique of drag prediction based on the linear momentum relation as

opposed to the traditional method of computing drag which involved simply integrating the pressure and friction forces acting on the aircraft (Gariépy et al., 2013), (Van der Vooren and SLOOFF, 1990). Such a technique allows for the decomposition of drag into various components i.e. wave drag, viscous drag, induced drag and spurious drag which is a drag caused due to numerical and truncation errors common in computational fluid dynamics simulations. This technique is important as it gives one a chance to physically visualise and identify the different sources of drag thereby increasing the accuracy of drag coefficients by identifying and removing the spurious drag. Simulation was performed using ANSYS-Fluent, a density-based solver was used for the discretization of the governing equations with a Roe Flux-Difference Splitting (Roe-FDS) scheme, implicit formulation with a second order spatial discretization. Convergence acceleration by using a multi-grid algorithm with an F cycle was used. A one equation Spalart-Allmaras turbulence model and *two equation  $k - \omega$  shear stress transport (SST)* turbulence model were used. The results obtained from their numerical investigation proved that the removal of the spurious drag improved the accuracy of the drag and was less sensitive to the mesh when compared to numerical simulation, that had the spurious drag. Several articles can be found on the use of CFD for drag prediction for interested readers. Please refer to Beechook and Wang, (2013), Barkmann, (2011a), Zhang et al., (2015b), Li et al., (2015), Vassberg et al., (2014), Görtz, (2005), Tinoco et al., (2017), Tate et al., (2017), Persson et al., (2017), Svoboda and Rozehnal, (2017), Lubis et al., (2017), Wang, (2015) etc.

Although computation time and meshing time still need improvement, the results obtained in the discussed and presented articles show how computational fluid dynamics has made much progress not only as an aerodynamic performance prediction tool for research purpose but also, importantly, as a flow characteristics prediction tool for the aerodynamic analysis of aircraft for industrial applications.

The Simulation approach adopted by Shankara and Snyder, (2012) has been employed for compressible flow analysis in this research and for incompressible flow analysis a modification using the segregated solver has been selected. More details on this are discussed in section 3.4.0. In the following section the governing equations which forms the basics of all CFD codes are discussed.

### **3.2. Theory**

The flow of Newtonian fluids can be described by the Navier-Stokes equations which can be solved numerically by using discretisation to provide numerical solutions to a fluid flow problem. To fully describe the flow around an aircraft wing and winglet to predict the aerodynamic performance in steady flow or unsteady flow, it is necessary to give an overview on the governing equations which are incorporated in all commercial CFD packages

and the involved Reynolds averaging procedure together with the turbulence closure models. Also, the finite volume method needs to be outlined together with various meshing techniques and the discretisation techniques used to analyse grids to produce numerical solutions for a fluid flow problem.

### 3.2.1. Governing Equations

Computational fluid dynamics is based on the governing equations of fluid dynamics. These governing equations symbolise the mathematical statements (forms) of the laws of conservation in physics. The following laws are fundamental to computational fluid dynamics.

- Conservation of Mass (continuity)
- Newton's second law (conservation of momentum)
- 1<sup>st</sup> Law of thermodynamics (conservation of Energy)

The partial differential form of the conservative forms of the governing equation in Cartesian co-ordinates for a control volume in space with particle(s) passing through it forms the basics of the equations that are solved in computational Fluid Dynamics packages as follows:

The Continuity equation (conservation of Mass equation) is derived from the conservation of mass laws which states that mass can neither be destroyed nor created. The derivation of this equation assumes a control volume fixed in space and time with fluid particles moving through the control volume and interacting with the surfaces of the control. The mass conservation law requires that the rate of mass in-flux into the control volume be equal to the rate of change of the accumulation of mass within the control volume plus the rate of mass leaving the control volume. The partial differential form of the equation (conservation form) is given as (Tu et al., 2012):

$$\frac{\partial \rho}{\partial t} + \frac{\partial(\rho u)}{\partial x} + \frac{\partial(\rho v)}{\partial y} + \frac{\partial(\rho w)}{\partial z} = 0 \quad (2)$$

The equation is given in terms of the velocity components  $(u, v, w)$  and Cartesian coordinates  $(x, y, z)$  respectively. This is the un-steady form of the equation assuming a change in density as a function of time. The steady form of the equation would assume a constant density as a function of time therefore  $\frac{\partial \rho}{\partial t} = 0$

The Momentum equation (conservation of momentum) is derived from Newton's second law of motion. The conservation of momentum law requires that momentum influx into the control volume be equals to the momentum out flux plus any change in momentum within the control volume. This equation is most times referred to as the Navier-Stokes Equation (conservation form of the equation) (Tu et al., 2012):

$$\begin{aligned} \frac{\partial(\rho u)}{\partial t} + \frac{\partial(\rho u u)}{\partial X} + \frac{\partial(\rho v u)}{\partial y} + \frac{\partial(\rho w u)}{\partial z} \\ = -\frac{\partial P}{\partial X} + \mu \left( \frac{\partial^2 u}{\partial X^2} + \frac{\partial^2 u}{\partial y^2} + \frac{\partial^2 u}{\partial z^2} \right) + \rho g X \end{aligned} \quad (3)$$

$$\frac{\partial(\rho v)}{\partial t} + \frac{\partial(\rho u v)}{\partial X} + \frac{\partial(\rho v v)}{\partial y} + \frac{\partial(\rho w v)}{\partial z} = -\frac{\partial P}{\partial y} + \mu \left( \frac{\partial^2 v}{\partial X^2} + \frac{\partial^2 v}{\partial y^2} + \frac{\partial^2 v}{\partial z^2} \right) + \rho g Y \quad (4)$$

$$\frac{\partial(\rho w)}{\partial t} + \frac{\partial(\rho u w)}{\partial X} + \frac{\partial(\rho v w)}{\partial y} + \frac{\partial(\rho w w)}{\partial z} = -\frac{\partial P}{\partial z} + \mu \left( \frac{\partial^2 w}{\partial X^2} + \frac{\partial^2 w}{\partial y^2} + \frac{\partial^2 w}{\partial z^2} \right) + \rho g Z \quad (5)$$

The momentum equations are written in 3-D for all velocity components ( $u, v, w$ ) for the Cartesian coordinates ( $x, y, z$ ) and has been written for the compressible un-steady state. The term on the left-hand side of the equation represents the convective terms and the steady-unsteady accelerations while the terms on the right-hand side represents the pressure terms, diffusive (viscous) terms and the body forces ( $x, y, z$ ) acting on the control volume.

The conservation of energy equation is derived from the 1<sup>st</sup> law of thermodynamics which states that the time rate of change of energy in a system is equal to the net rate of heat added to the system plus net rate of the work done by the system. The conserved form of the energy equation is given as (Wendt, 2008), (Anderson and Wendt, 1995):

$$\begin{aligned} \rho \frac{\partial}{\partial t} \left[ \rho \left( e + \frac{v^2}{2} \right) \right] + \frac{\partial}{\partial x} \left[ \rho \left( e + \frac{v^2}{2} \right) u \right] + \frac{\partial}{\partial y} \left[ \rho \left( e + \frac{v^2}{2} \right) v \right] + \frac{\partial}{\partial z} \left[ \rho \left( e + \frac{v^2}{2} \right) w \right] = \rho \dot{q} + \\ \frac{\partial}{\partial x} \left( k \frac{\partial T}{\partial x} \right) + \frac{\partial}{\partial y} \left( k \frac{\partial T}{\partial y} \right) + \frac{\partial}{\partial z} \left( k \frac{\partial T}{\partial z} \right) - p \left( \frac{\partial u}{\partial x} + \frac{\partial v}{\partial y} + \frac{\partial z}{\partial z} \right) + \lambda \left( \frac{\partial u}{\partial x} + \frac{\partial v}{\partial y} + \frac{\partial z}{\partial z} \right)^2 + \mu \left[ 2 \left( \frac{\partial u}{\partial x} \right)^2 + \right. \\ \left. 2 \left( \frac{\partial v}{\partial y} \right)^2 + 2 \left( \frac{\partial w}{\partial z} \right)^2 + \left( \frac{\partial u}{\partial y} + \frac{\partial v}{\partial x} \right)^2 + \left( \frac{\partial u}{\partial z} + \frac{\partial w}{\partial x} \right)^2 + \left( \frac{\partial v}{\partial z} + \frac{\partial w}{\partial y} \right)^2 \right] + \rho f_x x + \rho f_y y + \rho f_z z \end{aligned} \quad (6)$$

These equations are also known as the transport equations or the conservation equations. The forms of the governing equations that are generally used in computational fluid dynamics (CFD) are known as the Navier Stokes Equations. The Navier Stokes Equations include the effect of viscosity on the fluid flow. In most

commercial packages, the finite volume method is used to transform the continuous governing equations into a form that can be solved numerically. In STAR-CCM+ two approaches are taken to solve the governing equations. The segregated approach, where the flow equations are solved one after the other and linked using a correction equation, the coupled approach (density based coupled solver) where the coupled system of the governing equations is solved simultaneously at once.

Another equation worth mentioning is the equation for Reynolds number which is simply the ratio of the inertia forces to the viscous/ friction forces in the fluid.

$$\text{Re} = \frac{\rho u L}{\mu} \quad (7)$$

This equation is important as it determines the condition of the fluid field. i.e. if the flow field is laminar or turbulent. The determination of these conditions is the key for computational fluid dynamic as it directly affects what solvers, boundary conditions and flow physics models that is adopted for the simulation to obtain a numerical solution.

Another dimensionless parameter which is important is the Prandtl number which is the ratio of the molecular diffusivity of momentum and the molecular diffusivity of heat.

$$\text{Pr} = \frac{\text{Molecular diffusivity of momentum}}{\text{Molecular diffusivity of heat}} \quad (8)$$

### 3.2.2. Turbulence

Many real flows are turbulent in nature e.g. flows around an aircraft wing, boundary layers on wings of aircraft, jet streams and combustion. Turbulence is a difficult phenomenon to define but generally has the following characteristics such as being associated with large Reynolds number, irregular in nature, diffusive, possessing three-dimensional vorticity fluctuations and being dissipative. The rate of mass and momentum transfer in turbulent flow is much higher than that in Laminar flow.

Launder, (1991) gives the definition of turbulent flow as “at moderate Reynolds numbers the restraining effects of viscosity are too weak to prevent small, random disturbances in a shear flow from amplifying. The disturbances grow, become non-linear and interact with neighbouring disturbances. This mutual interaction leads to a tangling of vorticity filaments. Eventually the flow reaches chaotic non-repeating form describable only statistical terms. This flow is turbulent flow”.

Since Osborne Reynolds, it has well been known that flow behaviour can be categorised by the critical Reynolds number which governs the onset of turbulent flow. Based on the experimental work that was done by Reynolds on pipe flow and flow on a flat plate, the values for the various regimes were obtained. Thus, the flows can be effectively sub-divided into Laminar or turbulent flow.

The Navier Stokes equations given in Equations (2) are applicable to all fluid flow and thus would be able to handle turbulent flows in theory. Unfortunately, the actual numerical solutions to turbulent flows are more complex than for laminar flows because for turbulent flows the discretization of small steps in the flow in both time and space is important, which must to be performed down to the Kolmogorov scale, given by:

$$\eta = \left(\frac{\nu^3}{\epsilon}\right)^{\frac{1}{4}} \quad (9)$$

Nevertheless, it is accepted that the Navier Stokes equations can be used to directly solve turbulent flow fluid problems. This approach of modelling is generally called Direct Numerical Simulation. This fluid modelling approach to turbulent energy cascade by using the Navier Stokes equations requires that the turbulent length scales be larger than the grid spacing. Direct Numerical simulation tries to simulate all the scales of the turbulence itself. The grid size, quality and the maximum permitted time step for a Direct Numerical Simulation must be small enough to capture the Kolmogorov scales of the turbulent flow (Nichols, 2009). Direct Numerical Simulation is characteristically unsteady thus, it requires a long period to run to ensure that the obtained result for the simulation is statistically stable and independent of the initial conditions inputted at the beginning of the simulation. Direct Numerical Simulation requires grids that are uniformly spaced because otherwise the higher order numerical algorithms in Direct Numerical Simulation are invalid. Grid stretching should also be avoided as it reduces the order of the numerical grids and increases the numerical dissipation of the algorithm. It requires extremely large computational grids even for small Reynolds number simulation which could be a problem. Direct Numerical Simulation has only been used for problems with low Reynolds numbers and on very simple geometries due to computer limitations in terms of processing speed and memory required to perform numerical simulation for higher Reynolds number problems. Due to the complexity of most engineering problems it is impossible to simulate such problems with the Direct Numerical method and therefore, some form of modelling of the turbulence is often required so that solutions to engineering problems can be obtained for large scale problems.

As an alternative, Large Eddy Simulation tries to modify the approach of the Direct Numerical simulation by only modelling the smallest turbulence scales (Kolmogorov scales) in a computational fluid dynamic simulation

(Breuer, 1998). These small turbulence scales could be modelled with simple turbulence models because they are nearly isotropic. In Large Eddy Simulations, large scales are computed explicitly. An advantage of this approach is that large eddies, which are hard to model in a general way, due to the fact that, these large scales are anisotropic are calculated directly (resolved directly) while the small eddies are modelled since they are closer to isotropic and can easily adapt to maintain a dynamic balance with the rate of energy transfer imposed on the flow by the large eddies. In Large Eddy Simulations, the turbulence scales are resolved down to the inertial sub-range (Andersson et al., 2011). As a general rule of thumb suggested by Andersson et al., (2011) at least 80% of the turbulence energy should be resolved in the calculated velocities. Large Eddy Simulation are unsteady, they require to be run for large number of times steps in order to eliminate initial conditions dependency for the simulation to be statistically stable. Large Eddy Simulations can be used at much higher Reynolds number than Direct Numerical simulation. The governing equations for Large Eddy Simulations are obtained by spatially filtering over small scales. i.e. filtering the Navier Stokes equations of small scales. examples of the filters used are Gaussian and sharp spectral filters (Sagaut, 2001). The filter function determines the division of the turbulent spectrum into the grid realised and sub-grid regions i.e. (the turbulent scales that needs to be calculated directly and the ones that needs to be modelled). It also requires a low dissipation numerical scheme.

The filtered continuity equation is given by

$$\frac{\partial \bar{U}_j}{\partial x_j} = 0 \quad (10)$$

And the corresponding momentum equation is given by

$$\frac{\partial \bar{U}_i}{\partial t} + \frac{\partial \bar{U}_i \bar{U}_j}{\partial x_j} = -\frac{1}{\rho} \frac{\partial \bar{P}}{\partial x_j} + \nu \frac{\partial^2 \bar{U}_i}{\partial x_j \partial x_j} - \frac{\partial \tau_{ij}}{\partial x_j}. \quad (11)$$

In Large Eddy Simulation closure problems arises due to the presence of the residual stress tensor  $\tau_{ij}$  also known as the sub-grid stress tensor. This residual stress tensors describes the transfer of momentum by turbulence in the flow at turbulent scales that are smaller than the filter, and is given by:

$$\tau_{ij} = \overline{U_i U_j} - \bar{U}_i \bar{U}_j \quad (12)$$

The filtered velocities ( $\bar{U}_i$  and  $\bar{U}_j$ ) are solved for in the equation but the correlation term  $\overline{U_i U_j}$  is an unknown variable and a sub-grid stress model must be provided for the residual stress tensor ( $\tau_{ij}$ ) the simple models usually

involves modelling of a sub-grid viscosity (Andersson et al., 2011). An example of such models is the Smagorinsky-Lilly model (Canuto, 1994). In general, some challenges faced by using the Large Eddy Simulation is that it is still not capable of dealing with flight Reynolds number at reasonable turn-around times.

Hybrid RANS/LES models are a new kind of turbulence models which can be used for unsteady high Reynolds number flows. These models are extensions of the Large Eddy Simulation models (Nichols, 2009). The concept behind these models is to use a modified Reynolds Average Navier–Stokes turbulence model as a sub-grid model (i.e. turbulent scales that cannot be achieved on a computational grid) for the Navier-Stokes equations. The main aim of this model is to use Reynolds Average Navier-Stokes Simulations to calculate the boundary layer where very small turbulent scales are present, then use a Large Eddy Simulation type model to simulate the smaller turbulence scales that are away from the body used for the simulation; therefore, the large turbulent scales that are located away from the body are simulated using the unsteady Navier-Stokes equations. This model serves as a means to close the gap between the Reynolds Average Navier-Stokes Simulation model and the Large Eddy Simulation model. These models require a coarser mesh than the Large Eddy Simulation because the Reynolds Average Navier-Stokes Simulation type sub-grid model is valid for non-isotropic turbulent scales (Nichols, 2009). This model requires “spatial filtering of the Navier Stokes equations in order to determine the local values for the sub-grid turbulent viscosity” (Nichols, 2009). It does not require very low dissipation thus, so it can be easy to implement.

The following section of the report presents an overview of developments of the Reynolds Averaged Navier Stokes form of the Navier Stokes equation. This is discussed here as they are used in the numerical simulations presented in this report.

### **3.2.3. Reynolds Average Navier Stokes Equations**

Reynolds averaging is one of two averaging techniques used to simplify the Navier stokes equations the other one being Favre averaging (BILGER, 1975), (Ristorcelli and Morrison, 1996). These approaches involve using time averaged correlation terms which have to be modelled to be able to close the set of equations. Two other methods exist for closure. Namely: Hybrid Reynolds Average Navier Stokes modelling and the large eddy simulation both of which have been briefly discussed in Section 3.2.2.

The Reynolds Averaged Navier Stokes equations govern the transport of averaged fluid flow quantities, with the whole scales of turbulence being modelled (Fluent, 2012). The Reynolds Average Navier Stokes modelling

approach therefore reduces the required computational time and resources and it is widely used. Also, this modelling approach is adopted for the work presented in this report. RANS equations are usually used to compute time dependent flow conditions where the unsteadiness of the flow could be externally imposed i.e. time dependent sources or self-imposed e.g. vortex-shedding.

For Reynolds averaging the solution of the variables in the instantaneous Navier-Stokes equations is decomposed into the fluctuating components and the mean (ensemble-averaged or time averaged) components.

The velocity components can be broken down into (Andersson et al., 2011):

$$U_i = \langle U_i \rangle + u_i \quad (13)$$

Where  $\langle U_i \rangle$  is mean velocity and  $u_i$  is the fluctuating velocity components; similarly, for pressure, energy and other scalar quantities (Andersson et al., 2011).

$$\vartheta = \bar{\vartheta} + \vartheta' \quad (14)$$

Where  $\vartheta$  represents a scalar quantity such as energy, pressure etc.

By substituting the expression of the form shown above for the flow variables into the continuity and momentum equations and taking time average using the operator (Andersson et al., 2011).

$$\langle \vartheta \rangle = \frac{1}{\tau} \int_t^{t+\tau} \vartheta(x, \tilde{t}) d\tilde{t} \quad (15)$$

After a few manipulations, the general form of the Reynolds Averaged Navier Stokes equations for incompressible flow written in Cartesian tensors as (Andersson et al., 2011):

$$(16)$$

$$\frac{\partial \langle U_i \rangle}{\partial x_i} = 0$$

and

$$(17)$$

$$\frac{\partial \langle U_i \rangle}{\partial t} + \langle U_j \rangle \frac{\partial \langle U_i \rangle}{\partial x_j} = -\frac{1}{\rho} \frac{\partial}{\partial x_j} \left\{ \langle P \rangle \delta_{ij} + \mu \left( \frac{\partial \langle U_i \rangle}{\partial x_j} + \frac{\partial \langle U_j \rangle}{\partial x_i} \right) - \rho \langle u_i u_j \rangle \right\}.$$

Equations (16) and (17) are known as the Reynolds Averaged Navier Stokes equations. Additional terms or unknown appear in the equation that represents the effects of turbulence in the flow. These terms  $-\rho\langle u_i u_j \rangle$  are called the Reynolds stresses; it a very important term as it introduces a coupling between the mean and fluctuations components of the velocity field, this term must be modelled to close the equation.

### 3.2.4. Turbulence Closure

For turbulence closure several turbulence models exist in CFD which can be employed to perform this task, some of which will be discussed in this section of the report. The process of Reynolds averaging to turbulence modelling requires that the Reynolds stresses  $-\rho\langle u_i u_j \rangle$  "which is a second order tensor that represents a second-order moment of the velocity components at a single point in space" are appropriately modelled to obtain the desired solution (Andersson et al., 2011). The individual Reynolds stresses in the stress tensor has 9 components but since the Reynolds stress tensor is symmetric there are 3 normal stresses and 3 shear tensor stresses which means that the Reynolds tensors contains 6 unknowns that must be modelled. An ideal way to close the Reynolds Averaged Navier Equation would be to derive a transport equation for each of the Reynolds stresses, but this would result in third-order moments of velocity components requiring the derivation of equations for the third order moments would result in a fourth order moments; this goes on indefinitely and is regarded as the closure problem.

One of the common methods use to achieve closure is to use the Boussinesq hypothesis based on the assumption that the components of the Reynolds stress tensor  $-\rho\langle u_i u_j \rangle$  are proportional to the gradient of the mean velocity (Andersson et al., 2011). The Boussinesq hypothesis proposes that the transport of momentum by turbulence is a diffusive process and that the Reynolds stresses can be modelled by using a turbulence eddy viscosity; this is known as the eddy viscosity model (Fluent, 2012).

$$\tau_{ij} = -\rho\langle u_i u_j \rangle = \nu_T \left( \frac{\partial \langle U_i \rangle}{\partial x_j} + \frac{\partial \langle U_j \rangle}{\partial x_i} \right) - \frac{2}{3} k \delta_{ij} \quad (18)$$

Where  $k$  is the turbulence kinetic energy per unit mass and it is defined as the half trace of the Reynolds stress tensor;  $k = \frac{1}{2} \langle u_i u_i \rangle$ ;  $\nu_T$  is the eddy viscosity, which together with  $k$  need to achieve closure. This is achieved via turbulence models such as the Mixing length models, Spalart-Allmaras,  $k - \varepsilon$  and  $k - \omega$  and other eddy viscosity models. This approach has the advantage of reducing the computational cost which is related to determining the

eddy viscosity  $v_T$  via the turbulence models. The turbulent-viscosity models are based on characteristics velocity,  $u$ , and length scales,  $l$  describing the local turbulent viscosity  $v_T$ . An equation to show the relationship between the characteristic velocity, length scales and local turbulent viscosity is given below (Kinetic theory of gas):

$$v_T = C_v ul \quad (19)$$

Where  $C_v$  is a constant of proportionality; this equation makes sense since these scales are responsible for most of the turbulent transport. Therefore, all turbulence models based on the Eddy viscosity concept contain sets of additional equations required to determine the velocity and length scales to describe the eddy viscosity (local turbulence). For instance, in One equation turbulence model only one additional transport equation (Partial Differential Equation) is solved to determine the characteristic velocity,  $u$ , and, the length scale, most then be specified algebraically in exception of Spalart Allmaras model where the partial differential equation is solved to determine the turbulence eddy viscosity. For the  $k \omega$  and  $k \varepsilon$  models two additional transport equations are solved, one for the turbulence kinetic energy  $k$ , and the other for the turbulence dissipation rate  $\varepsilon$  or the specific dissipation rate known as  $\omega$  are solved and the turbulent viscosity is solved for, as a function of  $k$  and  $\omega$  or as  $k$  and  $\varepsilon$ . These are related to the turbulent viscosity mathematically by (Andersson et al., 2011):

$$v_T = C_v ul = C_v \frac{k^2}{\varepsilon} \text{ Since } \varepsilon = \frac{k^3}{l} \text{ for the } k \varepsilon \text{ model} \quad (20)$$

and

$$v_T = C_v ul = C_v \left(\frac{k}{\omega}\right)^{1/2} \text{ For the } k \omega \text{ model.} \quad (21)$$

Another approach which could be used to model the stress tensor and used to achieve closure to the RANS equations is the Reynolds Stress Models also known as the second moment closure models (Andersson et al., 2011). These models account for anisotropy due to swirling motion, streamline curves, rapid change in strain rate etc. but are computational expensive. The Reynolds Stress Models solve the transport equation for all components of the specific Reynolds Stress tensor. In addition to the Reynolds Stress Model an extra equation is needed for the turbulence dissipation rate  $\varepsilon$ , which means that seven additional equations must be solved for 3-D problems, this is because for 3-dimensions the Reynolds stress tensor is symmetric so that only six of the nine components

are unique (STAR-CCM+) plus the additional equation for the dissipation rate  $\epsilon$ . For 2-dimensions flows 5 equations are solved as only 3 of the Reynolds stress components need to be evaluated for 2-D flows. Examples of Reynolds stress turbulence models include; linear pressure strain model, Quadratic Pressure strain model and the Elliptic Blending model. In most engineering problem, the Boussinesq approximation approach works very well, and is less computationally expensive when compared to the Reynolds stress model. However, the Reynolds stress models tend to perform better in fluid flow conditions where anisotropy of the turbulence has a more predominant effect on the average flow. The computational results and simulations presented in this report used turbulence model based on the Boussinesq approximation approach.

### **3.2.5. One Equation Model (Spalart-Allmaras Turbulence Model)**

The Spalart-Allmaras turbulence model is a new type of one equation turbulence model which involves solving a single transport equation which determines the turbulent viscosity of the fluid flow. This model is different from other types of one equation models (i.e. the Baldwin-Lomax and the Johnson-King turbulence models) in the sense that it does not require an algebraic prescription of a length scale after solving the equation for the transport of turbulent kinetic energy in the fluid flow. The model was originally developed for Aerospace applications and has the advantage of being easily incorporated in an unstructured CFD solver. The authors of the original Spalart-Allmaras turbulence model presented results for attached boundary layer flows and slightly separated flows i.e. flows past an aerofoil. Wilcox, (1998) concluded that the model is not suitable for application to fluid flows involving jet-like free-shear regions. It is also mostly likely not suited for flows involving complex recirculation and body forces. A version of this model has been implemented for the validation of CFD tests that are presented in this report.

### **3.2.6. Two Equation model**

Two equation turbulence models have been used for many years and are well known in the aerospace industry. These are class of the eddy viscosity models that use the Boussinesq approximation approach to relate the Reynolds stress tensors to the mean flow quantities. Most two equation turbulence models solve for the transport equation for the Kinetic energy  $k$  and another transport equation which defines the turbulent length scale. Generally, the second transport equation solves for the turbulent dissipation rate  $\epsilon$  or the turbulent specific dissipation  $\omega$ . Some of the two equation models are valid down to the wall i.e. low Reynolds number models and others are only valid outside of the inside region of the boundary layer of the flow (high Reynolds number models)

### 3.2.6.1. Overview of Standard $k \varepsilon$

The standard  $k \varepsilon$  is a version of the two-equation model that involves solving the transport equations for turbulent energy  $k$  and the dissipation rate  $\varepsilon$ . The exact transport equation for  $k$  (turbulent kinetic energy) can be derived by Reynolds decomposition of the transport equation for  $k$  derived from the RANS equation. The derivation of the  $k \varepsilon$  equation assumes that the flow is fully turbulent and ignores the effect of molecular viscosity in the flow which means that this model is most suited for turbulent flow or high Reynolds number flow.

The exact transport equation for  $k$  is given as (Andersson et al., 2011):

$$\frac{\partial k}{\partial t} + \langle U_j \rangle \frac{\partial k}{\partial x_j} = -\langle u_i u_j \rangle \frac{\partial \langle U_i \rangle}{\partial x_j} - v \left\langle \frac{\partial u_i}{\partial x_j} \frac{\partial u_i}{\partial x_j} \right\rangle + \frac{\partial}{\partial x_j} \left( v \frac{\partial k}{\partial x_j} - \frac{\langle u_i u_i u_j \rangle}{2} - \frac{u_j P}{\rho} \right) \quad (22)$$

The first term on the left-hand side of the equation represents – the accumulation of  $k$ , the second term on the left-hand side of the equation represents – convection of  $k$  by the mean velocity. The first terms on the right-hand side of the equation is the term for the production of  $k$  (large eddies in the flow extracts energy from the mean flow), the second set of terms on the right-hand side of the equation represents the Dissipation of  $k$  (turbulent kinetic energy) by viscous stress whereby  $k$  is transformed into heat.

$v \frac{\partial k}{\partial x_j}$  – Represents the molecular diffusion of  $k$ ,  $\frac{\langle u_i u_i u_j \rangle}{2}$  – represents the turbulent transport by velocity fluctuations and the last term  $\frac{u_j P}{\rho}$  is the term for turbulent transport by pressure fluctuation in the fluid flow. The modelled equation is given as after closure of some of the un-known in equation (22) (Andersson et al., 2011):

$$\frac{\partial k}{\partial t} + \langle U_j \rangle \frac{\partial k}{\partial x_j} = v_T \left[ \left( \frac{\partial \langle U_i \rangle}{\partial x_j} + \frac{\partial \langle U_j \rangle}{\partial x_i} \right) \frac{\partial \langle U_i \rangle}{\partial x_j} \right] - \varepsilon + \frac{\partial}{\partial x_j} \left[ \left( v + \frac{v_T}{\sigma_k} \right) \frac{\partial k}{\partial x_j} \right] \quad (23)$$

The exact transport equation for  $\varepsilon$  is given as

$$\begin{aligned}
\frac{\partial \varepsilon}{\partial t} + \langle U_j \rangle \frac{\partial \varepsilon}{\partial x_j} &= -2v \left( \left\langle \frac{\partial u_i}{\partial x_k} \frac{\partial u_j}{\partial x_k} \right\rangle + \left\langle \frac{\partial u_i}{\partial x_k} \frac{\partial u_j}{\partial x_k} \right\rangle \right) \frac{\partial \langle U_i \rangle}{\partial x_j} - 2v \langle u_k \frac{\partial u_i}{\partial x_j} \rangle \frac{\partial^2 \langle U_i \rangle}{\partial x_k \partial x_j} \\
&\quad - 2v \left\langle \frac{\partial u_i}{\partial x_k} \frac{\partial u_i}{\partial x_j} \frac{\partial u_k}{\partial x_j} \right\rangle - 2vv \left\langle \frac{\partial^2 u_i}{\partial x_k \partial x_j} \frac{\partial^2 u_i}{\partial x_k \partial x_j} \right\rangle \\
&\quad + \frac{\partial}{\partial x_j} \left( v \frac{\partial \varepsilon}{\partial x_j} - v \langle u_j \frac{\partial u_i}{\partial x_j} \frac{\partial u_i}{\partial x_j} \rangle - 2 \frac{v}{\rho} \left\langle \frac{\partial p}{\partial x_j} \frac{\partial u_j}{\partial x_j} \right\rangle \right)
\end{aligned} \tag{24}$$

The first terms on the left-hand side of the equations can be physically interpreted as the accumulation of  $\varepsilon$ , the second terms on the left hand of the equation can be physically interpreted as the convection of  $\varepsilon$  by the mean velocity. The first and second set of terms on the right-hand side of the equation can be physically interpreted as the production of dissipation due to the interactions between the mean velocity and the products of the turbulent fluctuations. The third and fourth set of terms on the right-hand side of the equation can be physically interpreted as the destruction rate of the dissipation due to the turbulent velocity fluctuations in the fluid flow.

$v \frac{\partial \varepsilon}{\partial x_j}$  is the viscous diffusion of the energy dissipation  $\varepsilon$ ,  $v \langle u_j \frac{\partial u_i}{\partial x_j} \frac{\partial u_i}{\partial x_j} \rangle$  is the Turbulent transport of the energy dissipation rate  $\varepsilon$  due to the velocity fluctuation,  $2 \frac{v}{\rho} \left\langle \frac{\partial p}{\partial x_j} \frac{\partial u_j}{\partial x_j} \right\rangle$  is the Turbulent transport of  $\varepsilon$  as a result of pressure – velocity fluctuation in the fluid flow.

The modelled  $\varepsilon$  equation is given as Bengt, (2011):

$$\frac{\partial \varepsilon}{\partial t} + \langle U_j \rangle \frac{\partial \varepsilon}{\partial x_j} = C_{\varepsilon 1} v_T \frac{\varepsilon}{k} \left[ \left( \frac{\partial \langle U_i \rangle}{\partial x_j} + \frac{\partial \langle U_j \rangle}{\partial x_i} \right) \frac{\partial \langle U_i \rangle}{\partial x_j} \right] - C_{\varepsilon 2} \frac{\varepsilon^2}{k} + \frac{\partial}{\partial x_j} \left[ \left( v + \frac{v_T}{\sigma_k} \right) \frac{\partial \varepsilon}{\partial x_j} \right] \tag{25}$$

The First term on the left-hand side of the equation has the physical interpretation as the accumulation of the energy dissipation rate  $\varepsilon$ , the second term on the left-hand side of the equation can be physically interpreted as the convection of the energy dissipation rate by the mean velocity, the first term on the right-hand side of the equation is the production of the energy dissipation rate  $\varepsilon$ .  $C_{\varepsilon 2} \frac{\varepsilon^2}{k}$  is the term for the energy dissipation rate and finally  $\frac{\partial}{\partial x_j} \left[ \left( v + \frac{v_T}{\sigma_k} \right) \frac{\partial \varepsilon}{\partial x_j} \right]$  is the diffusion of the energy dissipation rate  $\varepsilon$ .

The modelling of the turbulent viscosity involves computing the turbulent or eddy viscosity  $v_T$  as a function of the kinetic energy ( $k$ ) and the dissipation rate ( $\epsilon$ ) by:

$$v_T = \rho C_\mu \frac{k^2}{\epsilon} \quad (26)$$

Where  $C_\mu$  is a constant.

The five closure coefficients ( $C_\mu = 0.09, C_{\epsilon 1} = 1.44, C_{\epsilon 2} = 1.92, \sigma_k = 1.00, \sigma_\epsilon = 1.30$ ) and are assumed to be constant and universal although it is suggested that they might be slightly different from one flow type to another.

### 3.2.6.2. RNG $k \epsilon$

The *RNG*  $k \epsilon$  model is a model obtained from a technique called renormalization group theory.

This model is in some ways similar to the Standard  $k \epsilon$  model which has been briefly discussed in section 3.3.6.1 but with some modifications. Modifications includes the addition of an extra term (Source term  $S_\epsilon$ ) to the  $\epsilon$  transport equation (dissipation of kinetic energy transport equation) to improve the accuracy of the strained flows. The addition of the source term in strained flows results in less destruction of kinetic energy dissipation  $\epsilon$ , hereby augmenting  $\epsilon$  and reducing  $k$  which in effect reduces the effective viscosity thereby adding the effect of swirling in flows in the model because the  $k \epsilon$  model is known to be too dissipative i.e. the turbulent viscosity in recirculation have been reported to be too high (Andersson et al., 2011). The model includes analytical formulae for the Prandtl numbers while the standard  $k \epsilon$  model uses constant values. The RNG theory provides an empirically derived differential formula or equation for the calculation of the effective viscosity in the fluid which takes into consideration the effects of low Reynolds number as opposed to the Standard  $k \epsilon$  model which is only ideal for High Reynolds number. The use of this feature depends on the accurate treatment of the near wall region in the fluid. The incorporation of these features makes the *RNG*  $k \epsilon$  model a more versatile model than the Standard model.

Modelled equation for the  $\epsilon$  with the addition of the source term is given as (Andersson et al., 2011):

$$\frac{\partial \epsilon}{\partial t} + \langle U_j \rangle \frac{\partial \epsilon}{\partial x_j} = C_{\epsilon 1} v_T \frac{\epsilon}{k} \left[ \left( \frac{\partial \langle U_i \rangle}{\partial x_j} + \frac{\partial \langle U_j \rangle}{\partial x_i} \right) \frac{\partial \langle U_i \rangle}{\partial x_j} \right] - C_{\epsilon 2} \frac{\epsilon^2}{k} + \frac{\partial}{\partial x_j} \left[ \left( v + \frac{v_T}{\sigma_k} \right) \frac{\partial \epsilon}{\partial x_j} \right] + S_\epsilon \quad (27)$$

### 3.2.6.3. Realisable $k - \varepsilon$ Model

The realisable model is different from the standard  $k - \varepsilon$  model in that it features a realisability constraint on the predicted stress tensor (Anderson and Wendt, 1995), (Andersson et al., 2011). The difference in both models comes from a correction to the  $k$  transport equation where the normal stress can become negative in the standard  $k - \varepsilon$  model for flows with large mean strain rates. To this effect, the realizable  $k - \varepsilon$  model uses  $C_\mu$  which is a variable to prevent the normal stresses from becoming negative. In the realizable  $k - \varepsilon$  model the  $C_\mu$  is not taken as a constant as in the case of the  $k - \varepsilon$  model, rather it is a function of the local state of the flow which ensures that the normal stresses are always positive at all flow conditions. Neither the  $k - \varepsilon$  model and the RNG  $k - \varepsilon$  model are realizable. The terms realisability means that stress tensor satisfies Schwarz's inequality and as a result the realisable  $k - \varepsilon$  model is more likely to perform better in flows involving separation and rotation. Also, this model generally, contains a modification the dissipation ( $\varepsilon$ ) equation, which involves adding a production term for turbulent energy dissipation that cannot be found in the  $k - \varepsilon$  model and RNG  $k - \varepsilon$  model. The standard  $k - \varepsilon$  model is known to predict the spreading rate in planar jets considerable well but the prediction of the spreading rate for axisymmetric jets very poorly, this under performance being considered to be mainly due to the modelled equation of the dissipation of kinetic energy. The realisable  $k - \varepsilon$  model is known to resolve the round-jet anomaly (it predicts the spreading rates for axisymmetric jets as well as that for planar jets). This model has been tested and validated for a wide range of flows i.e. free flows, boundary layer flows, separated flows and rotating homogeneous shear flows. For all these fluid flow cases, the Realisable  $k - \varepsilon$  model has been validated to perform better than the RNG  $k - \varepsilon$  and the Standard  $k - \varepsilon$  models. One limitation of the Realisable  $k - \varepsilon$  model is that the model produces non-physical turbulent viscosities in situations when the fluid flow computational domain contains both rotating and stationary fluid zones as the model contains the effect of the mean rotation when defining the turbulence viscosity.

### 3.2.6.4. Overview of the Standard $k - \omega$ model

The Standard  $k - \omega$  model is a two-equation model and is based on the transport equation for the turbulence kinetic energy ( $k$ ) and the specific dissipation rate ( $\omega$ ) which is defined as the dissipation rate per unit turbulent kinetic energy and is used as the length determining quantity. According to Andersson et al., (2011)  $\omega \propto \frac{\varepsilon}{k}$  and is interpreted as the inverse of the time scale on which dissipation occurs. The modelled  $k$  transport equation as consistent with the equation in the book by Andersson et al., (2011) is given as:

$$\frac{\partial k}{\partial t} + \langle U_j \rangle \frac{\partial k}{\partial x_j} = v_T \left[ \left( \frac{\partial \langle U_i \rangle}{\partial x_j} + \frac{\partial \langle U_j \rangle}{\partial x_i} \right) \frac{\partial \langle U_i \rangle}{\partial x_j} \right] - \beta k \omega + \frac{\partial}{\partial x_j} \left[ \left( \nu + \frac{v_T}{\sigma_k} \right) \frac{\partial k}{\partial x_j} \right] \quad (28)$$

And the modelled  $\omega$  equation is given as:

$$\frac{\partial \omega}{\partial t} + \langle U_j \rangle \frac{\partial \omega}{\partial x_j} = \alpha \frac{\omega}{k} v_T \left[ \left( \frac{\partial \langle U_i \rangle}{\partial x_j} + \frac{\partial \langle U_j \rangle}{\partial x_i} \right) \frac{\partial \langle U_i \rangle}{\partial x_j} \right] - \beta^* \omega^2 + \frac{\partial}{\partial x_j} \left[ \left( \nu + \frac{v_T}{\sigma_\omega} \right) \frac{\partial \omega}{\partial x_j} \right] \quad (29)$$

where the turbulent viscosity is calculated from the equation:

$$v_T = \frac{k}{\omega} \quad (30)$$

The model was developed by Wilcox, (1998). One advantage of the model over the  $k \varepsilon$  models is improved performance in boundary layers of flows when under adverse pressure gradients. The model also can be applied over the boundary layer including the viscous dominated regions of the flow without any required modification, without requiring the computing of wall distance in the computation. A disadvantage of the Standard  $k - \omega$  model is that in its original form, the boundary layer computations are sensitive to the specific dissipation rate in free stream. Over the years this model has been modified by adding production term to the turbulent kinetic energy ( $k$ ) and the specific dissipation rate ( $\omega$ ) equations which seem to have improved the accuracy of the model in predicting free stream flows or free shear flows.

### 3.2.6.5. Overview of Shear Stress Transport (SST) Model

The SST  $k \omega$  model was developed by Menter, (1994) to address the problem of the sensitivity of the Standard  $k \omega$  model to free stream or inlet conditions. To achieve this, Menter converted the  $k \varepsilon$  model into a  $k \omega$  formulation; this enables the Shear Stress Transport Model to achieve the accurate and robust performance of the  $k \omega$  model in the near wall region (viscous dominated region) with the free-stream independence and prudence of  $k \varepsilon$  model in the far field region. The SST model in many ways is similar to the  $k \varepsilon$  model but with some modifications made to the model. These modifications include multiplying the Standard  $k \omega$  model and the

transformed  $k - \varepsilon$  model with a blending function to combine the models. The blending function by which the models are multiplied is designed to have a zero away from the surface which then activates the transformed  $k - \varepsilon$  model and to be 1 at the near wall region of the fluid flow which activates the  $k - \omega$  model. The SST model implements a “damped cross-diffusion derivative term in the  $\omega$  equation” and applies the blending function which ensures that the transport equations of the model can perform well in both near and far field regions of the fluid flow problem (Fluent, 2012). Other modifications include modifying the way in which the turbulent viscosity is achieved to other to account for the transport of turbulent shear stresses in the fluid flow. Constants of modelling are also different in the SST model than in the Standard  $k - \omega$  model. The addition of these features makes the SST  $k - \omega$  Model more robust and accurate for a wider range of flow problems which includes flows around aerofoils and flows at high subsonic speed (transonic shock waves).

The Transport Equations for the SST  $k - \omega$  model is given below; the turbulence kinetic energy  $k$  and the specific dissipation rate  $\omega$  are obtained from the given transport equations and are given below as consistent with Menter et al., (2003), Launder and Sandham, (2002).

$$\frac{\partial(\rho k)}{\partial t} + \frac{\partial(\rho U_i k)}{\partial x_i} = \tilde{P}_k - \beta * \rho k \omega + \frac{\partial}{\partial x_i} \left[ (\mu + \sigma_k \mu_t) \frac{\partial k}{\partial x_i} \right] \quad (31)$$

And the  $\omega$  equation is given as:

$$\frac{\partial(\rho \omega)}{\partial t} + \frac{\partial(\rho U_i \omega)}{\partial x_i} = \alpha \rho S^2 - \beta \rho \omega^2 + \frac{\partial}{\partial x_i} \left[ (\mu + \sigma_\omega \mu_t) \frac{\partial \omega}{\partial x_i} \right] + 2(1 - F_1) \rho \sigma_{\omega 2} \frac{1}{\omega} \frac{\partial k}{\partial x_i} \frac{\partial \omega}{\partial x_i} \quad (32)$$

The blending  $F_1$  is defined by:

$$F_1 = \tanh \left\{ \left\{ \min \left[ \max \left( \frac{\sqrt{k}}{\beta^* \omega y}, \frac{500\nu}{y^2 \omega} \right), \frac{4\rho \sigma_{\omega 2} k}{CD_{k\omega} y^2} \right] \right\}^4 \right\} \quad (33)$$

With  $CD_{k\omega}$  which is the cross-diffusion term and it is given by:

$$CD_{k\omega} = \max\left(2\rho\sigma_{\omega 2} \frac{1}{\omega} \frac{\partial k}{\partial x_i} \frac{\partial \omega}{\partial x_i}, 10^{-10}\right) \quad (34)$$

Where  $y$  denotes the distance to the nearest wall. The blending Function ( $F_1$ ) = 0 away from the surface of the wall giving a  $k - \varepsilon$  model and switches over to ( $F_1$ ) = 1 inside the boundary layer giving a  $k - \omega$  model.

The turbulence eddy viscosity is calculated by:

$$v_t = \frac{\alpha_1 k}{\max(\alpha_1 \omega S F_2)} \quad (35)$$

$S$  is the invariant measure of the strain rate and  $F_2$  is the second blending function which is defined as:

$$F_2 = \tanh\left[\left[\max\left(\frac{2\sqrt{k}}{\beta^* \omega y}, \frac{500v}{y^2 \omega}\right)\right]^2\right] \quad (36)$$

A production limiter is used in the shear stress turbulence model to prevent the accumulation of turbulence in stagnation regions of the fluid flow. The production limiter is given as:

$$P_k = \mu_t \frac{\partial u_i}{\partial x_j} \left( \frac{\partial u_i}{\partial x_j} + \frac{\partial u_j}{\partial x_i} \right) \rightarrow \tilde{P}_k = \min(P_k, 10 \cdot \beta^* \rho k \omega) \quad (37)$$

All the constants of the equation are computed by a blending from the corresponding constants of the  $k - \varepsilon$  model and  $k - \omega$  model by:

$$\alpha = \alpha_1 F + \alpha_2 F(1 - F) \quad (38)$$

The constants for the shear stress turbulence model (SST model) are given as:  $\beta^* = 0.09, \sigma_{\omega 2} = 0.856, \sigma_{k2} = 1, \beta_2 = 0.0828, \beta_1 = 0.075, \sigma_{\omega 1} = 0.5, \sigma_{k1} = 0.85, \alpha_1 = 0.555$  or  $0.31, \alpha_2 = 0.44$

A version of this turbulence closure model is available in STAR-CCM+ and has been used for the main simulation presented in this thesis.

### 3.2.7. Near Wall Treatment

Turbulent flows are generally affected by the presence of walls; subsequently most fluid flow physics problems in CFD are bounded by the presence of walls as well, walls that affects the flow characteristics of the fluid flow adjacent to them. The mean velocity field in the flow is affected through the no-slip condition that must be satisfied at the wall. According to boundary layer theory (Riedeberger and Rist, 2012), (Schlichting et al., 1955), (Schlichting, 1968) the viscous forces that act in the fluid require a non-slip boundary at the bounding surface leading to the build-up of a layer in which the stream wise velocity increases progressive by normal to the wall and significant changes occurring in the fluid flow characteristics (i.e. velocity, stresses) can be observed. In the region close to the walls viscous damping reduces the tangential velocity fluctuations while the normal fluctuation of the velocity is reduced by kinematic blocking. Outside this region just beyond the near wall region, the turbulence is rapidly increased or augmented by the production of turbulence kinetic energy due to shearing in the flow or the presence of large gradients in the mean velocity.

Modelling of the near wall has a significant effect of the accuracy of the numerical simulations because walls are the main source of turbulence and main vorticity in the fluid flow. Also, at the near wall region the solution variables have the largest gradients in this region and most scalar transport occurs more strongly. To this effect, it is important to accurately represent the flow phenomenon in the near wall region in order to be able to successfully predict wall bounded turbulence flows. Turbulence closure models such as the  $k \varepsilon$  model, Large Eddy Simulation model and Reynolds stress models are valid for flows in the regions far away from the walls, and as a result when using these models, one needs to select appropriate wall-laws available in the CFD package to make these models suitable for wall-bounded flows or near wall flows. Models such as the Spalart-Allmaras and the  $k \omega$  models were developed to be capable of been applied and valid through-out the boundary layer provided the near wall mesh is properly sufficiently refined.

There are generally two approaches to modelling near wall regions in turbulent flows to ensure that the closure models can capture the large gradients of flow properties that are close to the walls. In the first approach, the viscous sub-layer and the buffer region are not resolved but rather walls functions (semi-empirical formulae) are used to bridge the viscosity affected inner region between the near wall and the outer region (fully turbulent region). The use of wall functions removes the needs to modify the turbulence model to account for the effect of the wall. This approach is ideal in most high Reynolds number flow as it saves computational resources; this is because the sub-viscous and buffer region of the flow do not need to be resolved as such. This approach is robust

and produces reasonably accurate results. The wall function treatment is not suitable for situations where low Reynolds effects are dominant and such situations require the use of the near wall treatment which is the second technique that is discussed in this report. In the second technique turbulence models are modified to enable the viscosity affected region to be resolved using mesh all the way down to the wall. Wall treatment is generally used together with Reynolds Average Navier-Stokes Simulations Model. The wall treatment options that are available in STAR CCM+ are;

High  $y^+$  wall treatment: Is the similar to the approach in which the near wall cells should be placed in the log-law region ( $30 \leq y^+ \leq 100$ )

Low  $y^+$  wall treatment: Best suited for low Reynolds turbulence models where the generated mesh is sufficient enough to resolve the viscous sub-layer ( $y^+ = 1$ ) with a recommended 10-20 cells within the boundary layer itself.

All  $y^+$  wall treatment: A hybrid or combination of high  $y^+$  and low  $y^+$  treatments. They are designed to give accurate results if the near wall cell centroid is in the viscous layer, the log law region or the buffer region.

### **3.2.7.1. Boundary Layer Velocity Profile**

The nature of the flow near the wall has been observed to be dominated by viscous forces while the influence of Reynolds stresses on the flow becomes significant further away from the wall where the impact of the viscous stresses have been significantly reduced (Riedeberger and Rist, 2012). Experiments from several sources have shown that the near-wall region of the fluid flow can be sub-divided into three or four layers. In the first layer called the viscous sub-layer, the flow in this region is almost laminar in nature. In this layer of the flow molecular viscosity plays a significant role in the heat, momentum and heat transfer in the fluid flow. In the outer layer known as the fully turbulent layer, turbulence plays a significant role in the flow. A region exists between the viscous sub-layer and the fully turbulent layer (region) or the log-law region where the effect turbulence and the molecular viscosity have equal significant. Fig. 47 illustrate the sub-divisions of the Near-wall Region obtained from ANSYS theory guide

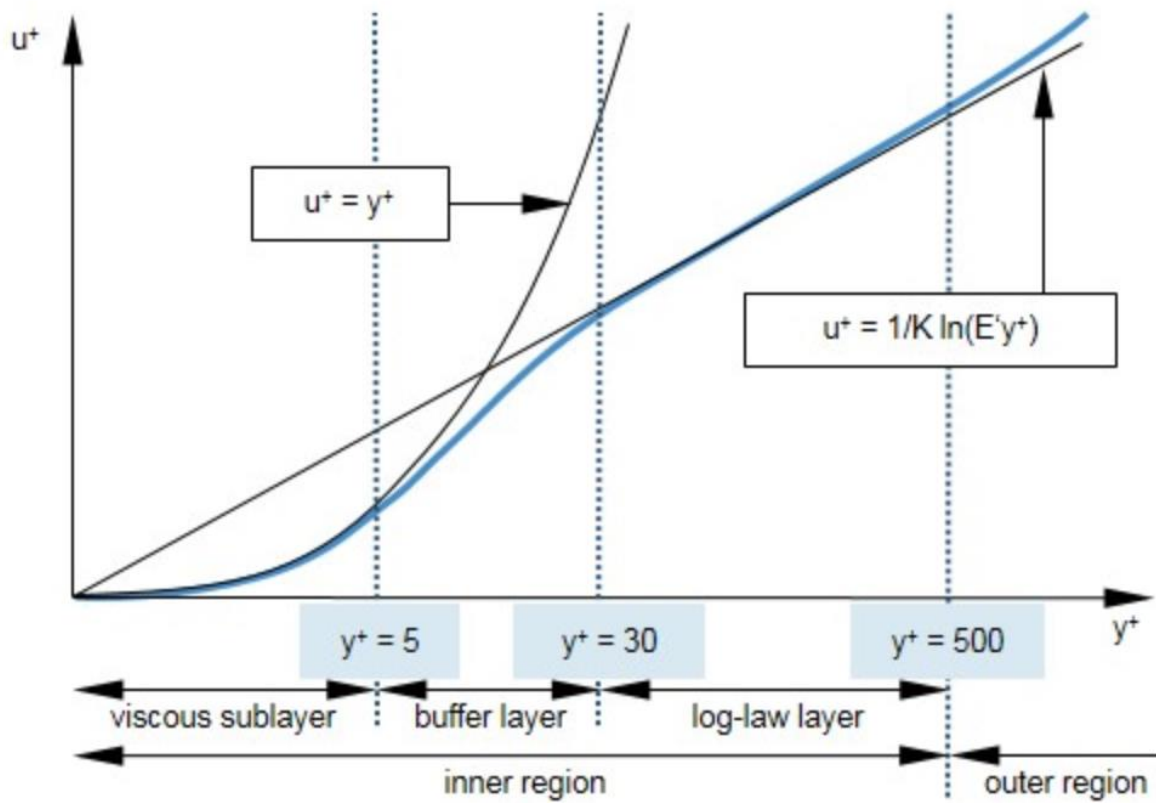


**Fig. 47: Illustrates the sub-divisions of the Near-Wall region (CD-ADAPCO, STAR-CCM+, 2015)**

This general division in the boundary layer means that one can generally distinguish between the very low and very high regions in the boundary layer. To study the regions, close to the wall an analysis of the scales and characteristics of the variables for the flow in the boundary layer is essential. Kinematic viscosity ( $\nu$ ) and shear stress  $\tau_w$  are very important parameters in studies involving flows in the near wall regions and as a result it is appropriate to use these parameters as references to introduce the scales of velocity and length.

Thus, the friction velocity can be defined as:

$$u_* = \sqrt{\frac{\tau_w}{\rho}} \quad (39)$$

Where the  $\tau_w$  shear stress can be obtained from re-arranging

$$\overline{cf} = \frac{\tau_w}{\rho U^2 / 2} \quad (40)$$

And the viscous length scale

$$\delta_v = \nu \sqrt{\frac{\rho}{\tau_w}} \quad (41)$$

Therefore, with these parameters the local non-dimensional distance to any cell centroid of the near wall cell can be found.

$$\mathbf{y}^+ = \frac{u^* y}{\nu} = \frac{y}{\delta_v} \quad (42)$$

This is equivalent to the Reynolds number term, it can be used to determine the level of viscous and Reynolds influences that are to be expected to have an effect on the region in the fluid flow (Pope, 2000). The different layers or regions as can be seen in Figure 12 in the near wall flow are defined based on the value of  $\mathbf{y}^+$ . In the viscous sub-layer  $\mathbf{y}^+$  less than 5 (molecular viscosity has a direct effect on the shear stress), in the log law region for  $\mathbf{y}^+$  greater than 30, the law log holds, while in the outer region where  $\mathbf{y}^+$  is greater than 50 or 60 (depending on the author) direct effect of viscosity can be ignored. The higher the Reynolds number, the smaller the section of the wall occupied by the viscous wall regions (Pope, 2000). This dimensionless variable is also important as the near wall treatment for a turbulence model in computational fluid dynamics simulation is usually selected based on the local dimensionless distance to the cell centroid of the near wall cell from the  $\mathbf{y}^+$  value.

Another non-dimensional variable which is used to describe the flow in the near wall region of the fluid flow is the dimensionless velocity in the near wall region which can be defined as:

$$\mathbf{u}^+ = \frac{u}{u^*} \quad (43)$$

*Inner layer* - Close to the wall  $\frac{y}{\delta} < 1$ , the non-dimensional velocity  $\mathbf{u}^+$  depends only on the dimensionless wall distance to the near wall  $\mathbf{y}^+$  (Pope, 2000), (Riedeberger and Rist, 2012) i.e.

$$\mathbf{u}^+ = \frac{u}{u^*} \equiv \mathbf{f}_w(\mathbf{y}^+) \quad (44)$$

This is known as the Law of the wall postulated by Prandtl, (1949) “that at high Reynolds number close to the wall the mean velocity profile is determined by the viscous scales independent of  $U_0$  and  $\delta$ ” (Pope, 2000). Thus, according to the Prandtl hypotheses the velocity profile in the region  $\frac{y}{\delta} < 1$ , of the boundary layer can be found only in terms of the non-dimensional wall distance.

In the viscous sub-layer, the non-slip condition at the walls and the use of a Taylor series expansion for  $f_w(\mathbf{y}^+)$  gives  $f_w(\mathbf{y}^+) = \mathbf{y}^+ + \mathcal{O}(\mathbf{y}^{+2})$  as a result yielding a linear relationship  $\mathbf{u}^+ = \mathbf{y}^+$

For  $\mathbf{y}^+$  less than 5

For higher Reynolds number i.e.  $\mathbf{y}^+$  greater than 30, a similar mathematical representation and analysis yields the logarithmic law of walls due to von KÁRMÁN and Burgers, (1935), Von Karman, (1930).

(45)

$$\mathbf{u}^+ = \frac{1}{k} \ln \mathbf{y}^+ + B$$

$k$  represents the von Karman constant. The values for the variables in the Log law have been known to vary in different literature but in general they can be taken to be in the range of 5% of  $k = 0.41$ , and  $B = 5.2$ . The mean velocity profile tends to agree very well with the DNS data for  $\mathbf{y}^+ > 30$  as stated by Pope (2000).

The buffer region as already discussed exists between  $5 < \mathbf{y}^+ < 30$ . The velocity profile of this region can be described by using the Law of walls together with a damping function (Pope, 2000). As the  $\mathbf{y}^+$  values approach 50 it has been observed that the mean velocity profile cannot be properly accounted for by the law of walls and as such the *velocity defect law due to Von Karman* (Von Karman, 1930) has to be used. The Velocity defect law due to the Von Karman is given by:

$$\frac{U_0 - U}{u^*} = F_D \left( \frac{y}{\delta} \right) \quad (46)$$

The *velocity defect law* is the difference between the mean velocity  $U$  and the centre line value or velocity at the outer edge of the boundary layer  $U_0$ . The law states that the velocity defect normalized by  $u^*$  depends on only  $\frac{y}{\delta}$  (Pope, 2000).

It is also essential to use the Law of wake to account for *the velocity defect law* effect (the difference between the mean velocity and the centre line value velocity at the outer edge of the boundary layer) by using the wake function  $w\left(\frac{y}{\delta}\right)$ . Since the velocity obtained is gained by adding the wake law and the log law, it can be put in the form of the velocity defect to give:

$$\frac{U_0 - U}{u^*} = \frac{1}{k} \left\{ -\ln\left(\frac{y}{\delta}\right) + \Pi \left[ 2 - w\left(\frac{y}{\delta}\right) \right] \right\} \quad (47)$$

$\Pi$  = the parameter that represents the wake strength. According to Pope, (2000) this relationship was found by him to accurately estimate the characteristics of the flow in the outer region of the boundary layer spectrum. Also, it can be used to derive the log-law as an asymptotic case.

### 3.2.8. Discretisation

Discretisation is one of two stages that are applied in computational fluid dynamics to obtain numerical solutions to a fluid flow physics problem. It involves the conversion of partial differential equations together with the boundary and initial conditions to form a system of discrete algebraic equations (Tu et al., 2012). The second step involves the implementation of numerical techniques or methods to obtain a solution to the system of algebraic equations that have been formed by discretization. Most CFD packages use the Finite Volume method as the main technique or method for numerical solution. The algebraic form of the governing equations for the fluid flow within the computational fluid dynamics package are approximated by applying finite difference type approximations to a finite volume cell in space. At the cell faces, surface fluxes of transport variables that are required for the simulation can be obtained by using various interpolation schemes (Tu et al., 2012). Some popular interpolation schemes that could be used are First Order Upwind (forward or backward difference approximation), Second Order Upwind, Quadratic Upstream interpolation of the Convective Kinetics (QUICK) and Second Order Central. It has been reported that some of these interpolation schemes do not perform very well on the upstream occurrence of the fluid flow and as a result only take into consideration the direction of the flow. There are other higher order interpolation scheme that exist which have reported to probably be able to achieve higher levels of accuracy for the evaluation at the cell face. Examples of such interpolation schemes are the SIMPLE, PISO algorithm and the SIMPLER. Interpolation schemes were developed for the purpose to act as a link between the pressure and the velocity which accounts for the conservation of mass within the simulation field. The Finite difference method and the finite element method are basic tools that are used in the solution of partial differential equation in general and in computational fluid dynamics, but the more popular method is the Finite volume method which has the characteristics of both the Finite element method and the finite difference method. The Finite Volume method or approach will be discussed in the next paragraphs since this method is the more commonly used method in most Computational Fluid Dynamics package including the CFD STAR-CCM+ code that was used for the simulations presented in the report.

### 3.2.9. Finite Volume Method

The finite volume method involves breaking down the solution domain into a finite number of small continuous control volumes which corresponds to the cells of a computational grid. The resulting statement expresses the exact conservation of the flow variables of each of the control volumes. At the centre of each of the control volume the desired or relevant variables are calculated. Discrete versions of the integral form of the continuum transport equations are applied to each of the control volumes. The reason for doing this process is to obtain a set of algebraic equations, where the sum of the number of un-knowns in each of the equation system or set corresponds to the total number of control volumes. If non-linear equations are obtained, iterative techniques that depend on linearisation strategies must be used. The obtained linear equations are solved by using an algebraic multi-grid solver. An advantage of the Finite volume method is that it can accommodate both structured and unstructured grids since it works well with control volume and not grid intersection points. Also, finite element type meshes can be used with this method of which the mesh can be formed by triangles or quadrilaterals for 2-D cases or hexahedra or a tetrahedral mesh for 3-D cases. The use of this un-structured mesh makes it more adaptive to more complex geometries.

### 3.2.10. Grid or Mesh Generation

Grid generation is basically the sub-division of the computational domain into a number of grid cells which covers all parts of the geometry of interest. Grid generation is the key to the computational fluid dynamics simulation process, as the type of grid and quality of the grid used for the simulation will determine the success or the failure of the simulation process in terms of obtaining the desired results. It also has a direct impact on the convergence and stability of the simulation. For grid generation, the mesh must be sufficiently fine to provide an appropriate resolution of the important fluid field features and properly capture the geometry to adequately represent the flow around the geometry. For wall bounded flows i.e. (flow around an aerofoil). It is recommended that mesh density be concentrated or properly refined around expected recirculation areas, vortices or steep flow gradients inside the viscous boundary layer to properly capture the flow characteristics in this region. As result, much time spent in CFD simulation both for research and industrial application is spent on the generation of the grid. It can be a computationally expensive process, but the introduction of cluster computing has significantly reduced the time in the process for CFD simulations.

Generally, there are two types of *Mesh structured and unstructured mesh* arrangements. A structured mesh consists of families or groups of grid lines with the property the members of each group should not cross each

other and are allowed to cross the members of other groups just once. The position of any grid point within the simulation domain is identified by a set of 2-D or 3-D indices i.e.  $i, j, k$ . An example of such a mesh in most CFD codes is the trimmer mesh. The number of grid points required to use a mesh of this type can be computationally expensive especially for more complex geometry. As a result, un-structured mesh types are more favoured as they provide a faster way of generating a mesh for more complex geometries and would generally require less computational effort to obtain an adequate mesh for a given fluid flow problem. Since the simulations presented in this report focus on complex geometry, the un-structured mesh (polyhedral, hexa-hedral mesh) and Body fitted mesh will be discussed in more details. In most aerospace problems (i.e. aircraft simulation or aerofoil simulation) the body fitted or un-structured mesh of either polyhedral, tetrahedral or hexahedral mesh is favoured since the structured mesh does have the tendency to generate highly skewed cells which can affect the stability or convergence of the simulation.

The topology of the body fitted mesh involves a mesh having been assembled from several structured blocks that are attached to each other. In this configuration, the attachment of each face of the adjacent block may be regular or arbitrary. Using this meshing approach provides the flexibility required to enable one to choose the best topology for each of the sub-divided blocks and as a result one can decide the appropriate grid structure based on C- grid, O-, or H- grid or unstructured mesh of Polyhedral, tetrahedral or hexahedral grids to fill each block. The use of *Chimera- grids* is another modern way of grid generation which is used. This type of mesh involves using block structured grids with overlapping blocks which are connected by an interpolation process. The Chimera grid has the advantage of been easily implemented in moving bodies (i.e. changing the angle of attack of an aerofoil without having to re-mesh or overtaking cars etc.) and complex geometries can be treated easily.

Un-structured meshes can be formed by using any of the three meshing algorithms: Delaunay meshing; the advancing-front method and the Quadtree / Octree method. In summary these meshing technique involves either using triangular meshing by the Delaunay method, or by forming a triangular mesh by adding individual elements one after the other to an existing front of already generated elements whose line segment forms the triangular mesh or simply by sub-dividing the physical space down to a desired resolution where vertices of the resulting octree or quadtree are then used as the node points and the octants are divided into tetrahedral elements for 3-D and the quadrants into triangles for 2-D. An Un-structured mesh such as the polyhedral mesh are formed by converting a tetrahedral mesh into a polyhedral mesh. The polyhedral meshes are created by using agglomeration thereby reducing the cell counts of the tetrahedral mesh. Polyhedral meshes are mostly favoured when compared to tetrahedral meshes and this type of un-structured mesh has been implemented in the numerical simulations

presented in this report as it has been reported to improve the resolution of the underlying tetrahedral mesh while at the same time reducing the number of mesh counts which directly reduces the computing time. Most commercial CFD packages also address the issues of near wall refinement which has been known to be an issue with using an un-structured mesh by using Prismatic cells types to resolve the boundary layer region of fluid flow.

For the simulation presented in this report and based on the type of geometry investigated the polyhedral mesh to capture the simulated geometry and fluid flow properties is used together with prism layers to resolve the near regions in the boundary layers.

## Chapter 4: Initial CFD results

In this chapter, the test cases to validate the numerical approach are also presented together with initial design studies of the devices. Section 4.1 presents CFD test cases to validate the numerical method, Section 4.2 presents the initial CFD results and proposed designs and Section 4.3 discusses the proposed design for the optimisation study and in Section 4.4 the effect of fuselage on wing aerodynamics is treated.

### 4.1. CFD Test cases to validate numerical method

The numerical investigation of the wing and wing-winglet configurations to be considered is done using the commercial CFD program STAR-CCM+ designed by CD-Adapco. STAR-CCM+ is a client-server-based software using object methods in C++ and java. The software uses a cell centred finite volume discretisation scheme applied to cells of regular and arbitrary mesh shapes. The software offers the options to create sketches or import 3-D geometries or 2-D shapes from other packages i.e. CATIA, mesh the geometry using the in-built automated grid generation algorithm which is capable of generating structured mesh (Trimmer mesh) and unstructured mesh (polyhedral, tetrahedral or hexahedral mesh) before solving for the generated grid with the offered 2-D or 3-D Reynolds Averaged Navier Stokes solvers for both steady or un-steady state problems and using the available turbulence model options as turbulence closure models.

To build some confidence on the numerical method that is adopted for this research, it was essential to carry out a number of test cases to predict the aerodynamic performance of a wing and or wing winglet configuration. The following test cases are presented.

- CFD work by Guerrero et al., (2012a) on a spiroid winglet using the Spalart Allmaras turbulence model
- CFD work by Beehook and Wang, (2013) on a blended winglet using Spalart Allmaras turbulence model
- Lift Prediction Workshop by NASA. A summary of the CFD campaign can be found in Rumsey et al., (2011a), Slotnick et al., (2011). The CFD work performed to replicate this work employed three turbulence models; the K-Omega ( $k - w$ ) model, Shear Stress Transition (*SST*) model and the Spalart Allmaras model. This was also used as a bench mark to check for any difference in aerodynamic performance prediction due to the various turbulence models.

The established mesh models, physics and solvers are discussed in the subsequent section which also includes the modelled design and configuration.

#### 4.1.1. Geometry

The geometries studied were identical to Guerrero et al., (2012a) for the spiroid winglet concept, Beechhook and Wang, (2013) for the blended winglet and Rumsey et al., (2011a), Slotnick et al., (2011) for the study to replicate work for the first lift prediction workshop (LPW). An isometric view of the geometries is shown in Figs. 48 – 50. The design parameters and specifications are presented in Table 1, Table 2 and Table 3 all the designs were performed in STAR-CCM+ CAD modeller software for easy compatibility with the CFD code.

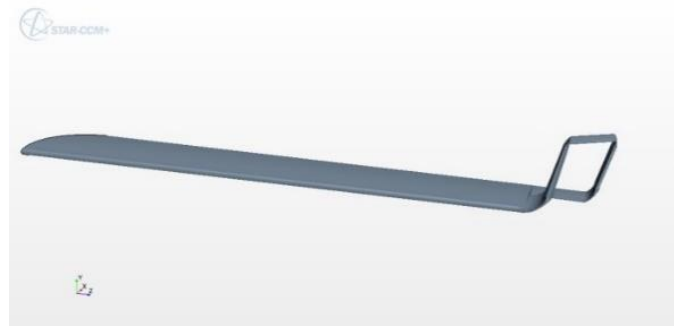


**Fig. 48: Wing with spiroid winglet**

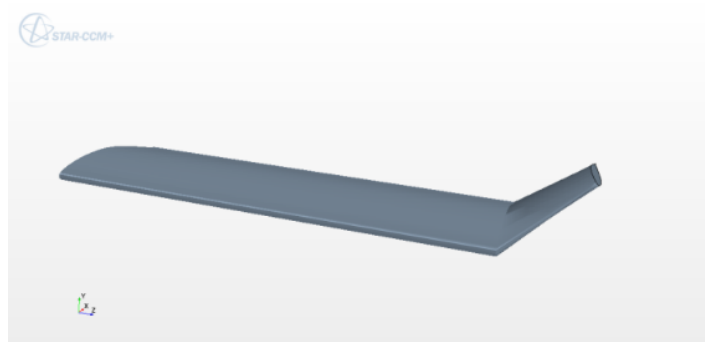


**Fig. 49: Wing with blended winglet**

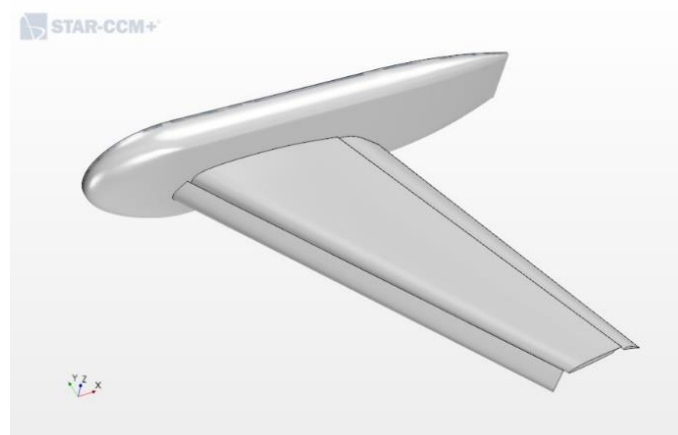


**Fig. 50: Wing and fuselage configuration Lift Prediction Workshop 1 (Rumsey et al., 2011b)**

**Table 1: Design parameters for clean wing and spiroid winglet**

Parameters	Clean wing	Spiroid equipped wing
<b>Semi-span</b>	4m	4.42m
<b>Tip chord</b>	0.7m	0.7m
<b>Sweep</b>	3.01 degrees	3.01 <i>degrees</i>
<b>Spiroid – Dihedral length</b>	N/A	0.451m
<b>Spiroid – top rectangular extension</b>	N/A	0.266m

**Table 2: Design parameters clean wing and blended winglet**

Parameters	
<b>Air-foil – section profile</b>	6-digit NACA series, NACA 65 <sub>3</sub> 218
<b>Wing semi-span</b>	330 mm
<b>Winglet root chord</b>	121 mm
<b>Winglet tip chord</b>	60.5 mm
<b>Winglet di-hedral angle</b>	45 <i>degrees</i>
<b>Winglet tip chord angled height</b>	55.1 mm
<b>Winglet tip chord vertical height</b>	39.0 mm
<b>Winglet tip chord horizontal length</b>	39.0 mm
<b>% to base used for the winglet</b>	16.67% of base wing used.

**Table 3: Lift Prediction Workshop 1 wing design specification**

Parameters	
<b>Reference area</b>	2.04646817m <sup>2</sup>
<b>Mean aerodynamic chord</b>	1.0067036 m
<b>Semi span</b>	2.1603716 m
<b>Aspect ratio</b>	4.561
<b>LE sweep</b>	33.89 degrees
<b>¼ c sweep</b>	29.97 degrees
<b>TE sweep</b>	16.24 degrees
<b>Tip cruise chord</b>	0.5363464 m
<b>Root cruise chord</b>	1.3582142 m

#### 4.1.2. Mesh and Computational Domain

Polyhedral elements formed from a transformed tetrahedral mesh were generated for all three models using the STAR-CCM+ mesh modeller. Several meshing options are available in the CFD code i.e. Trimmer mesh – structured mesh, hexahedral mesh – Un-structured mesh, tetrahedral mesh – un-structured mesh. The polyhedral mesh model was adopted based on its ability to adequately capture complex shapes such as the spiroid winglet with a lesser mesh count. A robust prism layer meshing algorithm was employed to capture the flow characteristics

in the boundary layer region *with*  $y^+$  value of less than 1 for all cases. The  $y^+$  value is calculated by using equations 36 – 39. Summary of the key mesh parameters are presented in Table 4.

**Table 4: Mesh specifications**

Mesh parameters	Clean wing & wing plus spiroid	Clean wing & wing plus blended winglet	Wing configuration for Lift Prediction Workshop 1
Mesh base size	0.06m	0.04m	0.02m
Surface refinement	12%	12%	12%
LE refinement	5%	5%	5%
TE refinement	5%	5%	5%
Number of prism layers	10	10	10 – 20
Total number of mesh count	2million	1.5million	20 million

Fig. 51 - Fig. 53 show the surface volumetric mesh density on the wing surface. By using the surface size modification options available within the automatic meshing algorithm in STAR-CCM+, the volumetric mesh was refined in regions around the leading and the trailing edges of all wing configurations to capture the geometry around the edges. Surface refinement was also defined on the surface of the wing by using a certain percentage (25%) of overall base size and the edges of the spiroid and blended wing-tip devices. Fig. 54 – Fig. 56 shows the domain and boundary conditions used to replicate the work in Guerrero et al., (2012a), Beechook and Wang, (2013) and Rumsey et al., (2011a) respectively.

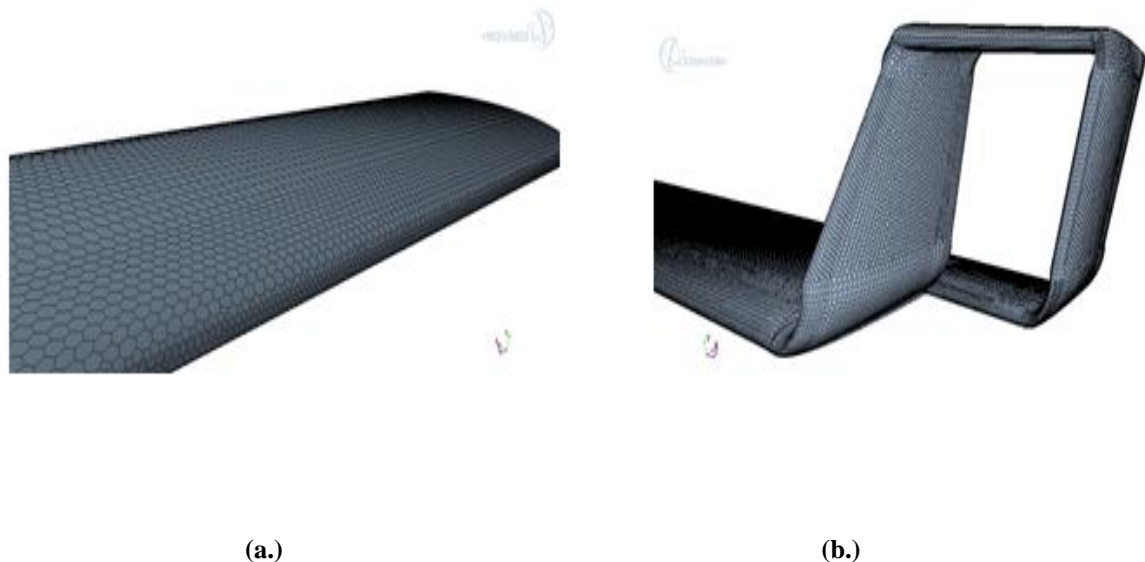
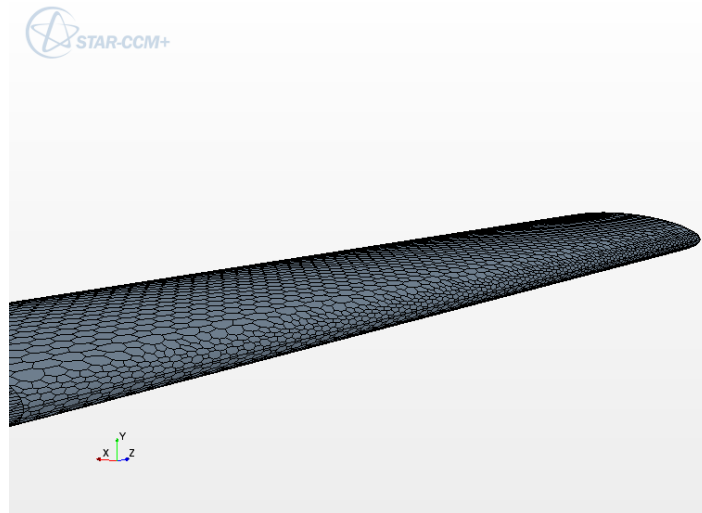


**Fig. 51: Volumetric mesh representation (a.) clean wing and (b.) spiroid winglet**



(a.)



(b.)

**Fig. 52: Volumetric mesh representation (a.) clean wing and (b.) blended winglet**

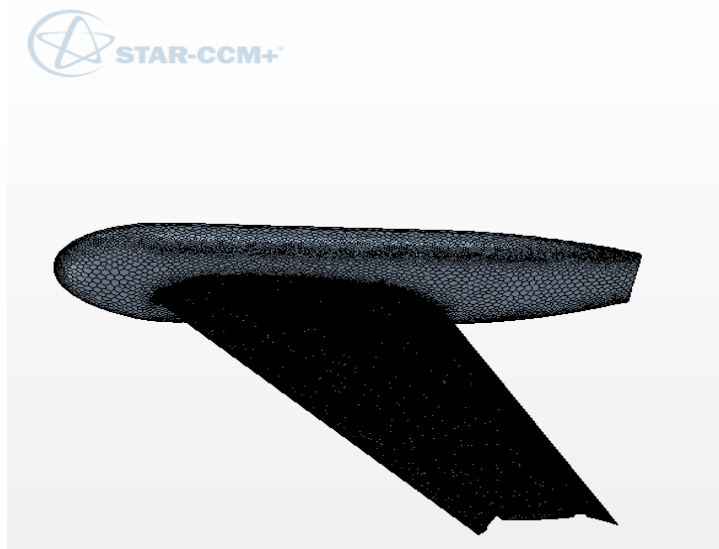


**Fig. 53: Volumetric mesh representation - Lift Prediction Workshop 1 (Rumsey et al., 2011b)**

The computational domain used for this study models both a wind-tunnel test section and open-air conditions (freestream). As shown in Fig. 54 and Fig 56, A symmetrical condition was used at the root chord region of the wing. Inlet conditions were specified as velocity inlet in the case of a wind-tunnel, the outlet was defined as pressure outlet and no-slip walls were specified at the sides of the domain. Table 5 summarises the boundary conditions and physics parameters applied.

**Table 5: Summarized boundary conditions**

Physics and boundary parameters	Clean wing & wing plus spiroid	Clean wing & wing plus blended winglet	Wing configuration for Lift Prediction Workshop 1
Velocity	1.5 m/s	35 m/s	
Mach number	-	-	0.201
Temperature	300 K	300 K	288 K
Angle of attack	0 – 15 degrees	0 – 12 degrees	
Pressure	101325 pascals	101325 pascals	10000 pascals
Turbulence intensity	1 %	1%	1%
Turbulence viscosity ratio	10 %	10%	10%
Turbulence closure model (s)	Spalart Allmaras	Spalart Allmaras	Spalart Allmaras, K-Omega Menter, Shear Stress Transition Model

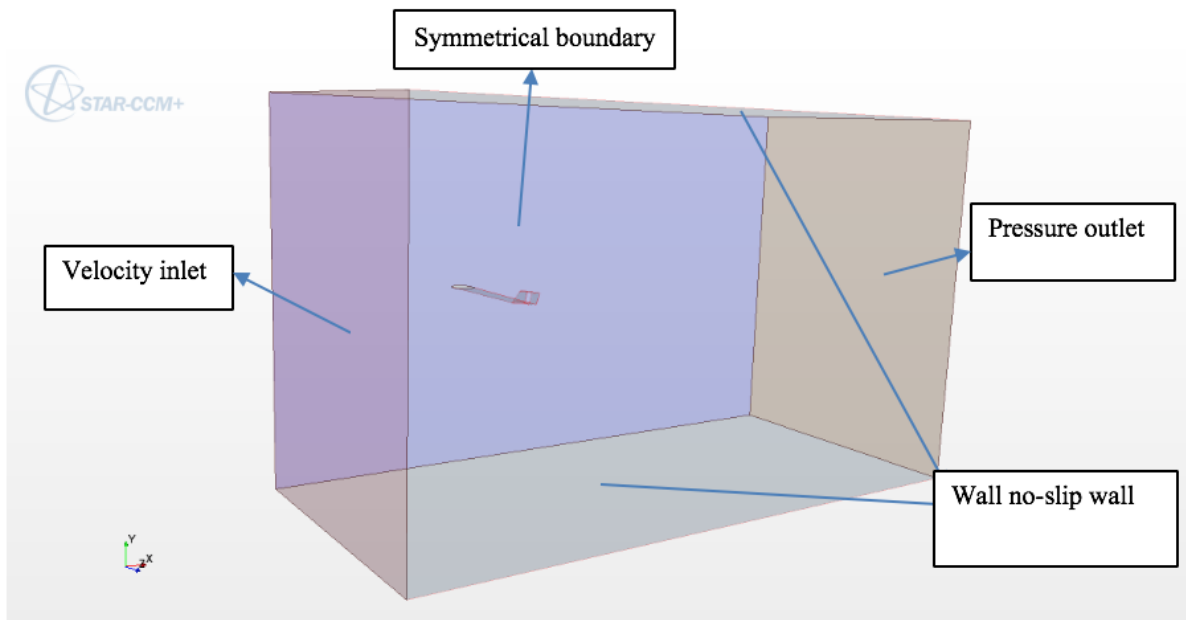


**Fig. 54: Domain and boundary conditions**

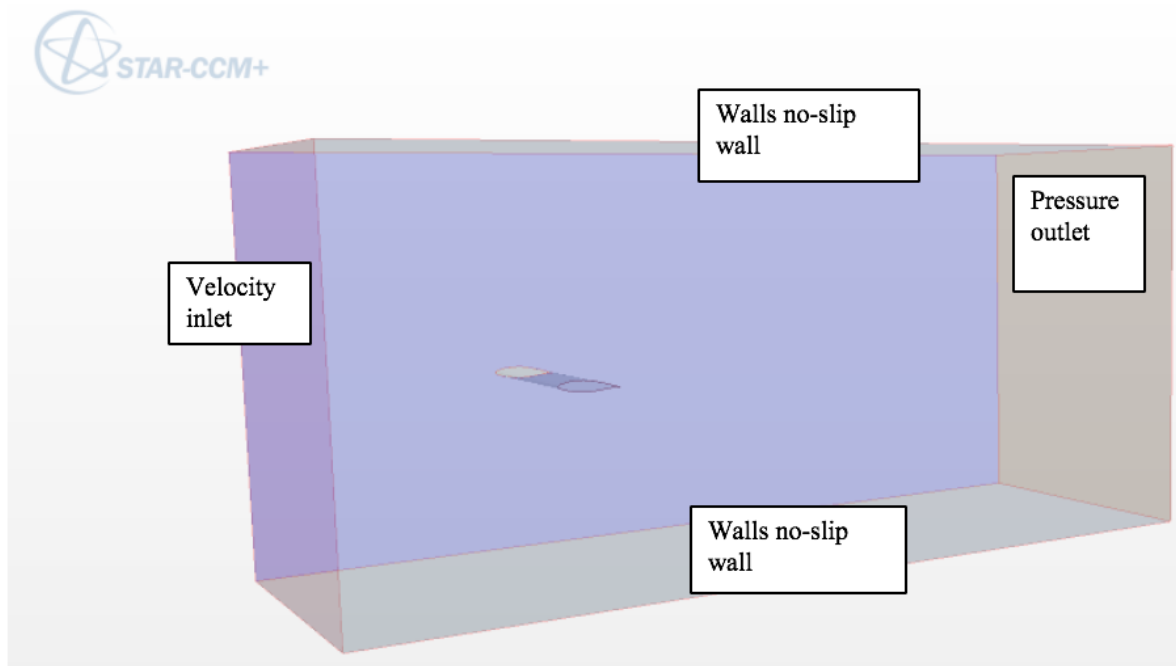


**Fig. 55: Domain and boundary conditions**

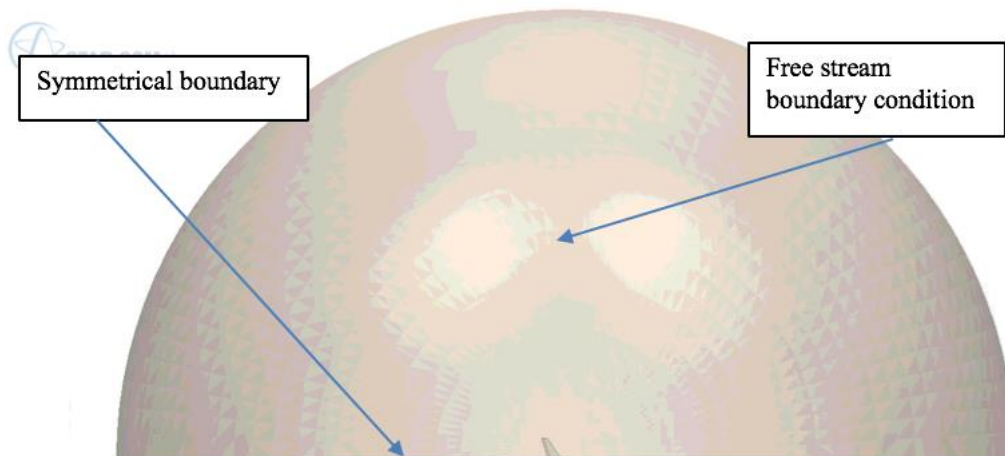


**Fig. 56: Domain and boundary conditions (Lift Prediction Workshop 1)**

#### **4.1.3. Computational Approach and Turbulence modelling**

Steady-state Reynolds Average Navier Stokes simulation was performed on the generated volumetric mesh by STAR-CCM+ version V9.02.06 and version 10.04.009. In STAR-CCM+, two flow solver options are available:

(1) Pressure based – using a segregated approach using Rhie and Chow, (1983) interpolation (pressure–velocity coupling together with a SIMPLE-type algorithm). The segregated flow model solves the flow equations in a segregated way where the bridge between the continuity and the momentum equations are achieved with a predictor corrector approach. This solver option has been suggested to work better for low speed to mid-speed flows (incompressible flows). (2) The density-based solver – coupled approach using the pre-conditioning of (Weiss and Smith, 1995). The coupled approach solves the conserved form of the governing equations for continuity, momentum and energy simultaneously using the pseudo-time marching approach. This approach has been known to work well for both incompressible and compressible flows. A wide range of turbulence closure models are also provided. This study uses the pressure based – segregated approach using a version of interpolation to solve the conserved form of the governing equations to replicate the work by Guerrero et al., (2012a) and Beechook and Wang, (2013) while the density based solver using the pre-conditioning of (Weiss and Smith, 1995) is adopted to replicate the Lift Prediction Workshop 1. The turbulence closure models used for the study can be seen in Table 5.

#### **4.1.4. Force coefficients ( $C_L$ and $C_D$ ) – Spiroid winglet**

Fig. 57 show the  $C_L$  as a function of the angle of attack. The results show good agreement with the ones obtained by Guerrero et al., (2012a) with deviation in the stall  $C_L$  at angle  $15^\circ$  which is slightly different from the data obtained for the clean wing. Overall the prediction and correlation of the  $C_L$  with (Guerrero et al., 2012a) were in good agreement which indicated that the simulation technique and meshing technique were appropriate.

$C_D$  as a function of the angle of attack is illustrated in Fig. 58. Again, a very good agreement may be seen with the results obtained by Guerrero et al., (2012a). The view was that this wing tip design was most effective in reducing the overall  $C_D$  at higher angle of attack of around  $10^\circ$  and above. Thus, further work has been done to improve the design and introduce other potentially better designs for analysis. These are presented in the later sections of this thesis. These designs will demonstrate the capability of improve the lift-to-drag ratio and  $C_D$  at lower angles of attack.

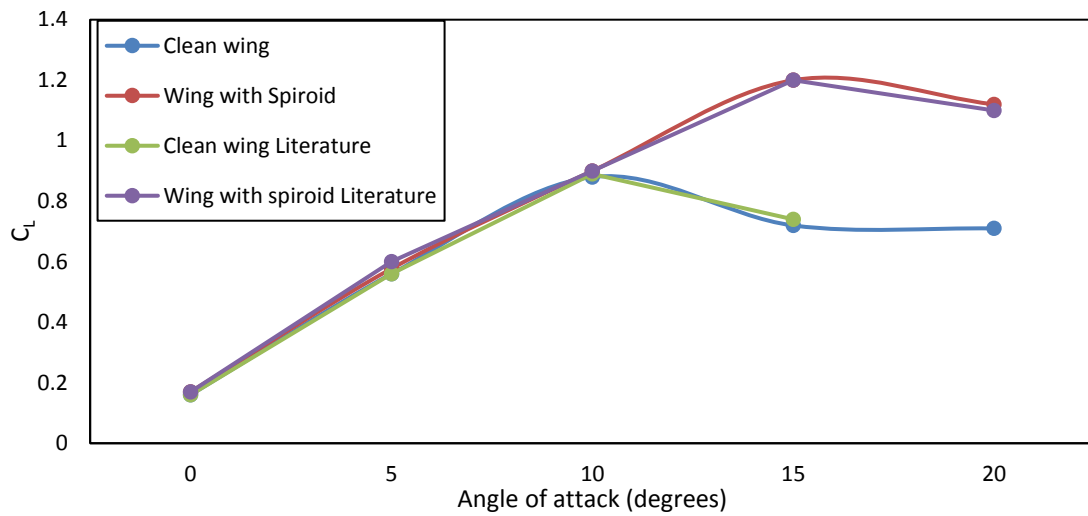


Fig. 57:  $C_L$  vs Alpha – numerical data and data from literature (Guerrero et al., 2012b)

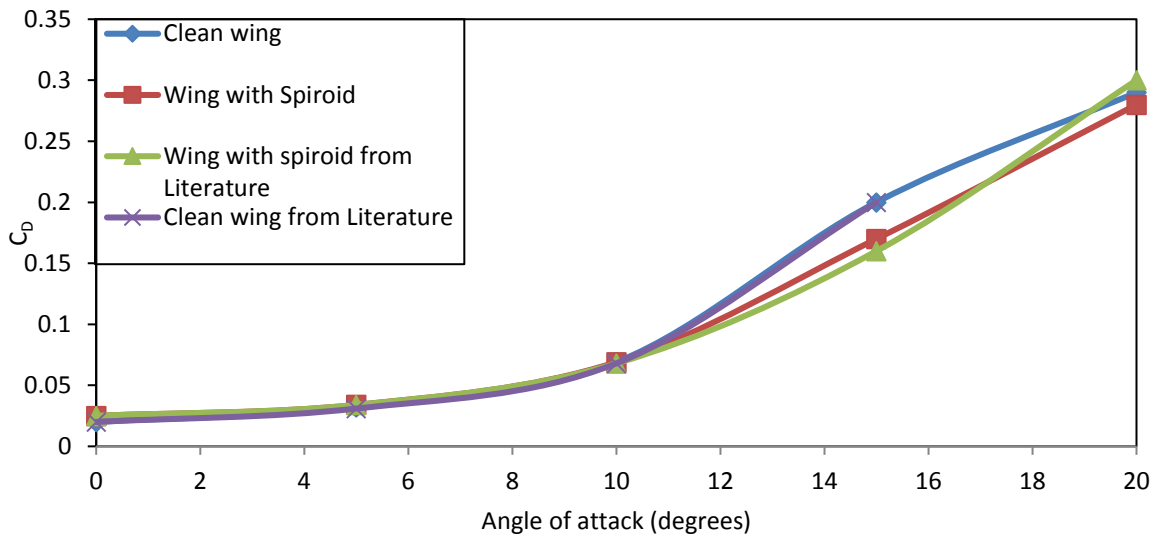
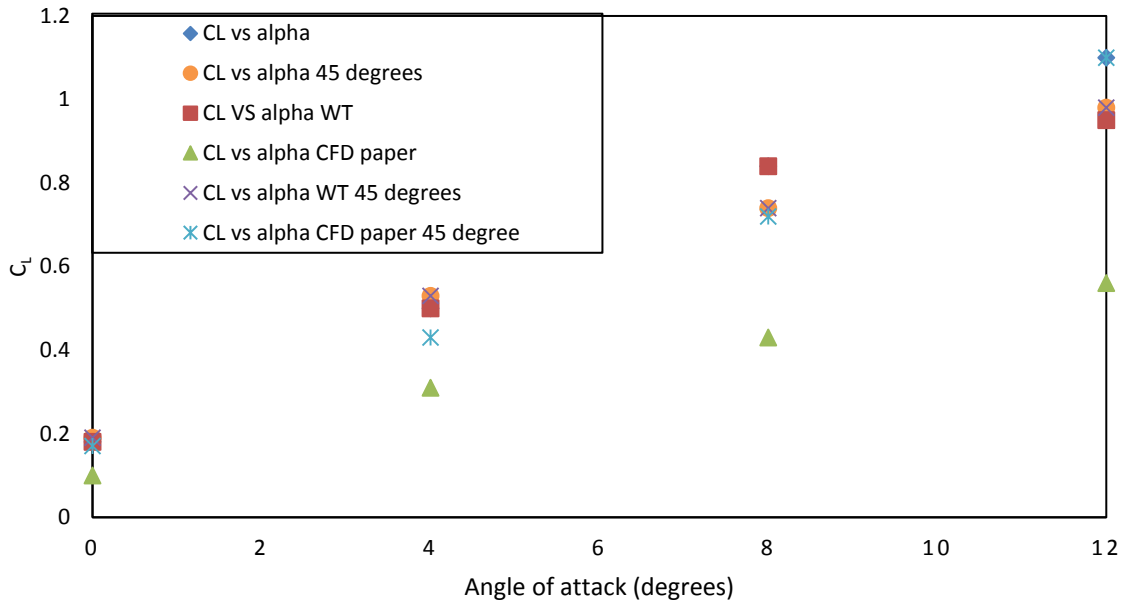


Fig. 58:  $C_D$  VS Alpha - numerical data and data from literature (Guerrero et al., 2012b)

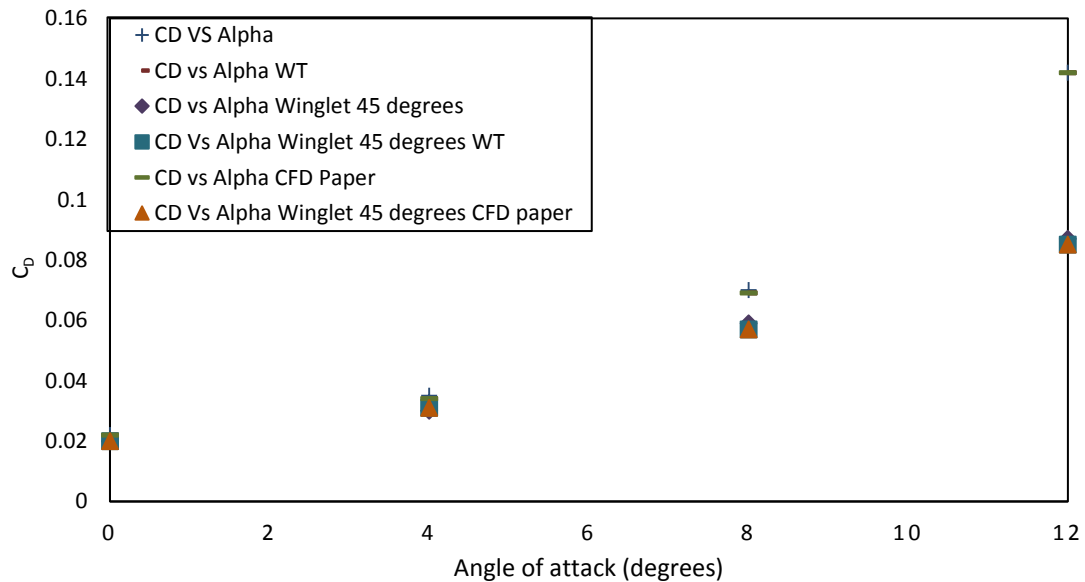
#### 4.1.5. Force Coefficients ( $C_L$ and $C_D$ ) – Blended winglet

Fig. 59 shows  $C_L$  plotted against the angle of attack for the clean wing and the wing equipped with a blended winglet, of di-hedral angle of 45 degrees. The result shows a good agreement with the results for the wind tunnel testing performed by Beechook and Wang, (2013). The  $C_L$  values were in better agreement with the wind-tunnel test results than the CFD results found in Beechook and Wang, (2013) as maybe seen in Fig. 59.

Fig. 60 depicts  $C_D$  as a function of the angle of attack. This also shows good agreement with the CFD results and Wind tunnel results found in Beechook and Wang, (2013). Overall, the results presented showed a drag reduction of 10 percent at  $0^\circ$  angle of attack, 15 percent at  $4^\circ$  angle of attack, 15.7 percent at  $8^\circ$  angles of attack and 53 percent drag reduction at  $12^\circ$  angles of attack by using the winglet.  $C_L$  was also improved by up to 11 percent.



**Fig. 59:  $C_L$  vs Alpha - numerical data and data from literature (Beechook and Wang, 2013)**



**Fig. 60:  $C_D$  VS Alpha - numerical data and data from literature (Beechook and Wang, 2013)**

#### 4.1.6. Force coefficients ( $C_L$ and $C_D$ ) – Lift Prediction Workshop 1

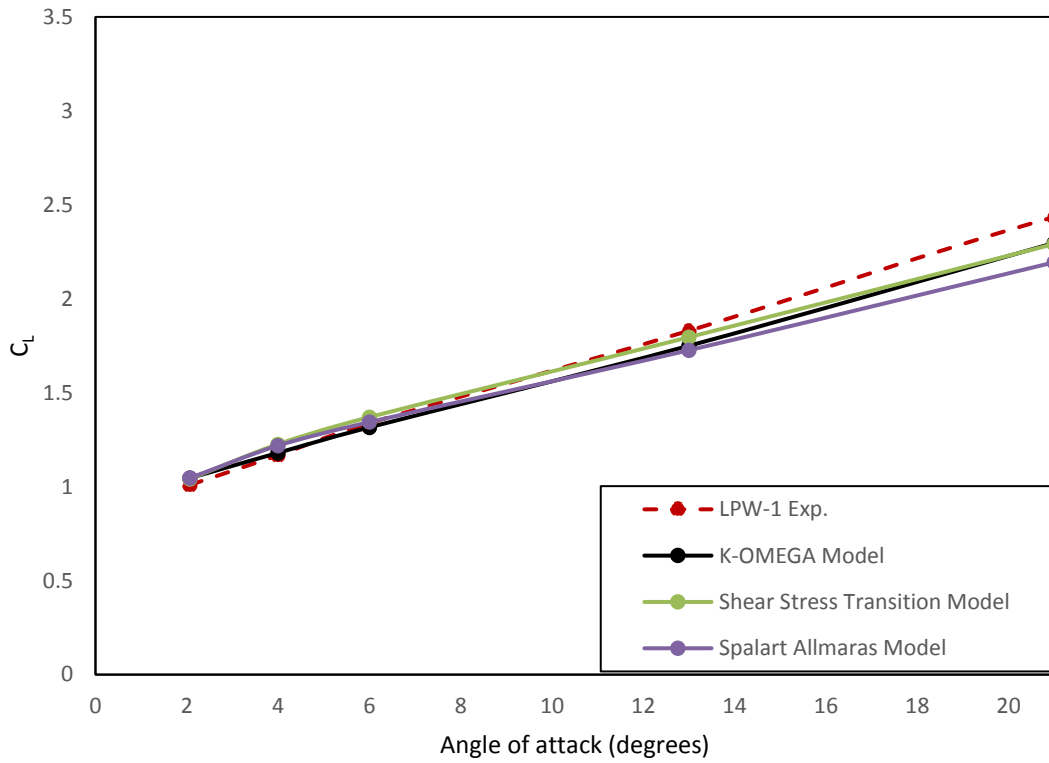


Fig. 61:  $C_L$  vs Alpha - numerical data and data from literature (Rumsey et al., 2011b)

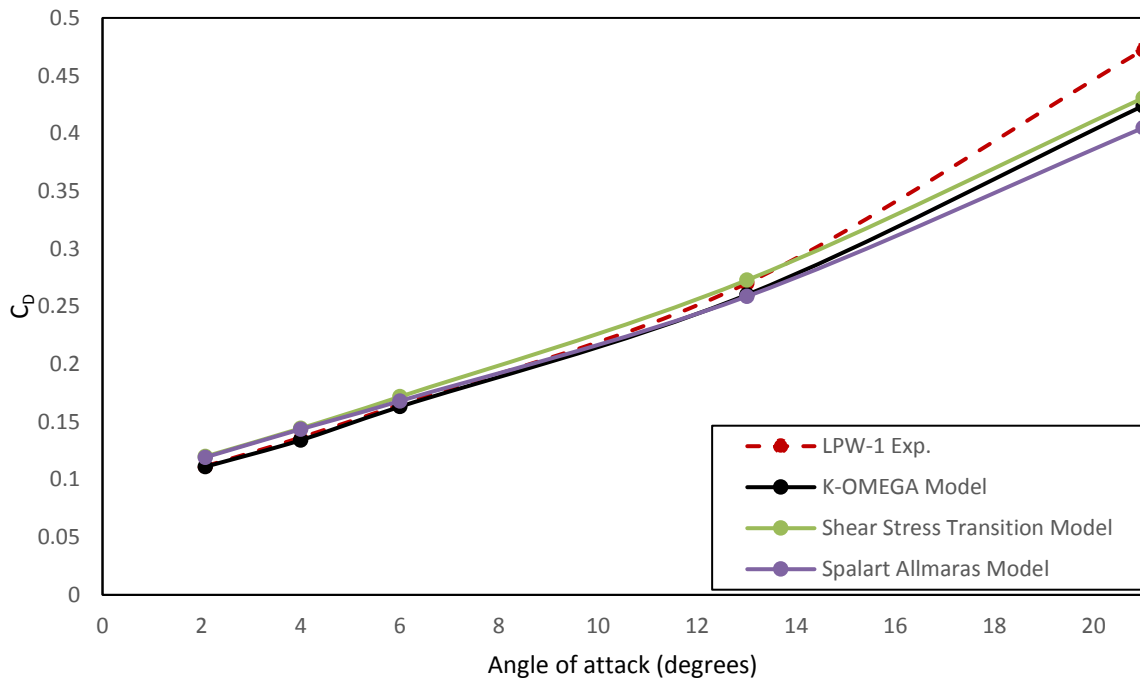


Fig. 62:  $C_D$  VS Alpha - numerical data and data from literature (Rumsey et al., 2011b)

**Table 6: Numerical data and data from literature (Rumsey et al., 2011b)**

Angle of attack	LPW-1		K-OMEGA model		Shear Stress Transition model		Spalart Allmaras model	
	$C_L$	$C_D$	$C_L$	$C_D$	$C_L$	$C_D$	$C_L$	$C_D$
2.074	1.0098	0.1114	1.0160	0.1112	1.0419	0.1159	1.0469	0.1152
3.996	1.1667	0.1363	1.1651	0.1351	1.2261	0.1443	1.2184	0.1435
6.002	1.3381	0.1653	1.3361	0.1642	1.3404	0.1717	1.3441	0.1680
13	1.8322	0.2712	1.7598	0.2611	1.7955	0.2727	1.7264	0.2586
21	2.4352	0.4722	2.2979	0.4238	2.2917	0.4305	2.1944	0.4047

Fig. 61 shows the results obtained from using the Shear Stress Transition (*SST*) model, Spalart Allmaras model, K-Omega ( $k - w$ ) Menter model which has been compared to the data collected from the wind tunnel experiment for  $C_L$  as a function of the angle of attack, this is also shown in Table 6. All of the turbulence models better predict  $C_L$  at lower angle of attack. The Shear Stress Transition model produces better results at higher angles of attack. Overall the prediction of  $C_L$  correlated well with the wind tunnel data. Fig. 62 shows the data for  $C_D$  with changing angle of attack, again the turbulence models performs better at lower angles of attack with the shear Stress Transition model performing slightly better than the other two models at higher angles of attack. This is might be anticipated as transition is expected to occur over the wing at higher angles of attack. The models are have also shown to be well suited for this present work since this work considers lower angles of attack and the results agree very well at lower angle of attack with Experiment.

## 4.2. Initial CFD results and proposed designs

Following a completion of the test cases to validate the numerical modelling approach, a new spiroid winglet design campaign was undertaken. An initial new set of scaled size wing and winglet models were investigated as a prerequisite to the new set of proposed designs which was developed and used as a base design for further optimisation research. This section of the work presents the research campaign on the spiroid design to establish potential new designs.

### 4.2.1. Geometry (Initial CFD results)

Two spiroid designs, blended and clean wing designs were created in the CFD package. The model of the clean wing used was a scaled model (3.5% of the full model) loosely resembling a Boeing 737 aircraft wing. The wing devices were incorporated into the already designed clean wing (retrofit). Most winglet designs are undertaken based on preference of the company or the preference of the modeller or design engineer. The design parameters for the wing and wing tip devices are given in Table 7.

**Table 7: Design specification**

Parameters	Clean wing	Blended winglet configuration	Spiroid Loop configuration	Spiroid Trapezium configuration
Semi-span	0.7m	0.7m	0.7m	0.7m
Wing root chord	0.3m	0.3m	0.3m	0.3m
Wing tip chord	0.07m	0.07m	0.07m	0.07m
Sweep	25 degrees	25 degrees	25 degrees	25 degrees
Spiroid – Dihedral length	-	-	0.15m	0.15m
Spiroid – top rectangular extension	-	-	0.035m	0.026m
Spiroid – top arc length	-	-	-	0.042m
Spiroid – second dihedral length	-	-	0.077m	0.063m
Spiroid – bottom rectangular extension	-	-	0.1m	0.1m
Aerofoil – section profile	NACA2412	NACA2412	NACA2412	NACA2412
Number of runs to arrive at this design	1	20+	20+	20+

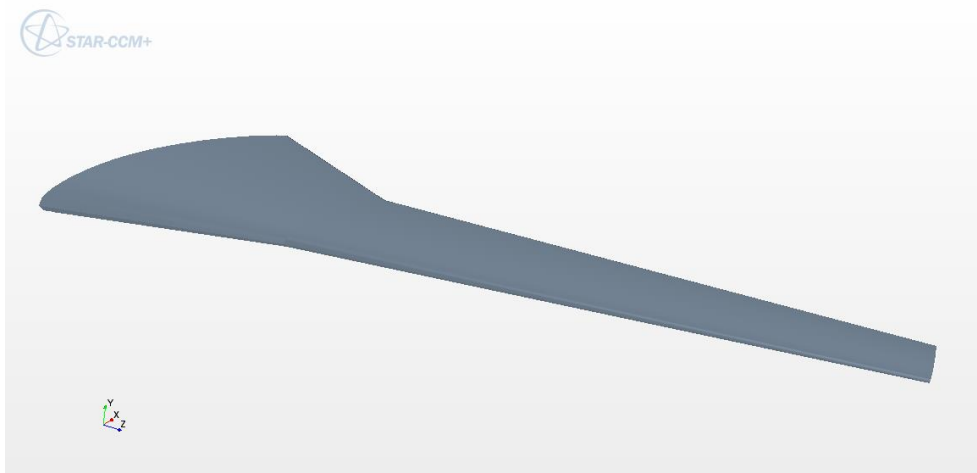


**Fig. 63: Clean wing configuration**

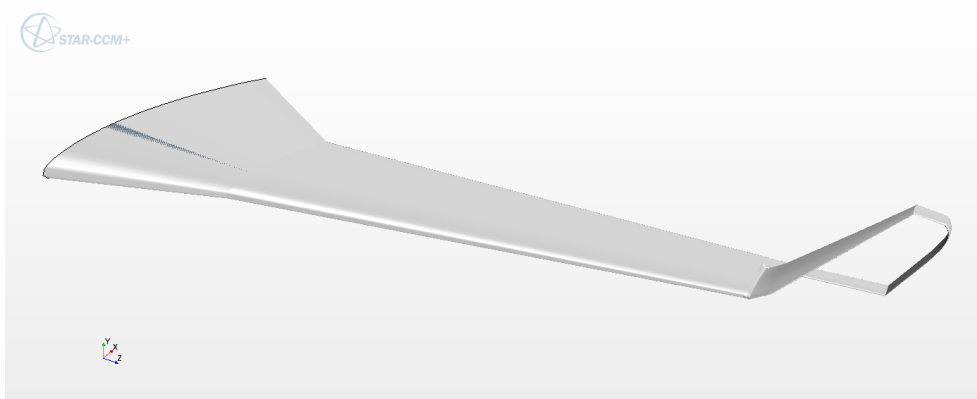


**Fig. 64: Spiroid Trapezium configuration**

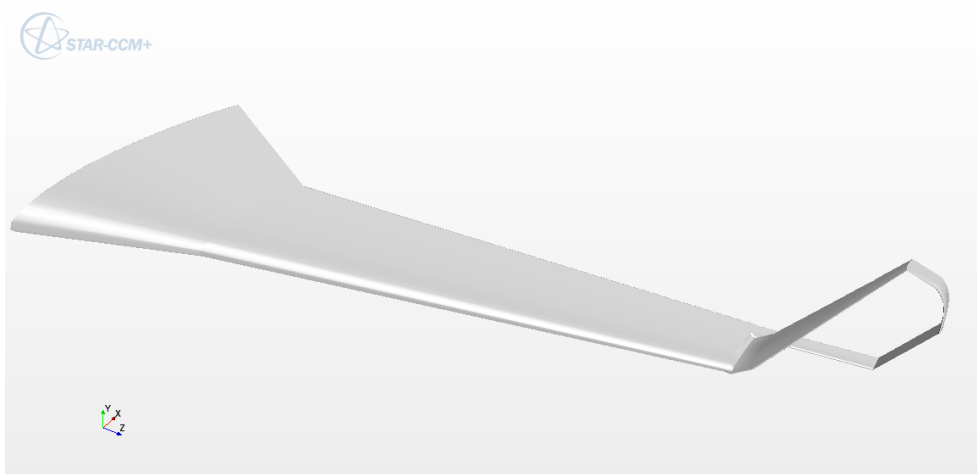


**Fig. 65: Spiroid Loop configuration**

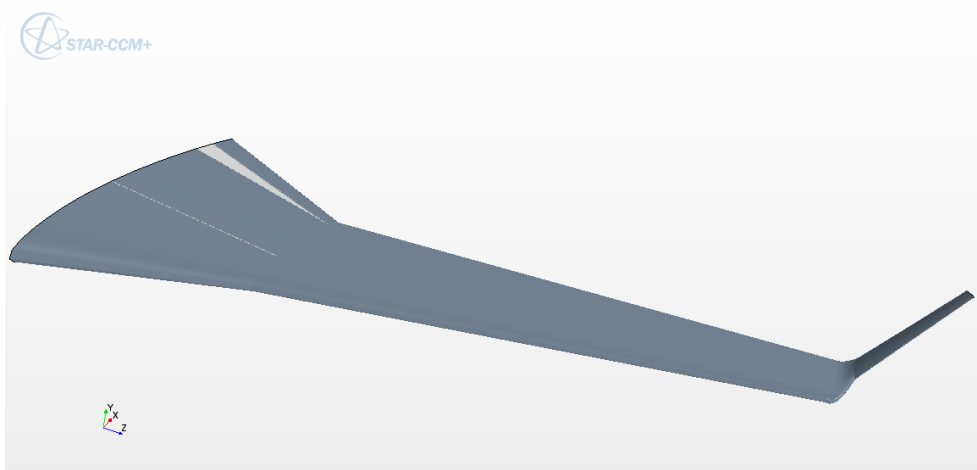


**Fig. 66: Blended winglet configuration**

Fig. 63 - Fig. 66 illustrate the wing and winglet configurations investigated as initial designs. A constraint was placed on the maximum allowable length of the winglet and was set to 20 -25 percent. This helps to prevent extremely large winglets guiding the design process to more practical device sizes.

The proposed designs developed based on a full-scale wing model of a loosely resembling Boeing 737 wing series is presented here. These designs were obtained after numerous CFD simulations of several designs to obtain a baseline configuration.

#### 4.2.2. Mesh and Computational Domain

The unstructured Tetrahedral transformed to polyhedral mesh option was created around all four geometries. As previously mentioned earlier this meshing option is ideal for arbitrarily shaped geometries and also required less grid points to resolve the flow around the wing and wing with winglet configurations. A Prismatic region near the wall was generated by using the robust automated prism layer algorithm to assure proper resolution of the boundary layers in the flow (see Fig.69). A total number of 10 prismatic layers were generated near wall. A non-dimensional wall distance  $y^+ < 1$  value which was calculated by using equations 40 – 42, was used which is sufficient to capture and resolve the flows in the boundary layer down to the wall. In addition, mesh refinement was defined around the spiroid device to capture the complicated flow around the devices, leading and trailing edge and wing tip refinement were generated by using the mesh refinement options available in STAR-CCM+. The Mesh was not customized for any particular angle of attack, rather the change in angle of attack was achieved by changing the free stream flow field direction while leaving the mesh generated un-changed (see Fig. 67 and Fig. 68). This was essential as it saved time to compute new mesh for every angle of attack which could be time consuming and computationally expensive. A total of  $8 \times 10^6$ –  $10 \times 10^6$  polyhedral un-structured arbitrary cells were generated. A mesh dependency test was performed at  $5 \times 10^6$ ,  $6 \times 10^6$ ,  $7 \times 10^6$ ,  $8.5 \times 10^6$  and  $10 \times 10^6$  cells at 0 degrees angle of attack and Mach 0.24, results obtained showed close agreement at  $8 \times 10^6$ –  $10 \times 10^6$  with negligible differences (see Fig..70 and Fig. 71).

**Table 8: Mesh specification**

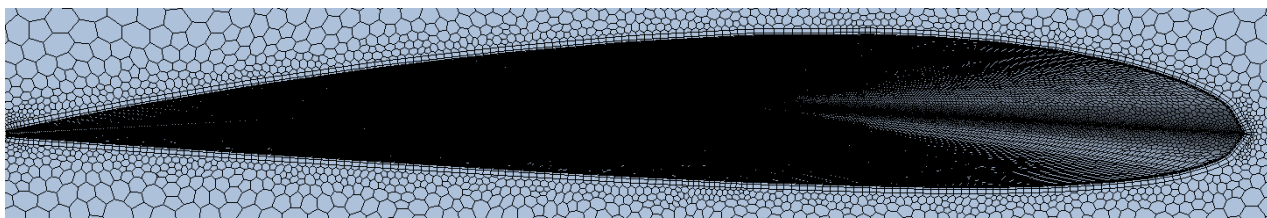
Mesh parameters				
Mesh base size	0.006m	0.006m	0.006m	0.006m
Surface refinement	12%	12%	12%	12%
LE refinement	12%	12%	12%	12%
TE refinement	12%	12%	12%	12%
Number of prism layers	10	10	10	10
Total number of mesh count	10 million	10 million +	10 million +	10 million +



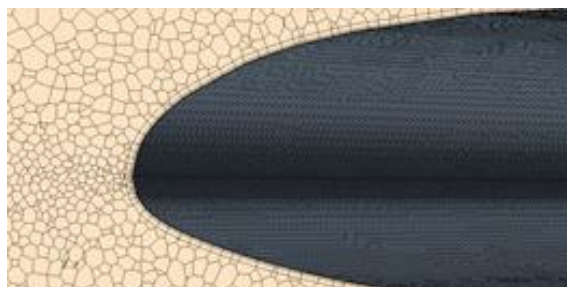
**Fig. 67: Mesh on Wing and spiroid trapezium model**



**Fig. 68: Spiroid loop and Blended winglet model**



**(a.)**



**(b)**

**Fig. 69: Cross-section of wing showing prism layers (a.) Whole aerofoil, (b.) zoomed leading edge view**

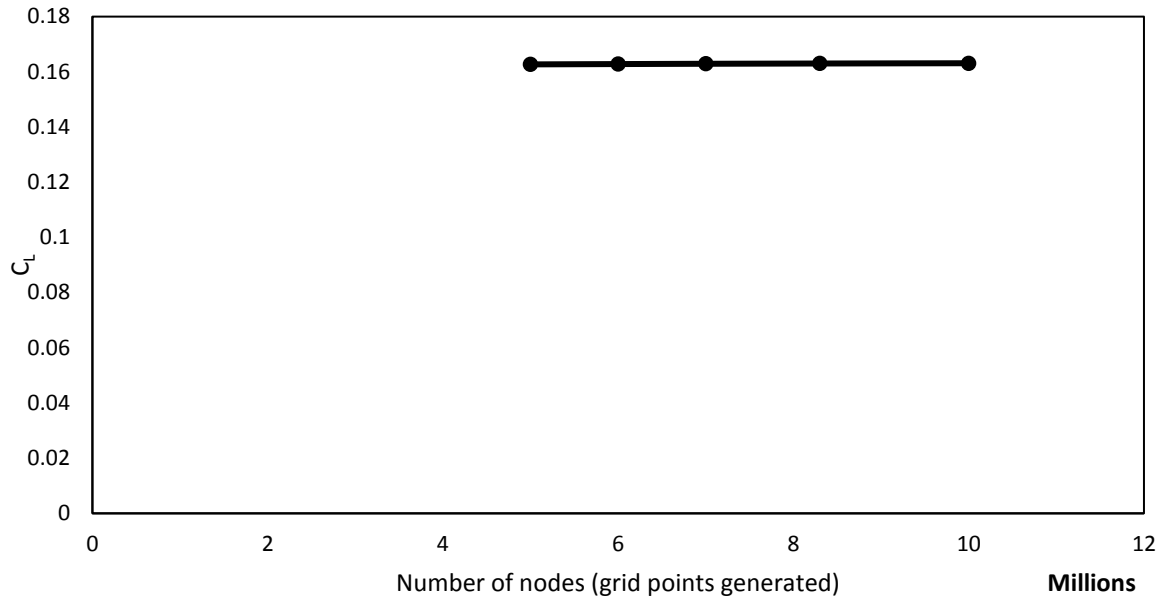


**Fig. 70: Graph showing  $C_L$  vs Number of nodes**

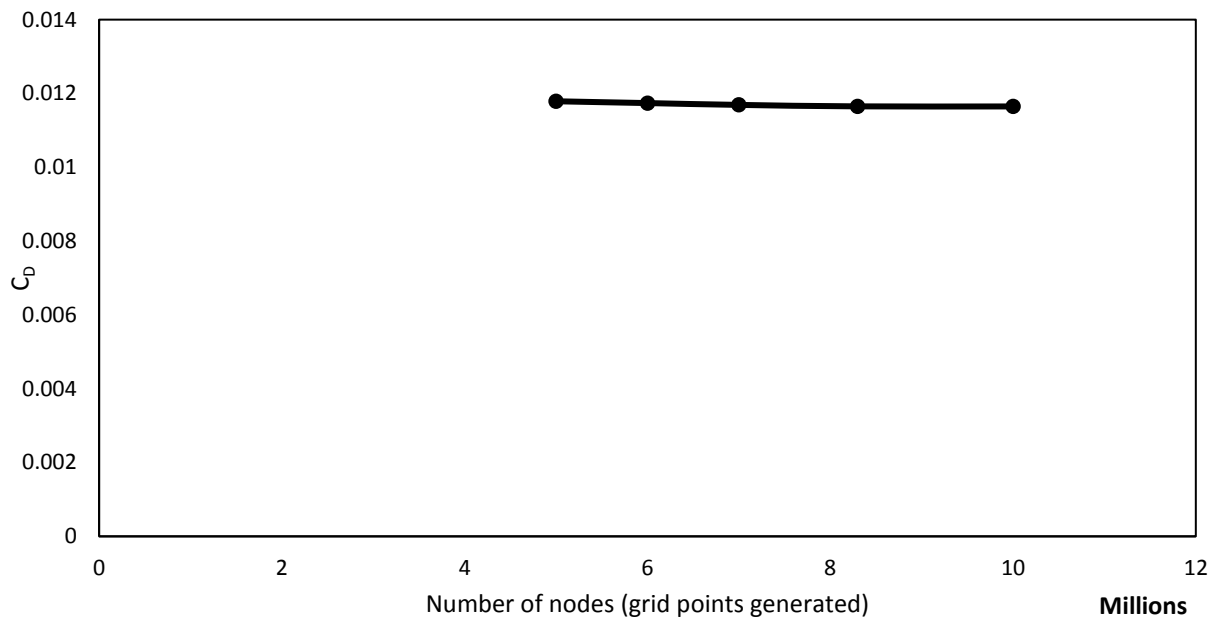


**Fig. 71: Graph showing  $C_D$  vs Number of nodes**

The computational domain used for this study models all inlet velocity conditions rather than the usual wind tunnel experiment set up. A symmetrical condition was used, and the domain extends approximately 30 times the wing root chord-length in all directions. Velocity boundary conditions specifying, direction, temperature, pressure and turbulence quantities are used at the far field conditions. The physics parameters are illustrated in Table 9.

**Table 9: Physics set-up**

Physics and boundary parameters	Clean wing & wing plus winglets
Velocity	80 <i>m/s</i>
Mach number	0.24
Temperature	300 <i>K</i>
Angle of attack	0 – 10 <i>degrees</i>
Pressure	101325 <i>pascals</i>
Turbulence intensity	1 %
Turbulence viscosity ratio	10 %
Turbulence model (s)	<i>K – Omega Menter model</i>

### 4.2.3. Computational approach

STAR-CCM+ is a client-based server system which uses structured code in object C++ and is java based. This study uses the pressure based – segregated approach with (Rhie and Chow, 1983) interpolation to solve the conserved form of the governing equations based on the AMG SIMPLE algorithm. The turbulence closure was achieved by using the two equation *SST Menter's turbulence model (K – Omega turbulence model)* details of this model has been discussed in section 3.2.6 of this report under turbulence closure models.

### 4.2.4. Force Coefficients

#### 4.2.4.1. Lift coefficient ( $C_L$ )

First is to consider  $C_L$  as a function of angle of attack (see Fig. 72). At an angle of attack of 0 degree there is a non-zero value for the coefficient of lift, and this is a usual characteristic of a cambered wing. It is also observed that the aerodynamic lift coefficient performance of the wing is slightly improved by all three winglet configurations. This is due to added effective wing span caused by the adding the winglets to the clean wing. The spiroid designs (Spiroid loop and Spiroid Trapezium) both performed better than the clean wing and the New concept blended winglet. This is mostly noticed at angles of attack of 0 degrees for all winglet configurations (see Table 10). For the spiroid devices  $C_L$  improvement of 4 – 8 percent was obtained for all angles of attack and for the blended winglet  $C_L$  improvement of 2-4 percent was obtained, this is shown in Table 10.  $C_L$  improvement for the winglets can be attributed to the extra effective wing area and modified lift distribution caused by the winglet.

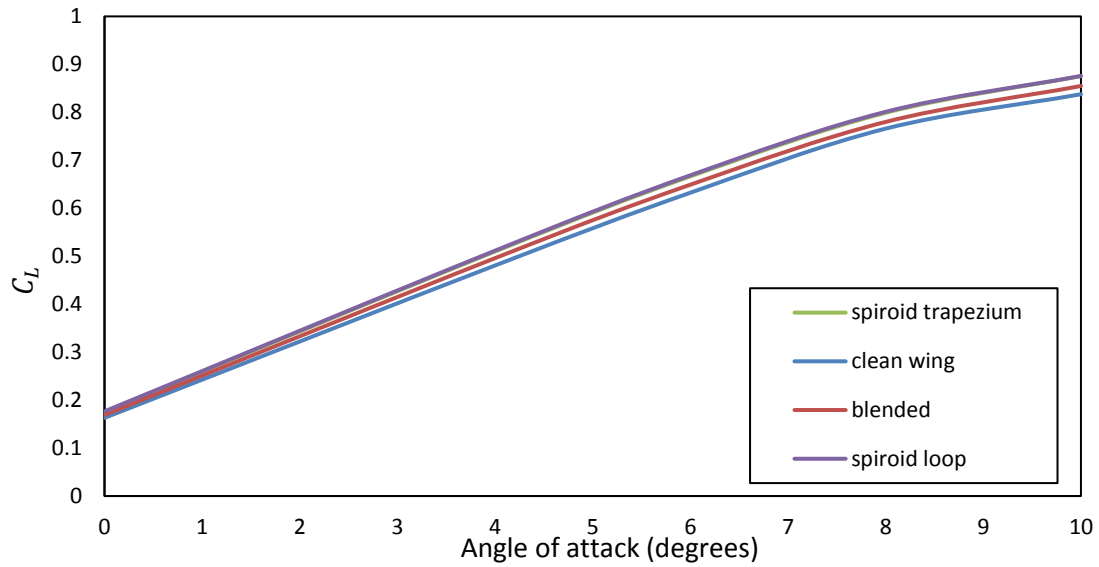


**Fig. 72: C<sub>L</sub> vs Angle of attack**

**Table 10: Lift coefficient**

Angle of attack	Clean wing	Blended winglet	% change	Spiroid trapezium	% change	Spiroid loop	% change
	C <sub>L</sub>	C <sub>L</sub>		C <sub>L</sub>		C <sub>L</sub>	
0	0.1630	0.1690	3.6%	0.1750	7.3%	0.1765	8.3%
2	0.3220	0.3331	3.4%	0.3448	7.1%	0.3450	7.1%
4	0.4805	0.4960	3.2%	0.5113	6.4%	0.5116	6.4%
6	0.6323	0.6491	2.7%	0.6684	5.7%	0.6686	5.7%
8	0.7659	0.7802	1.9%	0.7990	4.3%	0.8011	4.6%
10	0.8377	0.8549	2.1%	0.8756	4.5%	0.8758	4.5%

#### 4.2.4.2. Drag coefficient ( $C_D$ ) and drag polar

To analyse  $C_D$ , it is necessary to discuss the equations arising from Prandtl lifting line theory (Anderson, 2001) for the calculation of induced drag. The need to do this arises because, there is no direct approach to decompose the various types of drag values obtained from the calculations using computational fluid dynamics unless the Euler equations are solved explicitly. Also, this is because, the  $C_D$  or force value obtained from CFD solutions is a combination of all the types of drag forces associated with the fluid flow.

Generally, drag can be sub-divided into parasite and induced drag. These types of drag are well known and so would not be discussed here. The total drag on the wing can be written in the non-dimensionless form:

(48)

$$C_D = C_{D0} + C_{D_{induced}}$$

Where  $C_{D0}$  is the drag coefficient of parasite drag (the sum of the skin friction drag and the pressure drag). The second parameter  $C_{D_{ind}}$  is the coefficient of lift induced drag, which is mostly dependent on the generation of lift. The  $C_{D_{ind}}$  is defined by:

$$C_{D_{ind}} = \frac{C_L^2}{ARe\pi} \quad (49)$$

In the above equation,  $C_L$  is the lift coefficient,  $AR$  is the aspect ratio and  $e$  is the Oswald efficiency factor or the span efficiency,  $e$  may be estimated by using the equation obtained from (Raymer, 2005):

$$e = 1.78(1 - 0.045AR^{0.68}) - 0.64 \quad (50)$$

The aspect ratio is obtained by using:

$$AR = \frac{span^2}{Reference\ area} \quad (51)$$

with these equations the  $C_{D_{ind}}$  can be re-written as:

$$C_{D_{ind}} = KC_L^2 \quad (52)$$

Putting this back into the previous equation gives:

$$C_D = C_{D0} + KC_L^2 \quad (53)$$

For a cambered wing as used for this study, at 0-degree angle of attack, the wing generates a certain amount of lift as opposed to a non-cambered wing (Anderson, 1999), (Raymer, 1992). Fig. 73 shows  $C_D$  as a function of the angle of attack. The plot showed that the drag increases as the angle of attack increased. The increase in the  $C_D$  is not a rapid one but a gradual increase. The spiroid loop achieved a drag reduction of 1.0 percent at 6° angles of attack, the spiroid trapezium achieved a drag reduction of 1.7 percent at 6° angles of attack and 0.5 percent at an angle of 4°. The drag reduction at the angles of attack of 4° and 6° are encouraging as these are the angles adopted

by most commercial airline at cruise condition. The aim of most winglets is to reduce the drag at cruise conditions since this aspect of the flight phase covers most of the flying time. The blended winglets also showed encouraging drag reduction by 2.9 percent at  $4^\circ$  and  $6^\circ$ . The higher drag reduction observed for the blended winglet compared with the both spiroid winglets is due to the extra added wetted area by the geometry of the spiroid which increases the parasite drag perhaps also due to the interference drag added by the sharp corners on the spiroid design used for this study. Improving these parameters and optimization will improve the drag reduction capabilities of the spiroid winglet. The induced drag reduction potential of these device which were estimated by using equation (47) is shown in Fig. 74. The Spiroid Loop winglet reduced the induce drag by 12 percent at  $4^\circ$ , 18 percent at  $6^\circ$  and 15 percent at  $10^\circ$ . The Spiroid trapezium winglet reduced the induced drag by 11 percent at  $4^\circ$ , 16 percent at  $6^\circ$  and 14 percent at  $10^\circ$ . The encouraging percentage decrease of induced drag achieved by both spiroid winglets can be attributed to the fact that these devices dissipates the strength of the wing tip vortex. The large induced drag reduction can also be attributed to the modification of the lift distribution in the wing's span wise direction. As the induced drag is directly associated with lift production, a modification in the way the lift is distributed along the wing would be an ideal technique to reduce this form of drag which is what the spiroid wing design accomplishes. Therefore, it would be ideal to develop ways in which the parasite drag can be reduced while maintaining a desirable induced drag reduction at effective  $C_L$ . The blended winglet also showed good induced drag reduction of estimate 8 – 14 percent for angles of attack between  $0^\circ$  and  $10^\circ$ .

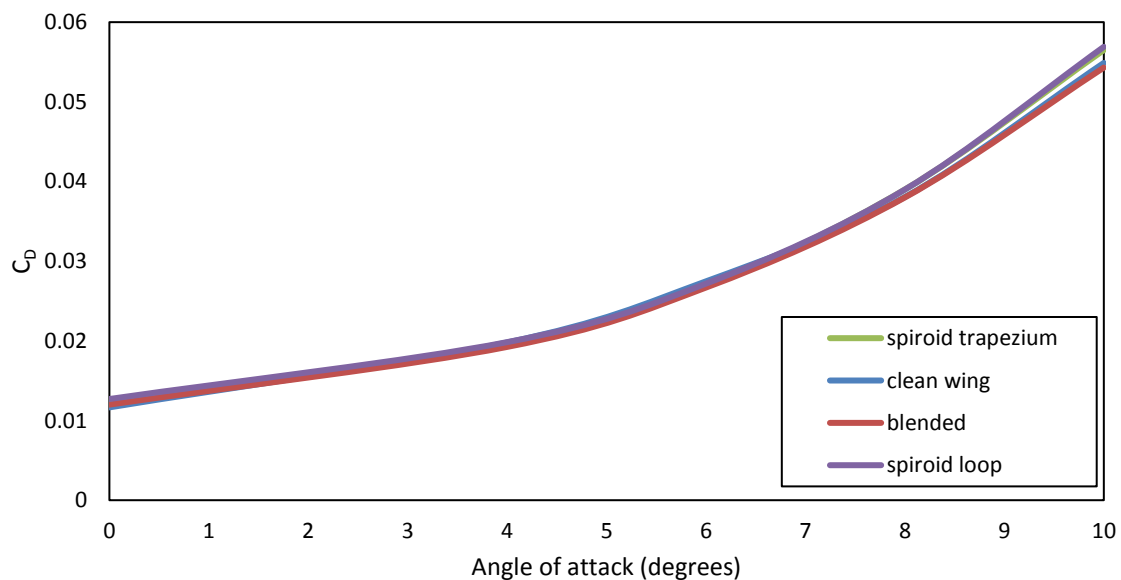


**Fig. 73:  $C_D$  vs Angle of attack**

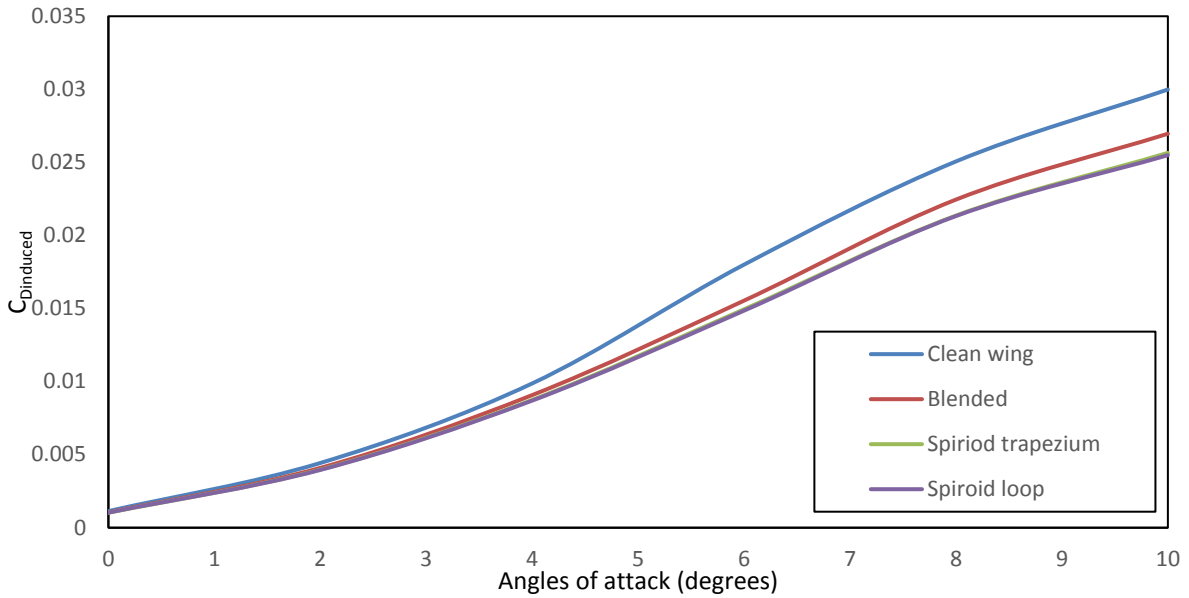


**Fig. 74: Induced drag reduction**

#### 4.2.4.3. Lift to Drag Ratio

The Lift-to-drag ratio is essential to determine the performance of the wing for a given flight condition. The Spiroid trapezium showed a 6 percent lift-to-drag improvement at  $4^{\circ}$  angle of attack, 6.7 percent lift-to-drag improvement at  $6^{\circ}$  angle, 1.7 percent at  $8^{\circ}$  and 1.5 percent at  $10^{\circ}$  while the Spiroid loop design demonstrated a 5 percent lift-to-drag improvement at  $4^{\circ}$ , 6.4 percent at  $6^{\circ}$ , 2.0 percent at  $8^{\circ}$  and 0.8 percent at  $10^{\circ}$  (see Fig. 75). These illustrates that the Spiroid design performs better or is well suited for cruise flight setting. The blended winglet gave a lift-to-drag ratio improvement of 5.8 percent at  $4^{\circ}$ , 5.3 percent at  $6^{\circ}$ , 1.97 percent at  $8^{\circ}$  and 3.0 percent at  $10^{\circ}$ . The blended winglet from these results, demonstrates better lift-to-drag ratio performance at higher angles of attack than both Spiroid winglets.

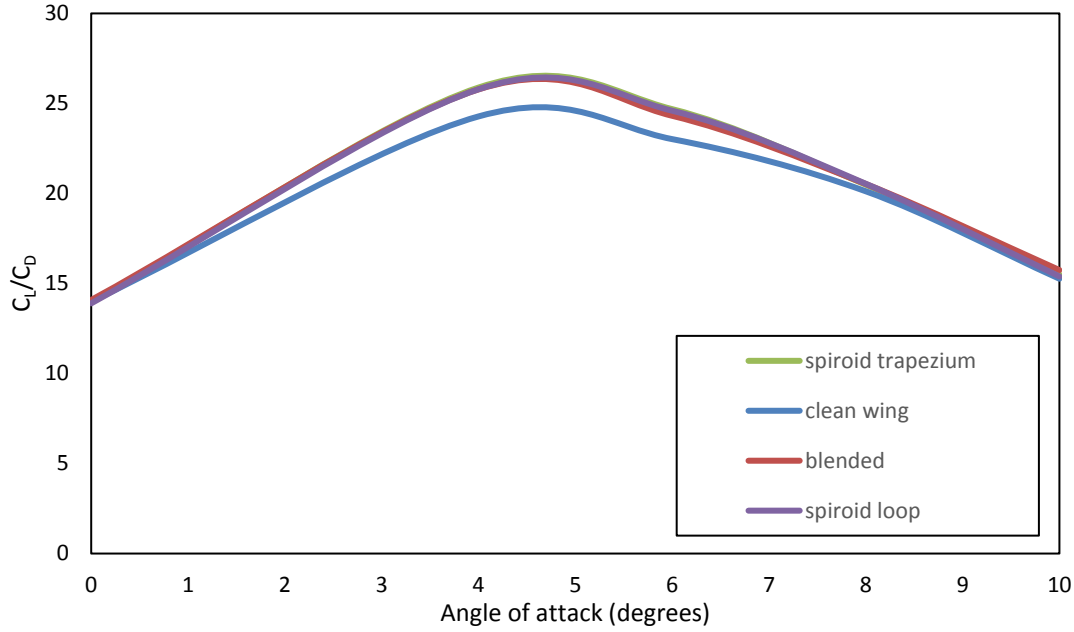


**Fig. 75: lift-to-drag ratio**

#### 4.2.4.4. Vortex

The visualization of the vortices pattern around the wing tip devices and clean wing is analysed by using the vorticity contour plots and the Q-criterion 3D representation. The Q-criterion scalar field function available in STAR-CCM+ has been used to visualise the vortices structure by using the volume Rendering technique which allows the visualisation of a scalar field in 3-D in a full volumetric way. ie. it gives the user a way to look inside the flow to observe what is happening in the region of interest.

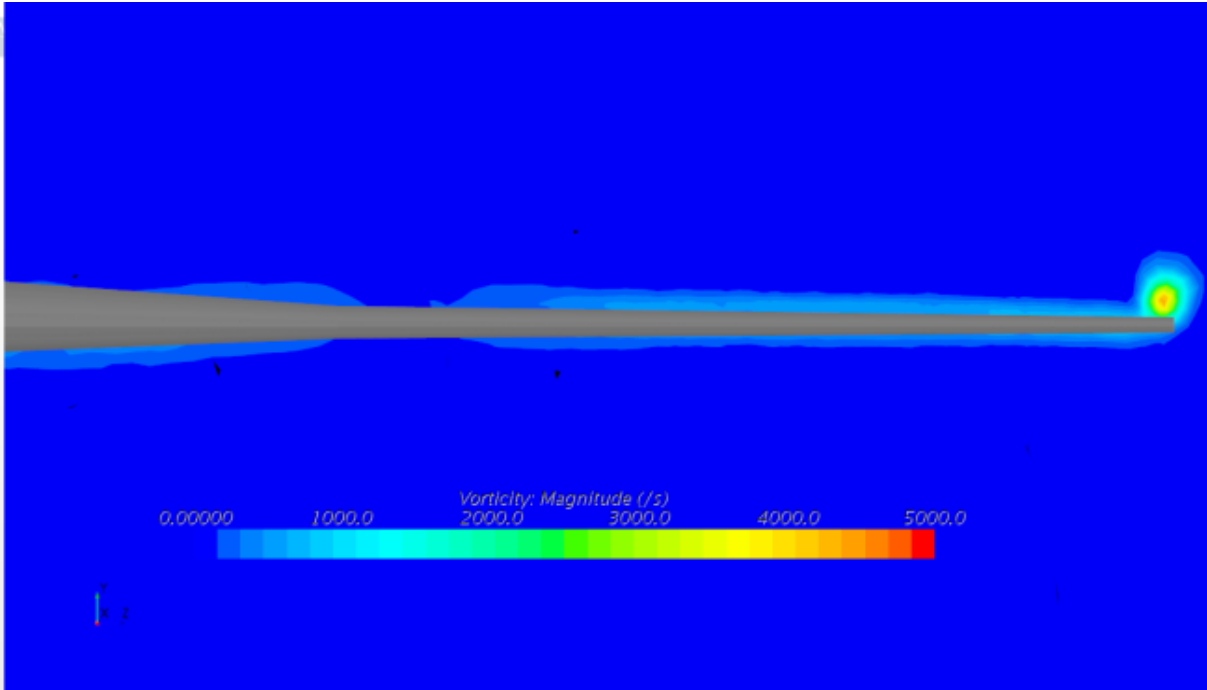
The Q-criterion scalar functions in STAR-CCM+ is defined by (Galilean invariant vortex definition):

$$Q = 1/2(\|\Omega\|^2 - \|S\|^2) \quad (54)$$

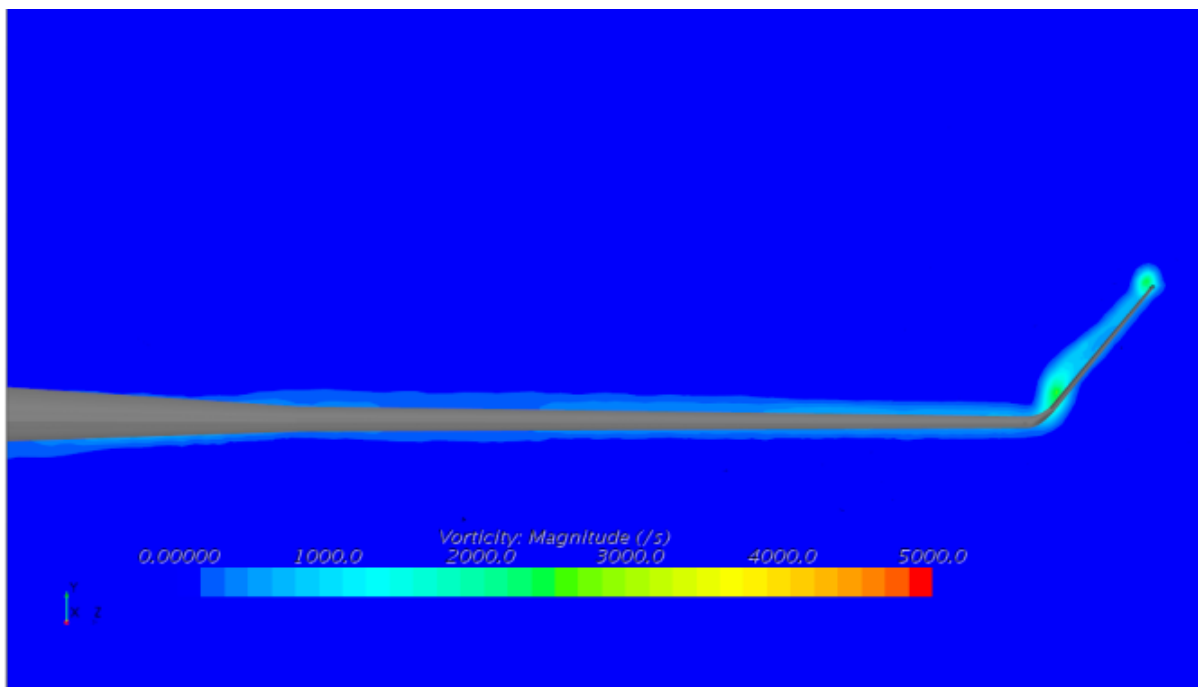
$\Omega$  Is the spin tensor (vorticity tensor) and  $S$  is the strain-rate tensor. A positive value implies that the flow is dominated by vorticity while a negative value implies a strain dominated flow.

Fig. 76 gives a graphical representation of the vortices flow pattern observed at the tip of the clean wing with a plane section cut in the span-wise direction of the wing at 0.4 m behind the wing. The concentration in magnitude of the vortices can clearly be seen at wing tip. A scale range of 0 – 5000 in vorticity magnitude is selected across all scalar contour plots for each of the devices for consistency. The vortices patterns around the wing tip with blended winglet are shown in Fig. 77, a clear reduction in vortices concentration around the tip is shown. A similar

pattern in the dissipation of the strength of the wing tip vortices is observed in Figs 78 – 79 for the spiroid trapezium device and Spiroid Loop device respectively. These plots give the indication that the Spiroid Loop dissipates the wing tip vortices better than the other devices as the concentration of vortices is less with this device, this is also evident in Fig. 74 as the Spiroid Loop winglet has the most induced drag reduction percentage followed by the Spiroid Trapezium then the Blended winglet compared to the clean wing.



**Fig. 76: Vorticity plot - Clean wing**



**Fig. 77: Vorticity scalar - Blended winglet**

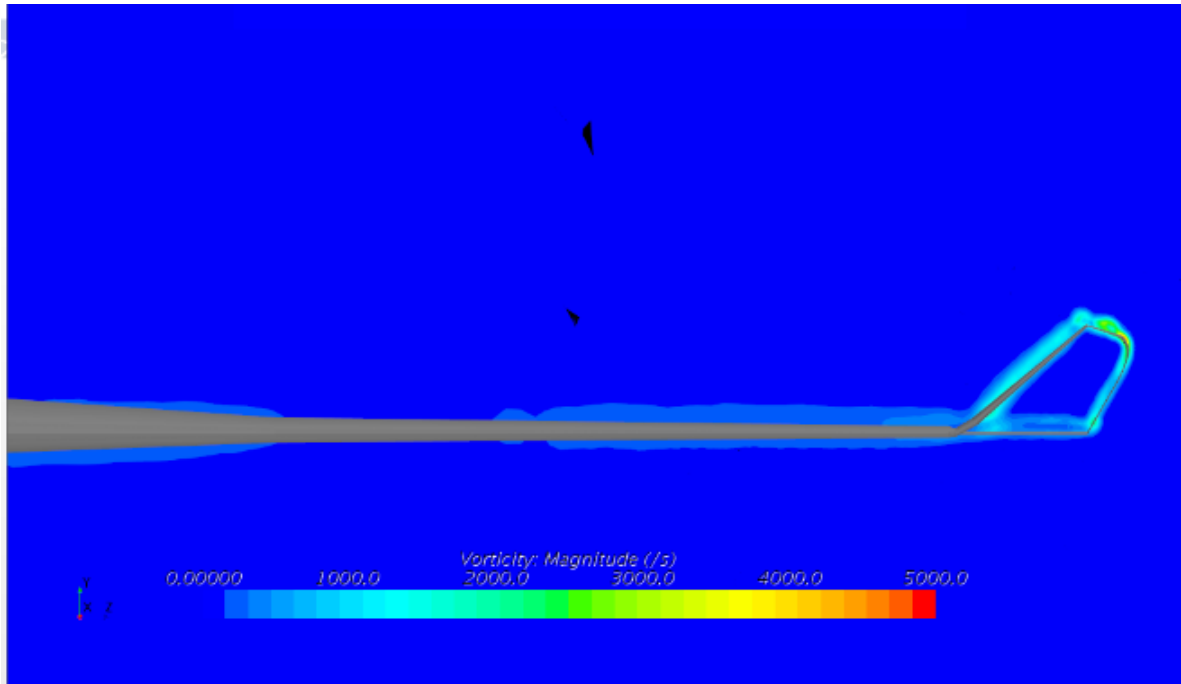


**Fig. 78: Vorticity scalar - Spiroid trapezium**

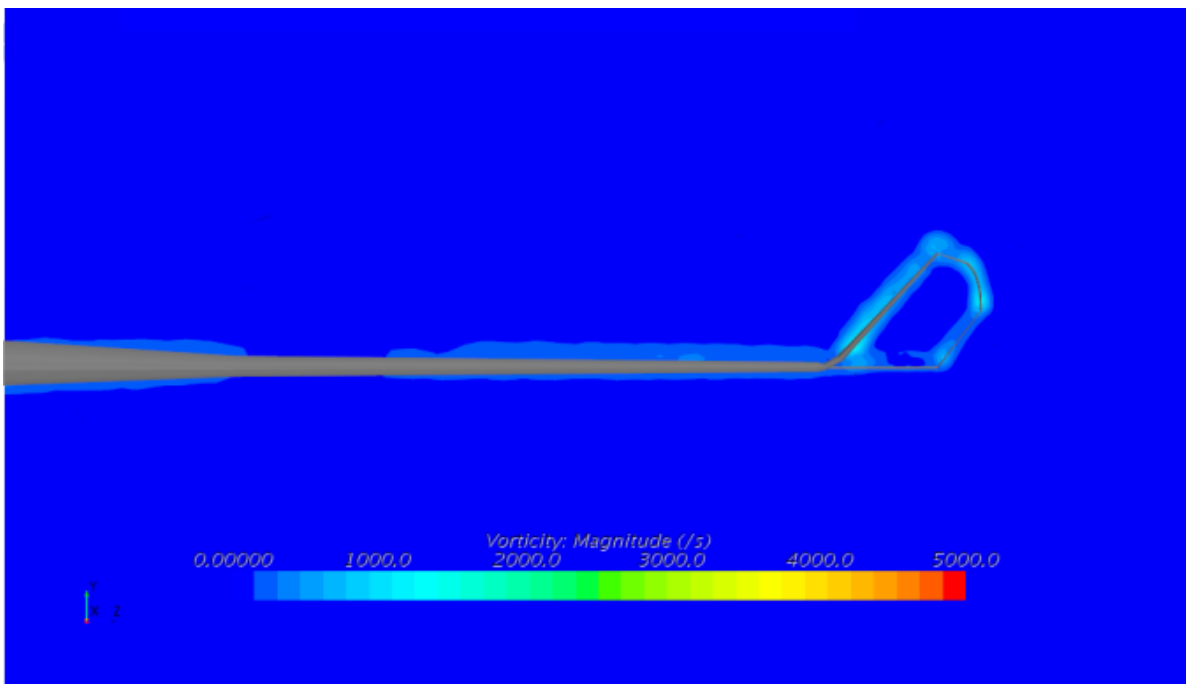


**Fig. 79: Vorticity scalar - Spiroid Loop**

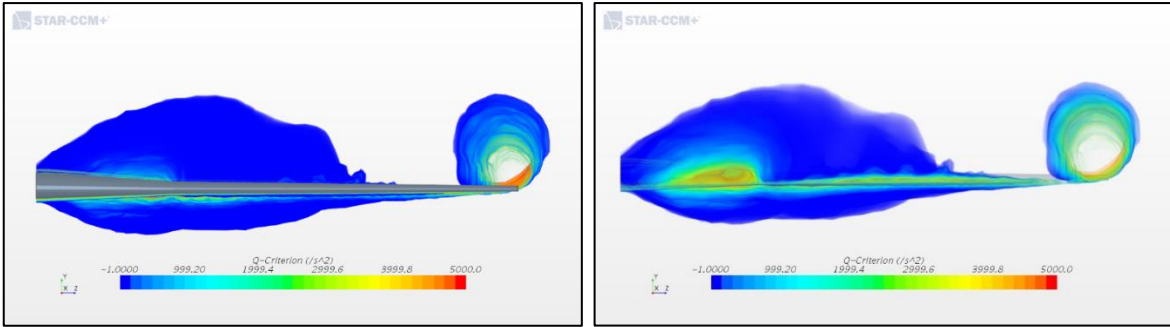


**Fig. 80: Q-Criterion 3D volume rendering - Clean wing (Left normal view and Right transparent view)**

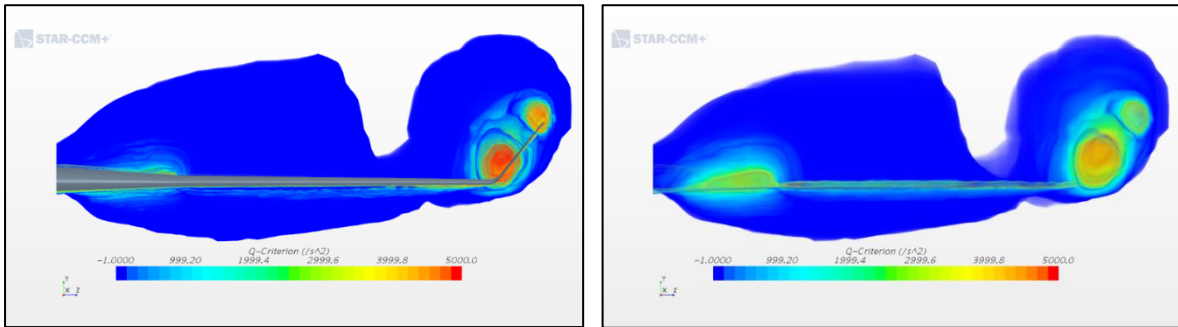


**Fig. 81: Q-Criterion 3D volume rendering – Blended winglet (Left normal view and Right transparent view)**

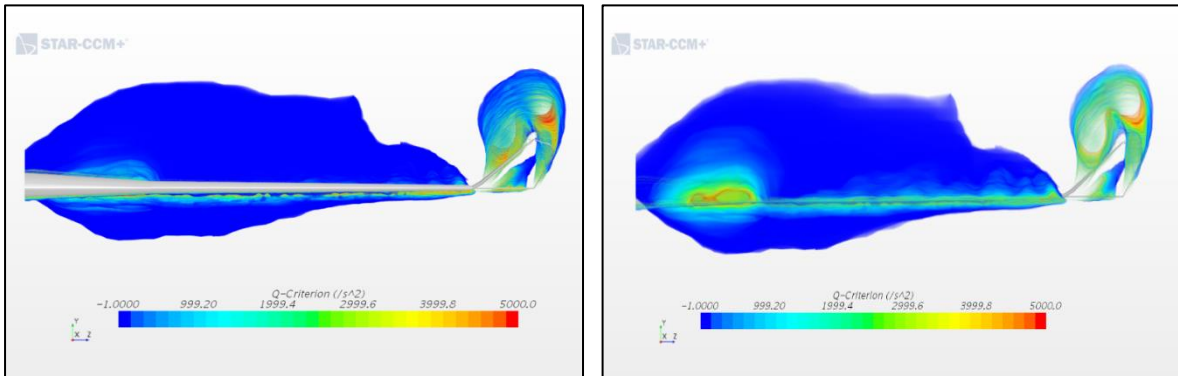


**Fig. 82: Q-Criterion 3D volume rendering – Spiroid trapezium (Left normal view and Right transparent view)**

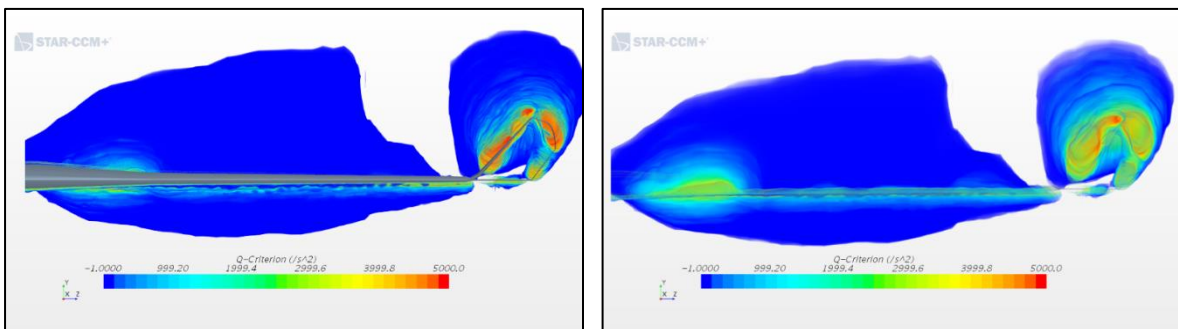


**Fig. 83: Q-Criterion 3D volume rendering – Spiroid Loop (Left normal view and Right transparent view)**

The Q-criterion 3D plots displayed in Figs. 80 – 83, shows a rapid dissipation of the vortices at the tip of all three studied designs with traces of vortices concentration around the edges of the device as indicated by the regions with higher positive Q-criterion values. These patches of vortices give an indication on the region of the design where further modification and optimisation can be performed to achieve better induced drag reduction percent.

#### 4.2.4.5. Range study

A brief range analysis under cruise flight conditions is helpful to indicate the value of an aircraft equipped with wing-tip devices in comparison with an aircraft without winglet. The range analysis has been performed at  $4^\circ$  because aircrafts cruising angle of attack is usually around this number and this was performed for all wing configurations by using an integrated form of Breguet range equation assuming constant altitude given as (Robert F. Stengel, 2004):

$$Range = \left( \frac{\sqrt{C_L}}{C_D} \right) \left( \frac{2}{c_T g} \right) \sqrt{\frac{2}{\rho S}} \left( m_i^{\frac{1}{2}} - m_f^{\frac{1}{2}} \right) \quad (55)$$

The Range is maximised when  $\left( \frac{\sqrt{C_L}}{C_D} \right) = maximum$ , in the equation (47)  $m_i$  is the mass (kg) of aircraft at the beginning of cruise and  $m_f$  is the final aircraft mass after the cruise (kg). The range improvement obtained is based on wing drag only and also neglects any increment due to adding high lift devices. This is given in Table 11 below.

**Table 11: Range of different wing tip devices at cruise at constant altitude**

Wing-tip type	$\frac{C_L^{0.5}}{C_D}$	% Improvement in Range
Clean wing	35.01643	0
Blended winglet	36.604609	4.338%
Spiroid Trapezium	36.24593	3.39%
Spiroid loop	36.051522	2.87%

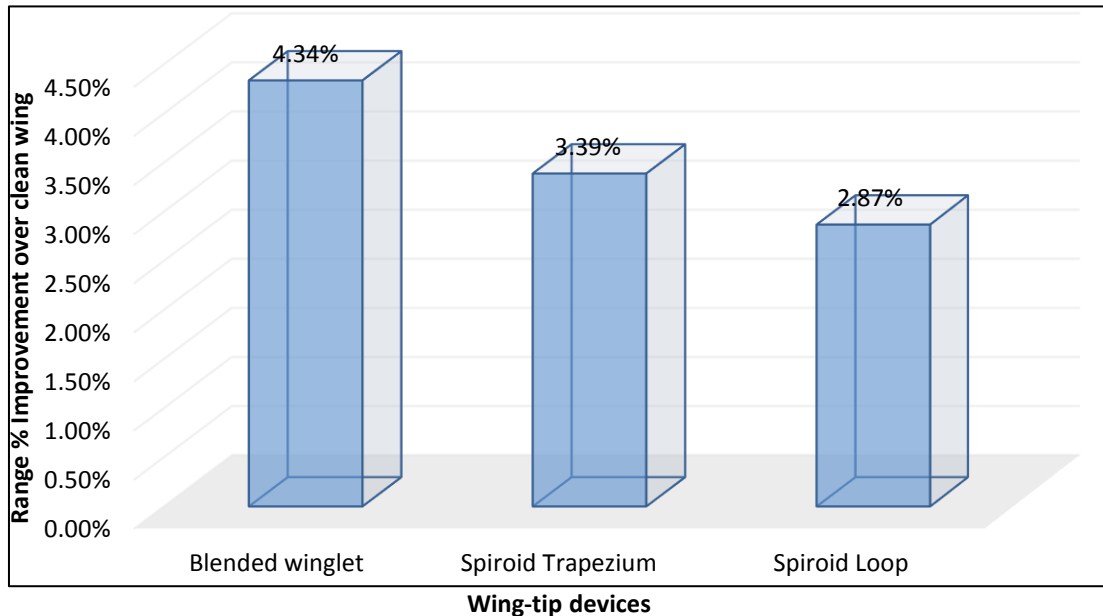
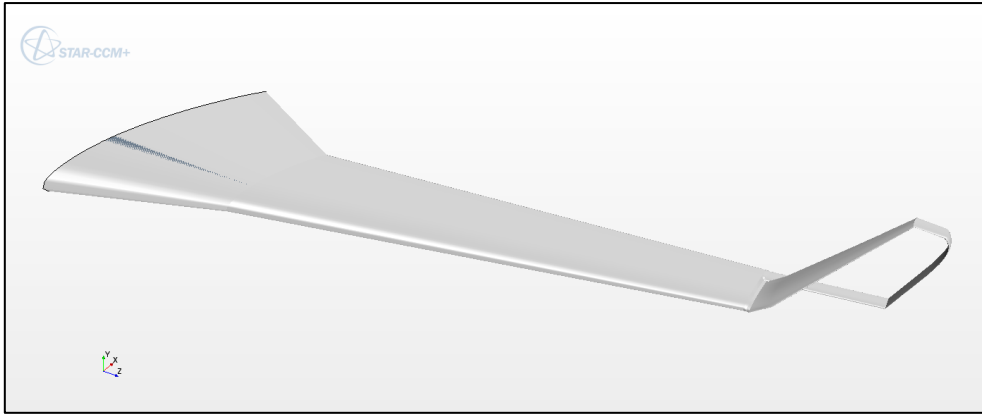


**Fig. 84: Clean wing range % improvement vs Wing-tip device**

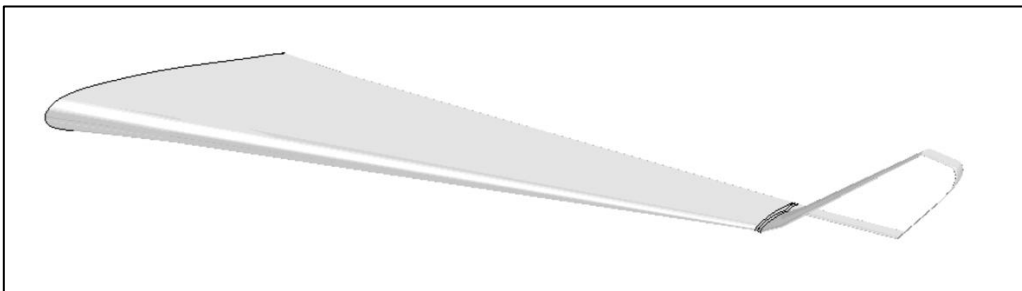
The factor that directly affects the range of an aircraft is the relation,  $\left(\frac{\sqrt{C_L}}{C_D}\right)$  from observing Table 11 and as evident in Fig. 84. The trade-off of maximum Range improvement based on the comparison of the clean wing against each studied wing-tip device showed an improvement of 4.34 percent for the blended winglet, 3.39 percent for the spiroid trapezium and 2.87 percent for the spiroid loop.

#### **4.3. Proposed designs for optimisation study**

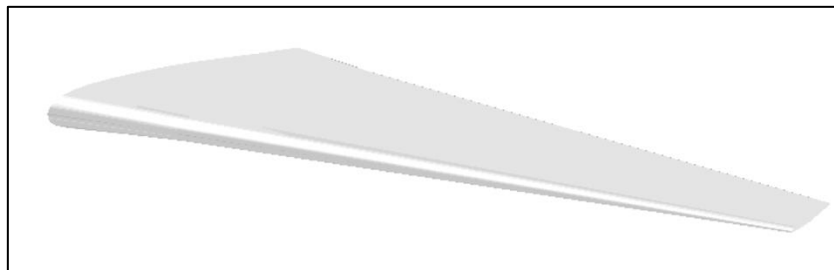
The designs in section 4.2.1. were scaled up to a full-size model and retrofitted on a wing model better resembling a Boeing 737 wing and checked to ascertain if the performance characteristics of the scaled model could be replicated on a full-size model (see Fig. 85). The device was tested at Mach 0.24 - 0.84 at  $4^\circ$  angles of attack at the specified operating conditions using CFD. Table 12 shows the data obtained. The trend in the results compared with those presented in section 4.2. showed the full-scale model of the spiroid trapezium winglet was effective in improving the lift-to-drag ratio at Mach numbers lower or equal to 0.64 and completely lost its benefits for Mach numbers above this number. It was suspected that the reason for the loss in performance was due to the high Mach number as evident in Table 12. The results also showed a drop-in lift-to-drag ratio at Mach 0.74 – 0.84, this is perhaps due to the wing design not been the exact replica of a Boeing 737 wing as well as the increment due to adding high lifting devices.



(a.)



(b.)



(c.)

**Fig. 85: (a) scaled spiroid trapezium winglet model in section 3.4.1. (b) Full scale model on a wing model resembling a Boeing 737 wing (c) Clean wing model for comparison**

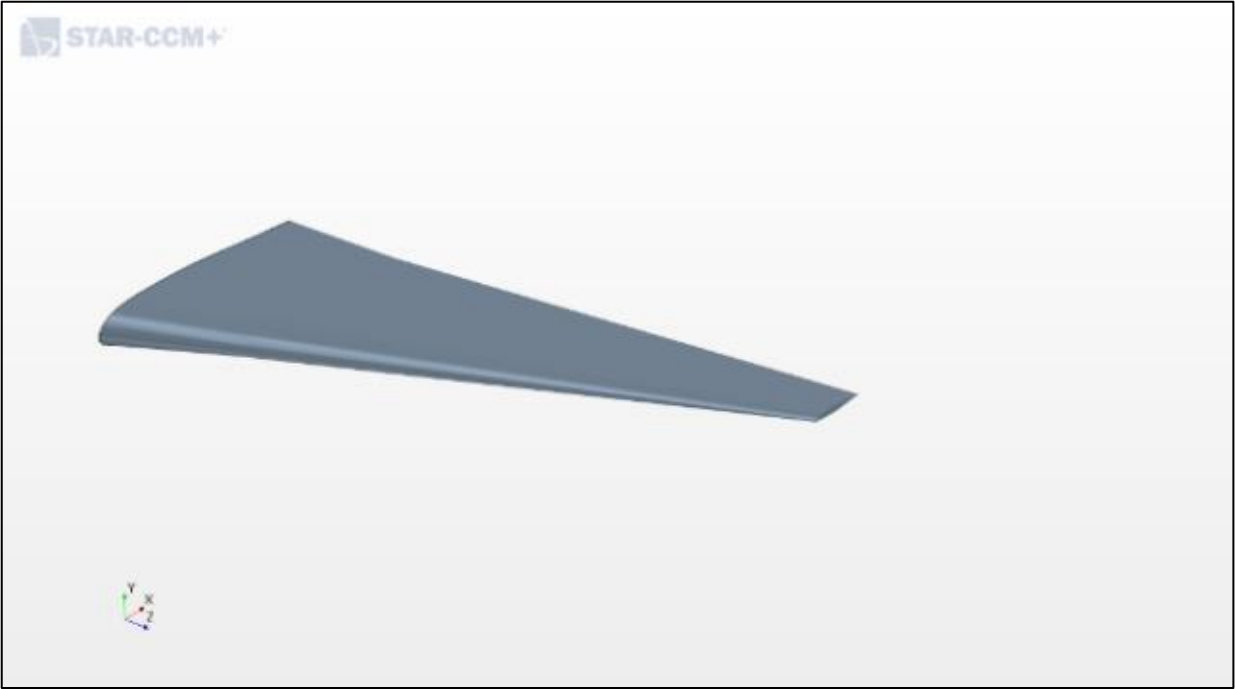
**Table 12: Performance of the full-scale trapezium spiroid winglet against a clean wing**

<b>Operating conditions – sea level, for several Mach numbers, 4-degree <math>\alpha</math></b>						
	<b>Clean wing</b>			<b>Spiroid Trapezium</b>		
<b>Mach number</b>	$C_L/C_D$	$C_L$	$C_D$	$C_L/C_D$	$C_L$	$C_D$
0.24	24.23698	0.45931	0.01895	25.99681	0.49226	0.01893
0.34	23.65175	0.44064	0.01863	25.60940	0.46938	0.01832
0.44	23.00117	0.46139	0.02005	24.82710	0.49217	0.01982
0.54	22.79646	0.49064	0.02152	24.66396	0.52591	0.02132
0.64	21.28800	0.52869	0.02485	22.38383	0.57621	0.02574
0.74	12.24934	0.54820	0.04475	12.09943	0.58927	0.04870
0.84	6.09662	0.53601	0.08791	6.06826	0.56739	0.09350

Due to its under-performance at Mach 0.74 and above, further investigations were carried out on other novel spiroid concepts which could be used at higher Mach numbers. This led to the set of designs proposed in addition to the spiroid trapezium for optimisation in the next session of the report. This new set of designs were discussed in section 2.4.1.6. Forty designs were investigated to find these new set of optimal designs. The wing tip devices were mounted on the same full - scale wing model that was used for the spiroid trapezium device. The design specifications are illustrated in Table 13.

**Table 13: Design specification wing with and without winglets**

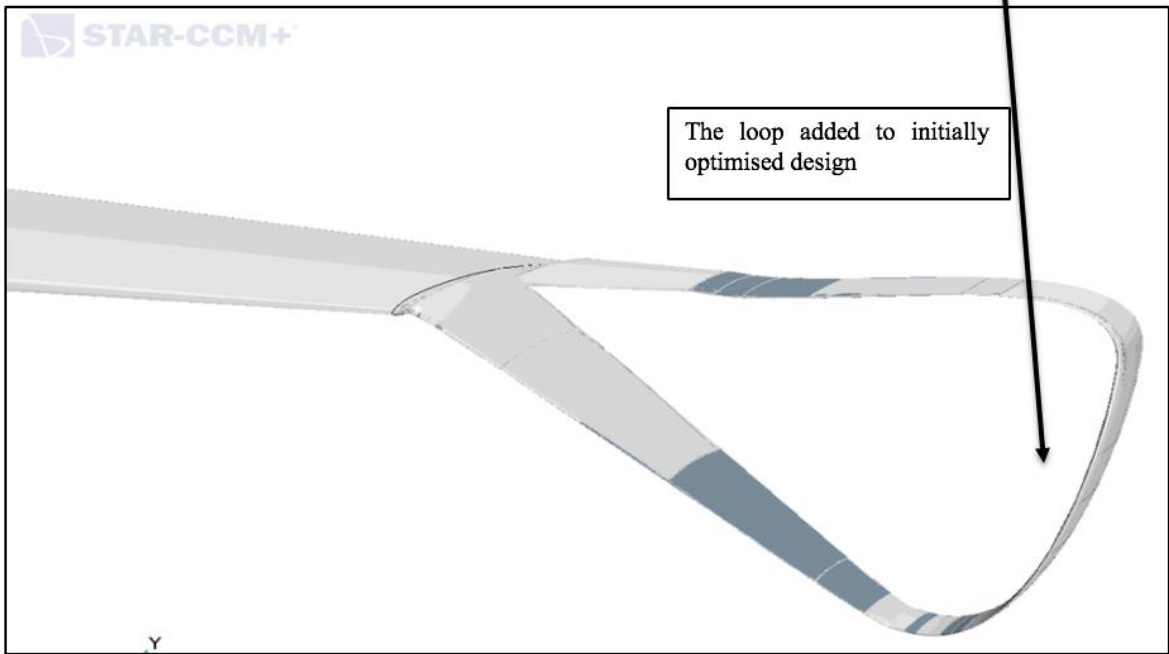
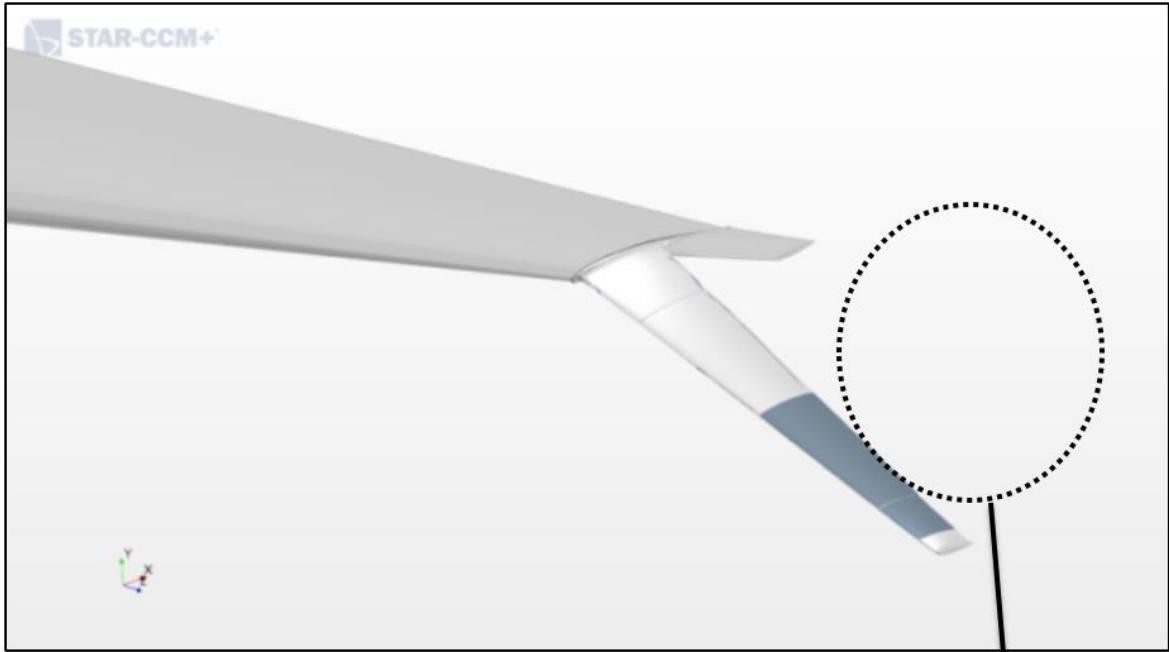
<b>Parameters</b>	<b>Clean wing</b>	<b>All winglets</b>
Semi-span	20m	20m
Wing root chord	7.5m	7.5m
Wing tip chord	1.7m	1.7m
Wing mid chord	4.3m	4.3m
Sweep	25 degrees	25 degrees
Dihedral	6 degrees	6 degrees



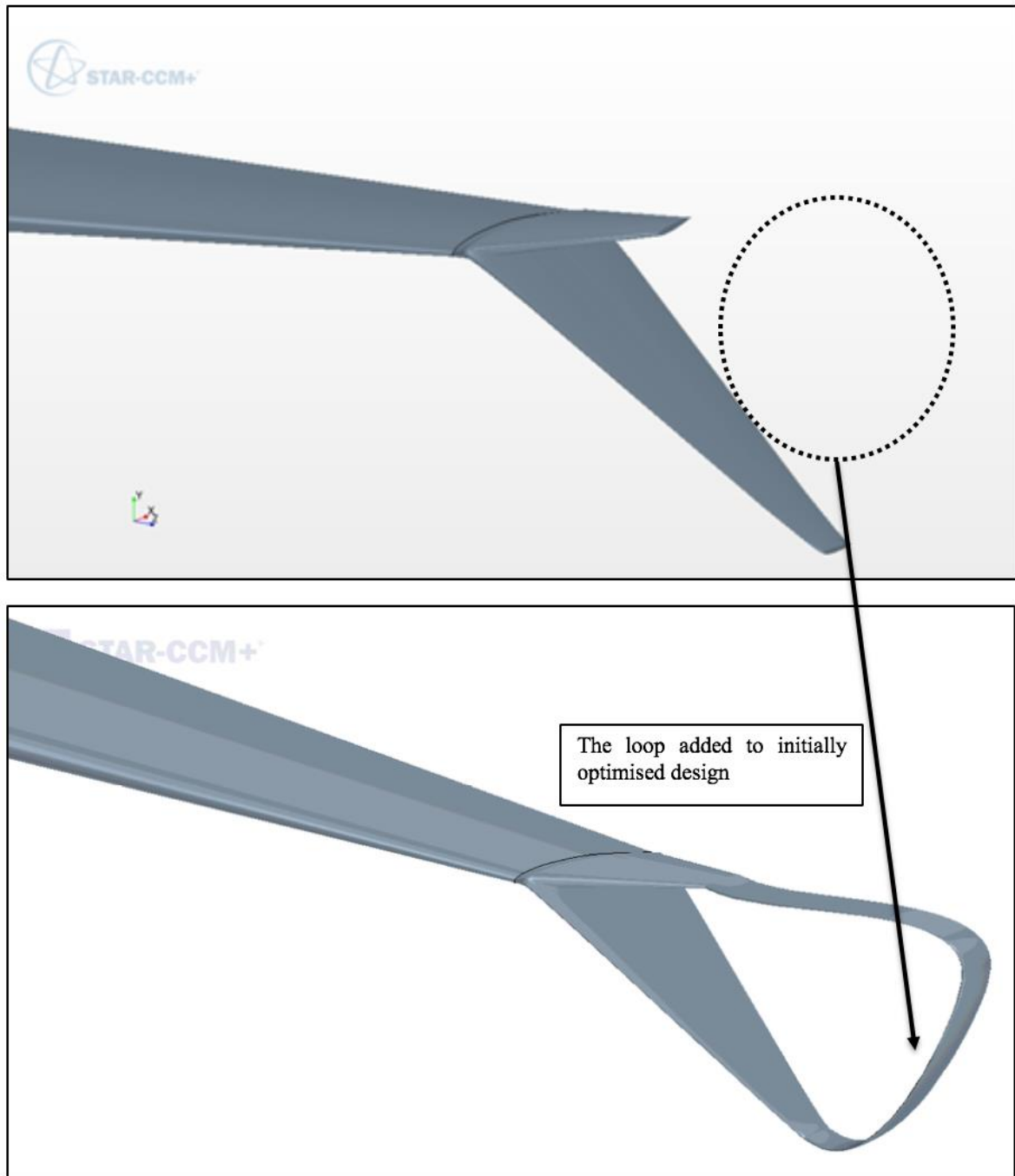
(a.)



(b.)



(c.)



(d.)

**Fig. 86: (a) clean wing (b) Design-1 (c) Design-2 (d) Design-3**

Fig. 85 (b) and Fig. 86 show the wing tip devices to be optimised, the devices were retrofitted on the clean wing. The performance of the devices shown in Fig. 86 compared against the clean wing at Mach 0.74 is shown in Table 14 while the performance of the spiroid trapezium is shown in Table 12.

**Table 14: Performance of the devices against the clean wing pre-optimisation at 4 degrees angle of attack and Mach 0.74**

Parameter	Clean wing	Design-1	Design-2	Design-2 Split-Tip	Design-3 Split-Tip	Design-3
$C_L$	0.537766039	0.506375372	0.54172188	0.543601871	0.554153442	0.558618248
$C_D$	0.044635076	0.042006001	0.044767644	0.044137806	0.044981524	0.045692284
$C_L/C_D$	12.04805921	12.05483412	12.10074574	12.31601485	12.31957899	12.22565831

These parameters were improved by using the optimisation algorithm discussed in section 5.2.4.

The optimisation process adopted, the final design models with results and analysis are presented in the next chapter of this report.

#### 4.4. Effect of fuselage on wing aerodynamic forces

Before the optimisation study was carried out, the impact that adding a fuselage to the wing would have on the wing tip was investigated. A fuselage was added to the wing model and is shown together with the mesh in Fig. 87.

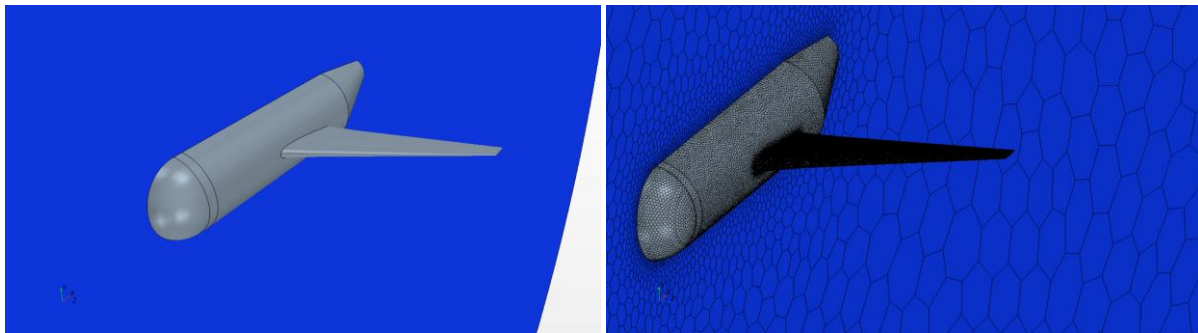


**Fig. 87: Fuselage plus wing and mesh**

The mesh type and configuration used in section 3.4.2 was adopted as well as the physics models in section 3.4.3. To analyse this effect, the following were considered: the lift-to-drag ratio, the wing per unit span, the drag per unit span, pressure and skin friction of the wing were studied. The lift-to-drag ratio of the wing only configuration was 12.4543 and 10.7928 for the fuselage plus wing configuration. This shows a drop-in value due to an increase in drag and a subsequent decrease in lift by adding the fuselage, this is shown in Table 15 and in Fig.88–Fig. 89. Fig. 88 shows the wing per unit span for both cases, the lift distribution at the wing tip region was shown to remain unchanged although the in-board wing section did show some modification due to the presence of the fuselage. Fig. 89 shows the drag per unit span in the span-wise direction, showing the comparison of both set-ups. The wing-tip regions once again seem to have not been affected by the addition of the fuselage. On the contrary, the in-board section of the wing shows higher  $C_D$  values on the plot. Fig. 90 gives a better clue as to the reason for

this occurrence; from analysis the pressure contours of the wing's top and bottom surface for both configurations, the pressure around the wing tip sections are identical but in-board of the wing. A higher-pressure region is observed near the wing's leading edge with fuselage top surface which causes the sudden drop in lift and increase in skin friction drag that is observed in Fig. 91. Based on these findings, it was concluded that the addition of the fuselage had no significant effect on the flow characteristics in the wing-tip region, therefore, it could be omitted during the optimisation process and for subsequent simulations. It was also helpful to do this as it saved computational time.

**Table 15: Aerodynamic coefficients wing only and wing plus fuselage**

	Wing only	Wing plus fuselage
$C_L$	0.5572	0.5245
$C_D$	0.0447	0.0486
$C_L/C_D$	12.4543	10.7928

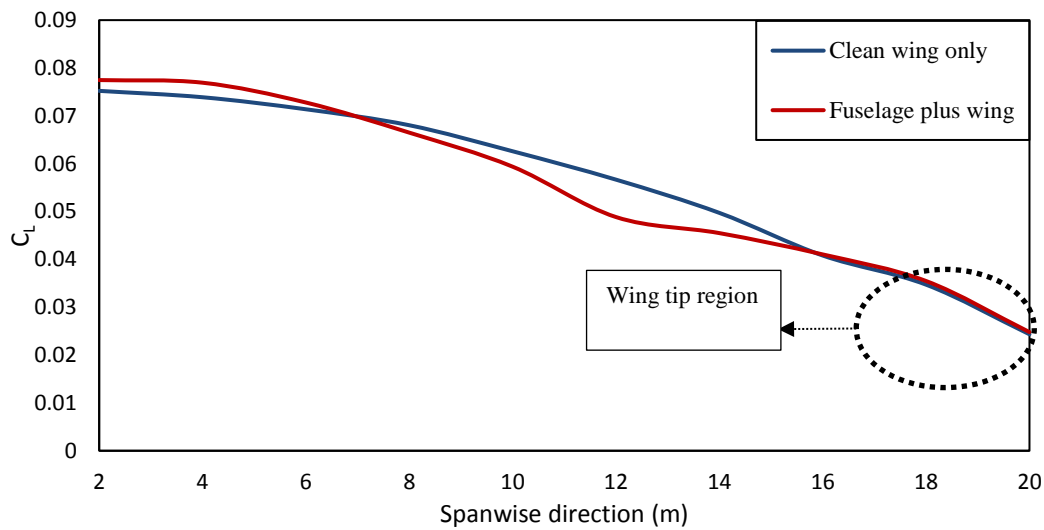


**Fig. 88: Lift per unit span**

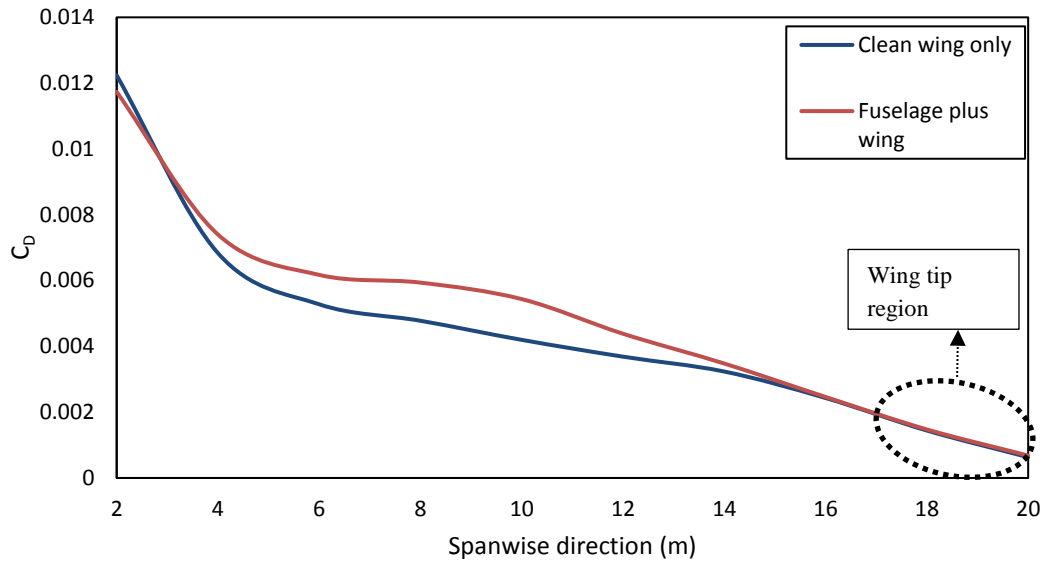
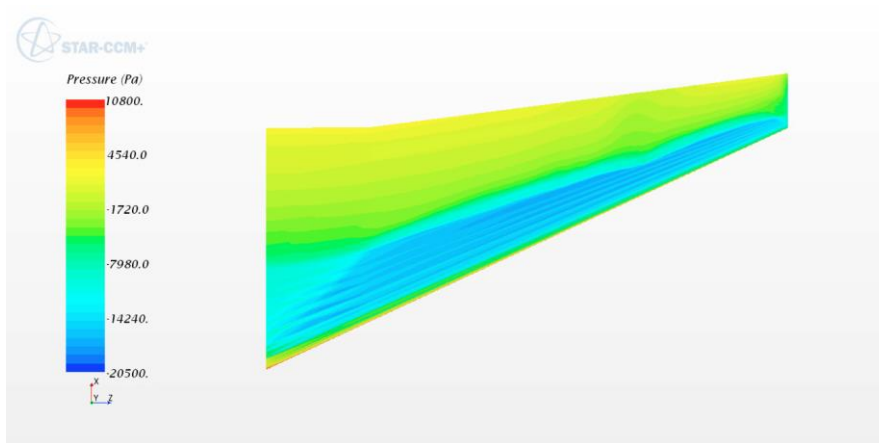
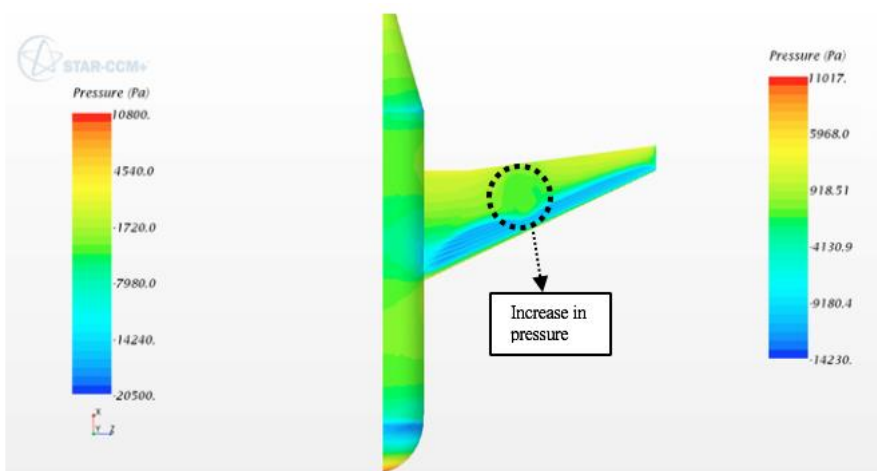


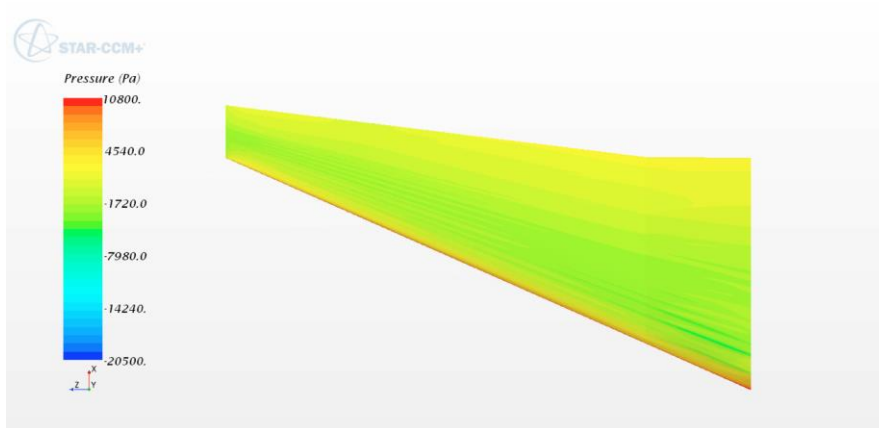
Fig. 89: Drag per unit span



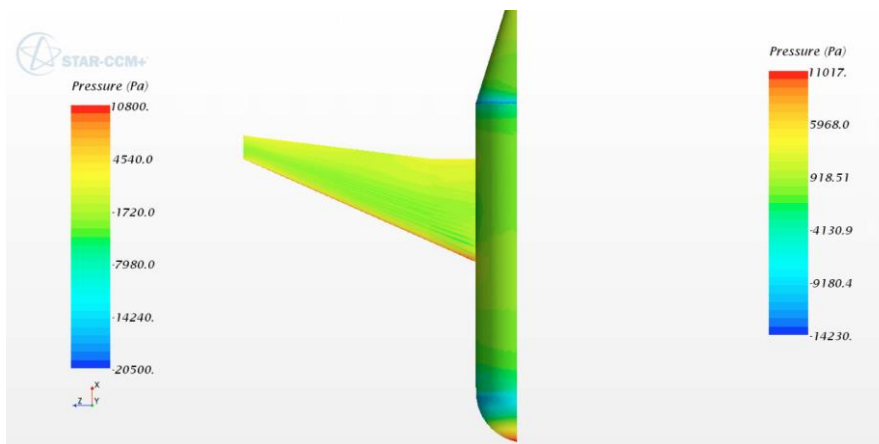
(i.) wing top surface



(ii.) Fuselage plus wing top surface

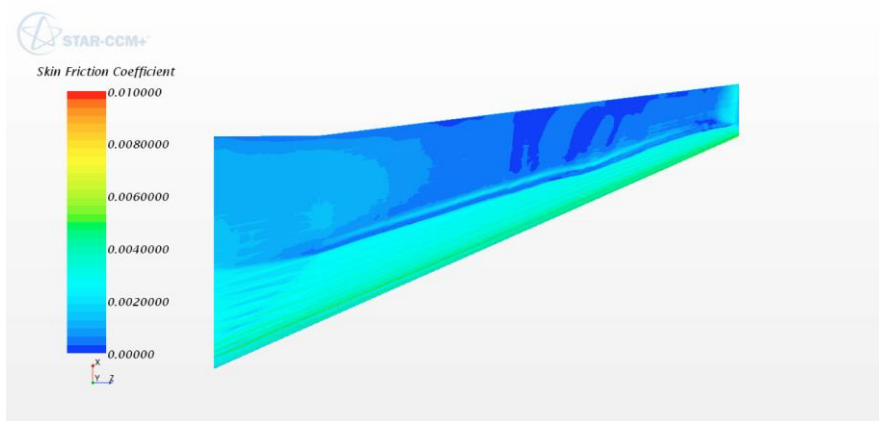


(iii.) wing bottom surface

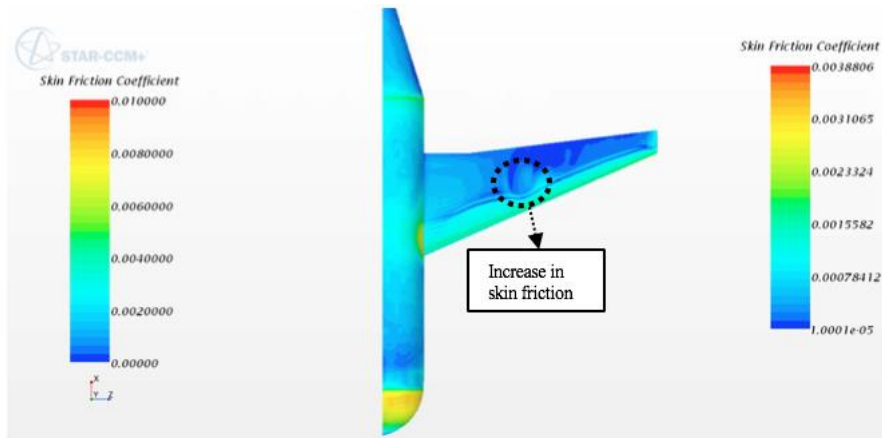


(iv.) Fuselage plus wing bottom surface

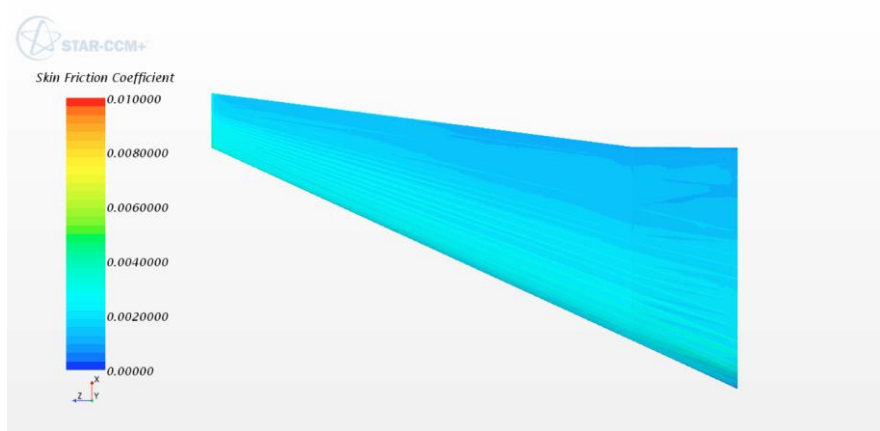
**Fig. 90: Pressure contour (i,ii,iii,iv)**



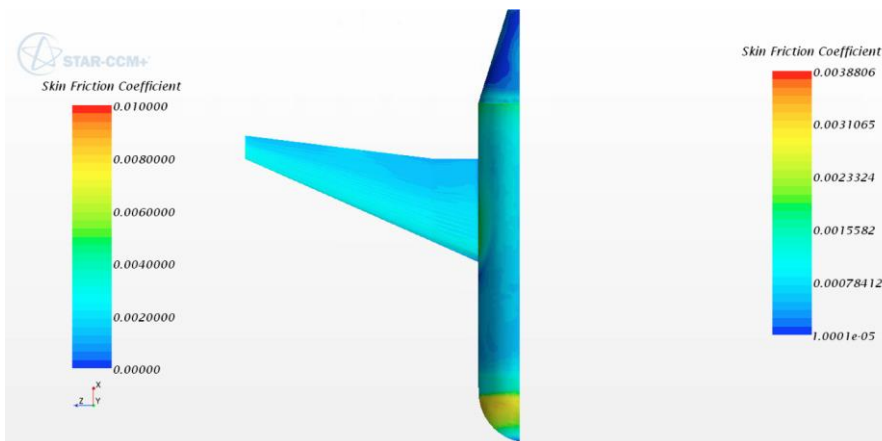
(i.) wing top surface



(ii.) Fuselage plus wing top surface



(iii.) wing bottom surface



(iv.) Fuselage plus wing bottom surface

**Fig. 91: Skin friction coefficient (i,ii,iii,iv)**

The optimisation process adopted, final design models with results and analysis are presented in the next chapter of this thesis.

## 4.5. Conclusion

Test cases to validate the numerical modelling approach has been performed in this chapter of this thesis with the results showing good correlation with the data reported in literature which was discussed in section 4.1. A new spiroid winglet design campaign was undertaken on a scaled wing and winglet models. This investigation was a prerequisite to the new set of proposed designs which was developed and used as a base design for further optimisation research presented in chapter 5. The qualitatively studied scaled wing and wing with winglet models had the following benefits and short comings:

- Improved generation of lift by increasing the lift coefficient ( $C_L$ ) significantly for the spiroid winglet technologies and the blended winglet with the spiroid winglet technologies achieving a  $C_L$  improvement of up to 8 percent.
- Improved lift-to-drag ratio.
- Reduced induced drag by up to 18 percent for the spiroid winglets and the blended winglet technologies
- Significant increased range by up to 5 percent.
- Slight reduction in cruise drag of up to 2 percent.
- Increased parasite drag for both spiroid wing-tip devices and the blended winglet due to increased wetted area.

Although results obtained are encouraging there is a lot of room for improvement in terms of increasing the drag reduction percentage of the spiroid devices by performing optimization studies which is addressed in chapter 5.

In addition to the spiroid trapezium technology, three new spiroid technologies (Designs 1-3) were introduced for optimisation due to the spiroid trapezium under performing at higher subsonic Mach numbers when the model was scaled up to a full size model and retrofitted.

Further, a comprehensive study on the effect of fuselage on wing aerodynamic forces with particular interest on the wing tip has been presented in this chapter of the thesis. Based on the findings, it is understood that the addition of the fuselage has no significant effect on the flow characteristics in the wing-tip region, therefore, it could be omitted during the optimisation process and for subsequent simulations. It was also helpful to do this as it saved computational time.

## Chapter 5: Aerodynamic optimisation of spiroid wing tip devices

In this chapter, the process that was adopted for the optimisation of the proposed designs in section 4.3 is discussed. The designs are further tested numerically by using the CFD method to validate their aerodynamic performance based on their capability to improve the lift to drag ratio, lift coefficient, drag coefficient and induced drag coefficient. Section 5.1. gives a general overview on optimisation, Section 5.2 describes aerodynamic shape optimisation, Section 5.2.1. describes the Gradient based optimisation methods, Section 5.2.2 discusses the Non-gradient based methods, Section 5.2.3. discusses the Surrogate based optimisation methods, Section 5.2.4, explains the optimisation method adopted for this research which was the SHERPA algorithm, Section 5.3. displays the Design Evaluation process, Section 5.3.1. presents the Optimisation Post Processing, Section 5.3.2. depicts the Effect of winglet on aerodynamic coefficient (cruise condition), Section 5.3.3. presents the Effect of winglet on aerodynamic coefficient (take-off condition). Section 5.3.4 displays the Effect of Mach number on winglet performance, Section 5.3.5. presents the lift per unit span and drag per unit span analysis and Section 5.3.6 the flow visualisation. Section 5.4. describes the Sensitivity of design variables on aerodynamic forces, Section 4.5 presents the conclusion of the chapter.

### 5.1. Introduction

The goal of an optimisation study is to obtain the best possible value for the objective function  $f(x)$  subject to given constraints; in this application, the function is a quantity which could be aircraft weight, drag, lift-to-drag ratio, profit, size, efficiency and shape etc. The objective function can be obtained from a given set of design variables denoted by a vector  $x$ . The design variables in this sense are regarded as the parameters which need to be altered in to optimise the objective function. From a practical sense, the values of these variables are bound by upper and lower limits. The optimisation problem can then include constraints; which are a function of the design variables. The constraints could be equality or inequality constraints. Mathematically, an optimisation problem can be formulated as:

$$\begin{aligned} \min f(x) & \hspace{15em} (56) \\ \text{s. t. } g_j(x) & \leq 0, j = 1, \dots, M \\ h_k(x) & = 0, k = 1 \dots, N \\ l & \leq x \leq u \end{aligned}$$

Where  $f(x)$  is the objective function,  $x$  is the vector of design variable,  $g_j(x)$  is an inequality constraint,  $M$  represents the number of inequality constraints,  $h_k(x)$  are the equality constraints and  $N$  is the number of equality constraints,  $l$  and  $u$  are the design variables lower and upper limits respectively.

## **5.2. Aerodynamic shape optimisation**

Aerodynamic shape optimization which is simply referred to as “ASO” here onwards involves employing advanced computer search algorithms in the design and investigation of aerodynamic surfaces. Such aerodynamic surfaces could include the aircraft wing, winglets, aircraft tail plane, turbine blades etc. Several solution technique or search algorithms exist which have been adopted for ASO; these includes gradient based (derivative) algorithms, non-gradient based methods (derivative free methods) and surrogate based methods. A quick overview of these methods is discussed in the following section.

### **5.2.1. Gradient based methods**

This search method is a non-stochastic search method with the search variables individually updated iteratively. Here the individual variables are updated by using the solution of a single simulation. One variable is updated based on a single simulation as such can result, in a large number of simulations runs to update all the variables (Chong and Zak, 2013). Therefore, the time taken to complete an optimisation run is largely dependent on the number of variables.

The key to using the gradient based optimisation method is in the use of ad-joint sensivity (Leifsson and Koziel, 2015). The use of ad-joint sensivity is independent of the number of variables; the ad-joint method functions by perturbing the fluid characteristics as opposed to directly working with the variables and determines the sensivity of the fluid flow field characteristics as a function of the objective function. Any changes obtained during this process are passed on to the gradient optimiser which uses the information to update the variables. The main advantage of using this method is that only a single CFD simulation is required in addition to an adjoint solution. The adjoint solution is comparable in complexity solving the CFD fluid flow equation (Tonomura et al., 2010), (Eyi et al., 1996).

Gradient based methods require the objective function to be differentiable and continuous and the optimum is dependent on the starting position. This method has been found to be unsuitable to handle variables which are discrete and has the tendency to get stuck in at a local optimum due to its reliance on the search starting point.

### **5.2.2. Non-gradient based methods (derivative-free methods)**

These are algorithms which do not require gradient information to find the problem optimum. The algorithms discussed here are based on guided random search as they use the information obtained from previous iterations to determine the next search point or direction. These can be sub-categorized as evolutionary algorithms. The most popular evolutionary algorithm that has been widely used for ASO is the genetic algorithm (GA). The genetic algorithm is based on bio-mimicry of the genetic process. Its fundamentals are based on Darwin's evolution theory of survival of the fittest. The genetic algorithm works with a set of populated points of which the fitness of each point within the population is computed. The set of points or simply points with higher fitness values are subject to cross-over and mutation with the hopes of producing points with better fitness values than their parents. The major advantage of GA over the gradient based method is that it does not get stuck at a local optimum but can give global optimum. Some examples on the application of GA for ASO can be found in references Elham and Van Tooren, (2014b), Reddy et al., (2014), Zhang et al., (2015a), Epstein et al., (2006). Other derivative free methods which have been adopted for ASO are: Simulated Annealing; an optimisation method based on the concept of heating metals to very high temperatures and then allowing them to cool slowly until the molecules of the metals arrive at a minimum energy state which leaves the solid free from defects. SA allows the process of hill climbing when the temperature is high making it possible for SA to escape getting stuck at local optima. See (Schramm et al., 2004), (Wang and Damodaran, 2001) for application on ASO. Particle Swarm is based on natural occurring events i.e. Flocking birds. This method is like GA in the sense that several search points are explored simultaneously in iterations to satisfy the objective function. The position of the individual points and the search group is tracked by the algorithm in terms of how well they fit in the objective function.

### **5.2.3. Surrogate based methods**

In surrogate optimisation, the high-fidelity expensive optimisation simulation is replaced by a computationally cheaper model which is iteratively updated and re-optimised. The main objective of using this optimisation method is to accelerate the optimisation process by using fewer optimisation runs (Leifsson and Koziel, 2015). The surrogates are typically functions which are constructed by using design of experiment (DOE) and by using data fitting methods. Several methods are available which can be used to construct the approximation surrogate function model. Some of these methods includes kriging, polynomial regression, radial basis function interpolation, support vector regression, corrected physics-based low-fidelity models (variable-fidelity optimisation; VFO). Once constructed, approximation models are fast to optimise. However, a lot of training

samples and a substantial amount of computing time and resources is required to gather the simulation data in order to ensure reasonable results. The most popular interpolation technique used for building surrogate model is the Kriging model.

The Kriging surrogate model technique is a geostatic method which is used for the interpolation of random surfaces based on a stochastic process to provide a confidence interval for predicted values. The interpolated random surfaces feature observed data at all sample points in the search space. This surrogate modelling technique have been found to be suitable for aerodynamic studies. The kriging model can be considered as a modelling technique which makes use of a global search model and a localised deviation variable.

$$\hat{y}(\vec{x}) = G(\vec{x}) + Z(\vec{x}) \quad (57)$$

$G(\vec{x})$  is the global model which could be a low order polynomial or a constant value and  $Z(\vec{x})$  is the localised deviation. It is suggested that no more than 50 parameters can be handled using the Kriging model (Simpson et al., 2001).

#### **5.2.4. SHERPA - Simultaneous Hybrid Exploration that is Robust, Progressive and Adaptive**

The optimisation algorithm adopted for this research is the Simultaneous Hybrid Exploration that is Robust, Progressive and Adaptive (SHERPA). SHERPA is a proprietary advanced and adaptive, non-gradient based search algorithm which uses multiple search methods simultaneously during a single optimisation case. The reason for using this optimisation search algorithm is to eliminate the need to rely on gradient based algorithms which are known for getting stuck at local minima and to reduce the computational expensiveness of using surrogate or derivative free algorithms. SHERPA is a multi-point adaptive algorithm which is well suited to handle multi-dimensional design space. Comparing SHERPA with other algorithms i.e. genetic algorithm, simulated annealing, non-linear sequential quadratic or response surface method has shown it to require no user defined functions and to produce better results and designs with fewer runs (Chase et al., 2010). Furthermore, for multi-objective design the algorithm can find the local and global pareto front and optimum design in less simulation time. The algorithm contains tuning parameters that are modified automatically based on the knowledge gained about the nature of the design space. For single objective optimisation studies, SHERPA uses several search methods which are combined simultaneously, not sequentially, in a unique and blended way (Chase et al., 2009), (Chase et al., 2010). This method makes use of the best characteristics of each search method; thus, if a search

method is deemed inefficient, the algorithm reduces the impact of the method on the process. The SHERPA algorithm uses a combination of the global and local search techniques. At any point during the optimisation process, SHERPA uses a range of 2 to 10 search methods. The algorithm performs all evaluation by using the actual model and not an approximate response surface model; although it is worth noting that is capable of performing optimisation analysis using surrogate models during sensitivity, design of experiment or optimisation studies. A comparison of the traditional and SHERPA search methods is shown in Fig. 92. The major difference between both methods is that the use of SHERPA removes the need to select a search algorithm and set tuning parameters to guide the search to the optimised design.

This algorithm has been employed for the successful optimisation of a composite wing box for high altitude aircraft (Arévalo, 2014), design of missile jet vane (Çitak et al., 2016), ship hull shape optimisation (Agrusta, 2015), (Enearu et al., 2017), (Ngo et al., 2015), (Kusterer et al., 2016), (Lange et al., 2014).

For post-processing of the results, proprietary software by Cader Technology called HEEDS is used. The HEEDS post-processor is embedded in Optimate + as the post processing platform which enables users to analyse the evaluated designs in terms of how well they meet the optimisation object function. This is called the performance plot as a function of the design identification number.

In HEEDS, each design is given a performance rating (s). The value in rating (performance) that is returned for the designated objective (s) and the degree to which a given design meets its constraints together determines the design's performance value. As such, a high-performance design is the one that satisfies all constraints and has a good rating based on the its objective (s). All the designs that satisfy the selected constraints essentially ignore the margin by which they meet those constraints. Once the constraints are satisfied, only the objectives contribute numerically to the performance evaluation. The performance value of each studied design is calculated by using the equation (HEEDS, 2017):

$$Perf. value = \sum_{i=1}^{Nobj} \left( \frac{LinWt_i * Sign_i * Obj_i}{Norm_i} \right) - \sum_{j=1}^{Ncon} \left( \frac{QuadWt_j * ConstrntViolation_j^2}{Norm_j^2} \right) \quad (58)$$

Where *perf.Value* is performance value, *Nobj* is the number of objective (s) in the optimisation study, *LinWt<sub>i</sub>* is the linear weight for the *i*<sup>th</sup> objective, *Sign<sub>i</sub>* is the sign of the *i*<sup>th</sup> objective. *Obj<sub>i</sub>* is the response value for the *i*<sup>th</sup> objective for that design, *Norm<sub>i</sub>* is the normalising value for the *i*<sup>th</sup> objective, *Ncon* is number of constraints in the

optimising study,  $QuadWt_j$  is the quadratic weight for the  $j^{\text{th}}$  constraint,  $ConstrntViolation_j$  is the amount by which the  $j^{\text{th}}$  constraint is violated and  $Norm_j$  is the normalising value for the  $j^{\text{th}}$  constraint. For given feasible designs (all constraints are satisfied), the performance function is a sum of the normalized objective (s) values. In the case where one or more constraints are violated, the performance of that design is reduced by a value that is based on the violation of that constraint (the second term in equation 3.0) (HEEDS, 2017).

The following section discusses the design evaluation approach.

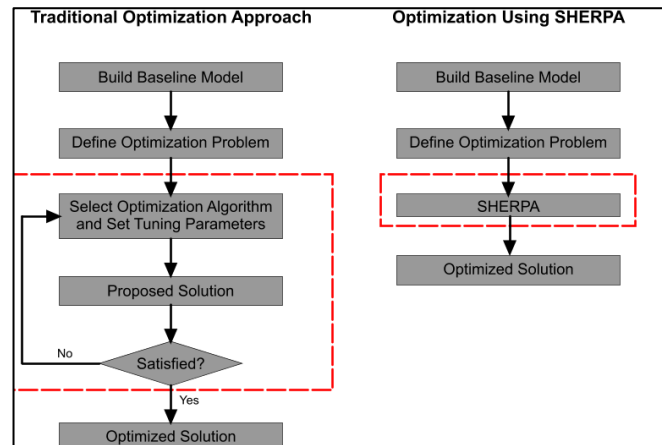


Fig. 92: Traditional and SHERPA optimisation approach (CD-ADAPCO, STAR-CCM+, 2015)

### 5.3. Design Evaluation

The SHERPA algorithm had been bench marked against other algorithms i.e. Genetic Algorithm, Simulated Annealing, Surrogate Based Response Surface Modelling see (Chase et al., 2010), (Chase et al., 2009) and was reported to be more efficient than the other algorithms. To optimise the wing tip devices discussed in section 4.3, the winglet geometries were parametrised by using the parameters shown in Table 16 – Table 19, these tables also includes the design parameters before and after the optimisation was performed on the devices.

The study considered the given operating condition of Mach 0.74 (for Designs 1-3) or Mach 0.24 (for the spiroid trapezium) and sought to *maximise*  $f(x) = L/D(x)$  subject to constraints on lift  $g_1(x) = \text{lift}_{\text{baseline-wing}} < \text{lift}_{\text{wing+winglet}}$  on the design variable vector.

The winglet design variables are constrained to restrict to sensible values the multi-dimensional search space used by the algorithm and to eliminate design errors which can be produced by the CAD modeller. These Mach numbers were used based on what was discussed in section 4.3.

In Optimate +, the design evaluation number, which is the number of design analyses required to successfully perform the design search is set between 40 -140 for each study. This number is selected based on the suggestions in (Mand, 2011) to use 17 – 25 runs per design parameter or a minimum of 40 optimisation runs. Simultaneous simulation with 4 core processors each is specified for the runs. After completing the optimisation process, further CFD simulation and analysis is performed on the baseline wing and the optimised designs at more refined mesh quality discussed in section 5.3, to affirm the obtained results.

**Table 16: Design 1 design variables with upper and lower limits**

Design variables	Lower limits	Upper limit	Before optimisation	After optimisation
Toe chord size-1	0.5 (scale factor)	3 (scale factor)	2 (scale factor)	1.3375(scale factor)
Toe chord size-2	0.5 (scale factor)	3 (scale factor)	2 (scale factor)	0.775 (scale factor)
Toe chord size-3	0.5 (scale factor)	3 (scale factor)	2 (scale factor)	1.1 (scale factor)
Toe chord size-4	0.5 (scale factor)	3 (scale factor)	2 (scale factor)	2.45 (scale factor)
Chord-1 thickness	0.2 (scale factor)	1 (scale factor)	0.5 (scale factor)	0.256 (scale factor)
Chord-2 thickness	0.2 (scale factor)	1 (scale factor)	0.5 (scale factor)	0.2 (scale factor)
Chord-3 thickness	0.2 (scale factor)	1 (scale factor)	0.5 (scale factor)	0.672 (scale factor)
Chord-4 thickness	0.2 (scale factor)	1 (scale factor)	0.5 (scale factor)	0.912 (scale factor)
Chord-2 position along the wing tip	0.05 (m)	1 (m)	0.5 (m)	0.91925 (m)
Chord-4 position along the wing tip	0.05 (m)	1 (m)	0.5 (m)	0.72925 (m)
Chord-2 twist	-5 deg.	5 deg.	0 deg.	5 deg.
Chord-3 twist	-45 deg.	45 deg.	0 deg.	2.8 deg.
Chord-4 twist	-5 deg.	5 deg.	0 deg.	2.8 deg.
Chord-2 span-wise position	0.15 (m)	0.17 (m)	0.17 (m)	0.1619 (m)
Chord-3 span-wise position	0.2 (m)	4 (m)	0.27 (m)	3.677 (m)
Chord-4 spam-wise position (device maximum length)	0.15 (m)	0.17 (m)	0.17 (m)	0.1667 (m)
Chord-1 vertical position	0.05 (m)	1 (m)	0.5 (m)	0.68175 (m)
Chord-2 vertical position	0.05 (m)	0.5 (m)	0.1 (m)	0.33125 (m)
Chord-3 vertical position	0.05 (m)	1 (m)	0.5 (m)	0.79575 (m)
Chord-4 vertical position	-0.5 (m)	-0.05 (m)	-0.1 (m)	-0.0995 (m)
Connection device thickness	0.2 (scale factor)	1 (scale factor)	0.5 (scale factor)	0.912 (scale factor)

**Table 17: Design 2 design variables with upper and lower limits**

Design variables	Lower limits	Upper limit	Before optimisation	After optimisation
Mid-point span-wise position (length)	2.25 (m)	5 (m)	3.4108 (m)	3.4325 (m)
Mid-point height	-2.26 (m)	-0.04 (m)	-0.929447 (m)	-0.2398 (m)
Chord 1 size	0.2 (scale factor)	1.129 (scale factor)	0.501925 (scale factor)	0.48799 (scale factor)
Toe 1 size	0.6 (scale factor)	1.129 (scale factor)	0.83308 (scale factor)	0.81689 (scale factor)
Toe-2 size	0.6 (scale factor)	1.129 (scale factor)	1.05004 (scale factor)	1.047 (scale factor)
Chord 3 size	0.2 (scale factor)	1.129 (scale factor)	0.604115 (scale factor)	0.566955 (scale factor)
Mid-point size	0.2 scale factor	1.129 (scale factor)	0.6 (scale factor)	0.566955 (scale factor)
Chord 1 height	-4 (m)	-1.2 (m)	-2.5 (m)	-2.292 (m)
Chord 3 height	-0.1 (m)	0.06 (m)	0.02 (m)	0.0176 (m)
Chord 1 length	0.8 (m)	3.3 (m)	2.2056 (m)	2.15 (m)
Chord 3 length	0.8 (m)	3.3 (m)	0.983 (m)	0.925 (m)
Chord 1 twist	-8 (deg.)	8 (deg.)	-0.6 (deg.)	-0.4 (deg.)
Chord 3 twist	-8 (deg.)	8 (deg.)	5.8 (deg.)	5.6 (deg.)
Mid-point twist	-10 (deg.)	10 (deg.)	0 (deg.)	0.2 (deg.)

**Table 18: Design 3 design variables with upper and lower limits**

Design variables	Lower limits	Upper limit	Before optimisation	After optimisation
Mid-point span-wise position (length)	2.25 (m)	5 (m)	3.4325 (m)	3.3362 (m)
Mid-point height	-2.26 (m)	-0.04 (m)	-0.2398 (m)	-0.3952 (m)
Chord 1 size	0.2 (scale factor)	2 (scale factor)	0.501925 (scale factor)	0.848 (scale factor)
Toe-2 size	0.2 (scale factor)	2.24 (scale factor)	2.24 (scale factor)	1.2914 (scale factor)
Chord 3 size	0.2 (scale factor)	2 (scale factor)	0.604115 (scale factor)	0.2 (scale factor)
Mid-point size	0.2 (scale factor)	2 (scale factor)	0.566955 (scale factor)	0.866 (scale factor)
Chord 1 height	-4 (m)	-1.2 (m)	-2.292 (m)	-2.432 (m)
Chord 3 height	-0.1 (m)	0.06 (m)	0.02 (m)	0.0048 (m)
Chord 1 length	0.8 (m)	3.3 (m)	2.15 (m)	1.4125 (m)
Chord 3 length	0.8 (m)	3.3 (m)	0.983 (m)	2.35 (m)
Chord 1 twist	-8 deg.	8 deg.	-0.6 deg.	2.88 deg.
Chord 3 twist	-8 deg.	8 deg.	5.8 deg.	6.08 deg.
Mid-point twist	-10 deg.	10 deg.	0.2 deg.	1.6 deg.
Chord 1 sweep	1.1	1.9	1.9	1.496
Chord 3 sweep	1.1	1.9	1.2	1.1975

**Table 19: Spiroid trapezium design variables with lower and upper limits**

Design Variables	Lower limit	Upper limit	Before optimisation	After optimisation
Chord 1 size	2.43 (scale factor)	6 (scale factor)	2.43 (scale factor)	2.4975 (scale factor)
Chord 2 size	2.43 (scale factor)	6 (scale factor)	2.43 (scale factor)	2.43 (scale factor)
Chord 3 size	2.43 (scale factor)	6 (scale factor)	2.43 (scale factor)	3.2154 (scale factor)
Chord 4 size	2.43 (scale factor)	6 (scale factor)	2.43 (scale factor)	2.8227 (scale factor)
Chord 5 size	2.43 (scale factor)	6 (scale factor)	2.43 (scale factor)	3.2154 (scale factor)
Chord 1 twist	-5 (deg.)	5 (deg.)	0 (deg.)	2.8 (deg.)
Chord 2 twist	-5 (deg.)	5 (deg.)	0 (deg.)	2.8 (deg.)
Chord 3 twist	-5 (deg.)	5 (deg.)	0 (deg.)	1.65 (deg.)
Chord 4 twist	-5 (deg.)	5 (deg.)	0 (deg.)	3.9 (deg.)
Chord 2 length	0.5 (m)	1 (m)	19.5129 (m)	20 (m)
Chord 4 length	0.475 (m)	1 (m)	20.0475 (m)	20.4185 (m)
Chord 5 length	0.5 (m)	1 (m)	19.5129 (m)	19.3382 (m)
Chord 5 sweep	6.5 (m)	7 (m)	6.9255 (m)	6.89 (m)

### 5.3.1. Optimisation Post-processing

In this section, the results from the optimisation process for the winglets is presented. Fig. 93-Fig.104, illustrates the history of the optimisation process using HEEDS post processing package. The designs analysed are each given a design number and a ranking number, based on how well it satisfies the objective function within the limits of the specified constraints. Fig. 93, Fig., 95, Fig. 97, Fig. 99, Fig. 101 and Fig. 103, explicitly shows the plot of lift-to-drag ratio as a function of the design identification number. The baseline design is given the design ID 1, the best design is ID 66 (Design-1), ID 20 (Design-2 mid part optimisation), ID 63 (Design-2 final design), ID 35 (Design-3 mid part optimisation), ID 100 (Design-3 final design) and ID 19 (spiroid trapezium) for each design. The mid-part optimisation refers to the optimisation of the loop shown in (Fig. 86 b and c). From analysing Fig. 93, Fig., 97, Fig. 99 and Fig., 103, SHERPA has found the best designs after 66, 63, 100 and 19 design evaluations for Designs 1 - 3 and the spiroid trapezium respectively. The performance of each of the designs based on how much lift-to-drag ratio improvement that was achievable is depicted in Fig. 94, Fig. 96, Fig. 98, Fig. 100, Fig. 102 and Fig. 104. The baseline wing and wing plus the optimised winglets are shown in Fig. 105 – Fig. 109, the devices before and after optimisation as well as a close view of each of the devices with dimensions and the design control points is illustrated. Within the designated multi-dimensional search space, SHERPA found a down-ward pointing winglet as the most effective winglet in terms of lift-to-drag ratio improvement for the

optimisation study carried out at Mach 0.74 with only an upward pointing configuration considered for the spiroid trapezium for Mach 0.24. The outcome of the study produced devices with substantial reduction in  $C_D$  and improvement in  $C_L$  as well as  $C_L/C_D$  improvement and are discussed in section 5.3.2 – 5.5.

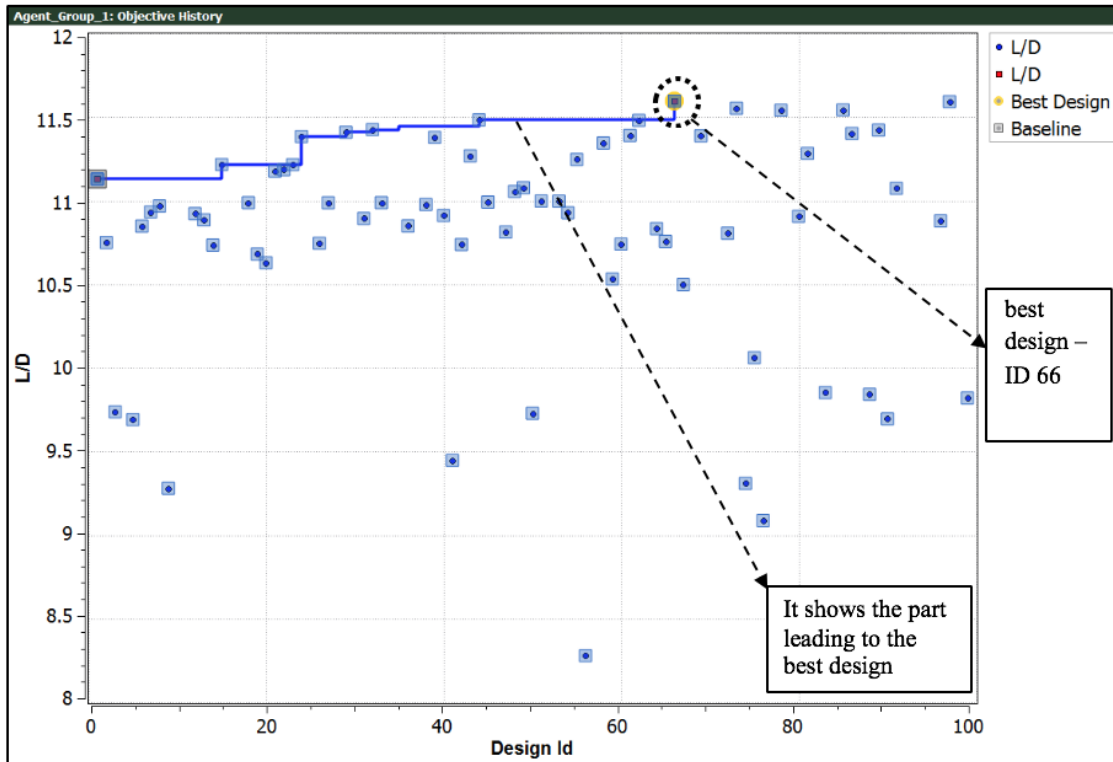


**Fig. 93: Lift-to-drag ratio as a function of the design number – Design-1**

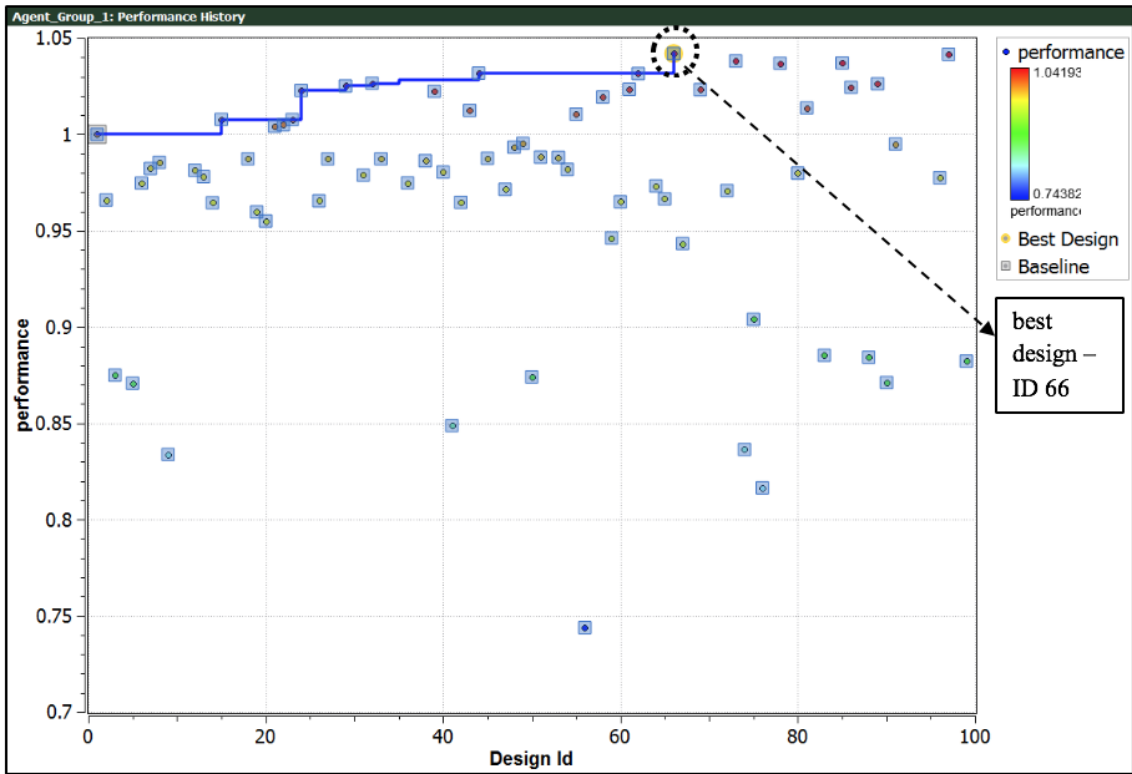


Fig. 94: Designs performance plot – Design-1

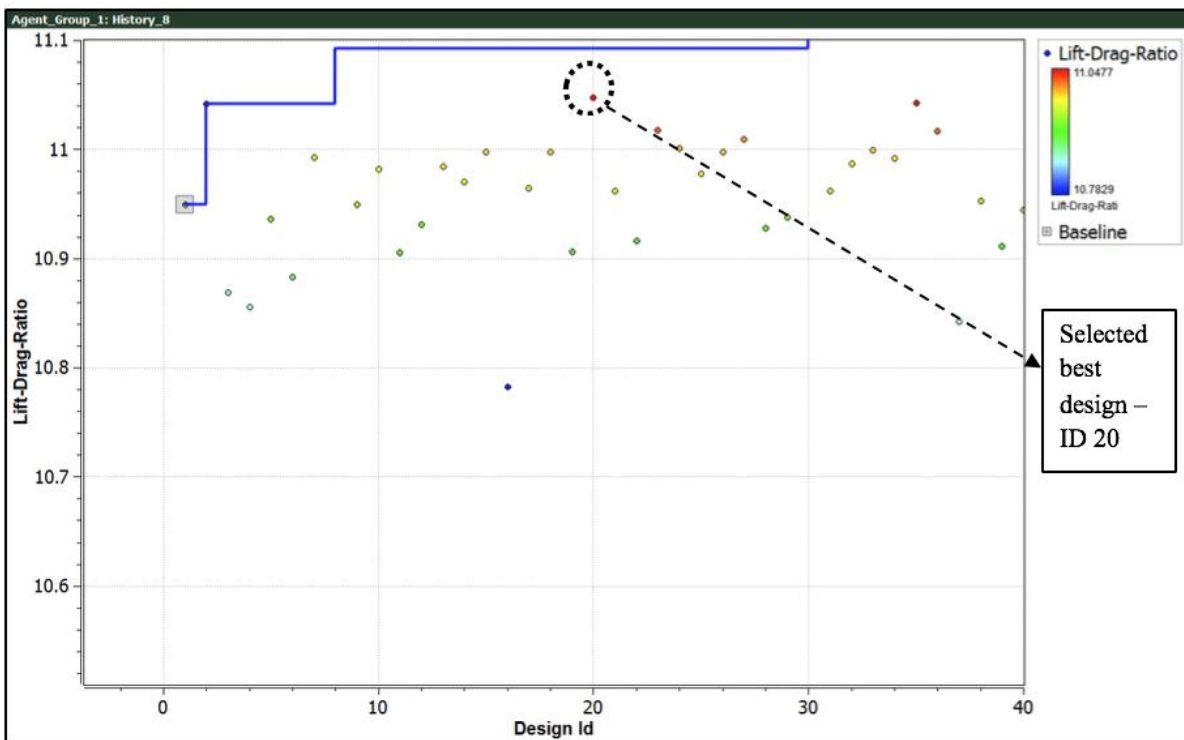


Fig. 95: Lift-to-drag ratio as a function of the design number – Design-2, Mid-point optimisation

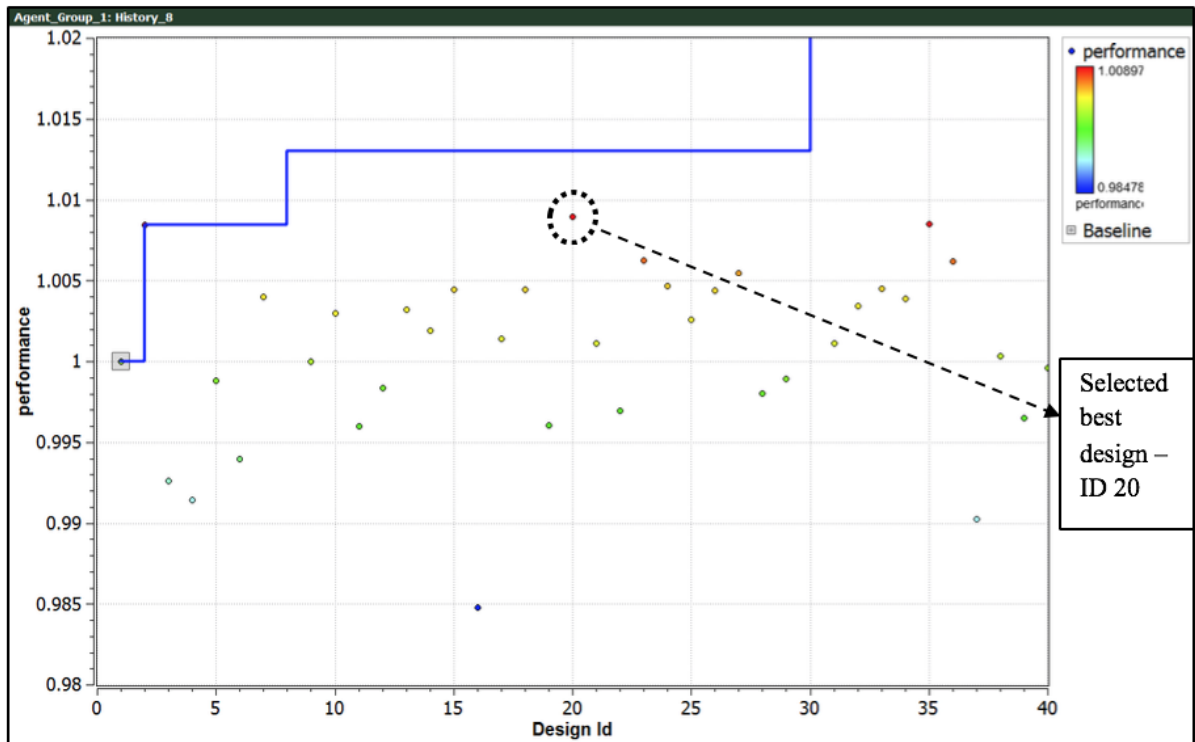


Fig. 96: Designs performance plot – Design-2, Mid-point optimisation

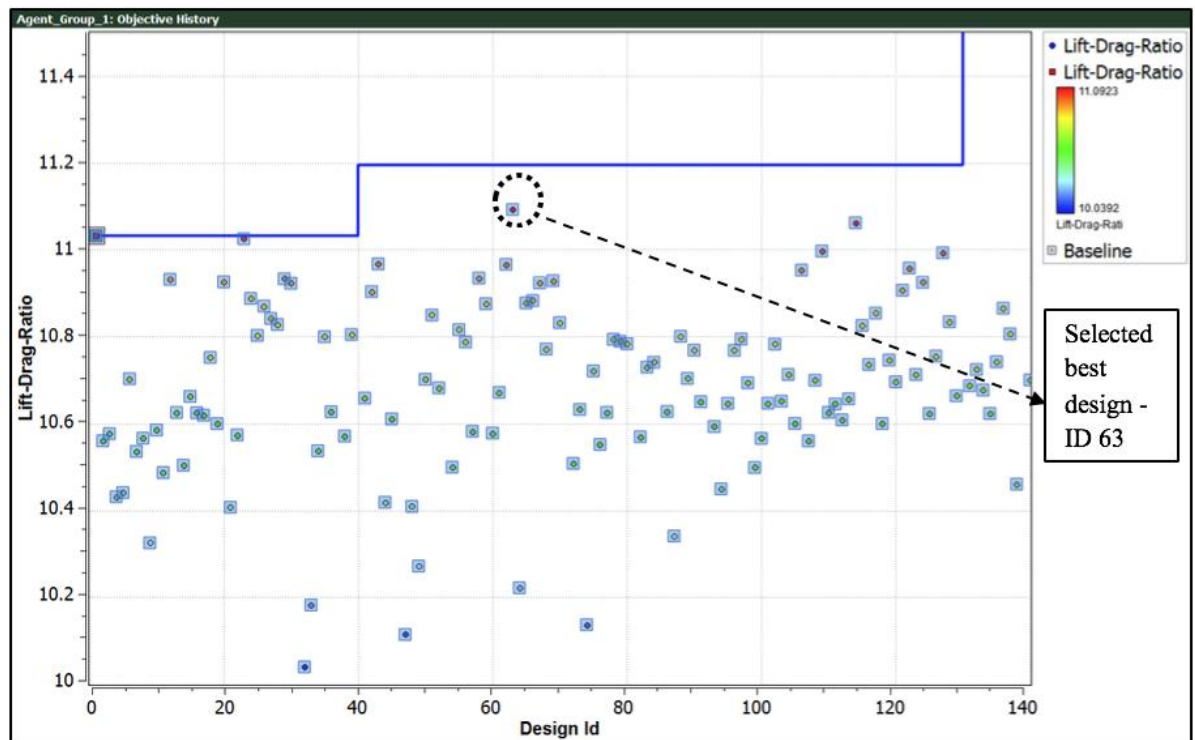


Fig. 97: Lift-to-drag ratio as a function of the design number – Design-2

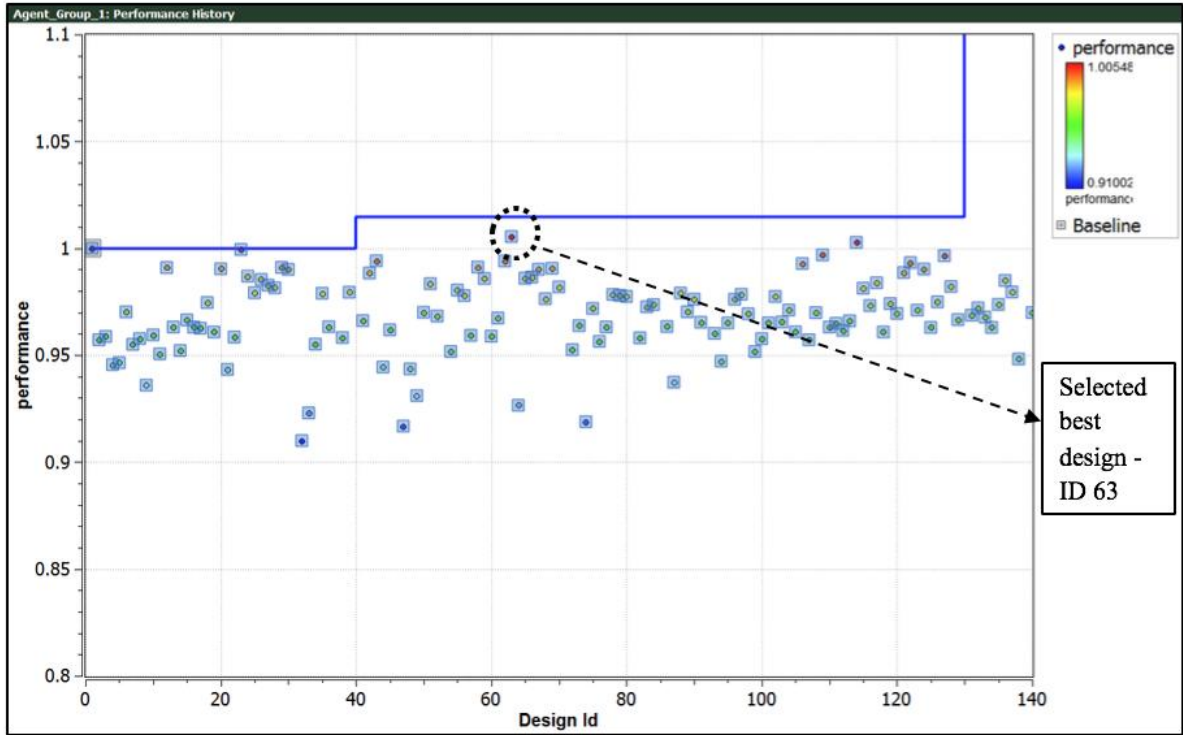


Fig. 98: Designs performance plot – Design-2

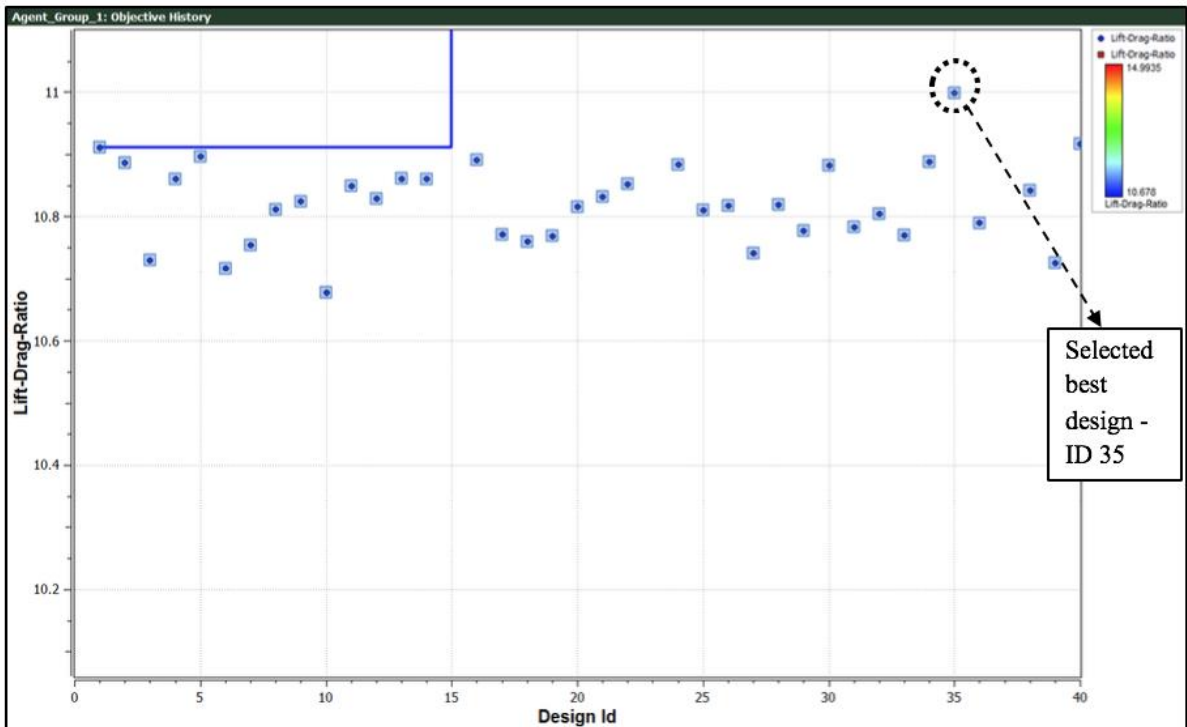


Fig. 99: Lift-to-drag ratio as a function of the design number – Design-3, Mid-point optimisation

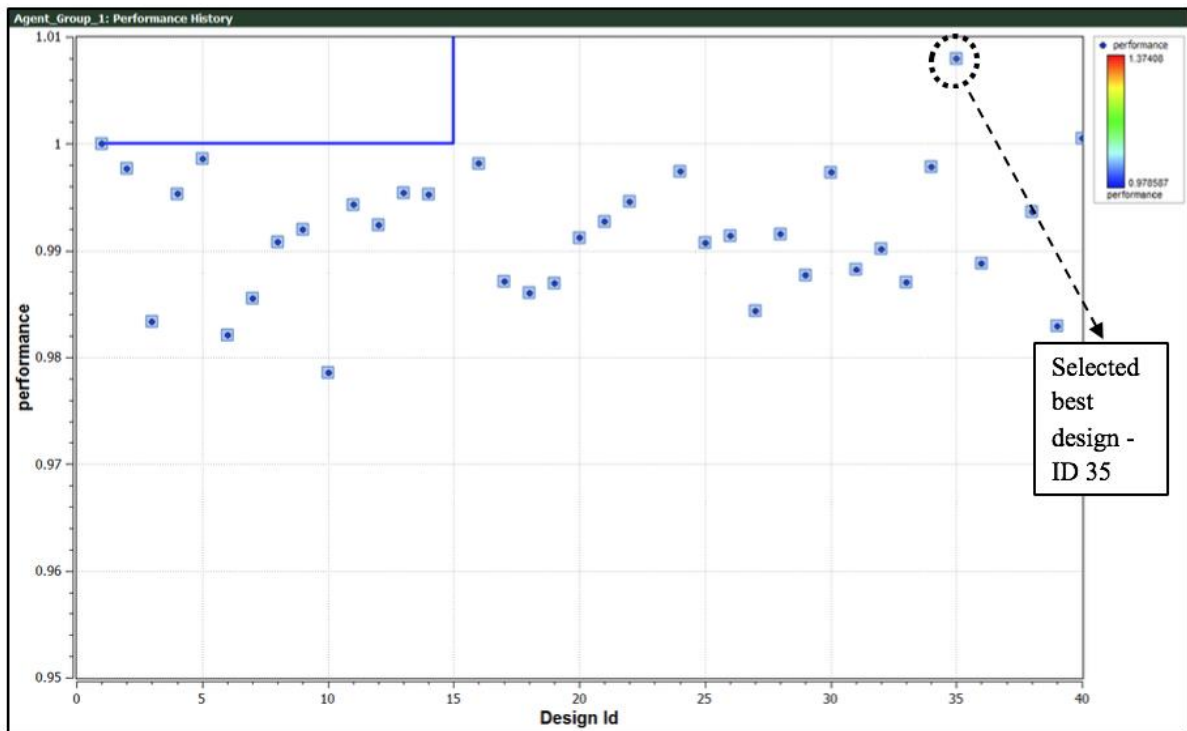


Fig. 100: Designs performance plot – Design-3, Mid-point optimisation

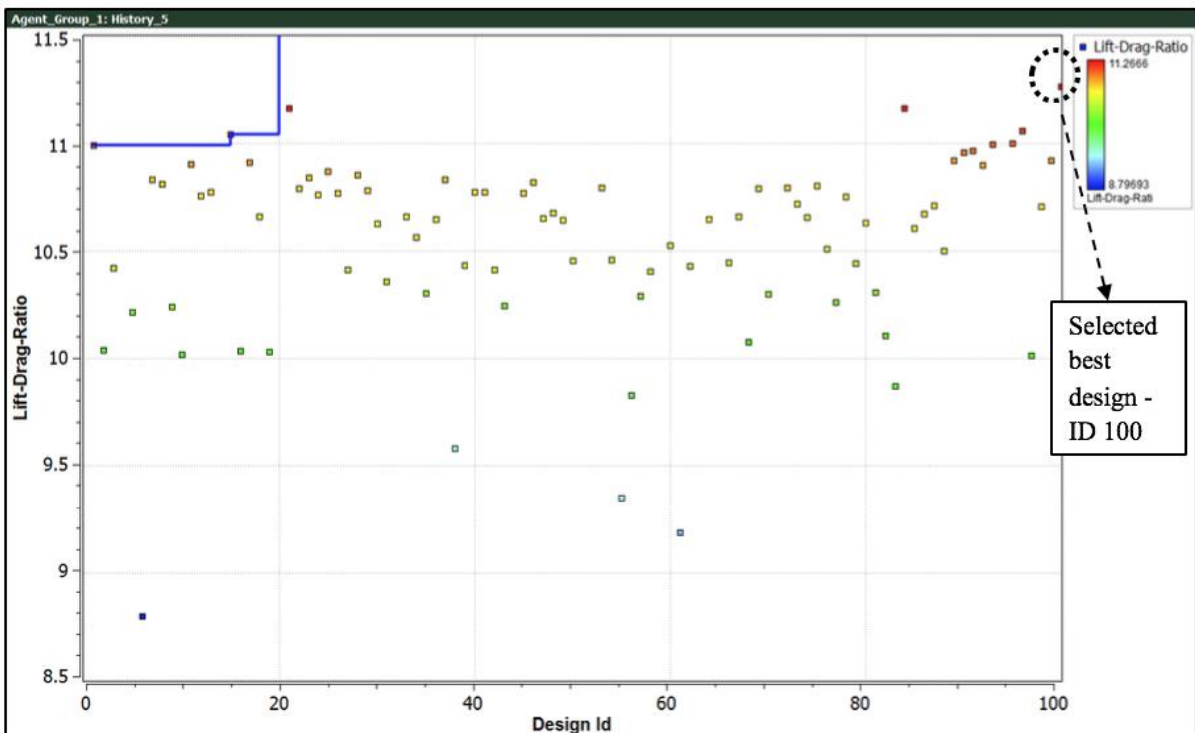


Fig. 101: Lift-to-drag ratio as a function of the design number – Design-3

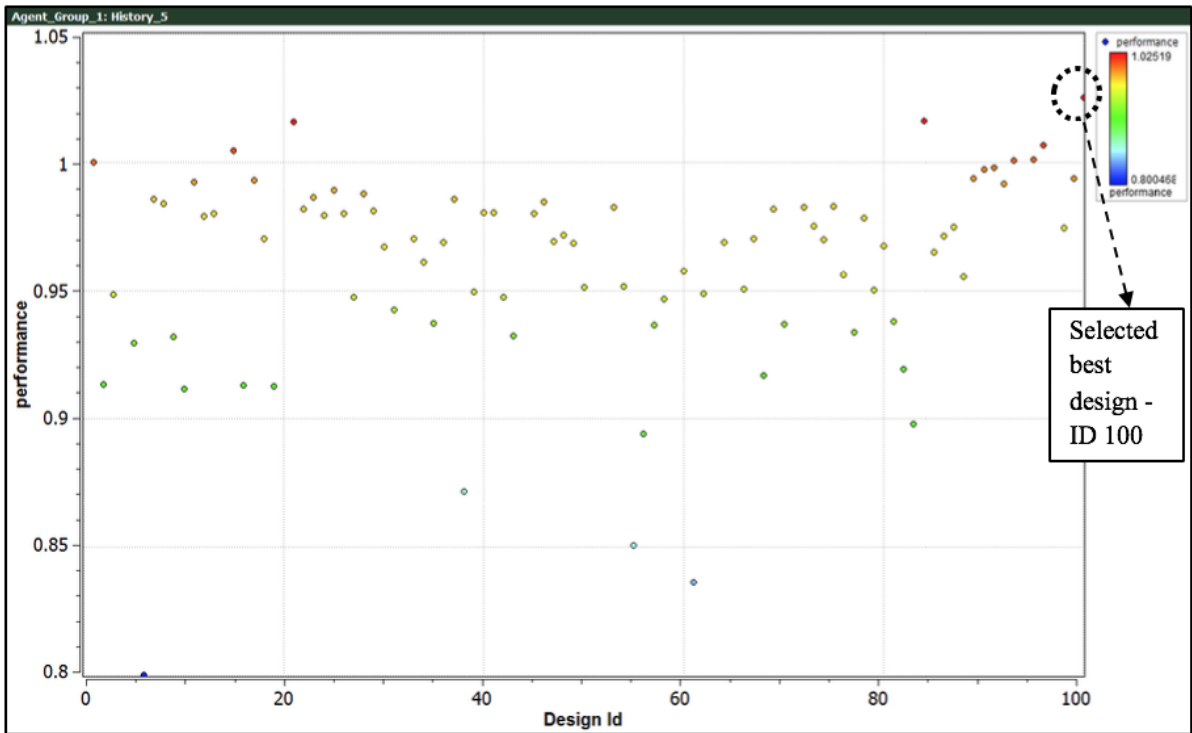


Fig. 102: Designs performance plot – Design-3

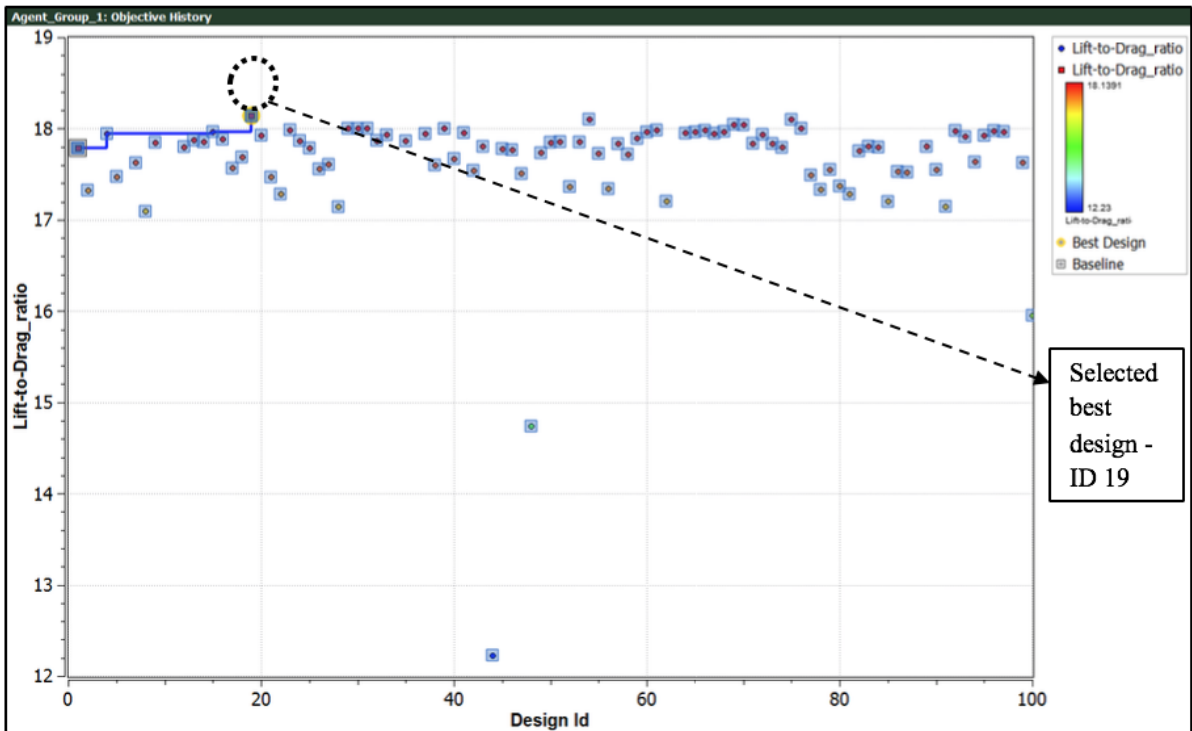


Fig. 103: Lift-to-drag ratio as a function of the design number – Spiroid trapezium

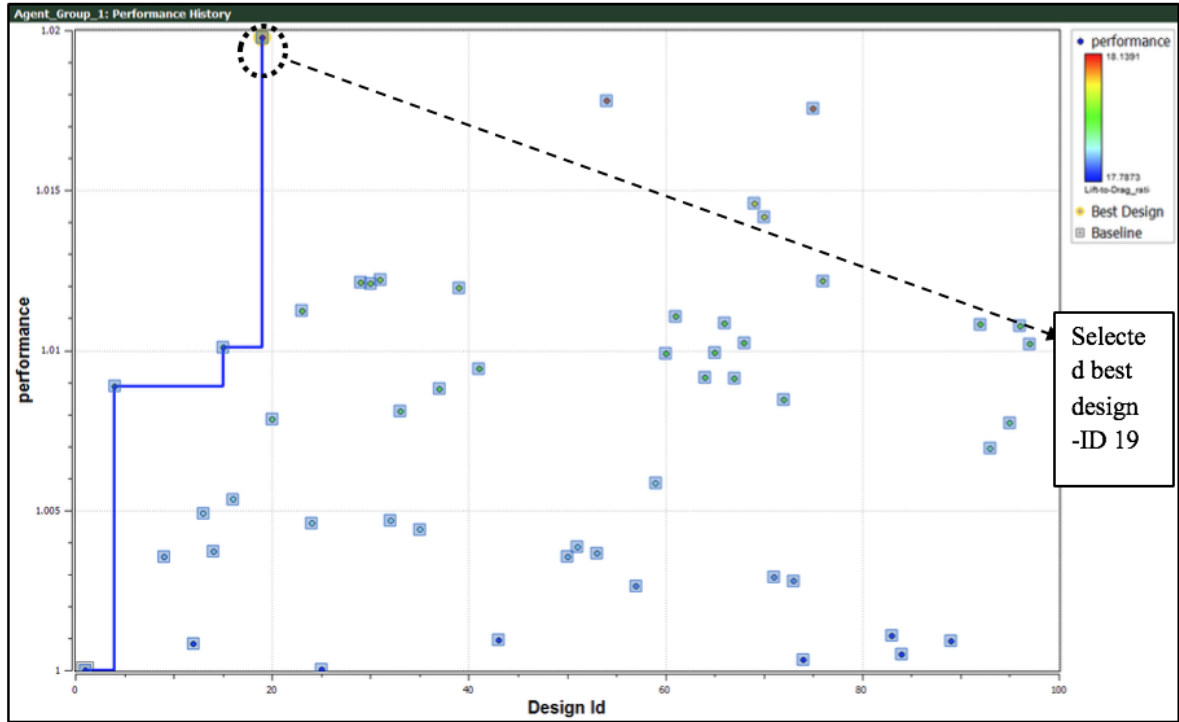
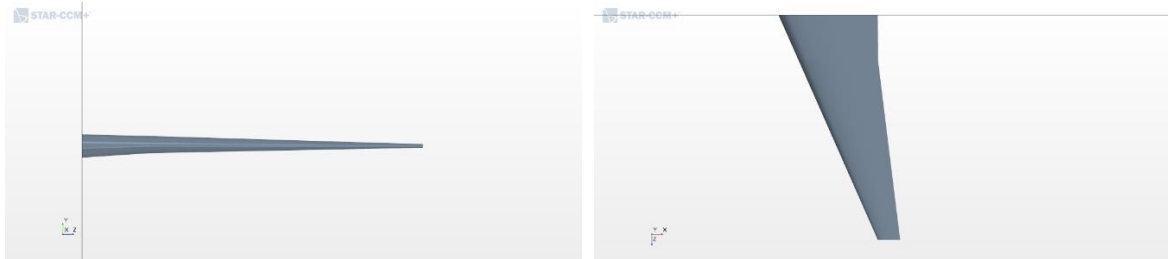
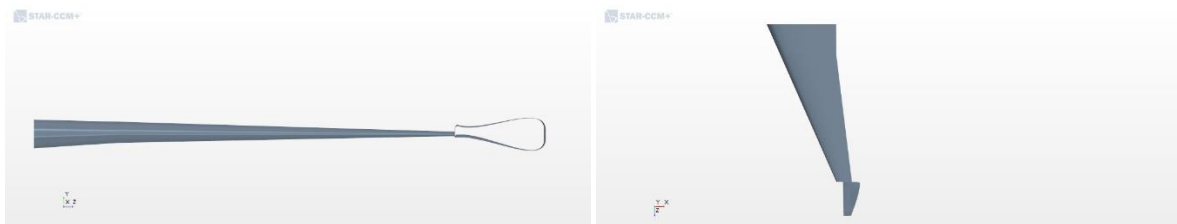


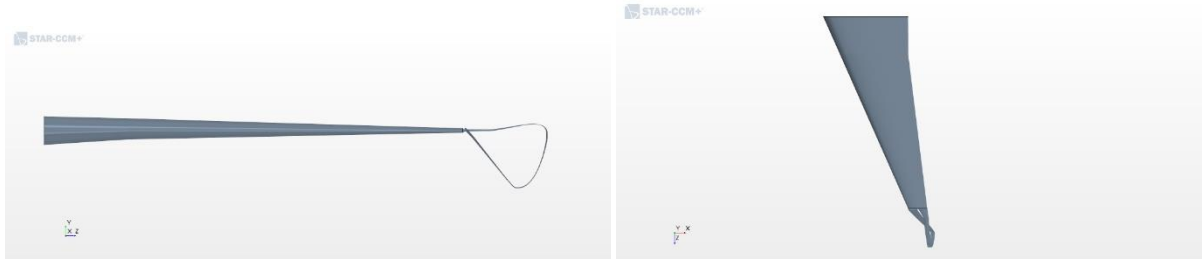
Fig. 104: Designs performance plot – Spiroid trapezium



(a.)



(b.)



(c.)

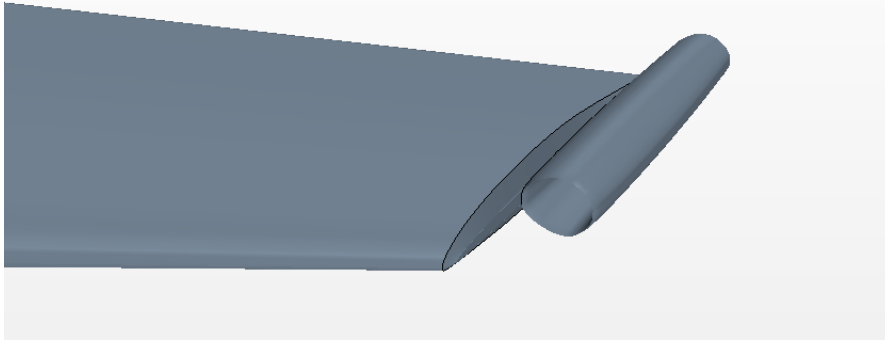


(d.)

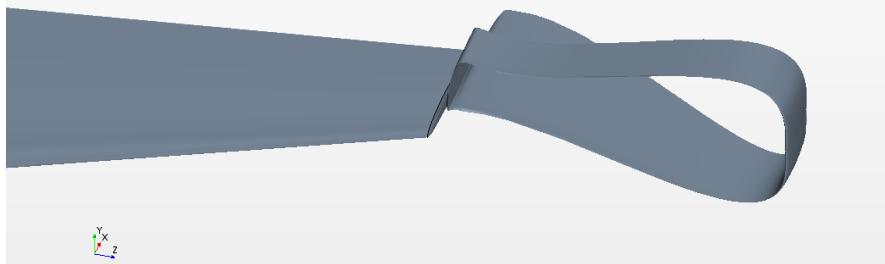


(e.)

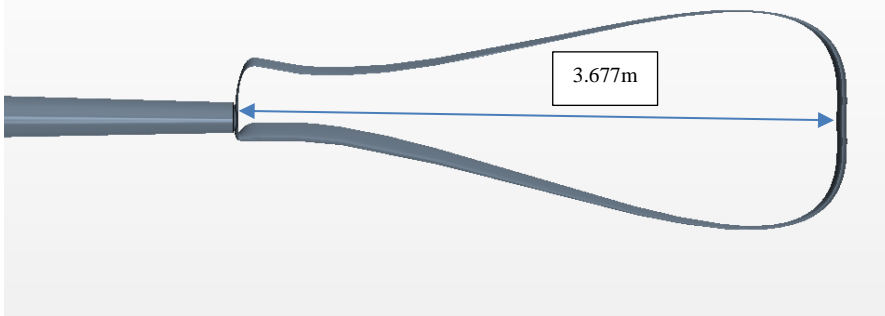
**Fig. 105: (a.) Clean wing, (b.) Design-1, (c.) Design-2, (d.) Design-3, (e.) Spiroid trapezium**



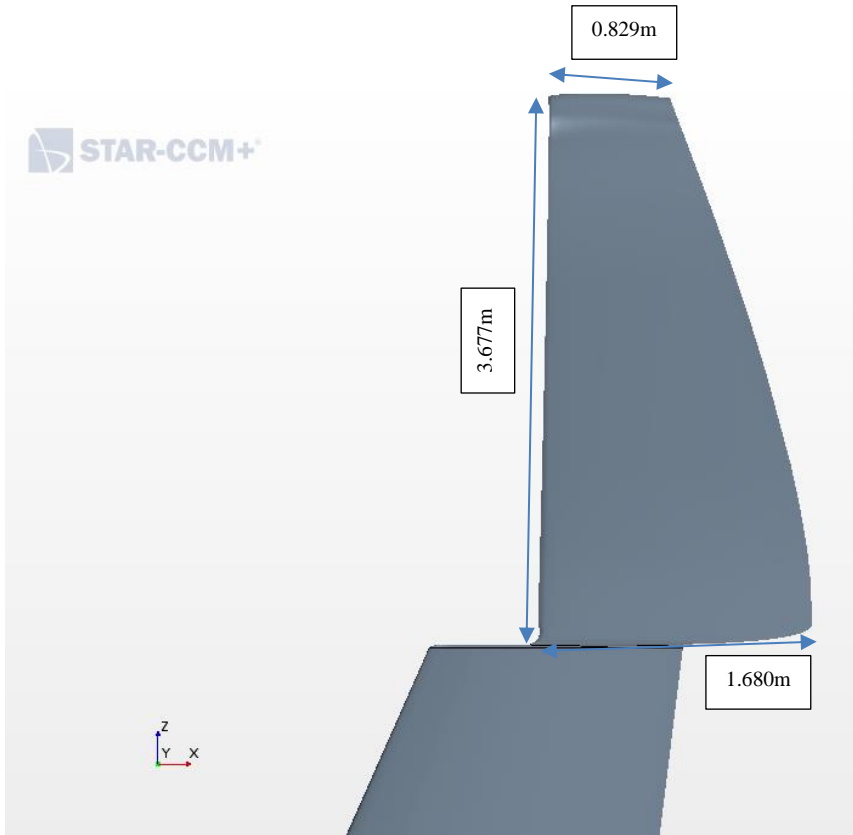
(a.) Design-1 – before optimisation



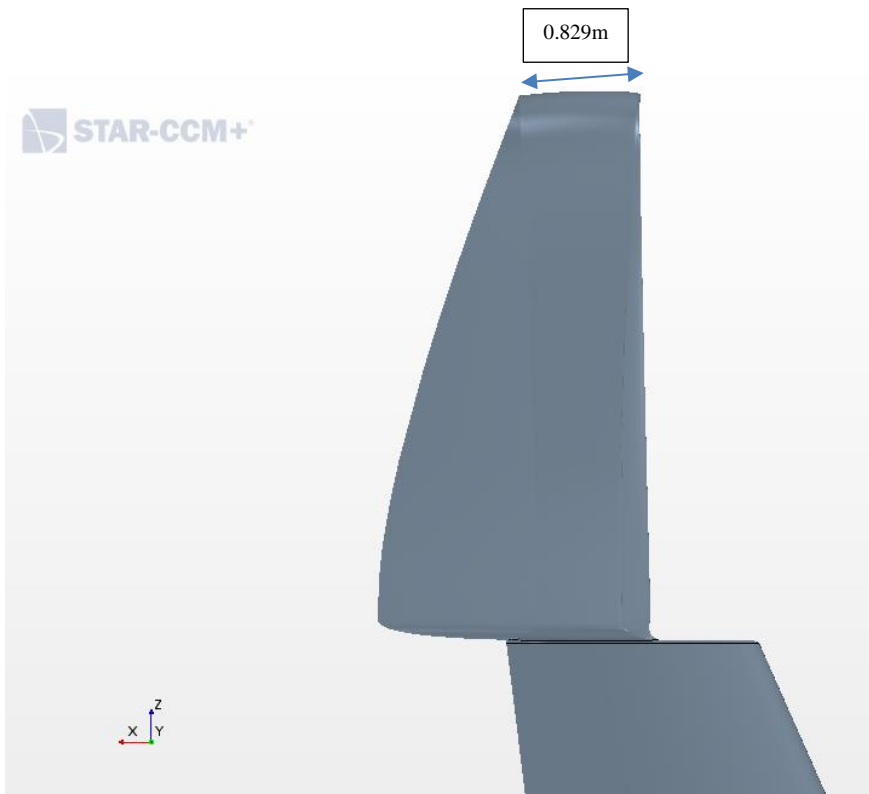
(b.) Design-1 – after optimisation



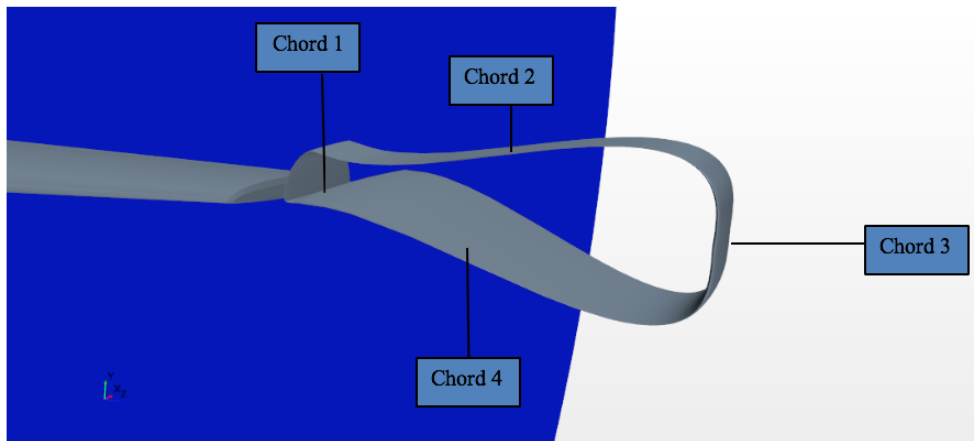
(c.) Design-1 with dimensions – front view



(d.) Design-1 dimensions – top view

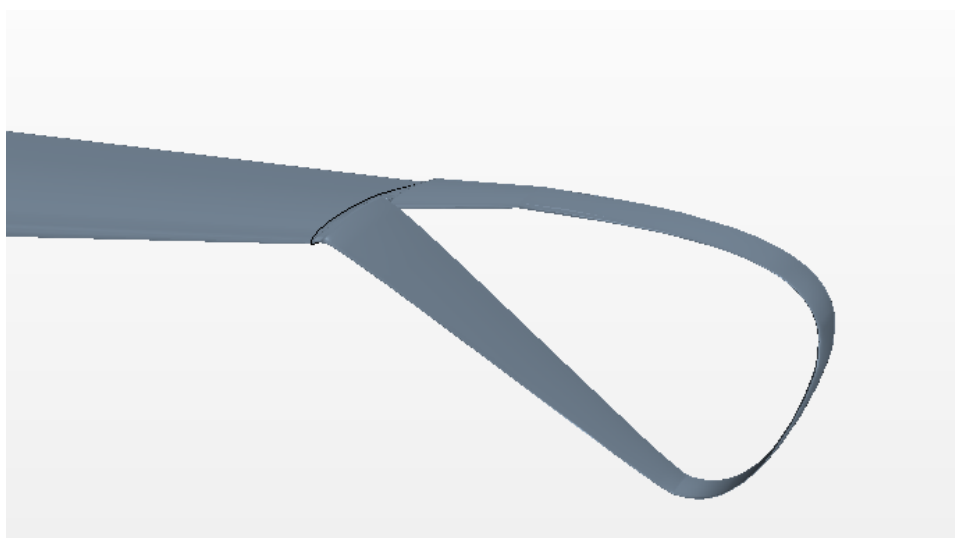


(e.) Design-1 dimensions – bottom view

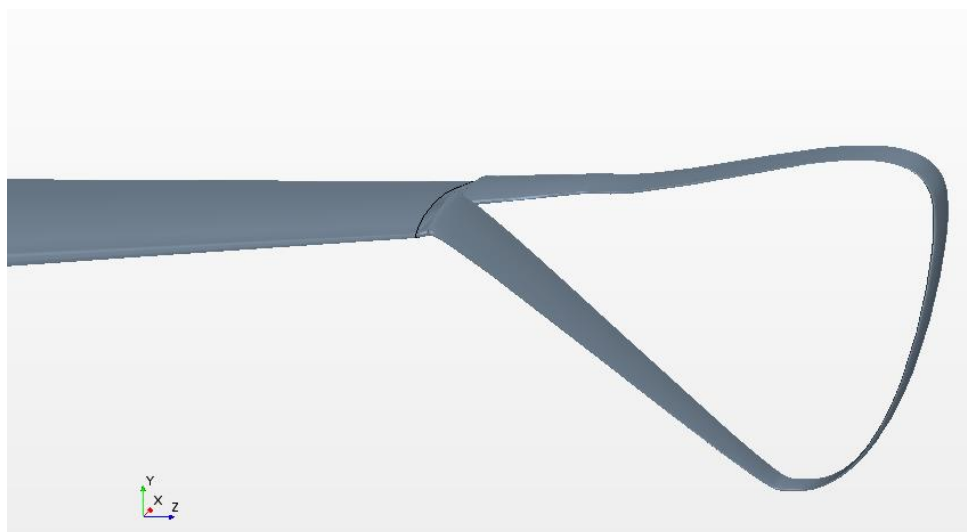


(f.) Close view with control points - Design-1

Fig. 106: Design-1 before and after optimisation as well as the design dimensions and control points



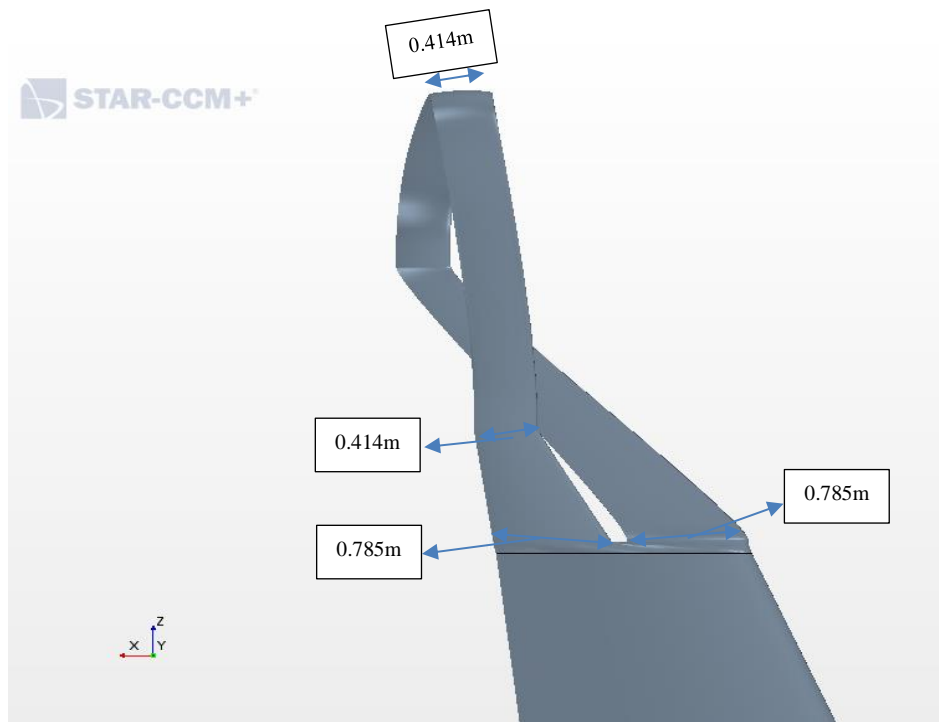
(a.) Design-2 – before optimisation



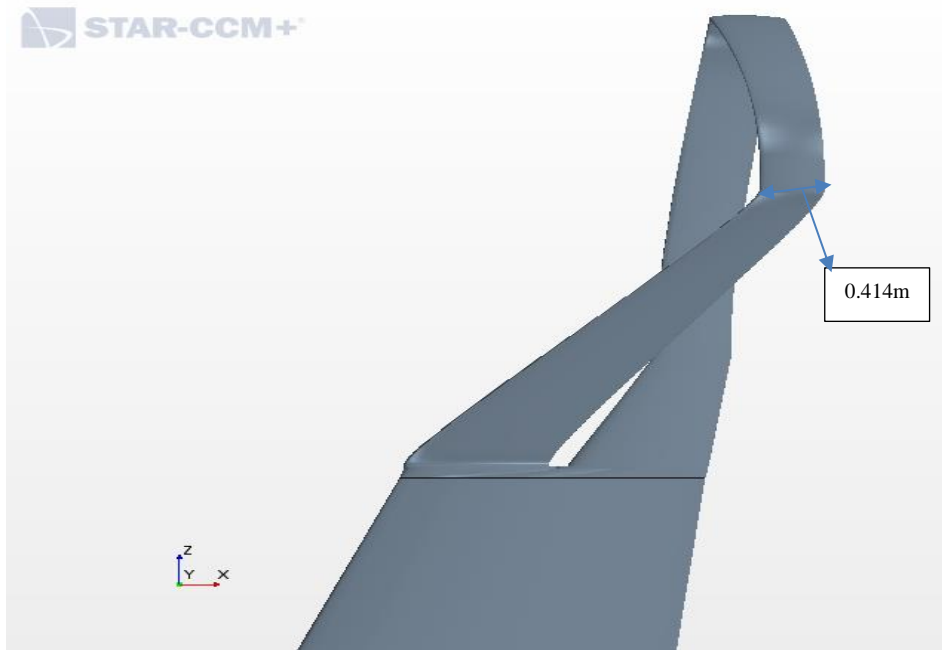
(b.) Design-2 – after optimisation



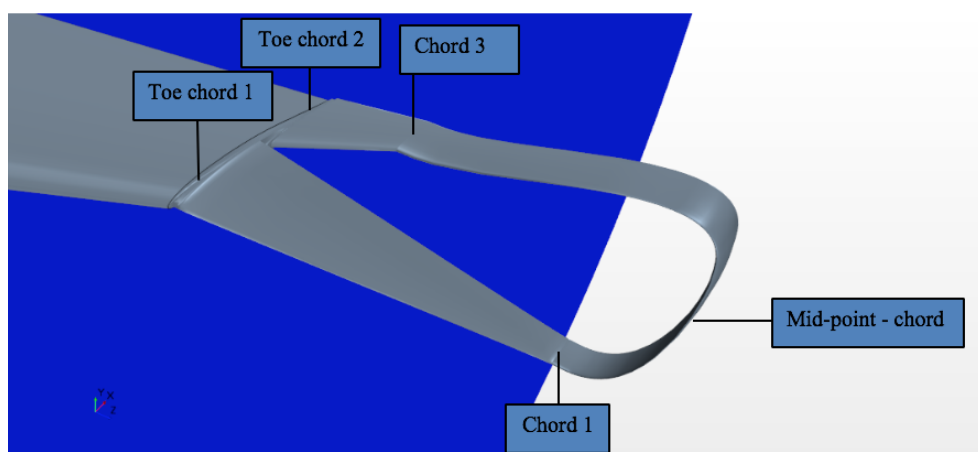
(c) Design-2 with dimensions – front view



(d.) Design-2 with dimensions – top view

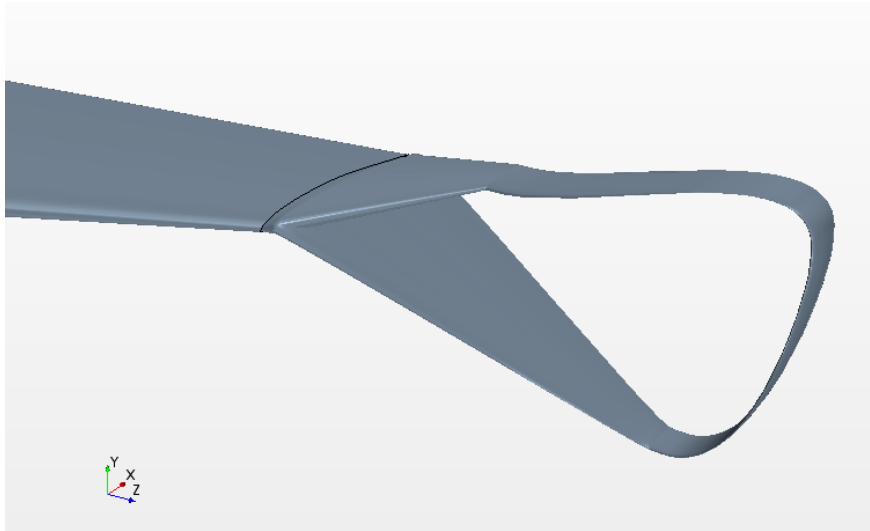


(e.) Design-2 with dimensions – bottom view

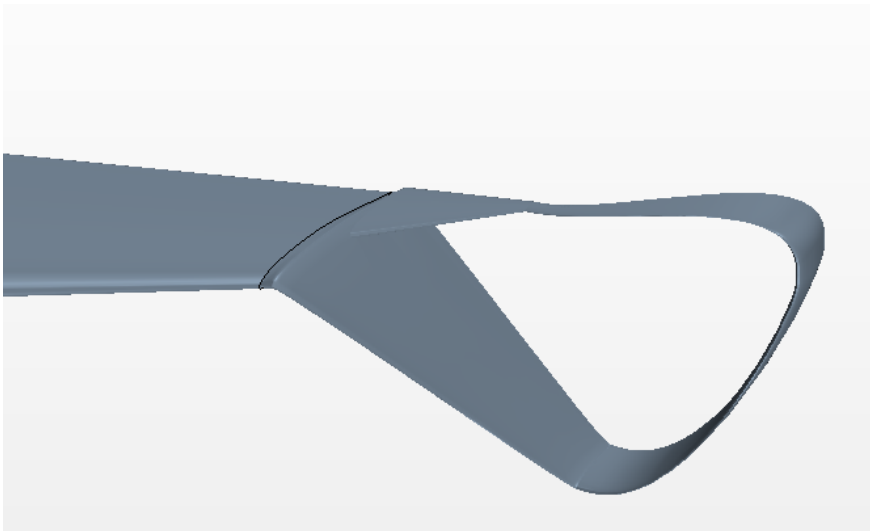


(f.) Close view with control points - Design-2

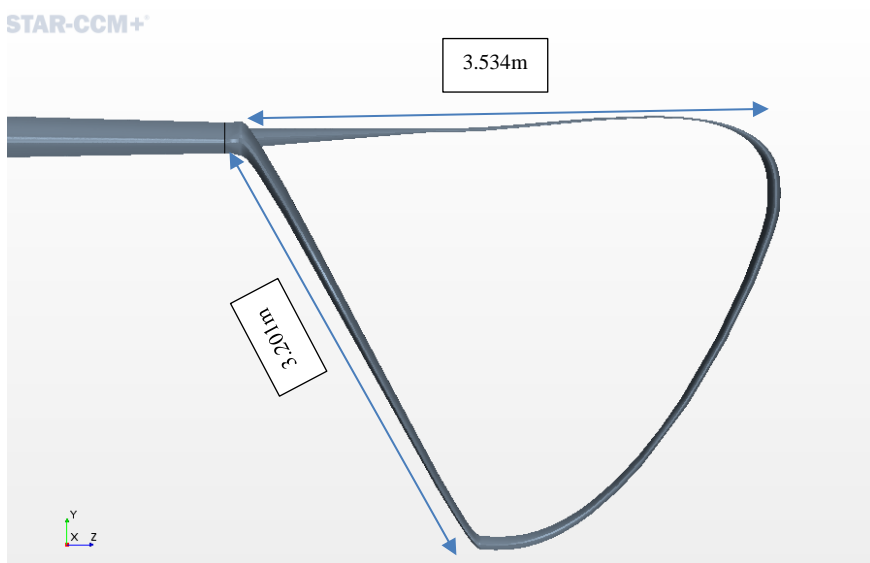
**Fig. 107: Design-2 before and after optimisation as well as the design dimensions and control points**



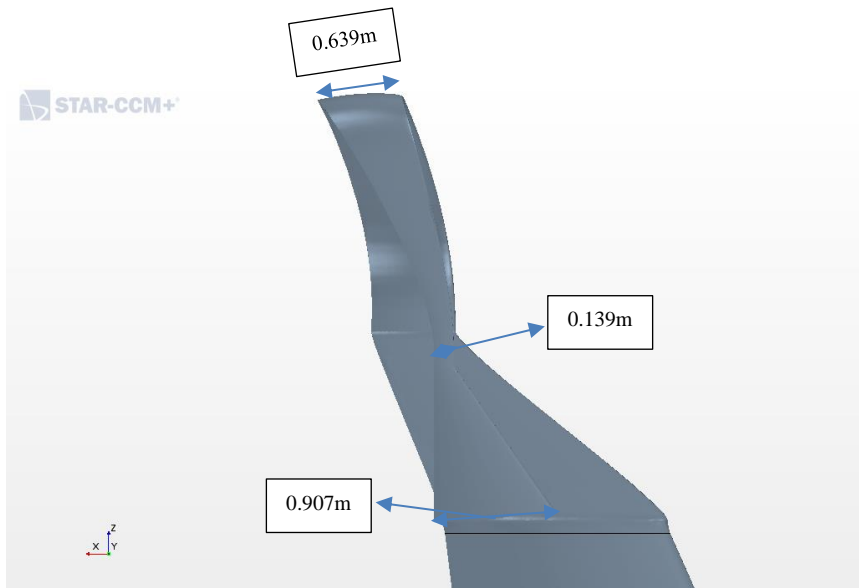
(a.) Design-3 – before optimisation



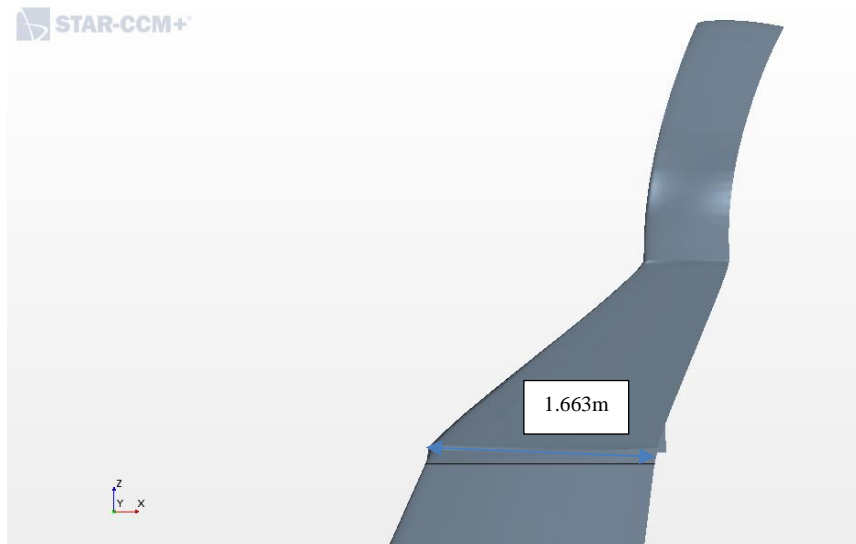
(b.) Design-3 – after optimisation



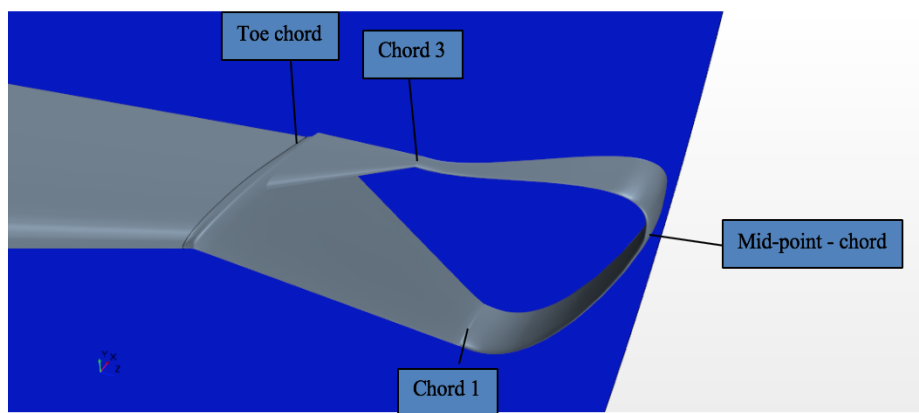
(c) Design-3 with dimensions – front view



(d.) Design-3 with dimensions – top view

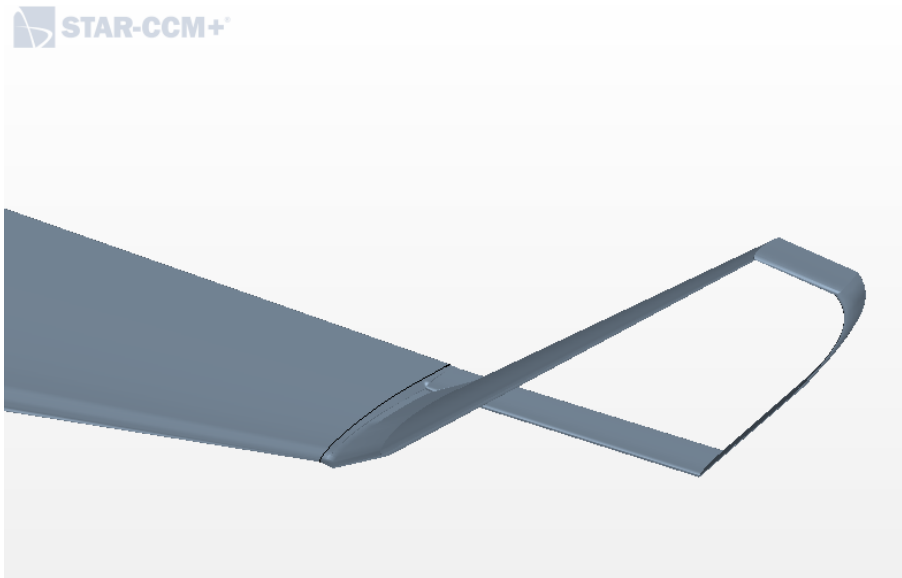


(e.) Design-3 with dimensions – bottom view

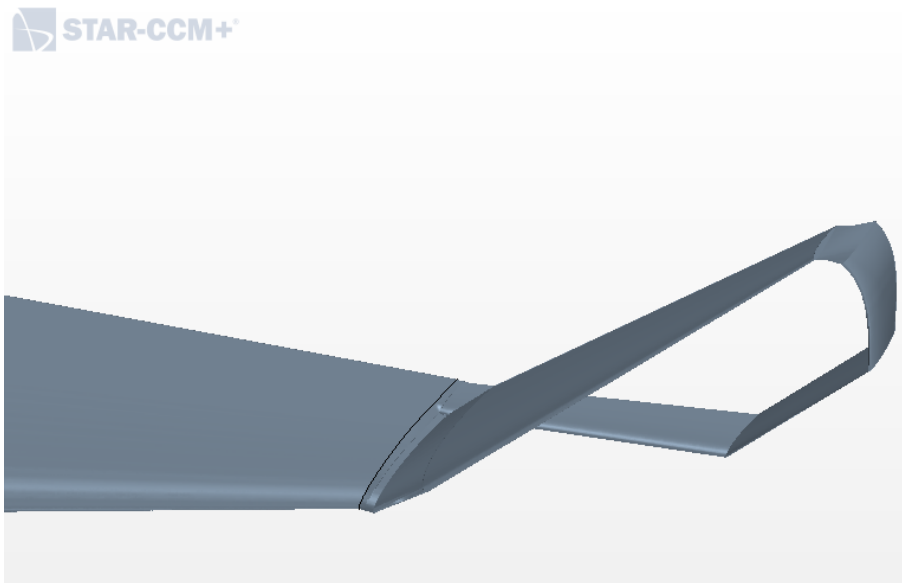


(f.) Close view with control points - Design-3

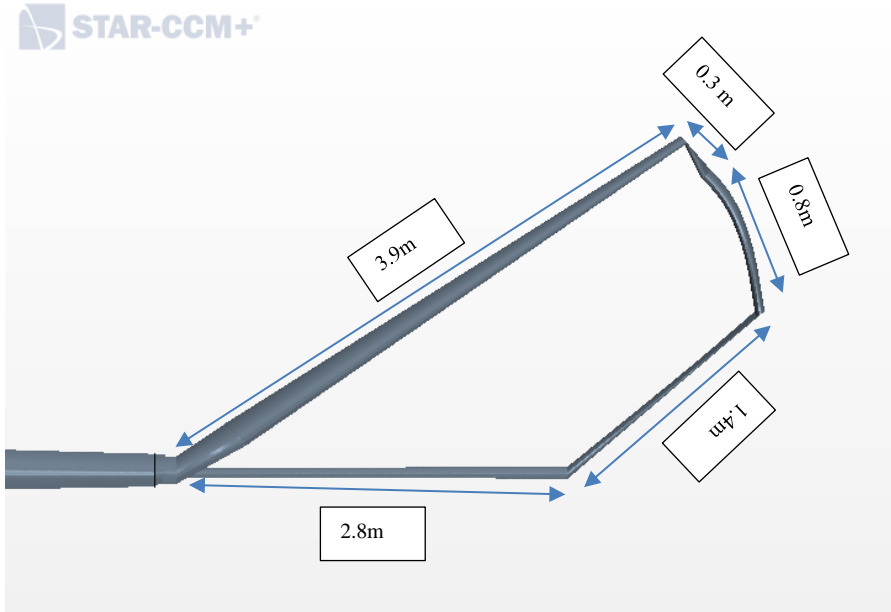
Fig. 108: Design-3 before and after optimisation as well as the design dimensions and control points



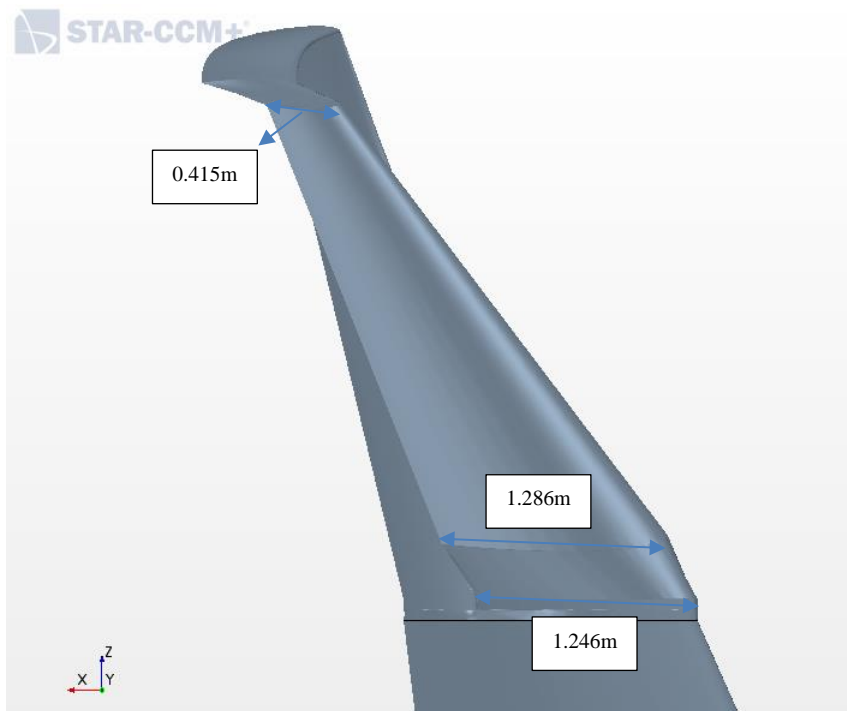
**(a.) spiroid trapezium – before optimisation**



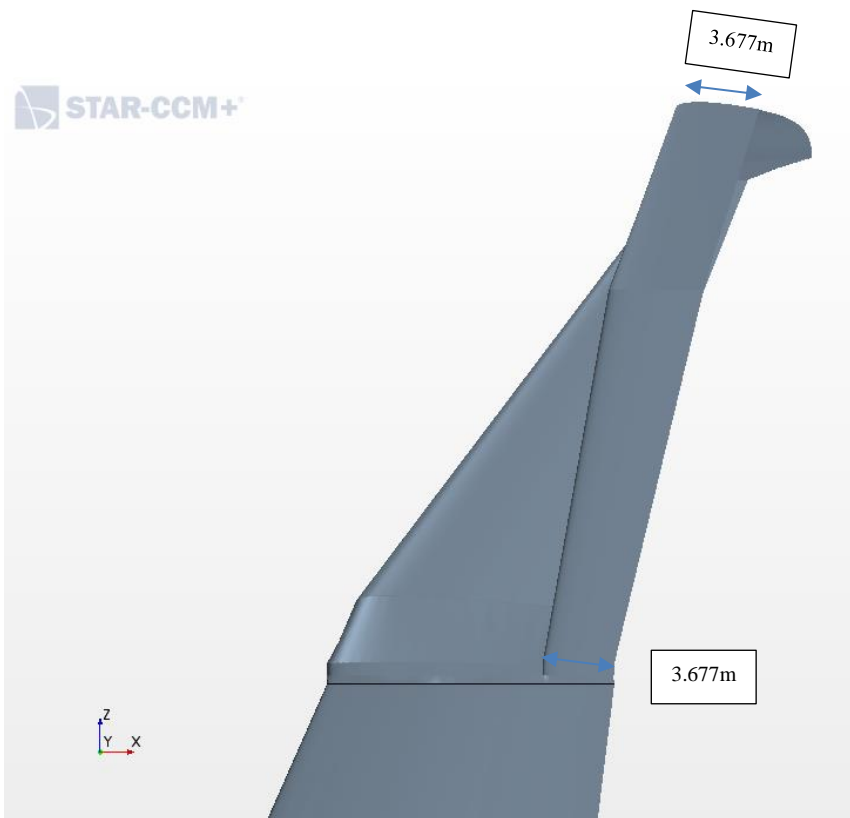
**(b.) spiroid trapezium – before optimisation**



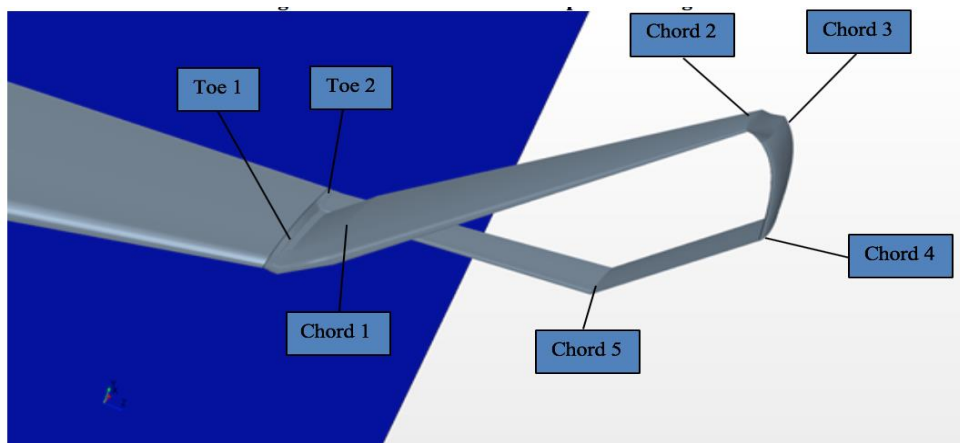
(c) Spiroid trapezium with dimensions – front view



(d.) Spiroid trapezium with dimensions – top view



(e.) Spiroid trapezium with dimensions – bottom view

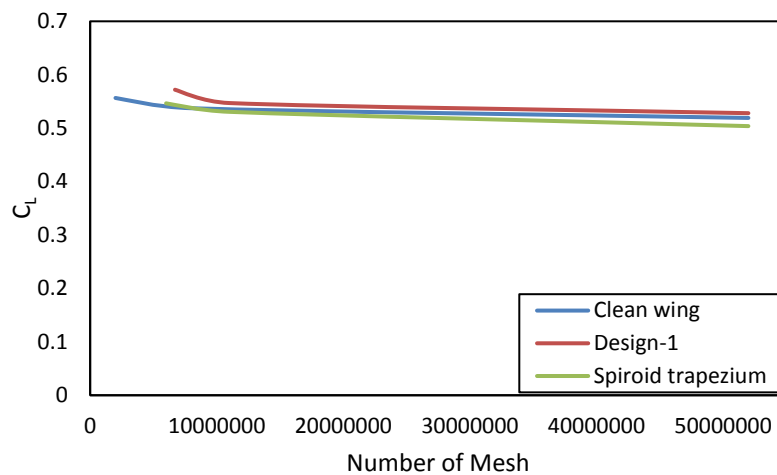


(f.) Close view with control points - spiroid trapezium

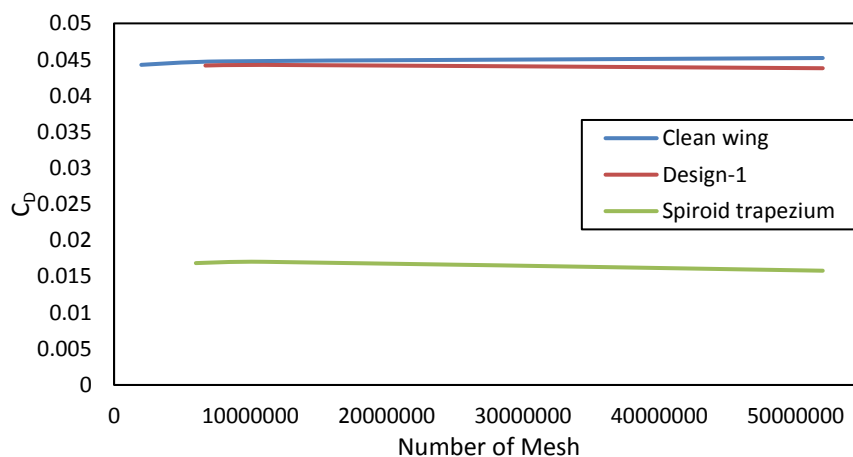
**Fig. 109: Spiroid trapezium before and after optimisation as well as the design dimensions and control points**

### 5.3.1.1. Mesh dependency study

The mesh dependency study was carried out and, the clean wing, Design-1 and Spiroid trapezium were used as the baseline for this study. It was assumed that these were sufficient to determine a mesh convergence for the various configurations since the wing was constant across all designs and also the mesh settings were the same. Three mesh counts were considered referred to as coarse, medium and fine mesh which corresponded to  $3 \times 10^6$ - $7 \times 10^6$ ,  $8 \times 10^6 - 11 \times 10^6$ , and  $50 \times 10^6 - 52 \times 10^6$  mesh counts respectively. The operating conditions used for this study is the same as those used for the device optimisation in section 5.3.1. The results for  $C_L$  and  $C_D$  are presented in Fig. 110 and Table 19, the force coefficient actually show convergence between 8 – 10 million mesh, in fact the medium mesh could be used for the remaining part of the study and the results will still be sufficiently accurate, but the fine mesh was used for all the results in this section of this thesis.



(a.)



(b.)

**Fig. 110: Mesh dependency study showing convergence - (a.) coefficient of lift and mesh count (b.) drag coefficient**

**Table 20: Coefficient of lift and drag mesh dependency study**

Parameters	Clean wing			Design-1			Spiroid trapezium		
	3 x10 <sup>6</sup>	8 x 10 <sup>6</sup>	50x10 <sup>6</sup>	6 x10 <sup>6</sup>	11 x 10 <sup>6</sup>	52x10 <sup>6</sup>	7 x10 <sup>6</sup>	11 x 10 <sup>6</sup>	52x10 <sup>6</sup>
C <sub>L</sub>	0.5565	0.5211	0.5191	0.5719	0.5221	0.5194	0.5464	0.5205	0.5038
C <sub>D</sub>	0.04426	0.04474	0.0438	0.04417	0.04426	0.0438	0.0160	0.0159	0.0158

### 5.3.2. Effect of winglet on wing aerodynamic coefficients – Mach 0.74 and 0.24 optimisation conditions

Table 21 and Table 22 show the characteristics of the aerodynamic coefficients for the optimised designs compared to the clean wing. In Table 21, the performance data for Designs 1 – 3 are presented, C<sub>L</sub>/C<sub>D</sub> ratio was improved by up to 3, 3 and 6 percent respectively. Also, C<sub>D</sub> was reduced by approximately up to 3 percent for Design-1, for Design 2 by 3 percent and 2 percent in Design-3. Coefficient of lift was also improved after optimisation, the new values showed a negligible increase for Design-1, while the other designs were increased by 0.5 percent for Design-2 and up to 3 percent for Design-3. Coefficient of induced drag was calculated using equation 47. The results obtained showed a reduction of 18 – 24 percent for all three designs with Design 1 at the upper end of this range. The reductions were predominately due to the aspect ratio and lift increase by using the wing tip devices on the clean wing as well as its impact on the wing tip vortices.

Also, in Table 21 is the coefficient of pitching moment (C<sub>M</sub>) which was taken about the ¼ mean aerodynamic chord (MAC), which for all the configurations was 4m. C<sub>M</sub> was taken about the same position on the wing for fair comparison. The results show that the configurations decrease this parameter by close to 40 percent compared with that of the clean wing.

Table 22 shows the performance data for the Spiroid trapezium device. The lift-to-drag ratio (C<sub>L</sub>/C<sub>D</sub>) was increased by 11 percent. C<sub>L</sub> was increased by 7 percent with a 4 percent decrease in C<sub>D</sub> and C<sub>D</sub><sub>Induced</sub> a reduction of 18 percent. The pitching moment coefficient (C<sub>M</sub>) was also presented with spiroid trapezium configuration achieving a reduction of up to 10 percent.

**Table 21: Aerodynamic coefficients for Designs 1 - 3**

Operating conditions – 32808ft, Mach 0.74, 4 degrees $\alpha$ , Mesh count – 50 - 52 million cells							
Aerodynamic coefficients	Clean wing	Design-1	% improvement, Design-1	Design-2	% improvement, Design-2	Design-3	% improvement, Design-3
$C_L/C_D$	11.4820	11.8404	3%	11.8639	3%	12.1150	6%
$C_L$	0.5191	0.5194	0.1%	0.5216	0.5%	0.5367	3%
$C_D$	0.0452	0.0438	3%	0.0439	3%	0.0443	2%
$C_{D_{induced}}$	0.0109	0.00837	24%	0.00838	23%	0.00895	18%
$C_M$	-0.4414	-0.2942	33%	-0.4291	3%	-0.3383	23%

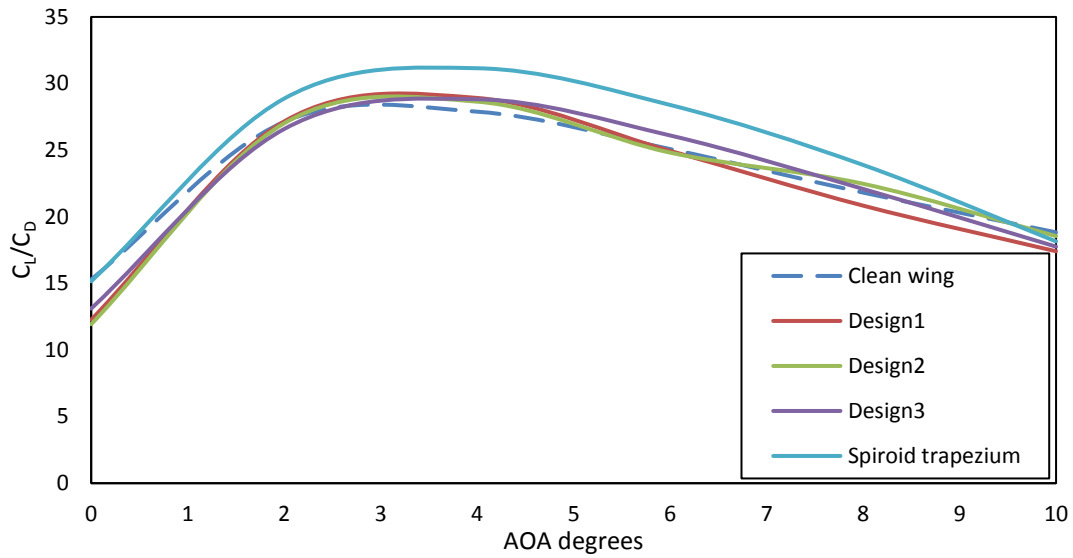
**Table 22: Aerodynamic coefficients Spiroid trapezium**

Operating conditions – sea level, Mach 0.24, 4 degrees $\alpha$ , Mesh count – 50 - 52 million cells			
Aerodynamic coefficients	Clean wing	Spiroid trapezium	% improvement Spiroid trapezium
$C_L/C_D$	28.8119	31.9935	11%
$C_L$	0.4766	0.5038	7%
$C_D$	0.0165	0.0158	4%
$C_{D_{induced}}$	0.00923	0.00764	18%
$C_M$	-0.3554	-0.1960	10%

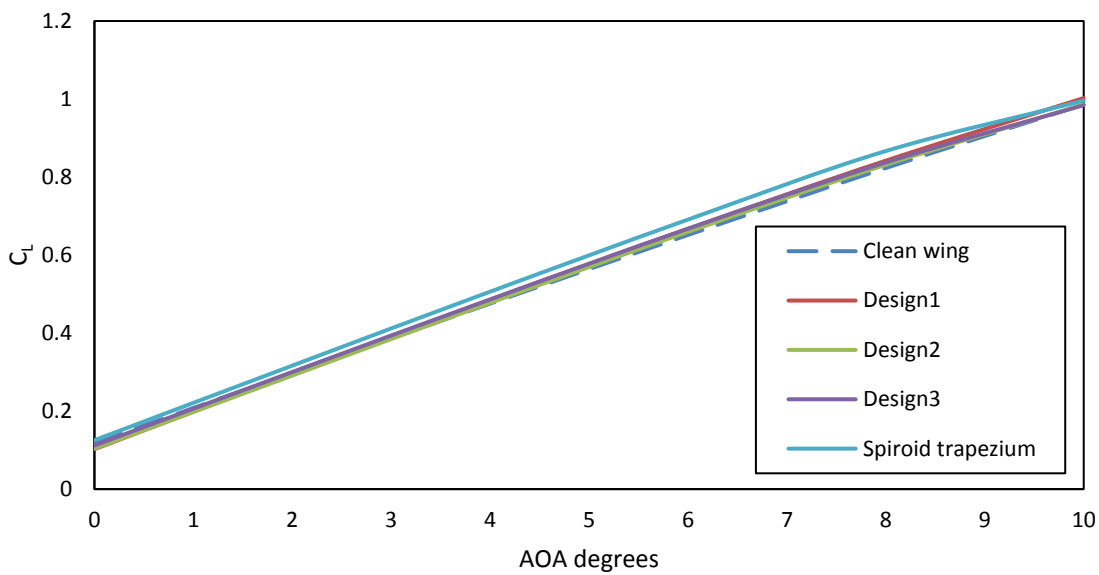
### 5.3.3. Effect of winglet on aerodynamic coefficients – Mach 0.24 (take-off condition)

Fig. 111 shows  $C_L/C_D$  ratio improvement logged at take-off operating conditions. The results showed that Designs 1- 3 were most effective for the cruise angle of attack selected for this study, which was  $4^\circ$  while the spiroid trapezium device was most effective at  $6^\circ$ . Designs 1- 3 were effective at angles of attack of  $2^\circ - 6^\circ$ . Beyond this point, Design-1 loses its effectiveness while Design-2 and Design-3 continues to be effective. On the contrary, the spiroid trapezium device was only effective at angles of attack between and including  $2^\circ - 8^\circ$ .

At  $4^\circ$ , the  $C_L/C_D$  ratio was increased by 4 – 3 and 11 percent for Designs' 1 - 3 and the spiroid trapezium respectively. Design-1 had the best lift-to-drag ratio at 4 degrees while Design-2 and Design-3 had a better performance at  $8^\circ$  and  $6^\circ$  with 3.0 percent and 4.0 percent increase respectively. The spiroid trapezium had its most impressive  $C_L/C_D$  ratio increase of 13 percent at  $6^\circ$ .



**Fig. 111:  $C_L/C_D$  ratio – take-off condition**



**Fig. 112: Lift coefficient – take-off condition**

Fig. 112 depicts the  $C_L$  of the winglets and the clean wing at several angles of attacks. Contrary to what was observed in Fig. 111,  $C_L$  was consistently improved for all AOA by the devices. At  $4^\circ$ , a noted increase of around 2 percent was observed for Design-1, while, an increase of about 0.3 percent was documented for Design-2, and an increase of 2 percent for Design-3 was obtained and up to 7 percent for the spiroid trapezium. Amongst the 4 configurations, the spiroid trapezium had the best  $C_L$  improvement with a value of around 7 percent suggesting

that this configuration is better suited for low speed flight conditions which in terms of other practical application could include but would not be limited to Unmanned Aerial Vehicles or Miniature planes.

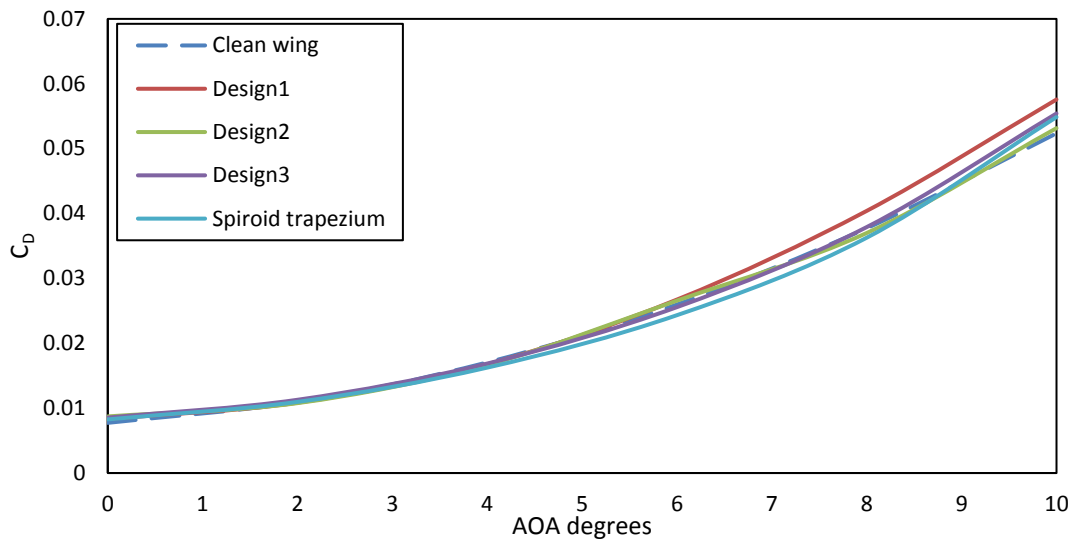


**Fig. 113: Drag coefficient – take-off condition**

$C_D$  as a function of the angle of attack is shown in Fig. 113 for all the devices. Designs 1 - 3 are shown to reduce the  $C_D$  consistently between  $2^\circ - 10^\circ$ . Design-1 achieved a  $C_D$  decrease of around 1 and 2 percent at  $4^\circ$  and  $6^\circ$ . On the other hand, Design-2 reduced the  $C_D$  by 2, 2 and 2 percent at  $4^\circ$ ,  $6^\circ$  and  $10^\circ$  angles of attack respectively. Furthermore, Design-3 had its most effective  $C_D$  at  $6^\circ$  and  $8^\circ$  for which the reductions were 1 and 2 percent. Again, as was the case in Fig. 112, the spiroid trapezium had the best  $C_D$  reduction with a value of up to 6.3 percent at  $6^\circ$  AOA and 4 percent at  $4^\circ$ .

The induced drag coefficient ( $C_{D_{induced}}$ ) is given in Fig. 114, the plot shows a consistent reduction of this parameter by all four devices which was as expected as they were designed for this purpose. The  $C_{D_{induced}}$  reduction percentage reduction observed for Design-1 was up to 43 percent, a similar value was recorded for Design-2 at 42 percent. Design-3 at best had a reduction of 32 percent and, the spiroid trapezium with a value of up to 26 percent at  $10^\circ$  AOA. Design – 1 had the largest aspect ratio with the second highest  $C_L$  curve and shared an e factor (Oswald efficiency factor) of 0.74 with the other devices, which is why it had the maximum induced drag reduction capability. These also demonstrates that  $C_{D_{induced}}$  is more dependent on the aspect ratio than  $C_L$  for a given wing configuration.

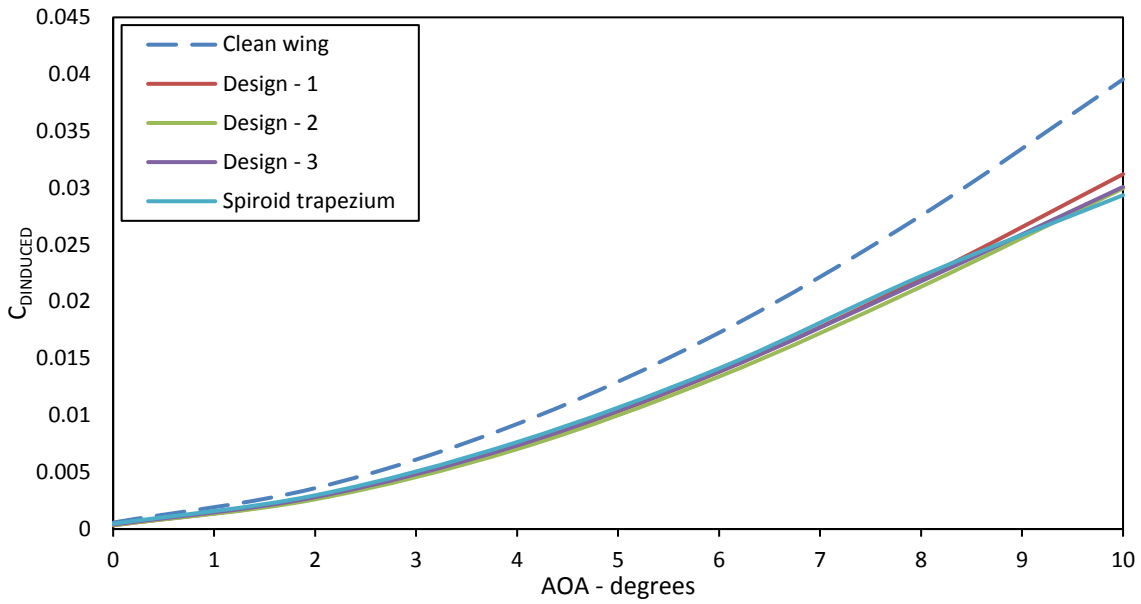


**Fig. 114:  $C_{DINDUCED}$  vs angle of attack – take-off condition**

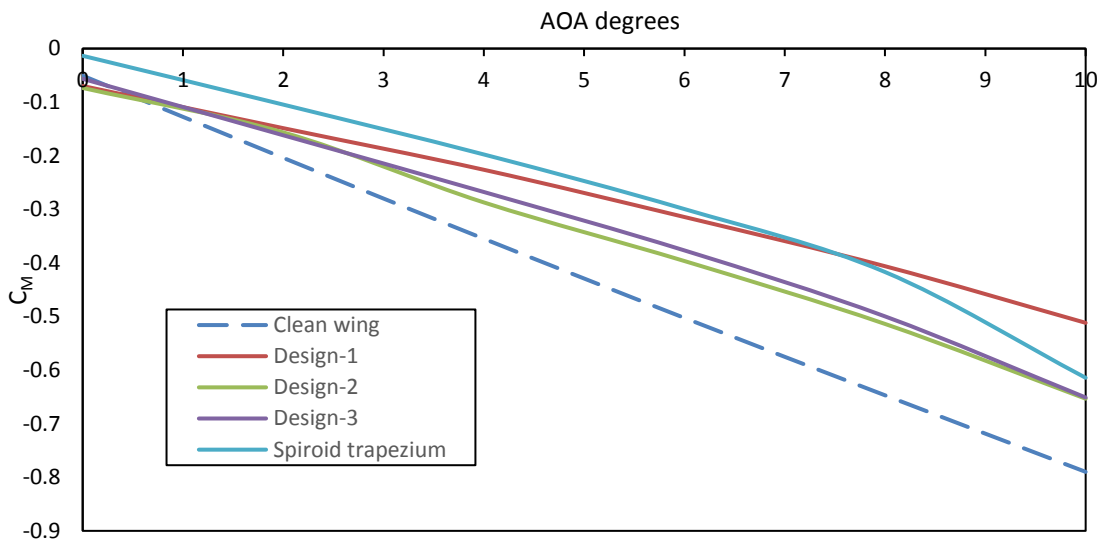


**Fig. 115: Coefficient of pitching moment ( $C_M$ ) vs angle of attack (AOA)**

The changes in the pitching moment coefficient as the angle of attack was increased is shown in Fig. 115. The results show longitudinal stability that is, it satisfies condition  $\frac{dC_M}{d\alpha} < 0$  for both clean wing and wing with wing tip devices. It also demonstrates that the wing with the wing tip devices attached would require less force to trim ( $\frac{dC_M}{d\alpha} = 0$ ) in flight state as evident with plots with the devices gravitating towards zero (trim state) as opposed to the one for the clean wing which has higher negative  $C_M$  values.

### 5.3.4. Effect of Mach number on winglet performance

The effect of Mach number on the characteristics of the devices are presented in this section of the report. As the Mach is a function of the air speed and the speed of sound, the effect of Reynolds number was also accounted for.

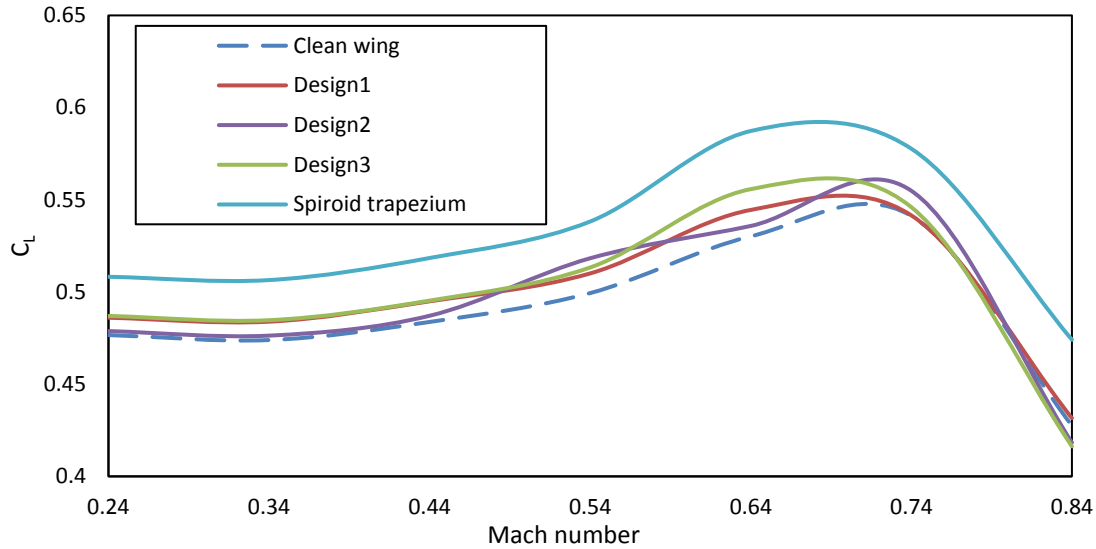
Fig. 116 shows the  $C_L$  as a function of Mach number with Table 23 showing the test conditions based on Reynolds number (Re), Mach No ( $M_\infty$ ) and air speed.

**Table 23 : Test conditions (Re, Mach No, air speed)**

Re	Mach Number	Air speed (m/s)
$2.1 * 10^7$	0.24	80
$3.1 * 10^7$	0.34	116.7
$4.0 * 10^7$	0.44	150
$4.9 * 10^7$	0.54	183.6
$5.8 * 10^7$	0.64	217.6
$6.7 * 10^7$	0.74	251.6
$7.6 * 10^7$	0.84	285.6

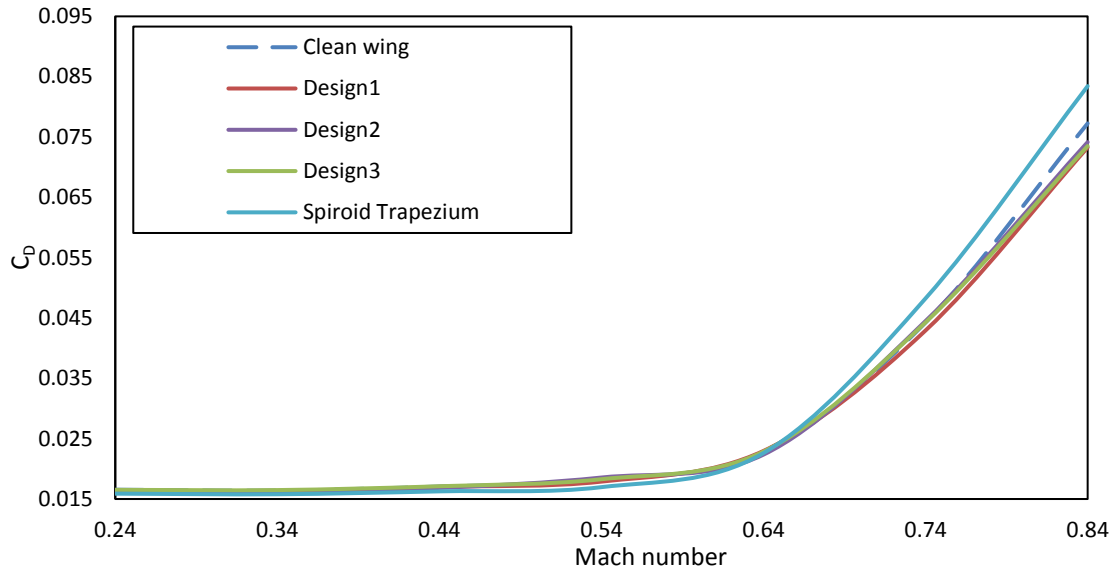
The  $C_L$  graph is shown in Fig. 116, the characteristic performance of each of the designs was consistent. The results follow a similar trend to the expected characteristics of a NACA aerofoil obtained from wind tunnel at NACA Langley Memorial Laboratory reported in books by (Anderson Jr, 2010), (Furlong and Fitzpatrick, 1947). In Fig. 116, at subsonic speeds the compressibility effect associated with increasing  $M_\infty$  resulted in increased  $C_L$ . A reason for this is to understand that the lift is mainly due to the pressure distribution on the wing and winglet surface. As the magnitude of  $M_\infty$  was increased, the pressure difference from one point on the top surface to another on the bottom wing surface becomes more evident. Therefore,  $C_L$  increases as  $M_\infty$  increases, this value of course could be calculated empirically but only for  $M_\infty$  away from 1 by using the Prandtl-Glauert rule (Anderson, 1999), (Raymer, 2005). The wing approached the transonic speed region at around  $M_\infty$  0.74 which is denoted by the galloping pattern in  $C_L$  curve as it approaches  $M_\infty$  1. This is typical of the transonic regime and its due to the shock wave boundary layer interaction, these characteristics are typical for transonic regime Mach numbers.

A close look at the benefits of the devices showed that Design-1 had a  $C_L$  increase of 2 percent at  $M_\infty$  0.24 to 3 percent at  $M_\infty$  0.64, Design - 2 had a maximum increase of 4 percent at Mach 0.54, Design-3 a maximum increase of 5 percent at Mach 0.64 and also the spiroid trapezium 10.7 percent at Mach 0.64. Amongst the designs, the spiroid trapezium had the better  $C_L$  improvement among the devices compared against the clean wing.



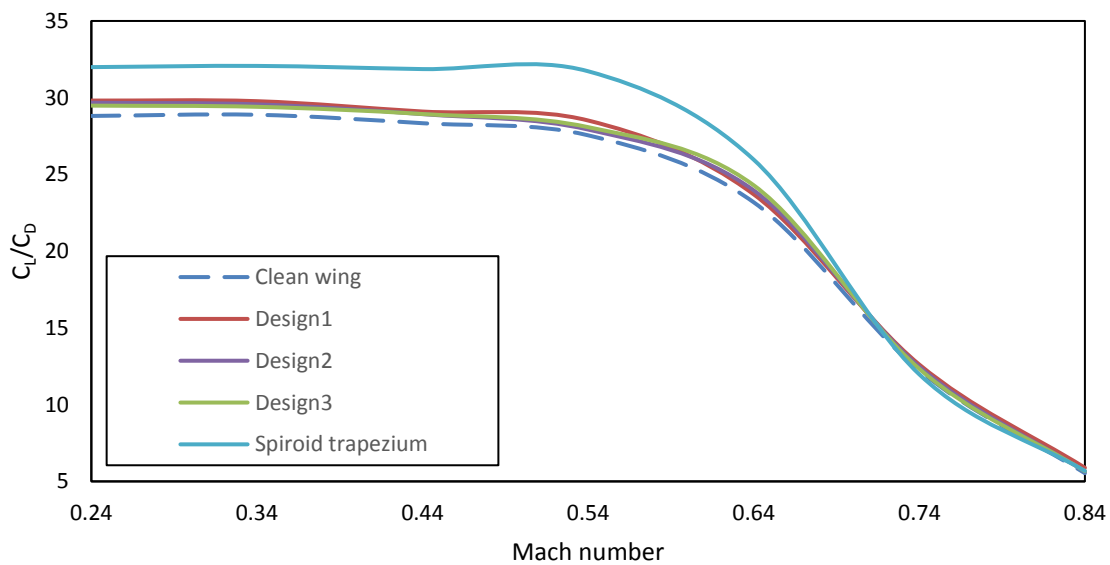
**Fig. 116: Lift coefficient as a function of Mach number**

The  $M_\infty$  effect on  $C_D$  is presented in Fig. 117, here contrary to what was observed in Fig. 116. The  $C_D$  is relatively constant until on and around the critical  $M_\infty$ , which is the free stream  $M_\infty$  where sonic flow is first experienced on the wing surface confirmed by the CFD results. It could be argued that the flow experienced in the subsonic regime is mostly dominated by skin friction and that the compressibility effect is negligible. The skin friction drags decreases as the  $M_\infty$  increases. The flow around this regime is attached and streamlined as evident in Fig. 117 for  $M_\infty$  0.24 to  $M_\infty$  0.64. Typically, as  $M_\infty$  increases beyond the critical  $M_\infty$ , large pockets of locally supersonic flows form above the wing surface, these supersonic flows are removed downstream by shock waves. The presence of the shock waves causes an increase in pressure drag which is intricately caused by the shockwave interacting with the flow boundary layers, thus causing the flow to separate from the wing surface. Hence, increasing the pressure drag, this explains what is seen in Fig. 117 in the range  $M_\infty$  0.64 – 0.84. The clean wing and the downward pointing devices appear to better cope with these transonic conditions in comparison with the Spiroid Trapezium configuration. A close analysis of the plot showed the configurations with the devices achieved consistent reduction of  $C_D$  with  $M_\infty$  with the least observed  $C_D$  for the spiroid trapezium at 6 percent reduction at  $M_\infty$  0.54 and Designs 1 – 3 with 5 percent at  $M_\infty$  = 0.84.



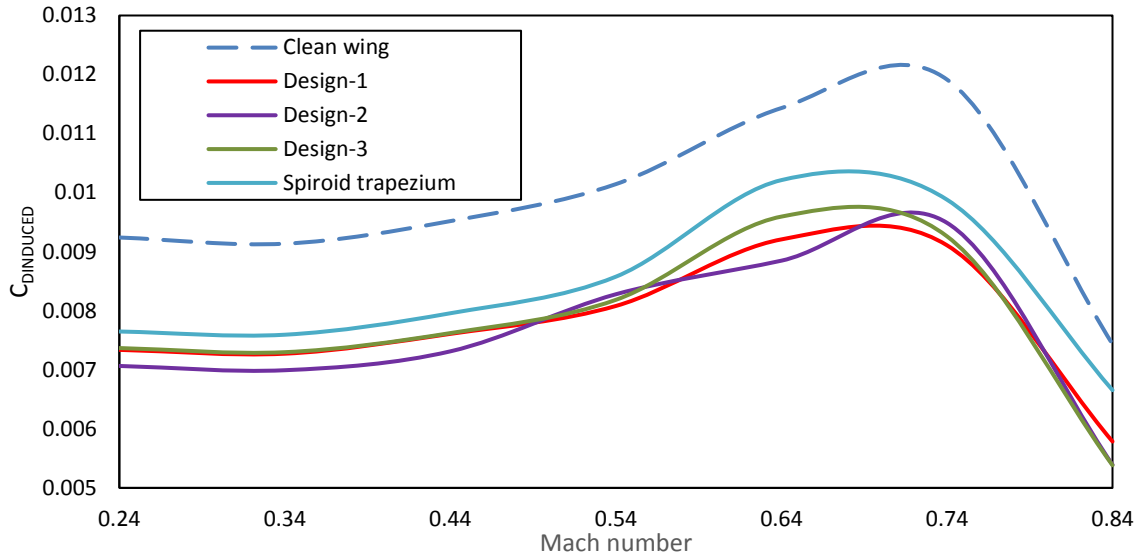
**Fig. 117: Drag coefficient as a function of Mach number**

Fig. 118 presents the  $C_L/C_D$  of the devices which shows the aerodynamic efficiency as a function of variable Mach number. The devices had different  $M_\infty$  at which they were most suited. For example, Design-1 was most effective at Mach 0.84 with a lift-to-drag ratio increase of 6.4 percent. Design-2 was most effective at Mach 0.64 with a  $C_L/C_D$  of 3 percent together with Design-3 at  $M_\infty$  0.64 with a value of 6 percent. The spiroid trapezium showed the biggest increase of up to 15 percent increase in  $C_L/C_D$  at  $M_\infty$  0.54. The spiroid trapezium under performed at  $M_\infty$  numbers above 0.64. At this Mach number all its benefits were lost, thus, suggesting that the device is not suited for high sub-sonic flight regimes. The overall consistency of the devices in improving  $C_L / C_D$  indicates that they are well suited for subsonic cruise conditions over a wide range of  $M_\infty$ .



**Fig. 118:  $C_L/C_D$  ratio as a function of Mach number**

In Fig. 119 Induced drag coefficient as a function of the Mach number is shown. Through using winglets, the induced drag is reduced substantially by between 11 - 28 percent as shown by the performance of the devices on the plot. The induced drag reduction is also consistent across the  $M_\infty$ .



**Fig. 119:  $C_{DINDUCED}$  as a function of Mach number**

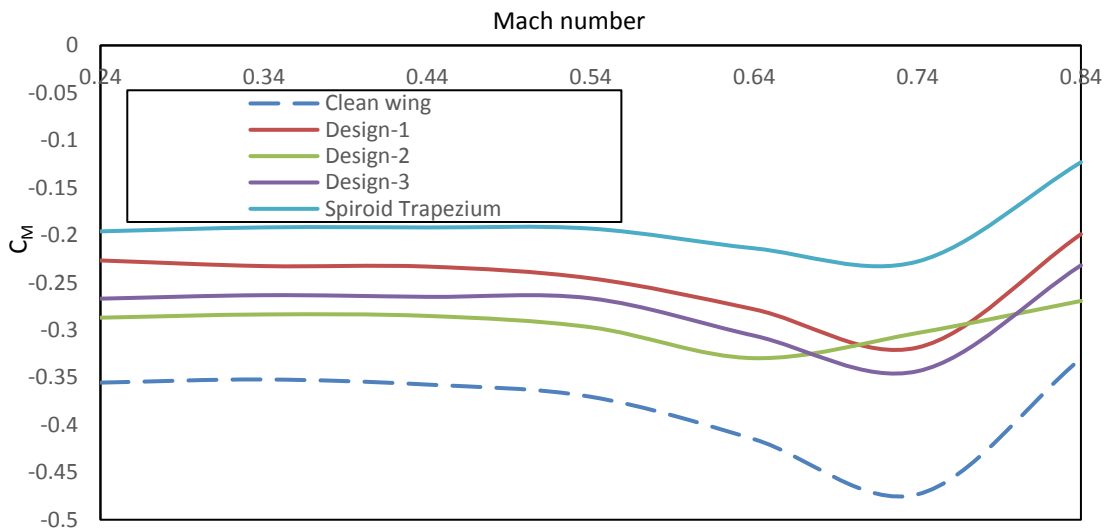


**Fig. 120:  $C_M$  as a function of Mach number**

Fig. 120 shows the effect of Mach number on  $C_M$ , the plot shows the configurations to be longitudinally stable.

i.e.  $\frac{dC_M}{d\alpha} < 0$  or  $\frac{dC_M}{dC_L} < 0$  when Fig. 120 is directly compared with Fig.116. The configurations with the devices

are shown to require less effort to achieve trim ( $\frac{dC_M}{d\alpha} = 0$ ).

The high fidelity CFD modelling and analysis of the optimised winglets has now been discussed in this section of the report. The next section of this chapter is focused on the sensitivity analysis of the winglet design variables.

### 5.3.5. Lift per unit span

Lift per unit span examines the lift distribution in the span-wise direction of the wing, which affects proportionally other wing performance factors such as rate of climb, velocity for the rate of climb, the flight velocity for  $(C_L/C_D)_{\max}$ , flight velocity for maximum  $(C_L^{3/2}/C_D)$ , stall speed as well as the induced drag. In fact, it can be argued that the induced drag does not explicitly depend on the aspect ratio but rather, on the lift per unit span (Anderson, 1999). A plot graph showing this parameter can also be used to distinguish the difference in lift distribution between the clean wing configuration and that with the wing tip devices. Fig. 121 shows plots of the lift per unit span for the studied designs. The plot was based on data obtained for the optimisation condition (i.e. Mach 0.74). A close examination of the plot illustrates that by using the wing tip devices, the lift distribution is modified across the entire wing and not just at the wing tip region. As expected, the in-board region of the wing generates the most lift, with the wing with winglet showing additional lifting regions due to added reference area. Fig. 122 shows similar characteristics as in the afore mentioned for a comparison of the clean wing and the spiroid trapezium device.

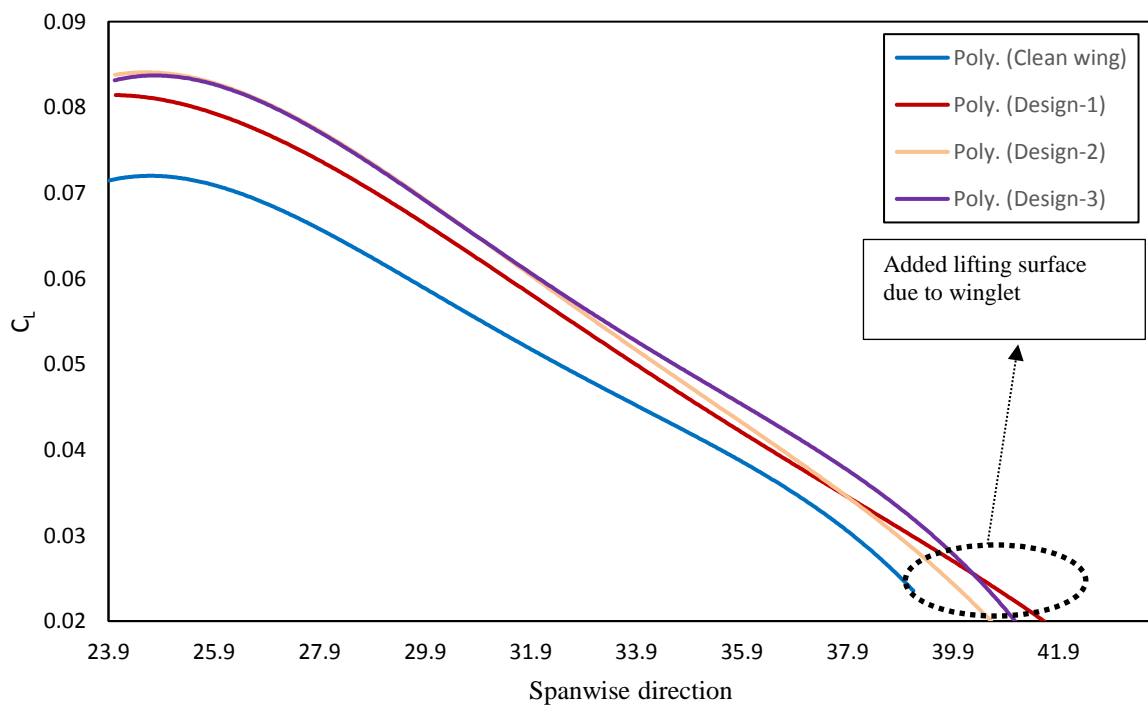


**Fig. 121: Lift per unit span - (Mach 0.74)**

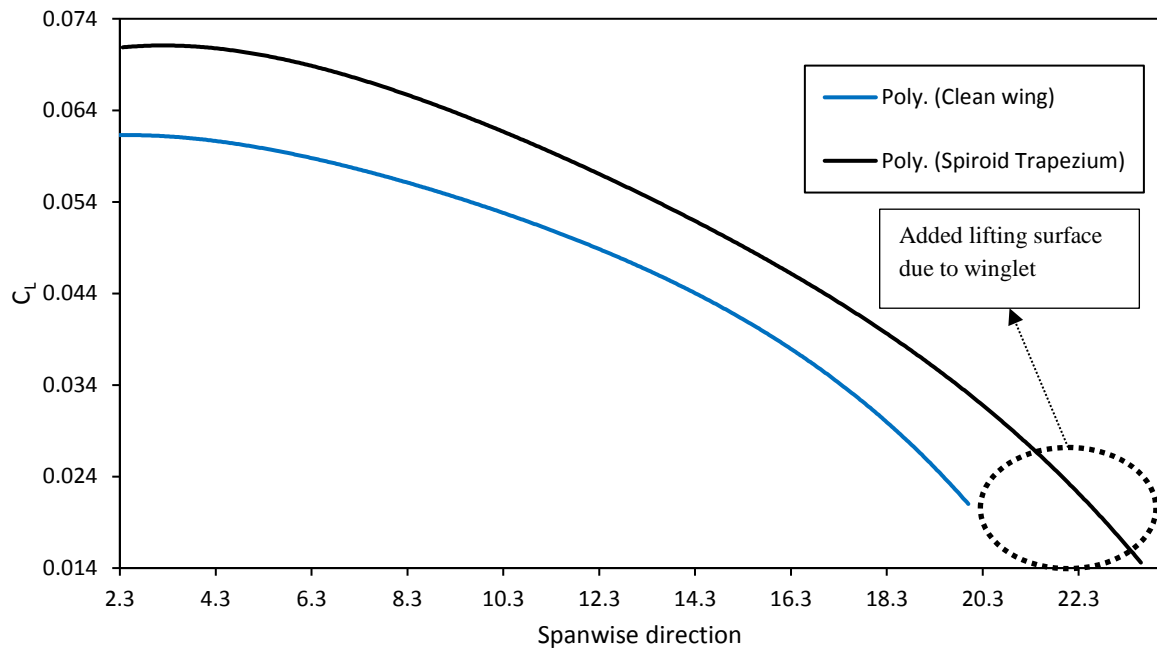


**Fig. 122: lift per unit span - clean wing and spiroid trapezium (Mach 0.24)**

### 5.3.6. Flow visualisation

The flow patterns around the wing tip region are presented in this section of the thesis. The flow characteristics are depicted by using the vorticity scalar contours and 3D volume rendering technique which has been discussed in section 4.2.4.4. First, consider the three designs, i.e. Designs 1 – 3 at Mach 0.74 which is then followed by the spiroid trapezium design (Mach 0.24). The strength of the vortices pattern is inversely proportional to the distribution or scattering of the vortices. That is, the wider the vortices spread out the less strong it becomes. Fig. 123 – Fig. 126 and Fig. 131 – Fig. 132 give the vorticity scalar contour plots showing a 2D representation of the flow at the rear of the wing on a cut plane section and on the wing.

Fig. 127 – Fig. 130 and Fig. 133 – Fig. 134 show a 3D representation of the flow around the wing tip region by using the volume rendering technique. The first colour bar in each figure is the vorticity experienced on the cut plane section and the other the vorticity on the wing. These showed that the strength of the vorticity was reduced by using the wing tip devices, this is evident with the vortices spreading out.

The pressure on the wing and wing tip devices are illustrated in Fig. 135 – Fig. 140. The pressure pattern on the wing and wing with the mounted devices are of broadly similar pattern. The observed difference is in the added pressure region created by the addition of the wing tip devices which causes the increase in lift that can be seen

in the lift coefficient improvement observed in section 5.3.1. Also, it was observed that the region with lower pressure corresponded with the higher vorticity regions observed on the vorticity contour plots. Furthermore, the pressure patterns observed on the wing is identical to that seen on the wing-tip devices. The wing tips therefore acting almost as an extension of the wing with favourable pressure gradients at the same time reducing the effect of the wing tip vortices.

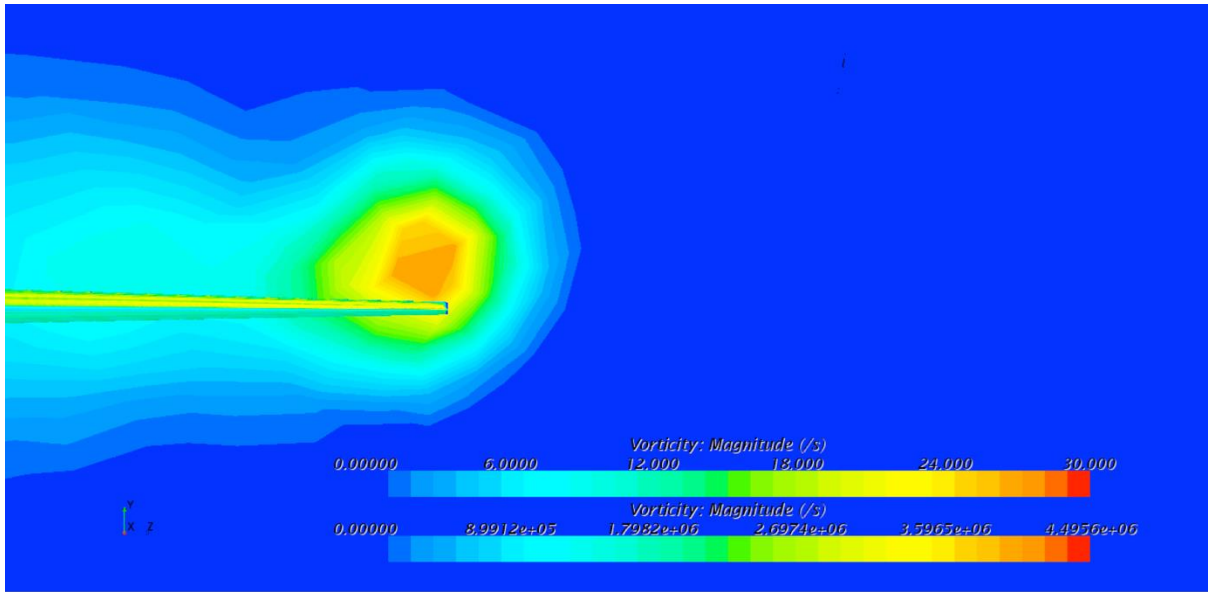


**Fig. 123 – Clean wing vorticity scalar contour**

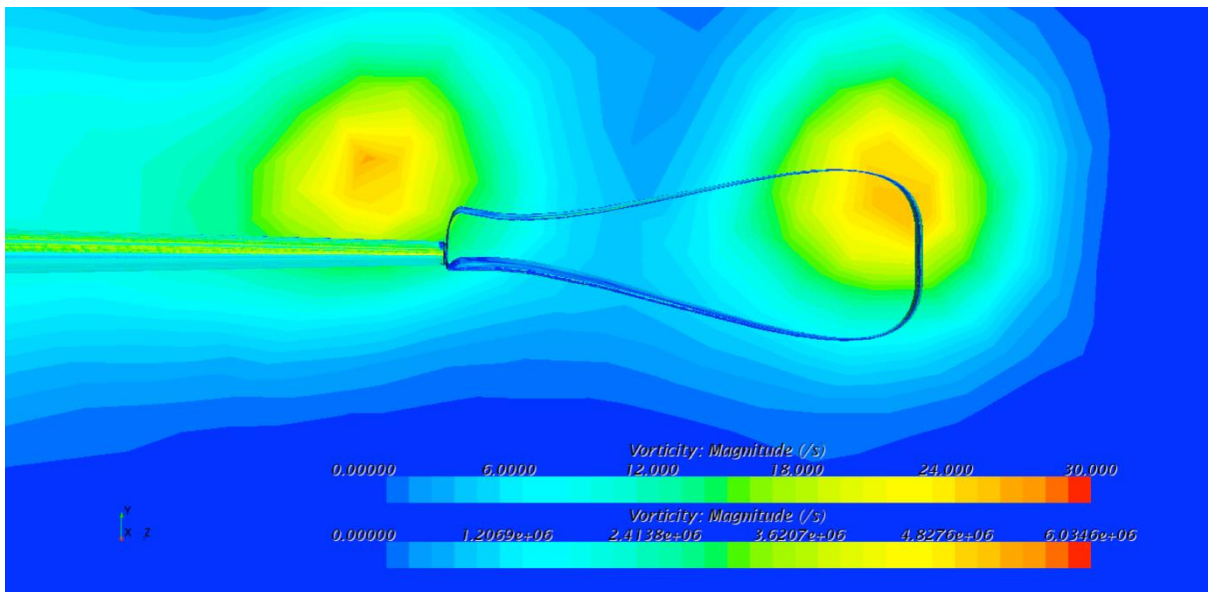


**Fig. 124 – Design – 1 vorticity scalar contour**

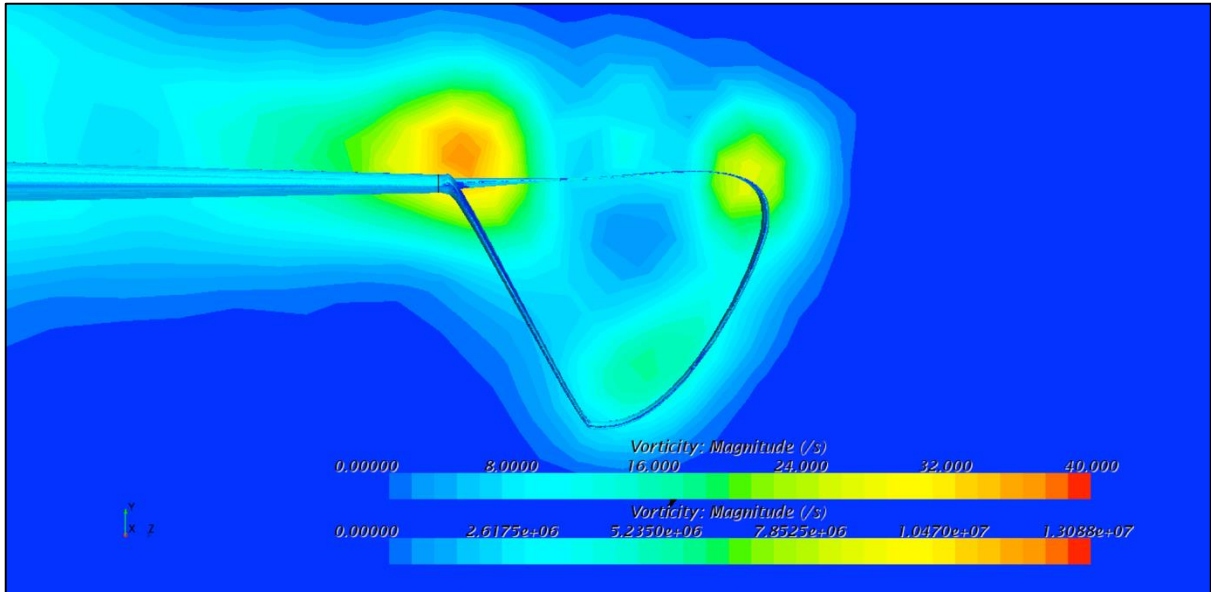


**Fig. 125 – Design – 2 vorticity scalar contour**

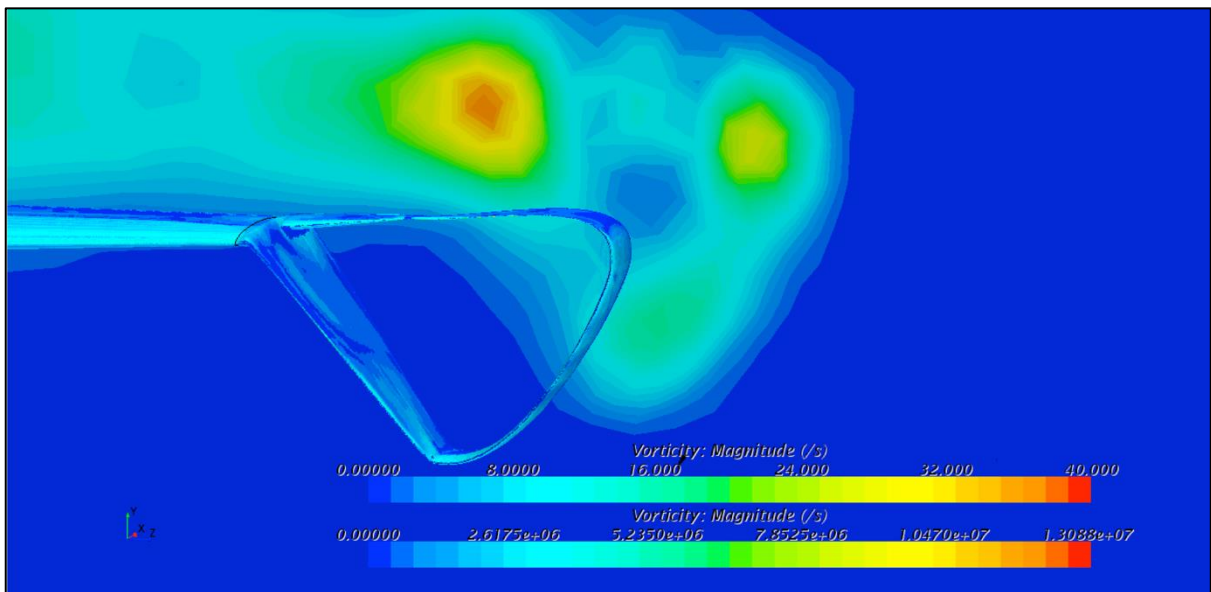


**Fig. 126 – Design – 3 vorticity scalar contour**

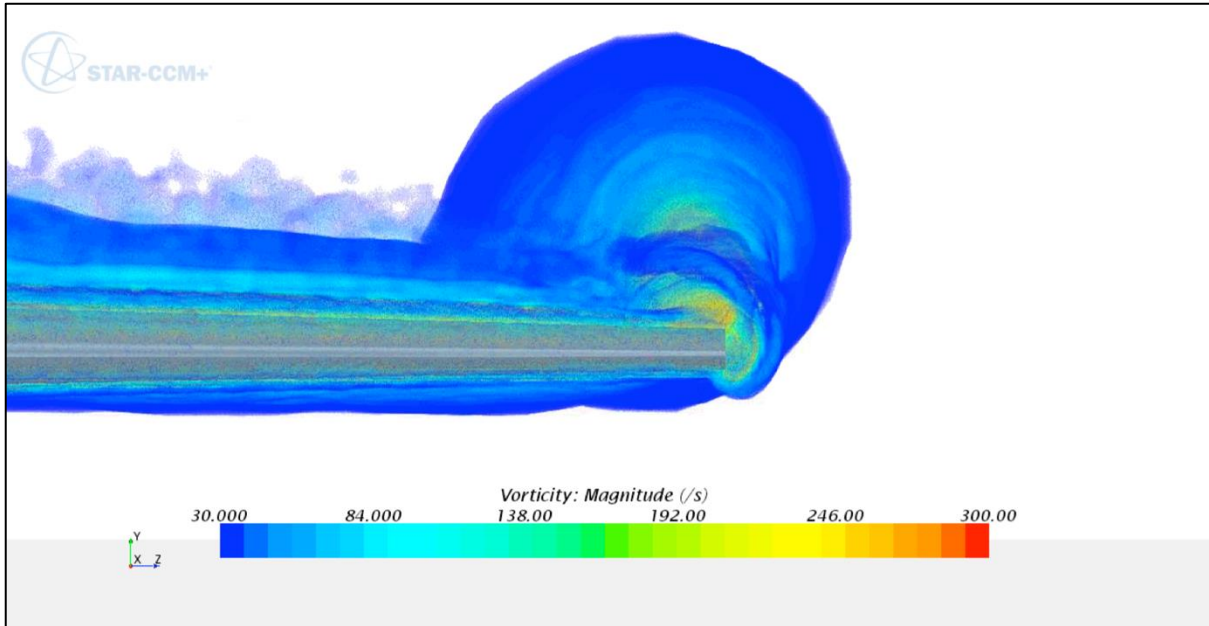


**Fig. 127: Clean wing vorticity volume rendering**

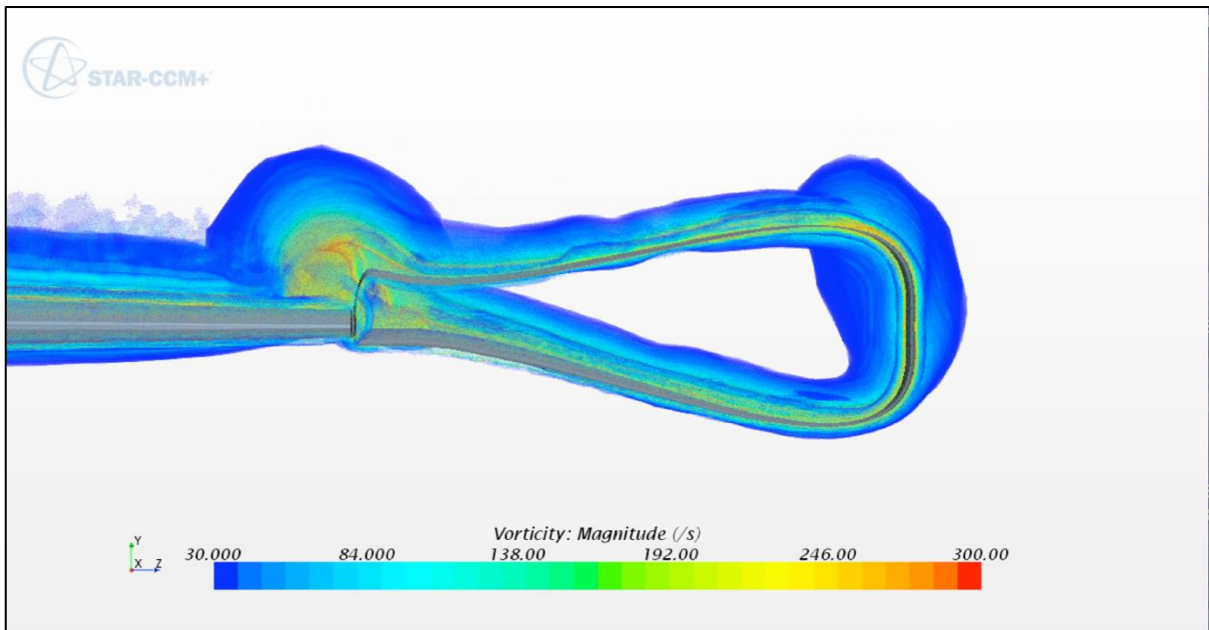


**Fig. 128: Design - 1 vorticity volume rendering**

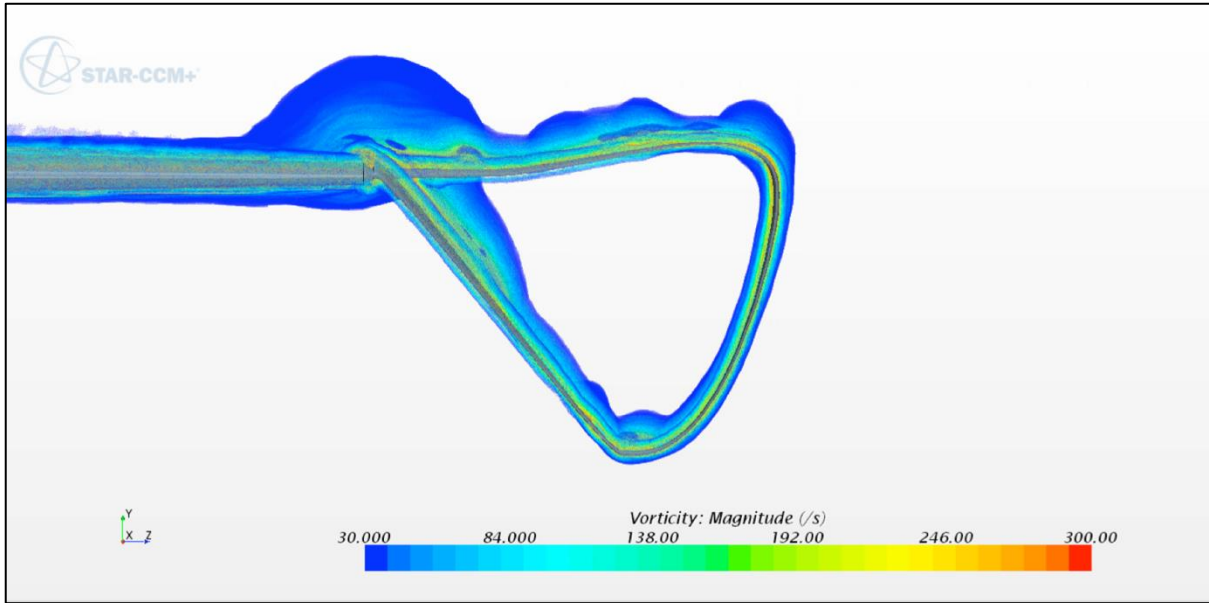


**Fig. 129: Design – 2 vorticity volume rendering**

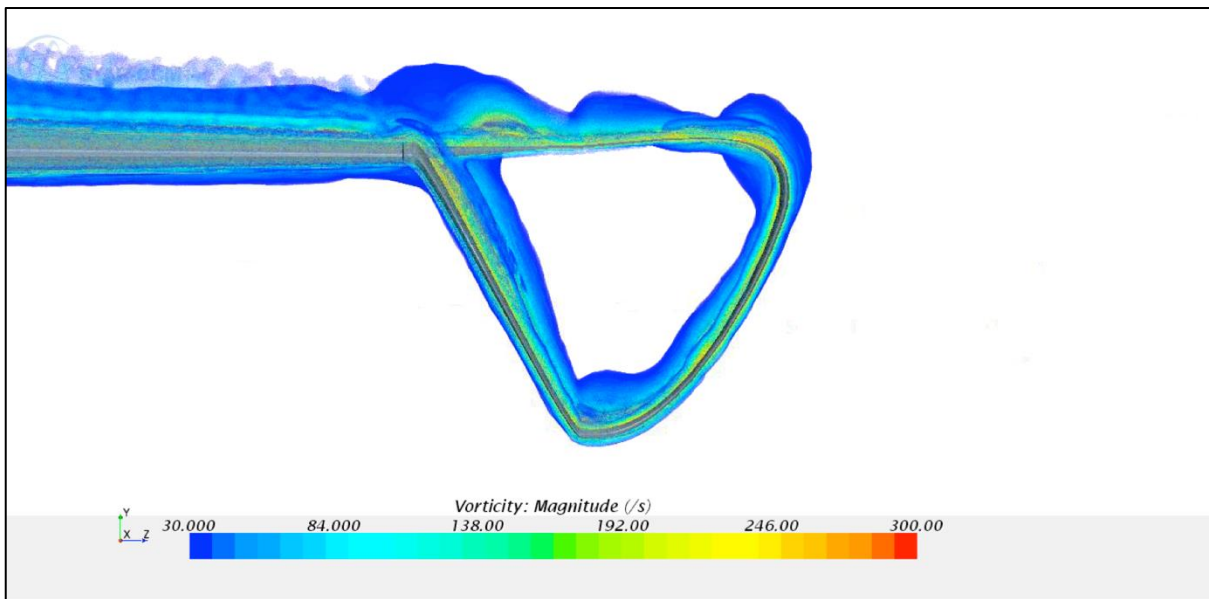


**Fig. 130: Design – 3 vorticity volume rendering**

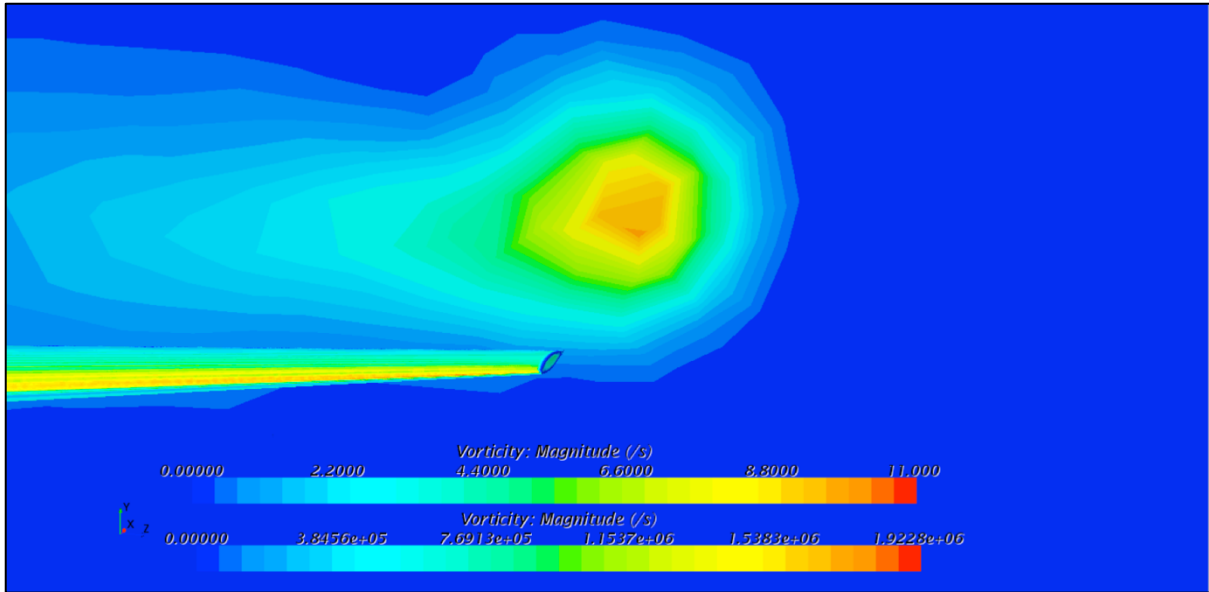


Fig. 131: Clean wing – vorticity scalar contour – Mach 0.24

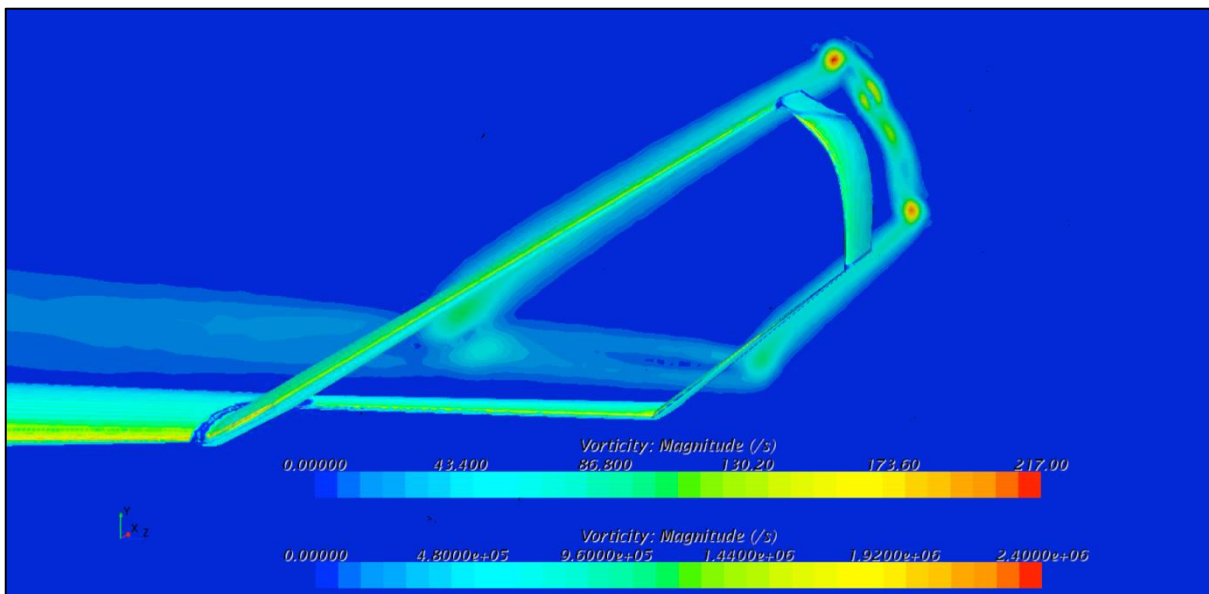
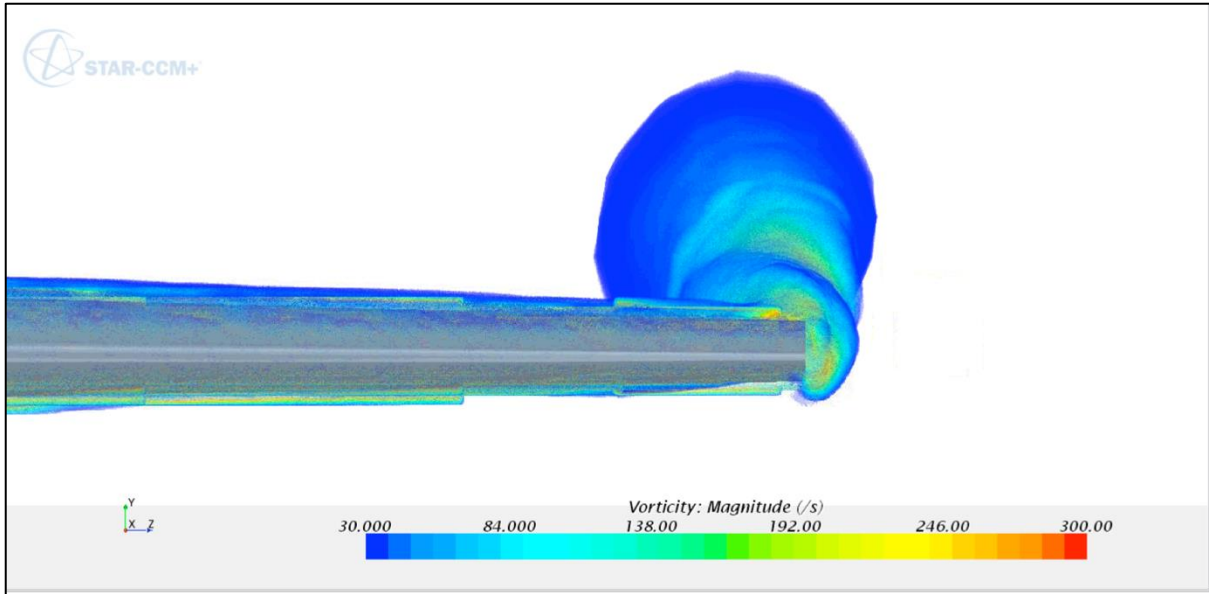
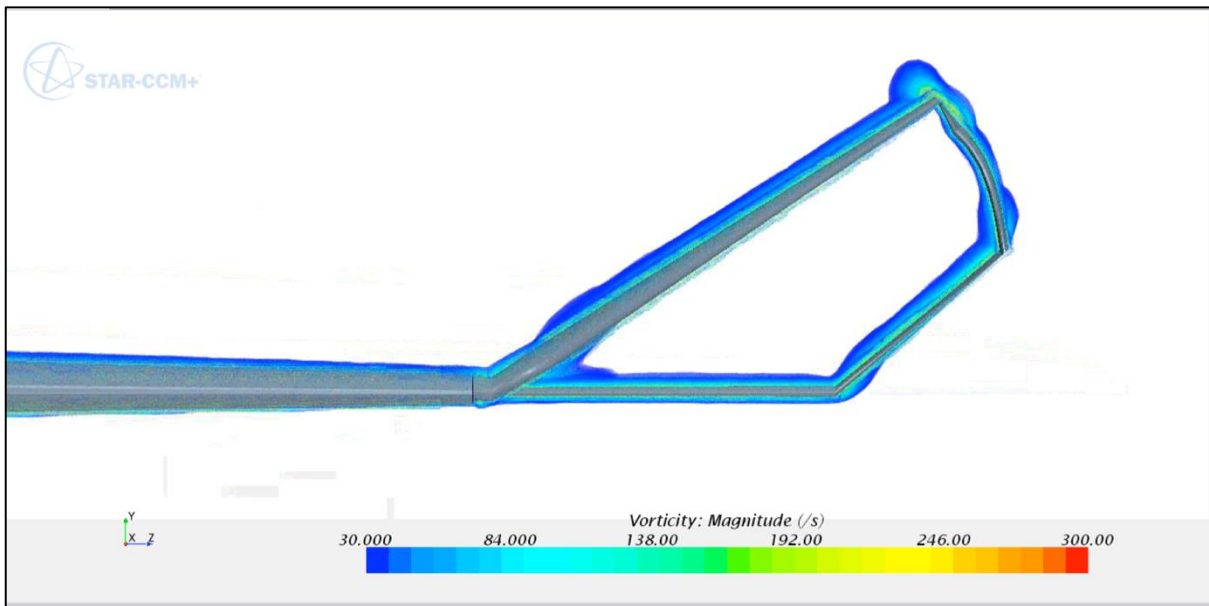


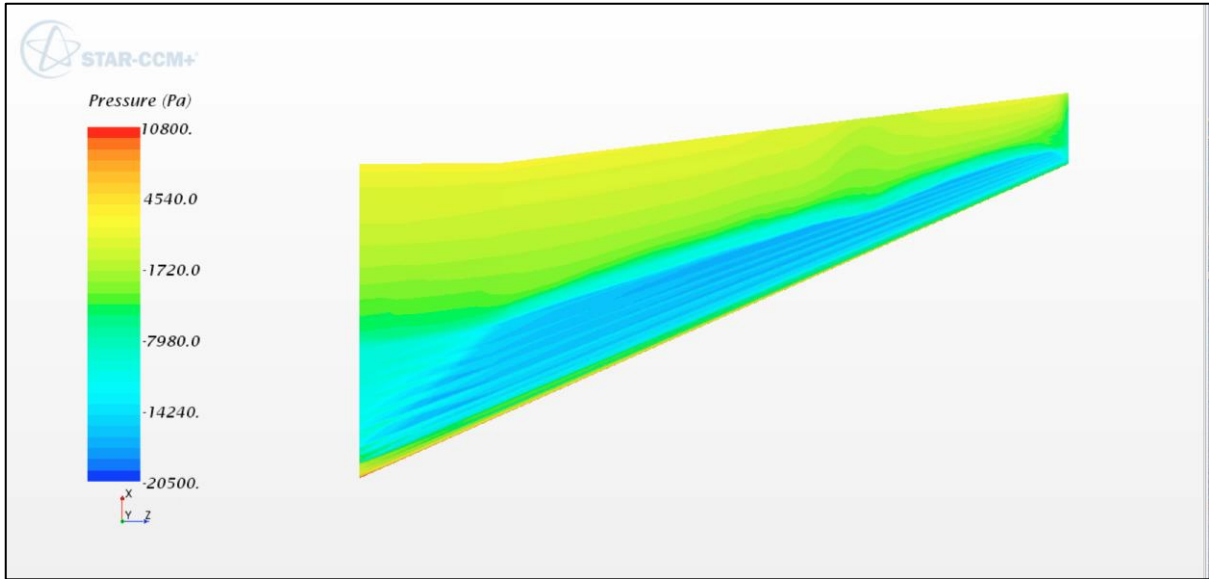
Fig. 132: Spiroid trapezium – vorticity scalar contour – Mach 0.24



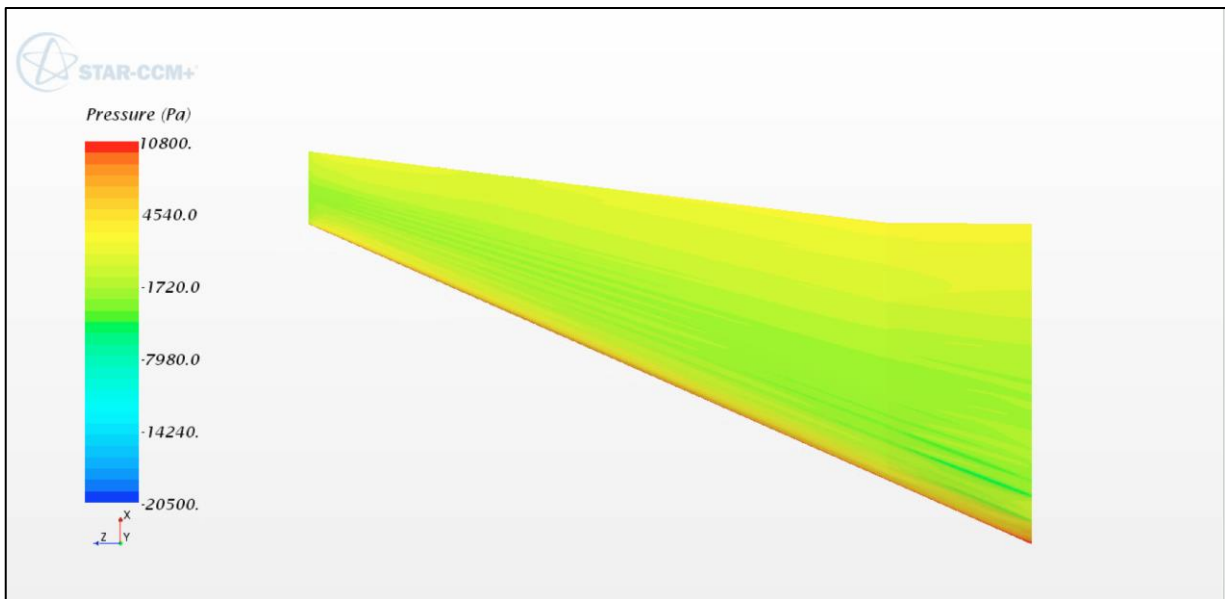
**Fig. 133: Clean wing – vorticity volume rendering – Mach 0.24**



**Fig. 134: Spiroid trapezium – vorticity volume rendering – Mach 0.24**

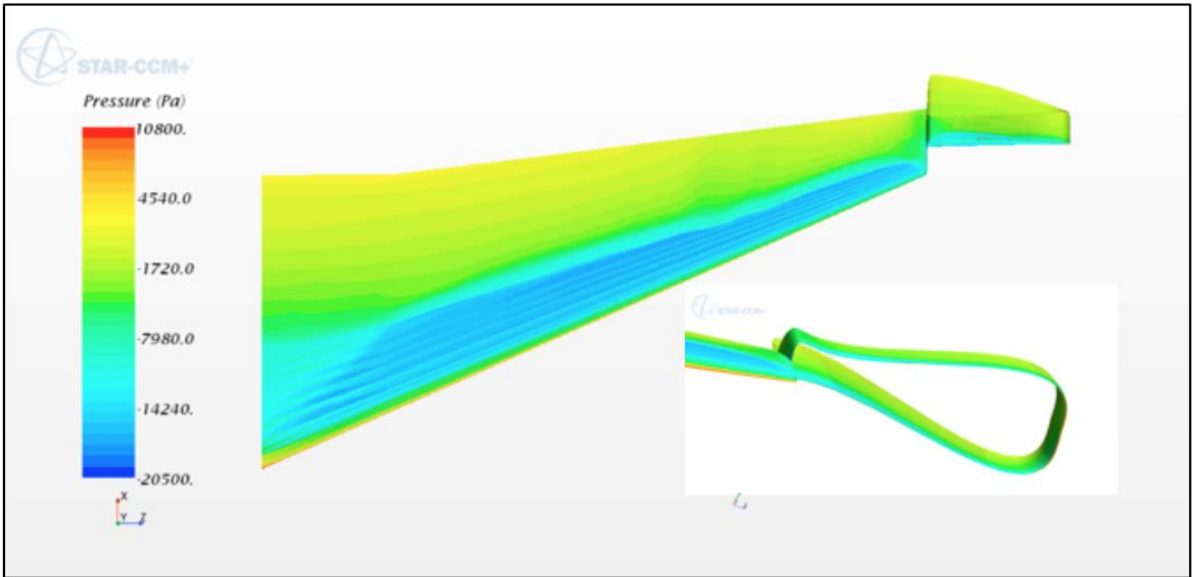


(a.)

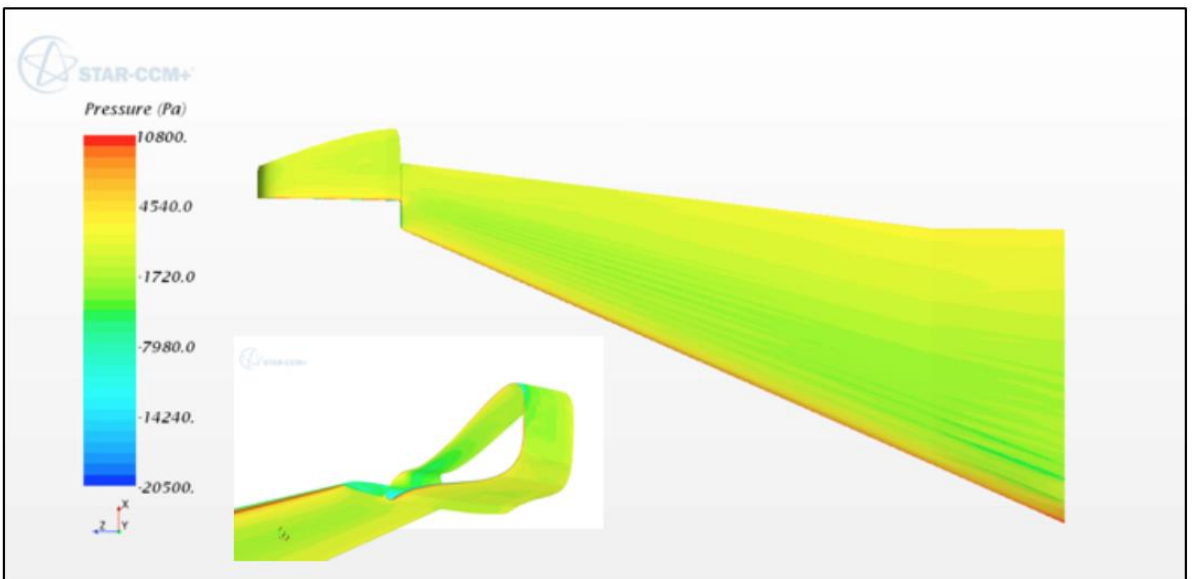


(b.)

**Fig. 135: Clean wing (a.) top, (b.) bottom – pressure contour – Mach 0.74**

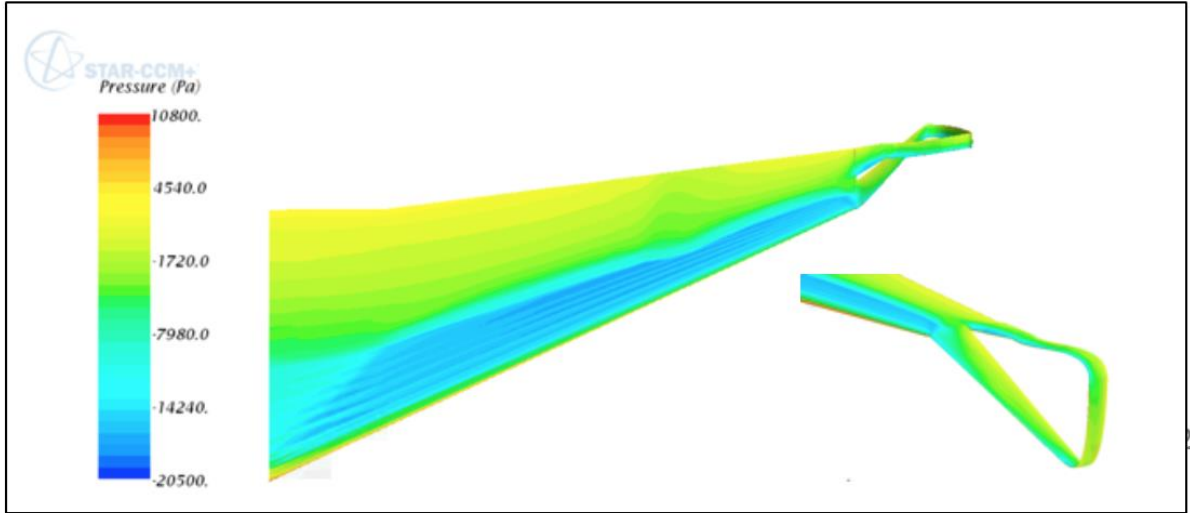


(a.)

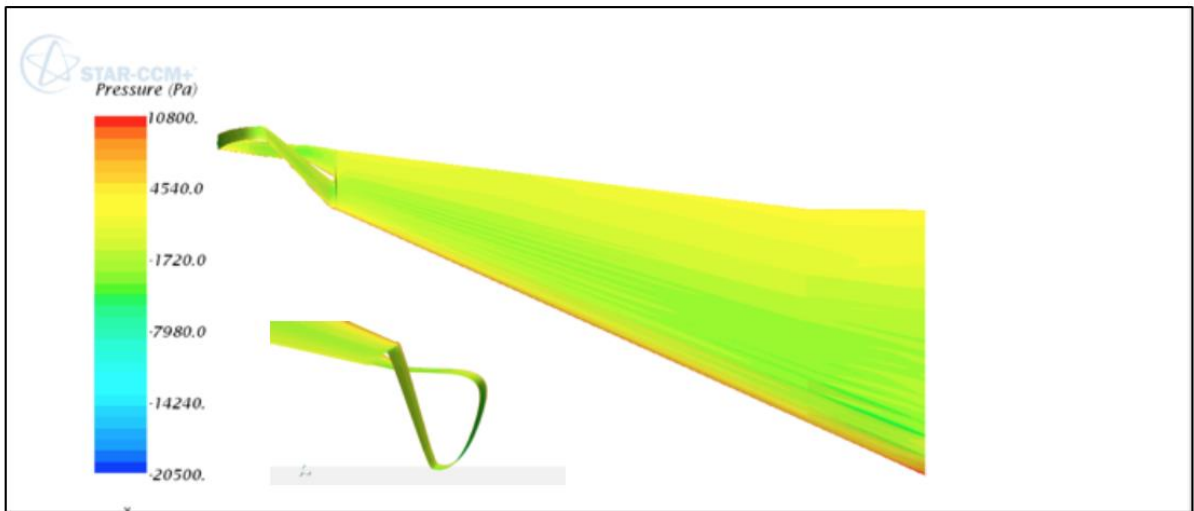


(b.)

Fig. 136: Design – 1(a.) top, (b.) bottom – pressure contour – Mach 0.74

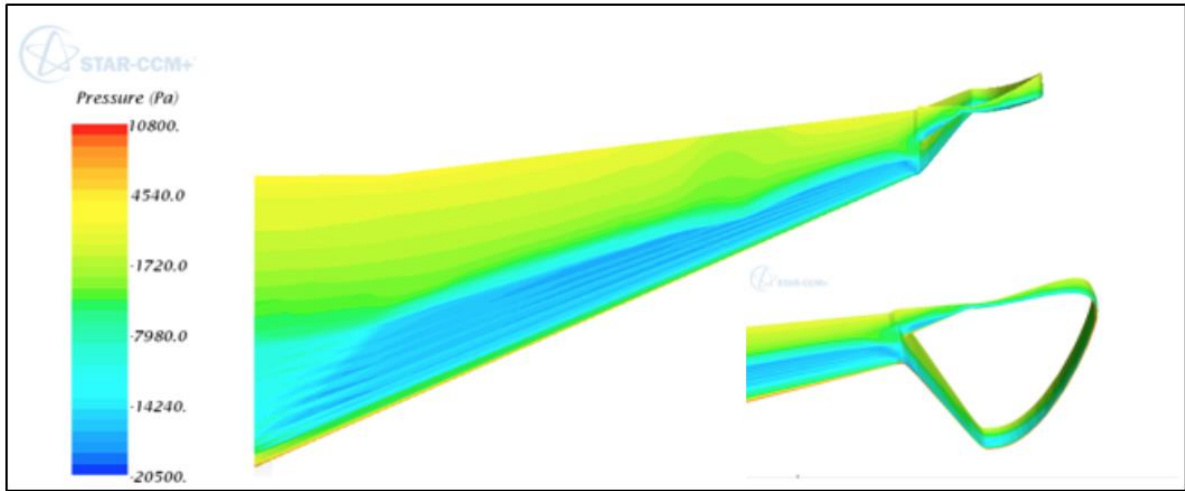


(a.)

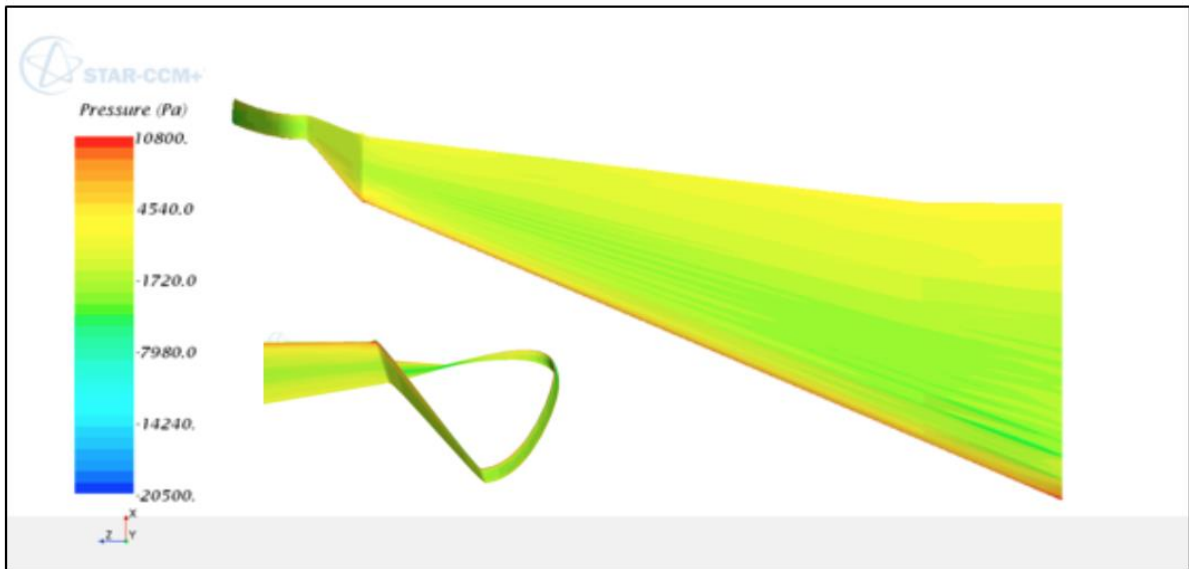


(b.)

**Fig. 137: Design – 2 (a.) top, bottom (b.) right – pressure contour – Mach 0.74**

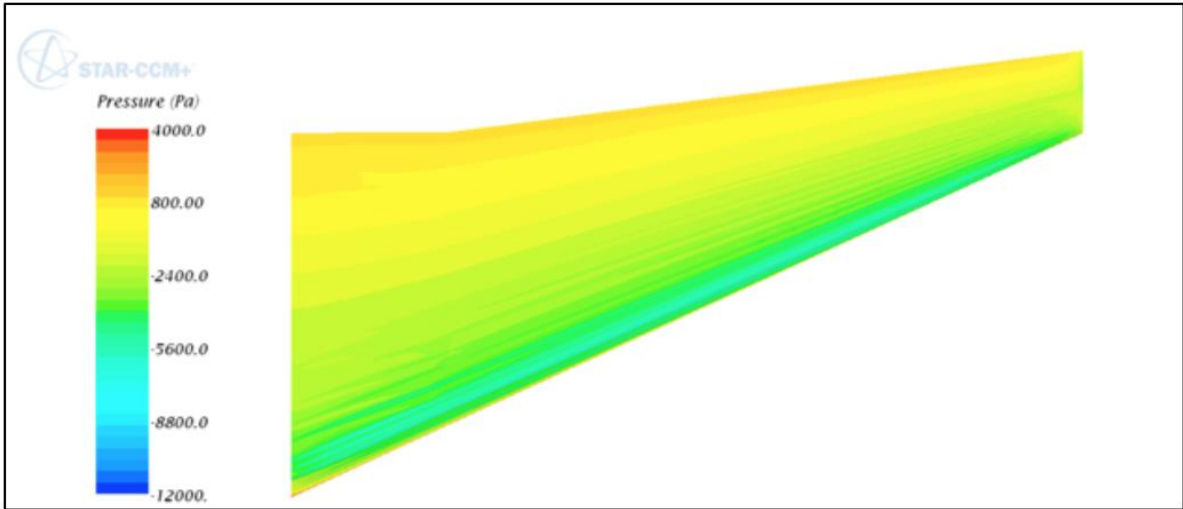


(a.)

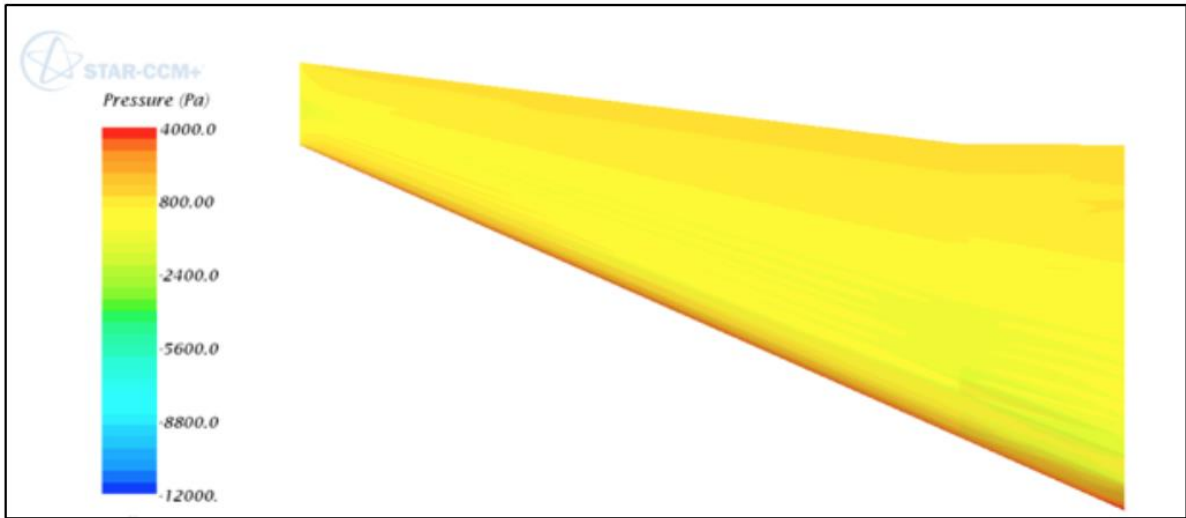


(b.)

Fig. 138: Design – 3 (a.) top, (b.) bottom – pressure contour – Mach 0.74

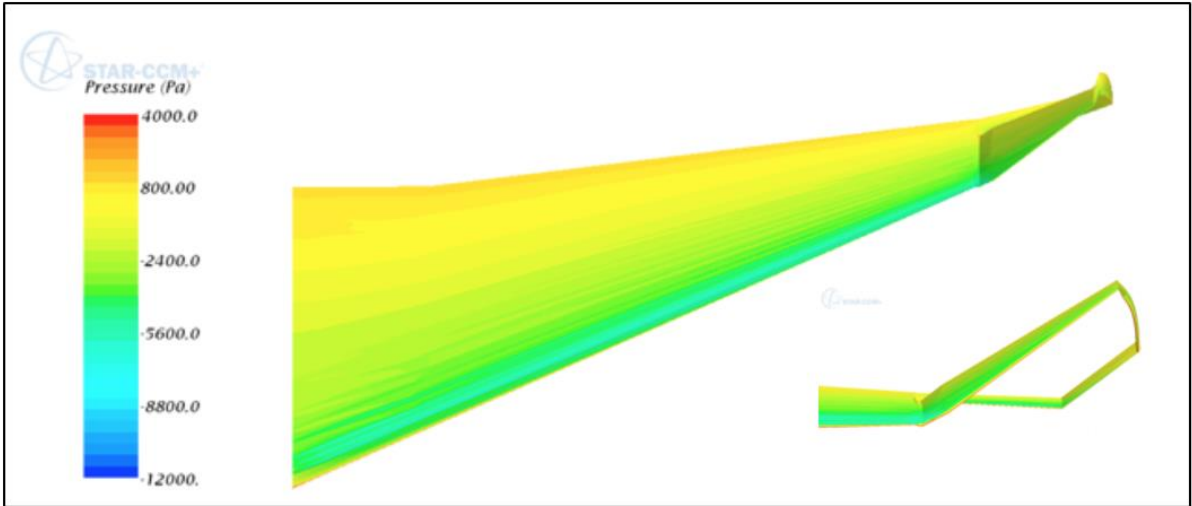


(a.)

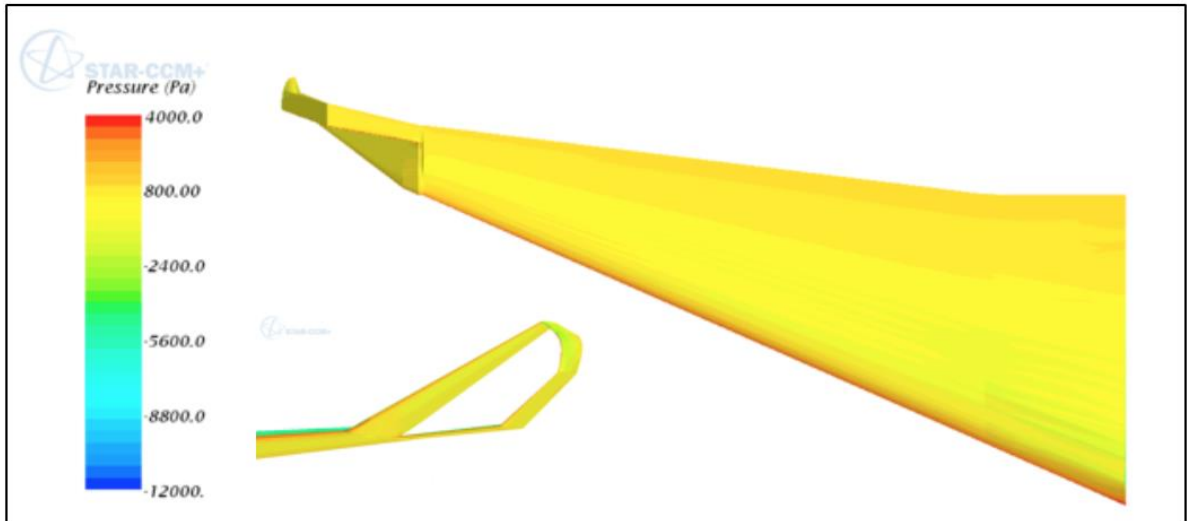


(b.)

**Fig. 139: Clean wing (a.) top left, (b.) bottom – pressure contour – Mach 0.24**



(a.)



(b.)

Fig. 140: Spiroid trapezium (a.) top, (b.) bottom – pressure contour – Mach 0.24

#### 5.4. Sensitivity of design variables on aerodynamic forces

The effect of changing the winglet design variables on the aerodynamic forces is presented in Fig. 141 – Fig. 156 and Appendices B-I to B-IV. To investigate these characteristic changes, a response surface based on a kriging surrogate model is generated (Kriging, 1951). The Kriging surrogate model technique is used for the interpolation of random surfaces based on a stochastic process. The interpolated random surfaces feature observed data at all sample points in the search space. This surrogate modelling technique has been found to be suitable for aerodynamic studies. The Kriging response surfaces were built in the HEEDs post processing package using computed data for the searched sample points. The kriging response surface depicts an approximate behaviour of the aerodynamic forces as a function of the design variables. The kriging response for the spiroid trapezium was used for a full 2<sup>nd</sup> level factorial Design of Experiment (DOE) study in HEEDS to observe the sensitivity of each of the design variables on the performance criteria (lift-to-drag ratio, lift and drag). The 2<sup>nd</sup> level factorial design are screening designs, it uses  $2^k$  (Montgomery, 2017) to determine the number of evaluations (possible combinations) for the screening; where  $k$  is the factor(s) which is also the design variables and each factor has two levels (Rushing et al., 2014), (Montgomery, 2017). The process involves screening a large number of factors that will affect the design(s), with the goal of identifying those factors most important to the response (aerodynamic forces). Eight thousand one hundred and ninety-two runs were carried out in HEEDs, this number was obtained by using  $2^k$ , the results are presented in Fig.141 – Fig. 155. This same number of runs was carried out for Design-2's initial optimisation in HEEDs with the results shown in Fig. 156 and Appendix B-I and B-II. A 2<sup>nd</sup> level factorial study was not performed on Design's 1 and 3 as it would have required millions of runs to obtain each set of results. The knowledge gained from this process is used as a baseline to further design and optimise Design-2. Alternatively, the 3-D response surface produced in HEEDs which is shown in appendices B-III and B-IV was deemed sufficient to observe the trend on how the variables impact on the aerodynamic forces.

The 2<sup>nd</sup> level factorial study on the spiroid trapezium devices showed the design drag, lift, and lift to drag ratio was most sensitive to chord 5 sweep by a 53, 52 and 69 percent respectively (see Fig. 141). These percentages are obtained based on how much change is attainable on the aerodynamic forces by changing the values of this factor (variable – chord 5 sweep). This process is done automatically within the algorithm and the same approach is used to obtain all the percentage values discussed here on. The next most sensitive parameter was chord 1 size at 38 percent for the lift and 21 percent for the drag, with the other parameters showing less sensitivity.

The result of doing the 2<sup>nd</sup> level factorial study on Design-2's initial optimisation stage demonstrated that the values of the lift-to-drag ratio is most dependent on the winglet chord size 3 by 84 percent. The drag is also most dependent on the winglet chord size 3 but by 43 percent, which is followed closely by the winglet toe 1 chord size at 41 percent. On the other hand, the lift is most dependent on winglet toe 1 chord size by 71 percent. Other variables which the performance parameters are less sensitive towards were the winglet toe 2 size, winglet chord 1 size, winglet sweep angle for chord 1 and for the other chords, winglet's vertical height (dihedral and anhedral) which is also the winglet's vertical height for chord 1, winglet twist angle (chord 1, chord 3, toe1 and 2). Also, less sensitive parameters are winglet chord 1 and 2 span-wise length. The response surfaces show that the drag value is highly affected by the winglet chord 3 size and toe 1 chord size. All the same, the other variables do have substantial impact on the drag value and should also be considered in the design process. The lift is more sensitive to the winglet toe 1 size, chord 1 size and chord 3 size with the other winglet design parameters been less sensitive.

Following the success of this design, Design-2 was optimised by closing the loop of this design. An analysis of the kriging response surface showed the drag is most dependent on the winglet chord 3 twist angle with winglet chord 3 vertical height, mid-point sweep and chord 1 vertical height following closely with the other parameters proving to be less sensitive, but It was also necessary to consider them during the optimisation process. The lift was most dependent on the winglet chord 3 twist angle with winglet Mid-point sweep angle and winglet toe 2 size following closely with the other parameters been less sensitive but also considered.

The kriging response surfaces produced during the optimisation process of Design-1 are depicted in Appendix B-III. First, the drag kriging response surfaces are presented then the lift kriging response surfaces. A detailed evaluation of the plots, demonstrate that the drag is most dependent on chord 3 sweep angle, followed by winglet chord 4 twist angle, then chord 2 sweep and size. The drag was sensitive to the other parameters but not as much as the ones mentioned initially. The least most sensitive parameter was the thickness of the connection device which had no effect on the drag. Also, chord 2 thickness, chord 4 sweep angle, length in the span-wise direction, vertical height and size fell into this category. The lift produced was mostly affected also by the winglet's chord 3 sweep angle, the next parameters with high sensitivity were chord 4 twist angles, chord 2 vertical height, chord 3 size and chord 2 twist angle, starting from high to low sensitivity. The following parameters had little effect on the lift: chord 4 sweep angle, the thickness of the connection device, chord 1 vertical height, chord 3 thickness and chord 4 thickness.

The kriging response surface of Design-3 with design parameters of the device shown on both horizontal axis of the 3-D plot as well as their corresponding drag and lift forces is shown in Appendix B-IV. It also shows the sensitivity to the drag and lift forces on the wing caused by changing the device design parameters. The results show that the drag is most dependent on winglet Mid-point sweep, followed by chord 3 twist and chord 1 twist angles. The drag value was less sensitive to the other parameters with the winglet mid-point length and chord 3 vertical height having the least sensitivity. In addition, the lift forces were also most dependent on the chord 1 twist angle, chord 3 twist angle and chord 1, chord 1 size and Mid chord twist angle. The least sensitive parameters were chord 3 sizes, mid-sweep angle and mid-point length in order of least sensitivity starting with the least sensitive. In respective of these findings, the other parameters were used in the optimisation process.

**Kriging response surface for spiroid trapezium device**

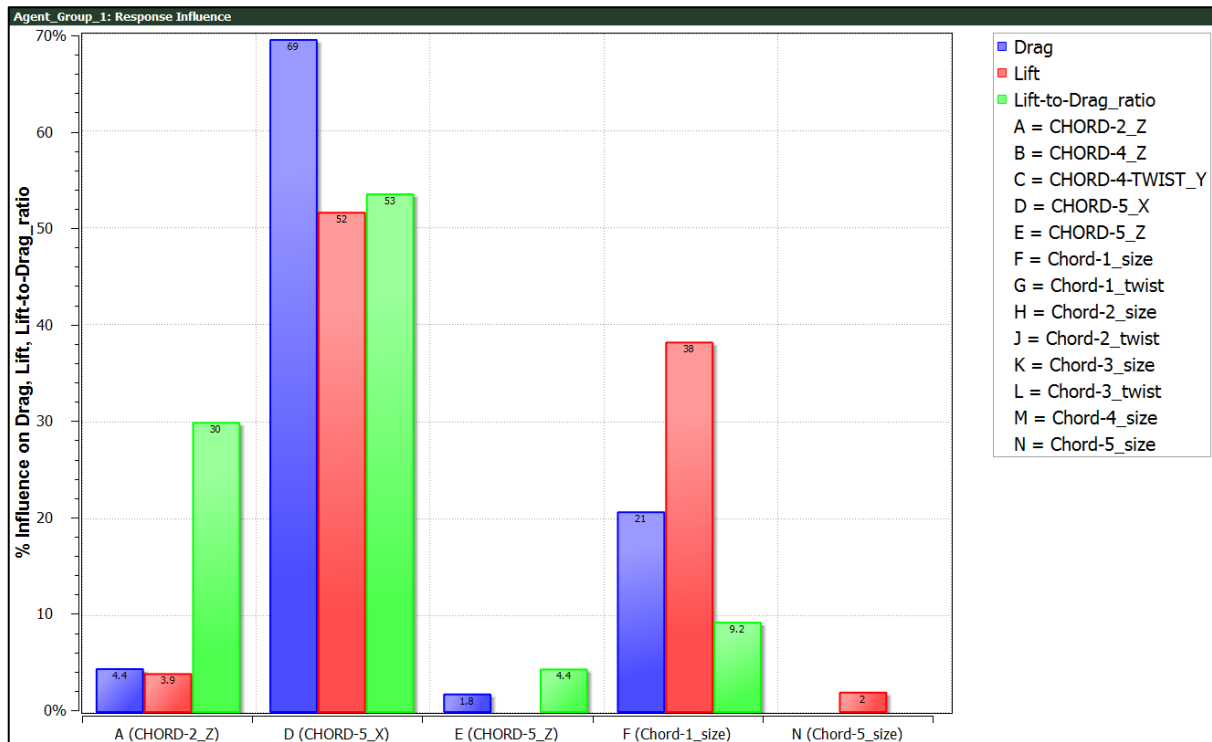


**Fig. 141: The influence of the factors (variables) on lift-to-drag ratio, lift (N) and drag forces (N)**

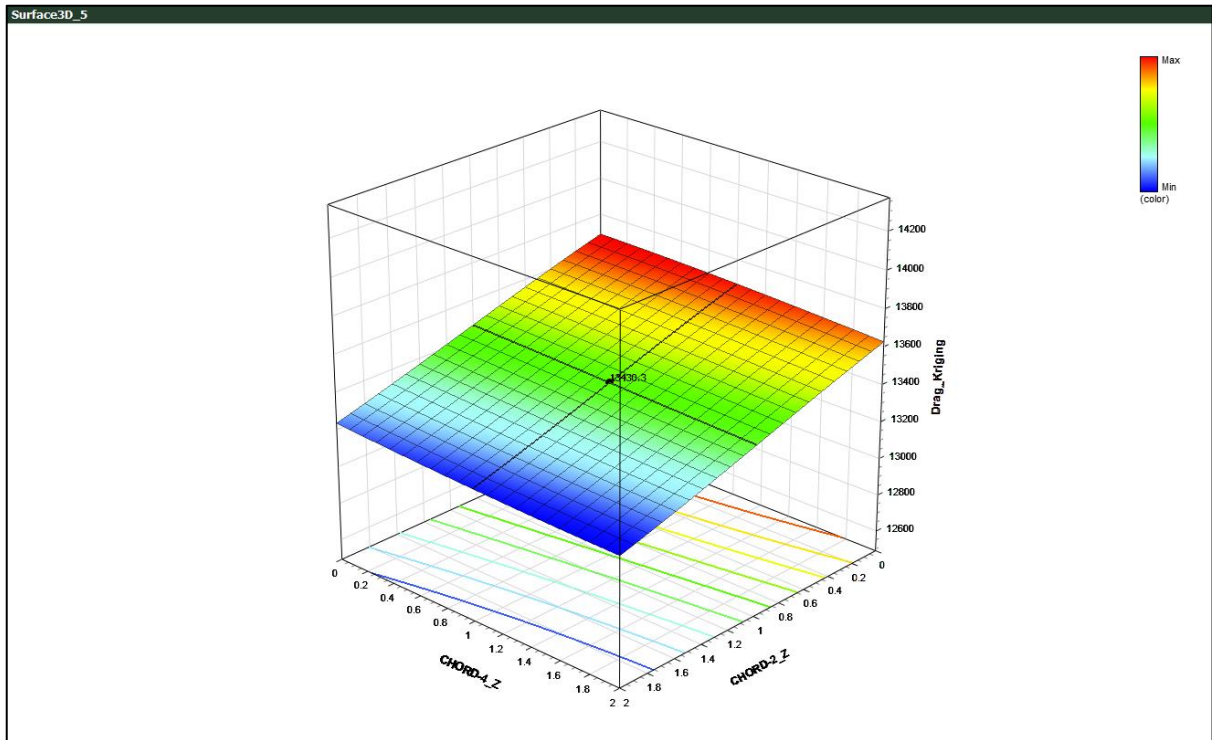


Fig. 142: Chord 4 length (m), Chord 2 length (m)

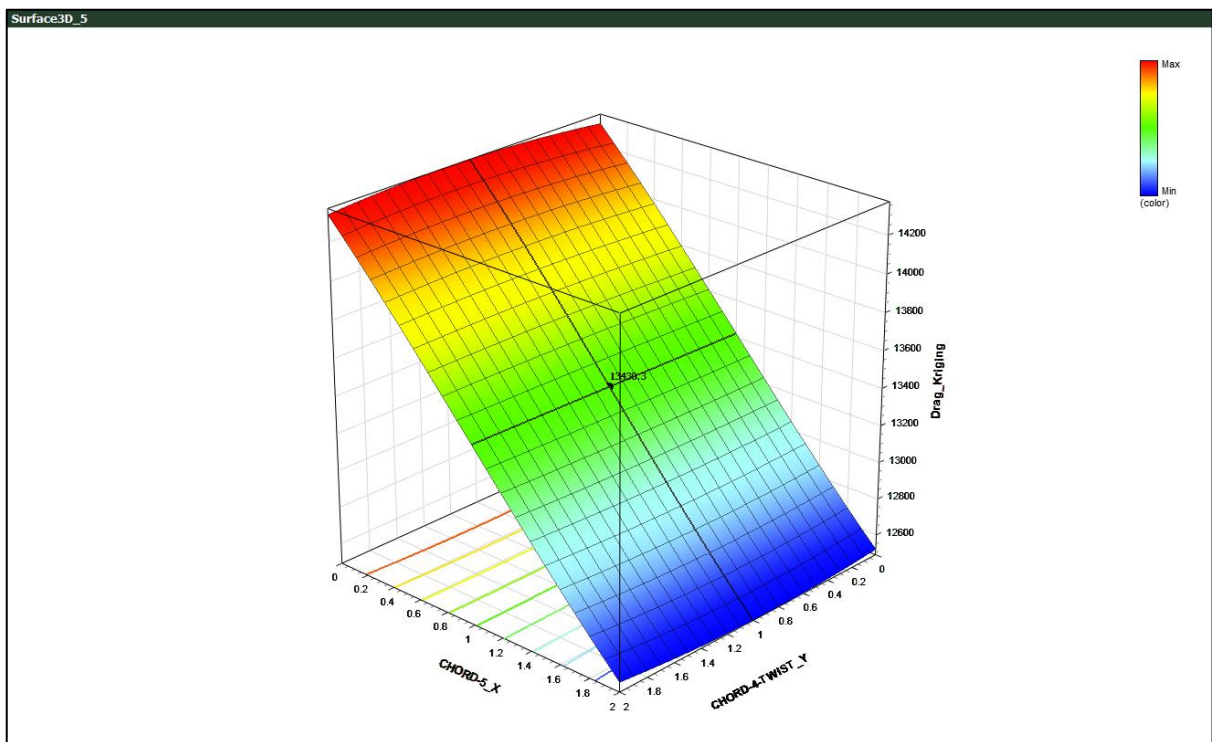


Fig. 143: Chord 5 sweep, Chord 4 twist

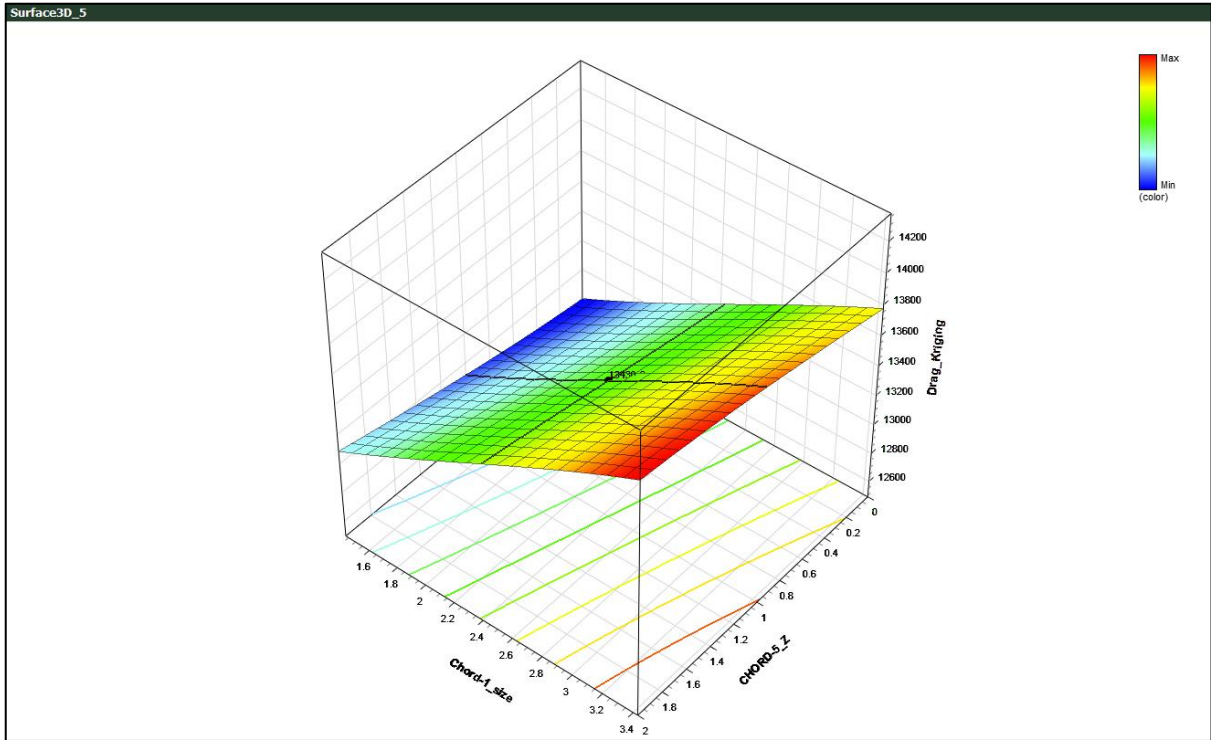


Fig. 144: Chord 1 size (m), Chord 5 length (m)

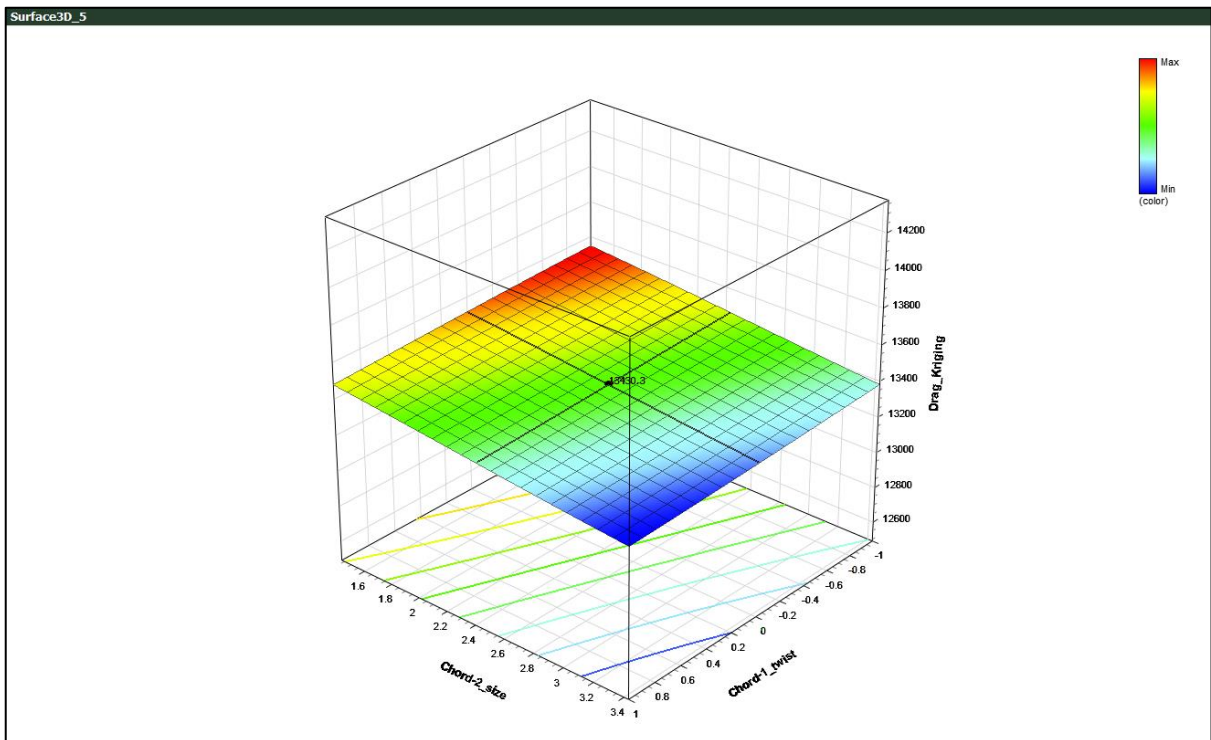


Fig. 145: Chord 2 size, Chord 1 twist

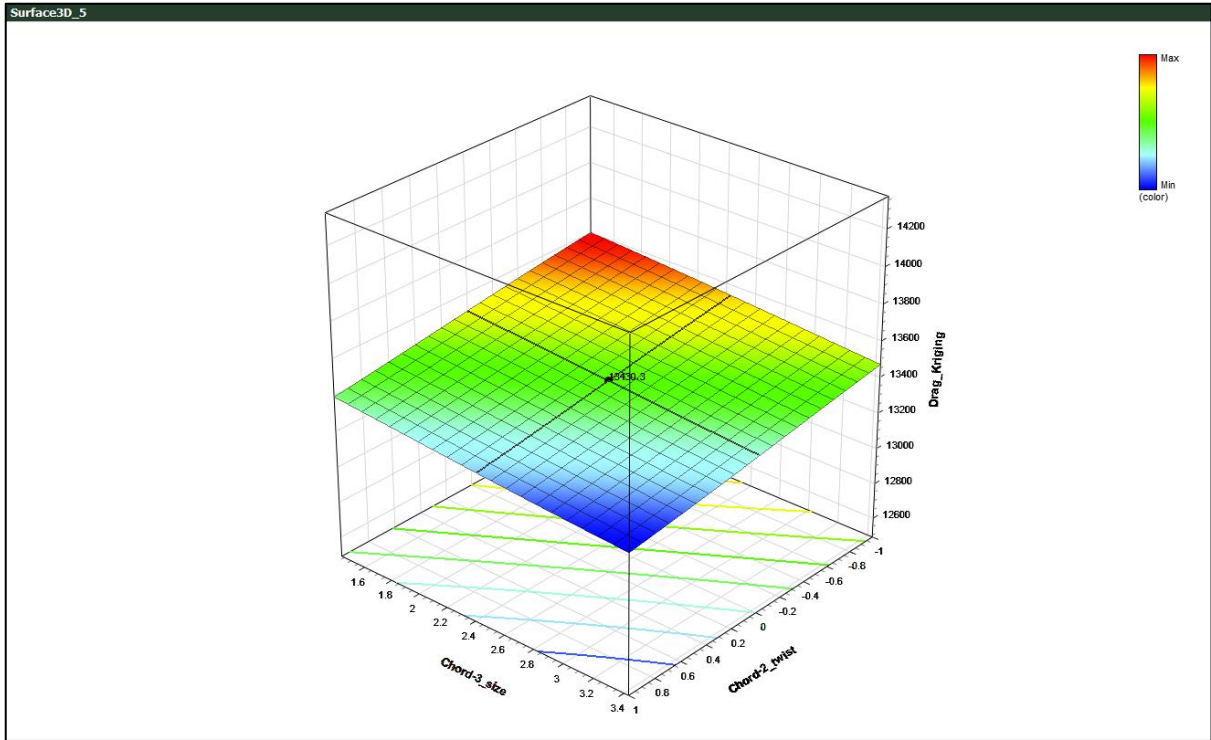


Fig. 146: Chord 3 size, Chord 2 twist

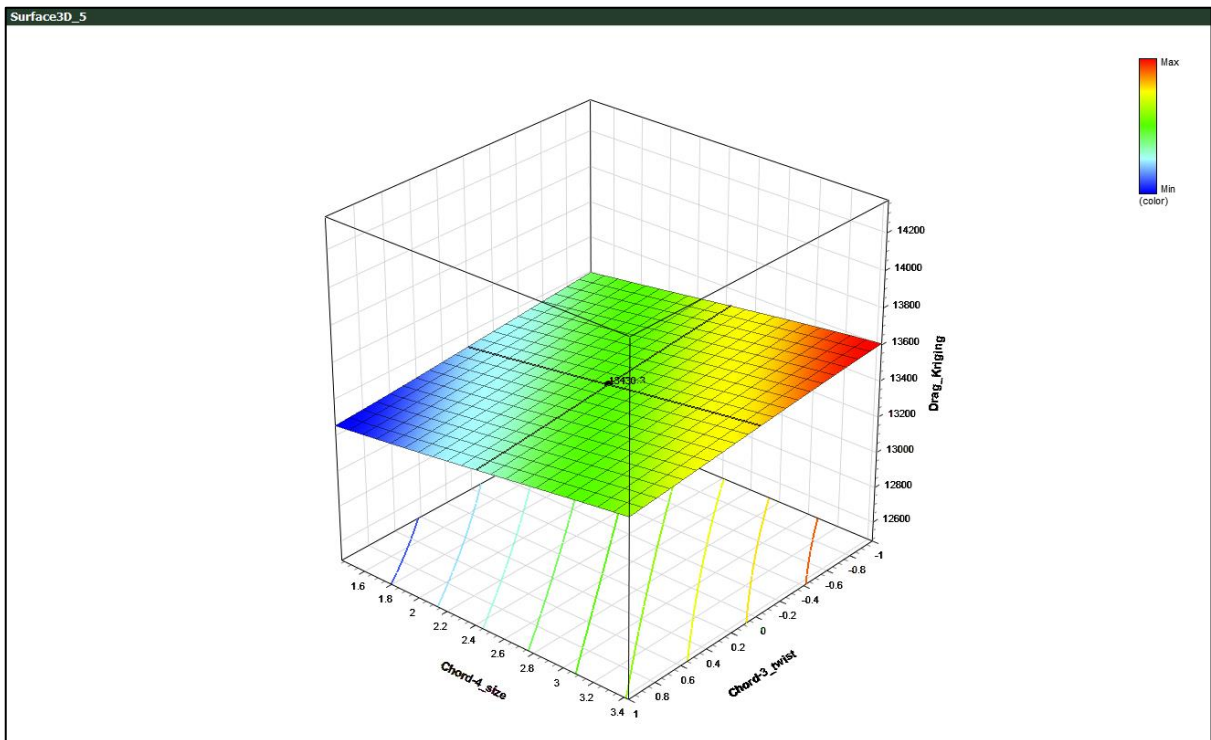
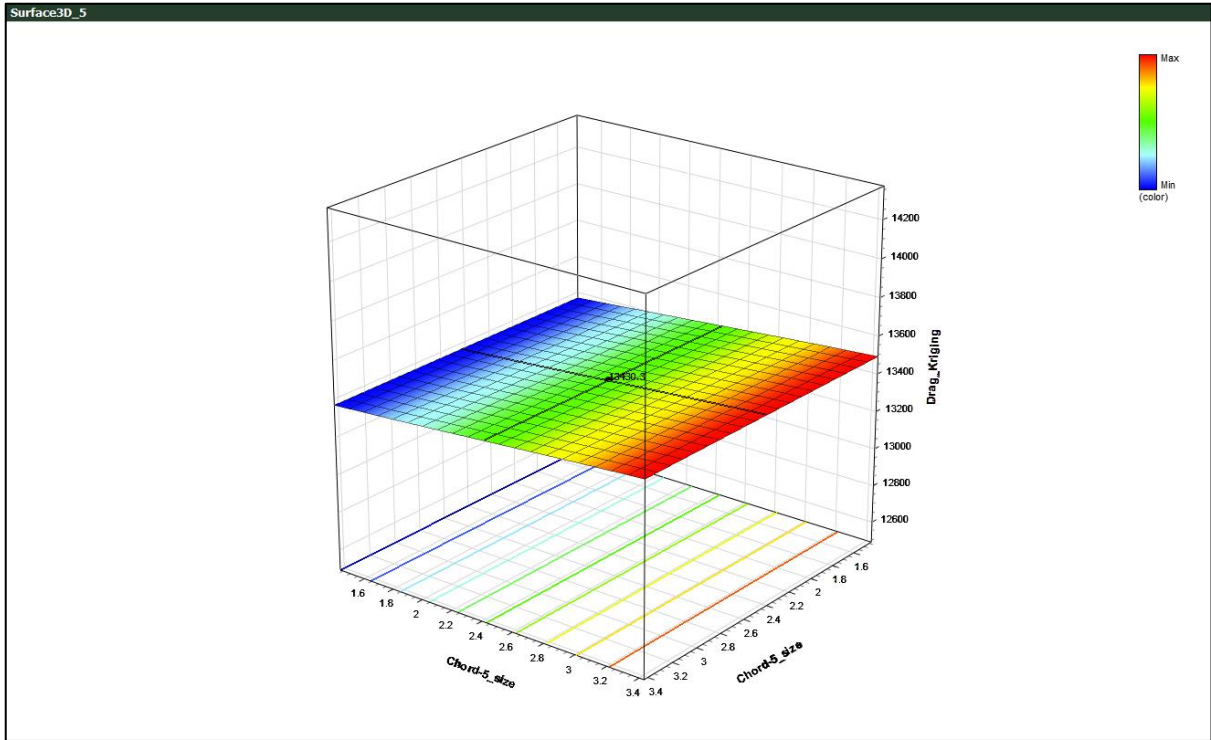
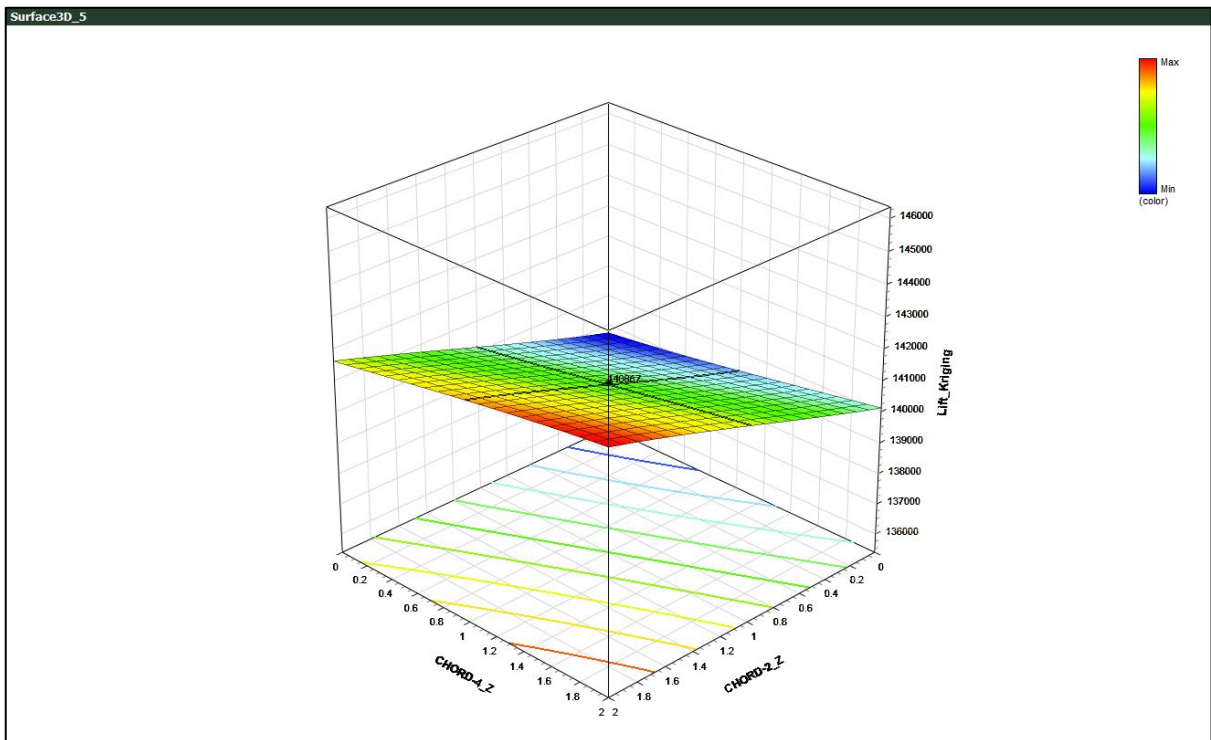


Fig. 147: Chord 4 size, Chord 3 twist



**Fig. 148: Chord 5 size, Chord 5 size**



**Fig. 149: Chord 4 length (m), Chord 2 length (m)**

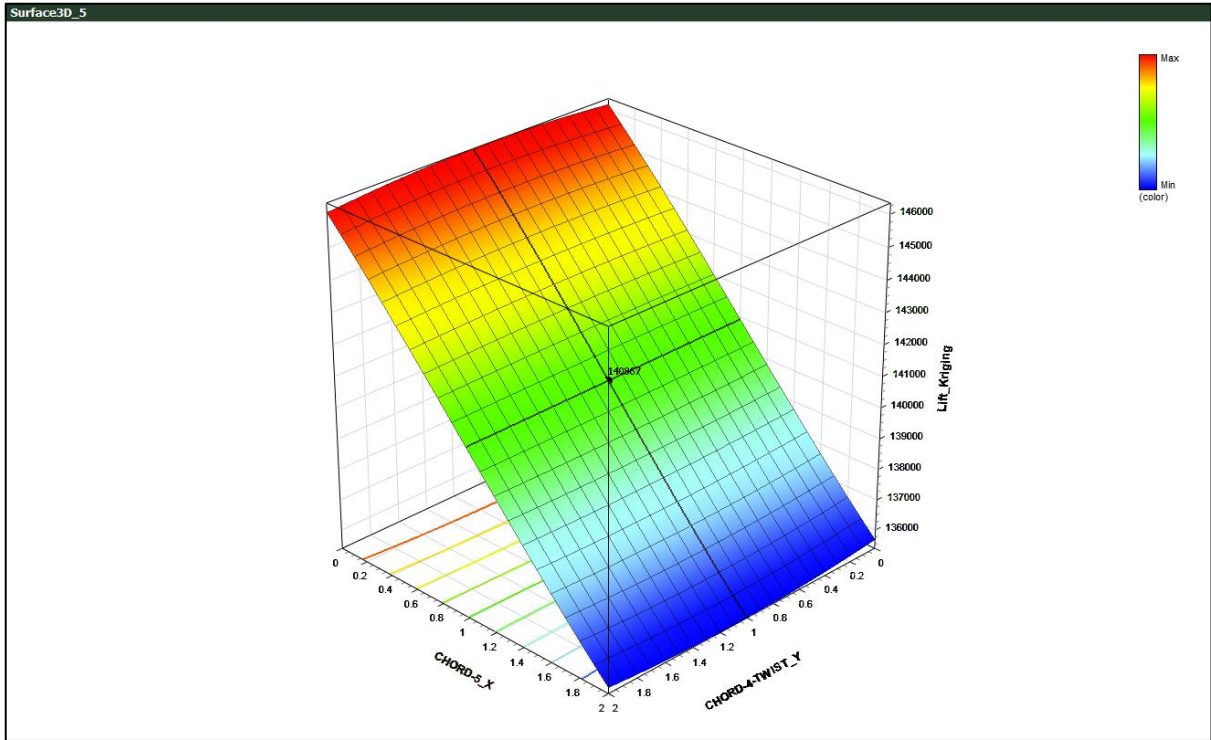


**Fig. 150: Chord 5 sweep, Chord 4 twist**

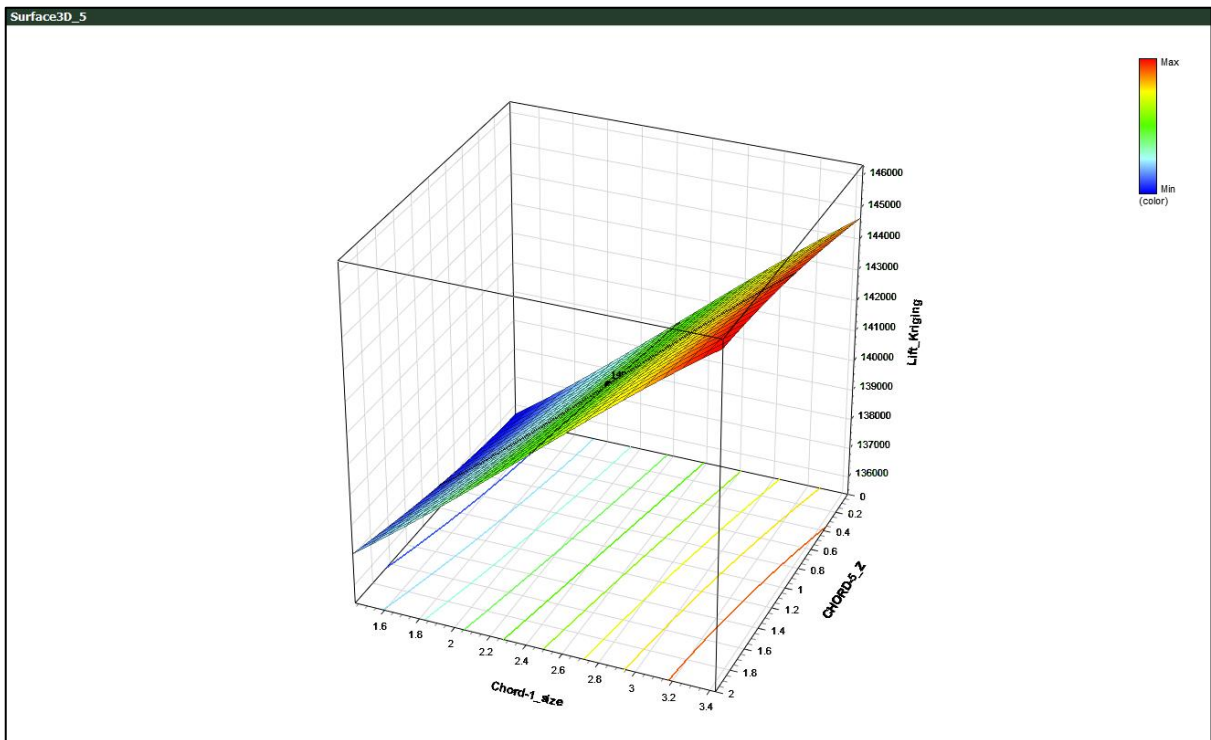


**Fig. 151: Chord 1 size, Chord 5 length (m)**

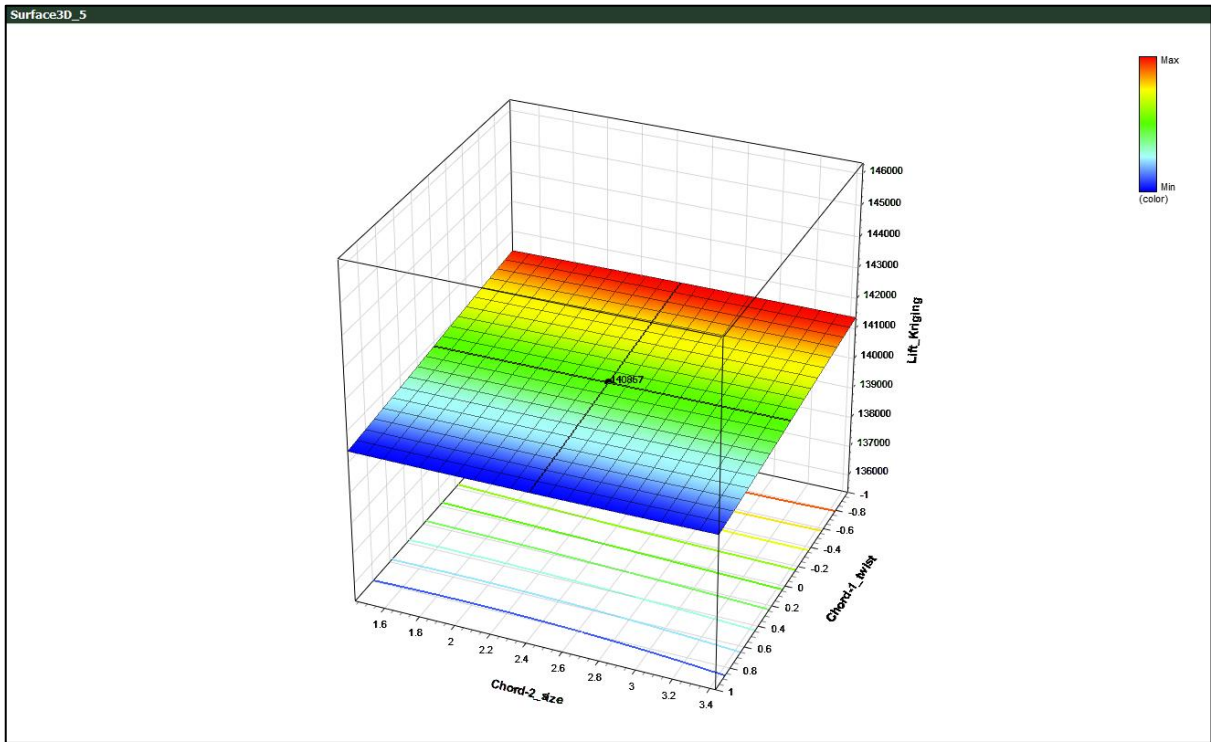


**Fig. 152: Chord 2 size, Chord 1 twist**

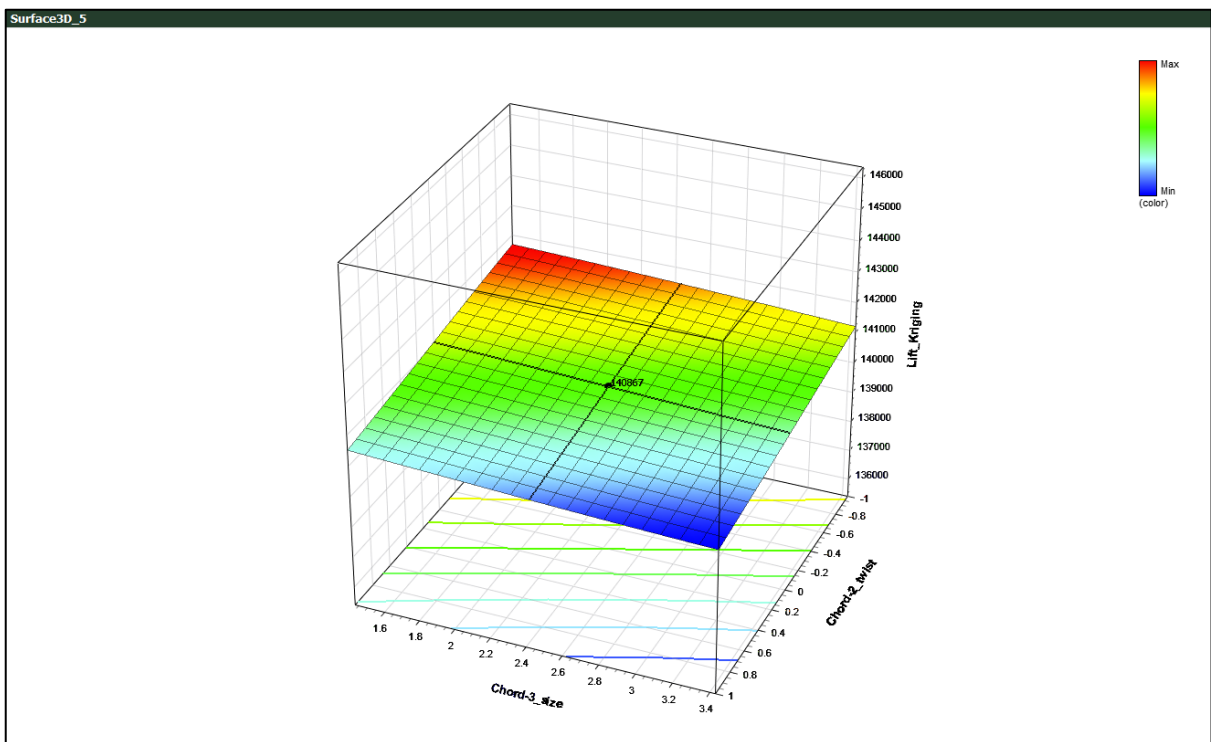


**Fig. 153: Chord 3 size, Chord 2 twist**

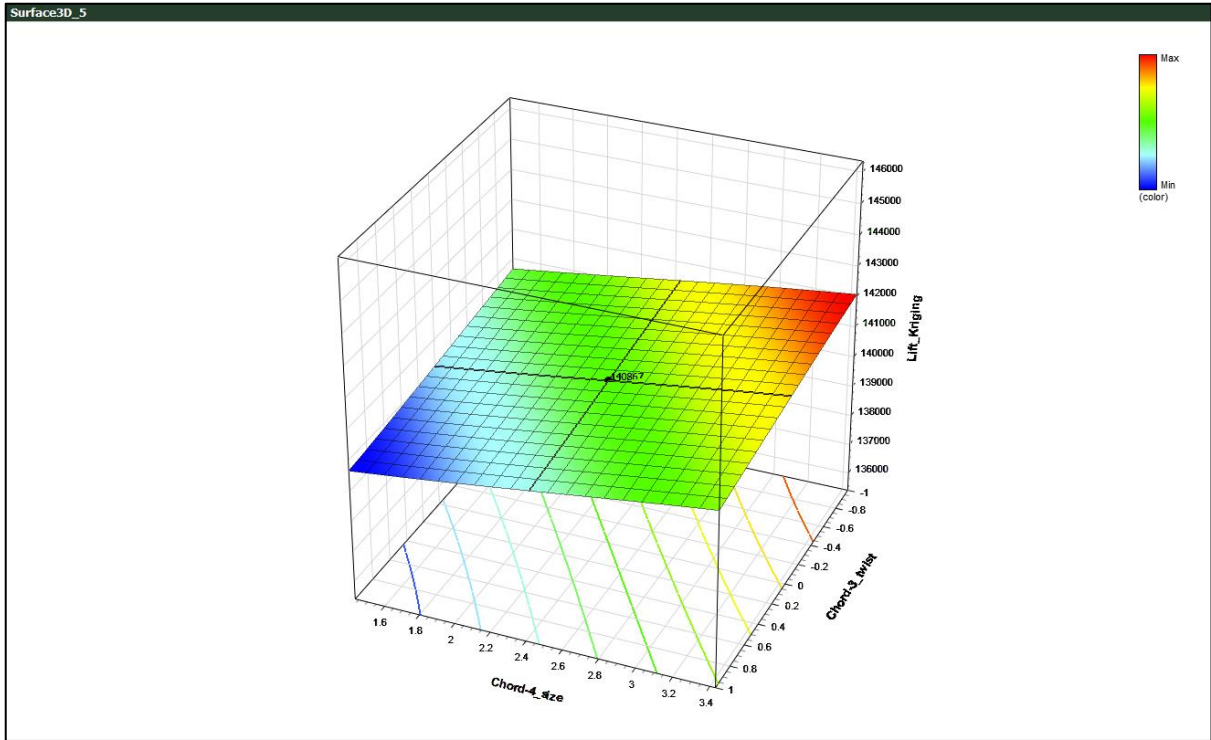


**Fig. 154: Chord 4 size, Chord 3 twist**

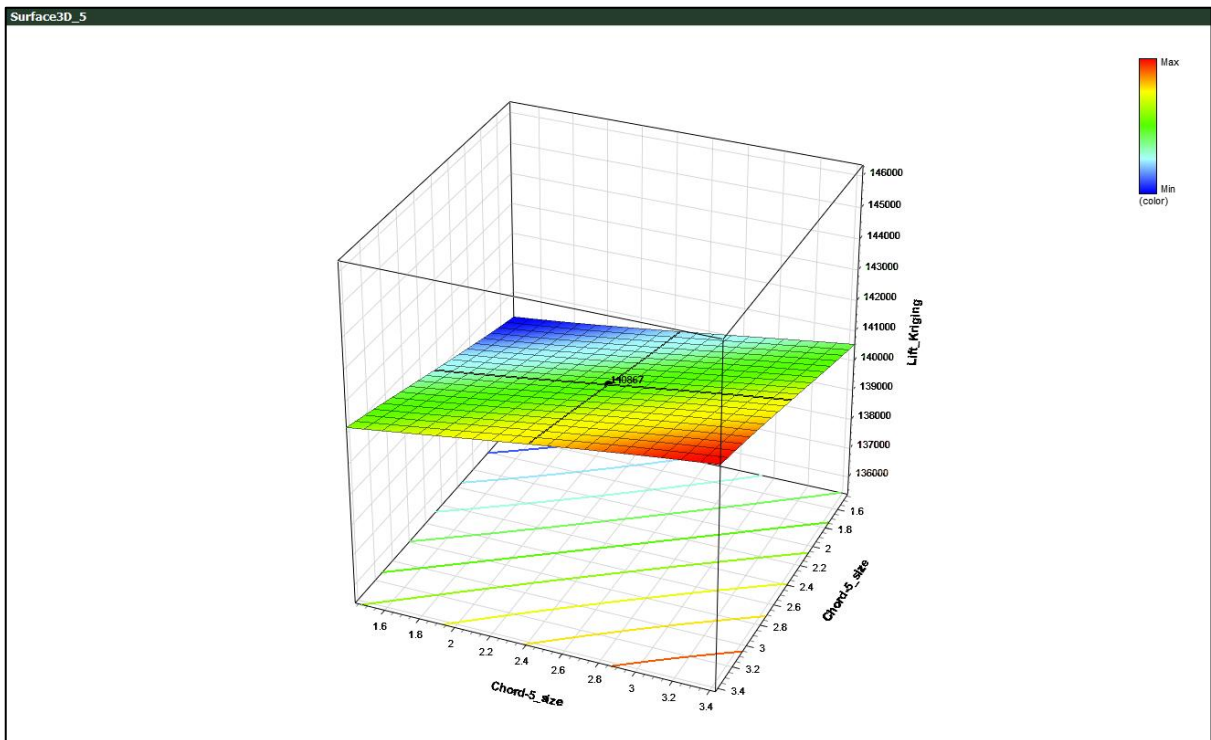


**Fig. 155: Chord 5 size**

## Kriging response surface for initial design phase of Design-2

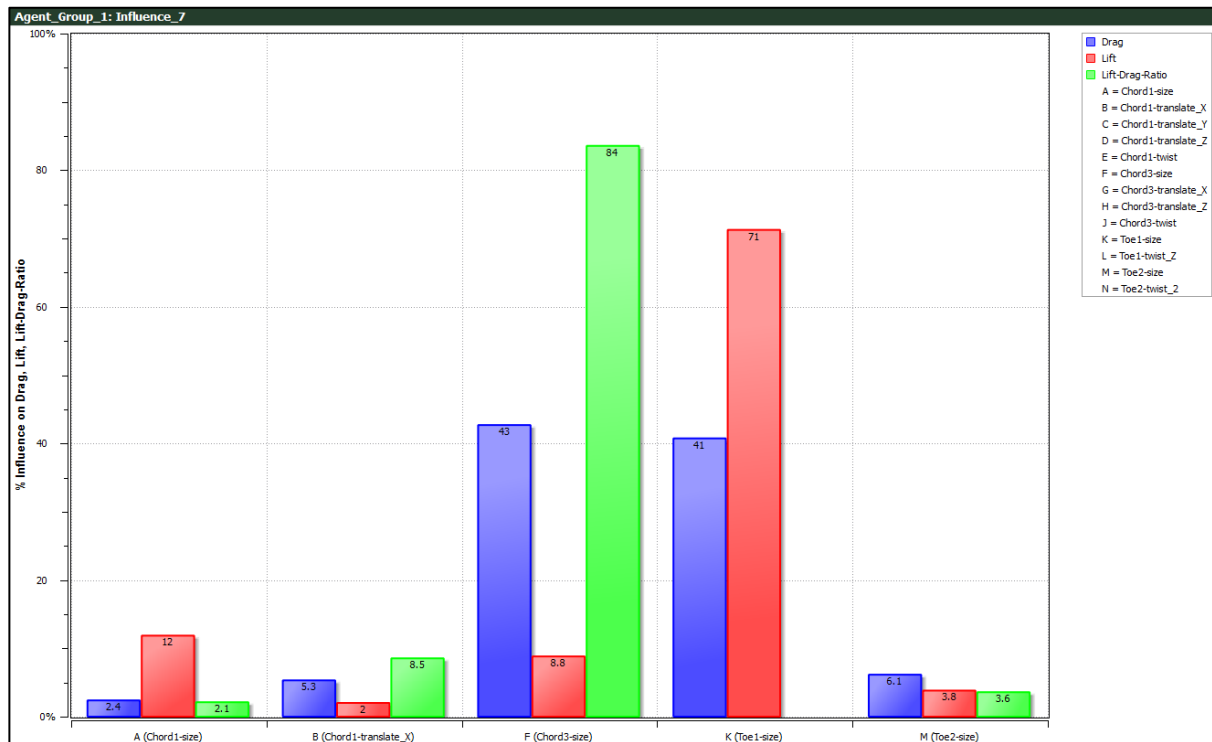


**Fig. 156: The influence of the factors (variables) on lift-to-drag ratio, lift (N) and drag forces (N)**

## 5.5. Conclusions

The optimisation process used for the design of four-novel induced drag reduction devices with the CFD results obtained from further analysis of the devices has been presented. The designs are labelled Designs-1- 3 and spiroid trapezium. The outcome of the investigation yielded the following benefits:

In section 5.3.2, a lift-to-drag improvement of up to 3, 3, 6, and 11 percent was attainable for Designs 1 – 3 and the spiroid trapezium respectively at the optimisation conditions.

- For the same conditions,  $C_D$  was reduced by up to 3, 3, 2 percent for Designs 1- 3 and also, the spiroid trapezium had a reduced  $C_D$  of approximately 4 percent.
- $C_L$  was improved by a maximum of 7 percent by using the wing spiroid trapezium configuration, there was also a consistent increase in  $C_L$  for Designs 1- 3.
- Attainable induced drag reduction up to 18 - 24 percent for both Designs 1-3 and the spiroid trapezium.

In section 5.3.3, the performance of the devices at assumed take-off condition of Mach 0.24 at several angles of attack was discussed. Each device had a certain range of angles of attack for which it was most effective, for example, Design's 1 – 3 were most effective at  $2^0 - 6^0$  and the spiroid trapezium at  $2^0 - 8^0$ .

- The most improved  $C_L/C_D$  ratio was obtained for the spiroid trapezium for 13 percent at  $6^\circ$  AOA while Design's 1 – 3 had an increase of up to 3 – 4 percent at  $4^\circ - 8^\circ$ .
- A consistent  $C_L$  improvement was observed for all the devices.
- Design – 1 produced the maximum induced drag reduction of up to 43 percent.

In section 5.3.4, a study on the effect of Mach number on the performance of the devices showed a consistent improvement in the  $C_L/C_D$  ratio and  $C_L$  with  $C_D$  and  $C_{D_{induced}}$  reduction across several Mach numbers.

- Design – 1 had a maximum  $C_L$  improvement of up to 3 percent at Mach 0.64 and up to 6.4 percent improvement of  $C_L/C_D$  ratio also at Mach 0.84 and up to 5 percent  $C_D$  reduction at Mach 0.84.
- Design – 2's highest  $C_L$  improvement was at Mach 0.54 with a value of 4 percent, a 3 percent improvement in  $C_L/C_D$  ratio at Mach 0.64 and up to 5 percent reduction in  $C_D$  at Mach 0.84.
- Design – 3 showed the most improvement in  $C_L$  at Mach 0.74 at 5 percent, a 6 percent increase in the  $C_L/C_D$  ratio for Mach 0.64 and up to 5 percent reduction in  $C_D$  at Mach 0.84.
- The spiroid trapezium had the most improvement among the other designs, its  $C_L$  modification was as high as 11 percent at Mach 0.54, with a  $C_L/C_D$  increase by up to 15 percent at the same Mach number and  $C_D$  reduction of 6 percent also at Mach 0.54.
- The induced drag reduction was between 11 – 28 percent for all configurations.

The sensitivity analysis of the four devices that was discussed in section 5.4 showed that for the spiroid trapezium, the most sensitive design variables were chord 5 sweep, chord 1 size (Fig. 109) with other parameters worth considering. Design-1 most sensitive variables amongst the 21 variables used were (Fig. 106):

- Drag – chord 3 sweep angle.
- Lift – chord 3 sweep angle.

For Design – 2 initial optimisation the following variables were most sensitive (Fig. 107):

- Drag – winglet chord 3 size.
- Lift – winglet toe 1 size.

Mid-point and closed loop optimisation most sensitive variable amongst the 14 design variables used were (Fig. 107):

- Drag – winglet chord 3 twist, chord 3 vertical height and winglet mid-point sweep.
- Lift – winglet chord 3 twist, winglet mid-point sweep angle and toe 2 size.

Also, for Design – 3, the most sensitive variables amongst the 15 design variables considered during the optimisation study were (Fig. 108):

- Drag – winglet mid-point sweep, chord 3 twist angle and chord 1 twist.
- Lift – chord 1 twist angle, chord 3 twist and chord 1 size.

It was also worth considering the other parameters (variables) as mentioned in section 5.4 under Chapter 5 during the optimisation process because their inclusion has some significance to the performance of the designs. It also allows for a comprehensive sensitivity analysis to be carried out on the designs' design parameters (variables) to better understand their effect on the drag and lift aerodynamic forces on the wing.

This study had successfully demonstrated the versatility of using these devices over a wide range of Mach numbers and flight speeds. It also demonstrated that the wing tip devices can be retrofitted on other wing types and still retain their performance. The prior knowledge on retrofitting winglets, had suggested that winglets could only be retrofitted on wing types for which they are designed. i.e. they are wing design specific.

Also, based on the results that have been discussed in this chapter of the thesis, the findings from this research suggests that downward pointing winglets (Designs 1-3) are best suited for aerodynamic performance improvement of aircraft wings in the higher subsonic flight regime while upward pointing winglets (spiroid trapezium) are better suited for lower subsonic flight regime. The study also showed that they are most suitable for cruise flight phase. In practice, an aircraft cruise phase is the longest time over the course of the aircraft journey. Therefore, applications of these technologies could include use on long range to short range aircraft, low subsonic flight regime aircraft, miniature planes, UAVs. The production of these technologies could be carried out in a similar way to how conventional winglets are produced, and retrofitting should be possible with a preferred option being to incorporate the technologies into the wing at the manufacturing stage where possible.

The next section of this thesis is focused on the investigation on the use of wing tip turbines as a wing aerodynamic performance improvement device, in order to ascertain how much aerodynamic performance in terms of lift to drag ratio, lift and drag improvements with respect to a number of parameters. These includes the propeller nacelle position (the distance that the propeller is aft the wing trailing edge), direction of the propeller rotation, Mach number, angle of attack and the propeller rpm on these aerodynamic forces and force ratio. This therefore provides evidence and an understanding of the significance of using such an aerodynamic performance improvement device.

## **Chapter 6: Investigation on the use of wing tip turbine as a wing aerodynamic improvement device**

### **6.1. Introduction**

In this chapter, the CFD investigation carried out on a turbine which was mounted on the tip of an aircraft wing model is presented. First, a test case to validate the numerical method adopted for the simulations is discussed, before the CFD simulations to investigate the possible drag reduction, lift improvement and lift-to-drag ratio improvement of using the wing tip turbine is presented. Section 6.2 describes the validation of CFD modelling approach, Section 6.2.1 describes the geometry, mesh and physics models and boundary conditions, Section 6.2.2 presents the comparison of the CFD results with experimental data. Section 6.3 presents the wind tunnel experiment at UH and CFD validation model, Section 6.3.1 presents the test description and CFD modelling approach, Section 6.3.2 presents the force coefficients. Section 6.4 describes the investigated design configuration, Section 6.4.1 describes the mesh and computational approach, Section 6.4.2 presents the results for the effect of propeller nacelle, Section 6.4.3 presents the effect of the direction of propeller rotation on wing aerodynamic characteristics, Section 6.4.4 displays the effect of Mach number on the wing propeller nacelle performance, Section 6.4.5. presents the effect of angle of attack on propeller wing aerodynamic performance at take-off condition, Section 6.4.6. describes the propeller rpm effect on wing performance and Section 6.5 presents the conclusion of the study.

### **6.2 Validation of CFD modelling approach with SVA Potdam experimental data of a controllable pitch propeller**

To validate the CFD modelling approach adopted for the investigation using the turbine, experimental test case results produced by the German company SVA Potdam (Barkmann, 2011b) was replicated. The company specialises on propeller design, development and testing. The investigation was carried out on a controllable pitch propeller VP1304 with the results used as a benchmark in the Second International Symposiums on Marine Propulsors (SMP11) workshop in 2011(Barkmann, 2011a), (Barkmann et al., 2011), (Klasson and Huuva, 2011). The open water test case from the experiment was replicated for this study and the data obtained was compared against the CFD results under the same conditions and design configurations which has been is presented in this thesis. The geometry and test conditions adopted are presented in the following.

### 6.2.1. Geometry, mesh, physics models

Fig. 224 depicts an identical version of the propeller model (Potsdam, 2011). The boundary conditions used for the numerical calculations are also highlighted on the model. The mesh type adopted is the same as presented in section 4.2.2, the main modifications made to the meshing approach are the two regions of the simulation domain (as shown in Fig224b) were meshed separately. The mesh models used includes extruder mesh model within STAR-CCM+, Polyhedral mesh, surface remesher and prism layer mesh models. The physics models used for the CFD modelling are similar to the one discussed in section 4.2.2 and this includes the main physics models given as: SST (Menter) K-Omega Turbulence model (Menter, 1994), segregated flow solver, steady state, constant density, material used is water. Modifications were made to the orientation of the simulation domain, here, two domains are specified; one with the rotating parts which includes the propeller blade, nose, and the other with non-rotating parts which included, the nacelle and the simulation domain containing the walls, inlet and outlet. The rotating and static regions are coupled using an interface which allows for physics values to be exchanged and updated within each region see Fig.224.

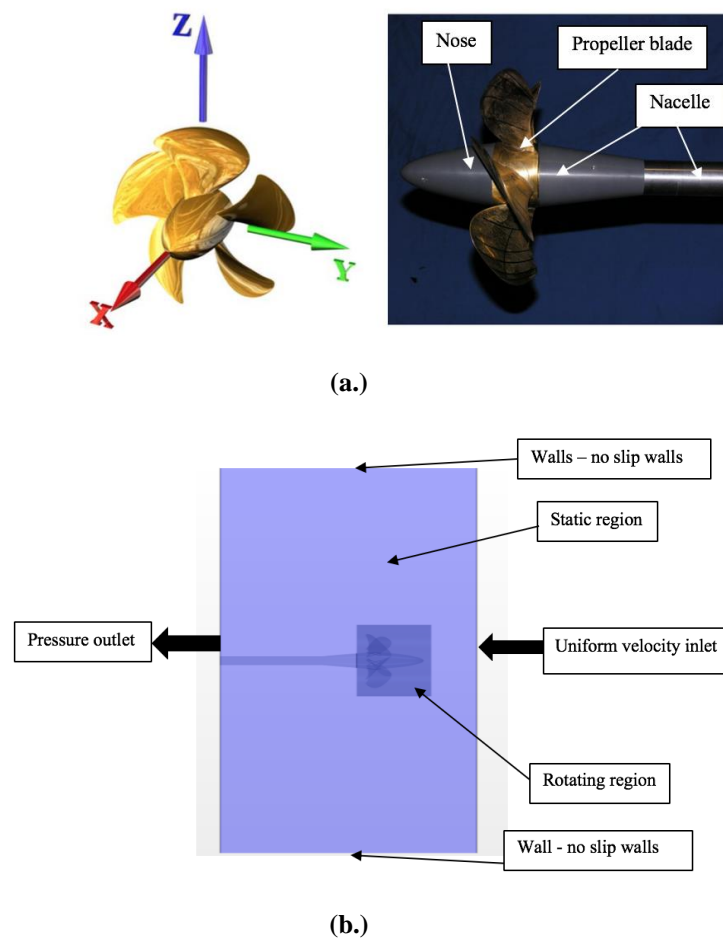


Fig. 157: (a.) Geometry (b.) boundary conditions

The values used in the boundary conditions and the initial propeller data to set-up the simulation are presented in Table 24. The propeller performance data consist of the advance coefficient, the torque coefficient, the thrust coefficient and efficiency. The velocity of the flow is driven by the advance coefficient,  $J$  (Houghton and Carpenter, 2003):

$$J = \frac{V_A}{nD} \quad (59)$$

$V_A$  is the advance velocity,  $n$  is the rate of revolution and the diameter of the propeller is  $D$

The thrust coefficient,  $K_T$  is given as (Houghton and Carpenter, 2003):

$$K_T = \frac{T}{\rho \cdot n^2 \cdot D^4} \quad (60)$$

$T$  is the thrust that is generated by the propeller,  $\rho$  is the density of the flowing fluid,  $n$  is the rate of propeller revolutions ideally written is revolutions per second and  $D$  is the propeller diameter.

The torque coefficient  $K_Q$  is defined as (Houghton and Carpenter, 2003):

$$K_Q = \frac{Q}{\rho \cdot n^2 \cdot D^5} \quad (61)$$

Where  $Q$  is the torque that is produced by the propeller.

The propeller efficiency is given as (Houghton and Carpenter, 2003):

$$\text{propeller efficiency} = \frac{J K_T}{2\pi K_Q} \quad (62)$$

**Table 24: Simulation initial conditions**

Parameter	Setting
$n$	15 rps
$D$	0.25 m
$V_A$	$J * n * D$ which
$J$	0.6 increment by 0.2 for every 500 iteration
water density $\rho$	1000 $\text{kg}/\text{m}^3$
$V_A$	2.25m/s, 3m/s, 3.75m/s, 4.5m/s and 6m/s

### 6.2.2. Comparison of CFD and experimental propeller performance data

The experimental propeller performance data was compared with the data obtained using CFD under similar conditions with both cases using water as their flowing fluid. Fig. 225 shows the correlation between the two set of data. The steady state CFD modelling approach adopted produces results showing good correlation with the experimental data obtained from (Potsdam, 2011). The  $K_Q$  and  $K_T$  are better predicted than the efficiency of the propeller. The numerical method employed for this case study was adopted for the subsequent investigation carried out on the wing with tip mounted turbine. A second test case study was carried out to validate the numerical approach by using a wind tunnel experiment carried out at the University of Hertfordshire (UH) and a CFD based model. This is discussed in more details in the next section.

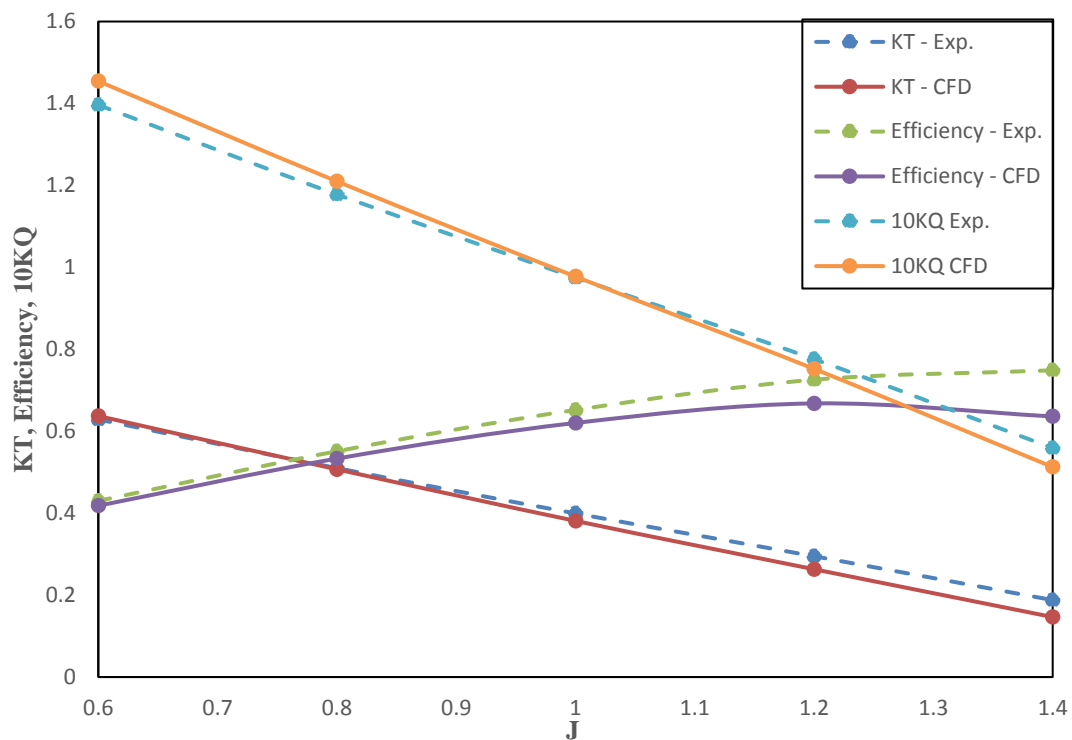


Fig. 158: Graph plot - Exp. (Barkmann, 2011b) and CFD propeller performance data

### 6.3. Wind tunnel experiment at UH and CFD validation model

A subsonic wind tunnel at the University of Hertfordshire was used for the experiment as shown in Fig. 226 (a.). The wind tunnel is closed loop and generates airspeeds in the range of 1- 24 m/s. The experiment was carried in a rectangular closed section 1.14 m by 0.83 m by 0.83 m. The forces and moments were measured by using an external balance. The model was set in the middle of the test section as shown in Fig.226. Incidence controlled by

moveable rear sting, this is shown in Fig. 226 (b.). The wind off conditions were set and it had aerodynamic force readings in the range of  $1-3\mu m$ . The data acquisition system takes readings over several seconds and then averages to reduce effect of noise on results. The wing and propeller specifications as well as the flow fluid conditions used for the study is shown in Table 25. Experiment at several angles of attack with the propeller configuration set in the pusher configuration and a clean wing only configuration was performed. A CFD model with identical configuration was carried out as well. The pusher configuration and not the puller was only considered because of the mounting system of the propeller and nacelle used which was better suited for the tractor position. Also, the aim of the experiment was for validation purpose, therefore, the pusher configuration data was deemed sufficient to obtain results which could be compared against the CFD data. The propeller rotation speed was measured by taking a video recording of the propeller rotation during the experiment which was then analysed using Android applications (Inshot – Video Editor and Video Marker, and Videoshop – Video Editor) to obtain the propeller revolution per second. The model set-up is presented in Fig.227, the mesh and physics models used are the similar to the one used in section 4.2.2 and the same in section 5.2.



(a.)

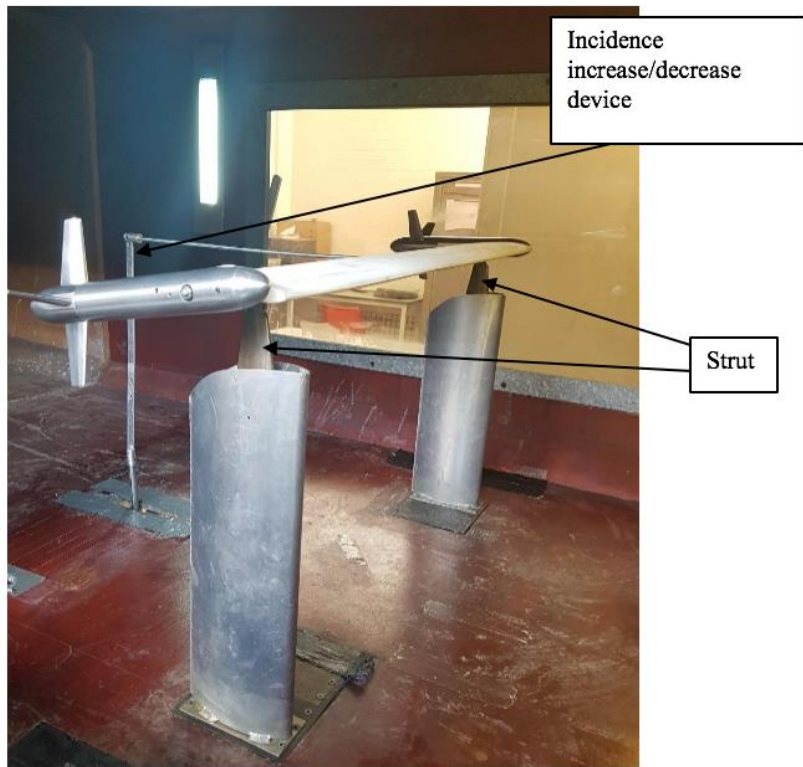
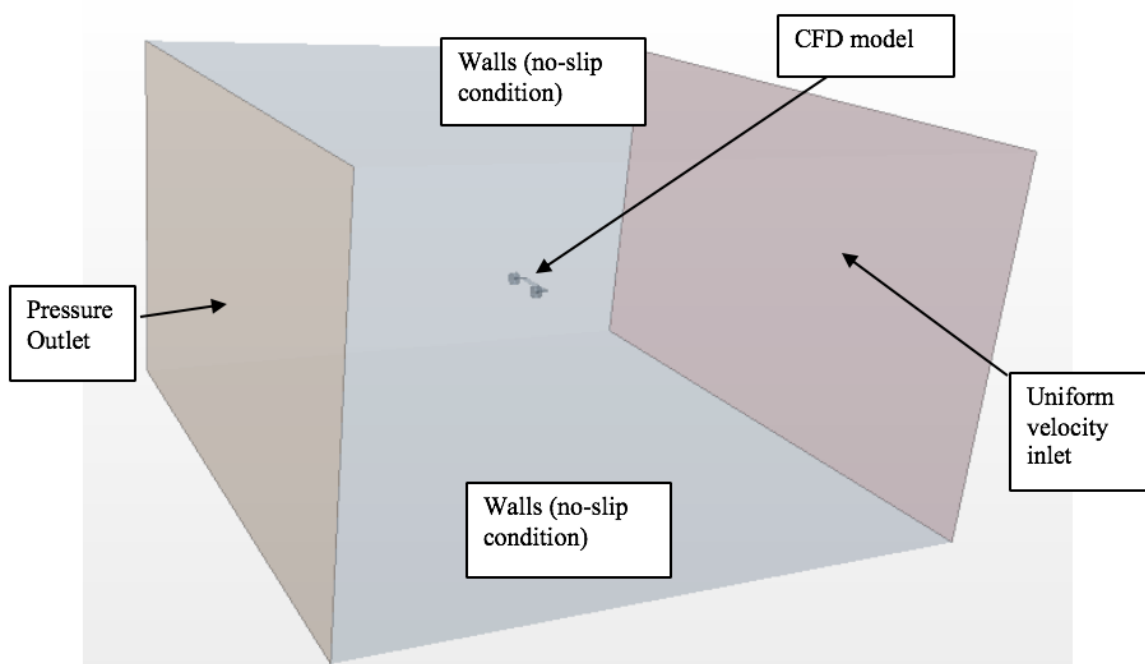
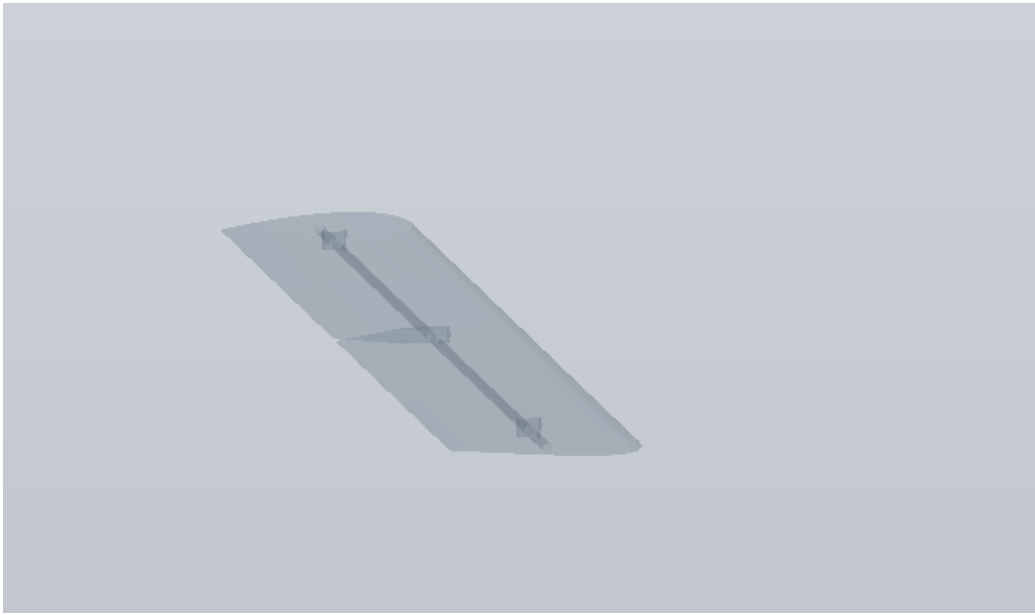


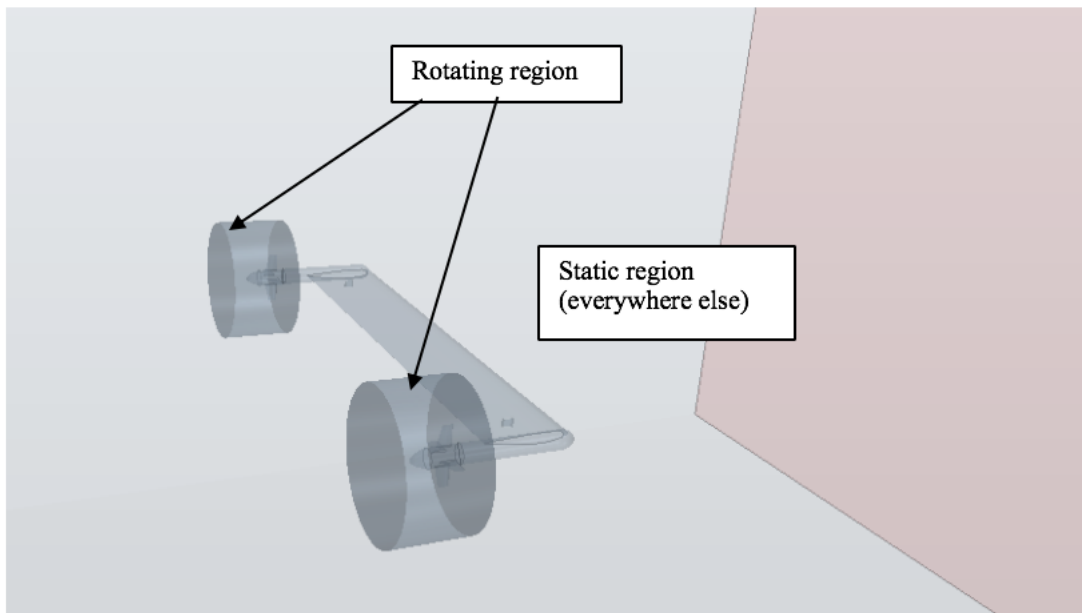
Fig. 159: (a.) wind tunnel set-up (b.) wind tunnel configuration showing the two strut and the incidence  
Strut



(a.)



(b.)



(c.)

**Fig. 160: CFD models (a.) simulation domain, (b.) clean wing (c.) wing plus propeller**

**Table 25: Wing and propeller specification**

Parameters	Wing	Wing plus propeller
Aerofoil	NACA2412	NACA2412
Wing span	0.71m	0.71m
Wing chord	0.123m	0.123m
Wing area	0.0873m <sup>2</sup>	0.0873m <sup>2</sup>
Wing platform	rectangular	rectangular
Blade	-	4
Propeller diameter	-	
RPM	-	760
Type of simulation	Steady state	Steady state and unsteady state
Velocity	15.6m/s	15.6m/s

### 6.3.1. Test description and CFD modelling approach

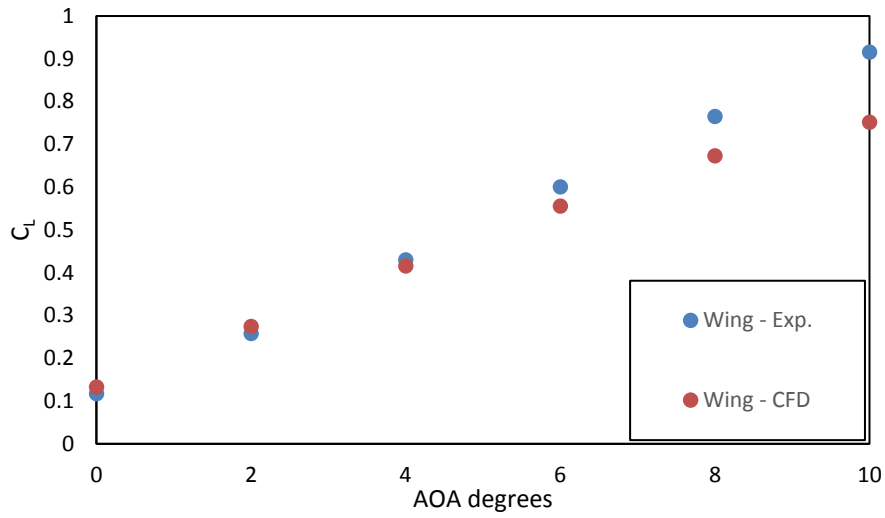
The results that were obtained from the experiment was compared with those from the CFD simulations. The wing was 3-D printed using ABS plastic with a surface finish (roughness) of  $200\mu\text{m}$ ; this value was taken into consideration in the CFD runs. The surface roughness value was obtained from the general surface finish for products printed using an ABS plastic material and was made available by the 3D printing company (3D ALCHEMY). The model was placed in the centre of the test section, with the aerodynamic forces measured by the external 3-axis force balance which was then transmitted by transducers to the lab software (Key sight VEE program) were the data was processed and stored.

For the CFD model, a full-scale model similar to the wind tunnel wing model and propeller was used, a half body model could also be used since the flow is symmetrical. The simulation domain was split into three regions with two rotating regions (containing the propeller blade, nose and hub) and one static region (wing and nacelle) as shown in Fig. 227. An internal interface was created between the rotating and static regions to allow for the exchange of physics values (pressure, velocity etc.). For the steady state simulation, the rotating motion was modelled by using the Moving Reference Frames technique in STARCCM+. This technique does not change the position of the cell vertices but rather it imposes the forces that are induced by the rotation. It gives a solution that represents the time averaged solution/ characteristics of the flow. The unsteady simulation was performed by employing the Rigid Body Motion method in STAR-CCM+; this technique is used to move rigidly the rotating region and mesh at a fixed displacement per time step, thus it is a transient simulation which considers the transient flow effect of the blades on the wing. A second order temporal discretization scheme was used with a time step of 0.00023 seconds corresponding to a one-degree movement of the blades. To account for surface roughness in STAR-CCM+, the wall surface specification was changed to rough with the roughness height specified at  $200\mu\text{m}$ .

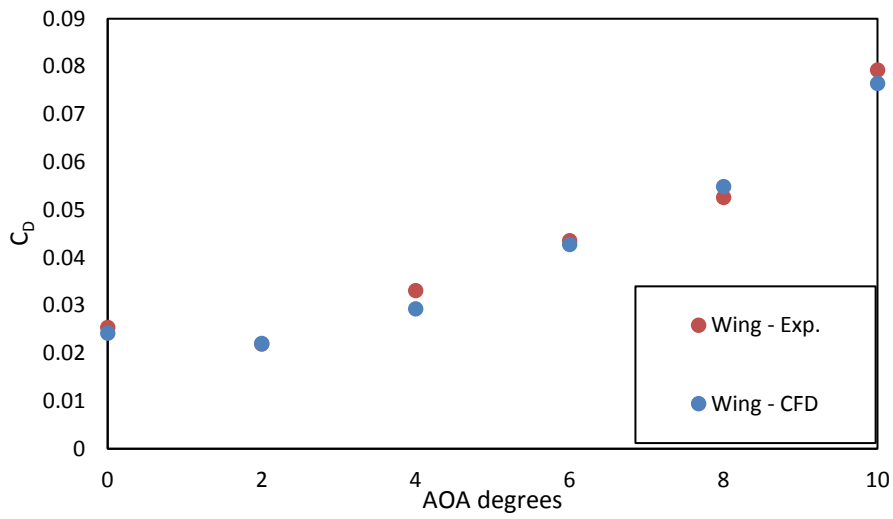
### 6.3.2. Force coefficients

Fig. 228 shows the comparison of the wind tunnel data against the CFD simulation data for both steady and unsteady runs. The results were obtained for  $C_L$  and  $C_D$  at several angles of attack (AOA). From analysing the plots, there is a good correlation between the wind tunnel results and the CFD results. This was more prominent at lower angles of attack for  $C_L$  as shown in Fig. 228 (a.) and (c.). The correlation for  $C_D$  values was consistent across all angles of attack (see Fig. 228 (b.) and (d.)), although CFD slightly under predicted this value at higher AOA. The discrepancies in the results can be attributed to the surface roughness/finish on the wing model from 3D printing. A  $200\mu m$  roughness height was used in the CFD models as mentioned earlier in section 5.3.1. This value was taken based on the general roughness height of 3D printed models which is usually within  $200\mu m$ . The presence of this roughness creates a more distorted and energetic flow region near the walls which becomes more prominent at higher AOA, CFD modelling tends to under – predict instabilities in flows. Also, for the work done in this thesis, low angles of attack of  $4^\circ - 6^\circ$  is of most importance anyways and the results correlate well for these angles.

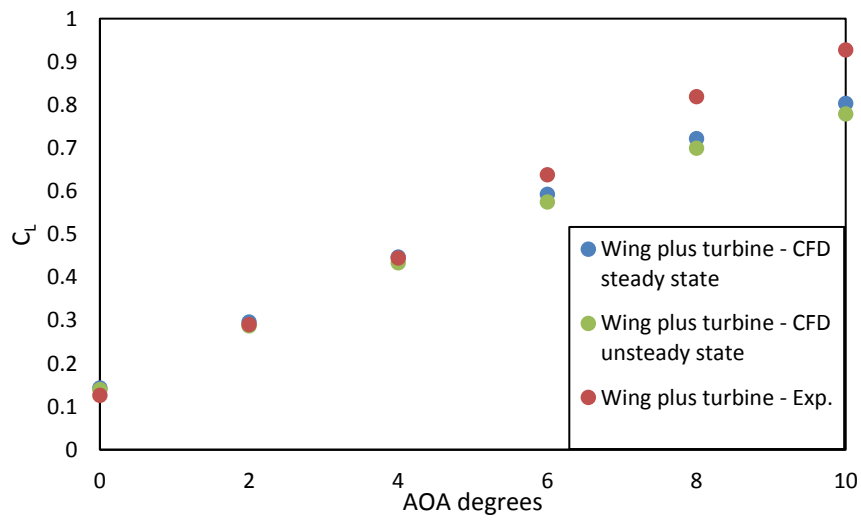
Furthermore, the steady and unsteady runs did correlate well with each other and the wind tunnel results with the data for the unsteady run slightly under predicting the wind tunnel data. All the same, it gives the indication that either method can produce good results. These methods were adopted for the CFD investigation carried out in the rest of this chapter.



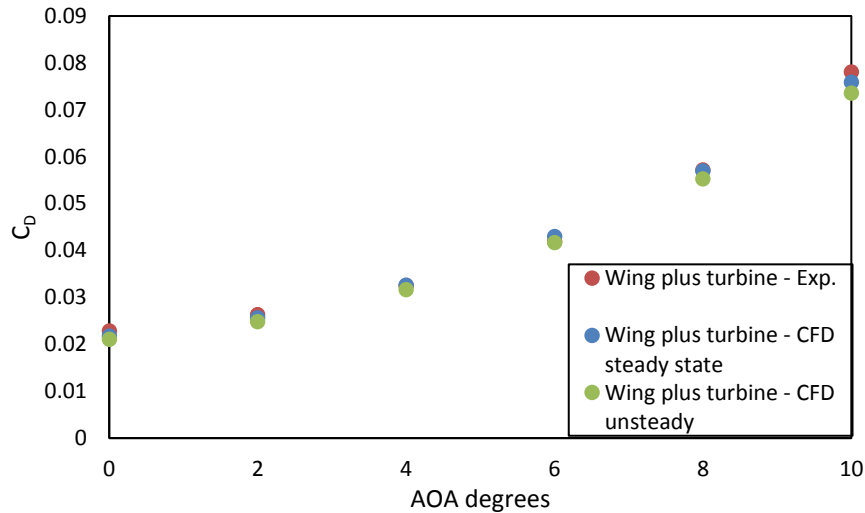
(a.)



(b.)



(c.)



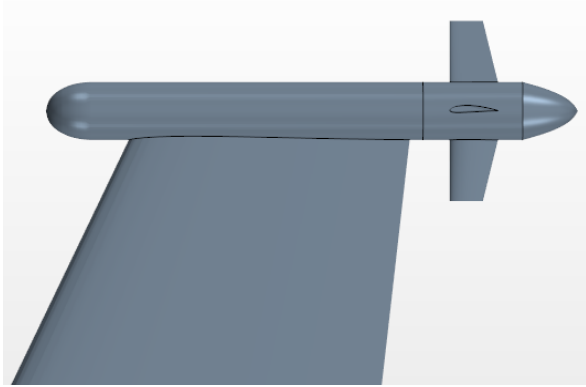
(d.)

**Fig. 161: Force coefficients (a.) Wing  $C_L$  from experiment and CFD (b.) Wing  $C_D$  from experimental and CFD (c.) Wing plus turbine  $C_L$  from experimental and CFD (steady and unsteady) (d.) Wing plus turbine  $C_D$  from experimental and CFD (steady and unsteady),**

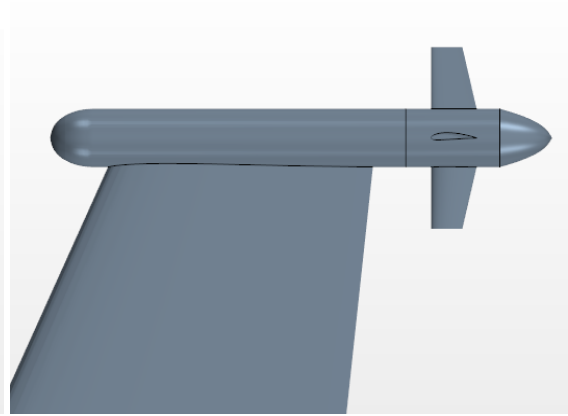
#### 6.4. Investigated design configuration

The investigated design configuration for the wing with mounted propeller at the tip is shown in Fig. 229. The following test conditions were considered:

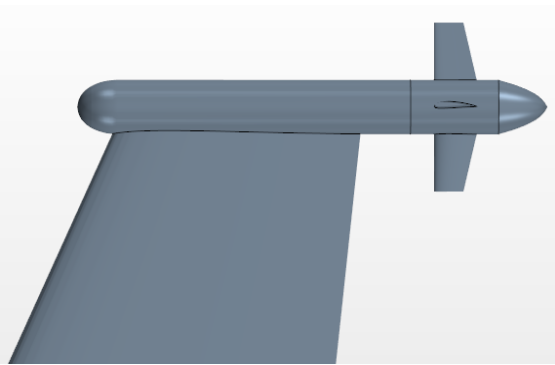
- The effect of propeller nacelle position on wing aerodynamic performance, this considers the distance that the propeller is aft of wing trailing edge.
- The direction of propeller rotation on wing aerodynamic characteristics.
- The effect of the Mach number on the wing propeller nacelle performance.
- Effect of angle of attack on propeller wing aerodynamic performance.
- Propeller RPM effect on wing performance.



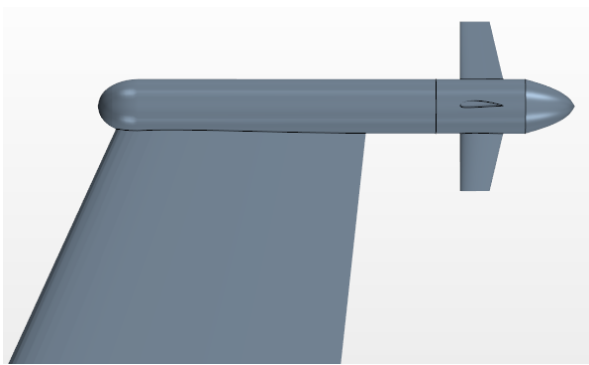
(a.)



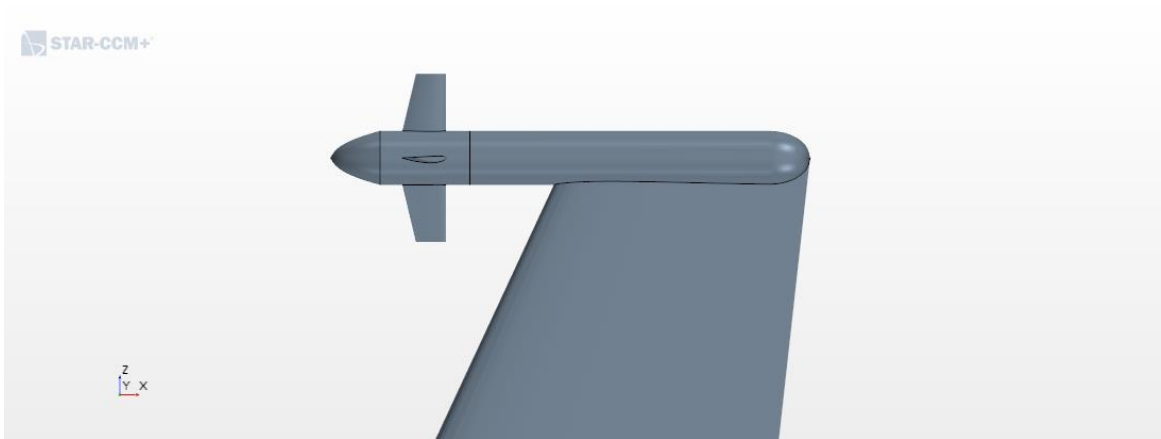
(b.)



(c.)



(d.)



(e.)



(f.)

**Fig. 162: Top view – the main difference in these is the distance that the propeller is aft the wing trailing edge (a.) propeller nacelle position 1 (b.) propeller nacelle position 2, (c.) propeller nacelle position 3, (d.) propeller nacelle position 4, (e.) propeller nacelle tractor position, (f) far view of configuration- propeller on wing tip**

In Fig. 229 (a), the distance that the propeller is aft of the wing trailing edge is 0.6m, Fig. 229 (b) shows this distance at 0.7m, Fig. 229 (c) shows it at 0.8m and Fig. 229 (d) depicts the configuration at 0.9m for the propeller distance aft of wing trailing edge.

The wing design that was used for this study is similar in specifications to that was used in section 4.3. The propeller design specifications and test conditions are given in Table 26.

**Table 26: Propeller design specification and test initial conditions.**

Parameters	
Nacelle	1.75m
Propeller diameter	0.86m
Hub length	0.46m
Nose length	0.28m
NACA	4412
Propeller nacelle positions	Position 1 – 4 and tractor propeller configuration
Angle of attack	0 – 10 degrees.
RPM studied	5000rpm – 9000rpm
Direction of propeller rotation	Clockwise and anti-clockwise rotations

#### 6.4.1. Mesh and computational approach

The mesh type is identical to that used in section 3.5 and section 5.3.1, the mesh setting used is given in Table 28. To determine the accuracy of the CFD solution, a mesh convergence study was performed on the wing design. The study was carried out using three different grids; medium, fine and very refined grids to predict the aerodynamic force coefficients  $C_D$  and  $C_L$ . The number of points/elements and corresponding force coefficient values are presented in Fig. 230 – Fig. 231 and are also shown in Table 27. The study revealed that a mesh count of 12 million was sufficient to produce a sufficiently high fidelity CFD result for this study.

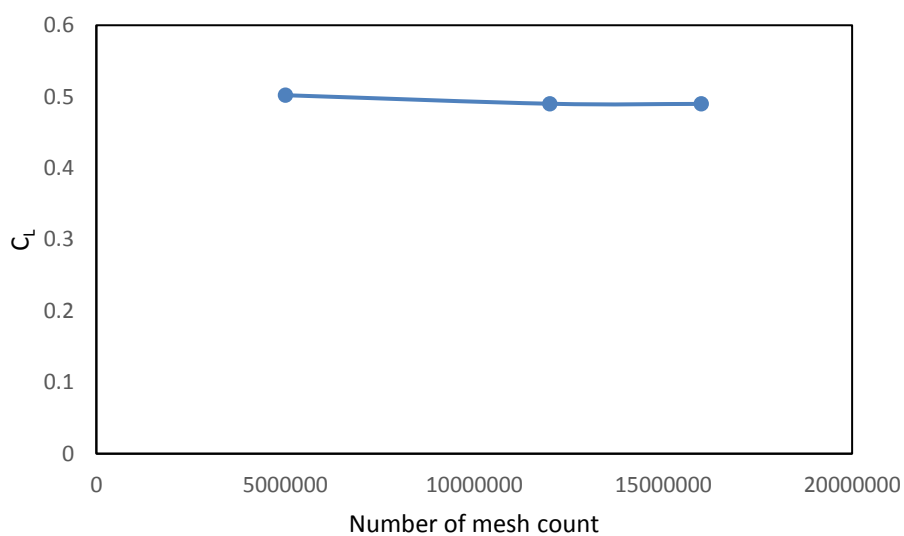


**Fig. 163: Coefficient of lift mesh dependency study**

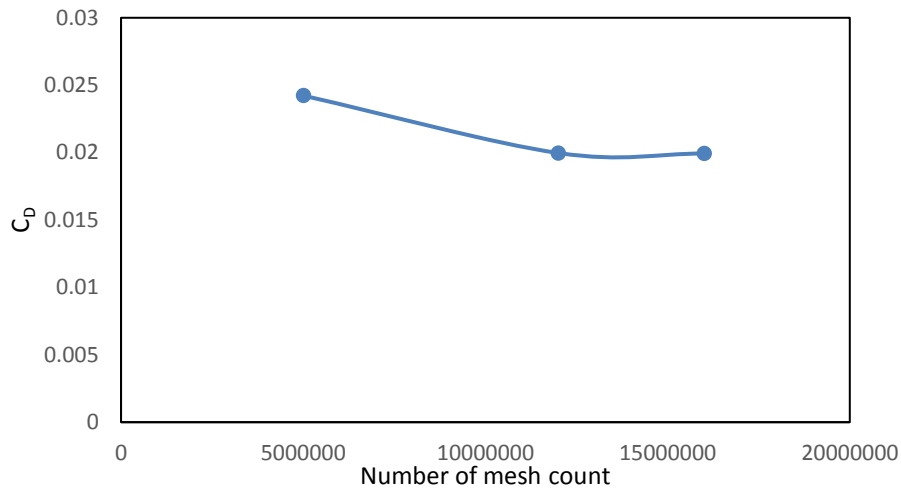


**Fig. 164: Coefficient of drag mesh dependency study**

**Table 27: Coefficient of lift and drag mesh dependency study**

Parameters	5x10 <sup>6</sup> (Medium mesh)	12 x 10 <sup>6</sup> (Fine mesh)	16x10 <sup>6</sup> (Very fine mesh)
C <sub>L</sub>	0.5020	0.49007	0.48987
C <sub>D</sub>	0.0242	0.01996	0.01993

**Table 28: Mesh settings**

Mesh parameters	
Mesh base size	0.1m
Surface refinement	25% of mesh base size
LE refinement	12% of mesh base size
TE refinement	12% of mesh base size
Number of prism layers	10
Total number of mesh count	12 million

The boundary conditions adopted for the simulation are shown in Fig. 232, and as was done in the test cases, the simulation domain was split into two regions: the static region and the rotating region with an interface coupling the two regions together allowing for the exchange of physics values. The rigid body modelling technique was applied for the unsteady simulation. In the rigid body motion, an unsteady motion problem is transformed to a steady state problem by imposing a moving reference frame on a static mesh, this method also allows moving the mesh vertices of a region during a transient simulation. The turbulence models and physics models employed for these simulations are the same as in section 4.2.2 which includes the main physics models as SST (Menter) K-

Omega turbulence model, ideal gas due to high speed and Mach numbers was used, material is air, all  $y^+$  wall treatment as well as coupled flow solver in STAR-CCM+ was also used. Both steady and unsteady state simulations were performed, for the unsteady state simulation, the time step is specified based on the time taken to complete  $1^0$  rotation of the propeller blades with a total time for 5 complete revolutions used. The number of revolutions per second was 116.7 rev/sec (7000rpm). It took 0.0086 seconds to complete one revolution and 0.000024 seconds to make a  $1^0$  rotation of the propeller blades and  $2^{\text{nd}}$  order temporal discretisation was also employed as before.

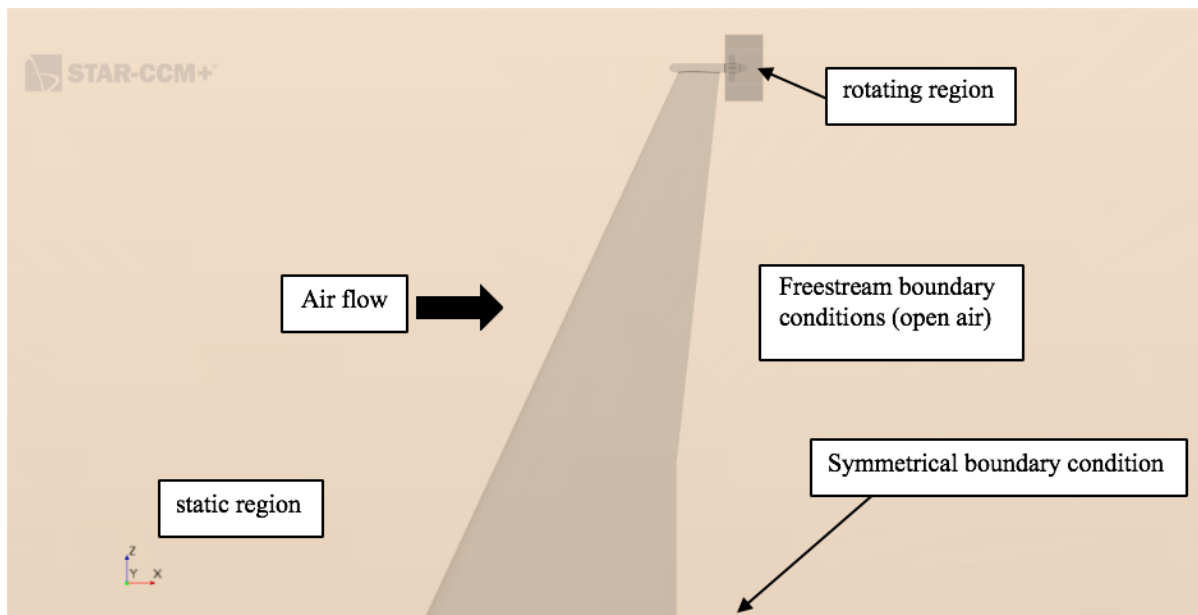


**Fig. 165: Simulation domain with boundary conditions**

#### **6.4.2. Results for the effect of propeller nacelle position on wing aerodynamic performance**

The steady state results obtained for the sensitivity of the propeller nacelle position as shown in Fig. 229 at the wing tip section at Mach 0.64 are presented in Table 29 (a). Based on the information in Table 29 (a), the propeller nacelle position 1 had the best performance in terms of  $C_D$  reduction with a value close to 1 percent and  $C_L / C_D$  improvement of up to 4.3 percent. Also, propeller nacelle position 2 had the best  $C_L$  improvement by up to 3.3 percent as shown in Table 29 (b). The results showed that the closer the propeller to the rear of the wing tip, the better the aerodynamic performance observed on the wing. Furthermore, the propeller nacelle pusher configuration was found to be better than the propeller nacelle tractor configuration based on the aerodynamic performance criteria used in this study.

**Table 29 (a): Propeller nacelle sensitivity to aerodynamic force coefficients and  $C_L/C_D$  ratio, the results for steady state simulation**

Parameters	Clean wing	Propeller nacelle position 1	Propeller nacelle position 2	Propeller nacelle position 3	Propeller nacelle position 4	Propeller nacelle - tractor position
$C_L$	0.4740	0.490075	0.490085	0.4897	0.4893	0.4788
$C_D$	0.02012	0.01996	0.01998	0.019987	0.01997	0.02017
$C_L/C_D$	23.5499	24.5420	24.51959	24.5055	24.4961	23.7397
$C_{D_{induced}}$	0.00720	0.006611	0.0065	0.006493	0.006481	0.00620

**Table 29 (b): Propeller nacelle sensitivity to aerodynamic force coefficients and  $C_L/C_D$  ratio, the results for steady state simulation showing percentage improvements**

Parameters	Clean wing - % improvement	Propeller nacelle position 1 - % improvement	Propeller nacelle position 2 - % improvement	Propeller nacelle position 3 - % improvement	Propeller nacelle position 4 - % improvement	Propeller nacelle - tractor position - % improvement
$C_L$	0	3.4%	3.4%	3.3%	3.2%	1.0%
$C_D$	0	0.8%	0.7%	0.7%	0.7%	0.25%
$C_L/C_D$	0	4.2%	4.1%	4.0%	4.0%	0.8%
$C_{D_{induced}}$	0	8.2%	9.7%	9.8%	10%	13.8%

**Table 30: Propeller nacelle sensitivity aerodynamic force coefficients and  $C_L/C_D$  ratio, the results for the unsteady state simulation**

Parameters	Clean wing	Propeller nacelle position 1	Propeller nacelle position 2	Propeller nacelle position 3	Propeller nacelle position 4	Propeller nacelle - tractor
$C_L$	0.4740	0.49003	0.49004	0.48974	0.48928	0.47879
$C_D$	0.02012	0.01982	0.019847	0.019847	0.019836	0.020029
$C_L/C_D$	23.5499	24.7131	24.6905	24.6763	24.6669	23.9051
$C_{D_{induced}}$	0.00720	0.00661	0.00650	0.00649	0.00648	0.0062

Table 30 describes the unsteady state simulation results obtained after 5 complete revolutions, a comparison with the state steady solutions in Table 29 (a), gives good correlation with a difference of 0.2 percent for  $C_L$  and 0.4 percent for the  $C_D$ . Based on this, it was assumed that a steady state simulation was sufficient to obtain reasonably

accurate solutions to this type of fluid problem. The next section of this report discussed the effect of the direction of rotation of the propeller blades on the aerodynamic force coefficients.

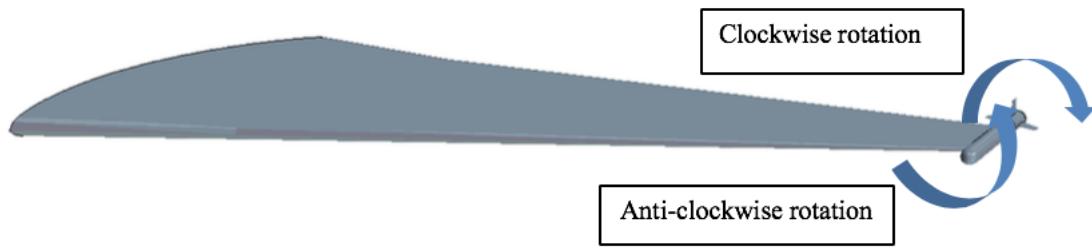
### 6.4.3. The effect of the direction of propeller rotation on wing aerodynamic characteristics

Fig. 233 gives an illustration of what is considered clockwise and anti-clockwise rotation in this study, the direction of rotation has a significant impact on how the rotating propeller interacts with the wing. This is because, the radial velocity component formed by the rotating blades contributes towards the pressure distribution on and around the wing thereby affecting the aerodynamic characteristics of the wing. Fig. 234 shows the velocity of the rotating blade; the direction of rotation is indicated by the velocity vector. The corresponding vorticity distribution experienced at the rear of the wing is shown in Fig. 235. Both sets of propeller rotation (clockwise and anti-clockwise) produced an expanded vortices distribution when compared with the one from the clean wing. In Fig. 236, the lift per unit span on the clean wing and wing with propeller are shown. Based on the analysis of the plot, the wing lift is improved across all parts of the wing, thereby giving suggesting that the force field created by the turbines does not only affect the wing tips but also all parts of the wing. Of course, as expected, the most significant changes are detailed around the wing tip region.

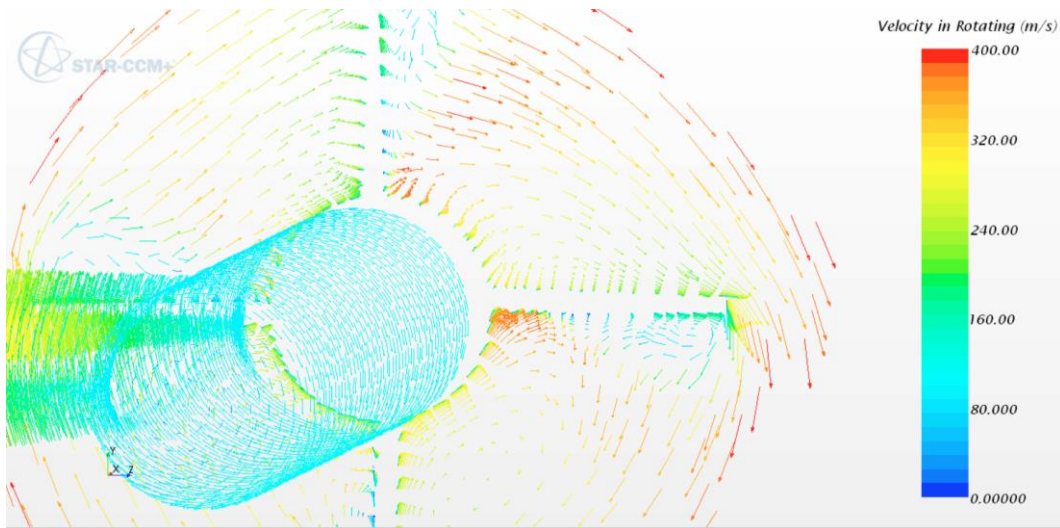
Table 31 presents the performance data for the clockwise and anti-clockwise rotation compared with that of the clean wing at Mach 0.64, and the results demonstrates the clockwise propeller rotation had a better overall performance. Because of these findings, only the clockwise rotation set-up was considered for the remaining part of this investigation.

**Table 31: Results clockwise and anti-clockwise rotation**

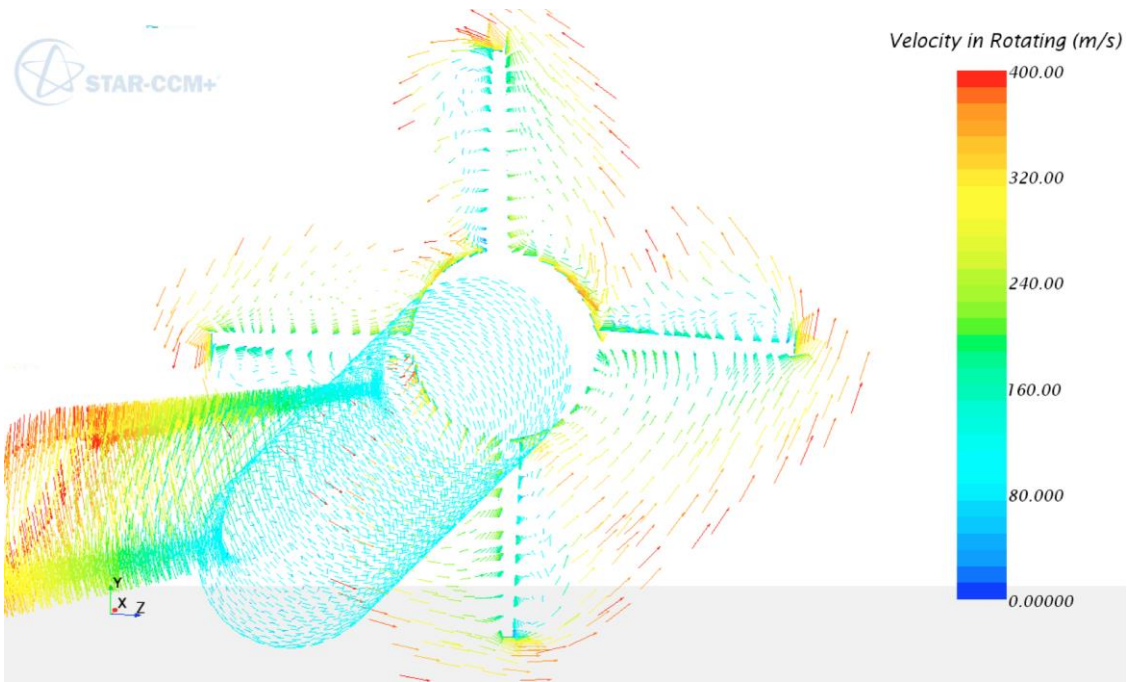
Parameters	Clean wing	Propeller nacelle clockwise rotation	Propeller nacelle anticlockwise rotation
$C_L$	0.4740	0.490075	0.48910
$C_D$	0.02012	0.01996	0.02010
$C_L/C_D$	23.5499	24.7131	24.4278
$C_{D_{induced}}$	0.00720	0.006611	0.006475



**Fig. 166: Wing and propeller geometry with rotation directions**

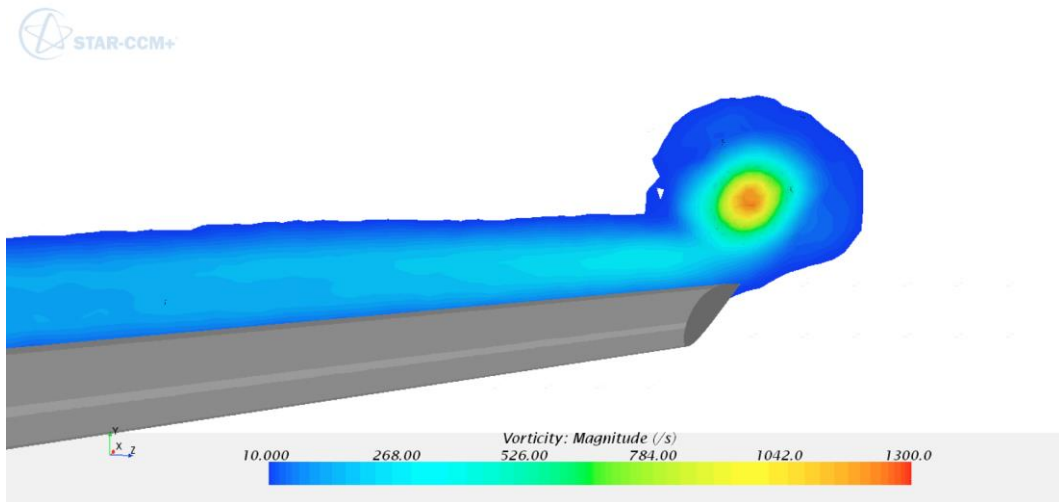


(a.) clockwise

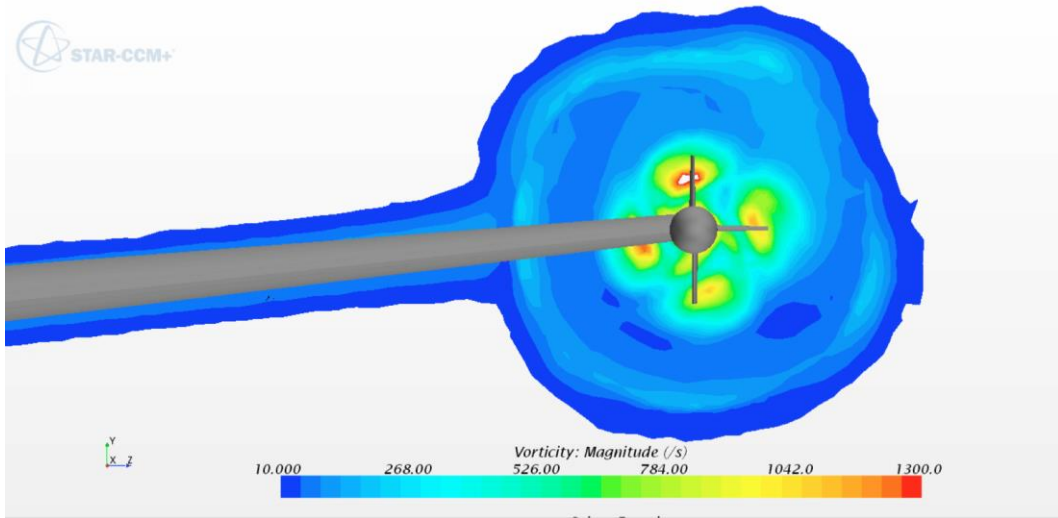


(b.) Anti – clockwise

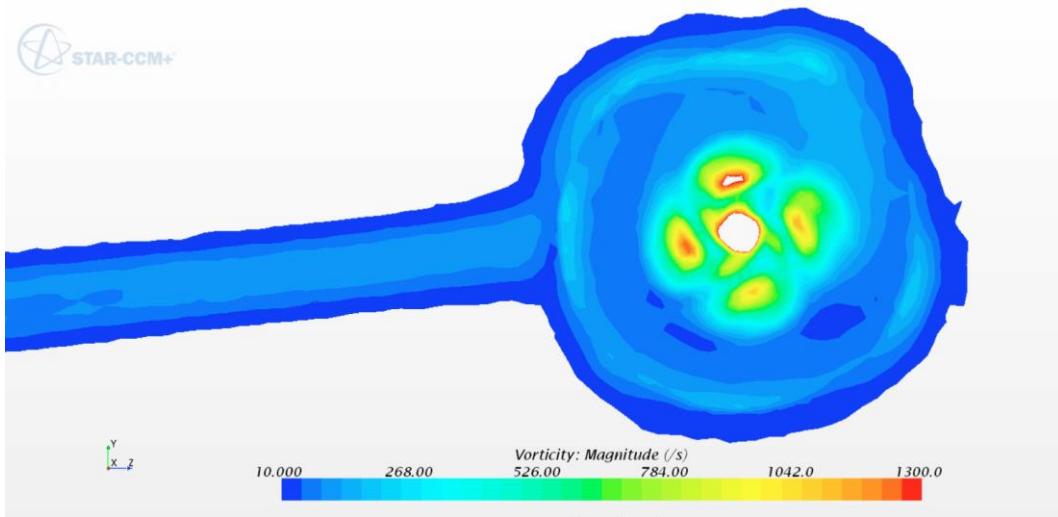
**Fig. 167: Velocity component of the rotating region – showing direction of blade rotation**



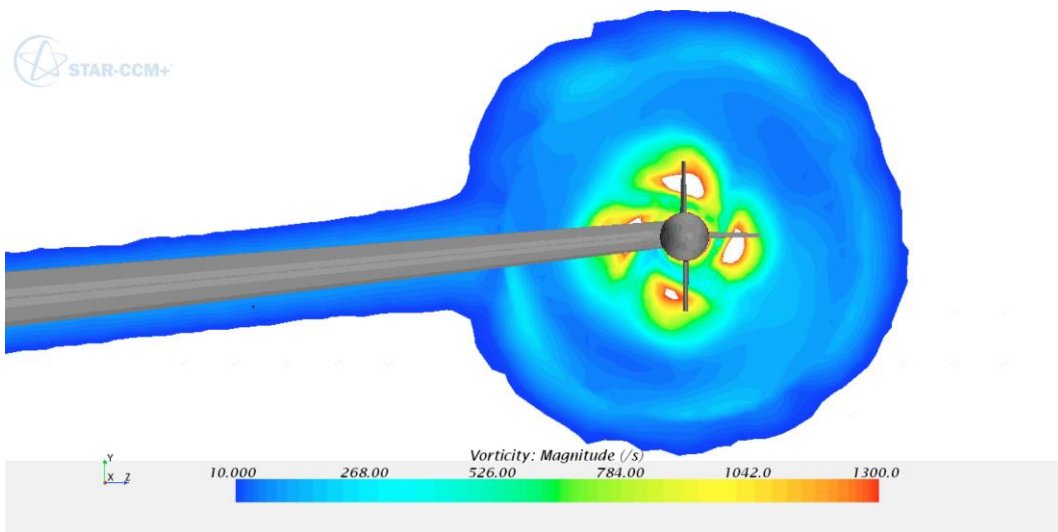
(i.) Clean wing – vorticity



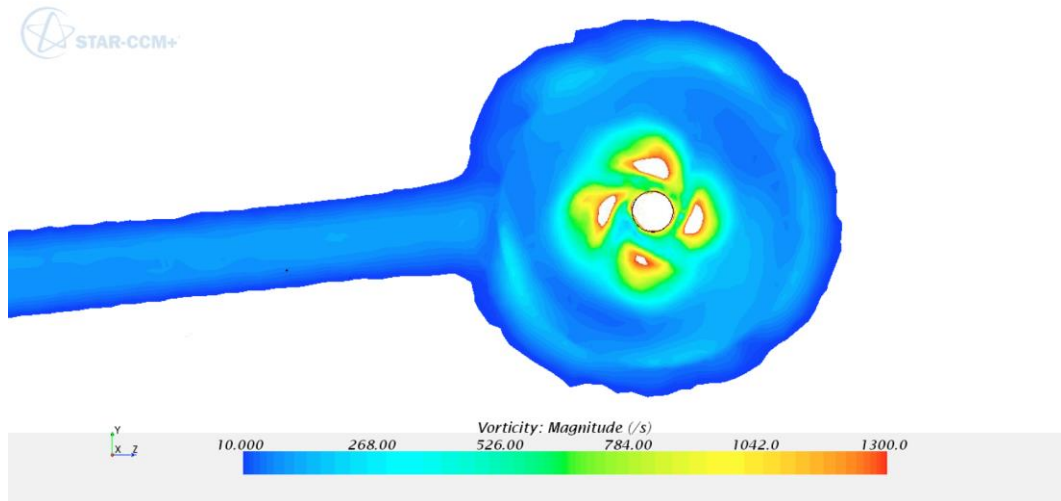
(ii.) Clockwise - rotation - vorticity



(iii.) Clockwise - rotation - vorticity



(iv.) Anti - clockwise rotation - vorticity



(v.) Anti – clockwise rotation – vorticity

**Fig. 168: Direction of rotation – Vorticity**

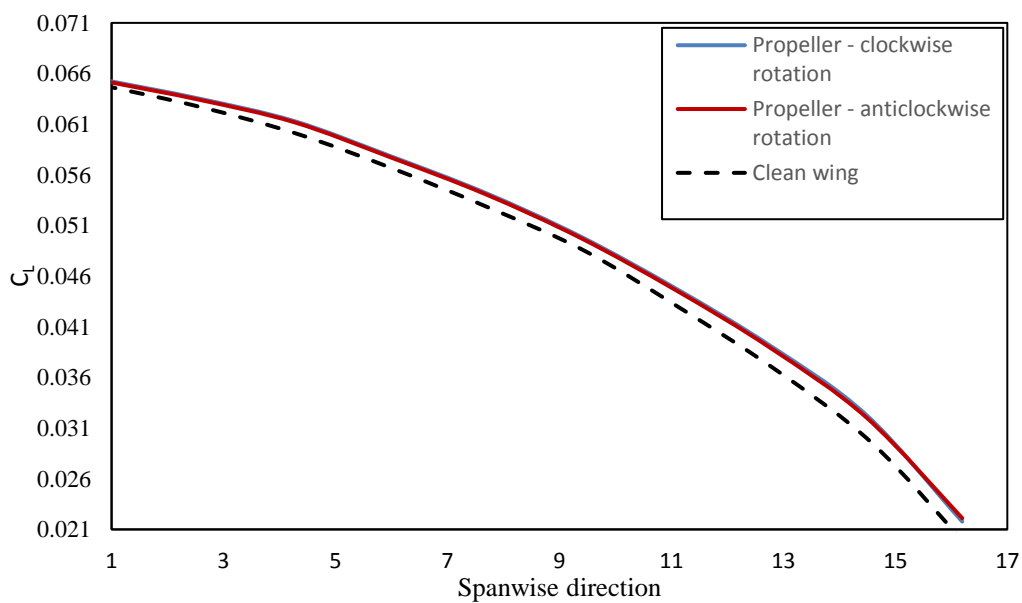


**Fig. 169: Lift per unit span**

#### 6.4.4. The effect of the Mach number on the wing propeller nacelle performance

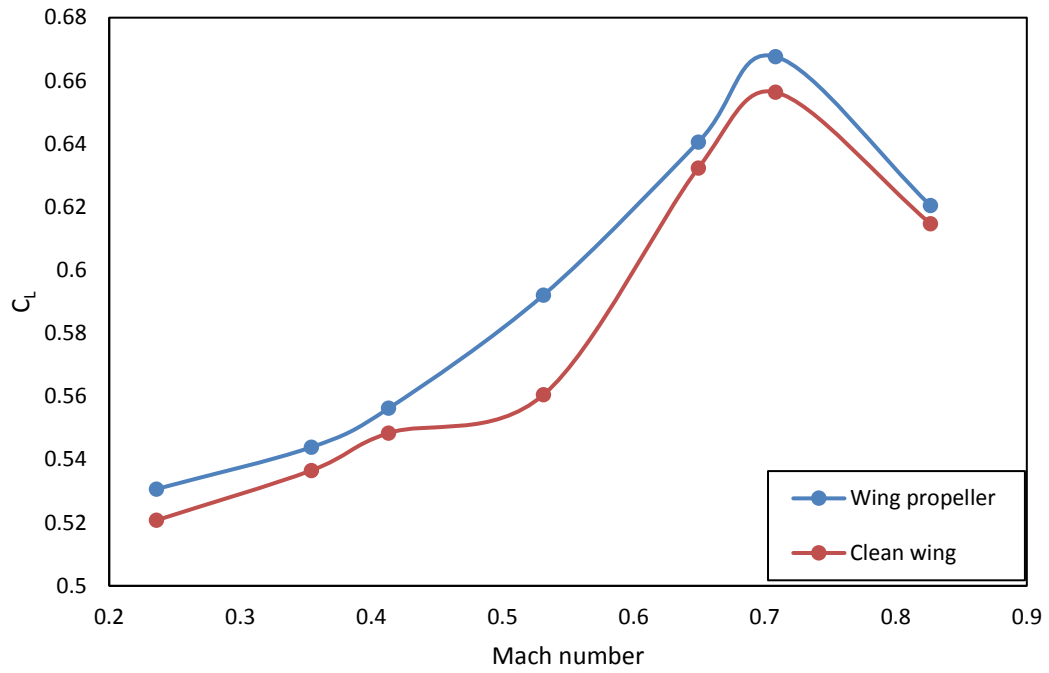
Fig. 237 depicts  $C_L$  against Mach number for the clean wing and wing propeller configuration. Analysis of the graph showed a consistent improvement in the  $C_L$  by using the propeller. The propeller is most effective in improving  $C_L$  between  $M_\infty$  0.44 – 0.64 with the maximum modification revealed at  $M_\infty$  0.54 at up to 5.6 percent.

The coefficient of drag ( $C_D$ ) for the clean wing and the wing propeller configuration is shown in Fig. 238, and up to 3.2 percent reduction in  $C_D$  was obtainable at  $M_\infty$  0.24 and at higher  $M_\infty$  0.74 – 0.84,  $C_D$  was increased by up to 2 percent. The reasons for this, are the high speed experienced by the propeller and the increased pressure on the wing due to the presence of shock waves which is typically present at or just before the critical Mach number (Anderson Jr, 2010). In Fig. 237 and Fig. 238, the critical Mach number occurred slightly past  $M_\infty$  0.64. Also, the clean wing is shown to have been able to better handle this condition.

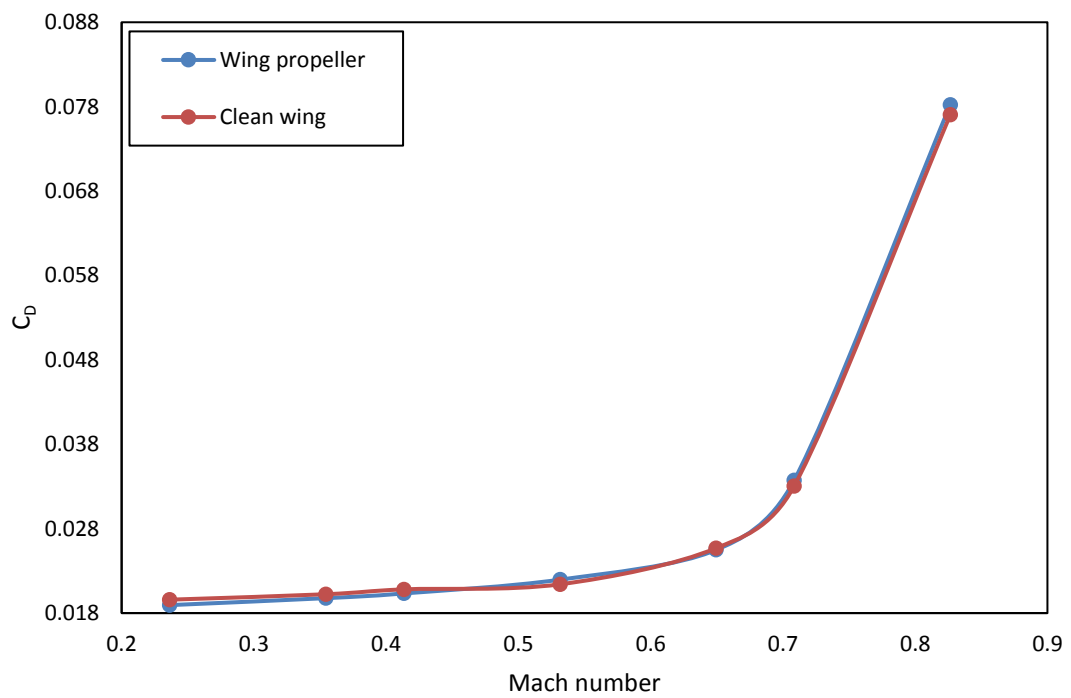
Fig. 239 shows  $C_L/C_D$  ratio, and an analysis of the graph illustrated that  $C_L/C_D$  ratio of the clean wing was modified by up to of 5.4 percent at Mach 0.24.

Fig. 240 shows the velocity experienced on and around the propellers, there is a gradual increase in speed by a magnitude of 9 – 10 velocity value for each Mach number with the exception of Mach 0.84 where this value is increased by almost 60. The speed around the propeller tip for Mach 0.74 – 0.84 were within the supersonic speed regime. This is due to the rotating velocity component from the propellers combining with the free stream velocity, thereby creating a higher resultant velocity component.

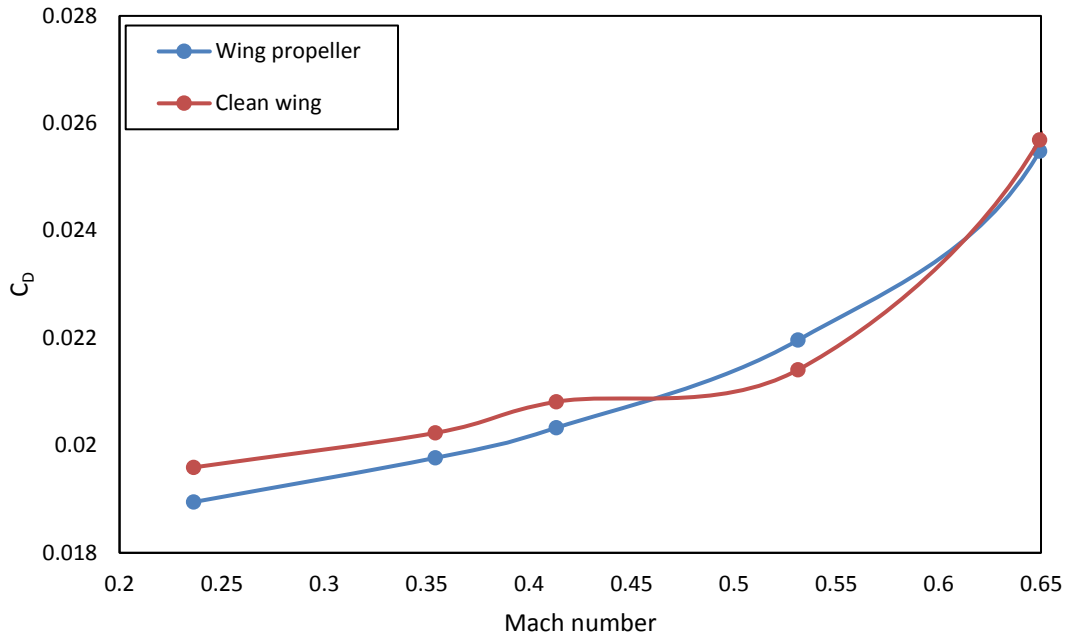
Fig. 241 shows the pressure distribution on the top and bottom surfaces of the wing under various conditions. Here one can observe a gradual increase in the area covered by a lower pressure region on the top surface and also an increase in a higher-pressure region at the bottom surface. This effect results an increase in lift as the Mach number increased as shown in Fig. 237. An increase in  $C_L$  is expected to produce an increase in the  $C_{D\text{induced}}$ , thereby subsequently increasing  $C_D$  value obtained. Fig. 242 shows the contour of the skin friction on the wing, from these, it is observed that a wider area of the wing experienced a lower skin friction as the Mach number increase with this being most noticeable at Mach 0.74 – 0.84, thereby highlighting that the major contributor to  $C_D$  as the  $M_\infty$  is increased was the increased pressure drag, this is also in agreement with (Anderson Jr, 2010), (Anderson, 1999).



**Fig. 170: Coefficient of lift as a function of Mach number**



(a.)



(b.)

**Fig. 171: (a.) Coefficient of drag as a function of Mach number for all studied cases (b.) Coefficient of drag as a function of Mach numbers < 0.65**

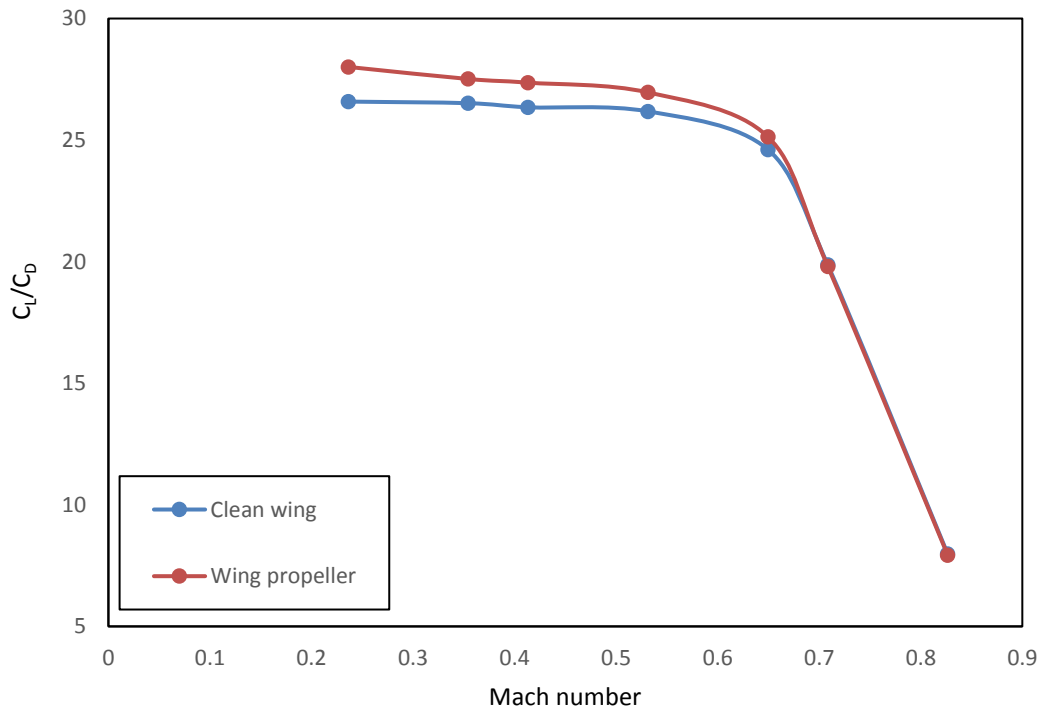
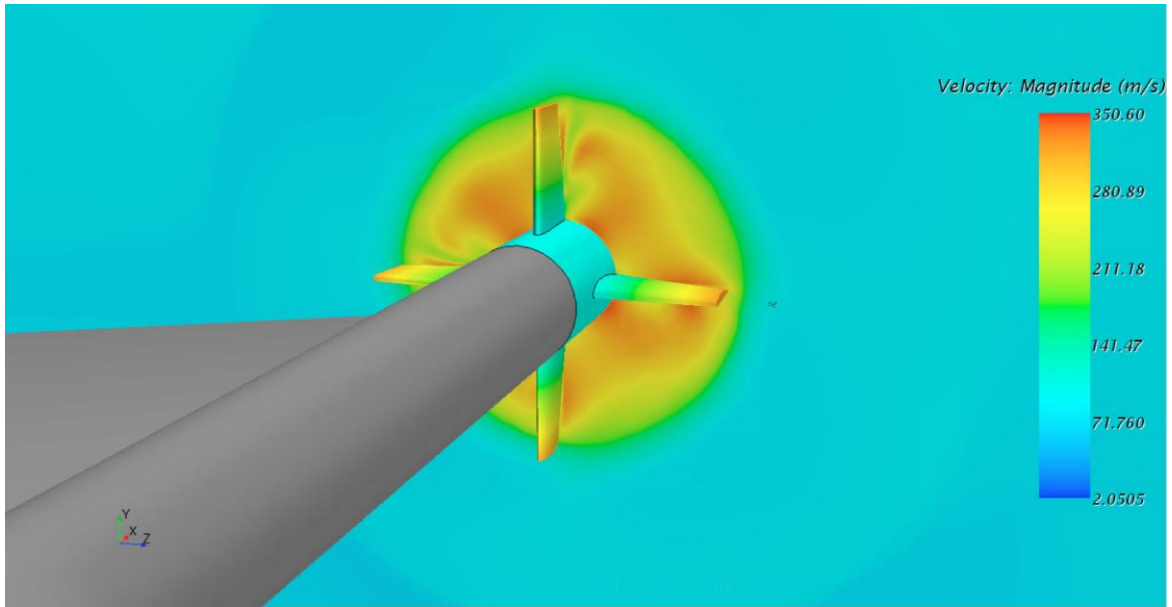
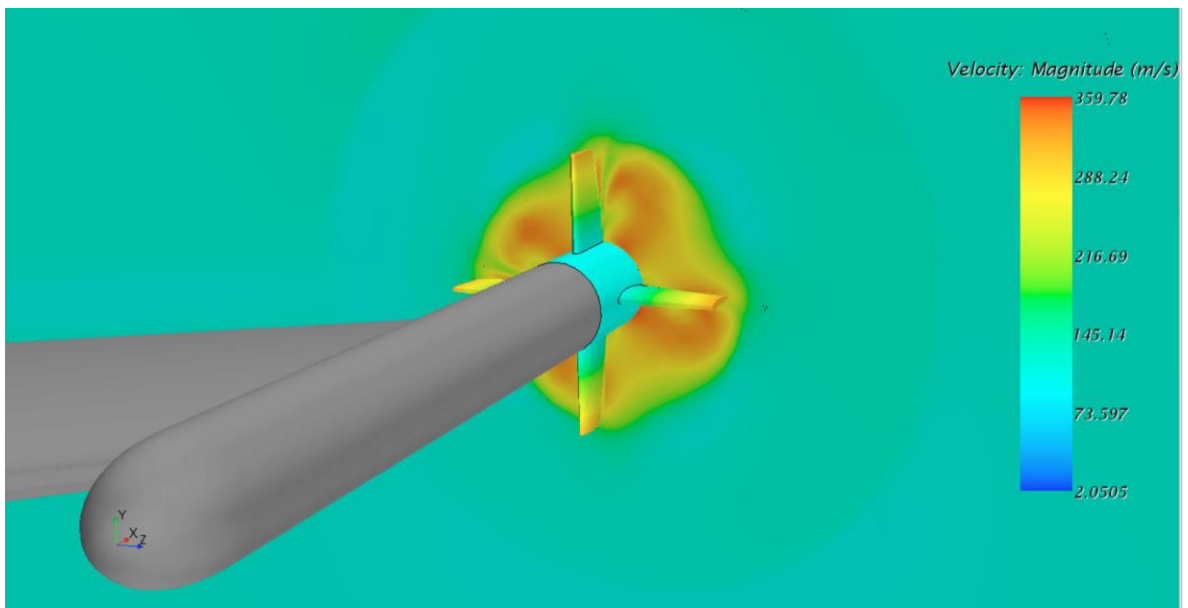


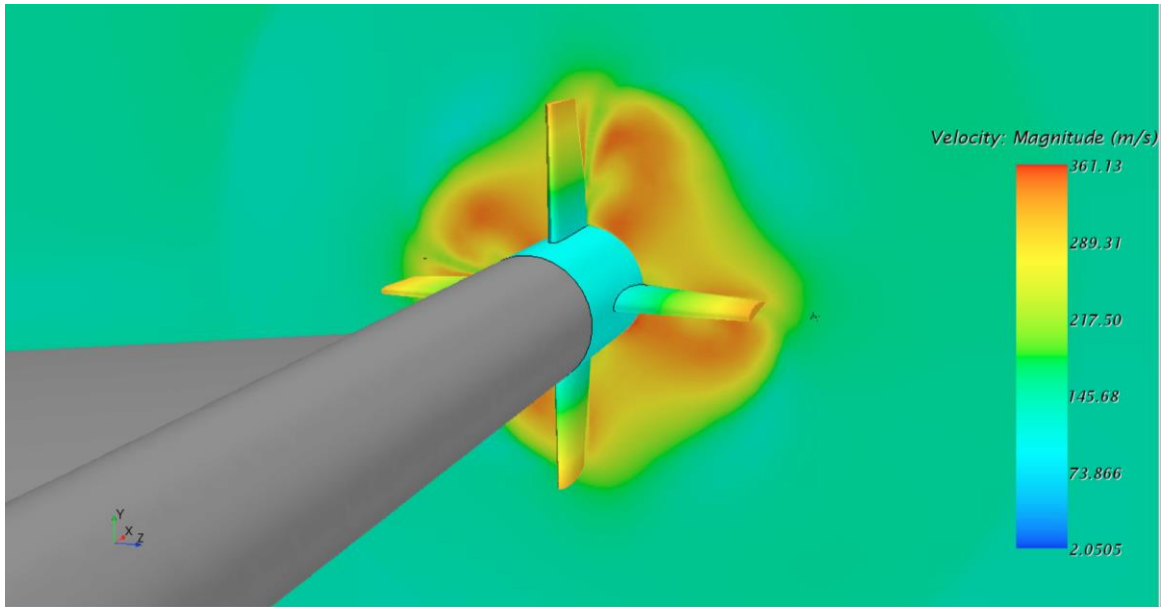
**Fig. 172:  $C_L/C_D$  ratio vs Mach number**



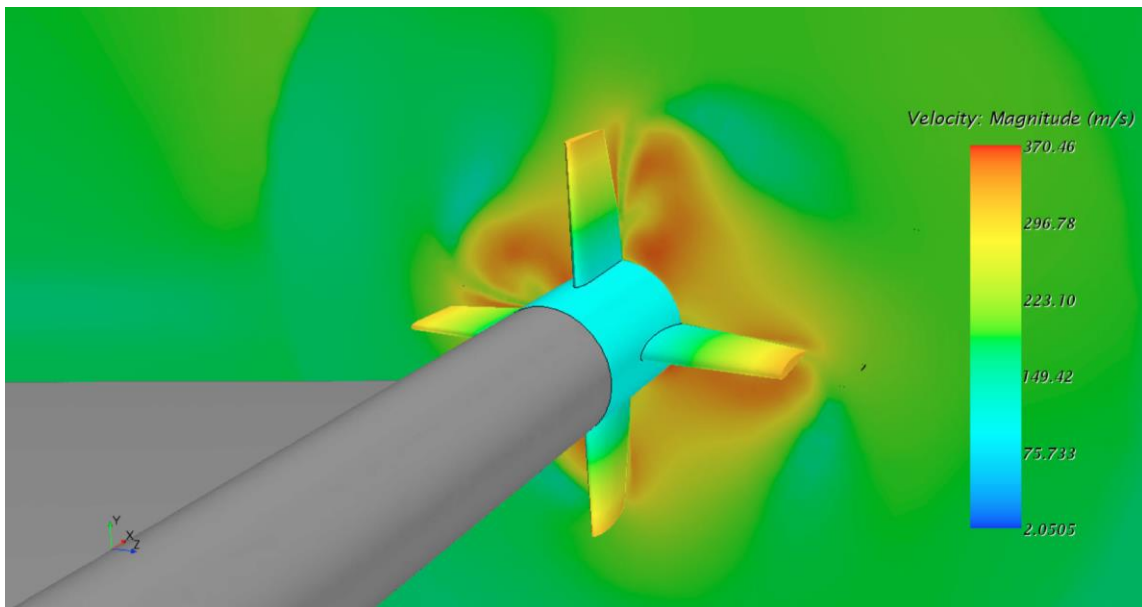
(i.) Mach 0.24



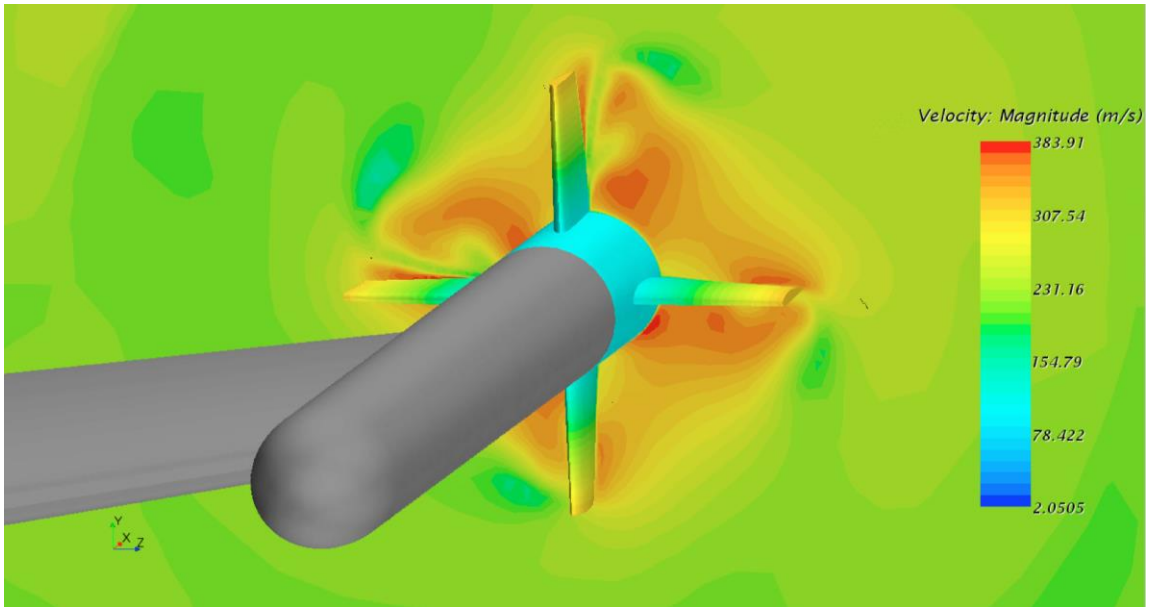
(ii.) Mach 0.34



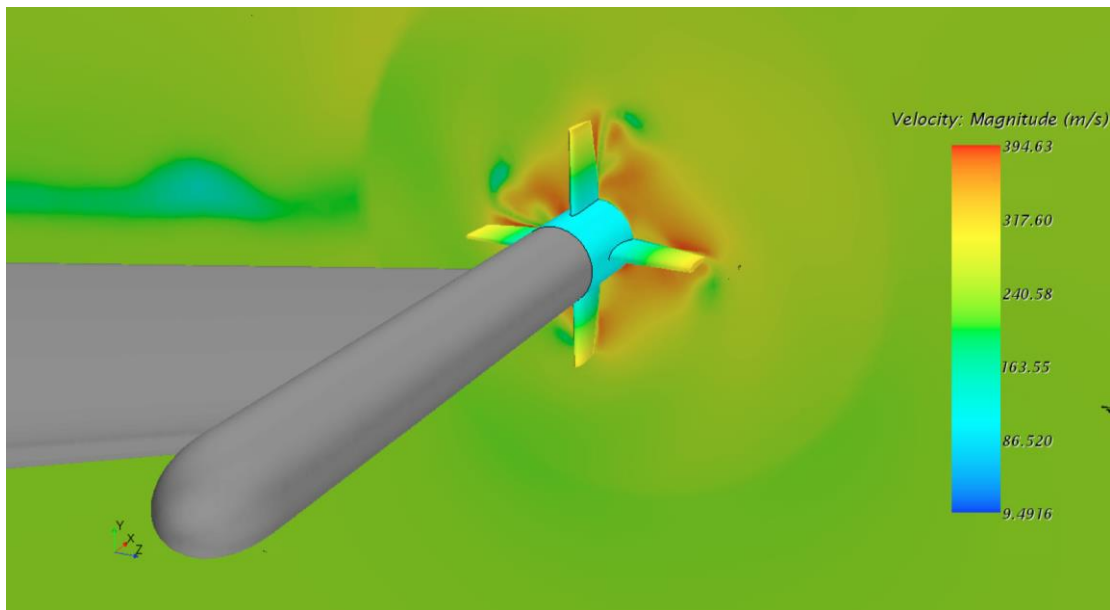
(iii.) Mach 0.44.



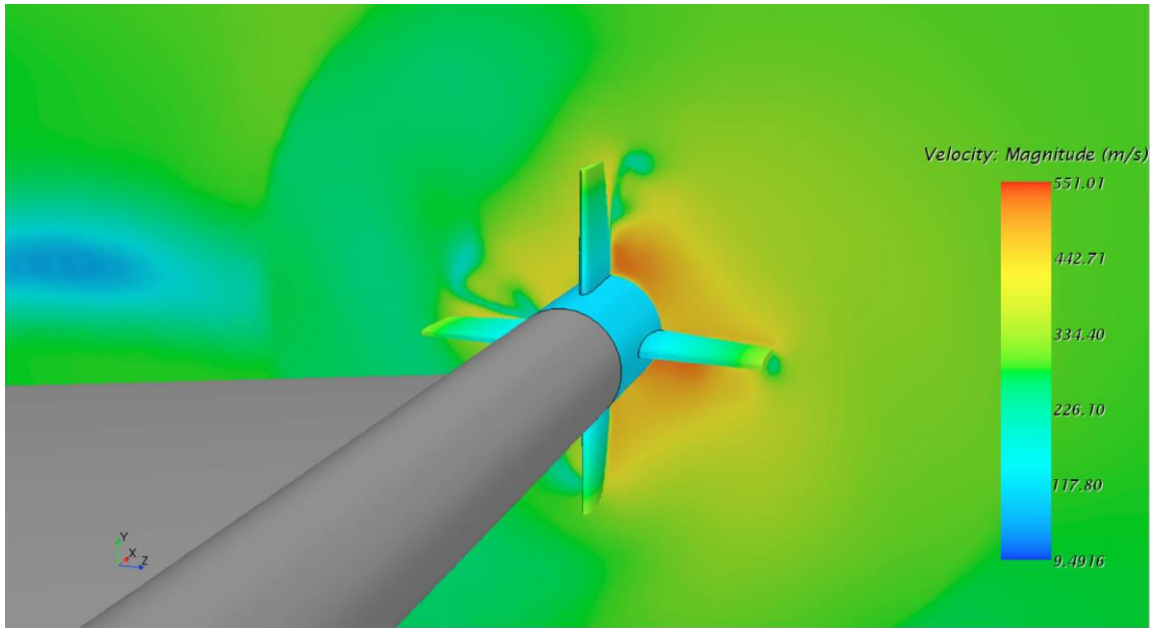
(iv.) Mach 0.54



(v.) Mach 0.64

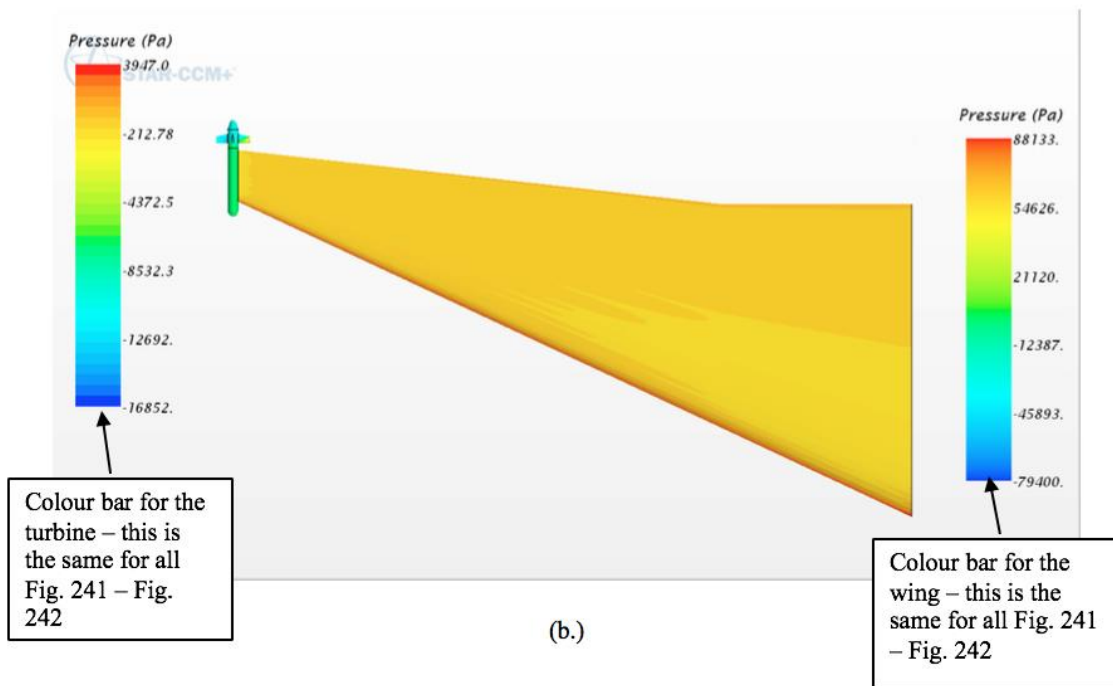
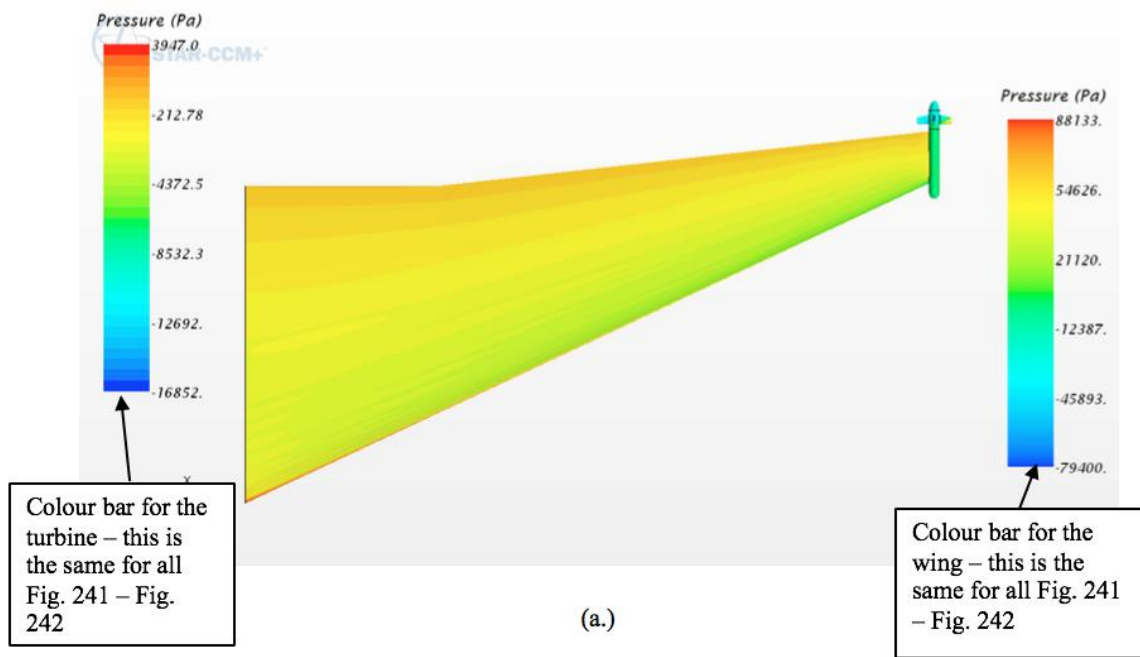


(vi.) Mach 0.74

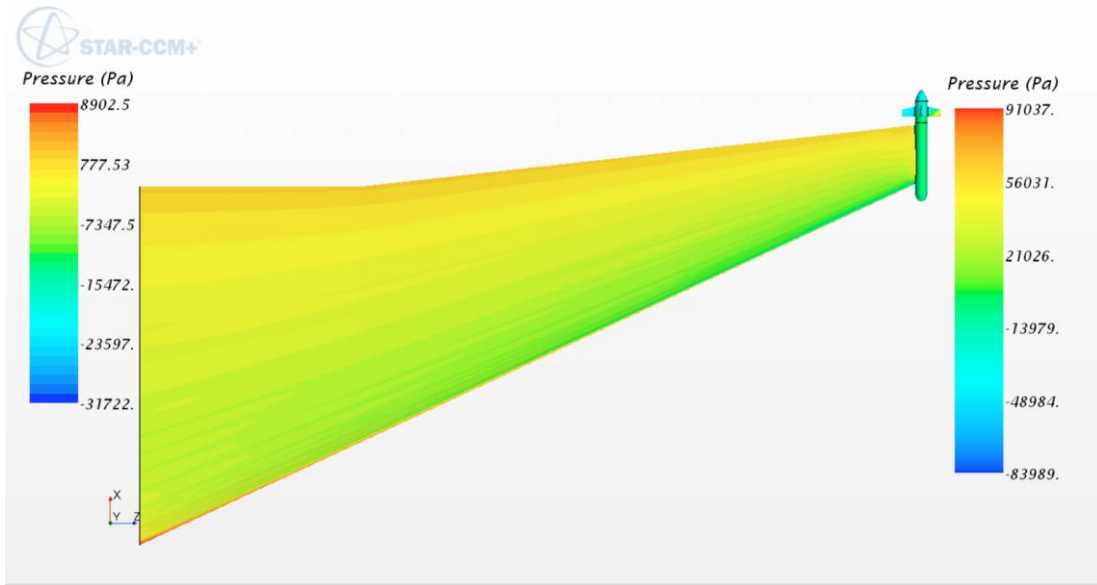


(vii.) Mach 0.84

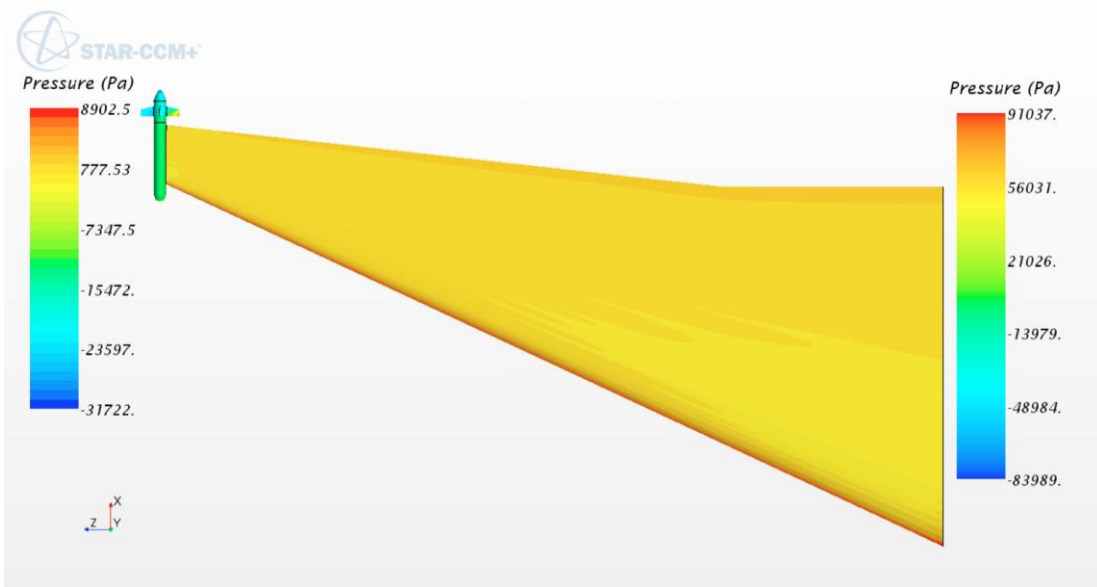
**Fig. 173: Velocity experienced by the propellers**



(i.) Mach 0.24 (a.) top and (b.) bottom wing surface

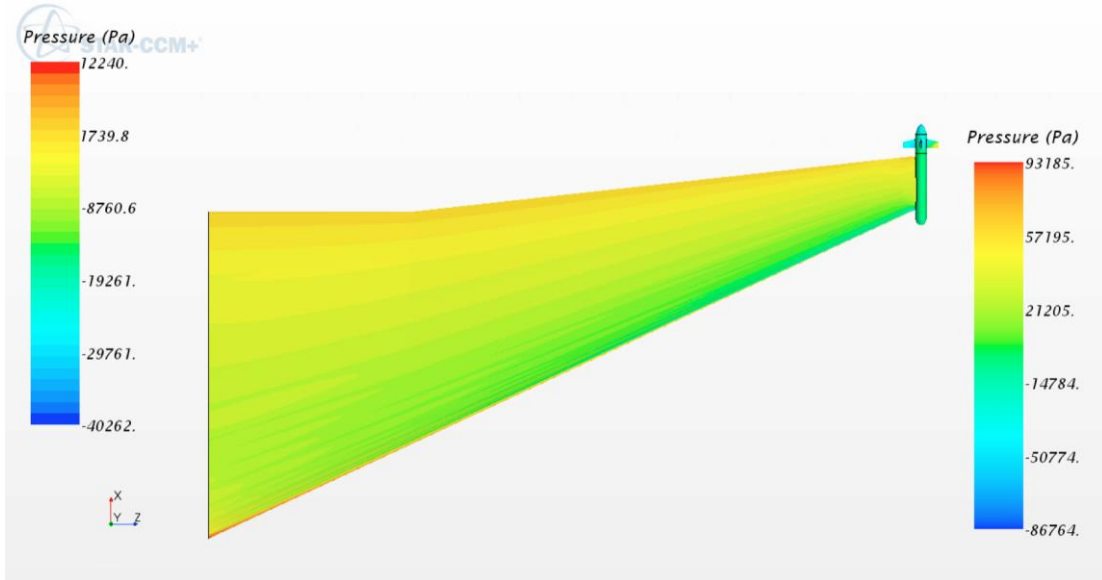


(a.)

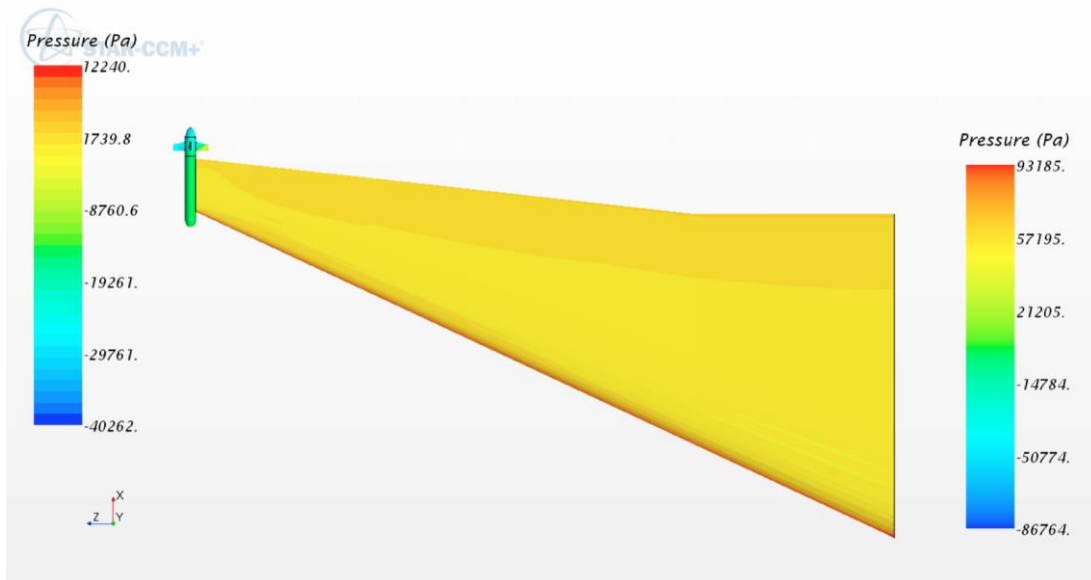


(b.)

(ii.) Mach 0.34(a.) top and (b.) bottom wing surface

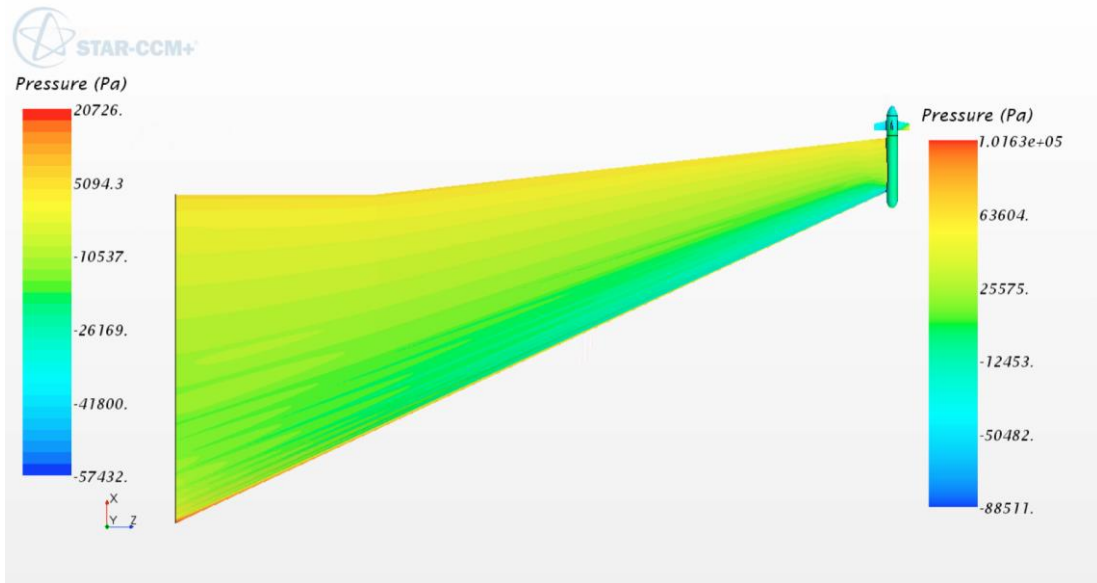


(a.)

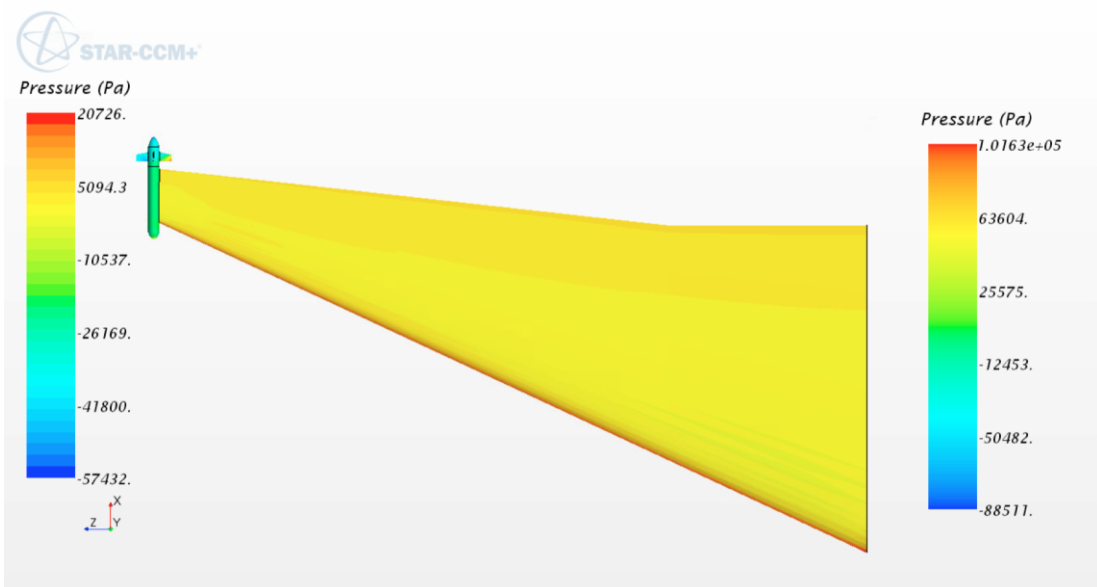


(b.)

(iii.) Mach 0.44 (a.) top and (b.) bottom wing surface

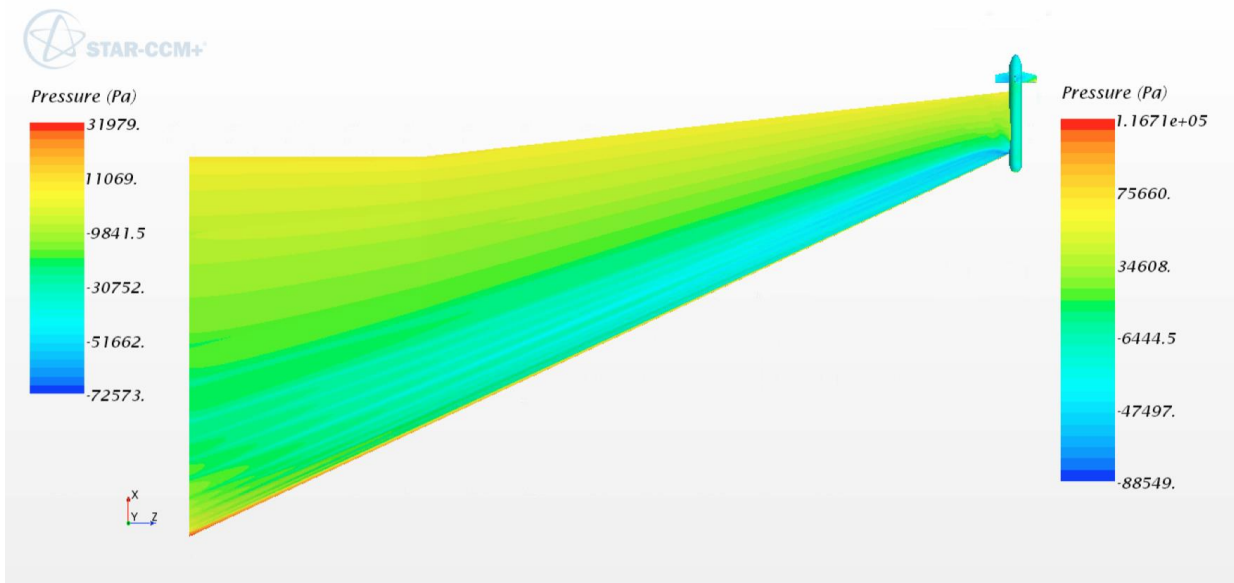


(a.)

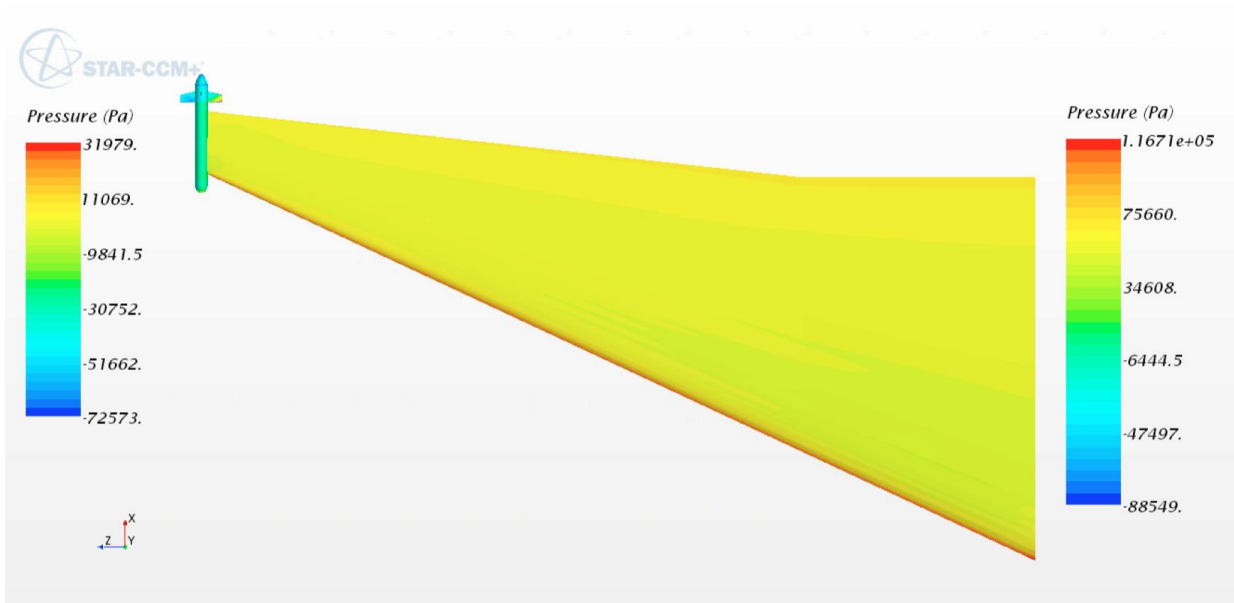


(b.)

(iv.) Mach 0.54 (a.) top and (b.) bottom wing surface

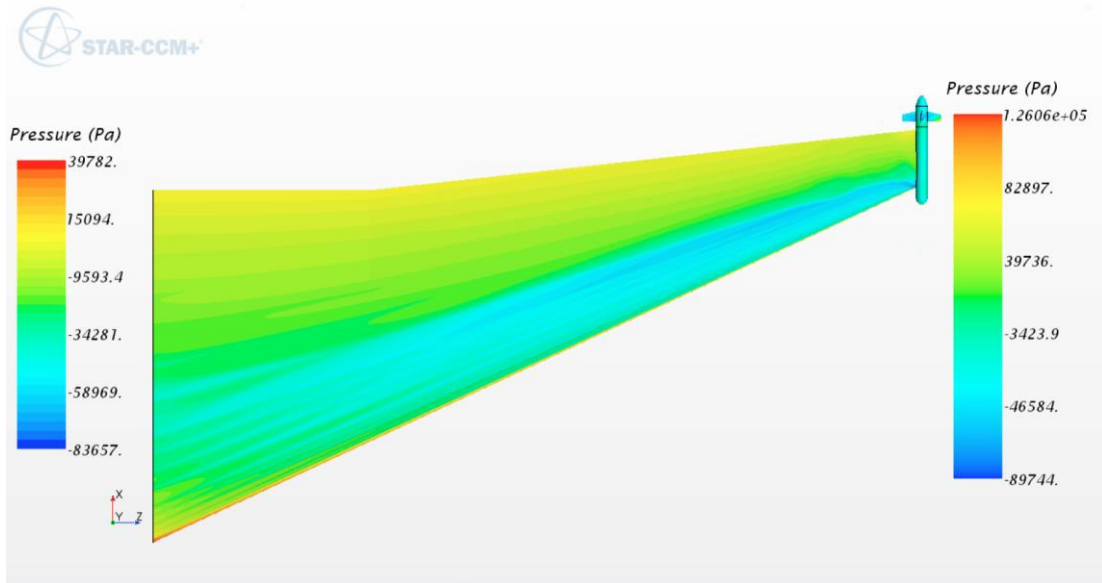


(a.)

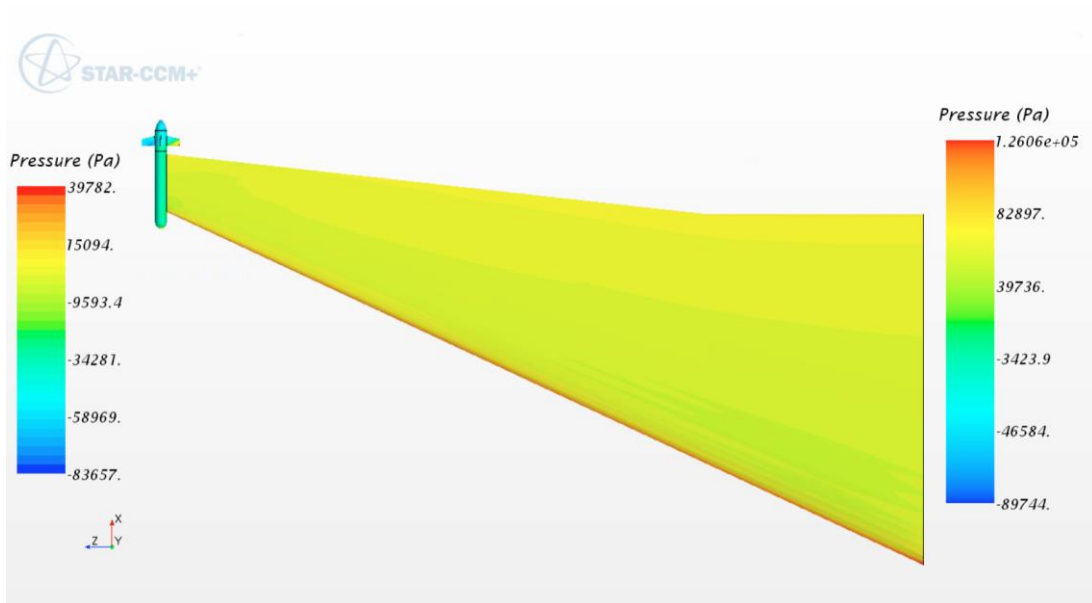


(b.)

(v.)Mach 0.64 (a.)top and (b.)bottom wing surface

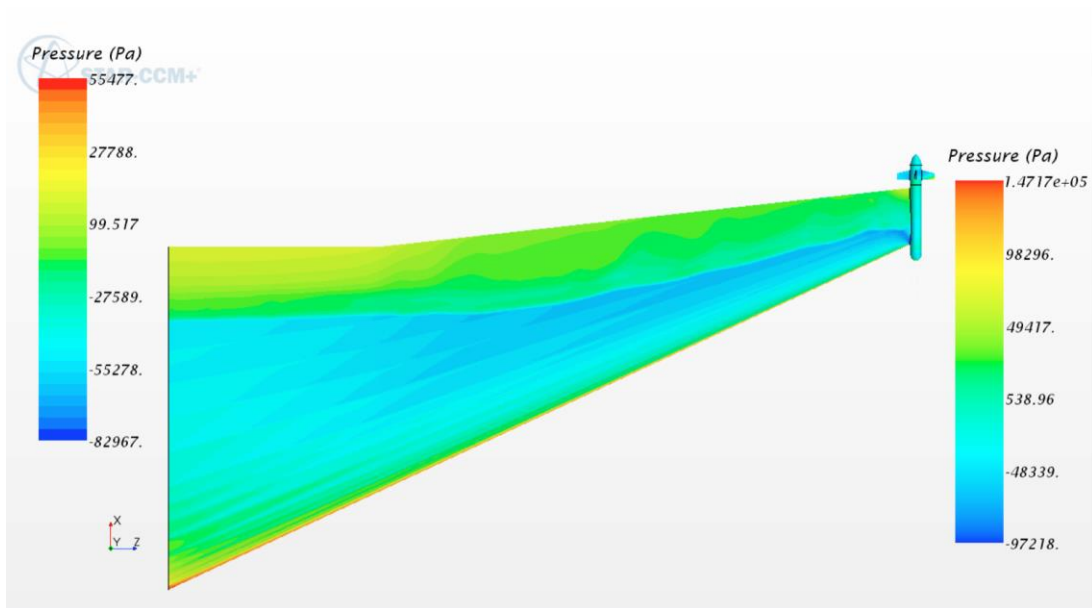


(a.)

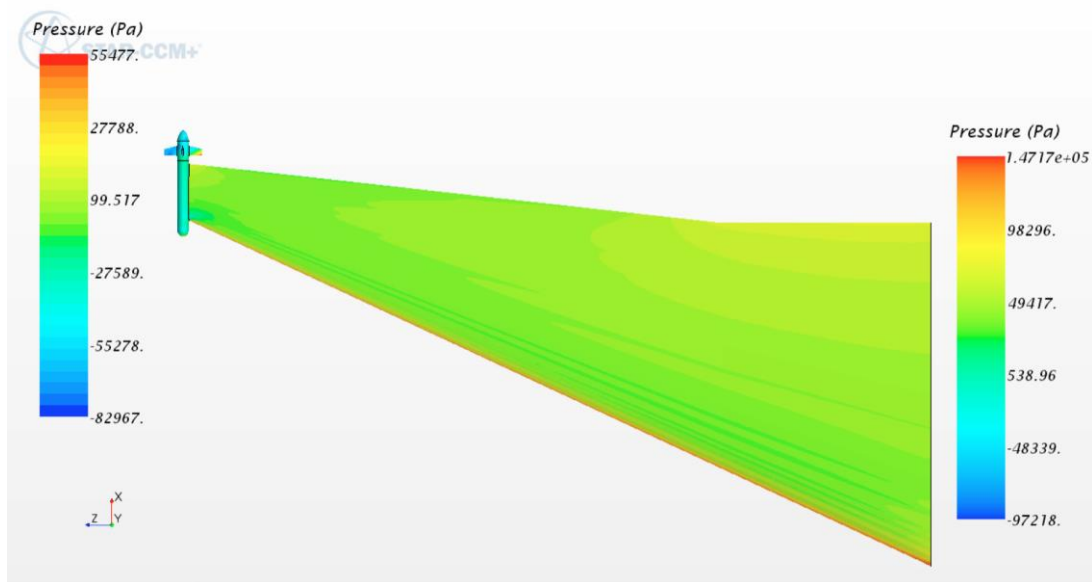


(b.)

(vi.) Mach 0.74 (a) top and (b) bottom wing surface



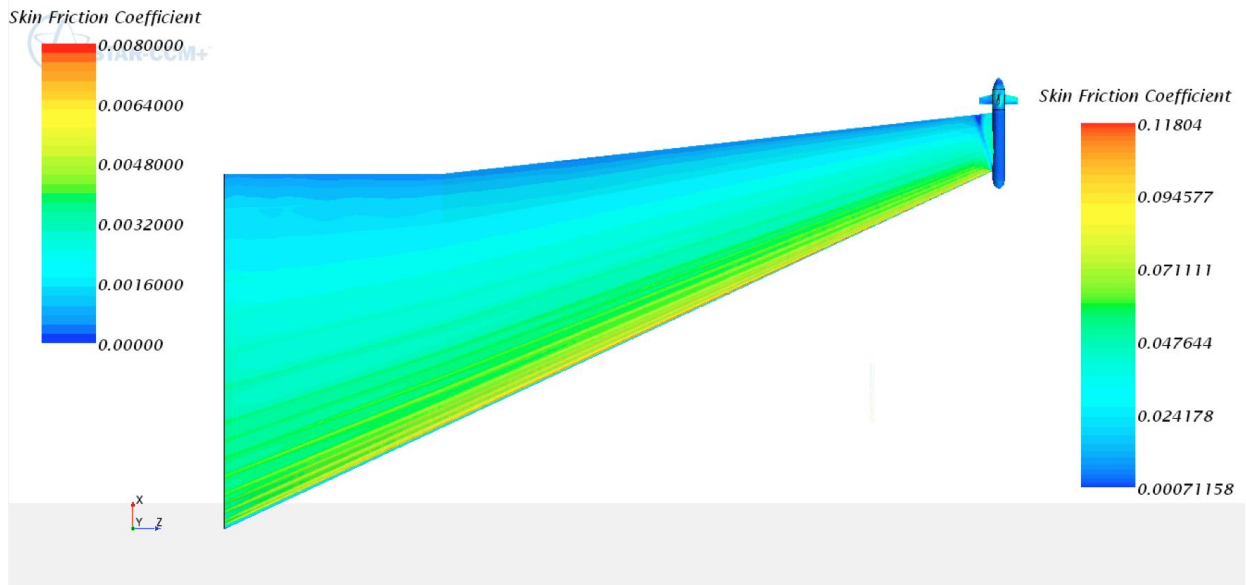
(a.)



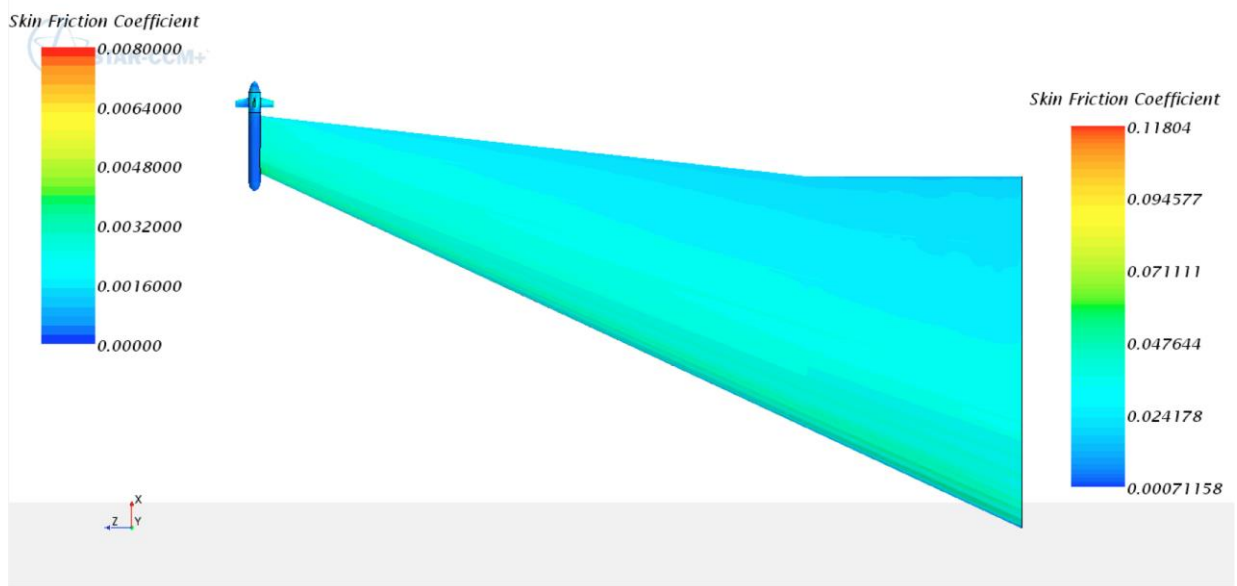
(b.)

(vii.) Mach 0.84 (a) top and (b) bottom wing surface

**Fig. 174: Pressure distribution of wing lifting surface**

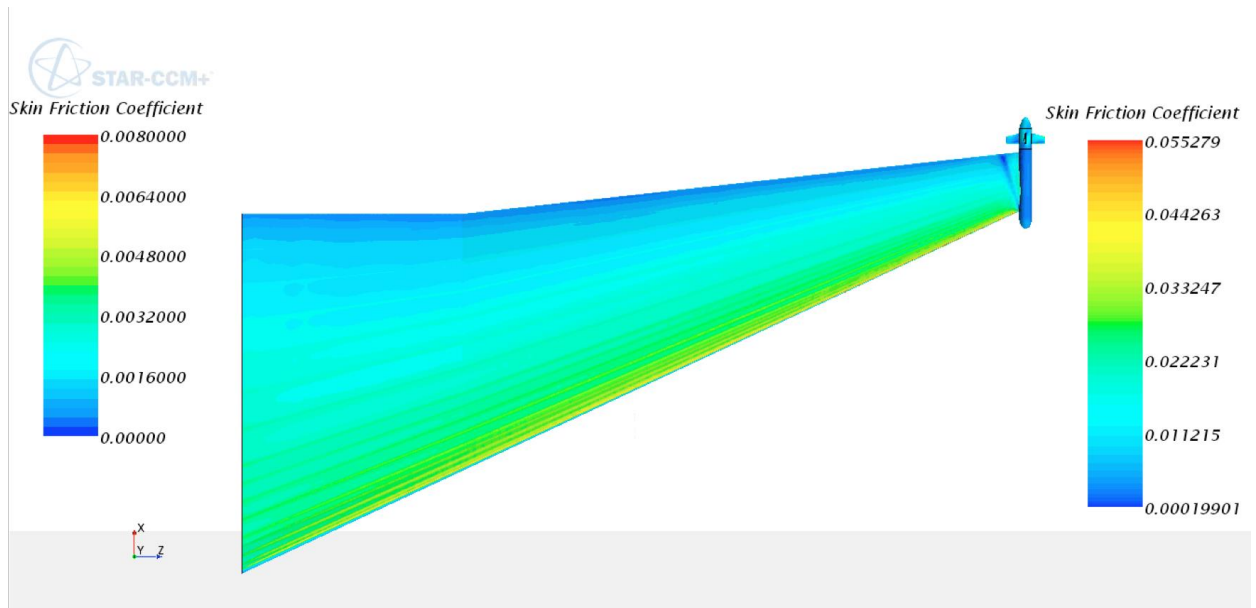


(a.)

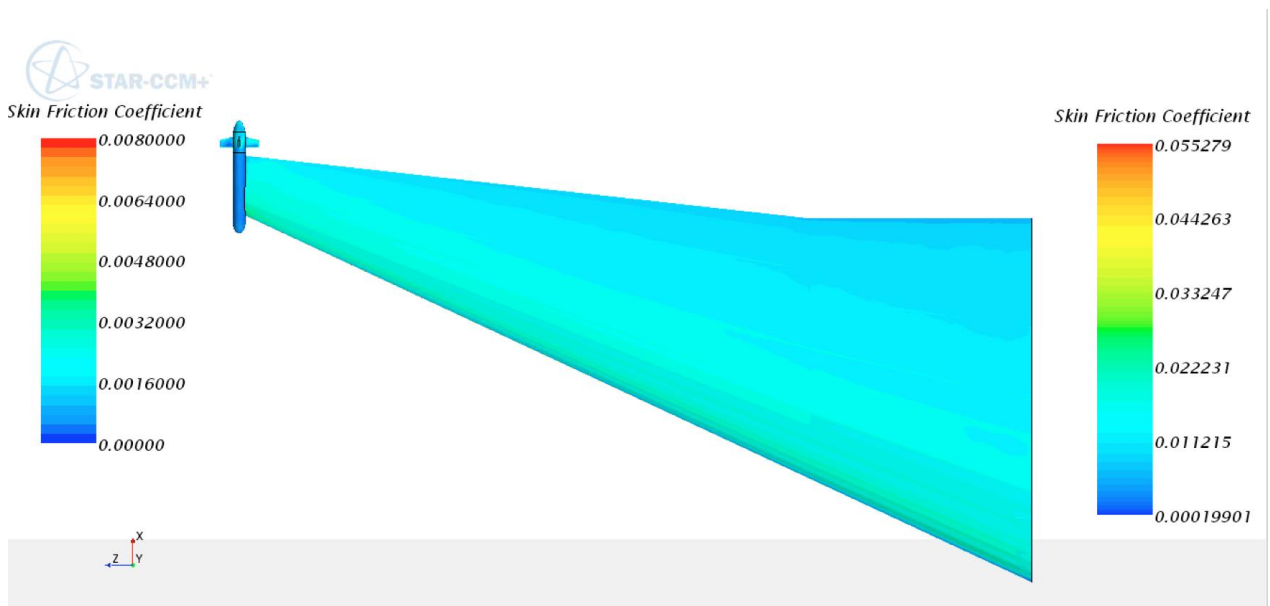


(b.)

(i.) Mach 0.24(a) top and (b) bottom wing surface

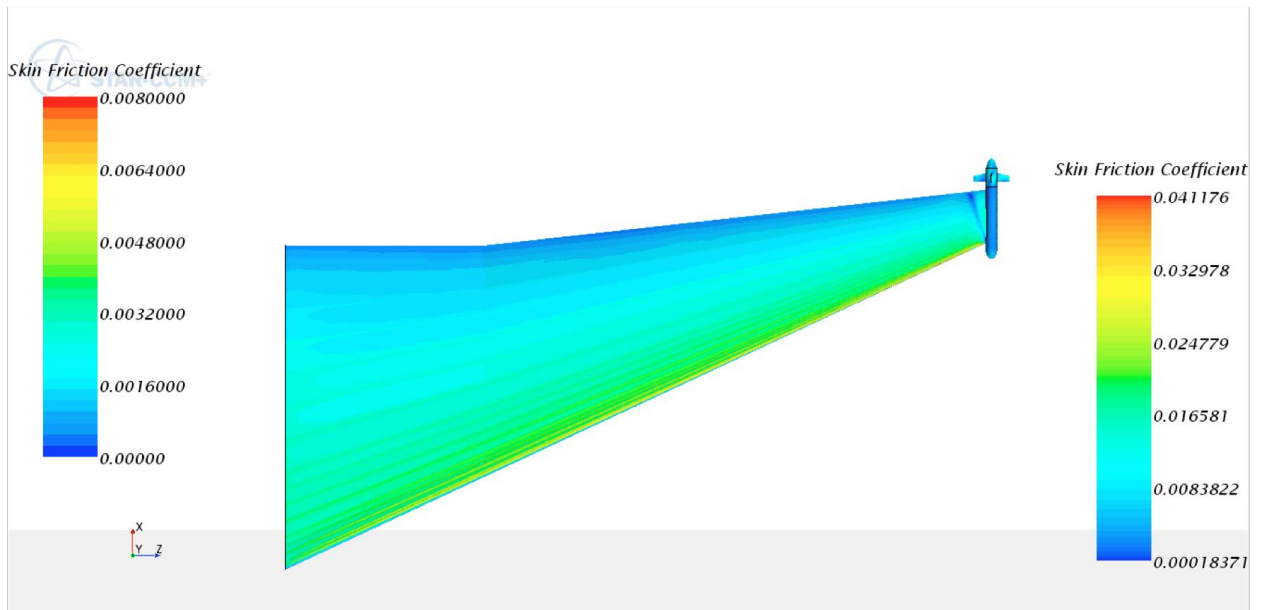


(a.)

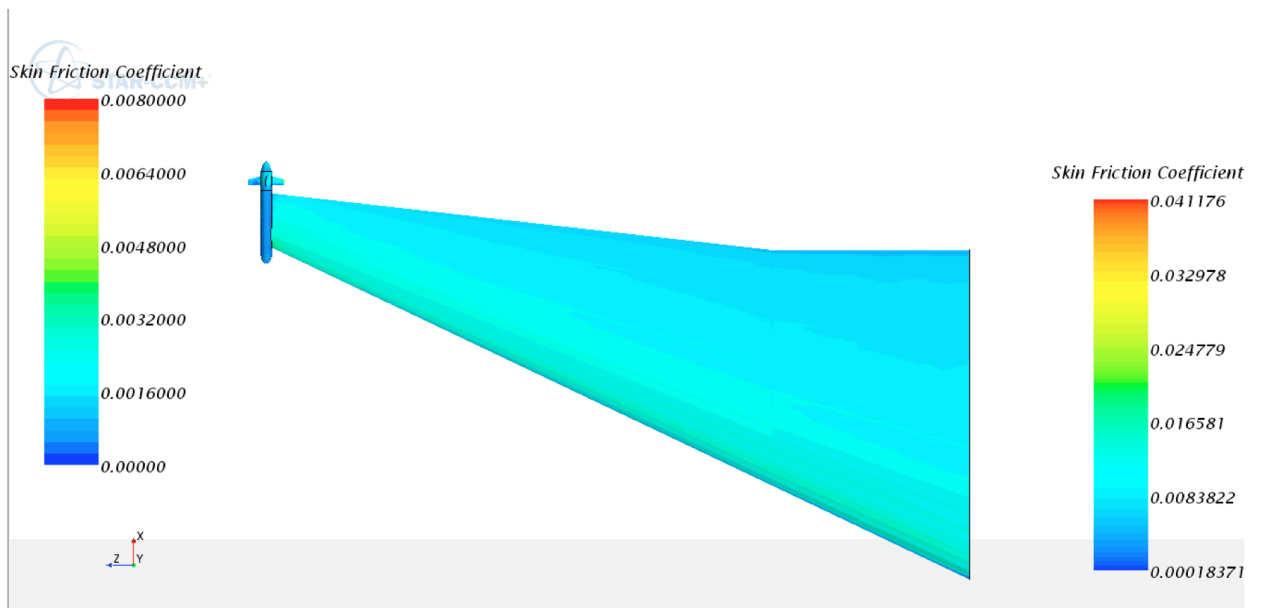


(b.)

(ii.) Mach 0.34 (a) top and (b) bottom wing surface

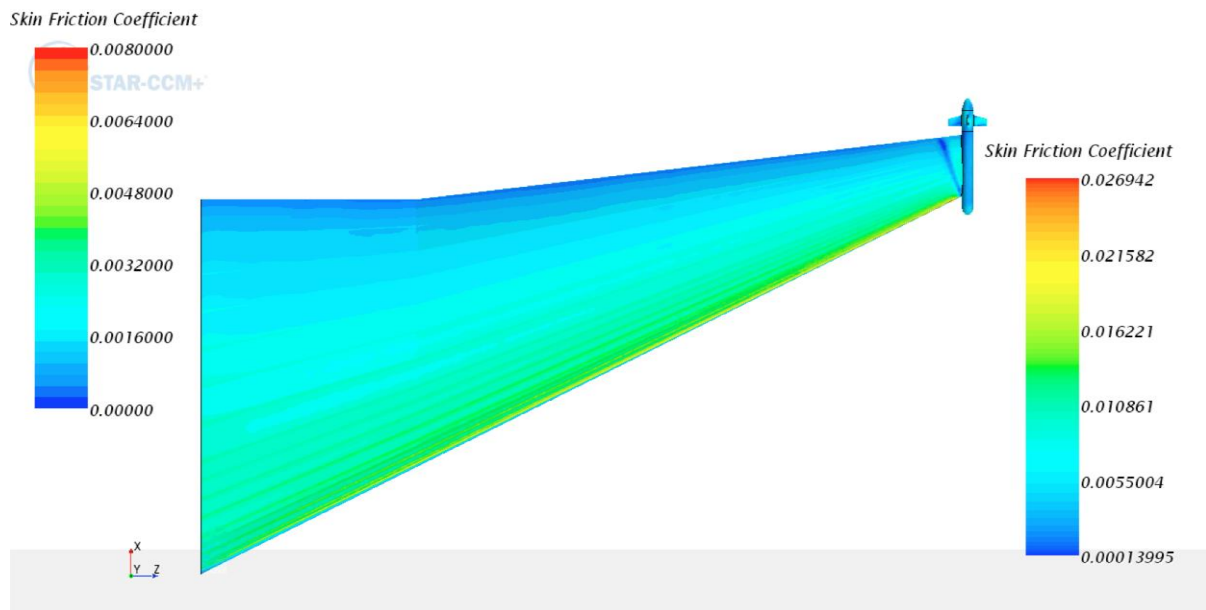


(a.)

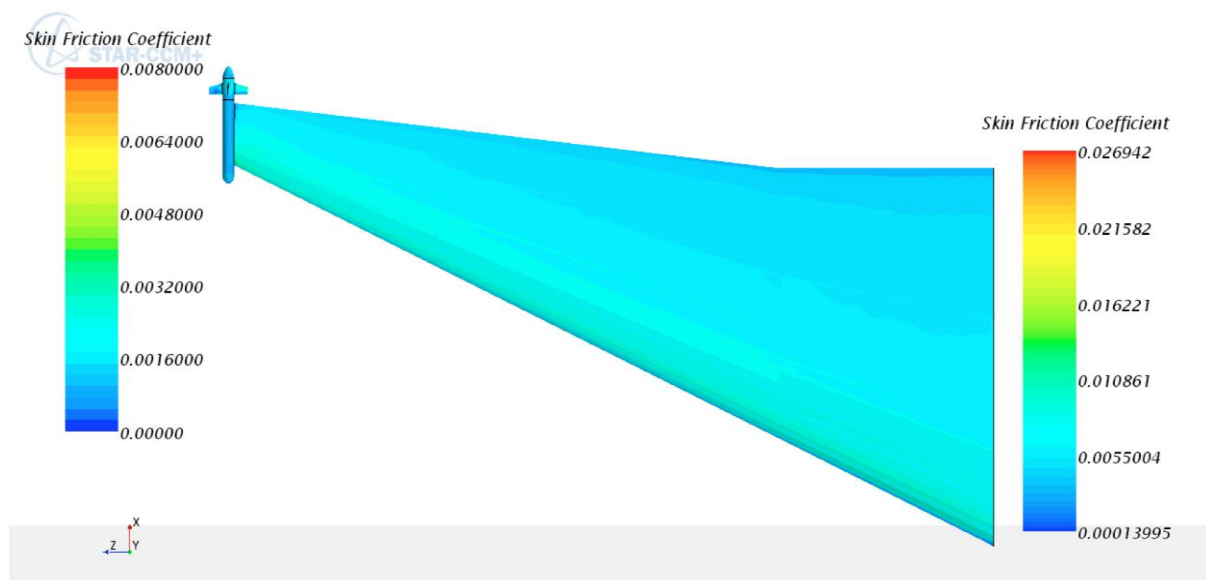


(b.)

(iii.) Mach 0.44 (a) top and (b) bottom wing surface

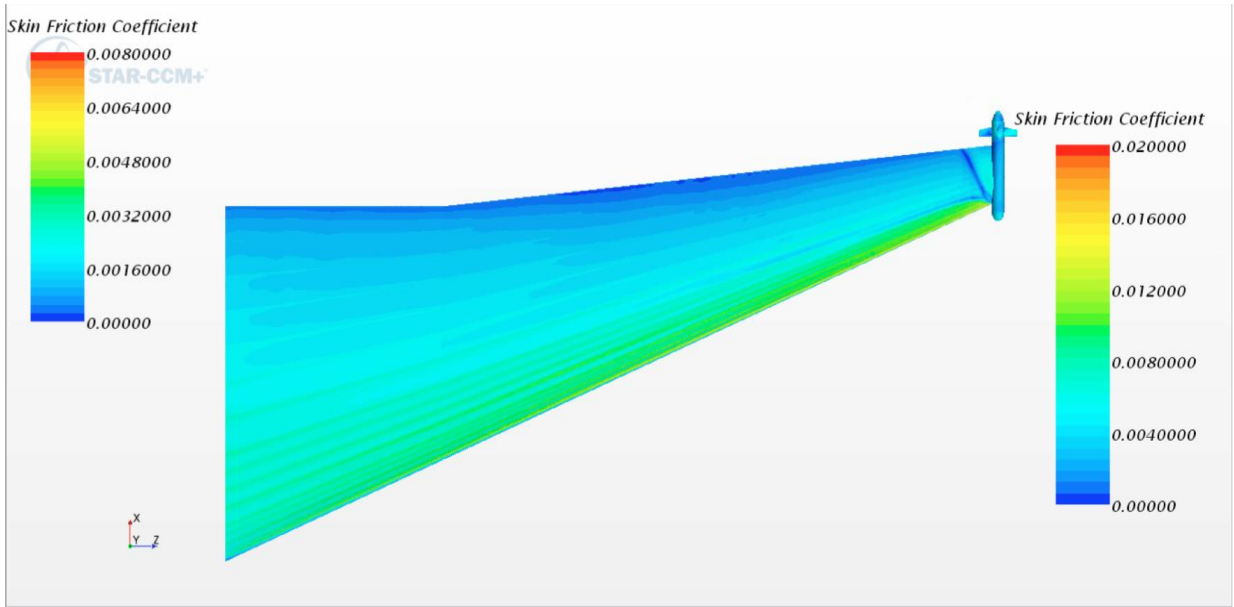


(a.)

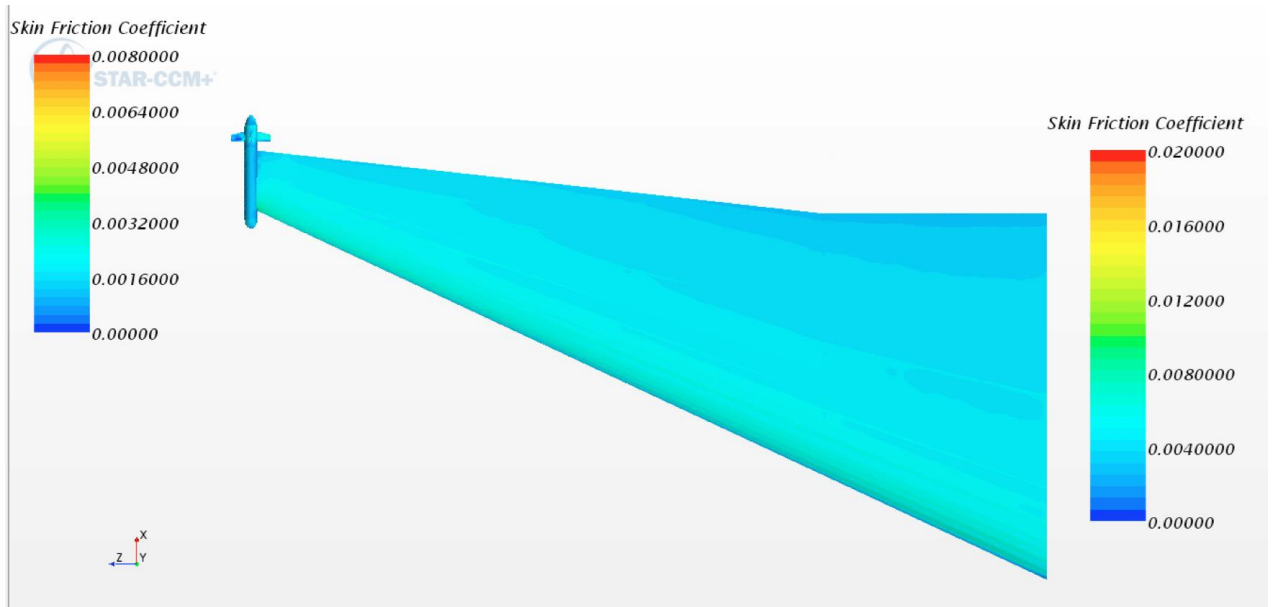


(b.)

(iv.) Mach 0.54(a) top and (b) bottom wing surface

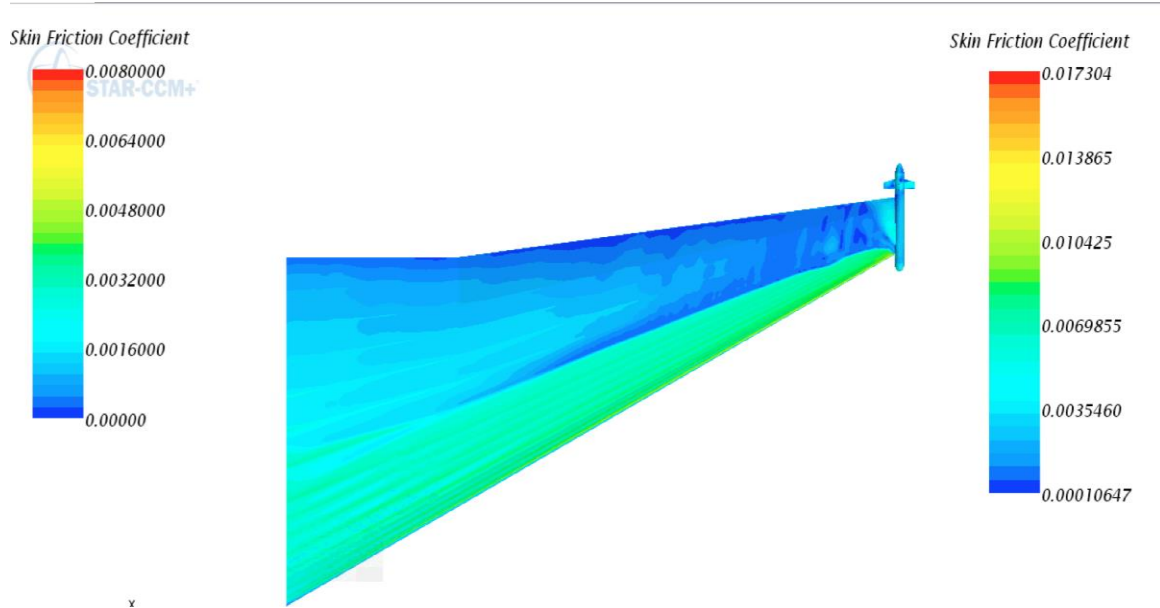


(a.)

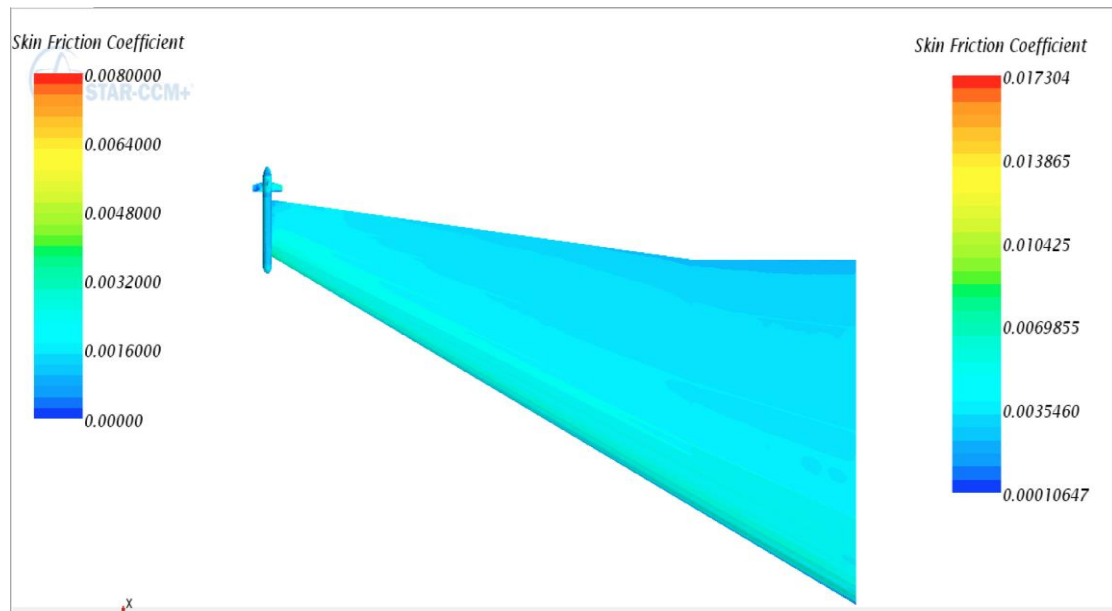


(b.)

(v.) Mach 0.64(a) top and (b) bottom wing surface

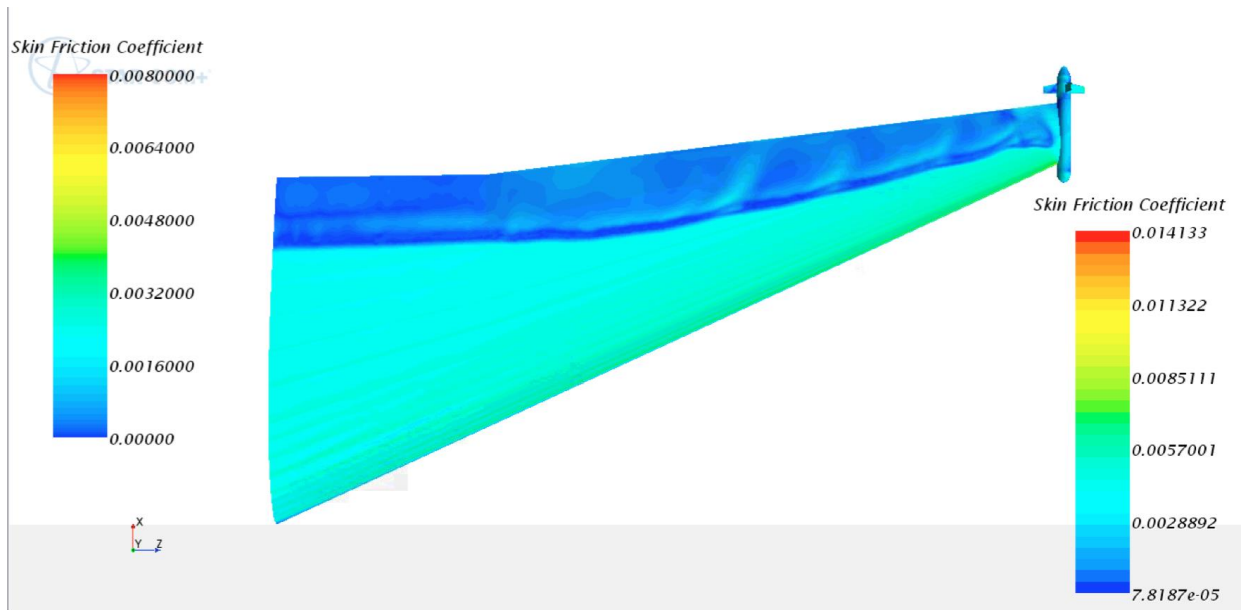


(a.)

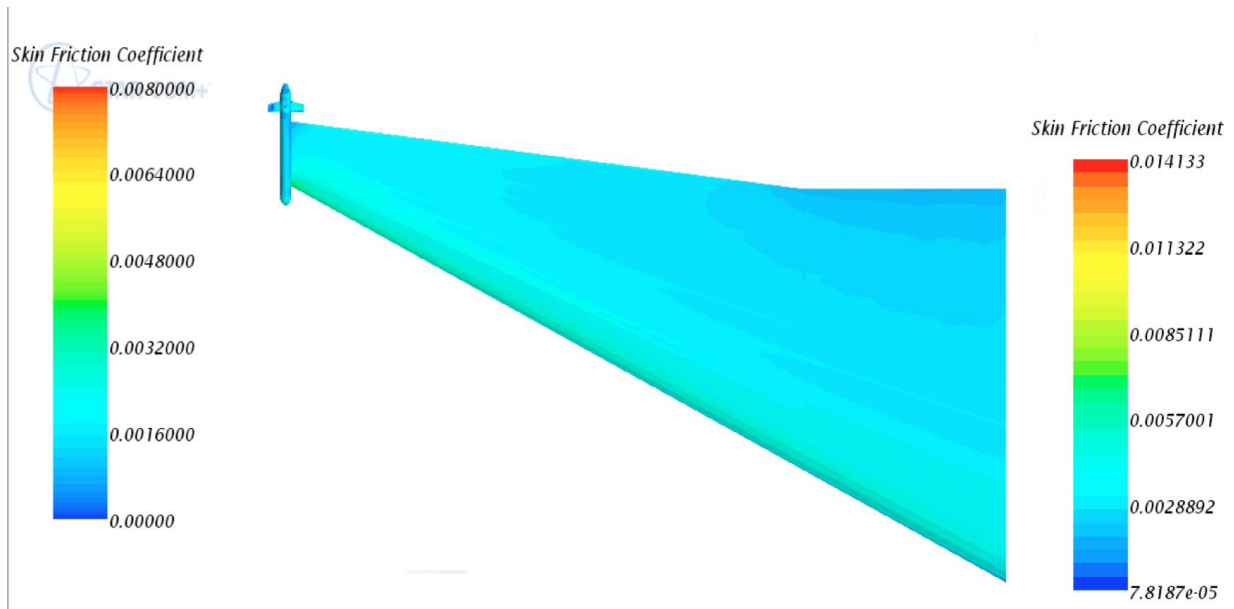


(b.)

(vi.) Mach 0.74 (a) top and (b) bottom wing surface



(a.)



(b.)

(vii.) Mach 0.84 (a) top and (b) bottom wing surface

**Fig. 175: Skin friction coefficient**

### 6.4.5. Effect of angle of attack on propeller wing aerodynamic performance – take-off condition

A further investigation was performed on the wing propeller configuration under take-off conditions which assumed a Mach 0.24 with sea level operating conditions. The results of the investigation are presented and discussed in this section of the report. The change in  $C_L$  with changing angle of attack is shown in Fig. 243, and the results show that the propeller consistently improves the clean wing  $C_L$  by up to 3.8 percent. Fig. 244 shows changes in  $C_D$  due to changing angle of attack, the clean wing  $C_D$  was reduced by up 3.3 percent at  $4^\circ$  using the propeller at the wing tip, and the best  $C_L/C_D$  ratio (5.3 percent) was also obtained at  $4^\circ$  angles of attack see Fig. 245. The propeller was less effective in reducing  $C_D$  above 6 degrees angle of attack. This indicates that these configurations are better suited for long haul flights at low angle of attacks.

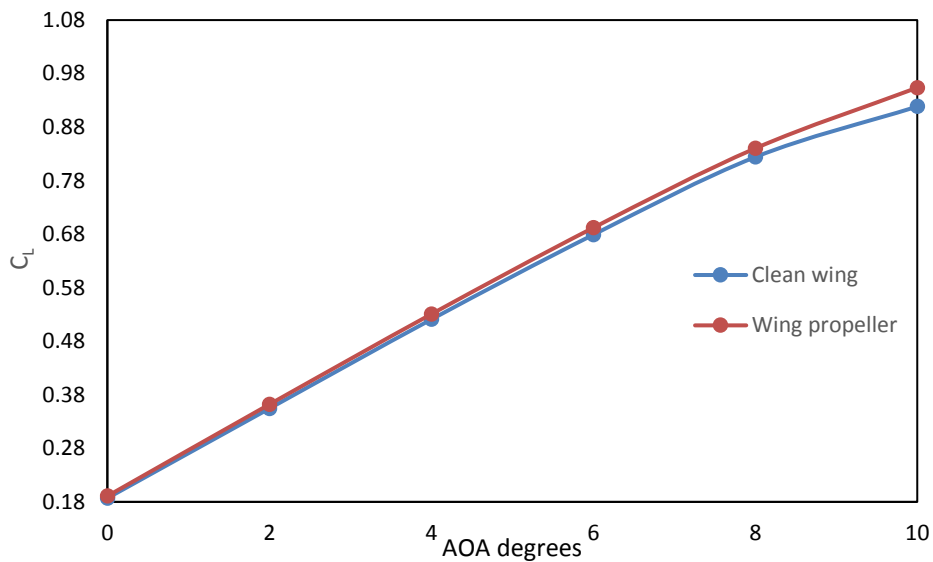
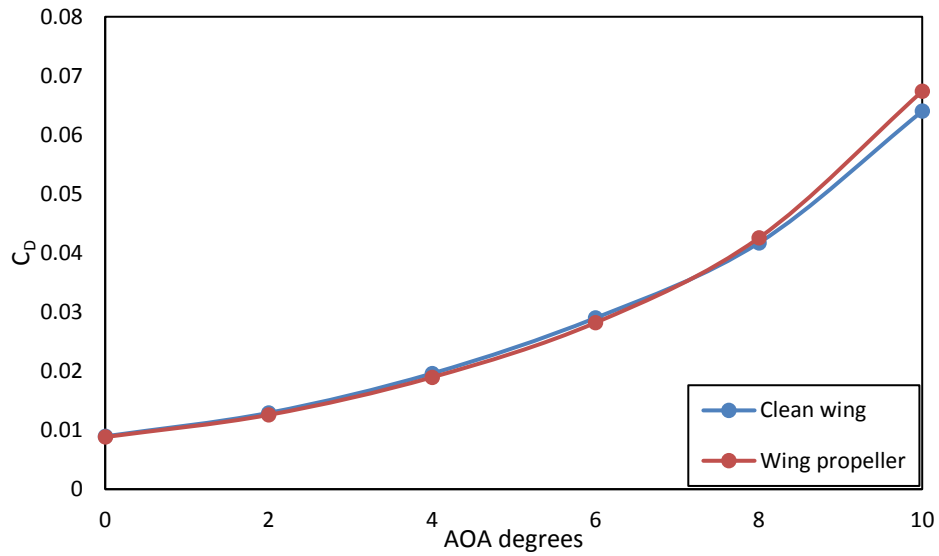
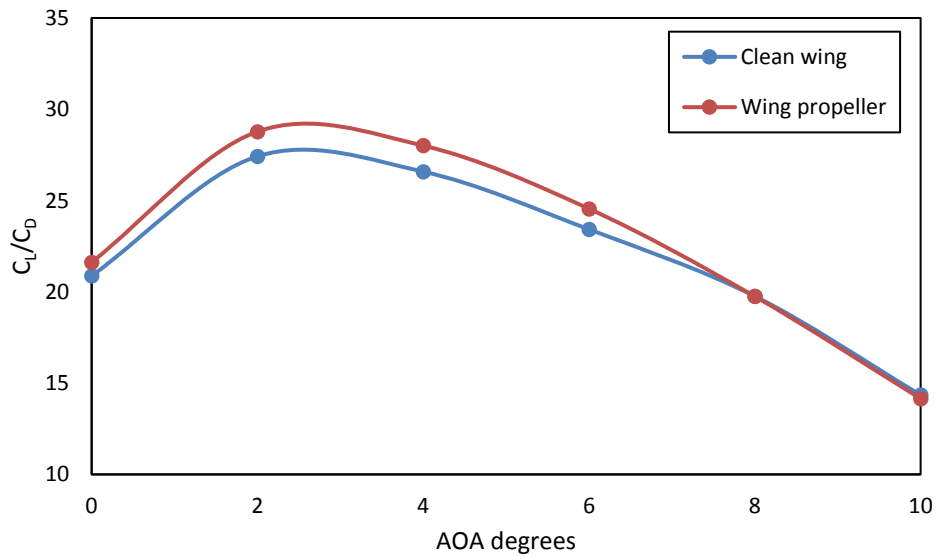


Fig. 176:  $C_L$  vs AOA



**Fig. 177:  $C_D$  vs AOA**



**Fig. 178:  $C_L/C_D$  vs AOA**

#### 6.4.6. Propeller RPM effect on wing performance

In this section, the results obtained from the investigation of the propeller rpm effect on the wing performance is presented. The performance data for the wing is presented in Table 32, and this table displays an interesting pattern to the behaviour of the studied performance parameters. Based on this set of data, the propeller rpm 8000 and 5000 produced the minimum  $C_D$  value on the wing while the maximum lift to drag ratio of 5.6 percent was obtained at rpm 8000 and maximum  $C_L$  at rpm 7000. The result showed no particular trend as the performance

parameters ( $C_L$ ,  $C_D$  and  $C_L/C_D$ ) are rather rpm specific, but the results do give the indication that the aerodynamic performance of the wing with propeller is sensitive to the rpm of the rotating propeller blades at the wing tip.

Also, it is worth mentioning that similar rpms that was used in this study were also adopted for other studies where experimental work was carried out using propellers on micro air vehicles (MAVs) or simply on a small clean wing, with the results showing considerable improvement in the aerodynamic performance of the MAV or wing. See the following articles and reports in references (Ananda Krishnan et al., 2013), (Ananda Krishnan et al., 2014), (Serokhvostov, 2013), (Brandt and Selig, 2011), (Chinwicharnam et al., 2013).

**Table 32: RPM effect on wing performance**

Parameters	Clean wing	Propeller rpm 9000	Propeller rpm 8000	Propeller rpm 7000	Propeller rpm 6000	Propeller rpm 5000
$C_L$	0.47403	0.48509	0.48594	0.490075	0.48528	0.48443
$C_D$	0.02012	0.01965	0.01954	0.019968	0.01957	0.01954
$C_L/C_D$	23.5499	24.6865	24.8689	24.5430	24.7971	24.7917

## 6.5. Conclusion

Investigations carried out on the aerodynamic performance of a wing mounted with tip turbine have been presented. The results discussed showed that the aerodynamic performance of the wing is dependent and sensitive to the propeller nacelle position at the wing tip with propeller nacelle position-1 (the distance that the propeller is aft of the wing trailing edge is 0.6m) the best configuration in this study. Also, it did demonstrate that the aerodynamic performance of the wing is also dependent on the rpm of the rotating propeller blade and on the direction of the rotation. The effect of Mach number, changes in angles of attack at take-off condition assumed at Mach 0.24 were also presented. The following conclusions could be drawn:

- The configuration was most effect at lower angles of attack between  $2^0 - 6^0$  which implies the set-up was mostly suited for cruise flight phase.
- The configuration improves the  $C_L$  by maximum 4 percent and reduced  $C_D$  by approximately 3.3 percent.
- A  $C_L/C_D$  ratio improvement of up to 5.6 percent was obtained at rpm 8000 at  $4^0$  angles of attack and Mach 0.64.
- The coefficient of drag reduction of up to 3.2 percent was achieved at Mach 0.24. The characteristics of the  $C_D$  curve showed that as was the case of the upward pointing winglets, the wing-tip propeller configuration is better suited for reducing drag at values below the critical Mach number.
- Induced drag reduction as high as the reduced overall drag was also achieved.

Based on the results presented and discussed in this chapter of thesis, it could be concluded that for practical application, the most ideal configuration of wing tip turbine technology for aerodynamic performance improvement would be to mount the technology with the propeller and nacelle close to the rear of the wing tip which would bring it in direct contact with the high vortex region of the wing tip. Together with this configuration the propeller rpm should potentially be on or below 8000rpm, with the direction of rotation in the clockwise direction taken from a point of view of an observer in front of the leading edge of the wing. Furthermore, applications should only be for subsonic flight Mach numbers below Mach 0.64 due to the tip speed of the propeller which approaches transonic speeds at higher Mach numbers and could result in noise pollution.

In addition, the kinetic energy generated by the rotating wing tip turbine could be harnessed and used to power electrical systems in the aircraft or UAV as well as being used as a drag reduction device on the aircraft.

The next chapter of this thesis is the discussion on feasibility and potential application of the induced drag reduction technologies studied in this thesis as well as the error analysis of the CFD results presented in this work.

Furthermore, the introduction of wing tip devices has other implications on aircraft design. For example, aeroelasticity. In recognition of this, an investigation of the flutter characteristics of using wing-tip devices on an aircraft wing was undertaken, providing evidence that by using such devices, the flutter characteristics of the wing changes little. This work is presented in Appendix A.

## Chapter 7: Discussion and error analysis of results

This chapter of this thesis discusses issues regarding error analysis, feasibility and potential applications of the technologies.

### 7.1. Re-introducing the wing-tip devices

Four novel spiroid induced drag reduction devices have already been presented and discussed in this thesis in chapter 5. Also, a detailed investigation to ascertain the extent of aerodynamic performance improvement capabilities of using a wing tip turbine on a clean wing has also been presented in chapter 6. To recapitulate on the four wing tip devices as well as the wing tip turbine configurations, an isometric view of the optimised designs and the wing tip turbine are presented in Fig. 179 – Fig. 183.

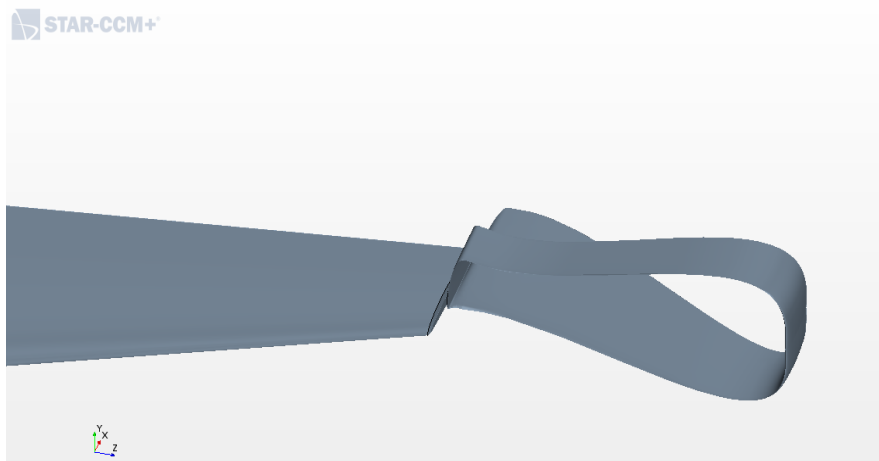


**Fig. 179: Design-1**

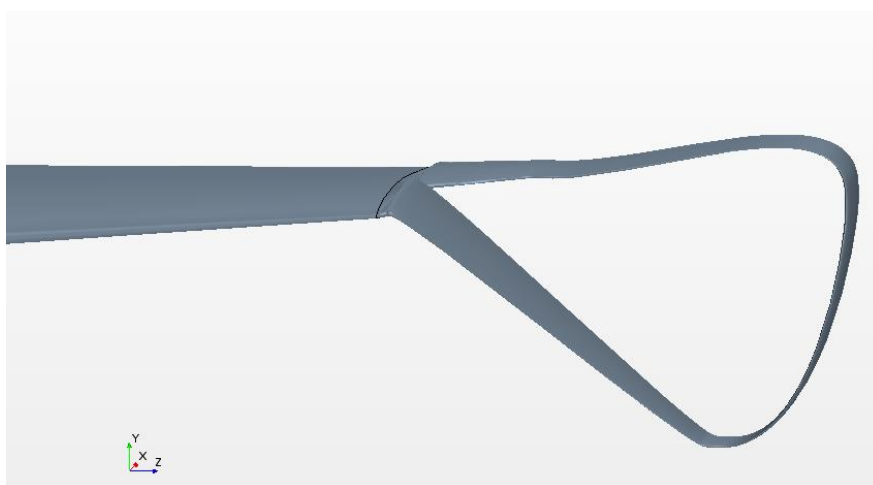


**Fig. 180: Design-2**

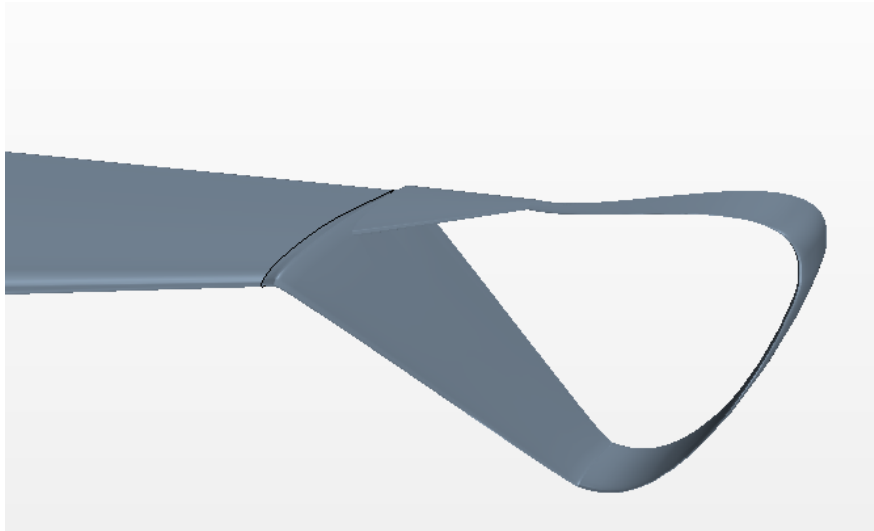


**Fig. 181: Design-3**

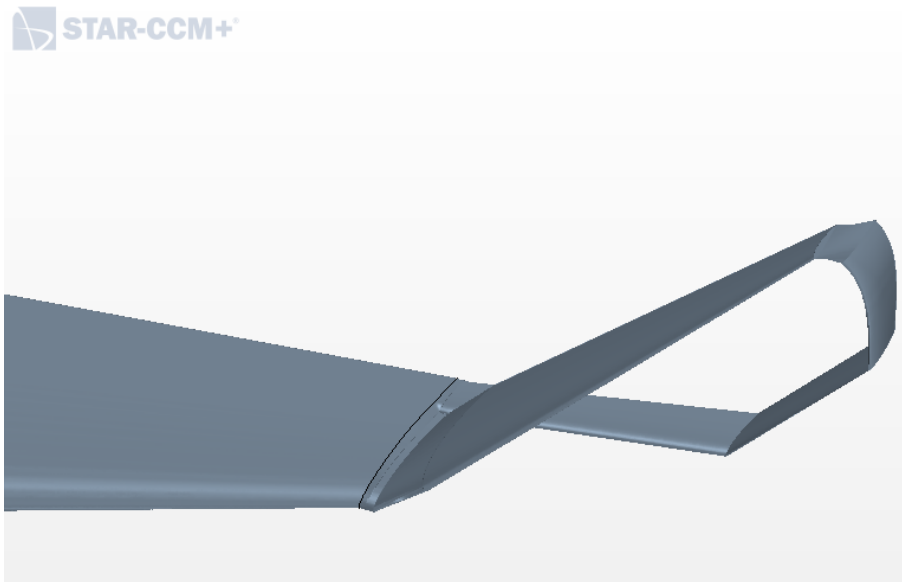


**Fig. 182: Spiroid trapezium**

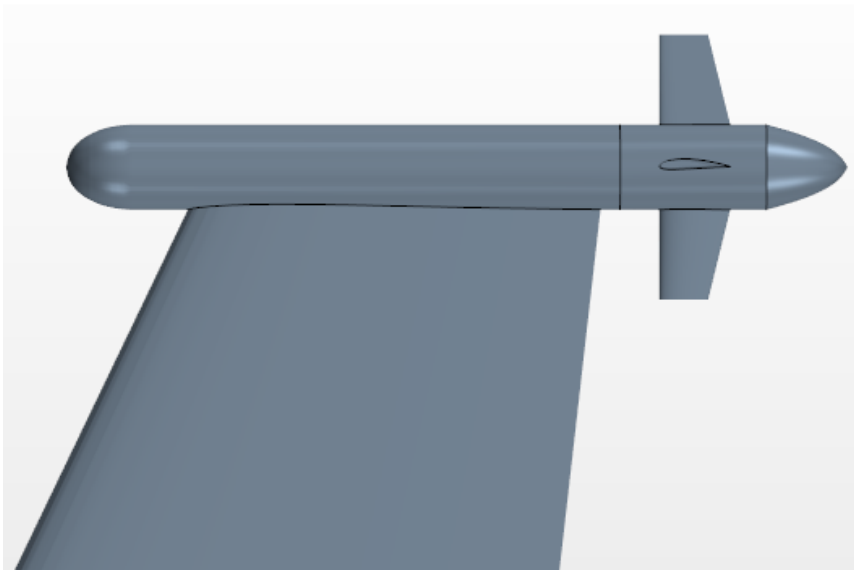


**Fig. 183: Wing tip turbine**

## 7.2. Error analysis and applied correction factors

To perform error analysis on the results obtained by using CFD for the designs 1 – 3 and spiroid trapezium which has been discussed in chapter 5 and wing tip turbine configurations in chapter 6, NASA experimental results in Rumsey et al., (2011b) for the first lift prediction workshop (LPW-1) are used to obtain a correlation factor which is used to correct the CFD results obtained for the same study with similar configurations in Rumsey et al., (2011b). The same correlation factor is then used to correct the results from chapter 5 and are presented in this section of the thesis. The results obtained from experimental work that was carried out in UH (see section 6.3) and the corresponding CFD work also discussed in section 6.3 is used to obtain a correction factor which is then used to correct the CFD results obtained for the wing tip propeller configurations in section 6.4. This was carried out because the type of simulation performed to replicate the experimental UH data and the work that was carried out in section 6.4 in chapter 6 are similar. This is in regard to the simulation being a multi-region (multi domain) simulation set-up with an interface created between the regions to allow for the exchange of physics values between the static and rotating regions within the domains at the wing tip and wing and nacelle regions.

First, the experimental results in Rumsey et al., (2011b) and the corresponding CFD results are presented in Table 33.  $C_L$  and  $C_D$  for the K-Omega model are corrected by using the following equations:

$$\frac{\text{Force coefficient}_{K-\omega \text{ model}}}{\text{Force coefficient}_{LPW-1}}$$

(63)

$$\text{Average of all } \frac{\text{Force coefficient}_{K\text{-omega model}}}{\text{Force coefficient}_{LPW-1}} \quad (64)$$

**Table 33: Numerical data and data from literature (Rumsey et al., 2011b)**

Angle of attack	LPW-1		K-OMEGA model		$\frac{C_{L-K\text{-omega model}}}{C_{L-LPW-1}}$	$\frac{C_{D-K\text{-omega model}}}{C_{D-LPW-1}}$
	C <sub>L</sub>	C <sub>D</sub>	C <sub>L</sub>	C <sub>D</sub>		
2.074	1.0098	0.1114	1.0160	0.1112	1.0061	0.9982
3.996	1.1667	0.1363	1.1651	0.1351	0.9986	0.9912
6.002	1.3381	0.1653	1.3361	0.1642	0.9985	0.9933

Equation 63 is used to determine the extent to which the C<sub>L</sub> and C<sub>D</sub> values of the LPW-1 differs from the values that are obtained using CFD and then the average of these values is calculated by using equation (64) to obtain a correction factor for each force coefficient. The correction factor applied for C<sub>L</sub> is 0.999 while C<sub>D</sub> is multiplied by 1.0057. These values are then used to correct the data obtained for the optimisation study of the spiroid technologies (Designs 1 – 3 and the spiroid trapezium design) that are presented in section 5.3.1 of this thesis. The data before the correction factor is applied is shown in Tables 34 – 35 and corrected results are presented in Table 36 and Table 37. The percentage improvement of the technologies compared against the clean wing has remained relatively unchanged, but their respective C<sub>L</sub>, C<sub>D</sub> and C<sub>L</sub>/C<sub>D</sub> values have been modified due to the applied correction factor. Therefore, there is no need to modify the percentage improvements stated section in 5.3.1 under chapter 5 for the spiroid technologies.

**Table 34: Aerodynamic coefficients for Designs 1 – 3, before correction was applied**

Operating conditions – 32808ft, Mach 0.74, 4 degrees α, Mesh count – 50 - 52 million cells							
Aerodynamic coefficients	Clean wing	Design-1	% improvement, Design-1	Design-2	% improvement, Design-2	Design-3	% improvement, Design-3
C <sub>L</sub> /C <sub>D</sub>	11.4820	11.8404	3%	11.8639	3%	12.1150	6%
C <sub>L</sub>	0.5191	0.5194	0.1%	0.5216	0.5%	0.5367	3%
C <sub>D</sub>	0.0452	0.0438	3%	0.0439	3%	0.0443	2%
C <sub>D</sub> induced	0.0109	0.00837	24%	0.00838	23%	0.00895	18%

**Table 35: Aerodynamic coefficients for Designs 1 – 3 corrected data**

Operating conditions – 32808ft, Mach 0.74, 4 degrees $\alpha$ , Mesh count – 50 - 52 million cells							
Aerodynamic coefficients	Clean wing	Design-1	% improvement, Design-1	Design-2	% improvement, Design-2	Design-3	% improvement, Design-3
$C_L/C_D$	11.4080	11.8465	3%	11.8023	3%	12.0344	6%
$C_L$	0.5185	0.5188	0.1%	0.5210	0.5%	0.5361	3%
$C_D$	0.0454	0.0440	3%	0.0441	3%	0.0445	2%
$C_{D_{induced}}$	0.01093	0.00837	24%	0.00836	23%	0.00893	18%

**Table 36: Aerodynamic coefficients Spiroid trapezium, before correction was applied**

Operating conditions – sea level, Mach 0.24, 4 degrees $\alpha$ , Mesh count – 50 - 52 million cells			
Aerodynamic coefficients	Clean wing	Spiroid trapezium	% improvement Spiroid trapezium
$C_L/C_D$	28.8119	31.9935	11%
$C_L$	0.4766	0.5038	7%
$C_D$	0.0165	0.0158	4%
$C_{D_{induced}}$	0.00923	0.00764	18%
$C_M$	-0.3554	-0.1960	10%

**Table 37: Aerodynamic coefficients Spiroid trapezium corrected data**

Operating conditions – sea level, Mach 0.24, 4 degrees $\alpha$ , Mesh count – 50 - 52 million cells			
Aerodynamic coefficients	Clean wing	Spiroid trapezium	% improvement Spiroid trapezium
$C_L/C_D$	28.6924	31.6736	11%
$C_L$	0.4761	0.5033	7%
$C_D$	0.01659	0.0158	4%
$C_{D_{induced}}$	0.00922	0.00750	19%

The results obtained from the experimental work that was carried out in the UH wind tunnel (see section 6.3) and the corresponding CFD work also discussed in section 6.3 are presented in Table 38 for the clean wing and Table 39 for the wing with propeller configuration. Equation 63 was applied on the data and the result are also shown in Table 38 and Table 39 for the clean wing and wing with turbine configurations respectively. A correction factor of 1.03 was obtained for the CFD  $C_L$  and 1.05 for the CFD  $C_D$  values by using equation 64 and the results are presented in Table 40 for the clean wing and Table 41 for the wing with turbine configurations. The results obtained from UH wind tunnel and the CFD results in Table 40 and Table 41 shows slight discrepancies in the results which can be attributed to the surface roughness/finish on the wing model from 3D printing. A  $200\mu\text{m}$  roughness height was used in the CFD models as mentioned earlier in section 5.3.1. This value was taken based

on the general roughness height of 3D printed models which is usually within 200  $\mu m$ . The presence of this roughness creates a more distorted and energetic flow region near the walls which becomes more prominent at higher AOA. For the work done in this thesis, low angles of attack of  $4^0 - 6^0$  are of most importance and the results correlate well for these angles.

**Table 38: UH wind tunnel experimental data and CFD results for the clean wing before correction**

Angle of attack	UH wind tunnel		CFD modelling		$\frac{C_{L-K-omega\ model}}{C_{L-LPW-1}}$	$\frac{C_{D-K-omega\ model}}{C_{D-LPW-1}}$
	$C_L$	$C_D$	$C_L$	$C_D$		
0	0.1169	0.0237	0.1329	0.0242	1.1364	1.0204
2	0.2576	0.0218	0.2743	0.0220	1.0651	1.0059
4	0.4301	0.0391	0.4155	0.0293	0.9664	0.7491
6	0.6006	0.0435	0.5553	0.0427	0.9245	0.9813
8	0.7651	0.0525	0.6732	0.0549	0.8798	1.0439
10	0.9152	0.0792	0.7517	0.0764	0.8213	0.9639

**Table 39: UH wind tunnel experimental data and CFD results for the wing with propeller before correction**

Angle of attack	UH wind tunnel		CFD modelling		$\frac{C_{L-K-omega\ model}}{C_{L-LPW-1}}$	$\frac{C_{D-K-omega\ model}}{C_{D-LPW-1}}$
	$C_L$	$C_D$	$C_L$	$C_D$		
0	0.1260	0.0239	0.1432	0.0217	1.1363	0.9091
2	0.2896	0.0293	0.2957	0.0256	1.0214	0.8730
4	0.4445	0.0325	0.4462	0.0325	1.0040	1.0022
6	0.6373	0.0419	0.5920	0.0429	0.9290	1.0250
8	0.8186	0.0572	0.7210	0.0569	0.8808	0.9966
10	0.9270	0.0781	0.8027	0.0758	0.8659	0.9714

**Table 40: UH wind tunnel experimental data and CFD clean wing corrected data**

Angle of attack	UH wind tunnel		CFD modelling		Correction factor obtained by using equation 64 for CFD $C_L$ values	Correction factor obtained by using equation 64 for CFD $C_D$ values
	$C_L$	$C_D$	$C_L$	$C_D$		
0	0.1169	0.0237	0.1367	0.0254	X 1.03	X 1.05
2	0.2576	0.0218	0.2826	0.0231	X 1.03	X 1.05
4	0.4301	0.0391	0.4280	0.0307	X 1.03	X 1.05
6	0.6006	0.0435	0.5720	0.0448	X 1.03	X 1.05
8	0.7651	0.0525	0.6934	0.0576	X 1.03	X 1.05
10	0.9152	0.0792	0.7743	0.0804	X 1.03	X 1.05

**Table 41: UH wind tunnel experimental data and CFD wing with propeller corrected data**

Angle of attack	UH wind tunnel		CFD modelling		Correction factor obtained by using equation 64 for CFD $C_L$ values	Correction factor obtained by using equation 64 for CFD $C_D$ values
	$C_L$	$C_D$	$C_L$	$C_D$		
0	0.1169	0.0237	0.1475	0.0226	X 1.03	X 1.04
2	0.2576	0.0218	0.3046	0.0266	X 1.03	X 1.04
4	0.4301	0.0391	0.4597	0.0339	X 1.03	X 1.04
6	0.6006	0.0435	0.6098	0.0447	X 1.03	X 1.04
8	0.7651	0.0525	0.7427	0.0592	X 1.03	X 1.04
10	0.9152	0.0792	0.8267	0.0789	X 1.03	X 1.04

**Table 42 : Propeller nacelle sensitivity to aerodynamic force coefficients and  $C_L/C_D$  ratio, the results for steady state simulation at 4 degrees AOA and Mach 0.64 data before corrections applied**

Parameters	Clean wing	Propeller nacelle position 1	Propeller nacelle position 2	Propeller nacelle position 3	Propeller nacelle position 4	Propeller nacelle - tractor position
$C_L$	0.4740	0.490075	0.490085	0.4897	0.4893	0.4788
$C_D$	0.02012	0.01996	0.01998	0.019987	0.01997	0.02017
$C_L/C_D$	23.5499	24.5420	24.51959	24.5055	24.4961	23.7397

**Table 43 : Propeller nacelle sensitivity to aerodynamic force coefficients and  $C_L/C_D$  ratio, the results for steady state simulation at 4 degrees AOA and Mach 0.64 corrected data**

Parameters	Clean wing	Propeller nacelle position 1	Propeller nacelle position 2	Propeller nacelle position 3	Propeller nacelle position 4	Propeller nacelle - tractor position
$C_L$	0.48822	0.50477	0.504788	0.504391	0.503979	0.493164
$C_D$	0.021126	0.02075	0.020779	0.020786	0.020769	0.020977
$C_L/C_D$	23.10991	24.31677	24.29293	24.26534	24.26616	23.50997

**Table 44: Propeller nacelle sensitivity to aerodynamic force coefficients and  $C_L/C_D$  ratio, the results for steady state simulation showing percentage improvements at 4 degrees AOA and Mach 0.64, before corrections applied**

Parameters	Clean wing - % improvement	Propeller nacelle position 1 - % improvement	Propeller nacelle position 2 - % improvement	Propeller nacelle position 3 - % improvement	Propeller nacelle position 4 - % improvement	Propeller nacelle - tractor position - % improvement
$C_L$	0	3.4%	3.4%	3.3%	3.2%	1.0%
$C_D$	0	0.8%	0.7%	0.7%	0.7%	0.25%
$C_L/C_D$	0	4.2%	4.1%	4.0%	4.0%	0.8%

**Table 45: Propeller nacelle sensitivity to aerodynamic force coefficients and  $C_L/C_D$  ratio, the results for steady state simulation showing percentage improvements at 4 degrees AOA and Mach 0.64, after corrections applied**

Parameters	Clean wing - % improvement	Propeller nacelle position 1 - % improvement	Propeller nacelle position 2 - % improvement	Propeller nacelle position 3 - % improvement	Propeller nacelle position 4 - % improvement	Propeller nacelle - tractor position - % improvement
$C_L$	0	3.4%	3.4%	3.3%	3.2%	1.0%
$C_D$	0	2%	1.7%	1.7%	1.7%	1.25%
$C_L/C_D$	0	5.2%	5.1%	5.0%	5.0%	1.8%

The factors presented in Tables 40 and 41 are used to correct the data for the wing tip propeller configurations in section 6.4 under chapter 6. The data in Tables 44 and 45 show that after the correlation factors has been applied to the CFD results, the percentage improvement of  $C_L$  remained largely unchanged. Thus, there is no need to modify this parameter in the data in section 6.4 under chapter 6 of this thesis. However, the percentage modification in  $C_D$  and  $C_L/C_D$  is increased by 1 percent from the original values. Therefore, it makes sense that any  $C_D$  values and  $C_L/C_D$  percentage modifications in section 6.4 in chapter 6 should be increased by 1 percent.

### 7.3. Potential application of the technologies

The wing tip spiroid technologies could be applied to a range of aircraft both short and long-range, miniature planes, airships, unmanned aerial vehicles, and even on car spoilers or race car spoilers to create a favorable drag reduction in this region of the car to improve efficiency.

The wingtip turbine technology could potentially also be used on small aircraft, in unmanned aerial vehicles as a performance improvement device. The kinetic energy generated by the propellers could be harnessed and use to power some electric systems in the air vehicle.

## Chapter 8: Conclusion

The aim of this project was to investigate aircraft drag reduction methodologies. The project objectives were to reduce aircraft drag by up to 4 percent by using novel drag reduction technologies. This is achieved by using an optimised spiroid winglet device(s) and a wing tip turbine. Wider implications of using wing tip devices on aircraft design was also considered by performing flutter analysis on an isentropic wing with added winglet variable masses to ascertain its influence on flutter speed and frequency.

First, a comprehensive literature of a number of drag reduction techniques has been conducted. A detailed literature on the underlying principles and application of CFD modelling techniques has also been reviewed, as well as a short but detailed overview of several optimisation methods. A comprehensive investigation of four novel aircraft induced drag reduction devices retrofitted on a representative commercial aircraft wing model has been presented, the designs are named within this thesis as Design-1 (see Fig. 106), Design-2 (see Fig. 107), Design-3 (Fig. 108) and the spiroid trapezium (see Fig. 109). The optimisation process which resulted in the production of these devices was carried out using STARCCM+ Optimate + built-in software, which uses a SHERPA search algorithm as its optimisation search tool. A total of one hundred or more design evaluations were carried out within the specified search space to produce each of the four designs. The SHERPA search algorithm produced three downward facing spiroid winglets and one dihedral winglet as the best designs within given constraints with the following benefits obtained after error analysis and the corrections of the results undertaken in chapter 7:

For the design conditions at Mach 0.74, three of the designs (Designs 1 – 3) and 0.24 (spiroid trapezium), the devices reduced the induced drag by up to 11 – 28 percent. Also, under the same operating conditions, the lift to drag ratio was improved by 3, 3 and 6 percent for Designs 1- 3 respectively and 11 percent for the spiroid trapezium.

The devices effectively reduced  $C_D$  by approximately up to 3 percent for Design-1, 3 percent for Design-2 and an increase of 2 percent was observed for Design-3 and a 4 percent reduction for the spiroid trapezium. In addition to this, the lift coefficient ( $C_L$ ) was improved with values recorded approximately up to 0.5, 3 percent for Designs 2 – 3 and a 7 percent increase in  $C_L$  was observed for the spiroid trapezium.

Further investigation on the devices at several Mach numbers at sea level conditions, showed Design-1 to have its most effective lift to drag ratio increase of 6.4 percent at Mach 0.84. Its  $C_L$  was increased by 3 percent at Mach

0.64, Design-2 had its most effective lift to drag ratio at Mach 0.64 with a 3 percent improvement. The best  $C_L$  change was logged at Mach 0.54 with a value of 4 percent. Design-3's most effective lift to drag ratio improvements was observed at Mach numbers 0.54 to 0.64 with a value of 6 percent and  $C_L$  value of approximately 5 percent improvement which was at Mach 0.64. The spiroid trapezium configuration had an improved  $C_L/C_D$  of up to 15 percent at Mach 0.54 and  $C_L$  improvement of 11 percent at Mach 0.64. The least  $C_D$  values were observed at Mach 0.54 for the spiroid trapezium at 6 percent reduction compared to that of the clean wing with Designs' 1 – 3 also showing  $C_D$  reduction of 5 percent at Mach 0.84. The four devices had an induced drag reduction up to 8 – 23 percent with Design-2 showing slightly better performance.

The sensitivity analysis of the four devices discussed in chapter 5 showed that for the spiroid trapezium, the most sensitive design variables are chord 5 sweep, chord 1 size (Fig.109) with other parameters having some impact also. For Design-1 most sensitive variables amongst the 21 used were (Fig. 106):

- Drag – chord 3 sweep angle.
- Lift – chord 3 sweep angle.

For Design – 2 initial optimisation the following variables are most sensitive (Fig. 107):

- Drag – winglet chord 3 size.
- Lift – winglet toe 1 size.

For mid-point and closed loop optimisation the most sensitive variables amongst the 14 design variables used were (Fig. 107):

- Drag – winglet chord 3 twist, chord 3 vertical height and winglet mid-point sweep.
- Lift – winglet chord 3 twist, winglet mid-point sweep angle and toe 2 size.

Also, for Design – 3, the most sensitive variables amongst the 15 design variables considered during the optimisation study were (Fig. 108):

- Drag – winglet mid-point sweep, chord 3 twist angle and chord 1 twist.
- Lift – chord 1 twist angle, chord 3 twist and chord 1 size.

In addition, it demonstrated that it was also worth considering other parameters (variables) as mentioned in section 5.4 under chapter 5 during the optimisation process, because their inclusion had some significance for the performance of the designs. It also allowed for a comprehensive sensitivity analysis to be carried out on the design parameters (variables) to better understand their effect on the drag and lift aerodynamic forces on the wing.

The spiroid trapezium had been successful retrofitted on two different wing models. Furthermore, the study showed that a downward pointing winglet is better suited for high subsonic flight regime while upward pointing winglets are most ideal for the lower subsonic regime.

The observations made from this investigation successfully demonstrate the effectiveness of these devices over a wide range of Mach numbers, thereby, indicating several potential applications which could include short and long-range aircraft, unmanned aerial vehicle, miniature planes high subsonic and transonic aircraft and potentially on car spoilers to create favourable drag at the rear of the car. Furthermore, this research work has successfully demonstrated the capability of using CFD modelling coupled with optimisation algorithms in the development of wing tip devices.

In addition to the novel spiroid concepts, detailed research on the use of wind tip turbines as an aerodynamic performance enhancement device on a clean wing has also been documented. This was based on using CFD modelling techniques to subsequently predict the wing and wing tip turbine flow interaction. To observe its effect on aerodynamic parameters such as the coefficient of lift, drag, and lift to drag ratio of the wing, two test cases using steady and unsteady CFD simulations were used to validate the CFD modelling approach adopted for the study by replicating the data for the experimental work carried out by the German company SVA Potsdam on a variable pitch propeller and experimental work at the University of Hertfordshire on a clean wing and a clean wing with mounted tip turbines.

A sensitivity study was carried out to observe the effect of the propeller nacelle position at the wing tip, on the aerodynamic performance of the clean wing at an assumed Mach number of 0.64, 4 degrees angle of attack, temperature, pressure and density settings for 32,808 feet altitude. The results revealed that the performance of the wing was improved in all studied nacelle positions including the pusher propeller configuration. Also, the trend was for the performance of the wing to be better when the nacelle and propellers were much closer to the aft the wing tip with such positions having the best documented impact with a lift to drag ratio increase of up to 5 percent after error analysis and correction had been performed on the results in chapter 7. Furthermore, the propeller pusher configuration was found to be more effective than the tractor configuration.

A study was also carried out to observe the effect of the propeller direction of rotation on the wing propeller interaction. By taking the direction of flow as the reference view of the observer, the clockwise propeller rotation

was found to be more effective in improving the aerodynamic properties of the clean wing than the anti-clockwise rotation.

Moreover, the effect of Mach number on the propeller wing performance was also presented. It was important to observe the performance of this configuration over a range of flight speeds. Mach numbers ranging from 0.24 to 0.84 were studied under sea level operating conditions. The outcome of the research showed that the lift coefficient was consistently modified between the Mach number of 0.44 to 0.64, with the maximum improvement up to 7 percent recorded at Mach 0.54. The drag coefficient was also consistently reduced between Mach 0.24 to 0.64, with the best modification of up to 3 percent observed at Mach 0.24. At higher Mach numbers of 0.74 to 0.84, the drag coefficient was noted to have increased by up to 2 percent. The reason for this increase is directly related to the tip speed of the propeller, which approaches the transonic speed regime, thereby causing a rapid increase in pressure around this region. In addition to the modifications to the coefficients of lift and drag, improvement in the wing's lift to drag ratio was also noted, a maximum value of 6 percent was seen.

The effect of changing the angle of attack on the performance of the configuration was also discussed. Results showed that the maximum lift to drag ratio, lift and drag coefficients were 6 percent, 4 percent and 4 percent respectively both at 4 degrees angle of attack. The configuration was shown to be less effective at reducing  $C_D$  beyond 6 degrees angle of attack. This gave the indication that this device is best suited for cruise flight phase.

The investigation on the rpm effect on the propeller performance on the wing aerodynamics was also documented. The results showed no trend in decreasing the rpm from 9000 – 5000. Rather, the performance was rpm specific and gives the indication that the performance of the wing in such configuration is rpm sensitive. That is, the maximum lift to drag ratio improvement was approximately 7 percent, the best coefficient of drag reduction was observed at 8000rpm and 5000rpm and the maximum lift coefficient recorded at 7000 rpm which was the rpm used throughout the study.

Based on the results presented and discussed in chapter 6 of this thesis, it could be concluded that for practical application, the most ideal configuration of the wing tip turbine technology for aerodynamic performance improvement would be to mount the technology with the propeller and nacelle close to the rear of the wing tip which would bring it in direct contact with the high vortex region of the wing tip. Together with this configuration the propeller rpm should be potentially on or below 8000rpm, with the direction of rotation clockwise. Furthermore, applications should only be for subsonic flight Mach numbers below Mach 0.64 due to the tip speed of the propeller which approaches transonic speeds at higher Mach numbers and could result in noise pollution.

Additionally, the kinetic energy produced by the rotating propeller blades could be used to power some aircraft systems. Also, this configuration could be adopted in small aircrafts at low speed, unmanned aerial vehicles or can simply be used as a propulsion system used to replace the concept of having the engines in-board of the wing, of course, the structural implication of such a concept needs to be taken into consideration.

The introduction of wing tip devices has other implications on aircraft design, such as aeroelasticity. A flutter analysis of an un-swept, uniform wing with and without variable winglet masses has been presented in Appendix A. The winglet's mass was increased from 0 to 1554 pounds, a fixed engine nacelle mass of 6000 pounds was located at the 46 percent chord position of the wing and the elastic axis was assumed at 40 percent chord. The flutter speed and natural frequencies were computed by using a numerical code run in MATLAB which solves the flutter equations using the p-k iterative method. The study suggested that installing winglets or other wing tip devices should not result in insurmountable aeroelastic issues.

## Chapter 9: Recommendations

Future work should focus on further investigating the devices on a full aircraft configuration or UAV to ascertain the amount of  $C_L/C_D$ ,  $C_L$  and  $C_D$  improvement achievable and also the impact on  $C_M$ . A scaled model aircraft or UAV retrofitted with the devices could also be tested in a wind tunnel for result validation purposes.

Furthermore, the structural impact on the wing by using such devices could be investigated by performing a structural optimisation study and or a multi-disciplinary optimisation study. This should include aero-structural analysis coupled by using the appropriate numerical code.

Future work could focus on the combination of wing tip devices with measures to reduce skin friction.

In addition, an investigation carried out to ascertain which decomposed drag component (s) is mostly affected or improved by using the spiroid wing tip technologies would be beneficial as future work.

More work could be focused on using other turbulence models such as Large Eddy simulation and Detached Eddy simulation models to predict the aerodynamic performance and flow characteristics around the devices and see how it compares with those in this thesis.

Moreover, investigation on the impact of using the spiroid devices on aircraft manoeuvring performance. E.g. rolling could be carried out

## References

- A. Abbas, J. D. V., E. Valero 2012. Aerodynamic technologies to improve aircraft performance. *Aerospace Science and Technology*.
- Abbas, A., De Vicente, J. & VALERO, E. 2013. Aerodynamic technologies to improve aircraft performance. *Aerospace Science and Technology*, 28, 100-132.
- Addoms, R. B. & Spaid, F. W. 1975. Aerodynamic design of high-performance biplane wings. *Journal of Aircraft*, 12, 629-630.
- Agrusta, A. A. 2015. Optimisation's techniques of hull shapes using CFD Rans simulations with low number of cells.
- Al-Atabi, M. 2006. Aerodynamics of wing tip sails. *Journal of Engineering Science and Technology*, 1, 89-98.
- Alba, C., Elham, A., German, B. J. & Veldhuis, L. 2018. A Surrogate-Based Multi-Disciplinary Design Optimization Framework Modeling Wing-Propeller Interaction. *Aerospace Science and Technology*.
- Alekseev, V., Gachechiladze, I., Kiknadze, G. & Oleinikov, V. Tornado-like energy transfer on three-dimensional concavities of reliefs-structure of self-organizing flow, their visualisation, and surface streamlining mechanisms. Transactions of the 2nd Russian Nat. Conf. of Heat Transfer, Heat Transfer Intensification Radiation and Complex Heat Transfer, 1998. 33-42.
- Ananda Krishnan, G. K., Deters, R. W. & Selig, M. S. Propeller Induced Flow Effects on Wings at Low Reynolds Numbers. 31st AIAA Applied Aerodynamics Conference, 2013. 3193.
- Ananda Krishnan, G. K., Deters, R. W. & Selig, M. S. Propeller-Induced Flow Effects on Wings of Varying Aspect Ratio at Low Reynolds Numbers. 32nd AIAA Applied Aerodynamics Conference, 2014. 2152.
- Anderson, J. 2001. Emeritus, "Fundamental of Aerodynamics". McGraw-Hill, New York, USA.
- Anderson, J. D. 1999. *Aircraft performance and design*, McGraw-Hill Science/Engineering/Math.
- Anderson, J. D. & Wendt, J. 1995. *Computational fluid dynamics*, Springer.
- Anderson Jr, J. D. 2010. *Fundamentals of aerodynamics*, Tata McGraw-Hill Education.
- Andersson, B., Andersson, R., Håkansson, L., Mortensen, M., Sudiyo, R. & Van Wachem, B. 2011. *Computational fluid dynamics for engineers*, Cambridge University Press.
- Arévalo, P. T. 2014. Design Optimization of a Composite Wing Box for High-Altitude Long-Endurance Aircraft.
- Arnal, D. & Archambaud, J. 2008. Laminar-turbulent transition control: NLF, LFC, HLFC. *Advances in Laminar-Turbulent Transition Modeling*.
- Arnal, D., Juillen, J., Reneaux, J. & Gasparian, G. 1997. Effect of wall suction on leading edge contamination. *Aerospace Science and Technology*, 1, 505-517.
- Arnal, D., Unckel, C.-G., Krier, J., Sousa, J. & Hein, S. Supersonic laminar flow control studies in the SUPERTRAC project. Proc. 25th Congress of the International Council of the Aeronautical Sciences ICAS, 2006a. 3-8.
- Arnal, D., Unckel, C.-G., Krier, J., Sousa, J. M. & Hein, S. Supersonic laminar flow control studies in the SUPERTRAC project. Proceedings of 25th Congress of International Council of the Aeronautical Science, 2006b. 2006.
- Bannasch, R. 2001. From soaring and flapping bird flight to innovative wing and propeller constructions. *Progress in Astronautics and Aeronautics*, 195, 453-471.
- Barkmann, U. 2011a. Potsdam Propeller Test Case (PPTC)-Open Water Tests with the Model Propeller VP1304. *Second International Symposium on Marine Propulsors*
- Barkmann, U., Heinke, H.-J. & Lübke, L. Potsdam Propeller Test Case (PPTC). Proceeding of the Second International Symposium on Marine Propulsors-smp'11, 2011. 36-38.
- Barkmann, U. H. 2011b. Potsdam Propeller Test Case (PPTC) Open Water Tests with the Model Propeller VP1304.
- Bechert, D. & Bartenwerfer, M. 1989. The viscous flow on surfaces with longitudinal ribs. *Journal of fluid mechanics*, 206, 105-129.
- Beechook, A. & Wang, J. Aerodynamic analysis of variable cant angle winglets for improved aircraft performance. Automation and Computing (ICAC), 2013 19th International Conference on, 2013. IEEE, 1-6.
- Bilger, R. 1975. A note on Favre averaging in variable density flows. *Combustion Science and Technology*, 11, 215-217.
- BLazek, J. 2015. *Computational fluid dynamics: principles and applications*, Butterworth-Heinemann.
- Boeing. 2015. *Introducing the 737 MAX 10* [Online]. Available: <http://www.boeing.com/commercial/737max/> [Accessed June 25 2015].
- Bohannon, K. S. 2006. Passive flow control on civil aircraft flaps using sub-boundary layer vortex generators in the AWIATOR programme. *AIAA Paper*, 2858, 2006.
- Brady, C. 1999. *Winglet* [Online]. Available: <http://www.b737.org.uk/winglets.htm> [Accessed June 20 2017].

- Brandt, J. & SELIG, M. Propeller performance data at low Reynolds numbers. 49th AIAA Aerospace Sciences Meeting including the New Horizons Forum and Aerospace Exposition, 2011. 1255.
- Braslow, A. L., Visconti, F. & Burrows, D. L. 1948. Preliminary Wind-Tunnel Investigation of the Effect of Area Suction on the Laminar Boundary Layer Over an NACA 64A010 Airfoil.
- Breuer, M. 1998. Large eddy simulation of the subcritical flow past a circular cylinder: numerical and modeling aspects. *International Journal for Numerical Methods in Fluids*, 28, 1281-1302.
- Bruse, M., Bechert, D., Van Der Hoeven, J., Hage, W. & Hoppe, G. Experiments with Conventional and with Novel Adjustable Drag Reducing Surfaces. Near-Wall Turbulent Flows Conference Proceedings (1993), 1993. Elsevier Science Publishers, Amsterdam, The Netherlands.
- Bushnell, D. 2003. Aircraft drag reduction—a review. *Proceedings of the Institution of Mechanical Engineers, Part G: Journal of Aerospace Engineering*, 217, 1-18.
- Bushnell, D. M., Hefner, J. N. & Ash, R. L. 1977. Effect of compliant wall motion on turbulent boundary layers. *The Physics of Fluids*, 20, S31-S48.
- Canuto, V. 1994. Large eddy simulation of turbulence: A subgrid scale model including shear, vorticity, rotation, and buoyancy. *The Astrophysical Journal*, 428, 729-752.
- Carpenter, P. W., Lucey, A. D. & Davies, C. 2001. Progress on the use of compliant walls for laminar-flow control. *Journal of Aircraft*, 38, 504-512.
- Caruana, D., Barricau, P., Hardy, P., Cambonne, J. & Belinger, A. 2009. The ‘plasma synthetic jet’ actuator aerothermodynamic characterization and first flow control applications. *AIAA*, 1307, 2009.
- Case, L., Jordan, C. N. & Wright, L. Effect of dimple depth on heat transfer enhancement in a rectangular channel ( $ar = 3:1$ ) with hemispherical dimples. 49th AIAA Aerospace Sciences Meeting including the New Horizons Forum and Aerospace Exposition, 2011. 825.
- Cerón-Muñoz, H. & Catalano, F. 2006. Experimental analysis of the aerodynamic characteristics adaptive of multi-winglets. *Proceedings of the Institution of Mechanical Engineers, Part G: Journal of Aerospace Engineering*, 220, 209-215.
- Chase, N., Rademacher, M., Goodman, E., Averill, R. & Sidhu, R. 2009. A benchmark study of multi-objective optimization methods. *BMK-3021, Rev*, 6.
- Chase, N., Redemacher, M., Goodman, E., Averill, R. & Sidhu, R. 2010. A benchmark study of optimization search algorithms. *MI, USA: Red Cedar Technology*.
- Chernyshev, S., Kiselev, A. & Kuryachii, A. Laminar flow control: TsAGI experience and investigations. 47th AIAA Aerospace Sciences Meeting including The New Horizons Forum and Aerospace Exposition, 2009. 381.
- Chinwicharnam, K., Ariza, D. G., Moschetta, J.-M. & Thipyopas, C. 2013. Aerodynamic characteristics of a low aspect ratio wing and propeller interaction for a tilt-body MAV. *International Journal of Micro Air Vehicles*, 5, 245-260.
- Choi, K.-S. 2000. European drag-reduction research—recent developments and current status. *Fluid Dynamics Research*, 26, 325-335.
- Chong, E. K. & Zak, S. H. 2013. *An introduction to optimization*, John Wiley & Sons.
- Çıtak, C., Akdemir, M. & Yumuşak, M. 2016. Multidisciplinary, Multiobjective Analysis and Optimization for the Design of Missile Jet Vane.
- Collier JR, F. 1993. An overview of recent subsonic laminar flow control flight experiments.
- Cortelezzi, L., Lee, K., Kim, J. & Speyer, J. 1998. Skin-friction drag reduction via robust reduced-order linear feedback control. *International Journal of Computational Fluid Dynamics*, 11, 79-92.
- Coustols, E. & Schmitt, V. 1990. Synthesis of experimental riblet studies in transonic conditions. *Turbulence control by passive means*. Springer.
- Creel, T. 1991. Effects of sweep angle and passive relaminarization devices on a supersonic swept-cylinder boundary layer. *AIAA Paper*, 91-0066.
- Durbin, P. 1996. On the k-3 stagnation point anomaly. *International journal of heat and fluid flow*, 17, 89-90.
- Elham, A. & Van Tooren, M. J. 2014a. Winglet multi-objective shape optimization. *Aerospace Science and Technology*, 37, 93-109.
- Elham, A. & Van Tooren, M. J. L. 2014b. Winglet multi-objective shape optimization. *Aerospace Science and Technology*, 37.
- Eliasson, P. Numerical validation of a half model high lift configuration in a wind tunnel. 45th AIAA Aerospace Science Meeting and Exhibit, 2007.
- Enearu, O., Chen, Y. K. & Kalyvas, C. A new approach to modelling of PEMFC flow field. Modelling, Identification and Control (ICMIC), 2017 9th International Conference on, 2017. IEEE, 958-964.
- Engert, M. & Nitsche, W. Active cancellation of Tollmien–Schlichting instabilities up to  $M = 0.40$ . International Congress of the Aeronautical Sciences, Paper, 2008.
- Epstein, B., Peigin, S. & Tsach, S. 2006. A new efficient technology for aerodynamic design based on CFD driven optimization. *Aerospace science and Technology*, 10, 100-110.

- Erdmann, R., Pätzold, A., Engert, M., Peltzer, I. & Nitsche, W. 2011. On active control of laminar–turbulent transition on two-dimensional wings. *Philosophical Transactions of the Royal Society of London A: Mathematical, Physical and Engineering Sciences*, 369, 1382-1395.
- Eyi, S., Lee, K., Rogers, S. & Kwak, D. 1996. High-lift design optimization using Navier-Stokes equations. *Journal of Aircraft*, 33, 499-504.
- Falcao Da Luz, L. F. B. 2013. Multidisciplinary Design Optimization of Adaptive Wingtip Devices for Greener Aircraft.
- Ferziger, J. H. & Peric, M. 2012. *Computational methods for fluid dynamics*, Springer Science & Business Media.
- Filippone, A. 2012. *Advanced aircraft flight performance*, Cambridge University Press.
- Fluent, A. 2012. 14.5, theory guide; ansys. Inc., Canonsburg, PA.
- Frediani, A., Balis Crema, L., Chiocchia, G., Ghiringhelli, G. & Morino, L. Development of an innovative configuration for transport aircraft; a project of five Italian universities. XVII Congresso Nazionale AIDAA III, Roma, Italy, 2003. 2089-2104.
- French, R. V. 1978. Vortex Reducing Wing Tip. *US Patent*, 4, 22.
- Frota, J. 2010. NACRE novel aircraft concepts. *The Aeronautical Journal*, 114, 399-404.
- Furlong, G. C. & Fitzpatrick, J. E. 1947. Effects of mach number and reynolds number on the maximum lift coefficient of a wing of NACA 230-Series airfoil sections.
- García-Mayoral, R. & Jiménez, J. 2011. Drag reduction by riblets. *Philosophical Transactions of the Royal Society of London A: Mathematical, Physical and Engineering Sciences*, 369, 1412-1427.
- Gariépy, M., Malouin, B., Trépanier, J.-Y. & Laurendeau, É. 2013. Far-field drag decomposition applied to the drag prediction workshop 5 cases. *Journal of Aircraft*.
- Gavrilović, N. N., Rašuo, B. P., Dulikravich, G. S. & Parezanović, V. B. 2015. Commercial aircraft performance improvement using winglets. *FME Transactions*, 43, 1-8.
- Godard, G., Foucaut, J.-M. & Stanislas, M. 2006. Control of a decelerating boundary layer. Part 2: Optimization of slotted jets vortex generators. *Aerospace Science and Technology*, 10, 394-400.
- Godard, G. & Stanislas, M. 2006a. Control of a decelerating boundary layer. Part 1: Optimization of passive vortex generators. *Aerospace Science and Technology*, 10, 181-191.
- Godard, G. & Stanislas, M. 2006b. Control of a decelerating boundary layer. Part 3: Optimization of round jets vortex generators. *Aerospace science and technology*, 10, 455-464.
- Görtz, S. 2005. *Realistic simulations of delta wing aerodynamics using novel CFD methods*. KTH.
- Gratzer, L. B. 1992. Spiroid-tipped wing. Google Patents.
- Grenon, R. & Bourdin, P. 2002. Numerical study of unconventional wing tip devices for lift-induced drag reduction. *Tiré à part- Office national d'études et de recherches spatiales*.
- Guerrero, J. E., Maestro, D. & Bottaro, A. 2012a. Biomimetic spiroid winglets for lift and drag control. *Comptes Rendus Mécanique*, 340, 67-80.
- Guerrero, J. E., Maestro, D. & Bottaro, A. 2012b. Biomimetic spiroid winglets for lift and drag Control. 340.
- Hackett, J. 1980. Vortex drag reduction by aft-mounted diffusing vanes. *ICAS paper*, 80, 13.4.
- Haines, A. 1968. Subsonic aircraft drag: An appreciation of present standards. *The Aeronautical Journal*, 72, 253-266.
- Hantrais-Gervois, J.-L., Grenon, R., Mann, A. & Büscher, A. 2009. Downward pointing winglet design and assessment within the M-DAW research project. *The Aeronautical Journal*, 113, 221-232.
- Hardy, P., Barricau, P., Caruana, D., Gleyzes, C., Belinger, A. & Cambronne, J. P. 2010. Plasma Synthetic Jet for flow control. Proceedings of the 40th AIAA fluid dynamics conference and exhibit. *AIAA*, 5103.
- Haynes, T. S. & Reed, H. L. 2000. Simulation of swept-wing vortices using nonlinear parabolized stability equations. *Journal of Fluid Mechanics*, 405, 325-349.
- Heeds. 2017. *HEEDS (Hierarchical Evolutionary Engineering Design System). Getting started manual*. [Online]. The Steve Portal, Documentation, HEEDS. Available: [https://documentation.thesteveportal.plm.automation.siemens.com/heeds\\_latest\\_en/HEEDSMDO/Welcome.htm](https://documentation.thesteveportal.plm.automation.siemens.com/heeds_latest_en/HEEDSMDO/Welcome.htm) 2017].
- Hein, S., Schüle, E., Hanifi, A., Sousa, J. & Arnal, D. Laminar flow control by suction at Mach 2. Seventh IUTAM Symposium on Laminar-Turbulent Transition, 2010. Springer, 189-194.
- Hemke, P. E. 1928. Drag of wings with end plates.
- Heyson, H. H., Riebe, G. D. & Fulton, C. L. 1977. Theoretical parametric study of the relative advantages of winglets and wing-tip extensions.
- Ho, S., Nassef, H., Pornsinsirak, N., Tai, Y.-C. & Ho, C.-M. 2003. Unsteady aerodynamics and flow control for flapping wing flyers. *Progress in Aerospace Sciences*, 39, 635-681.
- Hoerner, S. 1952. Aerodynamic shape of the wing tips. Air materiel command Wright-Patterson AFB OH Engineering DIV.
- Hossain, A., Arora, P. R., Rahman, A., Jaafar, A. A. & Iqbal, A. P. 2008. Analysis of longitudinal aerodynamic characteristics of an aircraft model with and without winglet. *JJMIE*, 2.

- Hough, G. R. 1980. *Viscous flow drag reduction*, American Institute of Aeronautics and Astronautics.
- Houghton, E. L. & Carpenter, P. W. 2003. *Aerodynamics for engineering students*, Butterworth-Heinemann.
- Iuliano, E., Salah El Din, I., Donelli, R., Quagliarella, D. & Arnal, D. Natural laminar flow design of a supersonic transport jet wing body. 47th AIAA Aerospace Sciences Meeting including The New Horizons Forum and Aerospace Exposition, 2009. 1279.
- Jahanmiri, M. 2011. Aircraft Drag Reduction: An Overview. Chalmers University of Technology.
- Jansen, P. W., Perez, R. E. & Martins, J. 2010. Aerostructural optimization of nonplanar lifting surfaces. *Journal of Aircraft*, 47, 1490.
- Jiménez, J. 1994. On the structure and control of near wall turbulence. *Physics of Fluids*, 6, 944-953.
- Joel, H. & Peric, M. F. 1999. Computational methods for fluid dynamics.
- Joseph, P., Amandolese, X., Edouard, C. & Aider, J.-L. 2013. Flow control using MEMS pulsed micro-jets on the Ahmed body. *Experiments in fluids*, 54, 1442.
- Joslin, R. D. 1998. Aircraft laminar flow control. *Annual review of fluid mechanics*, 30, 1-29.
- Jou, W., Huffman, W., Young, D., Melvin, R., Bieterman, M., Hilmes, C. & Johnson, F. Practical considerations in aerodynamic design optimization. 12th Computational Fluid Dynamics Conference, 1995. 1730.
- Jupp, J. 2001. Wing aerodynamics and the science of compromise. *The Aeronautical Journal*, 105, 633-641.
- Khosravi, S. & Zingg, D. W. A numerical optimization study on winglets. 15th AIAA/ISSMO Multidisciplinary Analysis and Optimization Conference, 2014. 2014-2173.
- Klasson, O. K. & Huuva, T. Potsdam propeller test case (PPTC). Second International Symposium on Marine Propulsors, SMP, 2011.
- Klug, H. G. 1988. Auxiliary wing tips for an aircraft. Google Patents.
- Kosorygin, V., Radeztsky, R. & Saric, W. 1995. Laminar boundary-layer, sound receptivity and control. *Laminar-turbulent transition*. Springer.
- Kravchenko, S. The application of the wing tip lifting surfaces for practical aerodynamic. ICAS PROCEEDINGS, 1996. 1338-1348.
- Kriging, D. G. 1951. A Statistical Approach to Some Basic Mine Valuations Problems on the Witwatersrand. *Journal of the Chemical, Metallurgical and Mining Engineering Society of South Africa*, 52, 119-139.
- Kroo, I. 2005. Nonplanar wing concepts for increased aircraft efficiency. *VKI lecture series on innovative configurations and advanced concepts for future civil aircraft*, 6-10.
- Kuhlman, J. & Liaw, P. 1988. Winglets on low-aspect-ratio wings. *Journal of Aircraft*, 25, 932-941.
- Kundu, A. K. 2010. *Aircraft design*, Cambridge University Press.
- Kurz, A., Grundmann, S., Tropea, C., Forte, M., Seraudie, A., Vermeersch, O., Arnal, D., Goldin, R. & King, R. 2013. Boundary layer transition control using DBD plasma actuators. *AerospaceLab*, p. 1-8.
- Kusterer, K., Dickhoff, J., Campana, N. T., Sugimoto, T., Tanaka, R., Kazari, M. & Bohn, D. Automated design space exploration of advanced-shaped film cooling holes using the sherpa algorithm. ASME Turbo Expo 2016: Turbomachinery Technical Conference and Exposition, 2016. American Society of Mechanical Engineers, V05CT12A004-V05CT12A004.
- Lange, K., Lueth, C., Godfrey, A. & Hartridge, S. Optimization of Component Material Properties and Flow Channel Geometric Parameters in a PEM Fuel Cell Cathode. Meeting Abstracts, 2014. The Electrochemical Society, 1106-1106.
- Lange, R., Cahill, J., Bradley, E., Eudaily, R., Jenness, C. & Macwilkinson, D. 1974. Feasibility study of the transonic biplane concept for transport aircraft application.
- Launder, B. 1991. Introduction to the Modeling of Turbulence: Introduction. *VKI An Introduction to Modeling Turbulence*.
- Launder, B. E. & Sandham, N. D. 2002. *Closure strategies for turbulent and transitional flows*, Cambridge University Press.
- Leifsson, L. & Koziel, S. 2015. Aerodynamic shape optimization by variable-fidelity computational fluid dynamics models: A review of recent progress. *Journal of Computational Science*, 46.
- Li, Z., Zhang, Y. & Chen, H. 2015. A low dissipation numerical scheme for Implicit Large Eddy Simulation. *Computers & Fluids*, 117, 233-246.
- Liebeck, R. H. 1973. A class of airfoils designed for high lift in incompressible flow. *Journal of Aircraft*, 10, 610-617.
- Lienhart, H., Breuer, M. & Köksoy, C. 2008. Drag reduction by dimples?—A complementary experimental/numerical investigation. *International Journal of Heat and Fluid Flow*, 29, 783-791.
- Lienhart, H., Breuer, M. & Köksoy, C. 2010. An Experimental/Numerical Investigation on Drag Reduction by Dimples. *PAMM*, 10, 31-34.
- Loftin JR, L. K. & Horton, E. A. 1952. Experimental investigation of boundary-layer suction through slots to obtain extensive laminar boundary layers on a 15-percent-thick airfoil section at high Reynolds numbers.

- Lubis, A., Rosley, M., Razak, M., Damanhuri, A. & Amin, A. 2017. Drag and lift evaluation on redesigned front area of 1990's land rover defender. *Proceedings of Mechanical Engineering Research Day 2017*, 2017, 48-49.
- Maksoud, T. & Seetloo, S. Wingtips and multiple wing tips effects on wing performance: theoretical and experimental analyses. 2014. International Conference on Heat Transfer, Fluid Mechanics and Thermodynamics.
- Mand, G. 2011. In SHERPA or MO-SHERPA, how does one decide on "Number of STAR-CCM+ runs"?
- Martin Bystrom, C.-G. U., DAN HENNINGSON, ARDESHIRE HANIFI. 2006. *Laminar Wings on Future Aircraft* [Online].
- Maughmer, M., Swan, T. & Willits, S. 2002. The design and testing of a winglet airfoil for low-speed aircraft. *Technical Soaring*, 26, 76-88.
- Mclean, D. Wingtip Devices: What they do and how they do it. Boeing Performance and Flight Operations Engineering Conference, 2005.
- McMasters, J. H. & Kroo, I. M. 1998. Advanced configurations for very large transport airplanes. *Aircraft Design*, 1, 217-242.
- Meheut, M., Grenon, G., Carrier, G., Defos, M. & Duffau, M. Aerodynamic design of transonic flying wing configurations. Proceeding of CEAS/KATnet II Conference on Key Aerodynamic Technologies, Bremen, Germany, 2009.
- Melber-Wilkending, S., Heidebrecht, A. & Wichmann, G. A new approach in CFD supported wind tunnel testing. 25th international congress of the aeronautical sciences, ICAS, 2006. 3-8.
- Menter, F., Kuntz, M. & Langtry, R. 2003. Ten years of industrial experience with the SST turbulence model. *Turbulence, heat and mass transfer*, 4, 625-632.
- Menter, F. R. 1994. Two-equation eddy-viscosity turbulence models for engineering applications. *AIAA journal*, 32, 1598-1605.
- Moens, F. & Gardarein, P. Numerical simulation of the propeller/wing interactions for transport aircraft. 19th AIAA applied aerodynamics conference, 2001. 2404.
- Montgomery, D. C. 2017. *Design and analysis of experiments*, John Wiley & sons.
- Morkovin, M. V. 1969. On the many faces of transition. *Viscous drag reduction*. Springer.
- Morkovin, M. V. 1985. Bypass transition to turbulence and research desiderata.
- Mostafa, S., Bose, S., Nair, A., Raheem, M. A., Majeed, T., Mohammed, A. & Kim, Y. A parametric investigation of non-circular spiroid winglets. EPJ Web of Conferences, 2014. EDP Sciences, 02077.
- Mullender, A. & Riedel, H. 1996. A laminar flow nacelle flight test programme. *ROLLS ROYCE PLC-REPORT-PNR*.
- Nasa. 2015. *What is Drag?* [Online]. Available: <https://www.grc.nasa.gov/www/k-12/airplane/drag1.html> [Accessed June 23 2015].
- Nazarinia, M., Soltani, M. & Ghorbanian, K. 2006. Experimental study of vortex shapes behind a wing equipped with different winglets. *Journal of Aerospace Science and Technology*, 3, 1-15.
- Ngo, L., Bello-Ochende, T. & Meyer, J. P. 2015. Numerical modelling and optimisation of natural convection heat loss suppression in a solar cavity receiver with plate fins. *Renewable Energy*, 74, 95-105.
- Nichols, R. 2009. Turbulence Models and their Application to Complex Flows, Revision 4.01. *University of Alabama at Birmingham (HPCMP/PET CFD Onsite-AEDC)*.
- Ning, S. A. & Kroo, I. 2008. Tip extensions, winglets, and c-wings: conceptual design and optimization. *AIAA paper*, 7052.
- Ning, S. A. & Kroo, I. 2010. Multidisciplinary considerations in the design of wings and wing tip devices. *Journal of Aircraft*, 47, 534.
- Patterson JR, J. C. & Bartlett, G. R. 1987. Evaluation of installed performance of a wing-tip-mounted pusher turboprop on a semispan wing.
- Perraud, J., Archambaud, J.-P., Schrauf, G., Donelli, R., Hanifi, A., Quest, J., Hein, S., Streit, T., Fey, U. & Egami, Y. High Reynolds number transition experiments in etw (telfona project). Seventh IUTAM Symposium on Laminar-Turbulent Transition, 2010. Springer, 553-556.
- Persson, A., Lindstrand, R., Muggiasca, S. & Larsson, L. 2017. CFD prediction of steady and unsteady upwind sail aerodynamics. *Ocean Engineering*.
- Pfenninger, W. 1965. Flow phenomena at the leading edge of swept wings. *Recent Developments in Boundary Layer Research, AGARDograph*, 97.
- Piot, E., Casalis, G. & Terracol, M. 2007. Direct numerical simulation of the crossflow instabilities induced by a periodic roughness array on a swept cylinder: receptivity and stability investigations. *AIAA Paper*, 3976.
- Poll, D. 1978. Some aspects of the flow near a swept attachment line with particular reference to boundary layer transition.
- Poll, D. Boundary layer transition on the windward face of Space Shuttle during re-entry. 20th Thermophysics Conference, 1985. 899.

- Pope, S. 2000. *Turbulent Flows*, 771 pp. Cambridge Univ. Press, Cambridge, UK.
- Potsdam, S. 2011. *PPTC smp'11 Workshop* [Online]. Available: <https://www.sva-potsdam.de/pptc-smp11-workshop/> [Accessed 2nd January 2017].
- Prandtl, L. 1949. Report on investigation of developed turbulence.
- Rakshith, B., Deshpande, S., Praveen, C., Narasimha, R. & Riethmuller, M. Aerodynamic Optimization of Wings for Propeller Driven Aircraft. Proceedings of the 3rd European Conference for Aero-Space Sciences, 2009.
- Raymer, D. P. 2005. *Aircraft Design: A Conceptual Approach*, Washington, D.C., AIAA.
- Reddy, S. R., Sobieczky, H., Abdoli, A. & Dulikravich, G. S. Winglets–Multiobjective Optimization of Aerodynamic Shapes. 11th World Congress on Computational Mechanics, 2014.
- Reid, E. G. 1925. The effects of shielding the tips of airfoils.
- Reneaux, J. 2004. Overview on drag reduction technologies for civil transport aircraft. *ONERA: Tire a Part*, 153, 1-18.
- Reneaux, J., Preist, J., Juillen, J. & Arnal, D. 1996. Control of attachment line contamination. *Tiré à part- Office national d'études et de recherches aérospatiales*.
- Rhie, C. & Chow, W. L. 1983. Numerical study of the turbulent flow past an airfoil with trailing edge separation. *AIAA journal*, 21, 1525-1532.
- Riedeberger, D. & Rist, U. 2012. Numerical Simulation of Laminar-Turbulent Transition on a Dolphin Using the  $\gamma$ -Re  $\theta$  Model. *High Performance Computing in Science and Engineering'11*, 379-391.
- Ristorcelli, J. & Morrison, J. 1996. The Favre–Reynolds average distinction and a consistent gradient transport expression for the dissipation. *Physics of Fluids*, 8, 2783-2785.
- Robert, J. Drag reduction: an industrial challenge. Special Course on Skin Friction Drag Reduction. 1992. AGARD.
- Rumsey, C., Long, M., Stuever, R. & Wayman, T. 2011a. Summary of the first AIAA CFD high lift prediction workshop.
- Rumsey, C. L. Recent developments on the turbulence modeling resource website. 22nd AIAA Computational Fluid Dynamics Conference, 2015. 2927.
- Rumsey, C. L., Slotnick, J., Long, M., Stuever, R. & Wayman, T. 2011b. Summary of the first AIAA CFD high-lift prediction workshop. *Journal of Aircraft*, 48, 2068-2079.
- Runyan, H. L. & Sewall, J. L. 1948. Experimental investigation of the effects of concentrated weights on flutter characteristics of a straight cantilever wing.
- Runyan, H. L. & Watkins, C. E. 1949. Flutter of a uniform wing with an arbitrarily placed mass according to a differential-equation analysis and a comparison with experiment.
- Rushing, H., Karl, A. & Wisnowski, J. 2014. *Design and analysis of experiments by Douglas Montgomery: a supplement for using JMP*, SAS Institute.
- Sagaut, P. 2001. *Large Eddy Simulation For Incompressible Flow, An Introduction*". Springer Publication.
- Samant, S., Bussolletti, J., Johnson, F., Burkhart, R., Everson, B., Melvin, R., Young, D., Erickson, L. & Madson, M. 1987. TRANAIR-A computer code for transonic analyses of arbitrary configurations.
- Saric, W. S., Carpenter, A. L. & Reed, H. L. 2008. Flight experiments on swept wing transition using distributed roughness. *ICAS Paper No. 2008-2.7*, 5.
- Saric, W. S., Carpenter, A. L. & Reed, H. L. 2011. Passive control of transition in three-dimensional boundary layers, with emphasis on discrete roughness elements. *Philosophical Transactions of the Royal Society of London A: Mathematical, Physical and Engineering Sciences*, 369, 1352-1364.
- Saric, W. S. & Reed, H. L. 2002. Supersonic laminar flow control on swept wings using distributed roughness. *AIAA paper*, 147, 2002.
- Saric, W. S. & Reed, H. L. 2003. Crossflow instabilities—theory & technology. *AIAA paper*, 771, 2003.
- Sawyers, D. Special Technology session 8; Drag reduction technologies; ECCOMAS CFD 2006. 2006.
- Schlichting, H. 1968. Boundary-layer theory.
- Schlichting, H., Gersten, K., Krause, E. & Oertel, H. 1955. *Boundary-layer theory*, Springer.
- Schramm, V., Denecke, J., Kim, S. & Wittig, S. 2004. Shape optimization of a labyrinth seal applying the simulated annealing method. *International Journal of Rotating Machinery*, 10, 365-371.
- Schrauf, G. H. & Horstmann, K. H. Simplified hybrid laminar flow control. European Congress on Computational Methods in Applied Sciences and Engineering, ECCOMAS, 2004.
- Schwamborn, D., Gerhold, T. & Heinrich, R. 2006. The DLR TAU-code: recent applications in research and industry.
- Selig, M. Modeling full-envelope aerodynamics of small UAVs in realtime. AIAA Atmospheric Flight Mechanics Conference, 2010. 7635.
- Serokhvostov, S. V. 2013. One idea of propeller for low Reynolds numbers. *Proc. IMAV*, 2013.
- Shankara, P. & Snyder, D. 2012. Numerical simulation of high lift trap wing using STAR-CCM+. *AIAA*, 2920, 2012.

- Simpson, T. W., Poplinski, J., Koch, P. N. & Allen, J. K. 2001. Metamodels for computer-based engineering design: survey and recommendations. *Engineering with computers*, 17, 129-150.
- Sinha, S. 2007. Optimizing wing lift to drag ratio enhancement with flexible-wall turbulence control. *AIAA Paper*, 25.
- Sinha, S. K. 1999. System for efficient control of flow separation using a driven flexible wall. Google Patents.
- Sinha, S. K. 2008. System and method for using a flexible composite surface for pressure-drop free heat transfer enhancement and flow drag reduction. Google Patents.
- Sinha, S. K. & Ravande, S. V. 2006. Drag reduction of natural laminar flow airfoils with a flexible surface deturbulator. *AIAA Paper*, 3030, 5-8.
- Sivaji, R. 2004. *Aerodynamic analysis of the joined-wing configuration of a high-altitude, long endurance (HALE) aircraft*. University of Cincinnati.
- Slotnick, J. P., Hannon, J. A. & Chaffin, M. 2011. Overview of the first AIAA CFD high lift prediction workshop. *AIAA Paper*, 862, 2011.
- Smith, M., Komerath, N., Ames, R., Wong, O. & Pearson, J. 2001. Performance analysis of a wing with multiple winglets. Georgia inst of tech atlanta school of aerospace engineering.
- Spillman, J. 1978. The use of wing tip sails to reduce vortex drag. *The Aeronautical Journal*, 82, 387-395.
- Stanislas, M. & Godard, G. Control of a decelerating boundary layer. comparison of different actuators using piv. TSFP digital library online, 2005. Begel House Inc.
- Stone, R. H. 2008. Aerodynamic modeling of the wing-propeller interaction for a tail-sitter unmanned air vehicle. *Journal of Aircraft*, 45, 198-210.
- STreit, T., Horstmann, K., Schrauf, G., Hein, S., Fey, U., Egami, Y., Perraud, J., El Din, I. S., Cella, U. & Quest, J. Complementary numerical and experimental data analysis of the ETW Telfona Pathfinder wing transition tests. 49th AIAA Aerospace Sciences Meeting including the New Horizons Forum and Aerospace Exposition, 2011. 881.
- Sui-Han, Z., Yong, Y. & Dong, L. Experiments of cross-flow instability in a swept-wing boundary layer. 27th Congress of the International Council of the Aeronautical Sciences, ICAS2010, Nice, 2010. 19-24.
- Svoboda, A. & Rozehnal, D. Modeling an unsteady flow over a pitching NACA 0012 airfoil Using CFD. Military Technologies (ICMT), 2017 International Conference on, 2017. IEEE, 452-456.
- Tate, E., Gargoloff, J., Duncan, B., Tummescheit, H., Griffin, J. & Batteh, J. Improved Aerodynamic Prediction Through Coupled System and CFD Models. Proceedings of the 12th International Modelica Conference, Prague, Czech Republic, May 15-17, 2017, 2017. Linköping University Electronic Press, 47-53.
- Taylor, J. W. 1976. *Jane's All the World's Aircraft, 1976-77*, Macdonald and Jane's Publishers Limited.
- Tinoco, E. N., Brodersen, O. P., Keye, S., Laflin, K. R., Feltrop, E., Vassberg, J. C., Mani, M., Rider, B., Wahls, R. A. & Morrison, J. H. 2017. Summary of Data from the Sixth AIAA CFD Drag Prediction Workshop: CRM Cases 2 to 5.
- Tonomura, O., Kano, M. & Hasebe, S. 2010. Shape optimization of microchannels using CFD and adjoint method. *Computer Aided Chemical Engineering*, 28, 37-42.
- Torenbeek, E. 2005. *Innovative configurations and advanced concepts for future civil aircraft: June 6-10, 2005*, Von Karman Institute for Fluid Dynamics.
- Torenbeek, E. 2013. *Advanced aircraft design: Conceptual design, technology and optimization of subsonic civil airplanes*, John Wiley & Sons.
- Traub, L. 2016. Effect of a pusher propeller on a delta wing. *Aerospace Science and Technology*, 48, 115-121.
- Tu, J., Yeoh, G. H. & Liu, C. 2012. *Computational fluid dynamics: a practical approach*, Butterworth-Heinemann.
- Tucker, V. A. 1993. Gliding birds: reduction of induced drag by wing tip slots between the primary feathers. *Journal of Experimental Biology*, 180, 285-310.
- Tucker, V. A. 1995. Drag reduction by wing tip slots in a gliding Harris' hawk, *Parabuteo unicinctus*. *Journal of Experimental Biology*, 198, 775-781.
- Ursache, N. M., Melin, T., Isikveren, A. T. & Friswell, M. I. Morphing winglets for aircraft multi-phase improvement. 7th AIAA ATIO Conference, 2007.
- Van Der Vooren, J. & Slooff, J. 1990. Cfd-based drag prediction: State-of-the-art, theory. *prospects. Tech. rep., NLR*, 4, 119.
- Van Leer, B. 1979. Towards the ultimate conservative difference scheme. V. A second-order sequel to Godunov's method. *Journal of computational Physics*, 32, 101-136.
- Vassberg, J. C., Tinoco, E. N., Mani, M., Rider, B., Zickuhr, T., Levy, D. W., Brodersen, O. P., Eisfeld, B., Crippa, S. & Wahls, R. A. 2014. Summary of the fourth AIAA computational fluid dynamics drag prediction workshop. *Journal of Aircraft*.
- Veldhuis, L. Review of propeller-wing aerodynamic interference. 24th International Congress of the Aeronautical Sciences, 2004.
- Viswanath, P. 2002. Aircraft viscous drag reduction using riblets. *Progress in Aerospace Sciences*, 38, 571-600.

- Von Karman, T. 1930. Calculation of pressure distribution on airship hulls.
- Von Kármán, T. & Burgers, J. M. 1935. *General aerodynamic theory. Perfect fluids.*
- Vos, J., Rizzi, A., Darracq, D. & Hirschel, E. 2002. Navier–Stokes solvers in European aircraft design. *Progress in Aerospace Sciences*, 38, 601-697.
- Wakayama, S. 2000. Blended-wing-body optimization problem setup. *AIAA Paper*, 4740, 2000.
- Walsh, M. 1990. Riblets. In: DB, B. & JN, H. (eds.) *Progress in astronautics and aeronautics*. Washington, DC: AIAA.
- Walsh, M. & Lindemann, A. 1984. *Optimization and application of riblets for turbulent drag reduction*, American Institute of Aeronautics and Astronautics Reston, VA.
- Wan, T. & Lien, K.-W. 2009. Aerodynamic efficiency study of modern spiroid winglets. *Journal of Aeronautics, Astronautics and Aviation. Series A*, 41, 23-29.
- Wang, G. 2015. *PIV experiment and CFD simulation of flow around cylinder.*
- Wang, X. & Damodaran, M. 2001. Aerodynamic shape optimization using computational fluid dynamics and parallel simulated annealing algorithms. *AIAA journal*, 39, 1500-1508.
- Warsop, C. AEROMEMS-An investigation into the viability of MEMS technology for boundary layer control. AIAA Applied Aerodynamics Conference, 1999. 08-02.
- Warsop, C. 2003. Active flow control using MEMS. United Kingdom, RTO-EN-AVT-105.2003.
- Warsop, C. 2006. Results and lessons learned from the European AEROMEMS II project. *AIAA Paper*, 3503.
- Warsop, C., Hucker, M., Press, A. J. & Dawson, P. 2007. Pulsed air-jet actuators for flow separation control. *Flow, Turbulence and Combustion*, 78, 255-281.
- Weiss, J. M. & Smith, W. A. 1995. Preconditioning applied to variable and constant density flows. *AIAA journal*, 33, 2050-2057.
- Wendt, J. F. 2008. *Computational fluid dynamics: an introduction*, Springer Science & Business Media.
- Whang, C. W. & Zhong, X. 1999. Direct numerical simulation of Görtler instability in hypersonic boundary layers. *Recent Advances in DNS and LES*. Springer.
- Whang, C. W. & Zhong, X. 2000. Direct Numerical Simulation of Görtler Instability in Hypersonic Boundary Layers. *Laminar-Turbulent Transition*. Springer.
- Whitcomb, R. Methods for reducing aerodynamic drag. NASA Conference Publication, 1981. 10-13.
- Whitcomb, R. T. 1976. A design approach and selected wind tunnel results at high subsonic speeds for wing-tip mounted winglets.
- Whomsley, J. 2018. *Aerodynamics simplified: Wingtip devices* [Online]. Available: <https://www.flitetest.com/articles/aerodynamics-simplified-wingtip-devices> 2018].
- Wilcox, D. C. 1998. *Turbulence modeling for CFD*, DCW industries La Canada, CA.
- Wild, J. Overview on the DeSIREH project. 5th European Conference for Aeronautics and Space Sciences EUCASS, Munich, 2013.
- William, S. & Ruben JR, B. Leading-edge roughness as a transition control mechanism. 36th AIAA Aerospace Sciences Meeting and Exhibit, 1998.
- Williams, M. D. 2009. Wind Tunnel Analysis and Flight Test of a Wing Fence on a T-38. Air force inst of tech wright-patterson afb oh dept of aeronautics and astronautics.
- Williams, M. H. & Cho, J. 1990. Propeller-wing interaction using a frequency domain panel method. *Journal of Aircraft*, 27, 196-203.
- Wilts, C. H. 1958. Incompressible flutter characteristics of representative aircraft wings.
- Wolkovitch, J. 1986. The joined wing: an overview. *J. Aircraft.*, 23, 161-178.
- Yates, J. E. & Donald, C. 1986. A fundamental study of drag and an assessment of conventional drag-due-to-lift reduction devices.
- Young, A. D. & Paterson, J. 1981. Aircraft excrescence drag. Advisory group for aerospace research and development neuilly-sur-seine (France).
- Young, T., Humphreys, B. & Fielding, J. 2001. Investigation of hybrid laminar flow control (HLFC) surfaces. *Aircraft Design*, 4, 127-146.
- Yu, M. & Yuan, X.-J. 2016. The effect of Görtler instability on hypersonic boundary layer transition. *Theoretical and Applied Mechanics Letters*, 6, 97-99.
- Zhang, Y., Fang, X., Chen, H., Fu, S. & Duan, Z. 2015a. Supercritical natural laminar flow airfoil optimization for regional aircraft wing design. *Aerospace science and Technology*, 43, 152 - 164.
- Zhang, Y., Fang, X., Chen, H., FU, S., Duan, Z. & Zhang, Y. 2015b. Supercritical natural laminar flow airfoil optimization for regional aircraft wing design. *Aerospace Science and Technology*, 43, 152-164.
- Zheng, X. & Yan, Y. 2010. A Biomimetic Smart Control of Viscous Drag Reduction. *Advances in Natural Science*, 3, 139-151.

## Appendices

### Appendix A: Flutter analysis of wing with winglet

Mounting wing tip devices has broad implications beyond the impact on aerodynamics. This explores one significant effect which is the impact on flutter characteristics.

The underlying theory and the flutter analysis of an un-swept wing model with and without applied concentrated mass (winglet mass) at the wing tip is presented. The wing model was assumed to be built at the root into a wall and was assumed to be of uniform aspect ratio. The wing was modelled as a uniform wing with the capability of bending and torsion. For the flutter analysis, incompressible Theodorsen theory unsteady aerodynamics was used. Appendix A-I describes the wing structural model, the aerodynamic modelling approach and the method used for solving the flutter equations. Appendix A-II presents the initial test case to validate the flutter model, Appendix A-III presents the investigated wing model, a description of the applied mass with results and analysis, Appendix A-IV depicts the conclusion.

#### A-I: Wing Structural Model, Aerodynamic modelling and solving the flutter equation

The wing geometry assumed to build the model is shown in Fig. A-I-1 and Fig. A-I-2, the wing is uniform, swept and has high aspect ratio, and the wing is built in the root. The structure is modelled using isotropic thin plate theory and equations of motion formulated based on the Rayleigh-Ritz method. The deformation is given as a weighted sum of assumed mode shapes. The strain energy and kinetic energies of the wing are then determined and the Lagrangian approach is used to develop the equations of motion. The wing coordinate system is also shown in A-I-1 the origin is the wing root chord, the x-axis lies in the root plane of the wing, the y-axis runs in the span-wise direction of the wing along the line of the aerofoil mid chord location and the z-axis is defined as vertically upwards (Fig. A-I-1 and Fig. A-I-2). The assumption is that the displacement of any point on the wing may be represented by a bending deflection  $h(y)$  which is regarded as been positive downwards along the y-axis together with a rotation  $\alpha(y)$ , also positive nose up about this axis. The wing chord-wise sections, perpendicular to the y-axis are assumed rigid.

The wing aerodynamics are modelled as inviscid unsteady incompressible using Theodorsen theory. The p-k method or approach is used to solve the flutter equations, the process is iterative. Here, the aerodynamic stiffness and damping matrices are functions of the reduced frequency k, which is dependent on the frequencies of oscillation and is obtained from the analysis of the eigenvalues. For each given flight speed, for each of the

eigenvalue, the reduced frequency is computed based on the value of its imaginary part. The aerodynamic matrices are re-calculated, and the eigenvalue analysis repeated, and the reduced frequency is again calculated. The process is repeated until the change in reduced frequency at each successive iteration falls below some acceptable level.

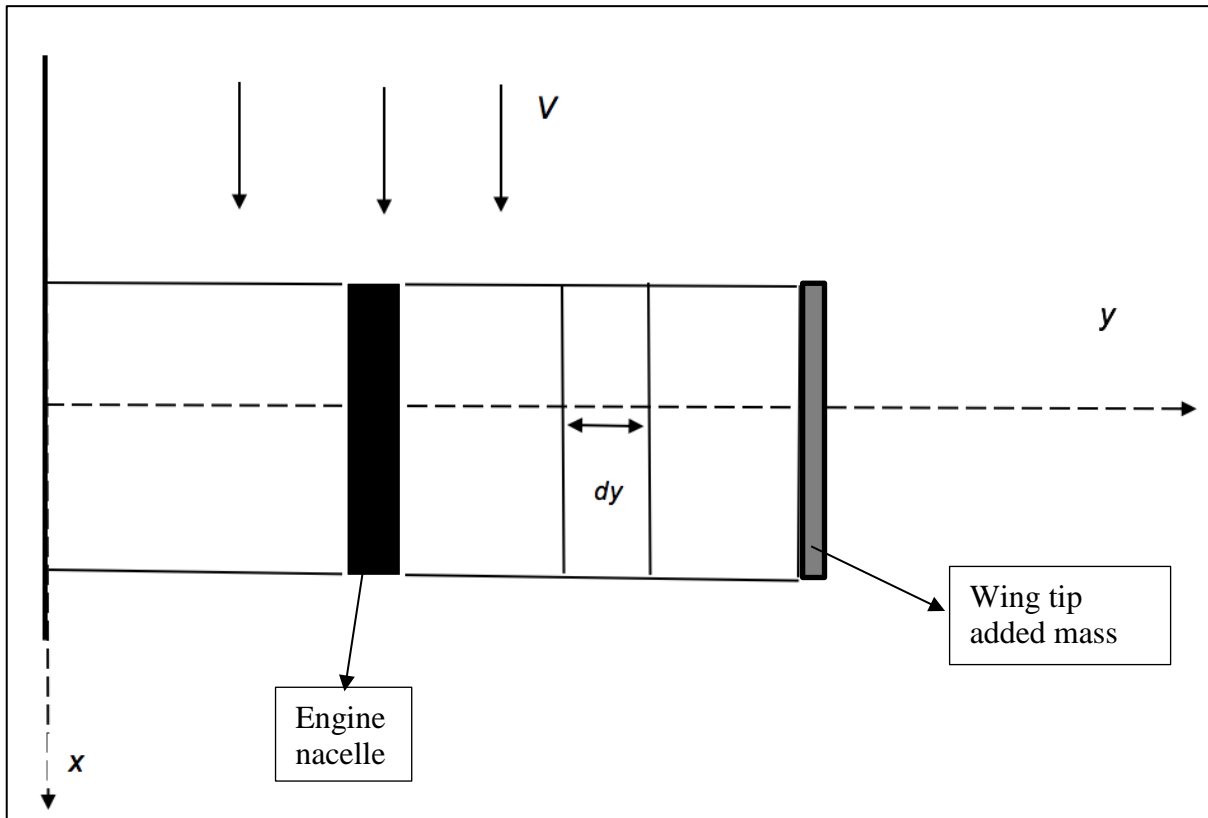


Fig. A-I-1: Un-swept Wing used for the study

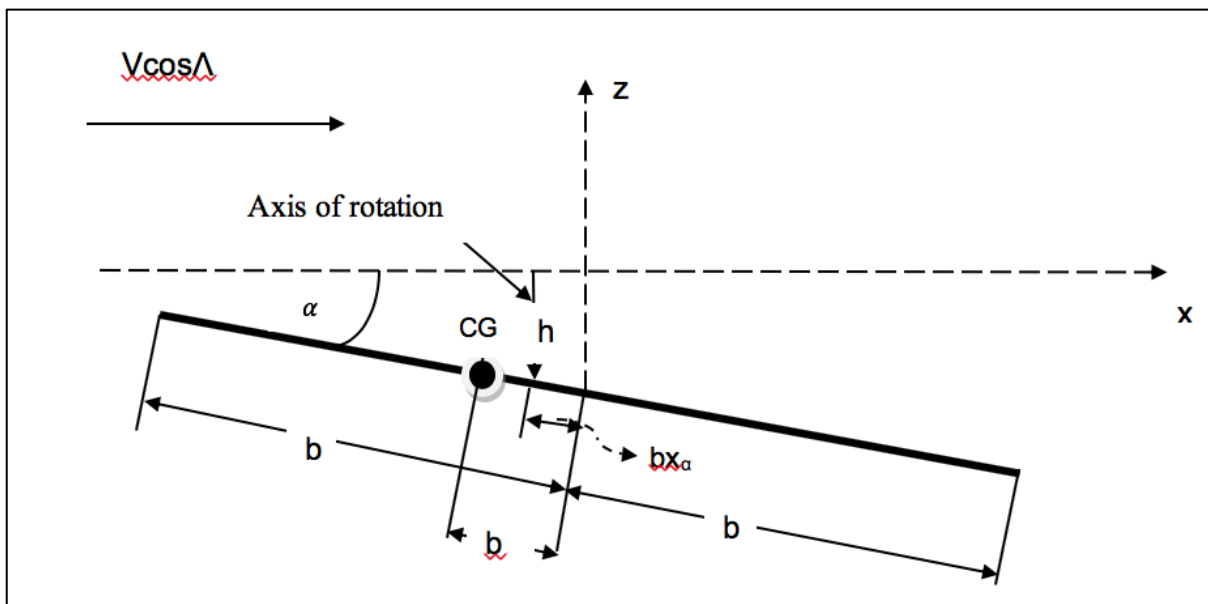


Fig. A-I-2: Definition of Displacement of Aerofoil Section

## A-II: Initial test case to validate Flutter Model

The initial test case to validate the model is described here. The work presented replicates the experimental and numerical results in (Wilts, 1958), the flutter characteristics of a uniform un-swept wing with variable concentrated mass position is studied. The wing geometry is assumed to be built in at one end. The physical characteristics of the uniform cantilever wing is shown in Table A-II-1.

**Table A – II – 1: Physical characteristics of the uniform cantilever wing**

Parameter	
Half chord, ( <i>inches</i> )	4
Span, ( <i>inches</i> )	48
Mass per unit length, ( <i>lb sec<sup>2</sup>/sq. inches</i> )	$1.877 \times 10^{-4}$
Pitching inertia per unit length, ( <i>lb sec<sup>2</sup></i> )	$8.00 \times 10^{-4}$
Flexural rigidity, <i>EI</i> , ( <i>lb sq. inches</i> )	$1.407 \times 10^5$
Torsional rigidity, <i>GJ</i> , ( <i>lb sq. inches</i> )	$0.692 \times 10^5$
Elastic-axis position, ( <i>inches</i> )	-0.504
Center of mass position, ( <i>inches</i> )	0.156
Mass of concentrated mass, <i>lb sec<sup>2</sup>/inches</i>	$8.23 \times 10^{-3}$
Pitch inertia of concentrated mass, ( <i>lb sec<sup>2</sup> inches</i> )	0.1636
Center of mass of concentrated mass, ( <i>inches</i> )	-3.274
Air density, ( <i>lb sec<sup>2</sup>/inches<sup>4</sup></i> )	$1.55 \times 10^{-7}$

The flutter speed and frequency are computed using the method discussed in Section A-I. The model is run within MATLAB using input data as defined in Table A-II-2, Table A-II-3 and Table A-II-4. The program determines the stiffness matrices. The needed integration process is performed using symbolic tool within MATLAB. The natural frequencies of the wing are determined within MATLAB and the flutter analysis is then performed. This process involves finding the aerodynamics damping and stiffness matrices for the values which have been assumed for frequency before the integration process is performed with MATLAB again. The flutter equations are constructed and the stability analysis for the wing is performed for the given range of flight speeds by using the p-k method.

**Table A – II – 2: Wing structural and stiffness data**

<b>Wing Structure Mass and Stiffness Data</b>	<b>Units</b>	
Mass per unit span (m)	kg/m	$1.877 \times 10^{-4}$
Pitching moment of inertia per unit length about elastic axis ( $I_a$ )	kgm	$8.00 \times 10^{-4}$
Wing flexural rigidity (EI)	Nm <sup>2</sup>	$1.407 \times 10^5$
Wing torsional rigidity (GJ)	Nm <sup>2</sup>	$0.692 \times 10^5$
Wing cross-coupling rigidity (K)	Nm <sup>2</sup>	0

**Table A – II – 3: Wing Geometry Data**

<b>Wing Geometry Data</b>		
Wing semi-chord (b)	m	4
Wing span (l)	m	48
Sweep angle ( $\Lambda$ )	degrees	0
Location of CG forward of wing mid-chord non-dimensionalised by b ( $x_a$ )	-	0.034
Distance of wing elastic axis forward of wing mid-chord non-dimensionalised by b (a)	-	-0.126

**Table A – II – 4: Aerodynamic Data**

<b>Aerodynamic Data</b>		
Air density $\rho_\infty$	kg/m <sup>3</sup>	$1.55 \times 10^{-7}$
Aerofoil section lift curve slope ( $C_{L\alpha}$ )	-	6.28319

The flutter speed and frequency were computed for 9 mass locations, the data produced are compared with the experimental and numerical data from reference (Wilts, 1958) and is given in Table A-II-5.

**Table A – II – 5: Computed results showing comparison with Experimental and Calculated values from (Wilts, 1958)**

Mass location per unit span	Calculated using method discussed in this report		Calculated values (Wilts, 1958)		Experimental (Runyan and Sewall, 1948), (Runyan and Watkins, 1949)	
	$v_f, mph$	$f_f, cps$	$v_f, mph$	$f_f, cps$	$v_f, mph$	$f_f, cps$
0	221.59	24.37	227	25.27	228	22.1
0.167	201.7	21.1			221	19.1
0.229	200.3	18.9	226	19.23	221	17.4
0.292	220.1	16.9			233	16.3
0.333	276	15.5			256	15.5
0.354	divergence	divergence	277	28.04	260	Divergence or 16.3 – 26.8
0.625	divergence	divergence	359	30.68		Divergence
0.938	-		273	25.67	261	Divergence
0.959			251	24.87	251	21.8
0.979					231	21.6
1	212	19.9	205	23.60	218	21.4

The results show good correlation with the experimental data, with the results illustrating a better agreement with the flutter frequency ( $f_f, cps$ ) and slight over prediction of the flutter speed ( $v_f, mph$ ). This approach is adopted for the remaining work presented in this section.

### **A-III: Investigated wing model with concentrated mass (winglet) at wing tip**

In this appendix, the investigation on a uniform cantilever wing with and without applied concentrated mass at the wing tip is presented. The wing geometry is assumed to be un-swept, built in, the wing span and tip chord is the same as that for the aircraft considered in reference (Wilts, 1958). The concentrated masses on aircrafts usually consist of the engine nacelle and in some cases fuel tanks, electrical systems. For aircraft structures, engines, nacelles, fuel tanks, electrical systems are modelled as concentrated mass on the wing. It is known that these masses have an impact on the wing flutter characteristics and such improvement can be made to the flutter characteristics of a wing by simply selecting an appropriate mass location though other constraints will apply.

The basic concentrated engine nacelle mass for the wing is assumed as 6,000 pounds and is assumed to be at the 46 percent span position and 60 inches in front of the elastic axis as in reference (Wilts, 1958). A variable

concentrated mass (winglet mass) applied at the wing tip is assumed to be in the range of 375 – 518 pounds and is increased until 1554 pounds. The weight of the winglet is based on the estimated value provided in reference (Brady, 1999).The characteristics of the wing are given in Table A-III-1.

**Table A–III–1: Physical characteristics of wing**

<b>Wing Structure Mass and Stiffness Data</b>	<b>Units</b>	
Mass per unit span (m)	lb sec <sup>2</sup> /sq in.	$3 \times 10^{-2}$
Pitching moment of inertia per unit length about elastic axis ( $I_a$ )	lb sec <sup>2</sup>	$8.0 \times 10^1$
Wing flexural rigidity (EI)	lb sq in.	$2.5 \times 10^9$
Wing torsional rigidity (GJ)	lb sq in.	$3.33 \times 10^9$
Wing cross-coupling rigidity (K)	lb sq in.	0

<b>Wing Geometry Data</b>		
Wing semi-chord (b)	inches	40
Wing span (l)	inches	845
Sweep angle ( $\Lambda$ )	degrees	0
Location of CG forward of wing mid-chord non-dimensionalised by b ( $x_a$ )	-	0.3
Distance of wing elastic axis forward of wing mid-chord non-dimensionalised by b (a)	-	-0.2

<b>Aerodynamic Data</b>		
Air density $\rho_\infty$	lb sec <sup>2</sup> /in <sup>3</sup>	$1.55 \times 10^{-7}$
Aerofoil section lift curve slope ( $C_{L\alpha}$ )	-	6.28319

#### **A-IV: Location of centre of mass, Elastic axis location, concentrated mass with results and conclusion**

The concentrated masses used for this study are the engine nacelle and wing tip masses. No recorded research has been presented on the effect of using wing-tip devices on the flutter characteristics of a wing. Hence aside from the aerodynamic effect of using such devices, it was worth considering for this study briefly the effect of such variable masses on the flutter characteristics of a wing.

The elastic axis location relative to the quarter chord length which is the aerodynamic centre on the aerofoil is an important factor which determines the nature of the coupling between the aerodynamic forces and the structure. A change in one would require a corresponding change in the other and a change in the centre of mass. It is common knowledge that the aerodynamic and structural coupling with the aerodynamic centre at a forward

position from the elastic axis may have an undermining influence while an aerodynamic centre which is behind (aft) of the elastic axis usually has a stabilising effect.

Also, the location of the centre of mass influences the flutter speed of an aircraft wing. The general concept is that the flutter speed increases as the centre of the concentrated mass position is moved forward from the elastic axis. However, for the purpose of this study, the centre of mass of the wingleet was assumed to be the elastic axis or 40 percent of the chord. This was based on suggestions in reference (Wilts, 1958) which suggested that the centre of mass location near the elastic axis or slightly aft the elastic axis generally is practical and typical also the aerodynamic centre was assumed at the quarter chord length. Variation in centre of mass locations between the 25 percent chord to the 50 percent chord was carried out.

The flutter speed and flutter frequencies were computed for several concentrated masses by using the method discussed in A-III. The results are shown in Fig. A – IV – 1 and Fig. A – IV – 2. The flutter characteristics are illustrated in terms of the flutter frequency, the flutter speed, the applied variable mass and location of concentrated mass. The purpose of this study as mentioned initially, was to observe the characteristics trend in the flutter of a wing with and without applied variable weight concentrated at the wing tip. The first case that was studied was the wing with mounted engine nacelle and without concentrated mass at the wing tip. The data obtained was used as a baseline and was compared against the configurations with variable concentrated masses.

The result showed there was no significant impact on the flutter speed and frequency by adding the wingleet masses at the wing tip.

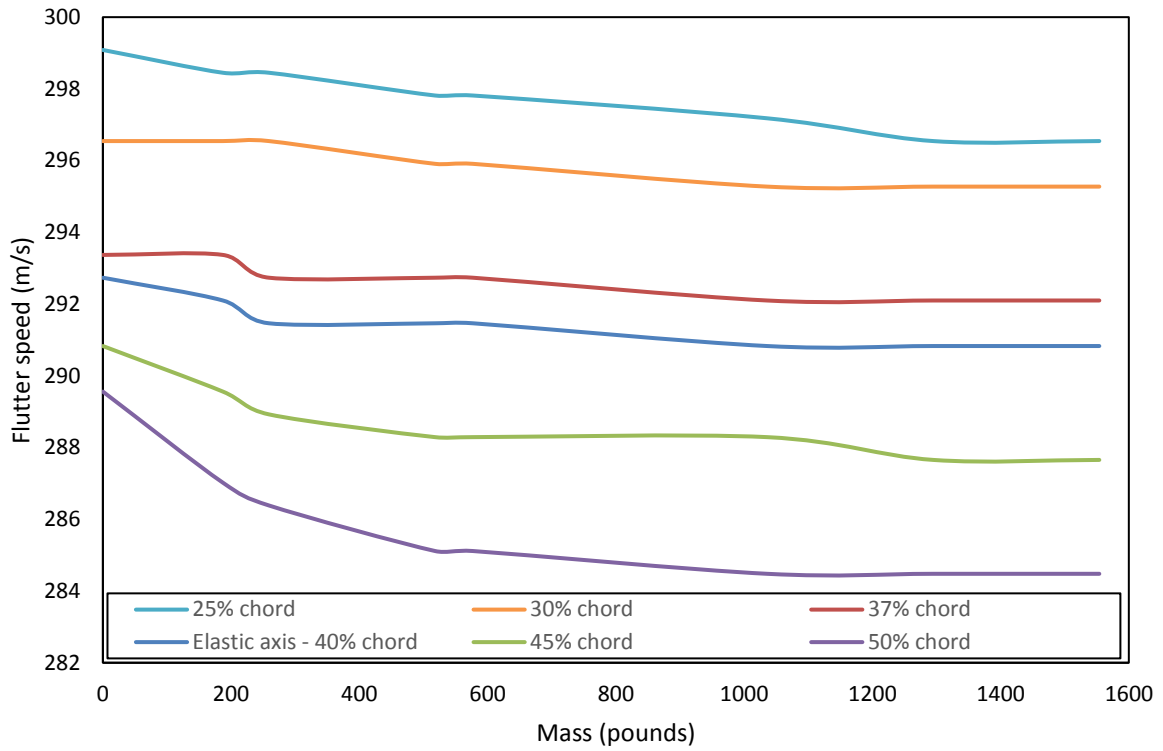


**Fig. A – IV – 1: Flutter speed as a function of winglet variable mass**

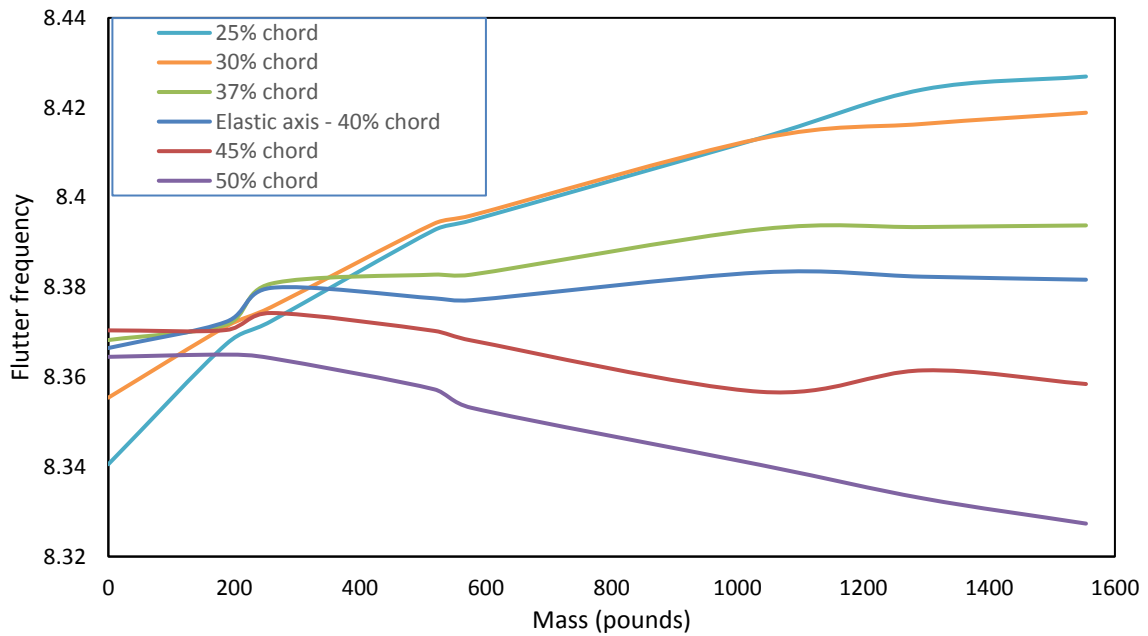


**Fig. A – IV – 2: Flutter frequency as a function of winglet variable mass**

## Appendix B: Kriging response surfaces

### B-I: Kriging response surface for initial design phase of Design-2

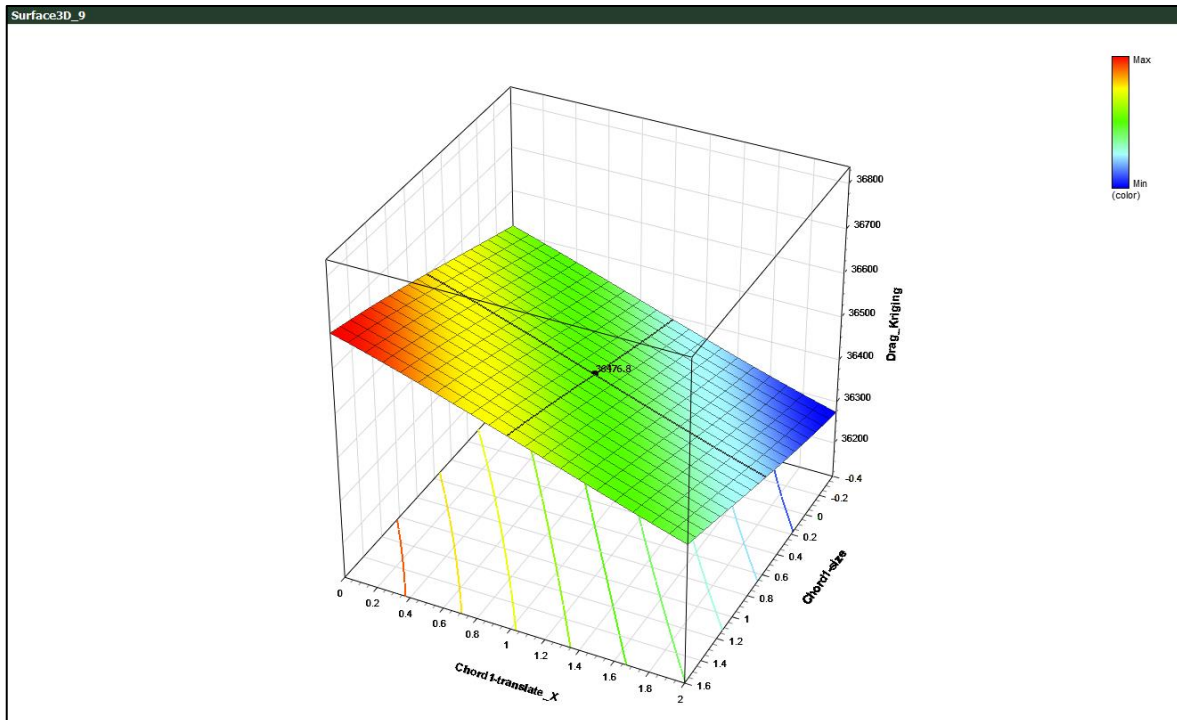


Fig. B-I-1: Chord 1 sweep (chord 1-translate\_x), Chord 1 size

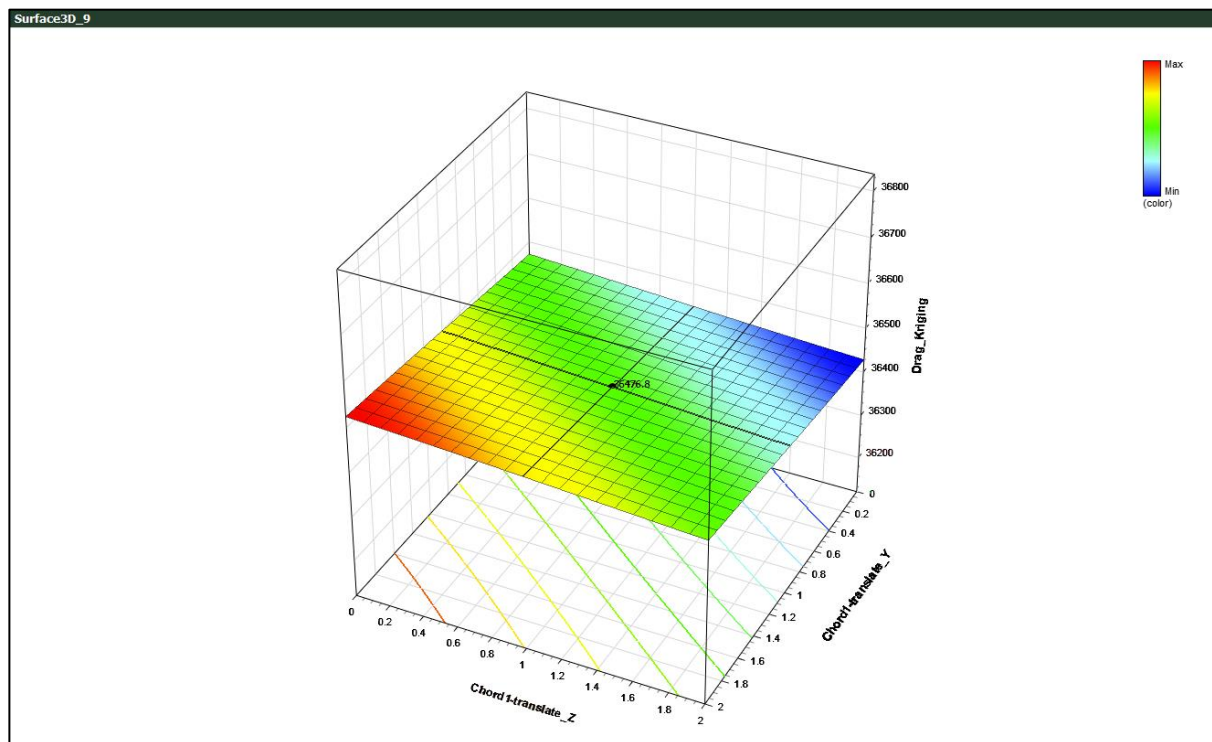


Fig. B-I-2: Chord 1 length (Chord 1-translate\_z), Chord 1 height (Chord1-translate\_Y)

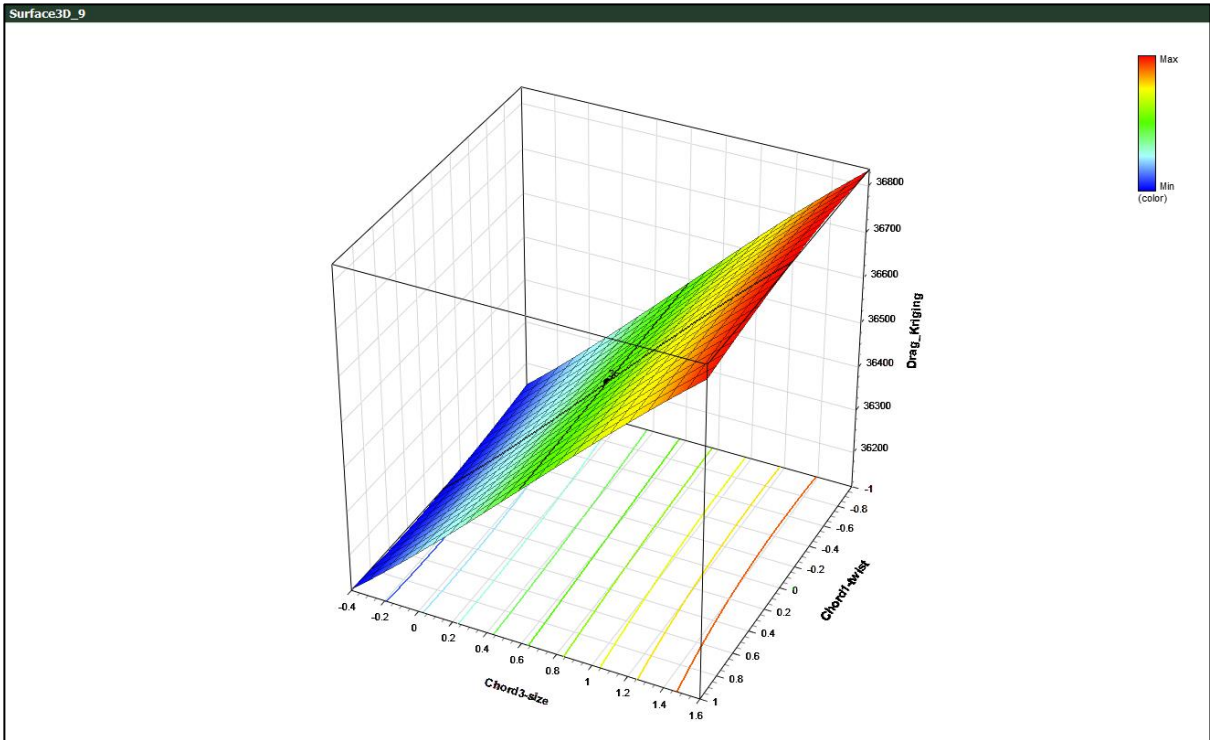


Fig. B-I-3: Chord 3 size, Chord 1 twist

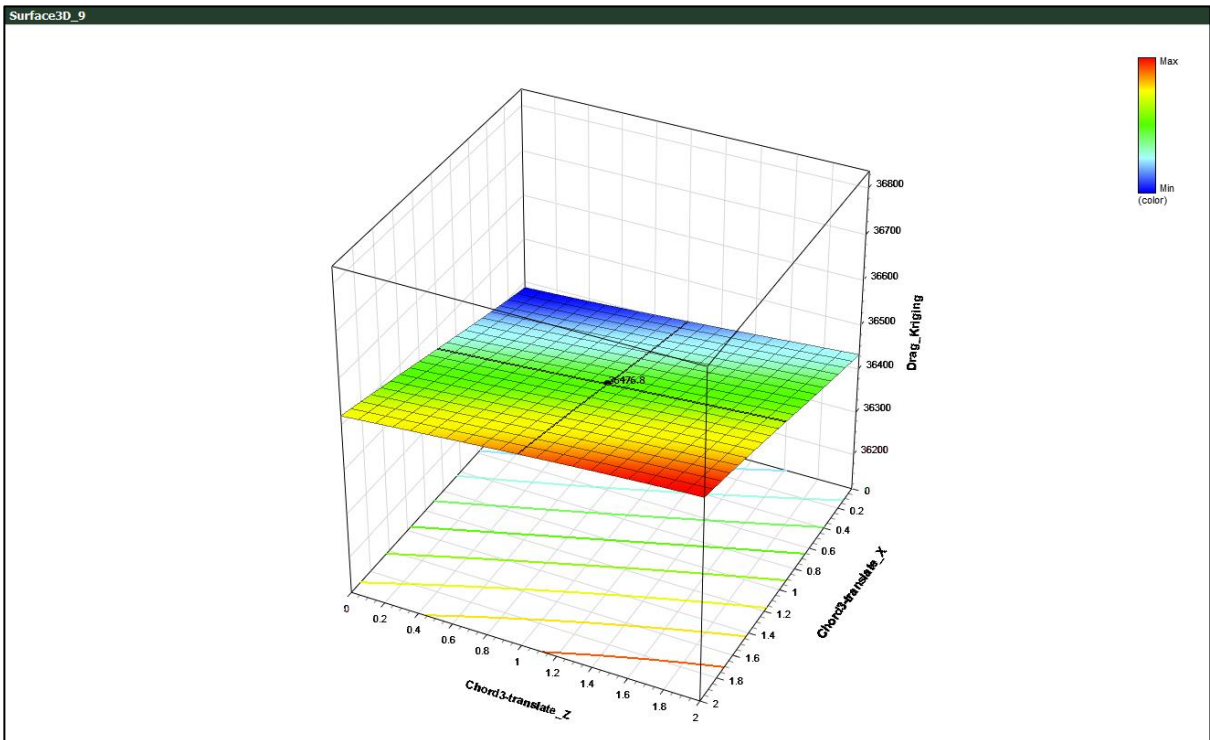
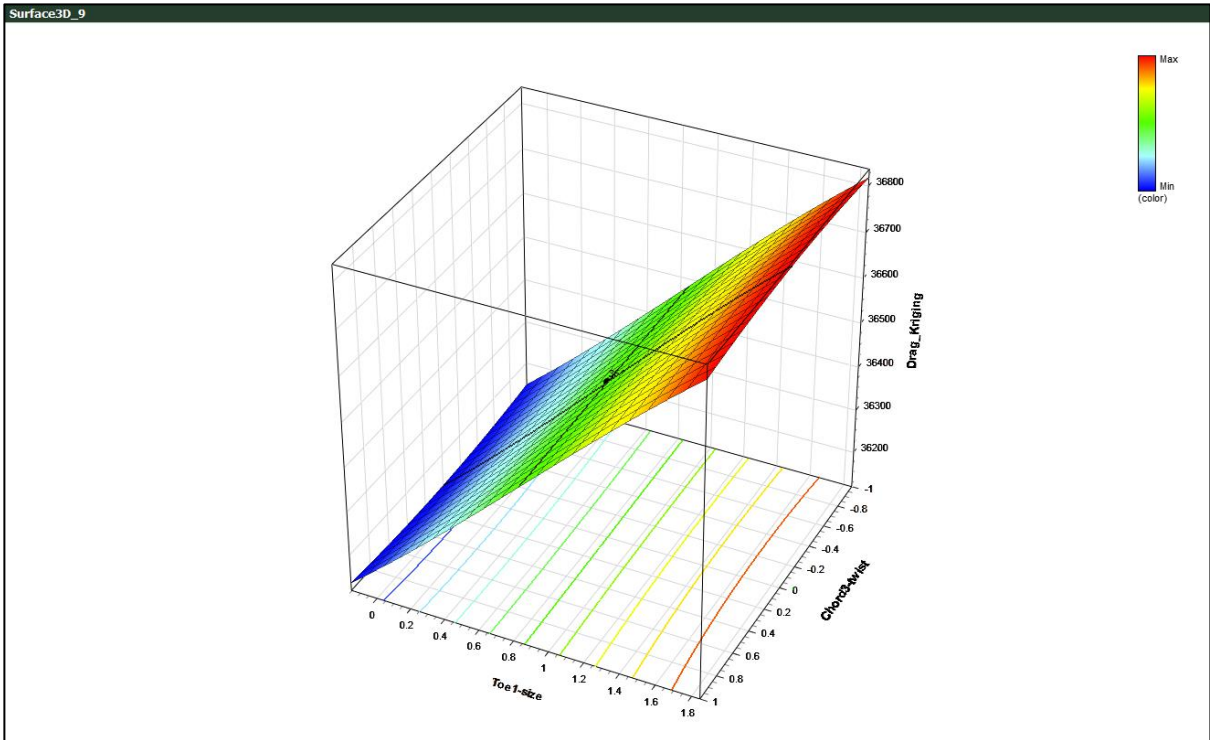
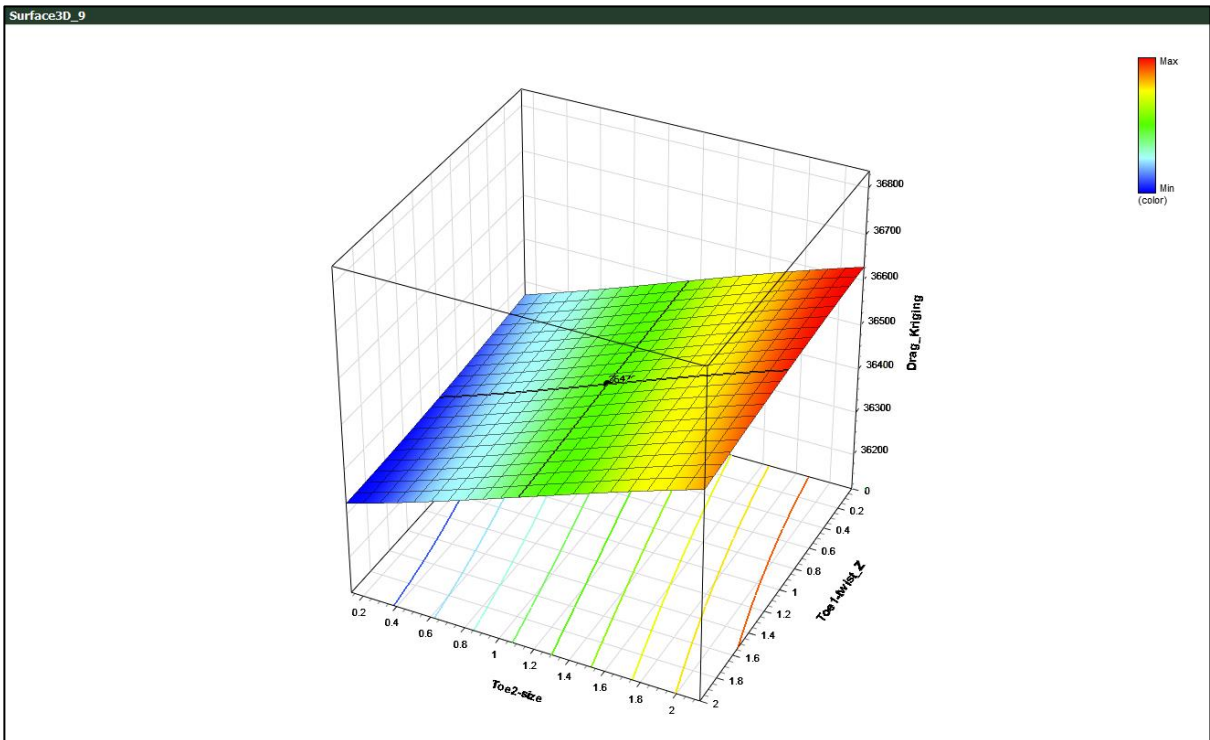


Fig. B-I-4: Chord 3 length (chord 3-translate\_z), Chord 3 sweep (Chord 3-translate\_x)



**Fig. B-I-5: Toe1 size, Chord 3-twist**



**Fig. B-I-6: Toe 2 size, Toe 1 twist (Toe 1-twist\_z)**

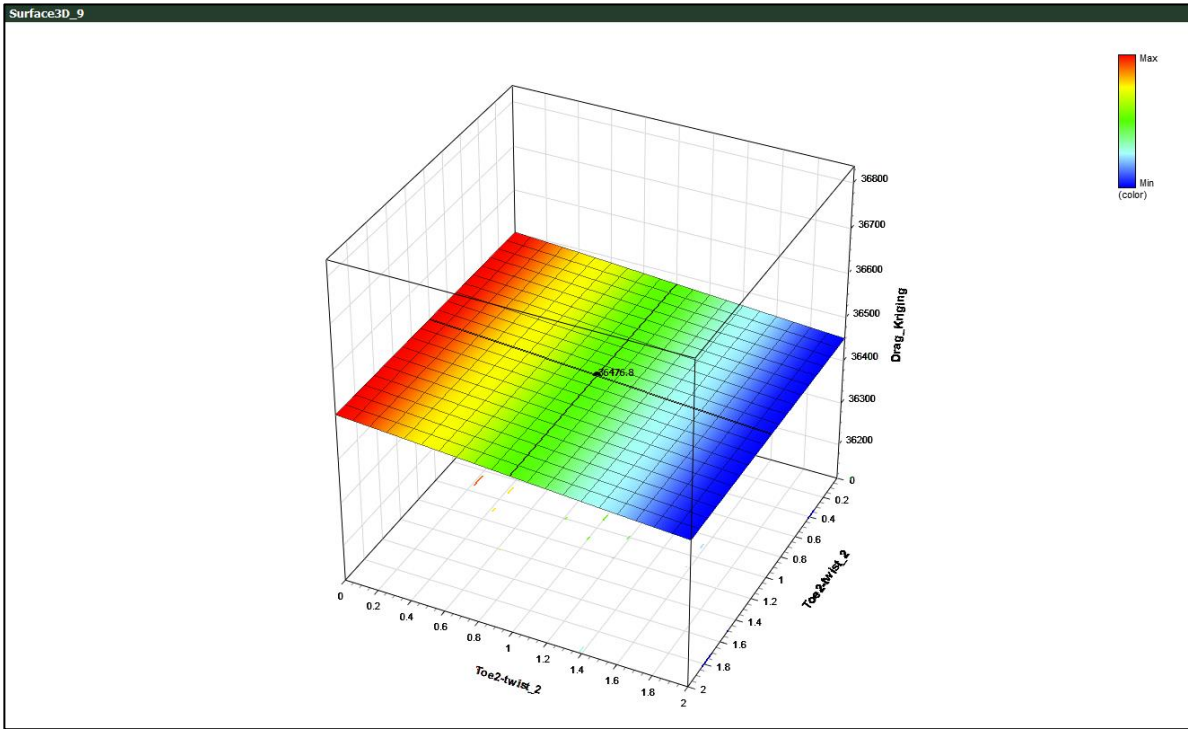


Fig. B-I-7: Toe 2 twist (Toe2-twist\_2)

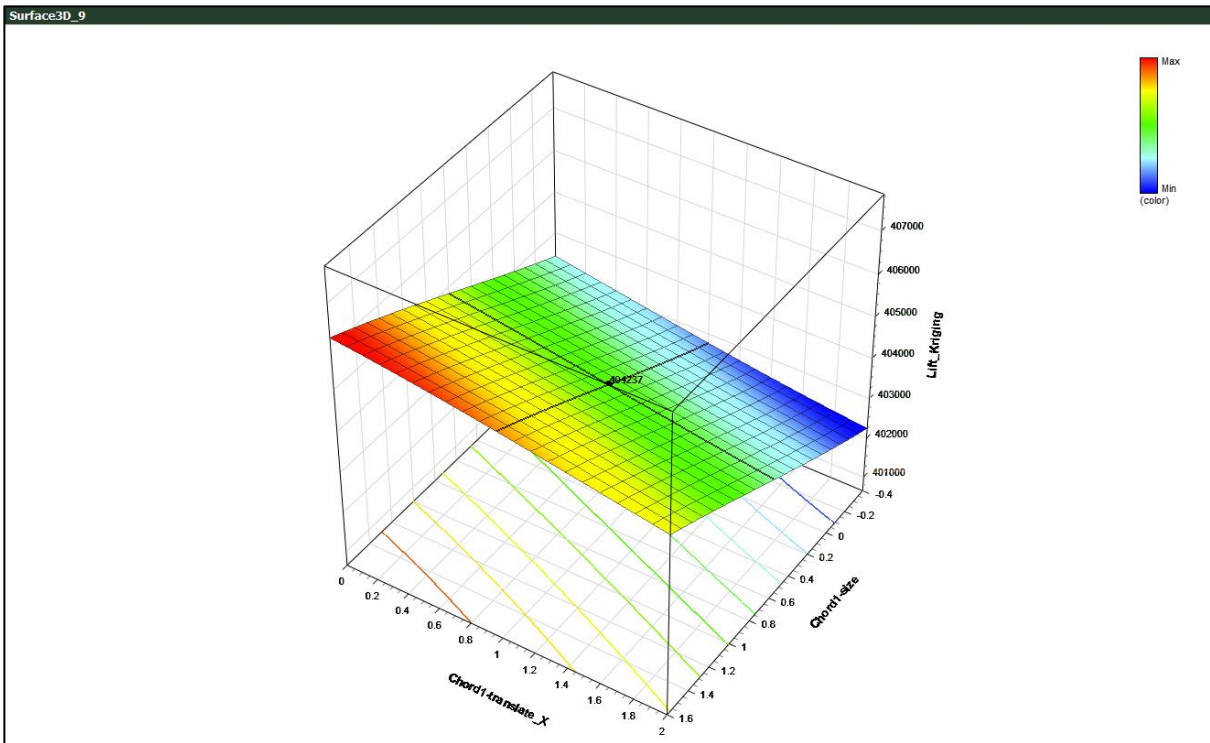


Fig. B-I-8: Chord 1 sweep (chord 1-translate\_x), Chord 1 size – Lift kriging

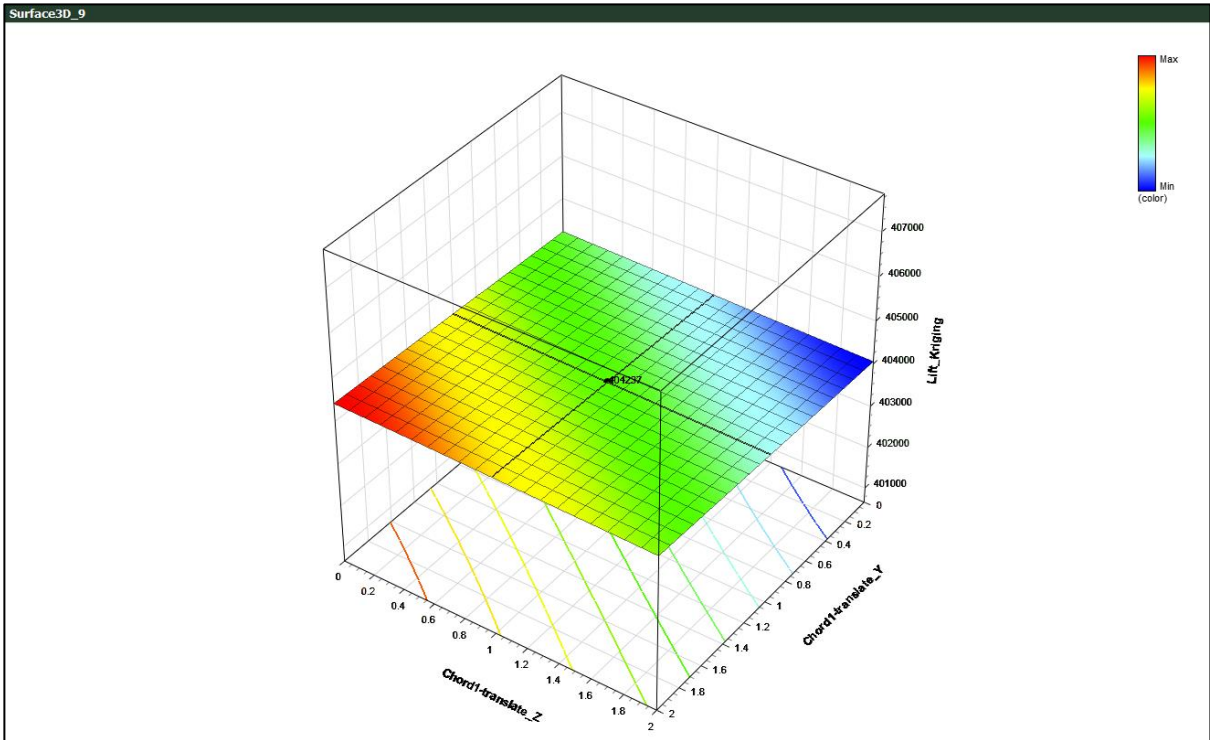


Fig. B-I-9: Chord 1 length (Chord 1-translate\_z), Chord 1 height (Chord1-translate\_Y) – Lift kriging

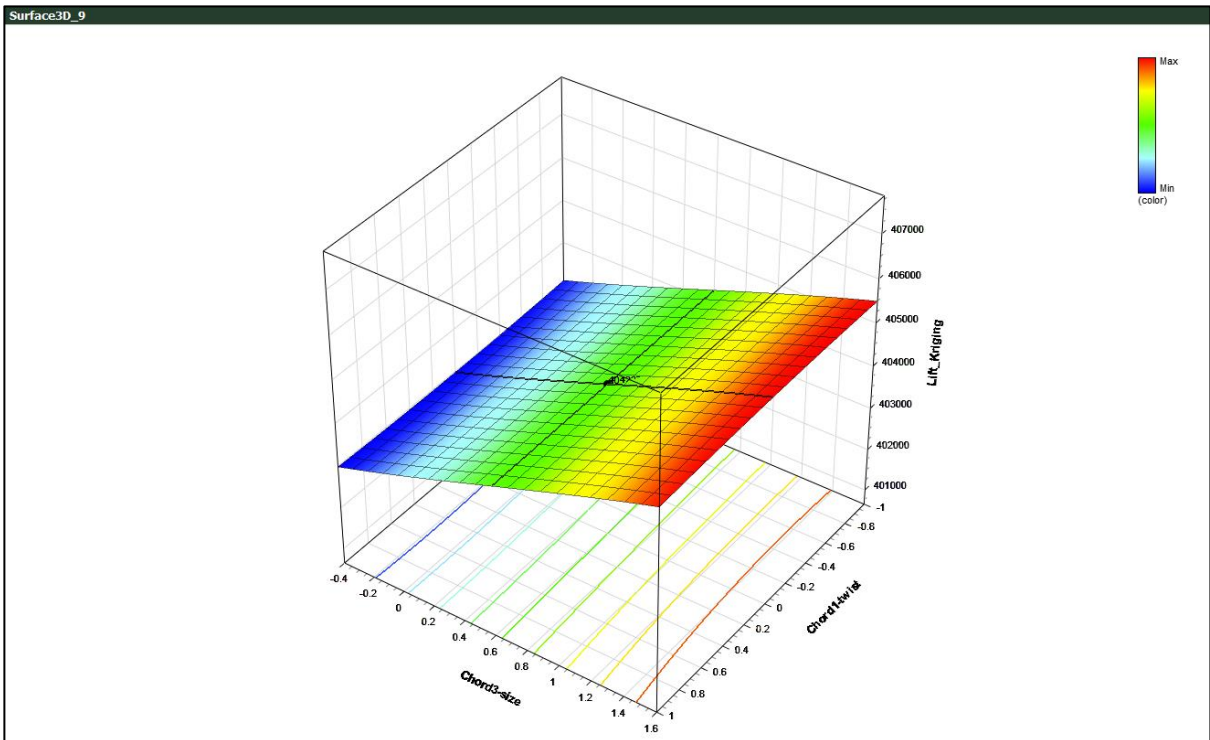


Fig. B-I-10: Chord 3 size, Chord 1 twist – Lift kriging

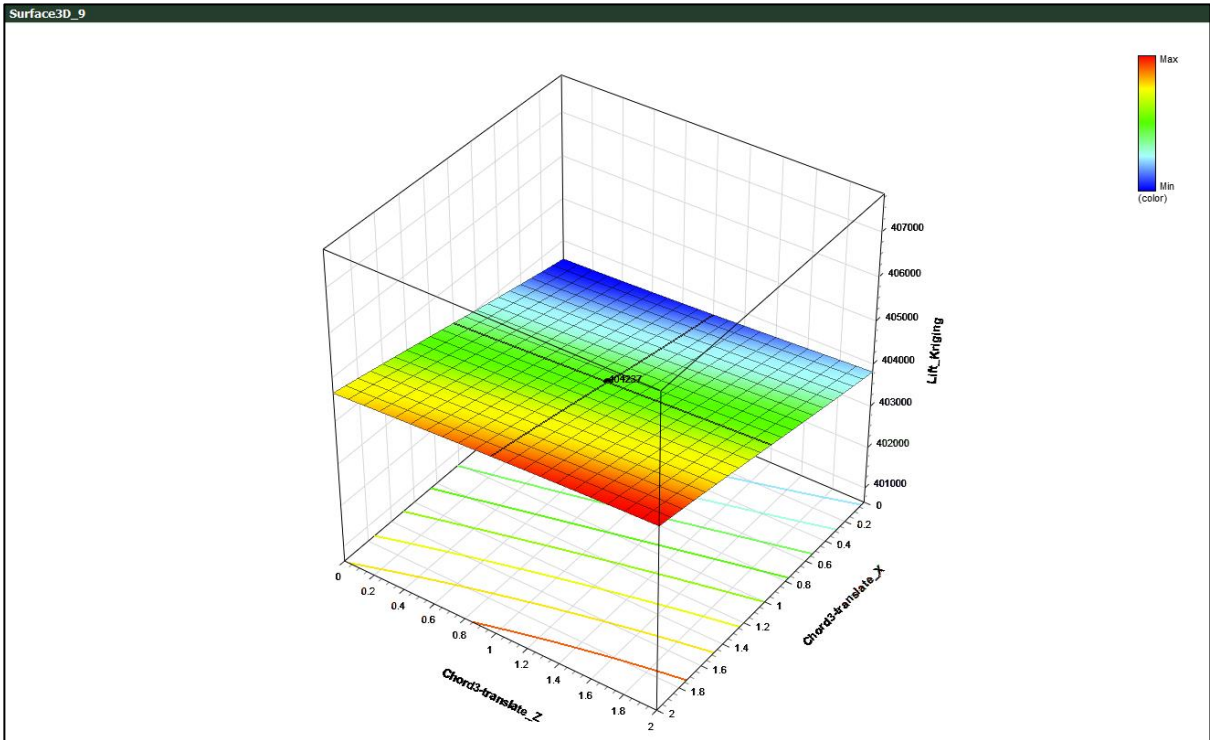


Fig. B-I-11: Chord 3 length (chord 3-translate\_z), Chord 3 sweep (Chord 3-translate\_x) – Lift kriging

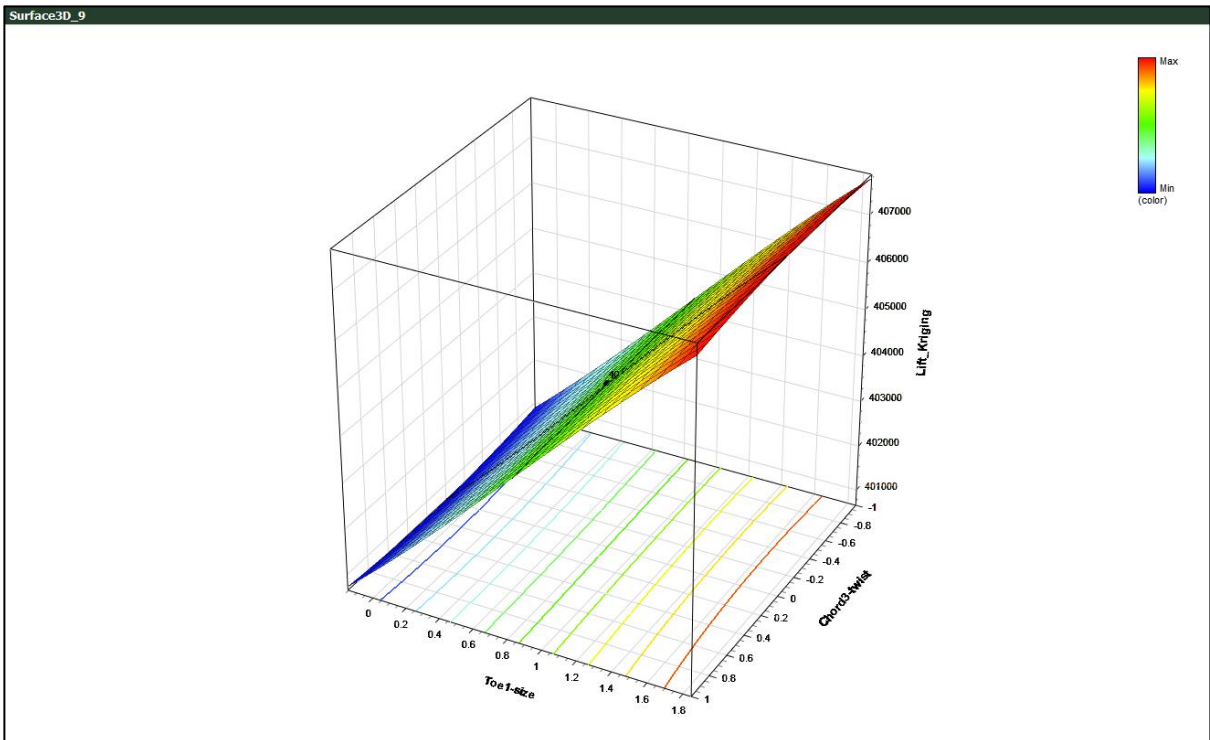


Fig. B-I-12: Toe 1 size, Chord 3 twist – Lift kriging

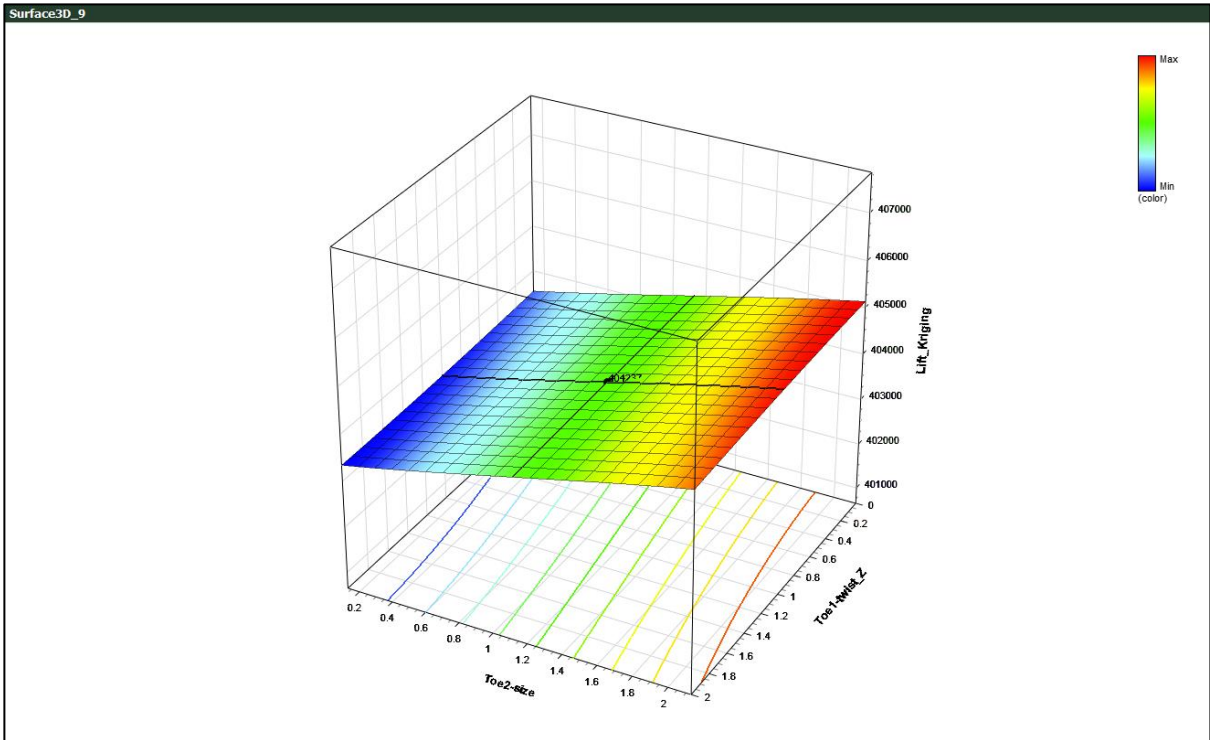


Fig. B-I-13: Toe 2 size, Toe 1 twist (Toe1-twist\_z) – Lift kriging

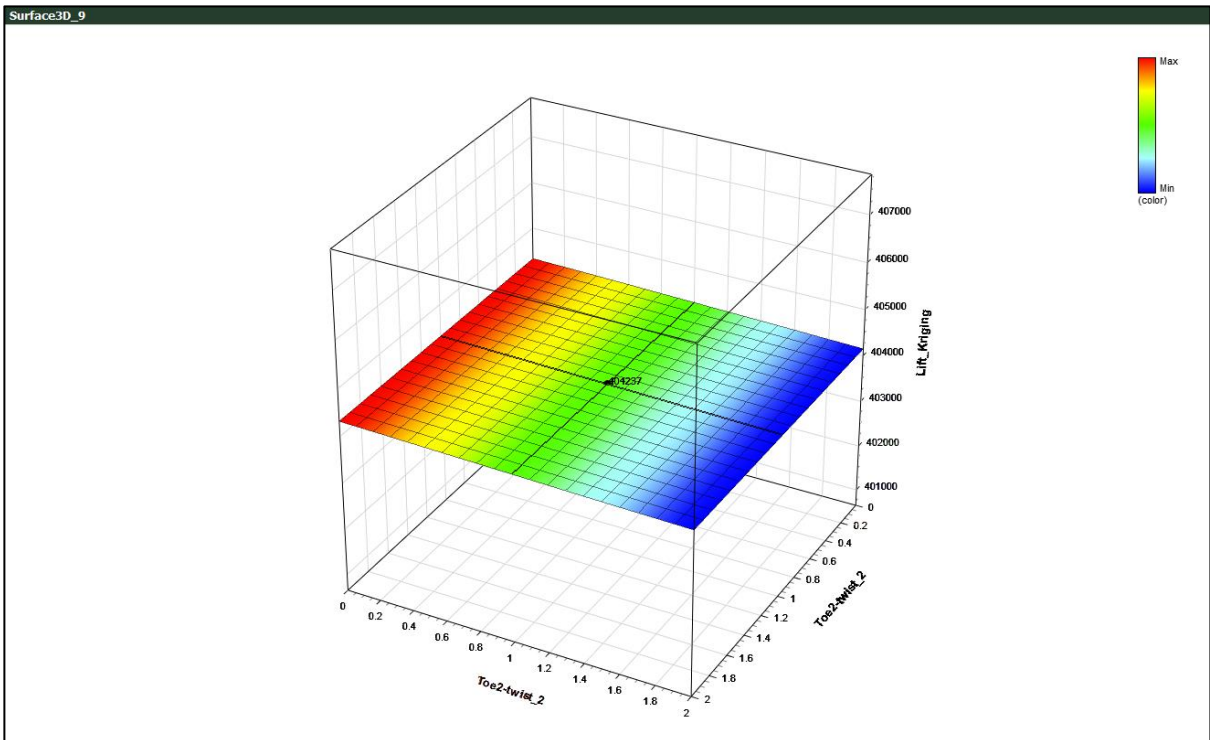


Fig. B-I-14: Toe 2 twist (Toe2-twist\_2) – Lift kriging

## B-II: Kriging response surface for the second phase of the optimisation process of Design-2

The mid-point was first optimised, Fig. B-II-1– Fig. B-II-2, before the other factors (design parameters) were optimised.

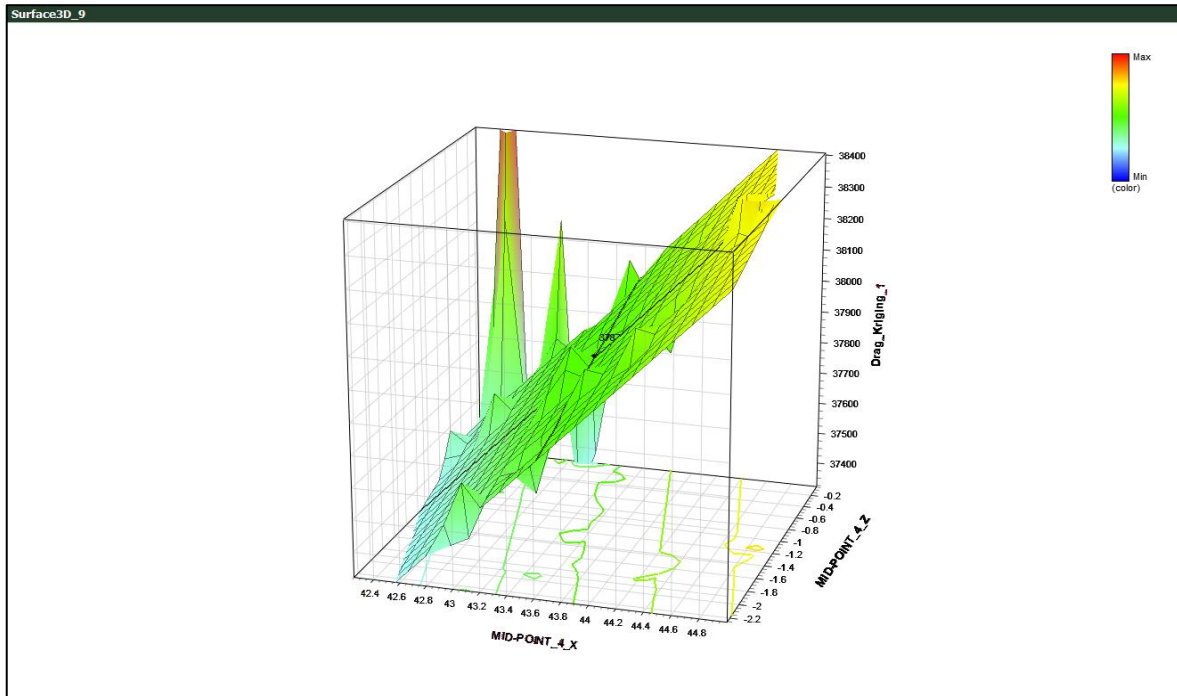


Fig. B-II-1: Mid-point sweep (MID-POINT\_4\_X), Mid-point length (MID-POINT\_4\_Z)

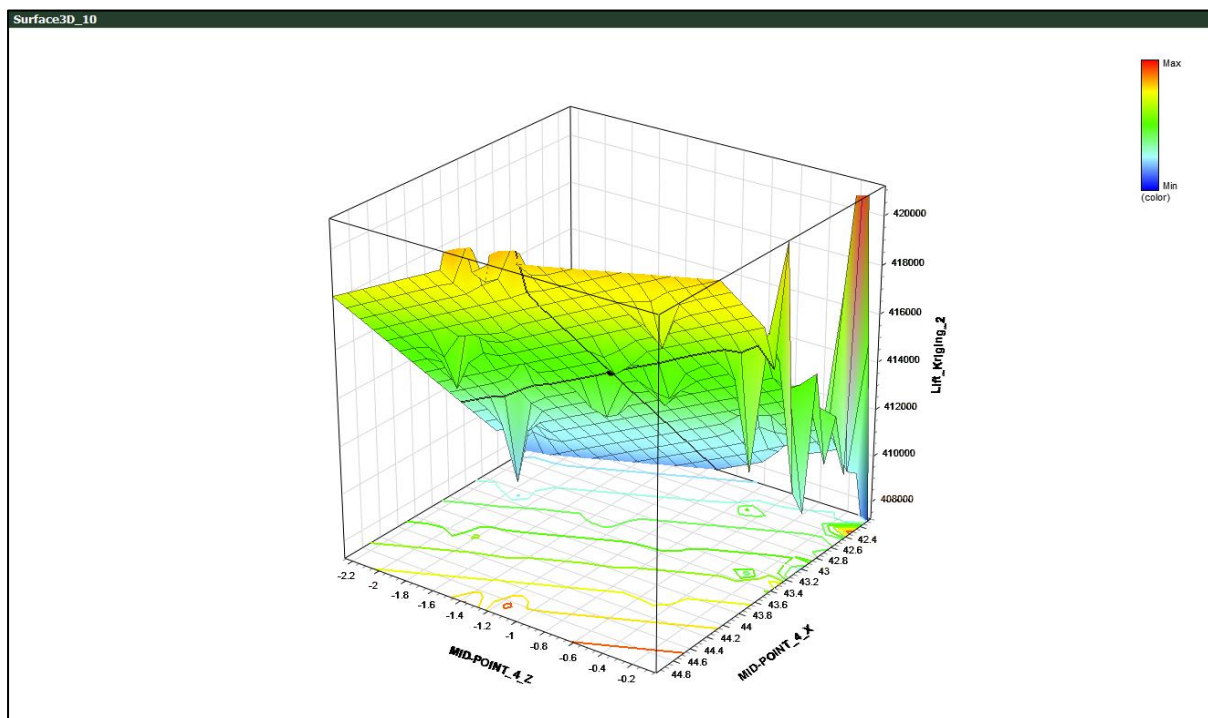


Fig. B-II-2: Mid-point sweep (MID-POINT\_4\_X), Mid-point length (MID-POINT\_4\_Z)

Fig. B-II-3 - Fig. B-II-14 depicts the kriging surrogate model for the rest of the parameters (variables) for the optimisation of Design-2.

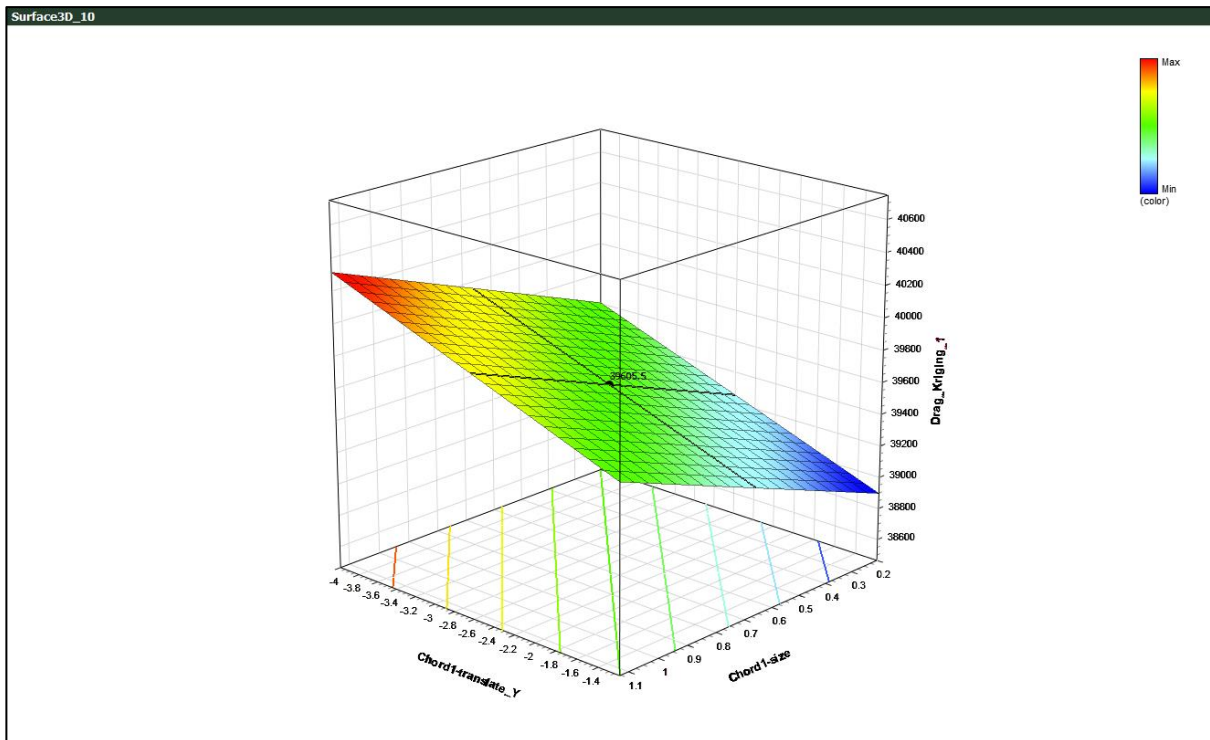


Fig. B-II-3: Chord 1 vertical height (Chord1-translate\_Y), Chord 1-size

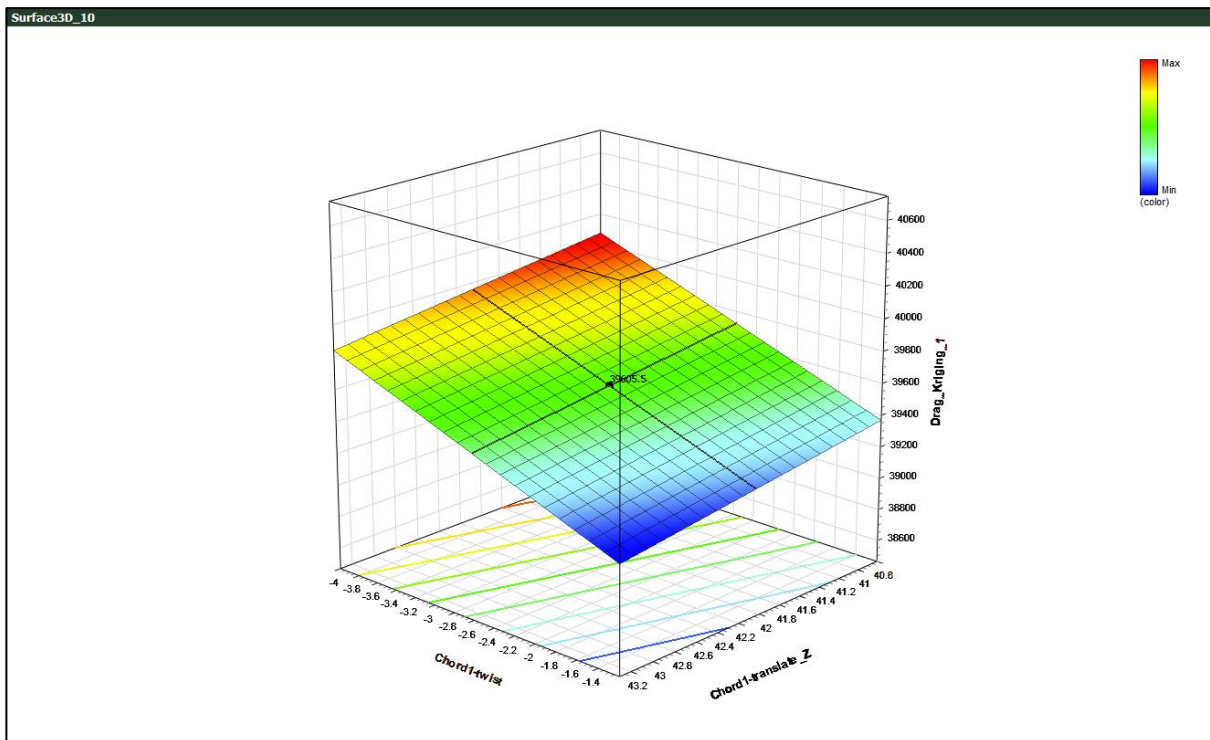


Fig. B-II-4: Chord 1 twist, Chord 1 length (Chord1-translate\_z)

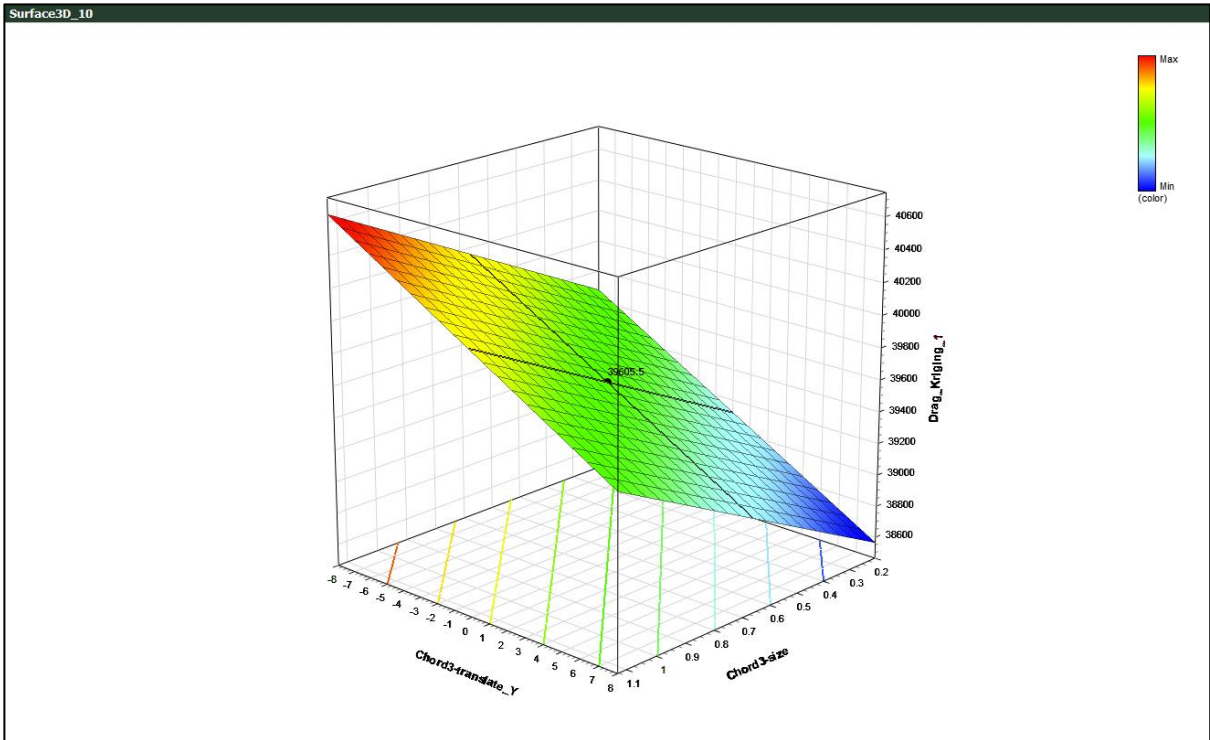


Fig. B-II-5: Chord 3 vertical height (Chord3-translate\_Y), Chord 3 size

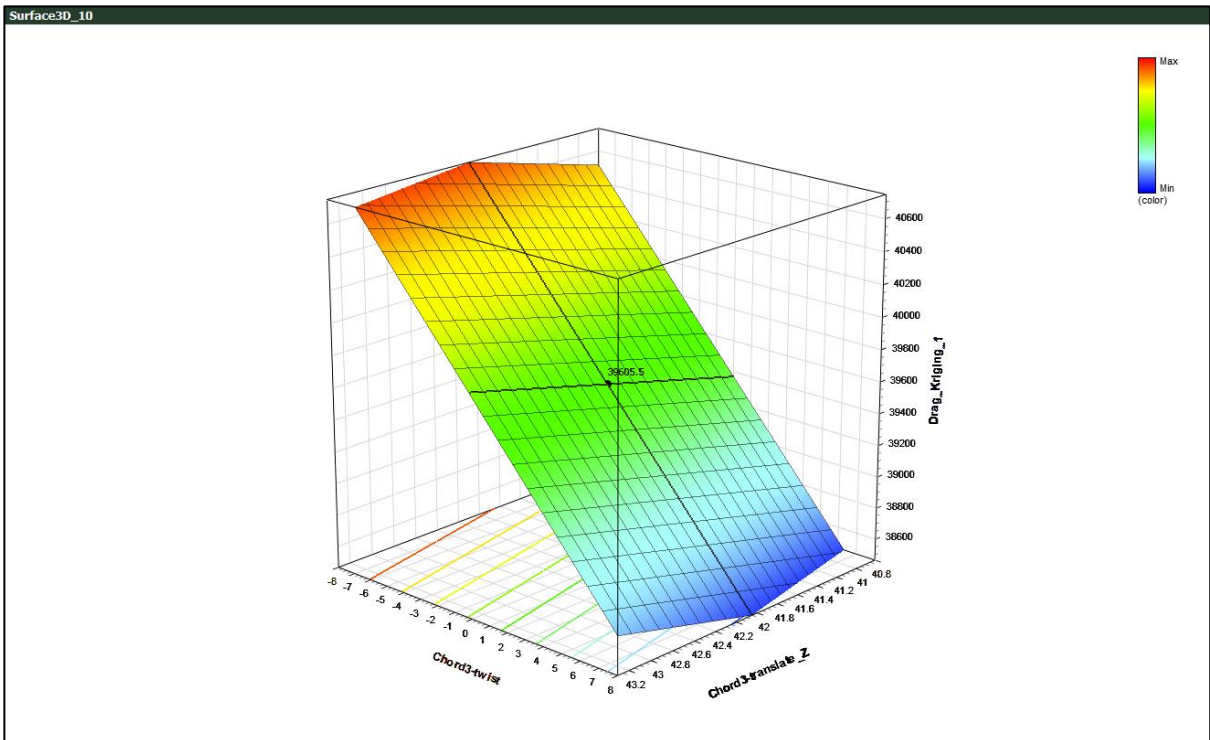


Fig. B-II-6: Chord 3 twist, Chord 3 length (Chord3-translate\_z)

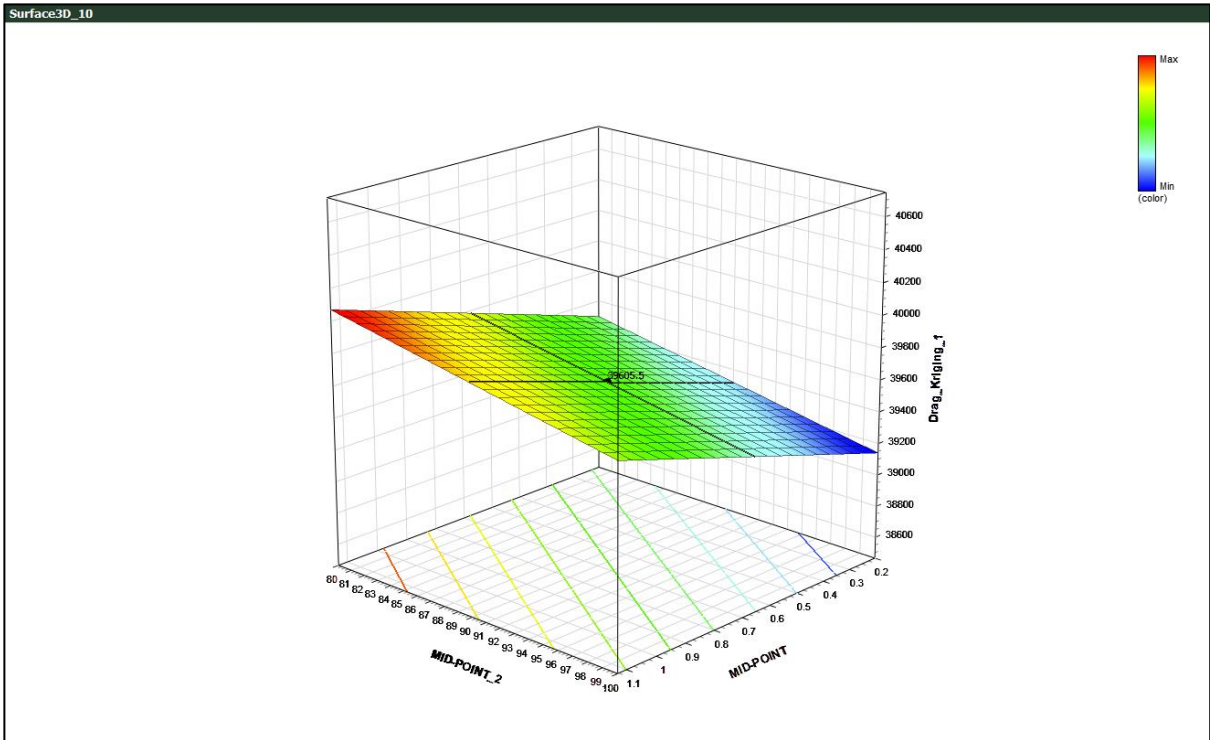


Fig. B-II-7: Mid-point twist (MID-POINT\_2), Mid-point size (MID-POINT)

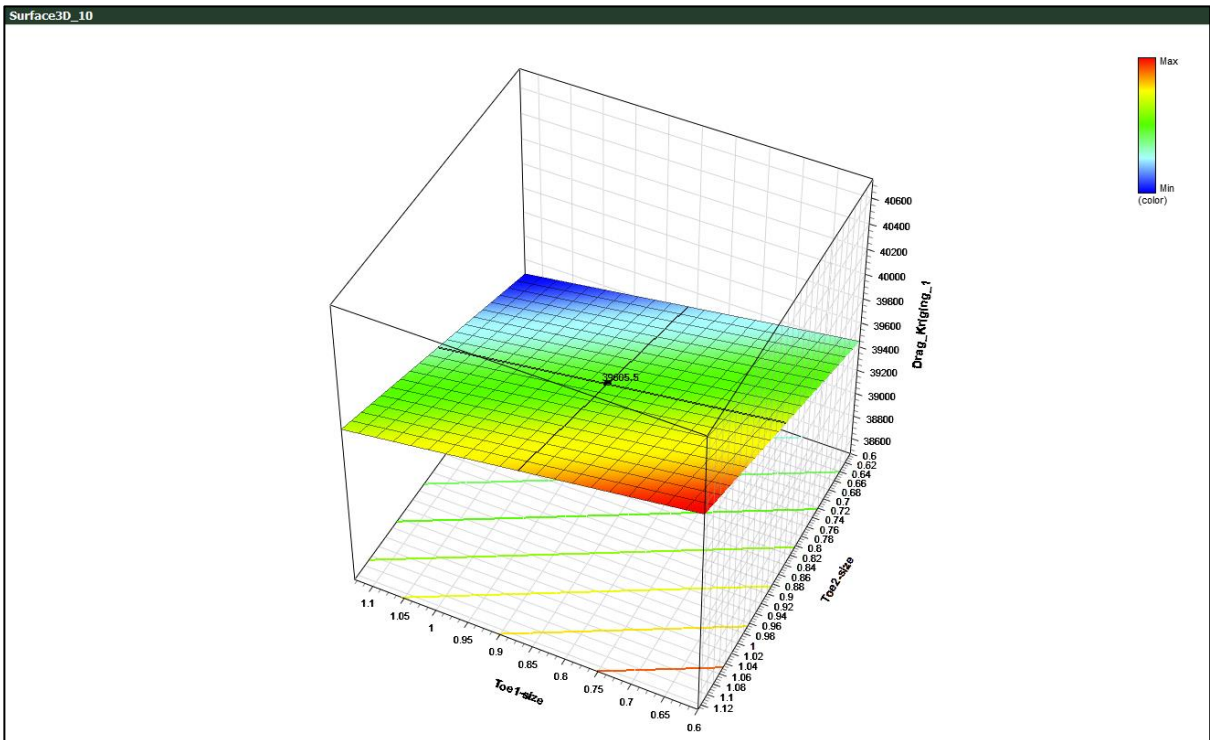


Fig. B-II-8: Toe 1 size, Toe 2 size

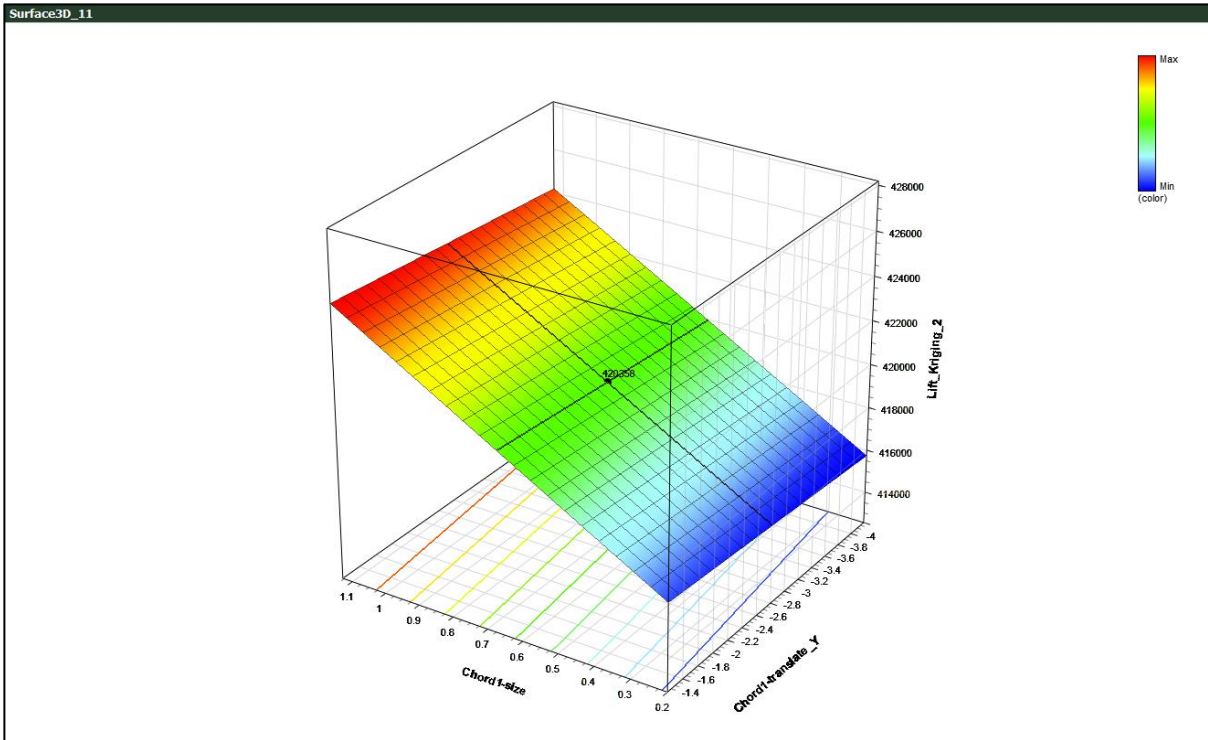


Fig. B-II-9: Chord 1 size, Chord 1 length (Chord1-translate\_Y) – Lift kriging

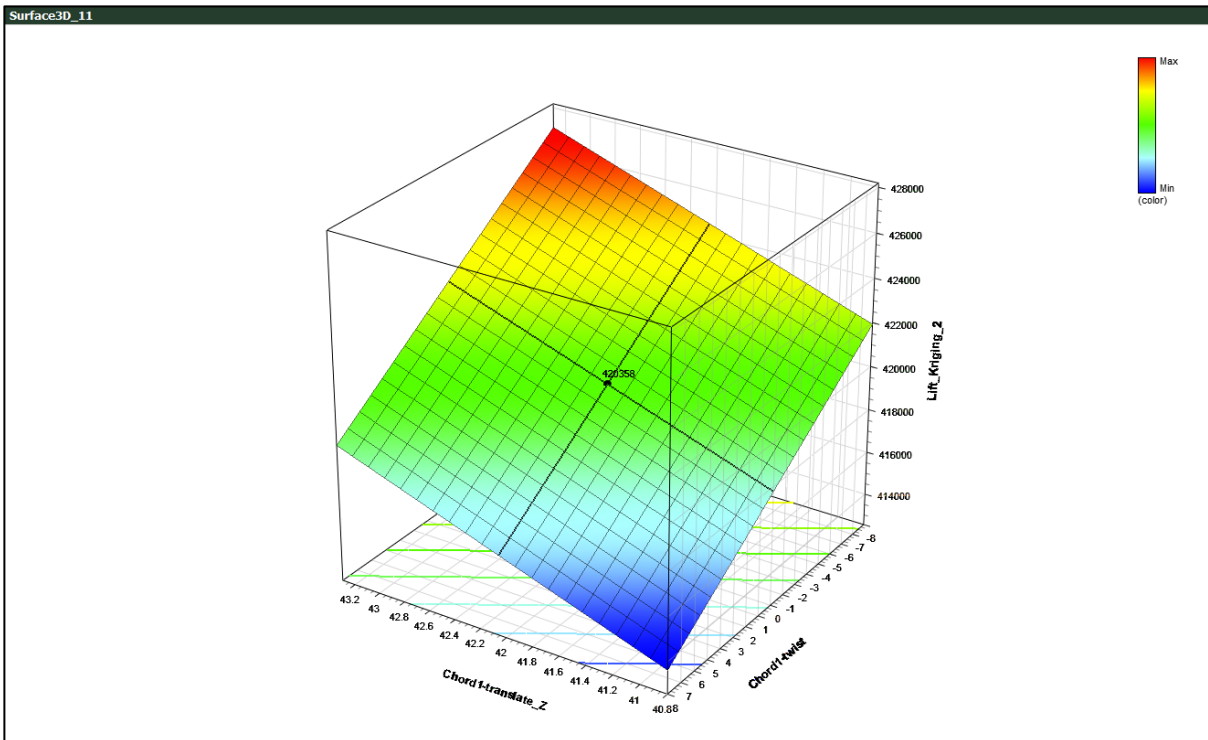


Fig. B-II-10: Chord 1 length, (Chord 1-translate\_z), Chord 1 twist – Lift kriging

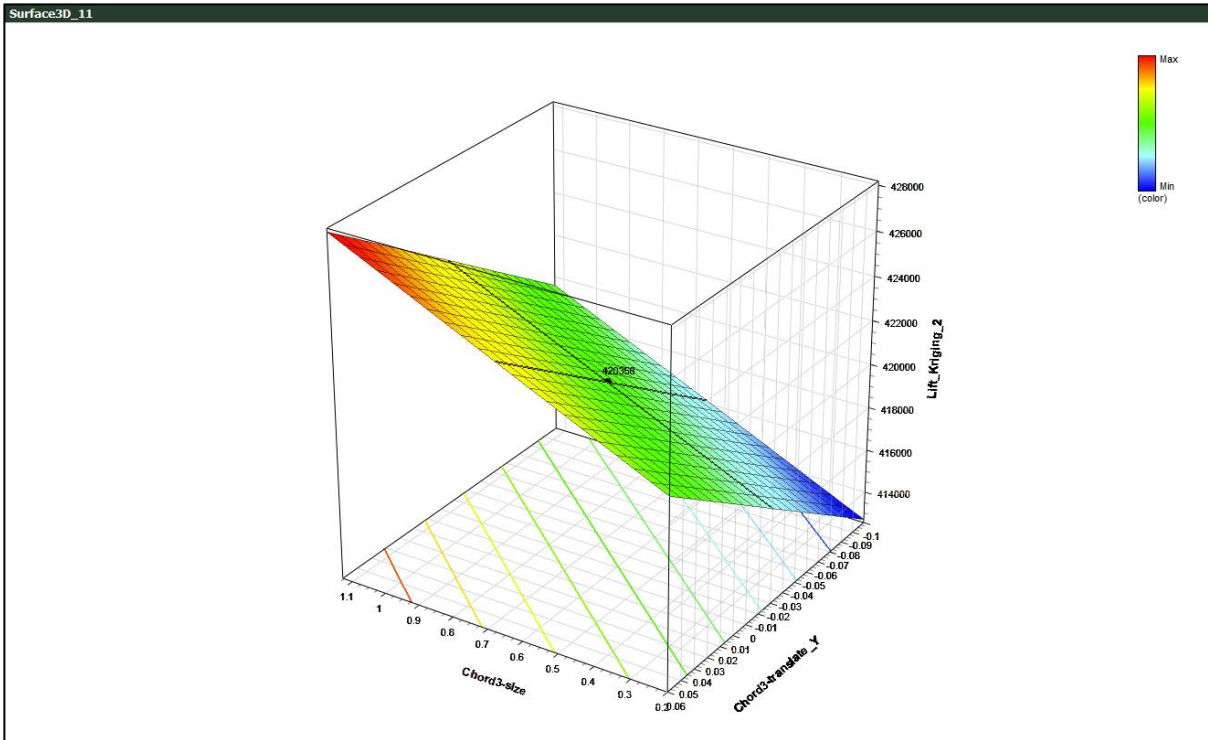


Fig. B-II-11: Chord 3 size, Chord 3 vertical height (Chord3-translate\_Y) – Lift kriging

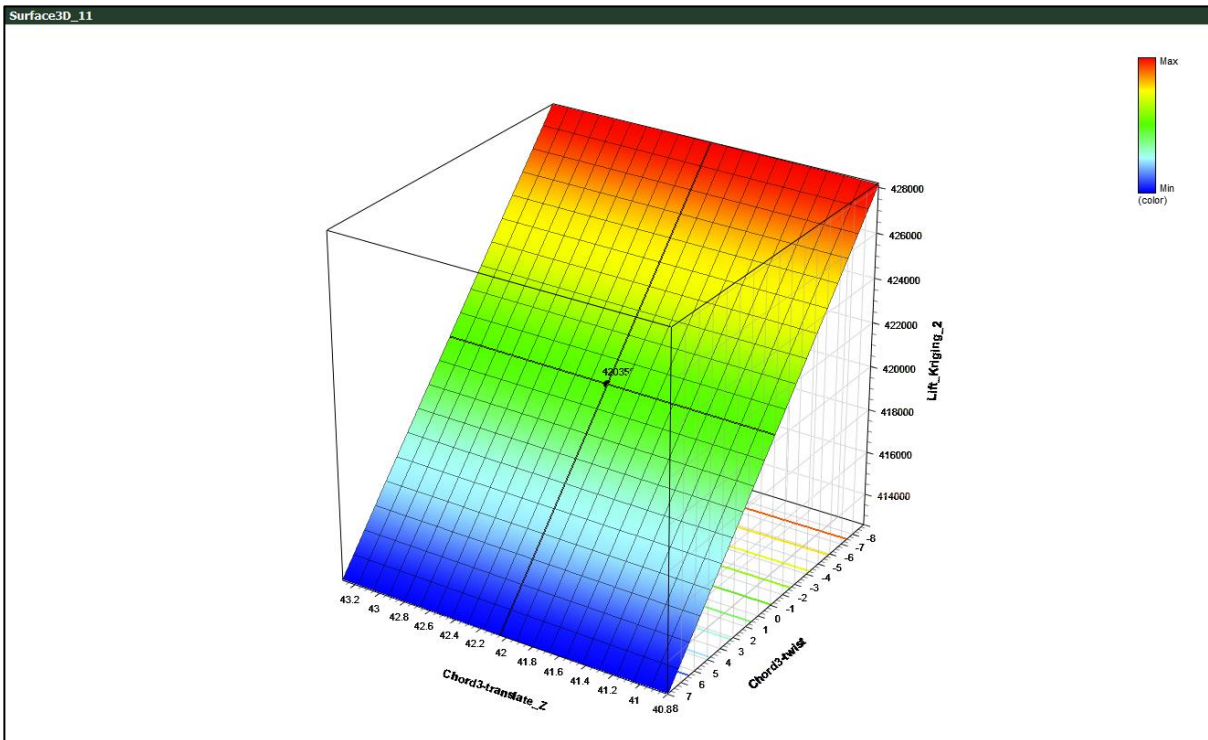


Fig. B-II-12: Chord 3 length (Chord3-translate\_z), Chord 3 twist – Lift kriging

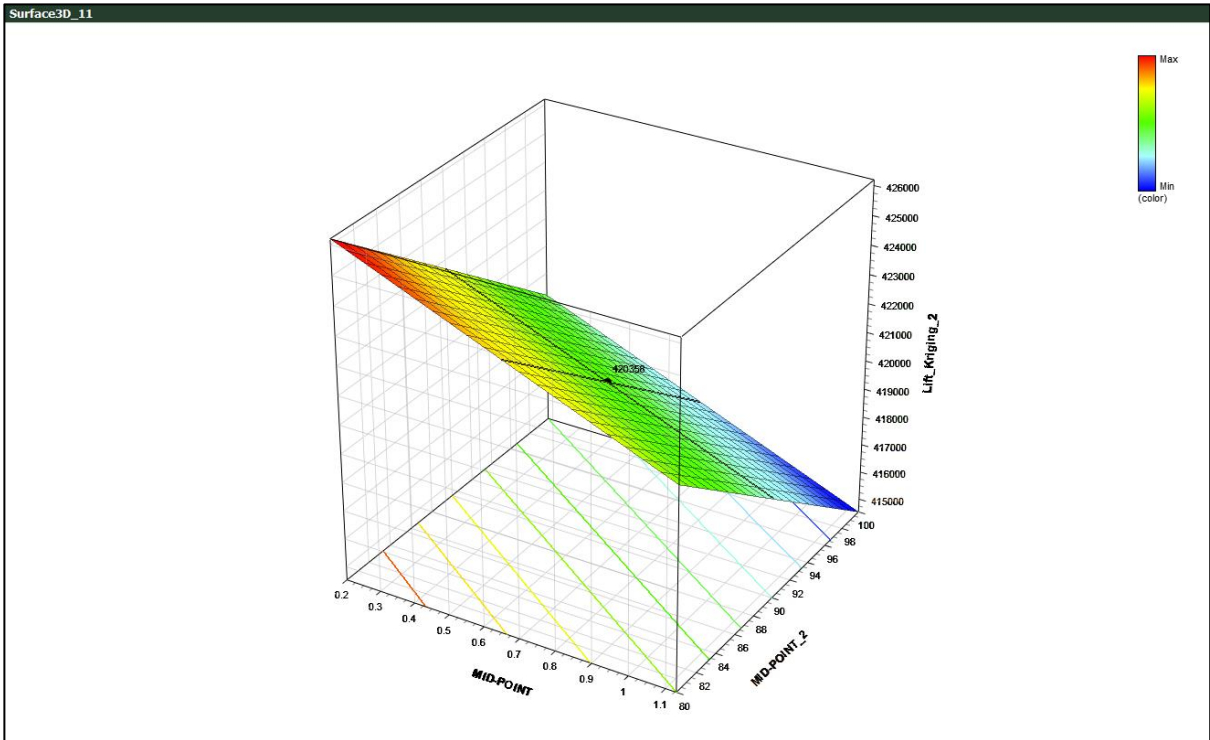


Fig. B-II-13: Mid-point size (MID-POINT), Mid-point twist (MID-POINT\_2) – Lift kriging

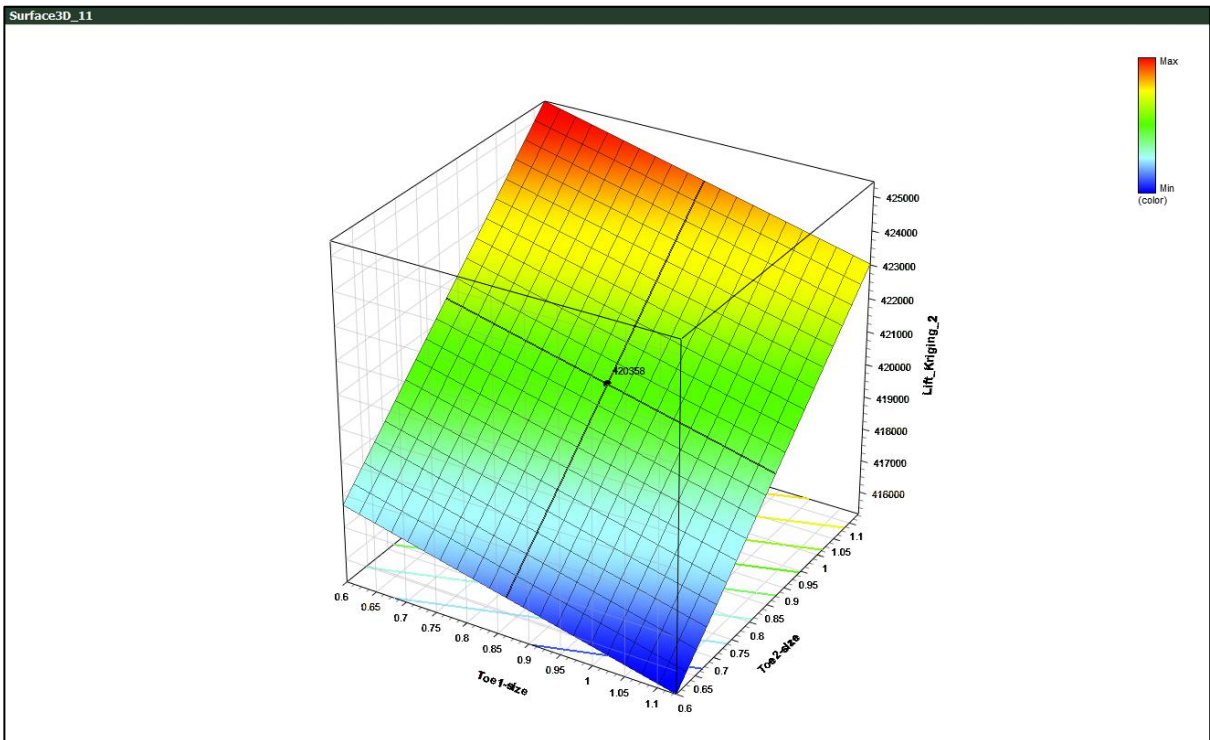


Fig. B-II-14: Toe 2 size, Toe 1 size

### B-III: Kriging response surfaces produced for Design-1

First, the drag kriging response surfaces are presented then the lift kriging response surfaces.

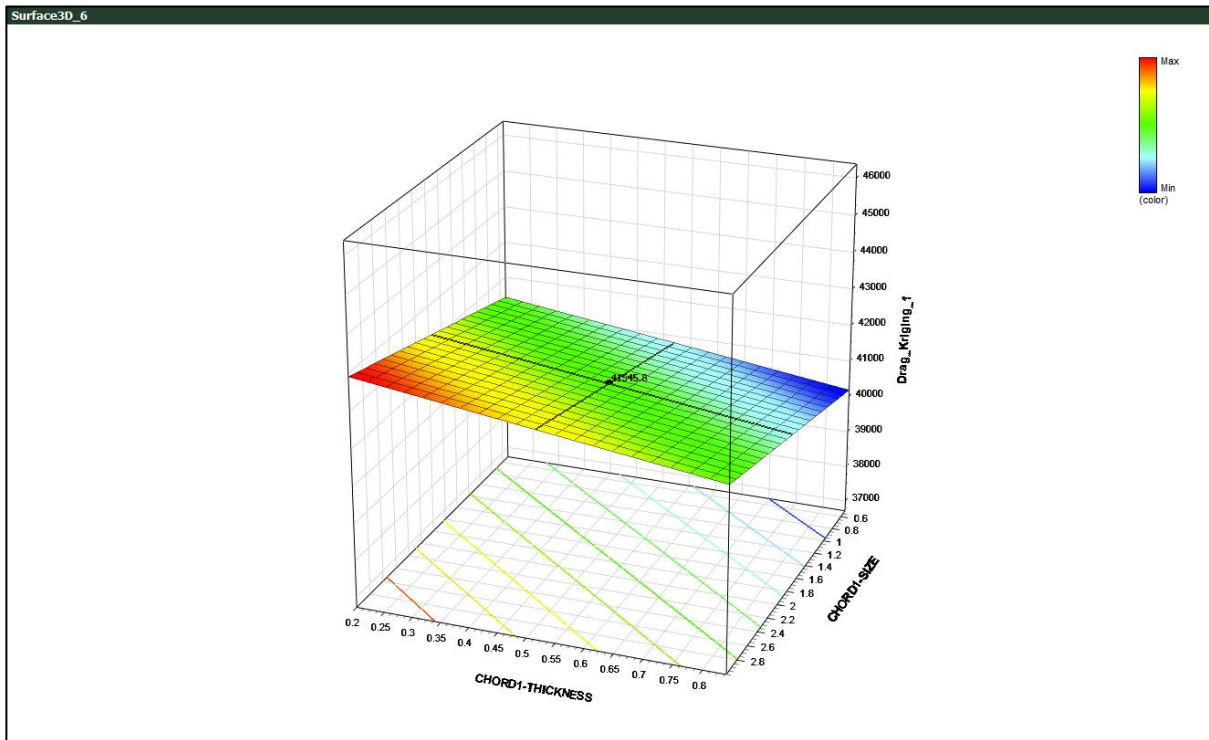


Fig. B-III-1: Chord 1 thickness, Chord 1 size

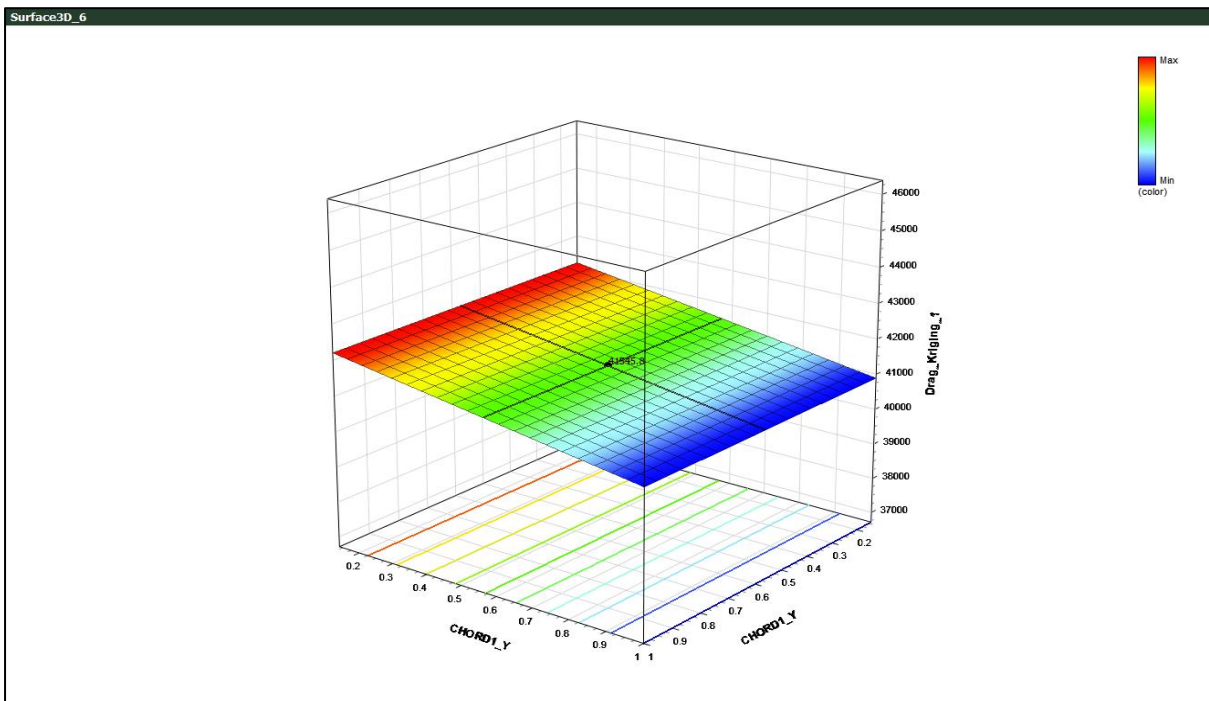


Fig. B-III-2: Chord 1 vertical length

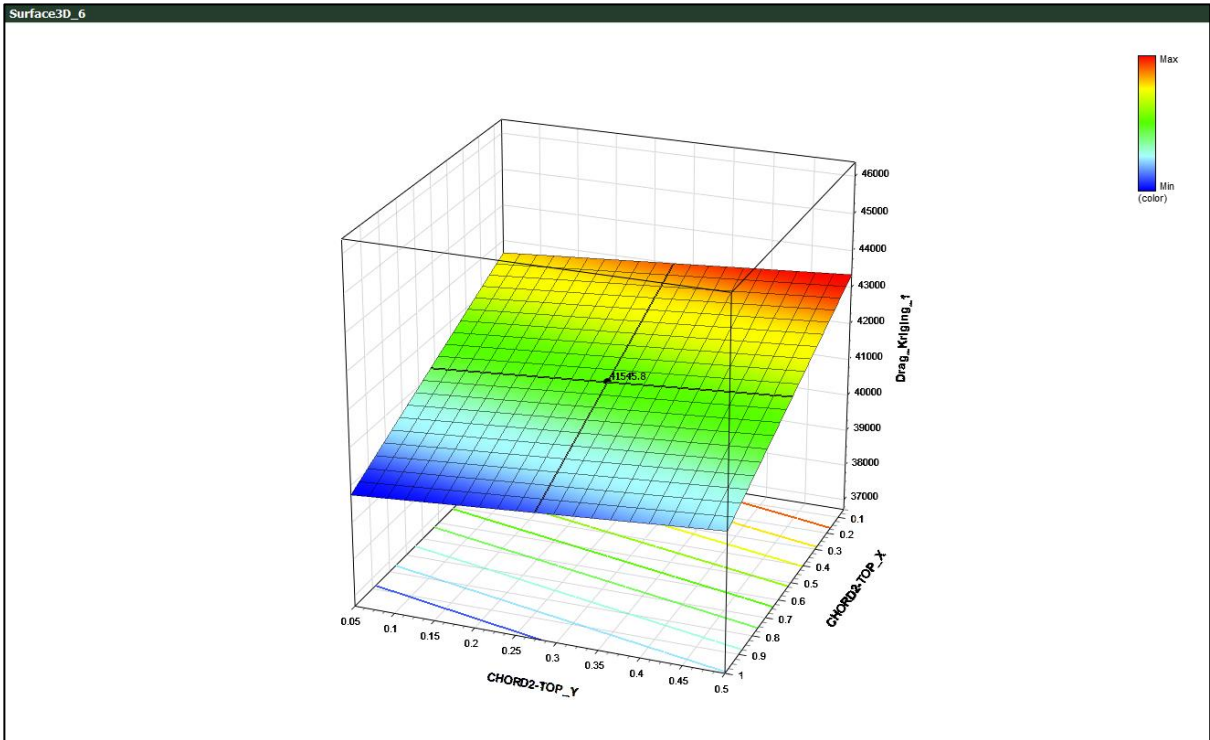


Fig. B-III-3: Chord 2 vertical height (CHORD2-TOP\_Y), Chord 2 sweep (CHORD2-TOP\_X)

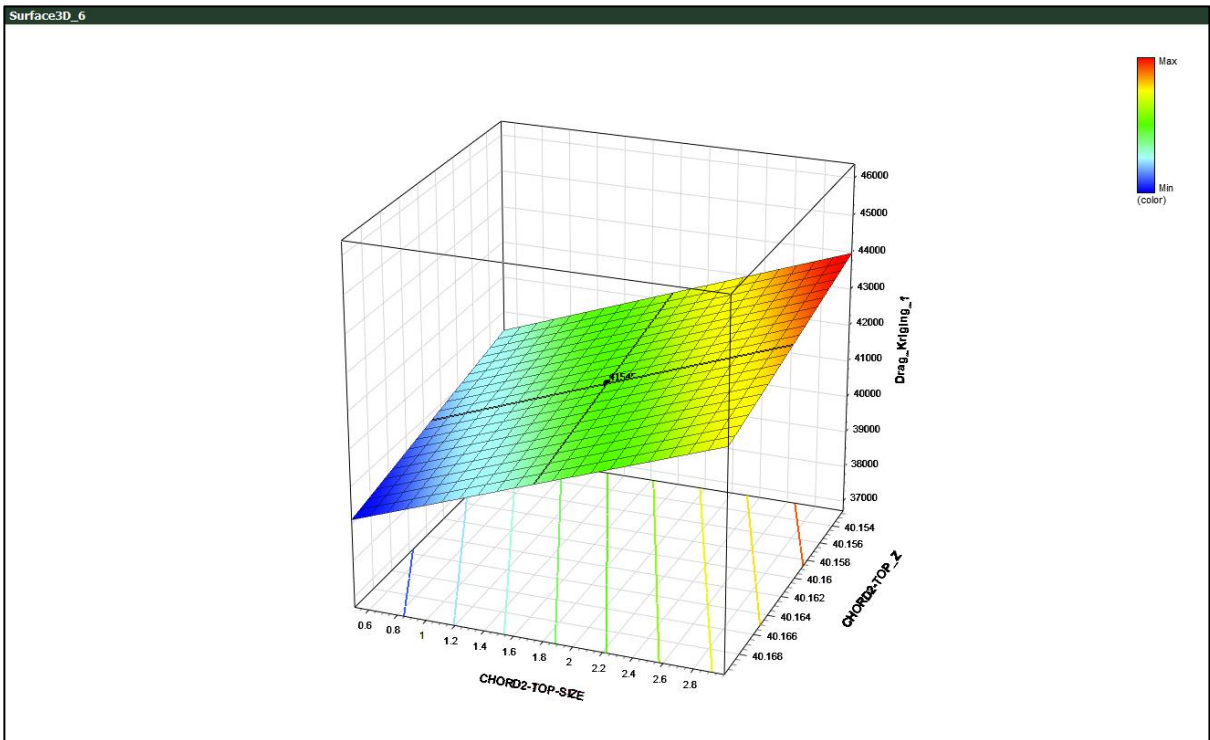


Fig. B-III-4: Chord 2 top size, Chord 2 top – length (CHORD2-TOP\_Z)

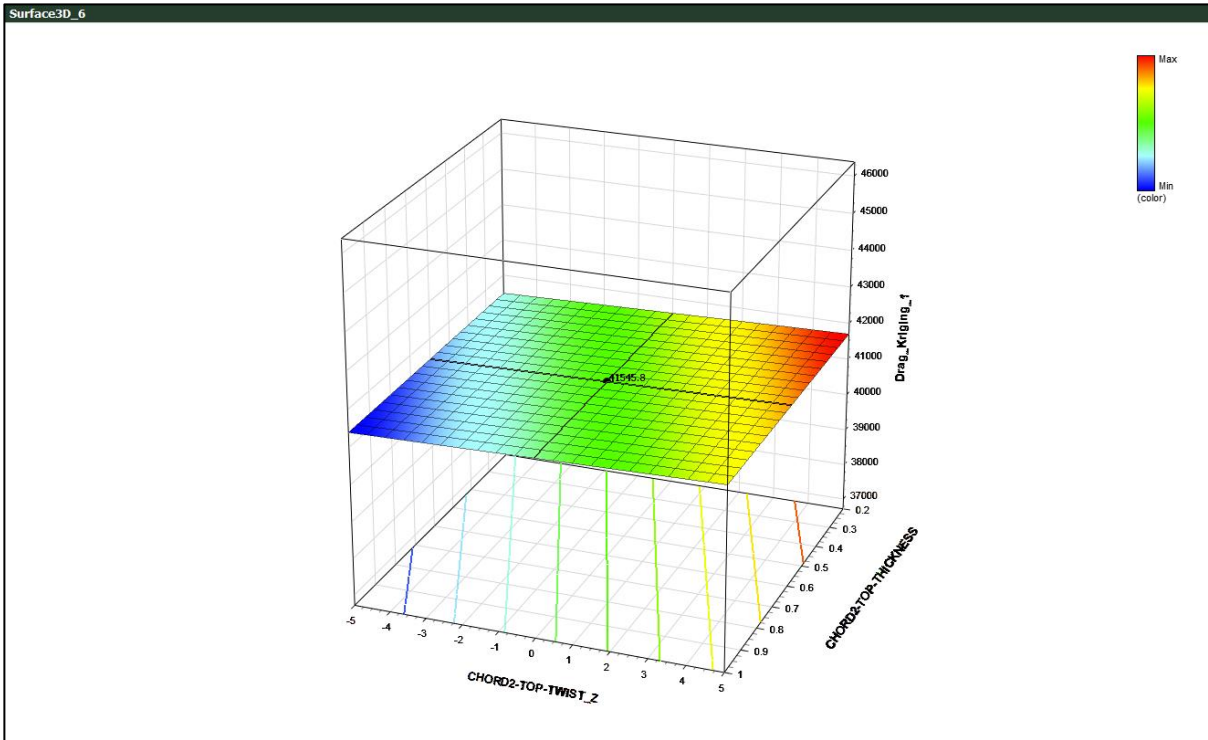


Fig. B-III-5: Chord 2 top twist (CHORD2-TOP\_Z), Chord 2 top thickness

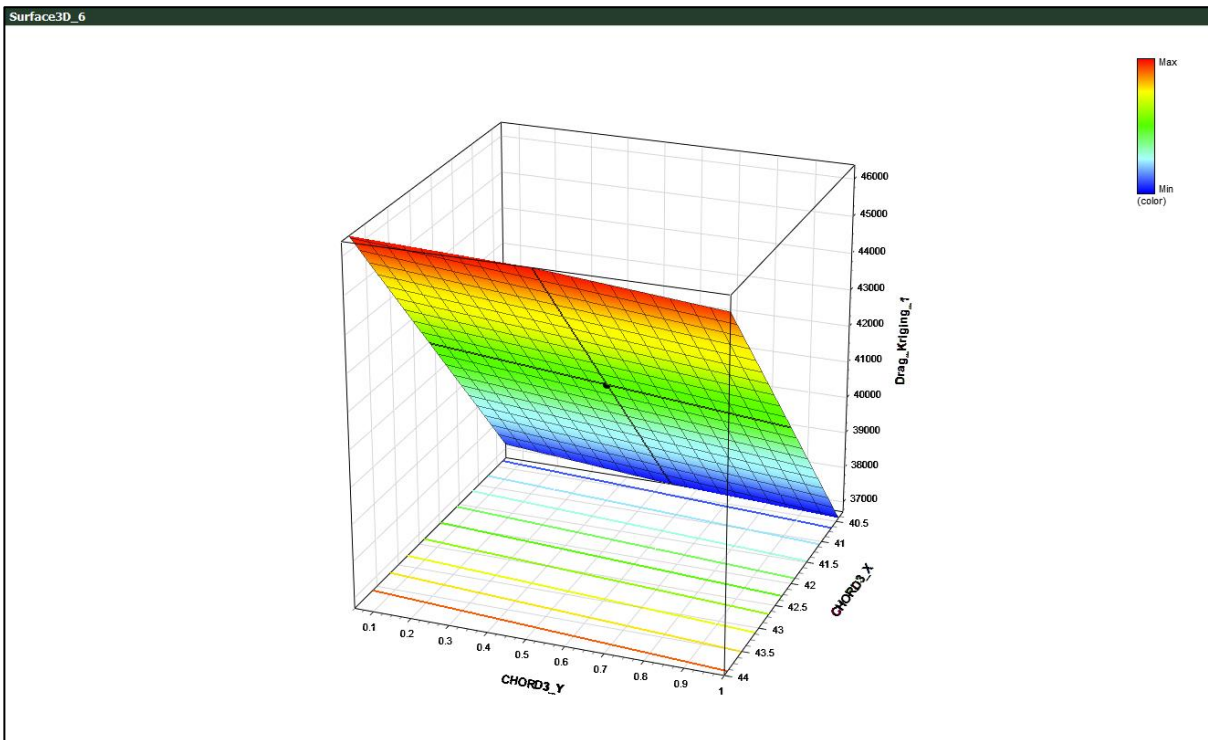


Fig. B-III-6: Chord 3 vertical height (CHORD3\_Y), Chord 3 sweep (CHORD3\_X)

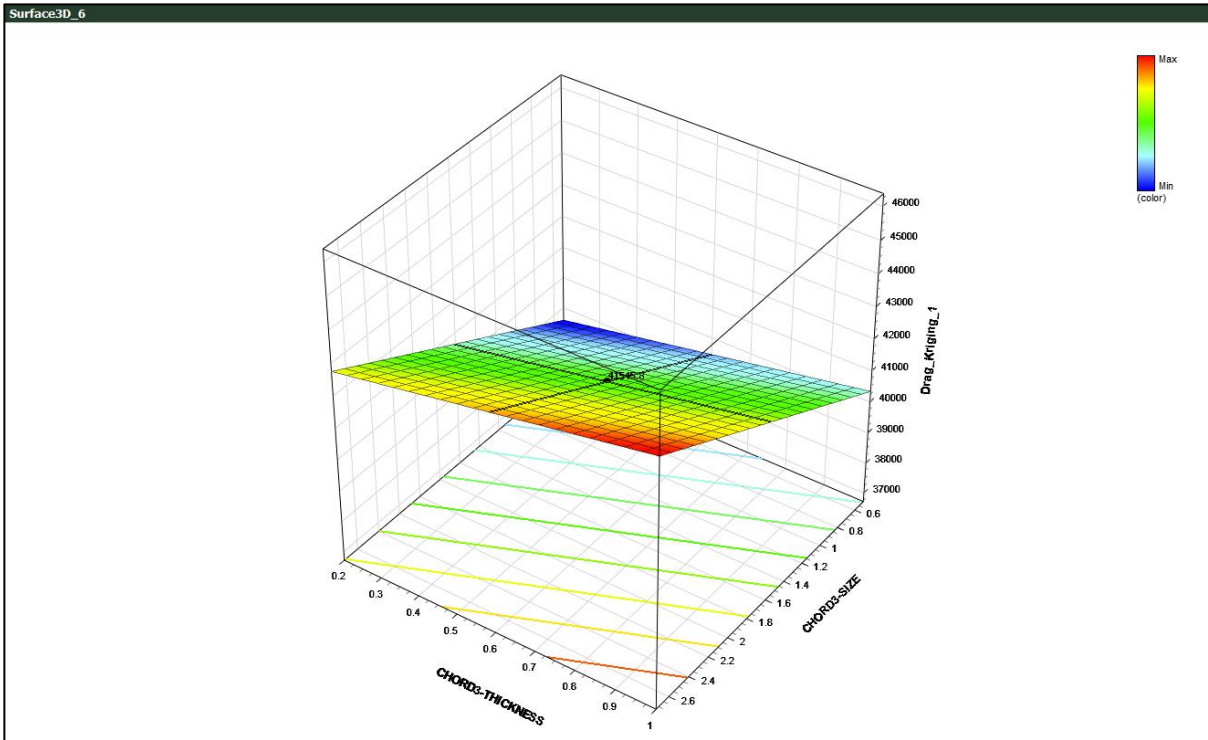


Fig. B-III-7: Chord 3 thickness, Chord 3 size

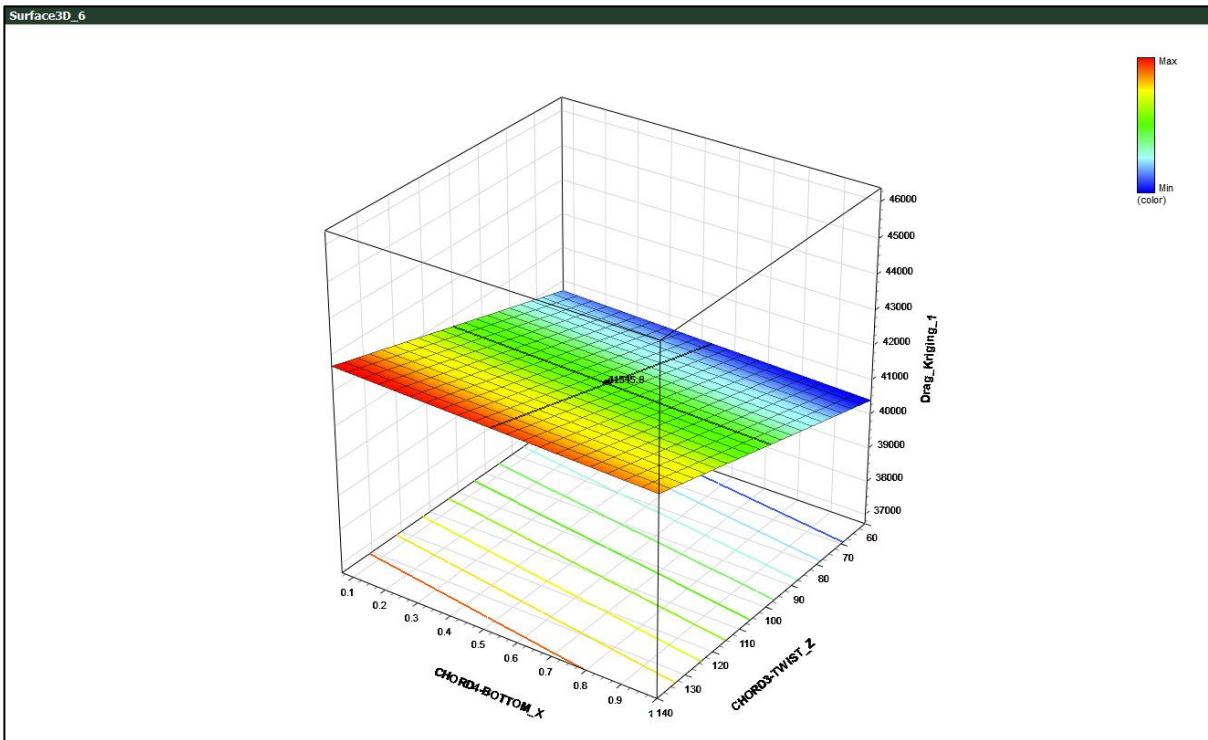


Fig. B-III-8: Chord 4 bottom sweep (CHORD4-BOTTOM\_X), Chord 3 twist (CHORD3-TWIST\_Z)

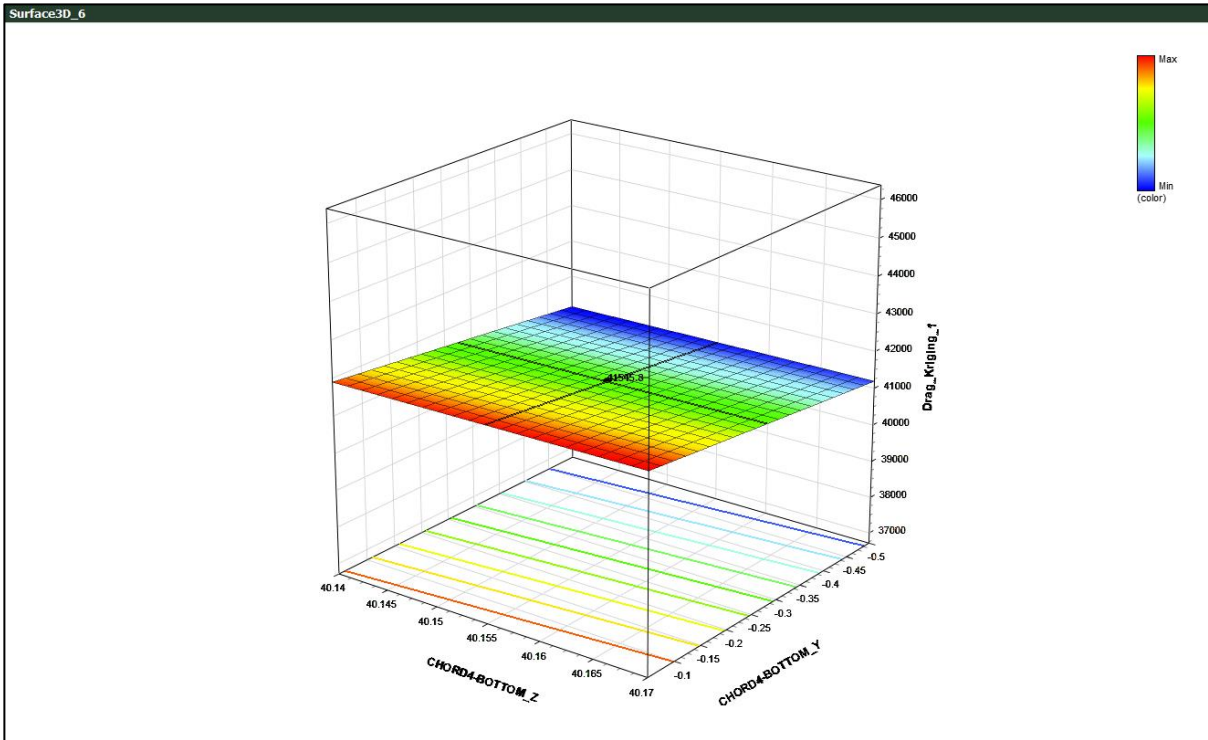


Fig. B-III-10: Chord 4 bottom – length (CHORD4-BOTTOM\_Z), Chord 4 bottom – vertical height (CHORD4-BOTTOM\_Y)

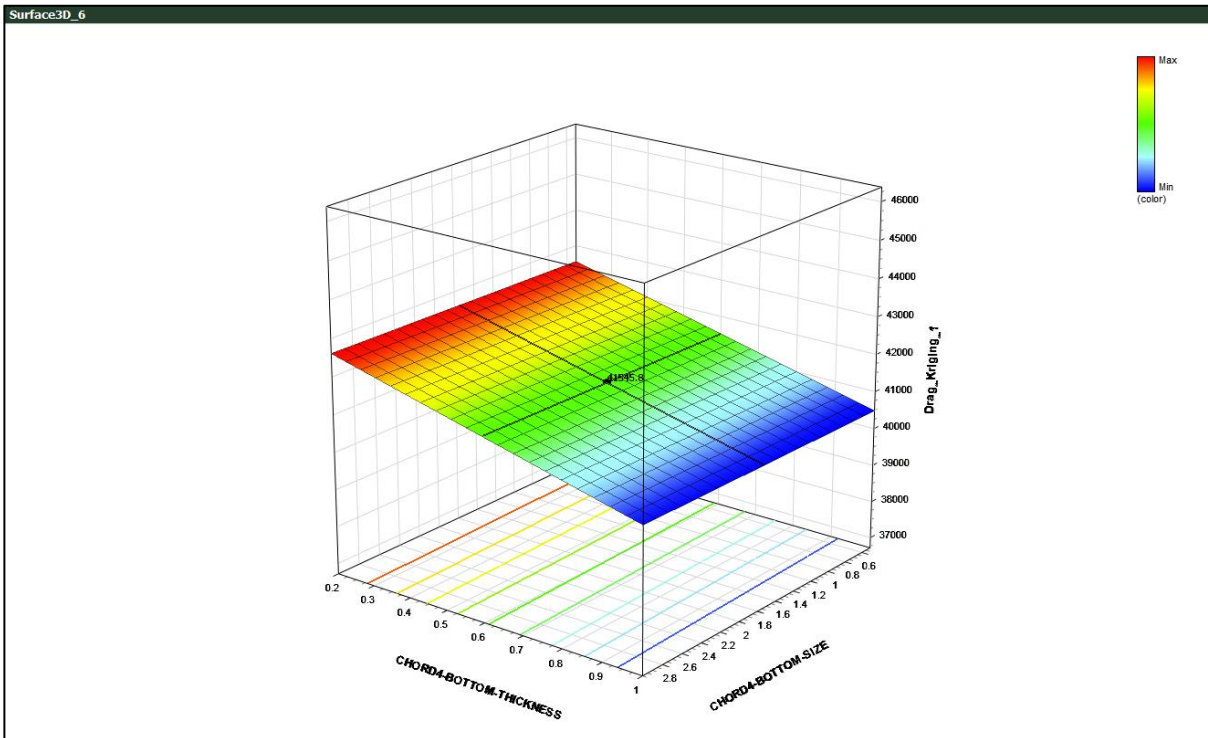


Fig. B-III-11: Chord 4 bottom thickness, Chord 4 bottom size

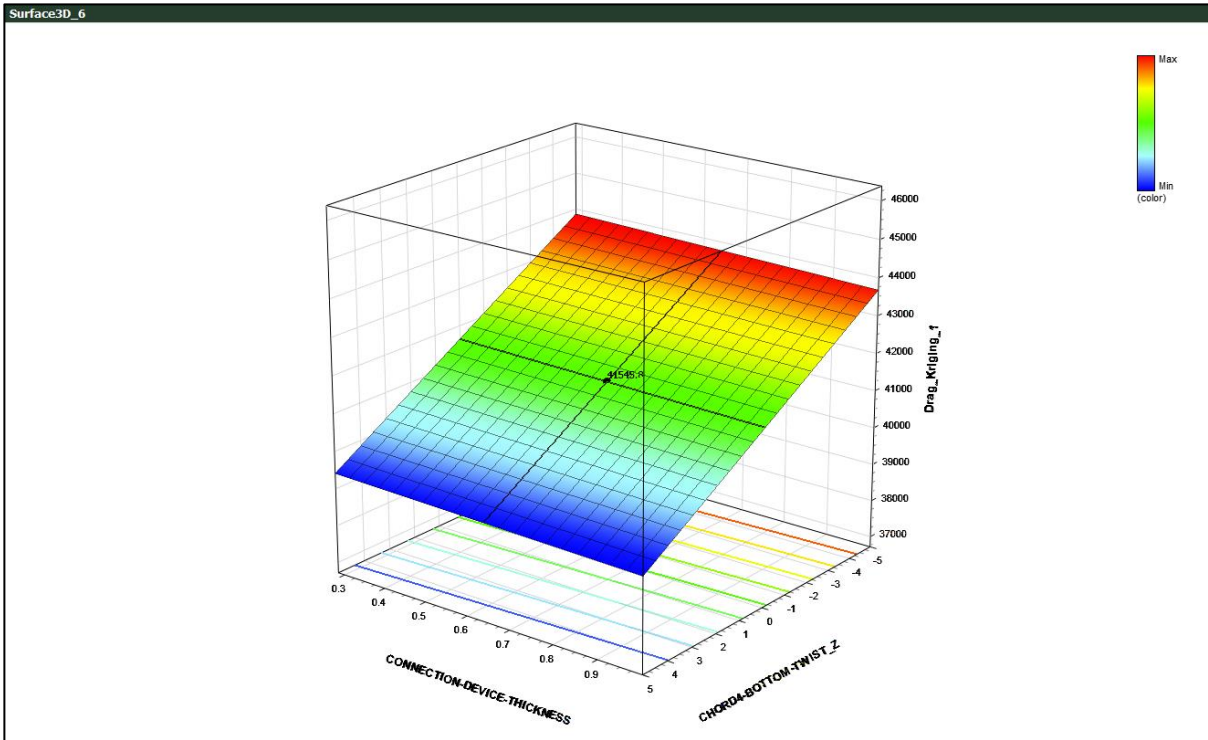


Fig. B-III-13: Connection device thickness, Chord 4 bottom twist (CHORD4-BOTTOM-TWIST\_Z)

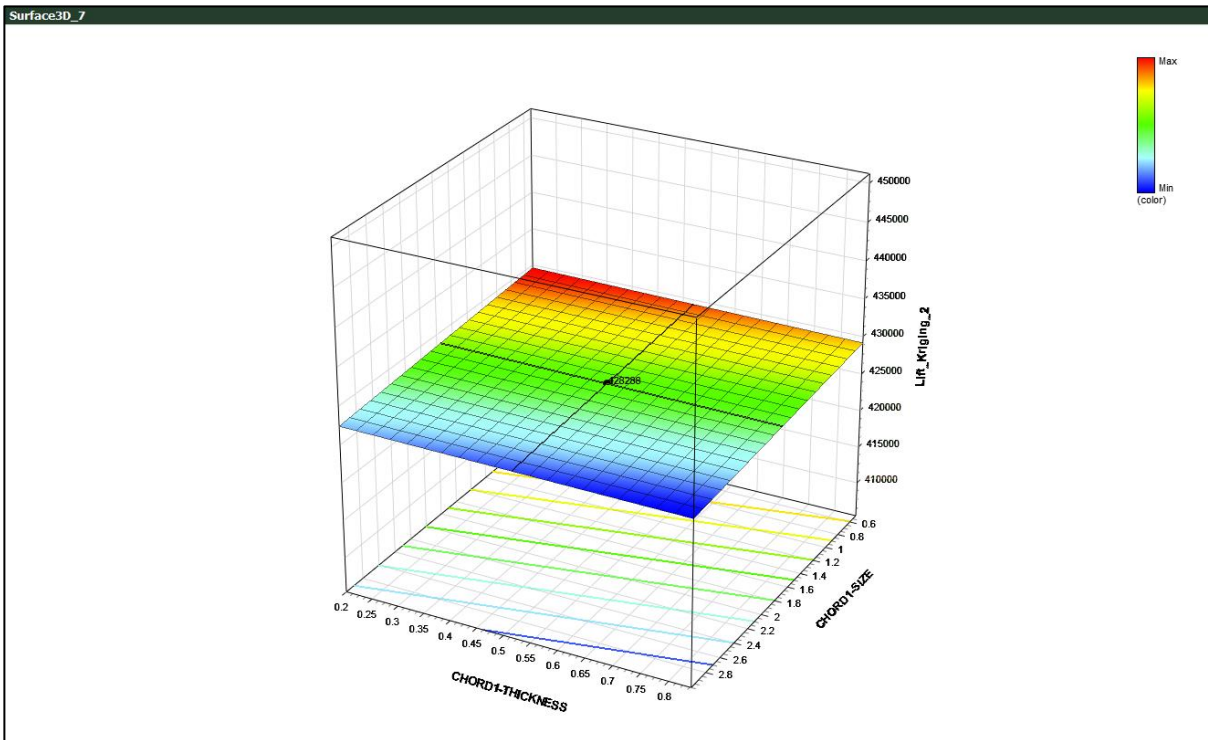


Fig. B-III-14: Chord 1 thickness, Chord 1 size – Lift kriging

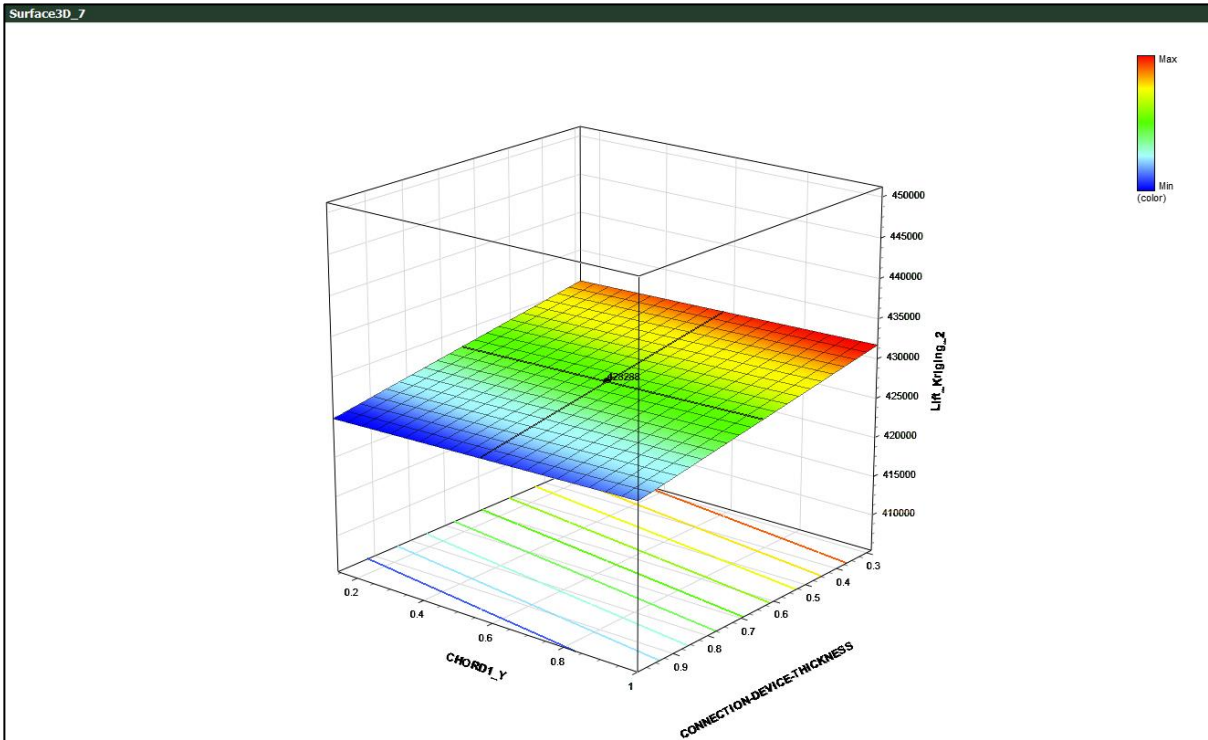


Fig. B-III-15: Chord 1 vertical height (CHORD1\_Y), Connection device thickness – Lift kriging

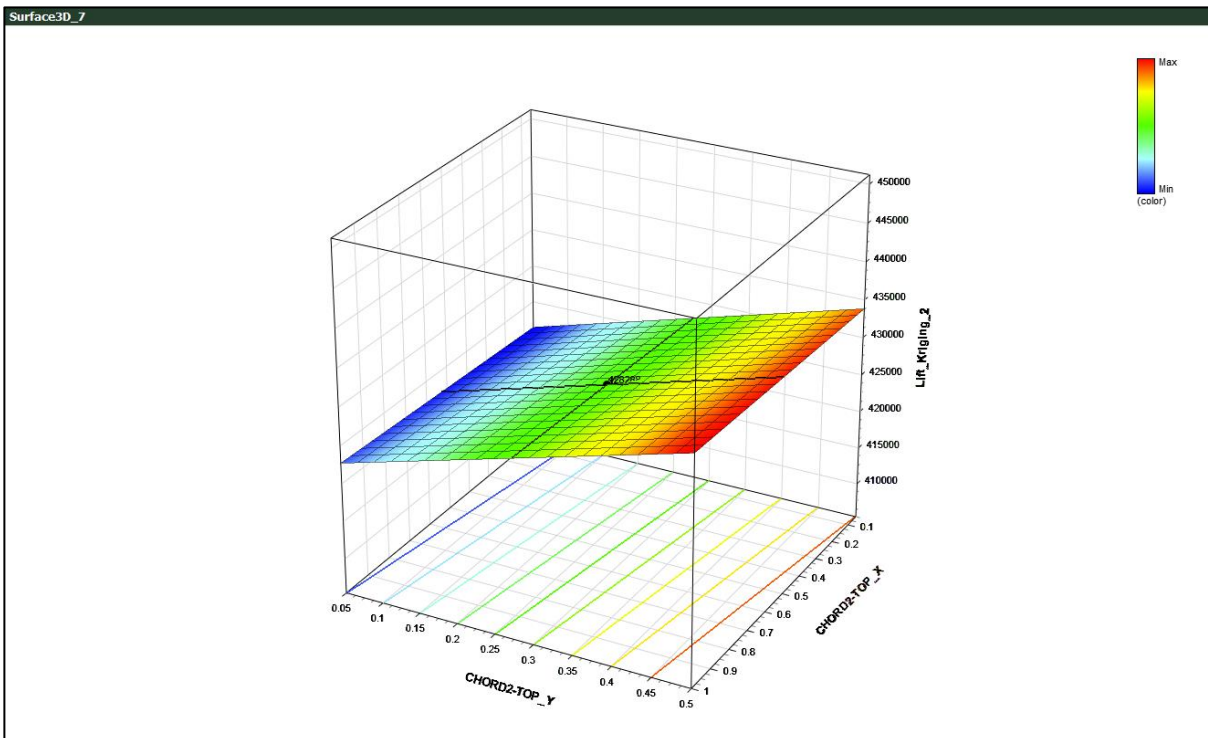


Fig. B-III-16: Chord 2 top – vertical height (CHORD2-TOP\_Y), Chord 2-top sweep (CHORD2-TOP\_X) – Lift kriging

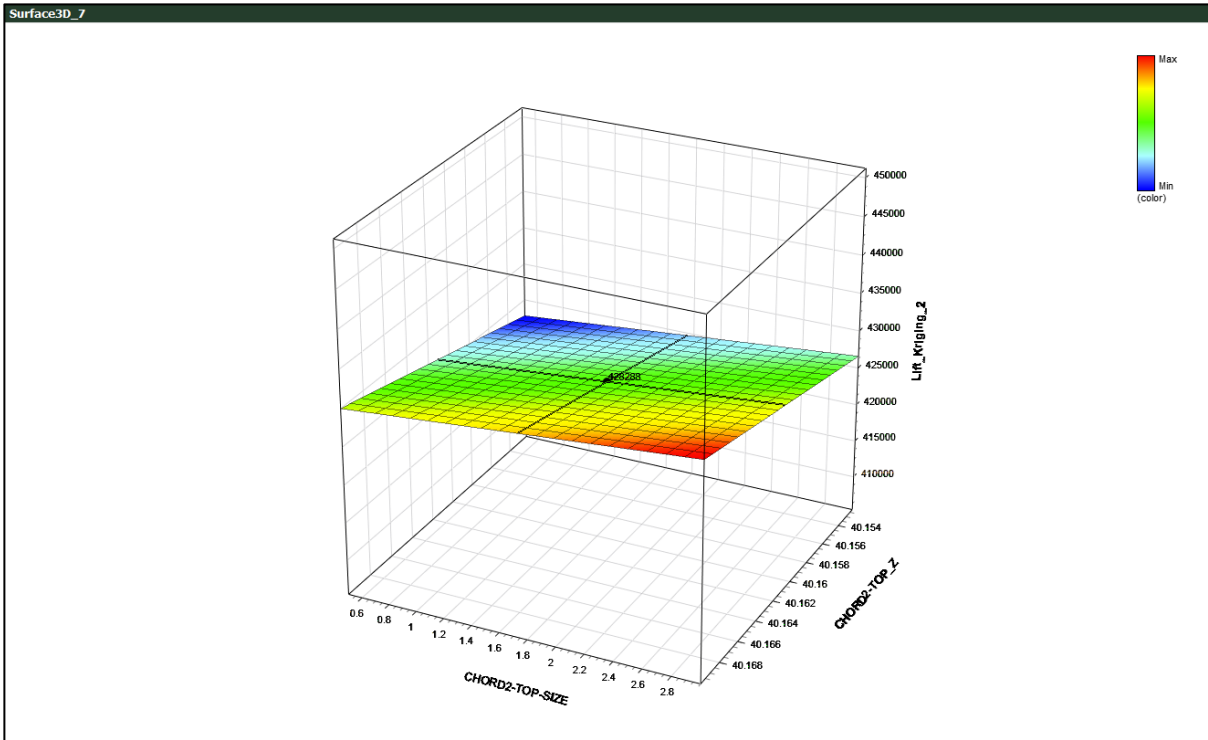


Fig. B-III-17: Chord 2 top size, Chord 2 top length (CHORD2-TOP\_Z) – Lift kriging

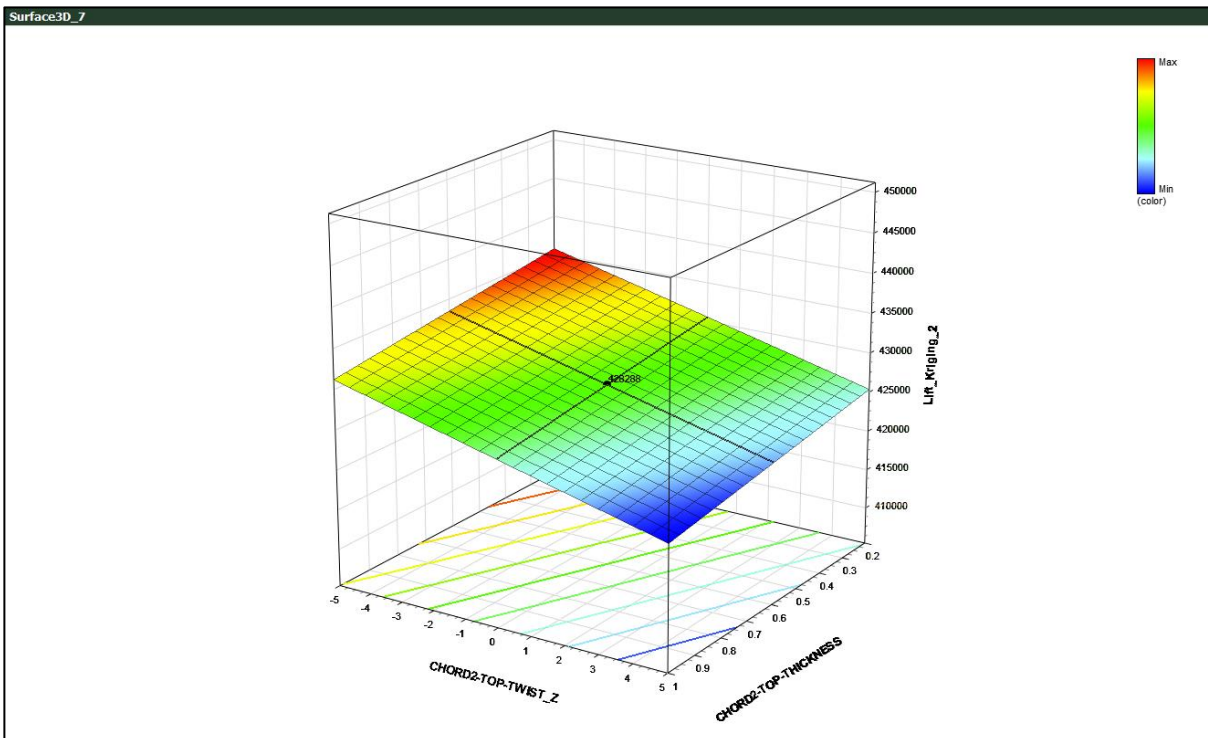


Fig. B-III-18: Chord 2 top twist (CHORD2-TOP-TWIST\_Z), Chord 2 top thickness (CHORD2-TOP-THICKNESS) – Lift kriging

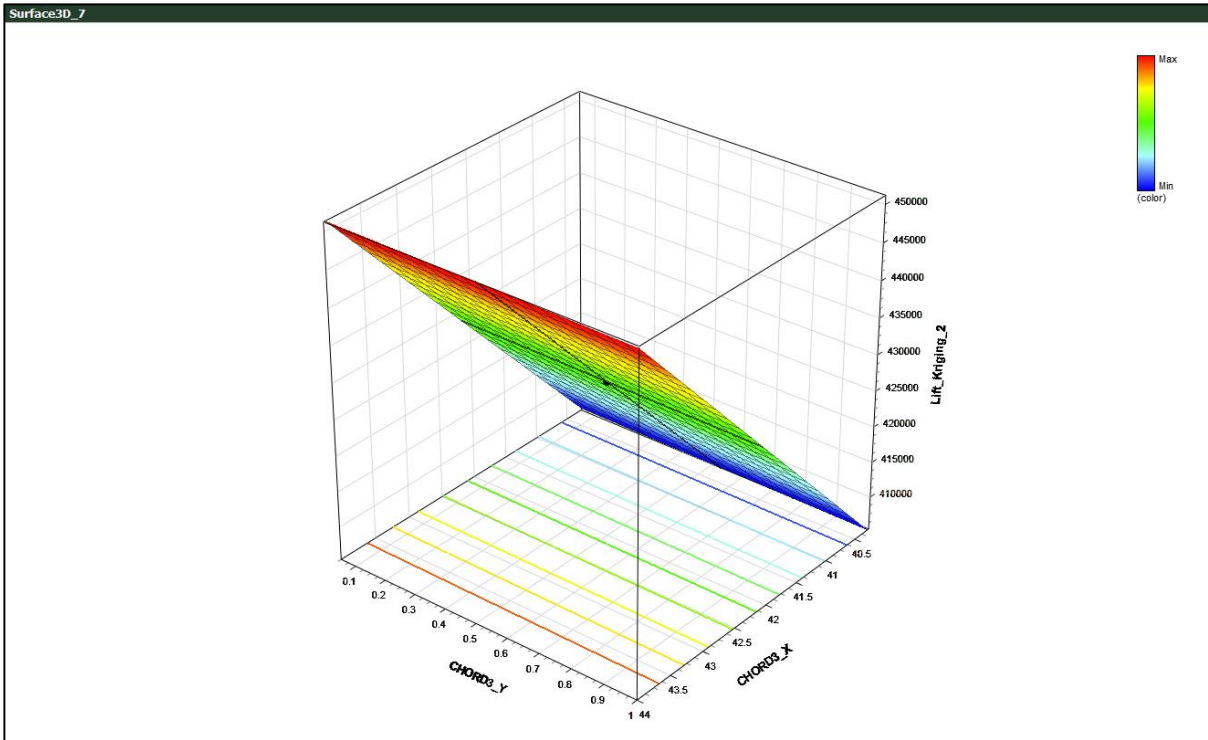


Fig. B-III-19: Chord 3 – vertical height (CHORD3\_Y), Chord 3 sweep (CHORD3\_X) – Lift kriging

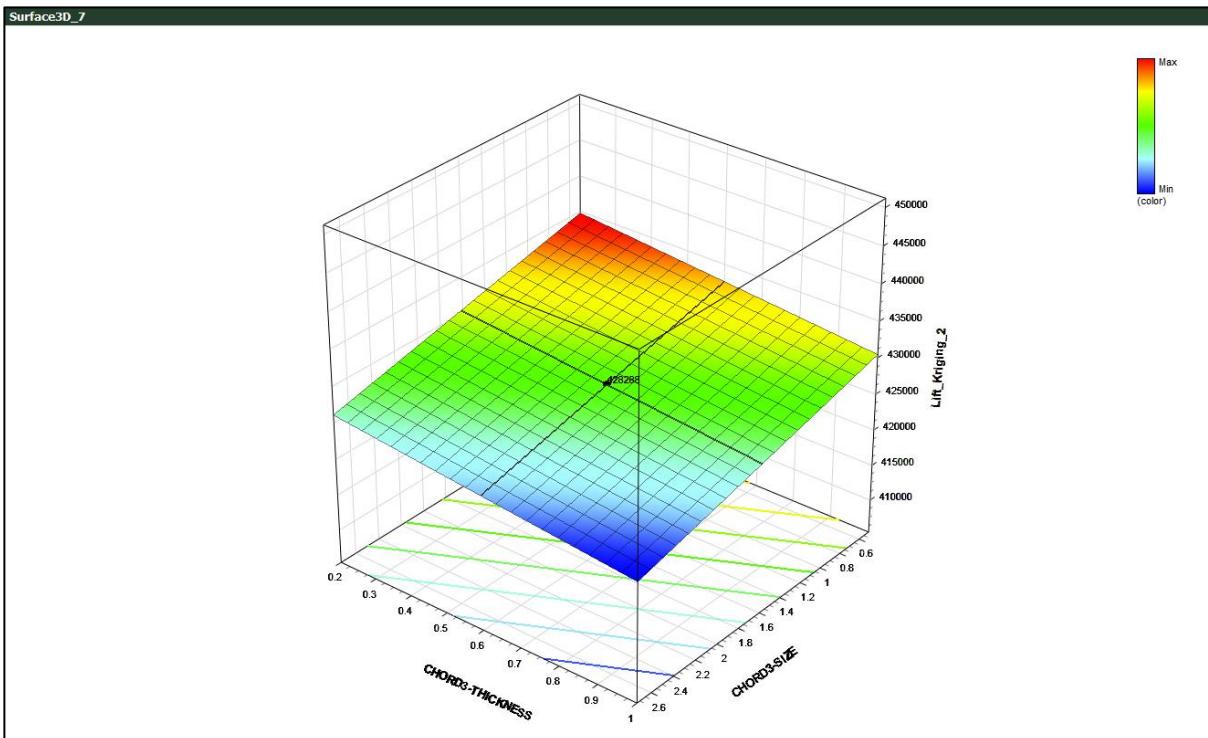


Fig. B-III-20: Chord 3 – thickness, Chord 3 size – Lift kriging

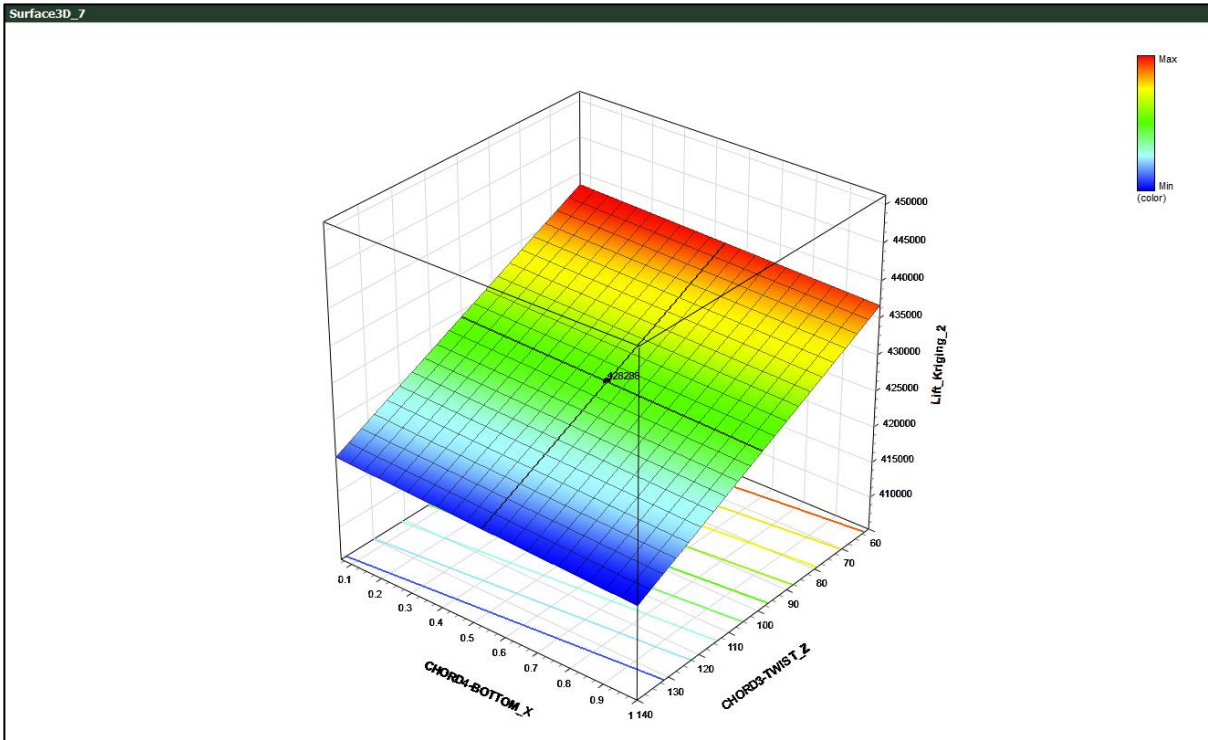


Fig. B-III-21: Chord 4 bottom sweep (CHORD4-BOTTOM\_X), Chord3-twist (CHORD3-TWIST\_Z) – Lift kriging

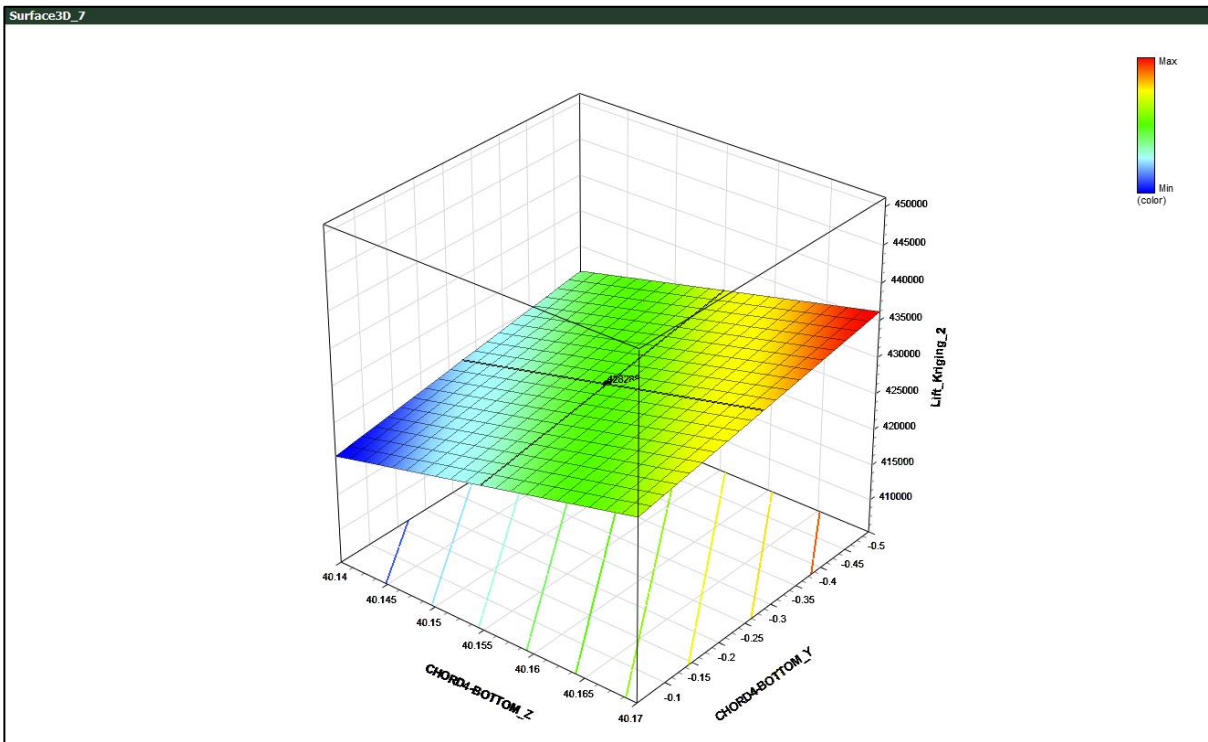


Fig. B-III-22: Chord 4 bottom length (CHORD4-BOTTOM\_Z), Chord 4 bottom vertical height (CHORD4-BOTTOM\_Y) – Lift kriging

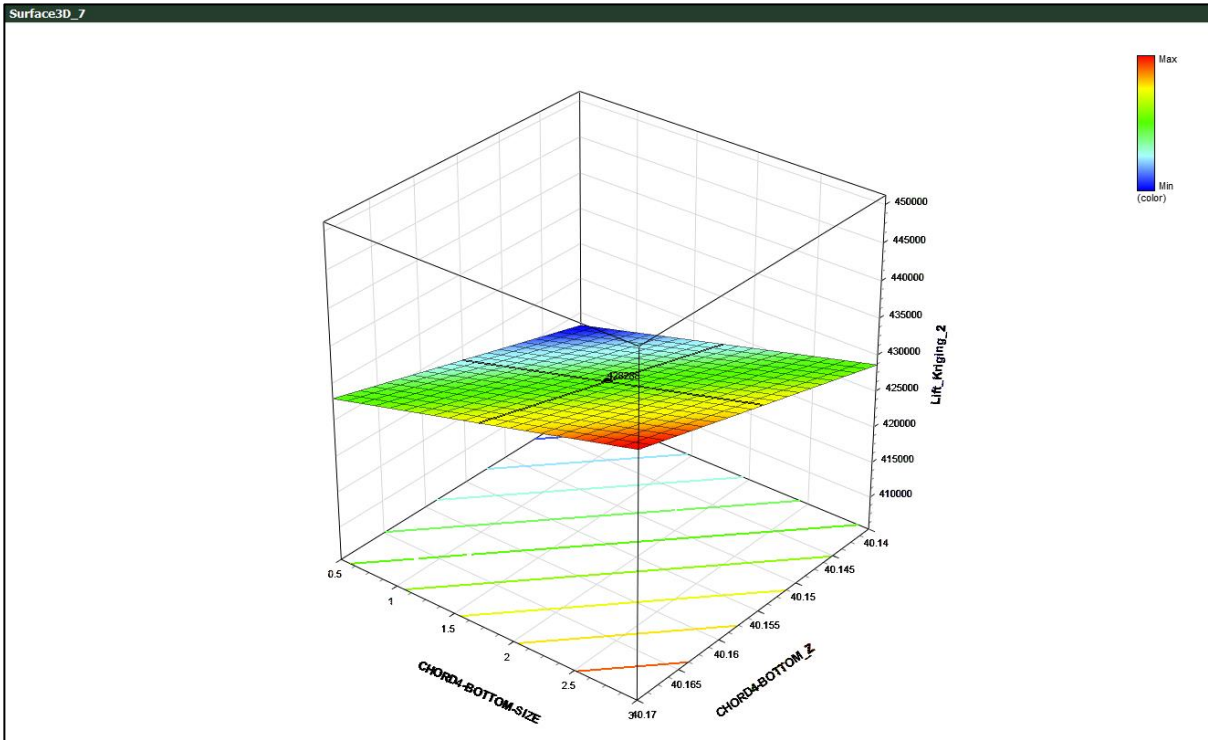


Fig. B-III-23: Chord 4 bottom size, Chord 4 bottom length (CHORD4-BOTTOM\_Z) – Lift kriging

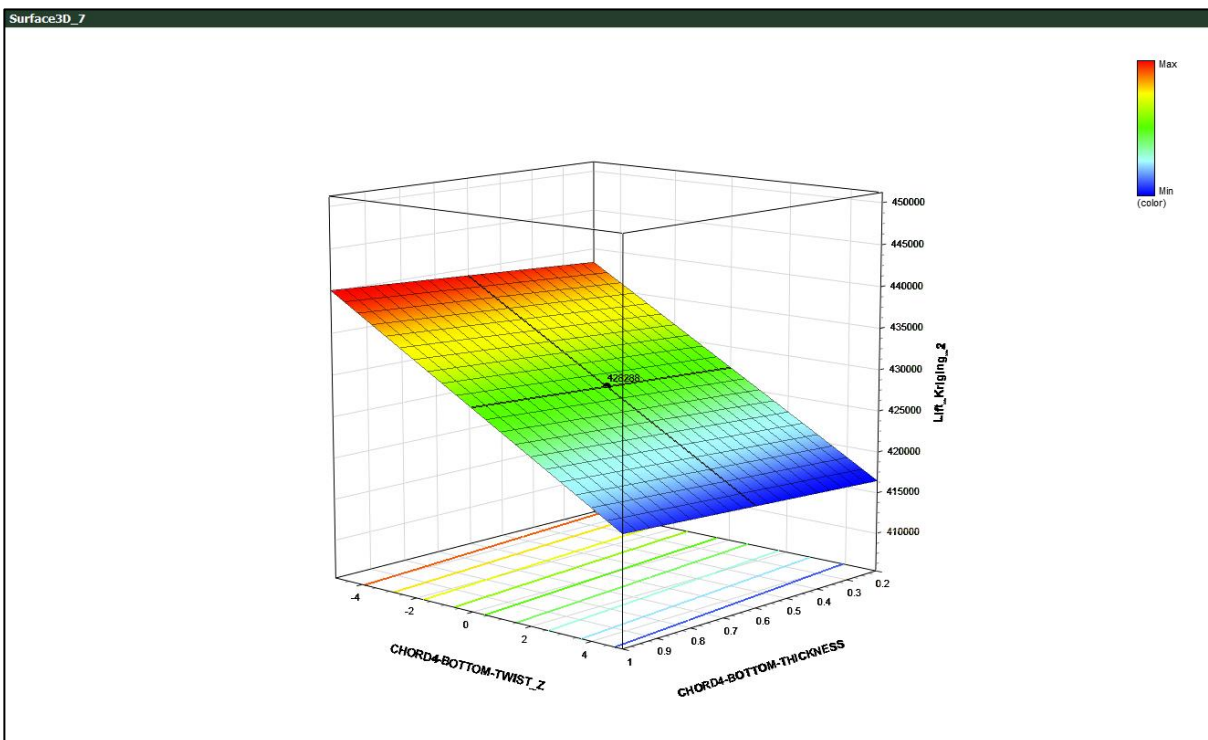


Fig. B-III-24: Chord 4 bottom twist (CHORD4-BOTTOM-TWIST\_Z), Chord 4 bottom thickness – Lift kriging

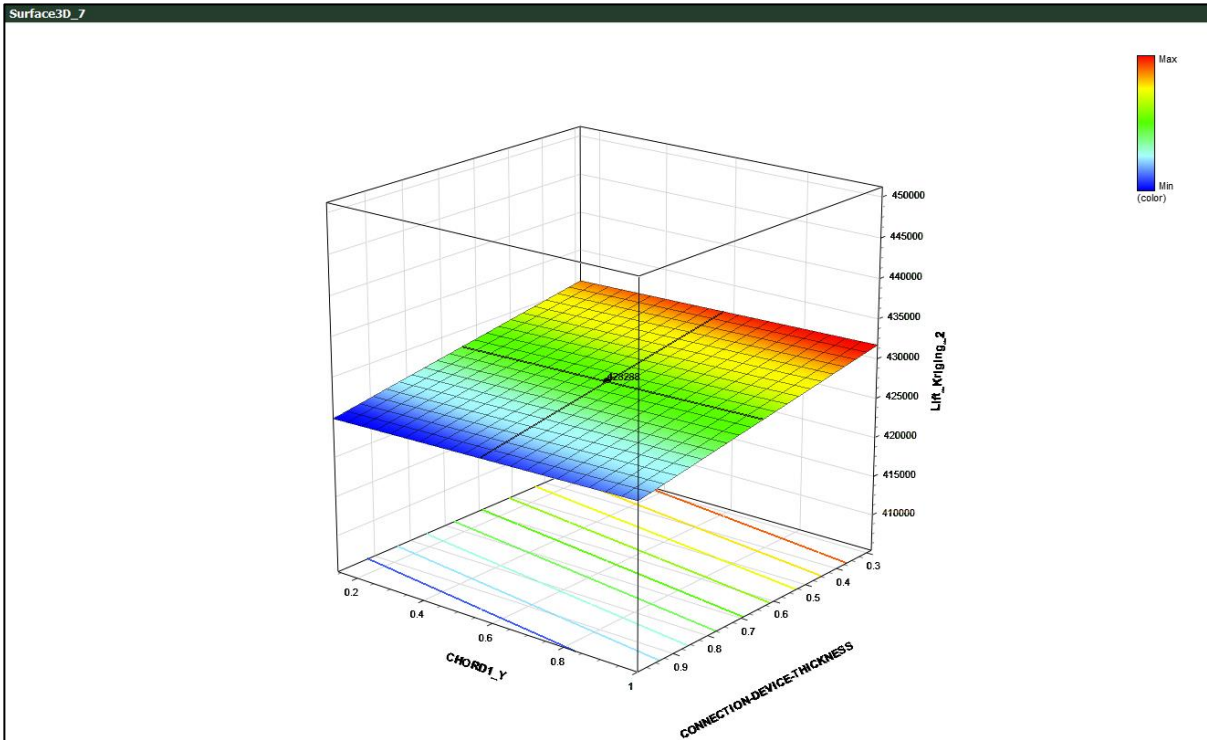


Fig. B-III-25: Chord 1 vertical height (CHORD1\_Y), Connection device thickness – Lift kriging

**B-IV: Kriging response surfaces for Design-3**

First, the response surface of the mid-point section is presented which is then followed by the ones for the other parts of the design.

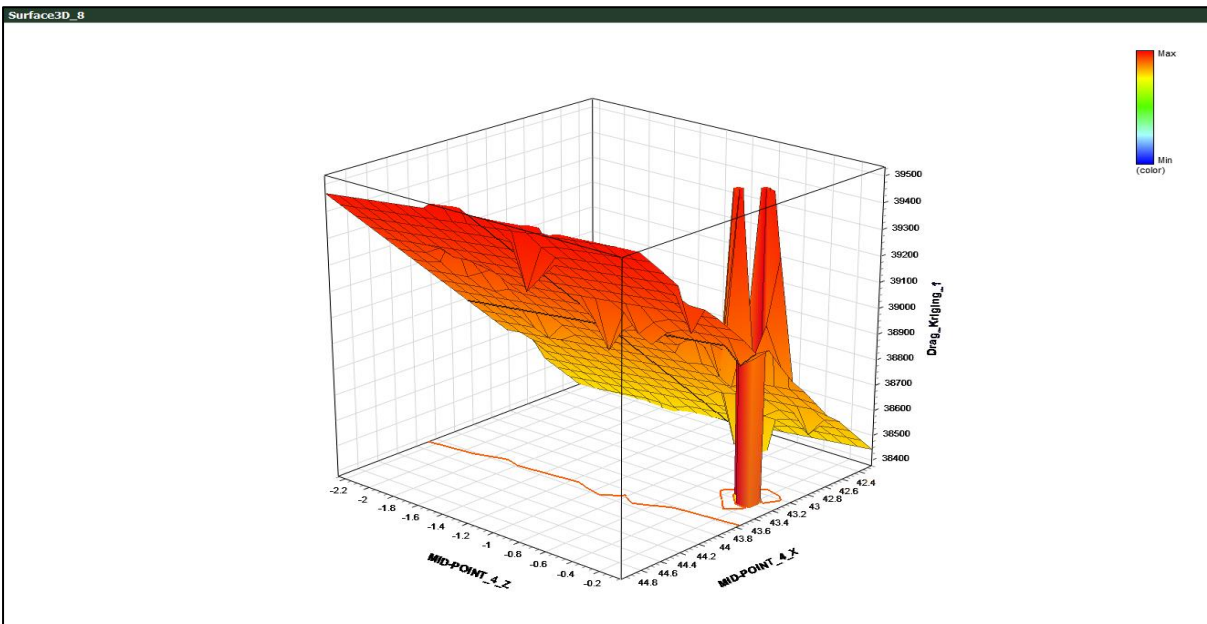
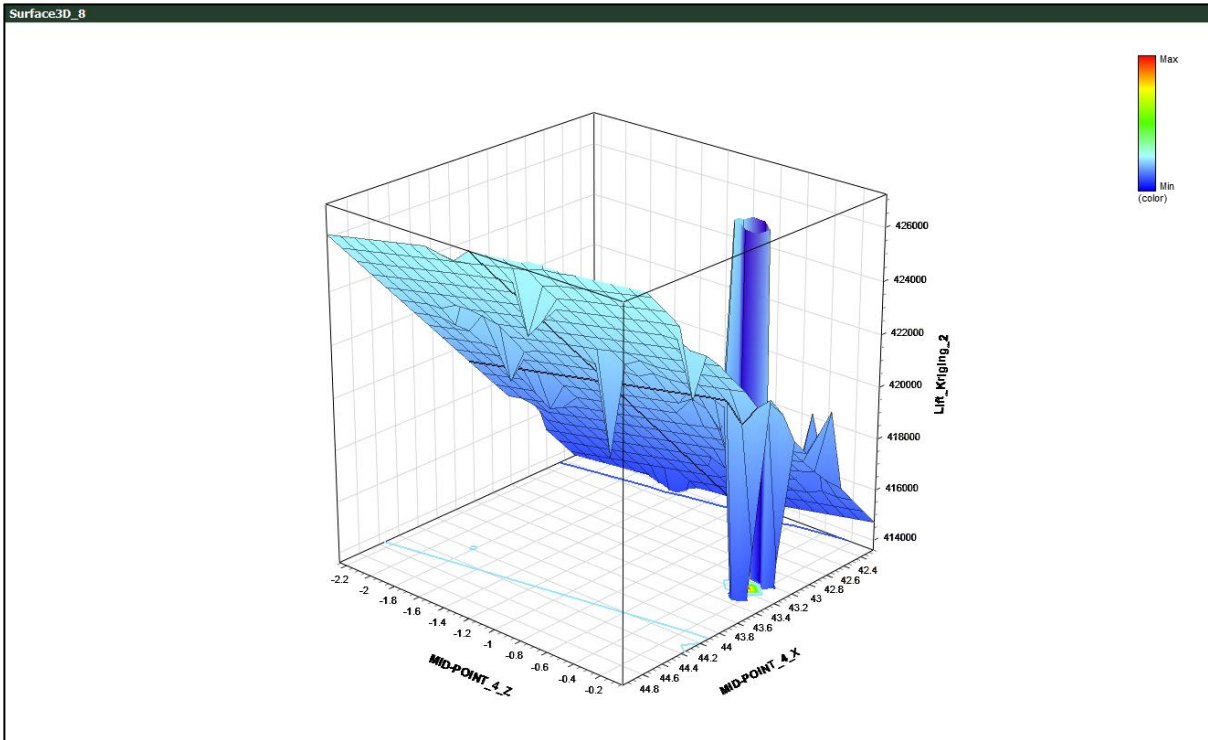
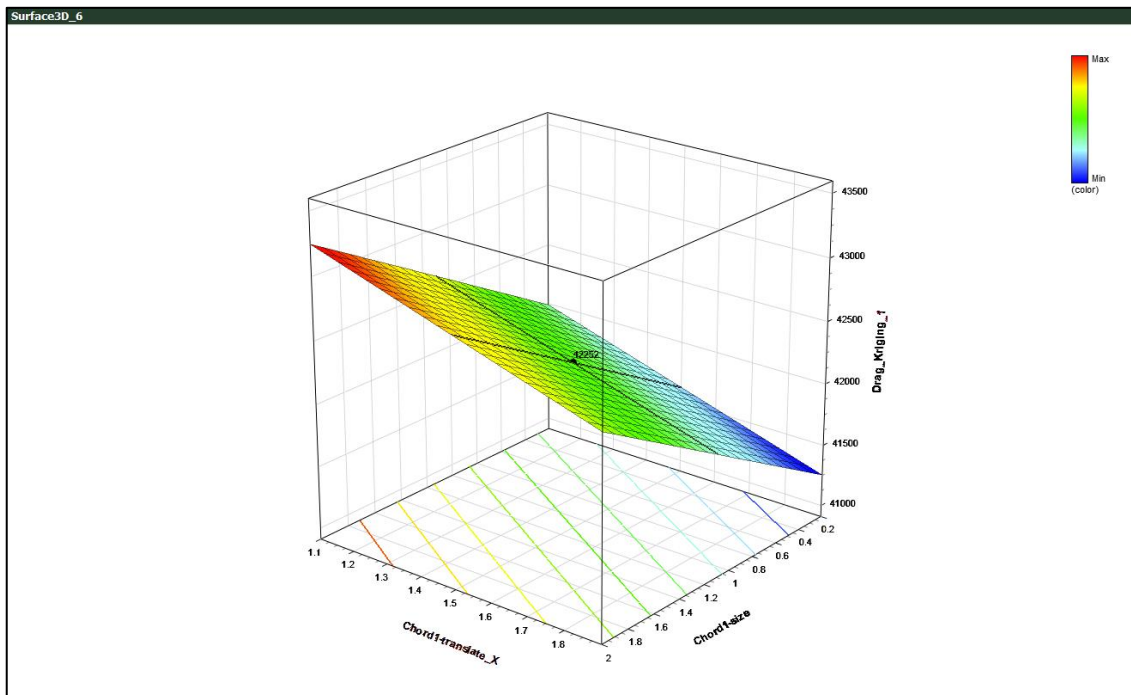


Fig. B-IV-1 : Mid-point length (MID-POINT\_4\_Z), Mid-point sweep (MID-POINT\_4\_X)



**Fig. B-IV-2: Mid-point length (MID-POINT\_4\_Z), Mid-point sweep (MID-POINT\_4\_X) – Lift kriging**

The kriging surrogate response surfaces produced for the optimisation of the other design parameters for Design-3 is presented in this section.



**Fig. B-IV-3: Chord 1 sweep (Chord1-translate\_x), Chord 1 size**

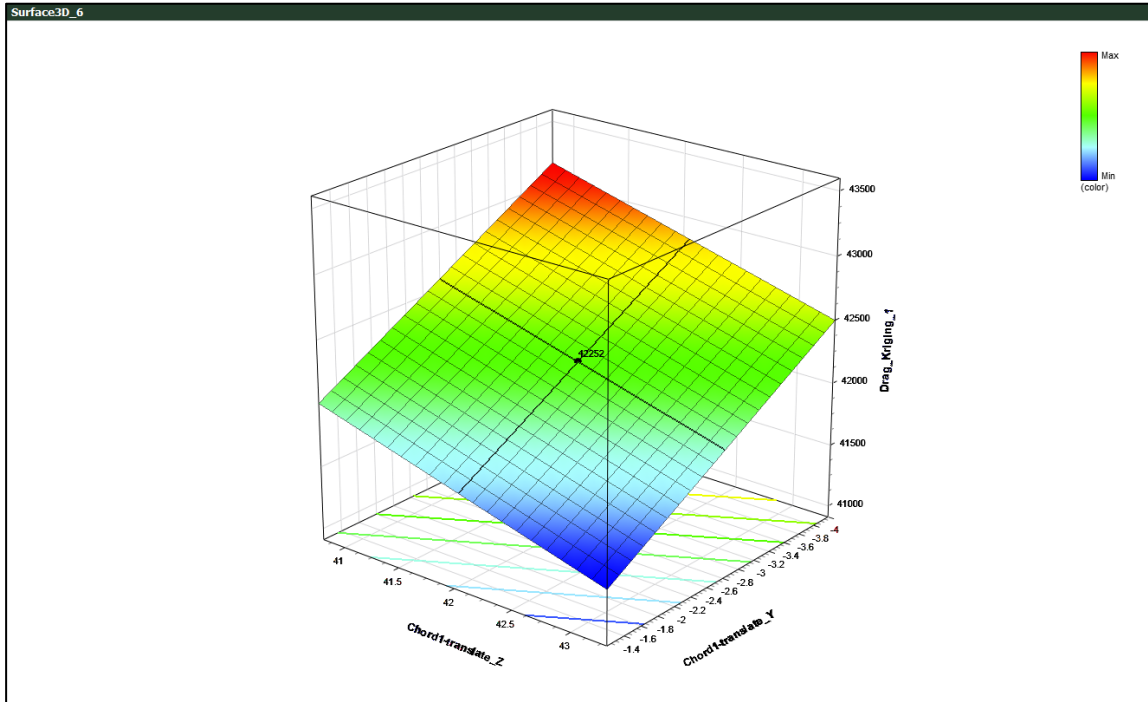


**Fig. B-IV-4: Chord 1 length (Chord1-translate\_z), Chord 1 vertical height (Chord1-translate\_Y)**

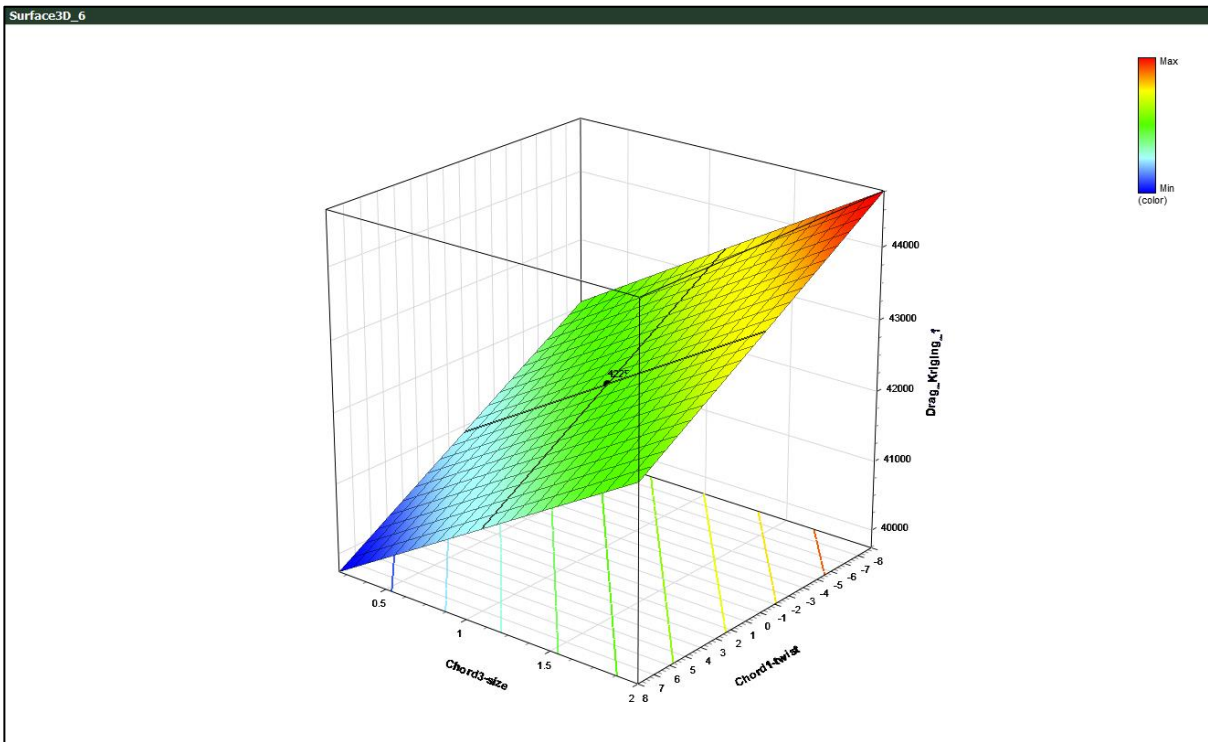


**Fig. B-IV-5: Chord 3 size, Chord 1 twist**

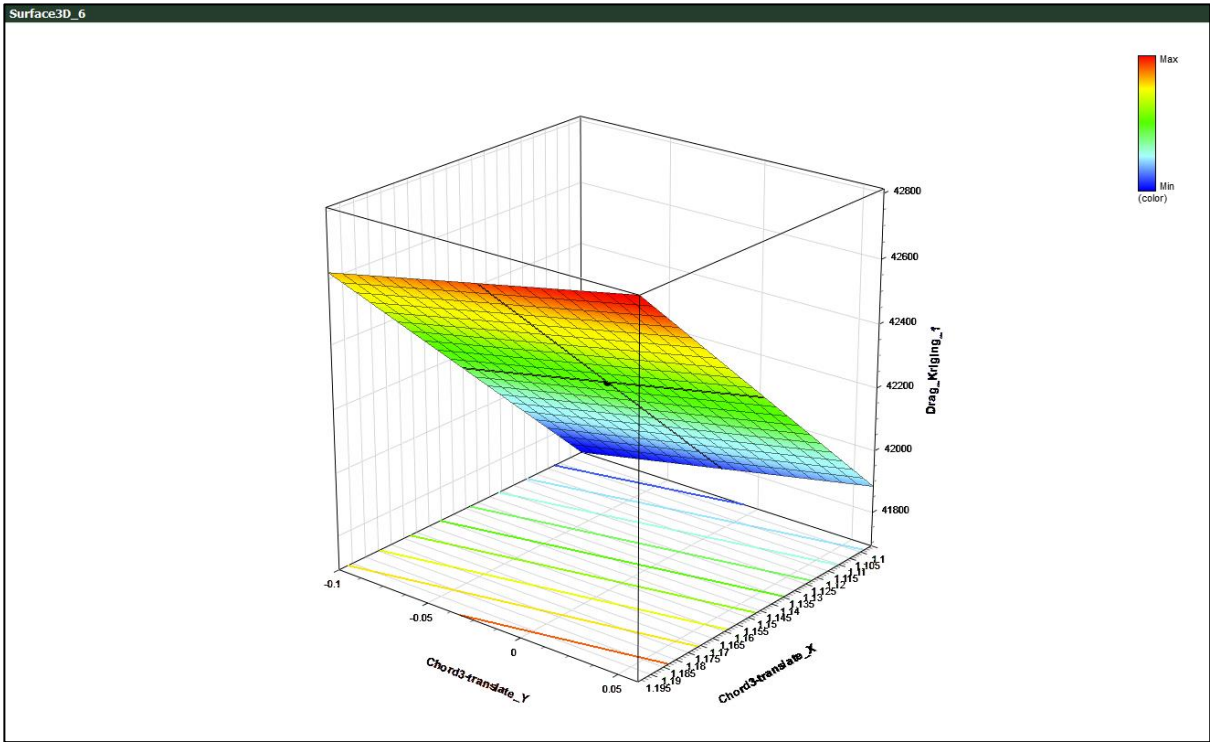


Fig. B-IV-6: Chord 3 vertical height (Chord3-translate\_Y), Chord 3 sweep (Chord3-translate\_x)

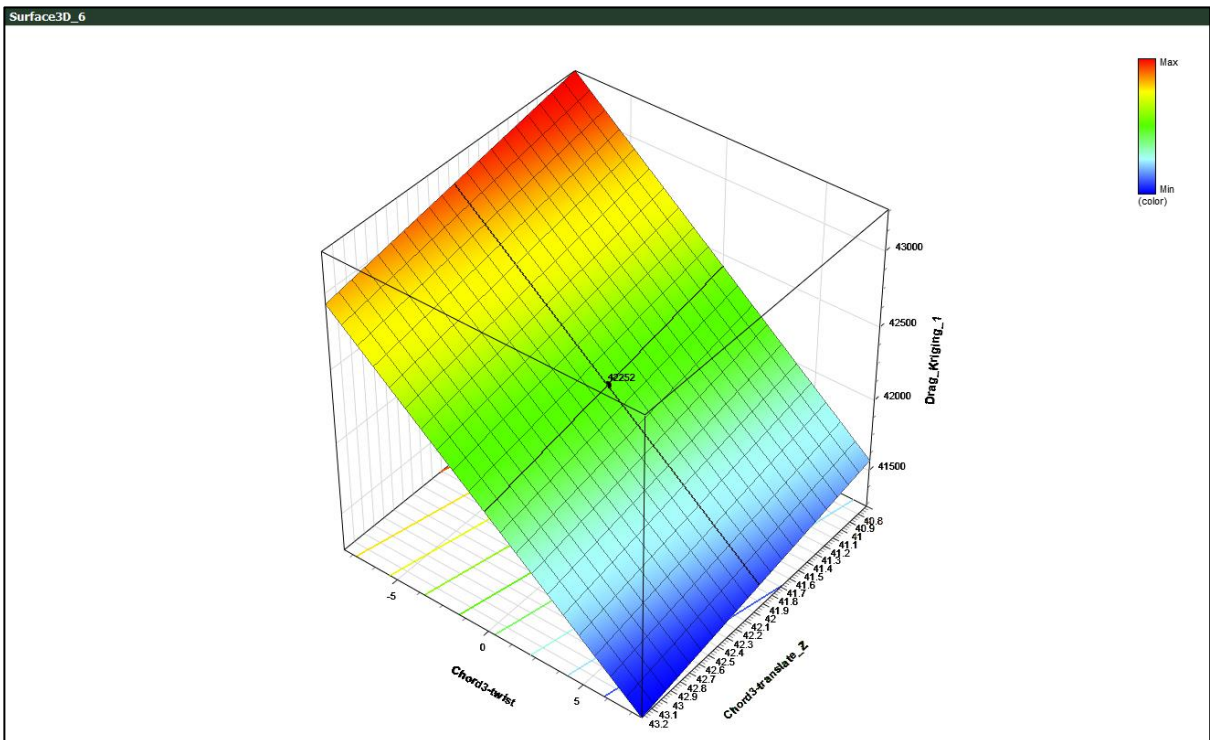


Fig. B-IV-7: Chord 3 twist, Chord 3 length (Chord3-translate\_z)

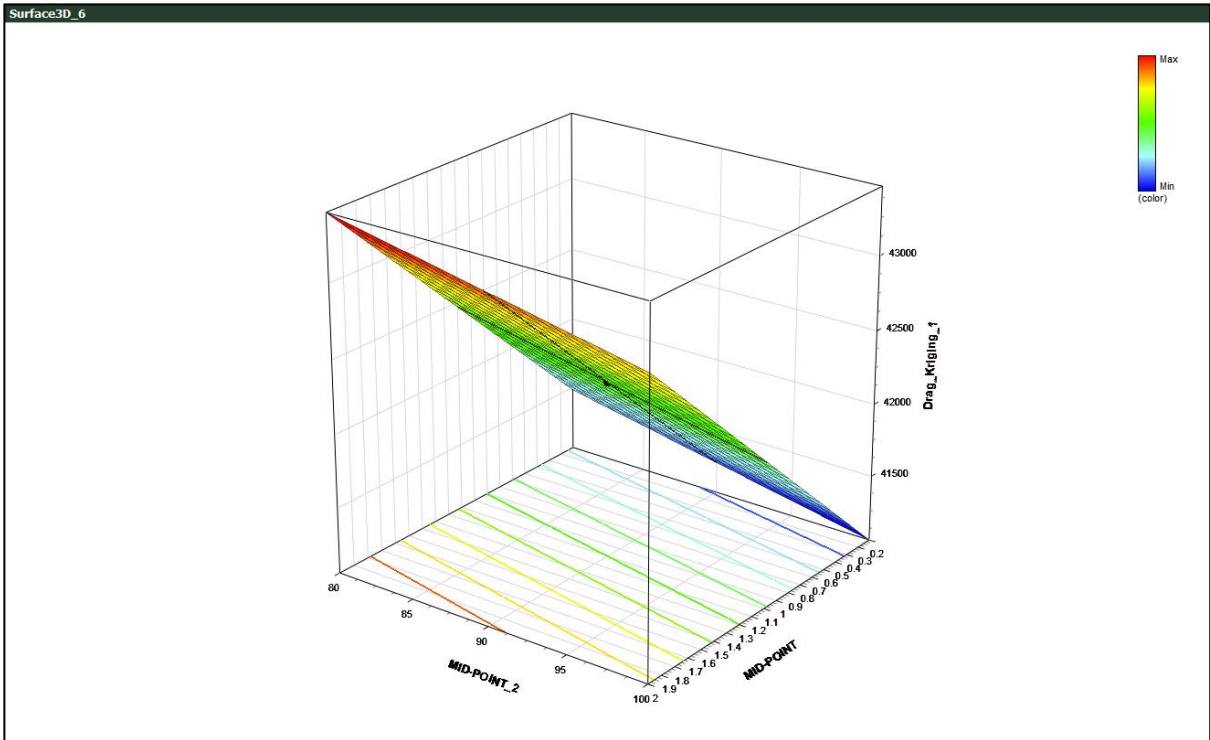


Fig. B-IV-8: Mid-point twist (MID-POINT\_2), Mid-point size (MID-POINT)

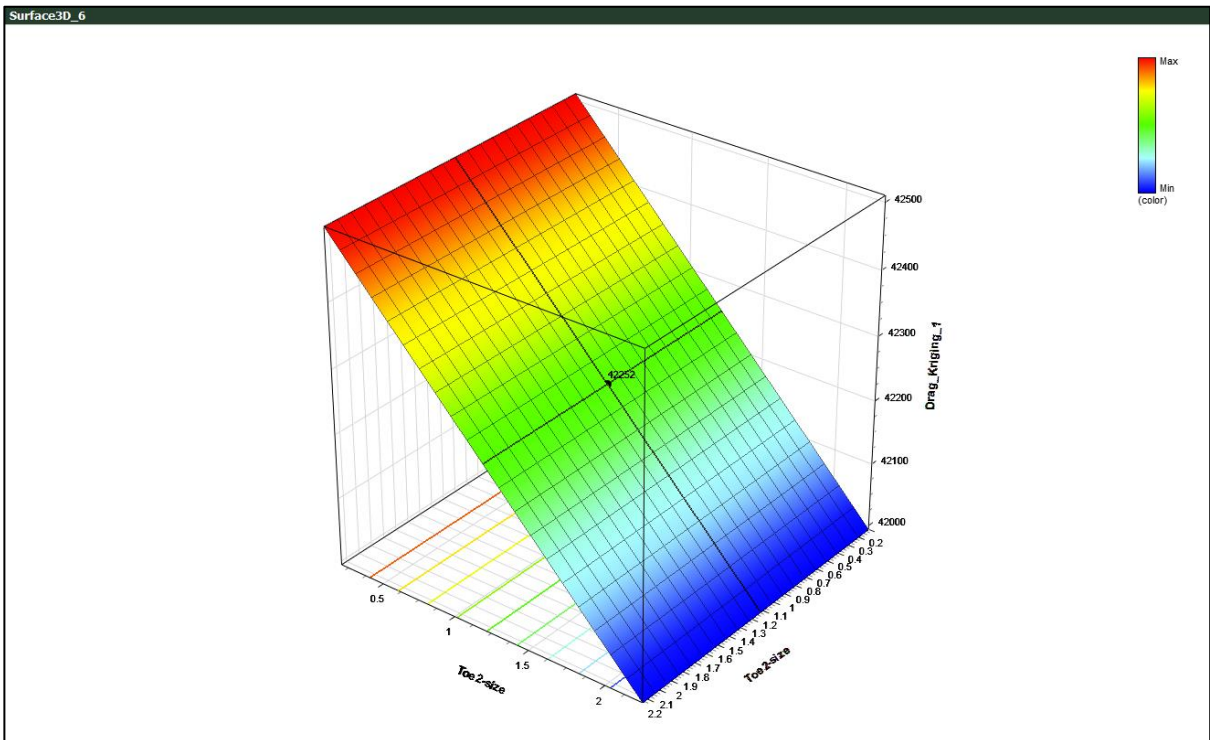


Fig. B-IV-9: Toe 2 size

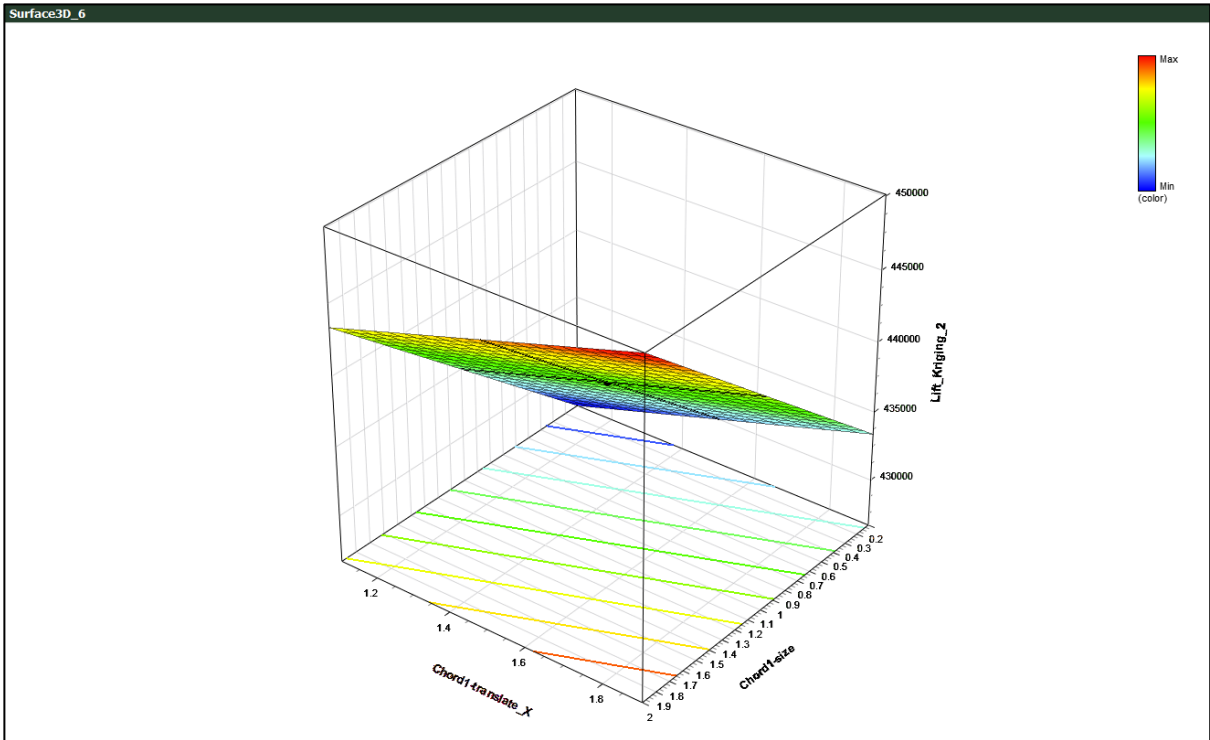


Fig. B-IV-10: Chord 1 sweep (Chord1-translate\_x), Chord 1 size – Lift kriging

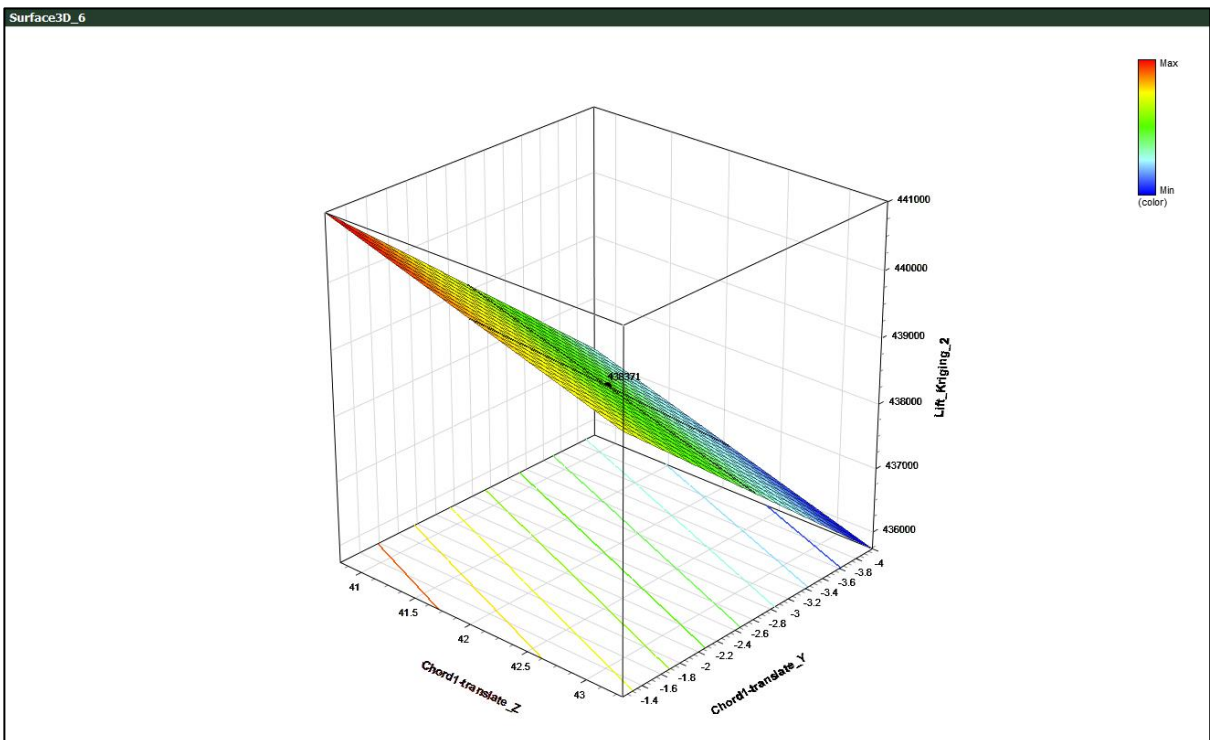


Fig. B-IV-11: Chord 1 length (Chord1-translate\_Z), Chord 1 vertical height (Chord1-translate\_Y) – Lift kriging

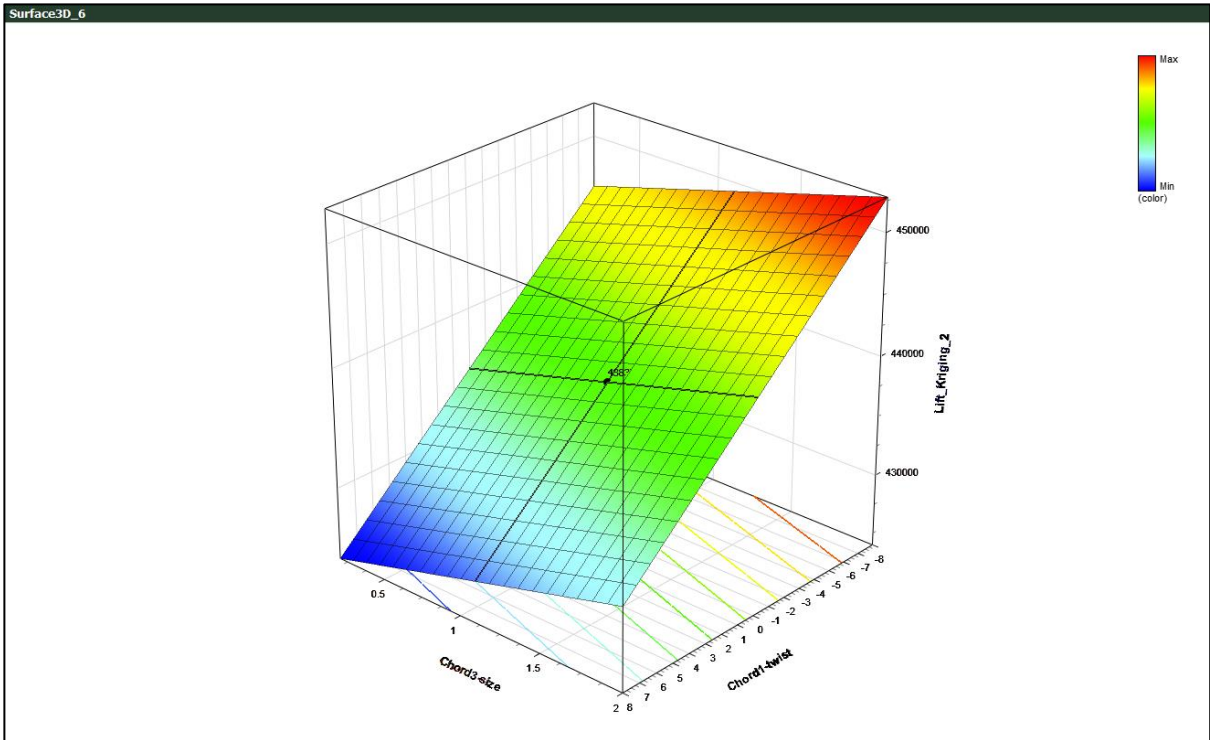


Fig. B-IV-12: Chord 3 size, Chord 1 twist – Lift kriging

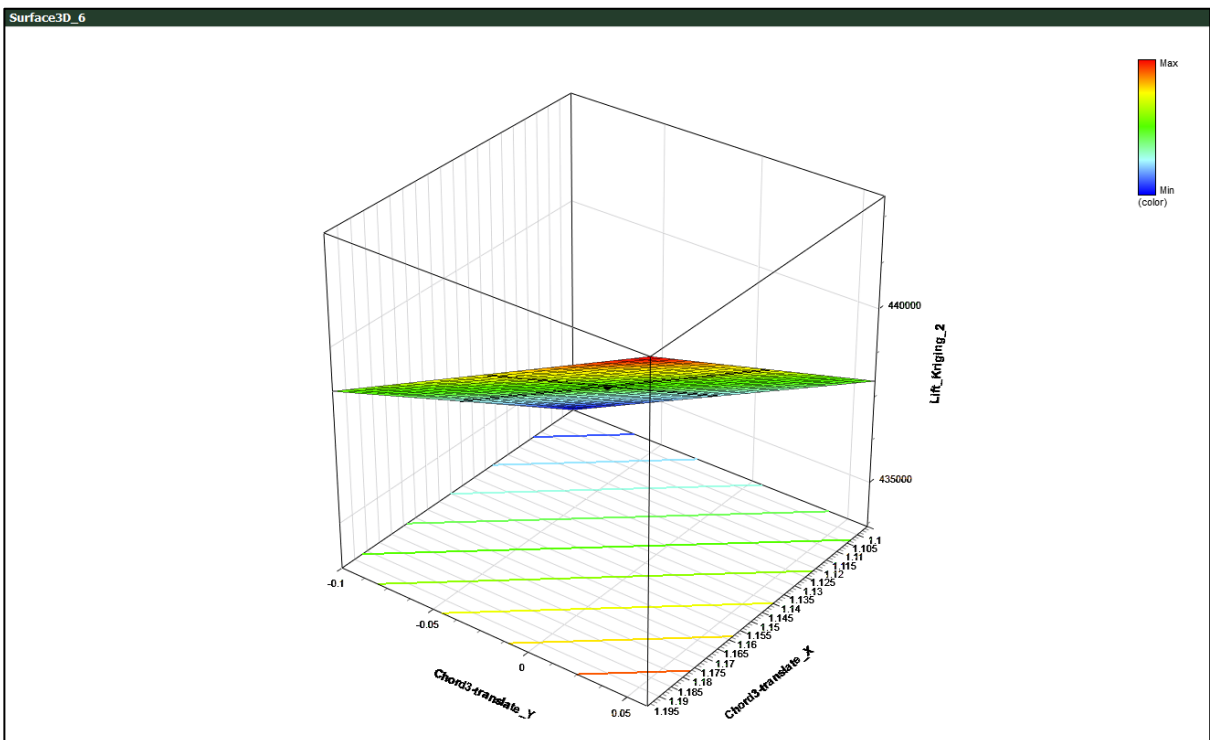


Fig. B-IV-13: Chord 3 vertical height (Chord3-translate\_Y), Chord 3 sweep (Chord3-translate\_x) – Lift kriging

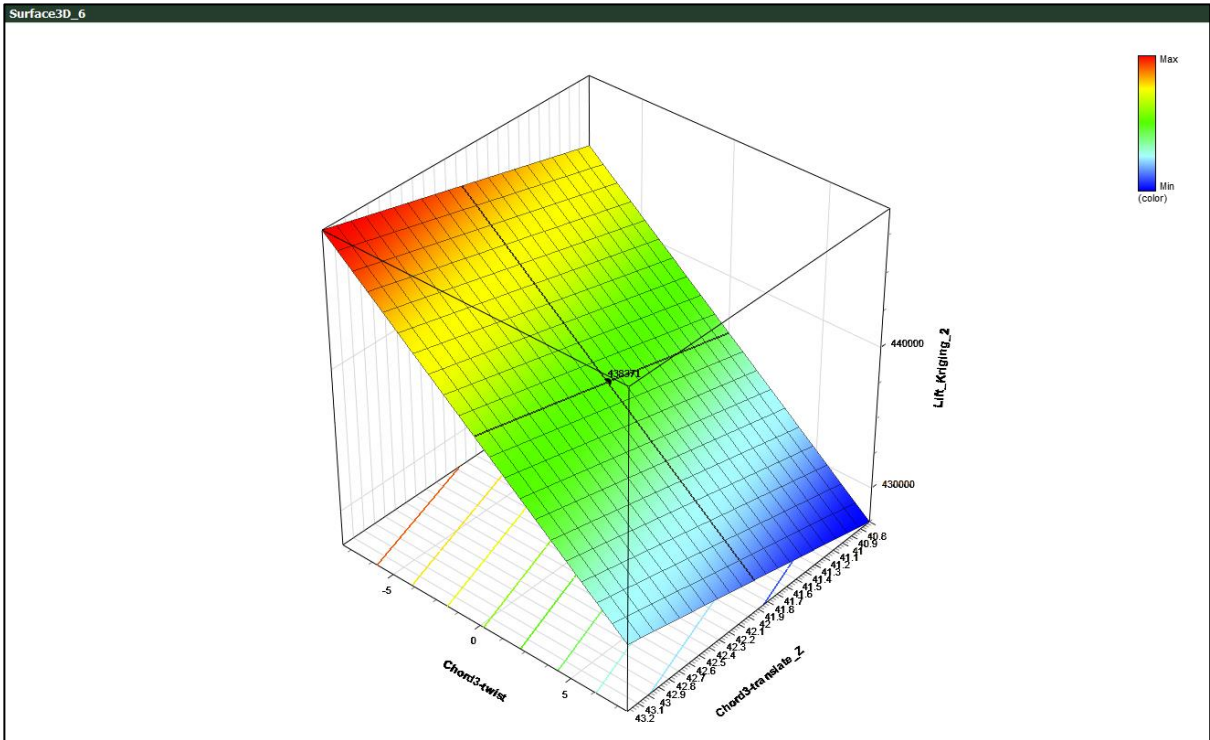


Fig. B-IV-14: Chord 3 twist, Chord 3 length (Chord3-translate\_z) – Lift kriging

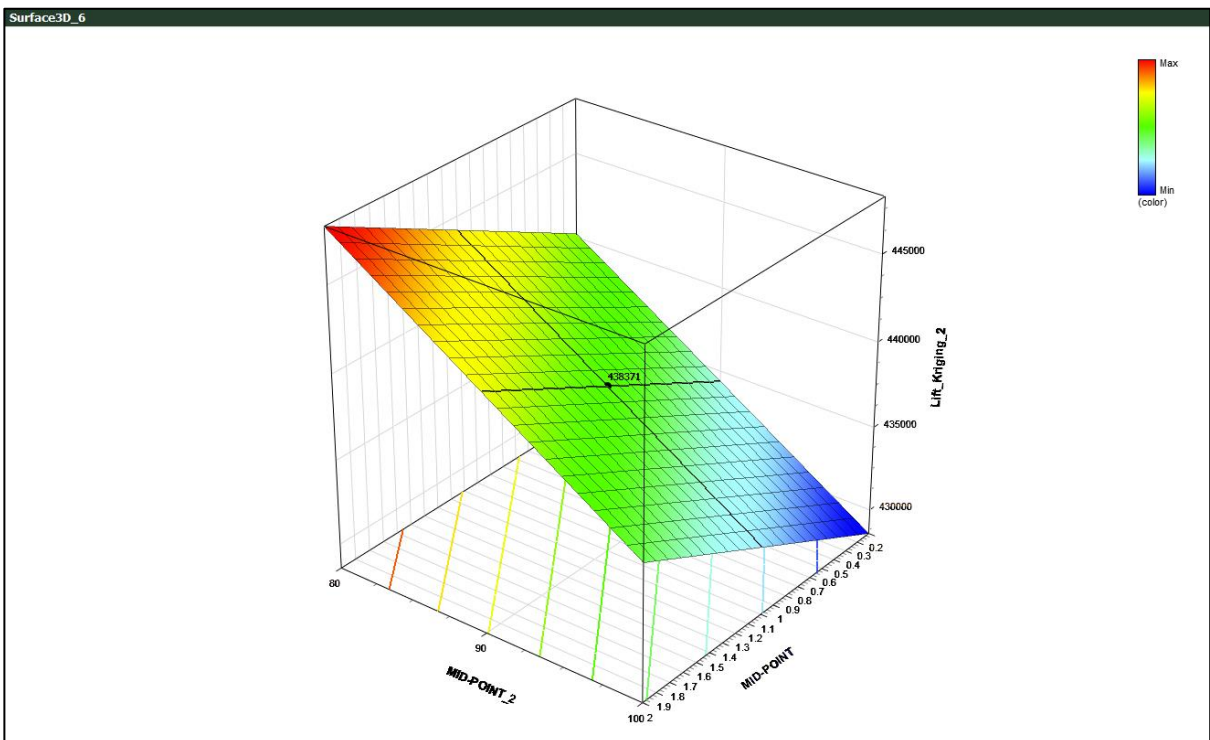
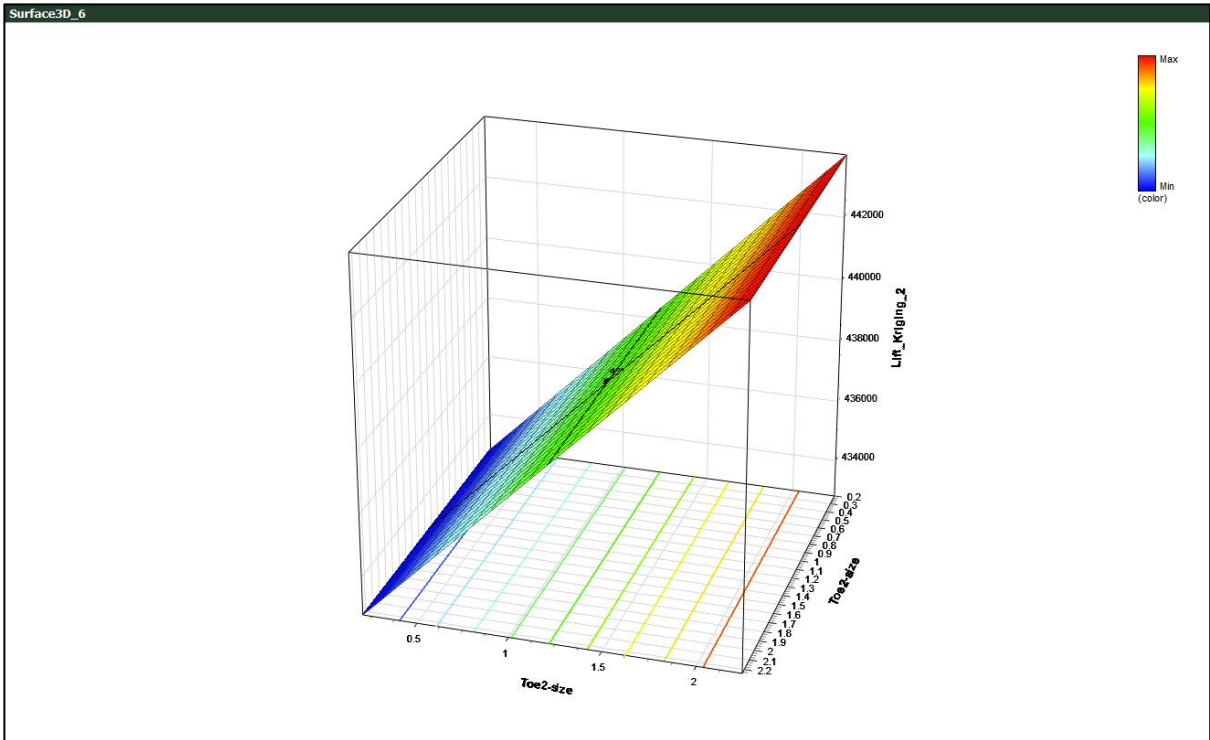


Fig. B-IV-15: Mid-point twist (MID-POINT\_2), Mid-point size (MID-POINT) – Lift kriging



**Fig. B-IV-16: Toe 2 size (scale factor) – Lift kriging**